minerals

Special Issue Reprint

Igneous Rocks and Related Mineral Deposits

Edited by
Claire Wade and Alexander R Cruden

mdpi.com/journal/minerals

MDPI

Igneous Rocks and Related Mineral Deposits

Igneous Rocks and Related Mineral Deposits

Guest Editors

Claire Wade
Alexander R Cruden

MDPI

Basel • Beijing • Wuhan • Barcelona • Belgrade • Novi Sad • Cluj • Manchester

Guest Editors

Claire Wade
Department for Energy and Mining
Geological Survey of South Australia
Adelaide
Australia

Alexander R Cruden
School of Earth Atmosphere and Environment
Monash University
Melbourne
Australia

Editorial Office
MDPI AG
Grosspeteranlage 5
4052 Basel, Switzerland

This is a reprint of the Special Issue, published open access by the journal *Minerals* (ISSN 2075-163X), freely accessible at: https://www.mdpi.com/journal/minerals/special_issues/851KI1H20T.

For citation purposes, cite each article independently as indicated on the article page online and as indicated below:

Lastname, A.A.; Lastname, B.B. Article Title. *Journal Name* **Year**, *Volume Number*, Page Range.

ISBN 978-3-7258-8921-1 (Hbk)
ISBN 978-3-7258-8922-8 (PDF)
https://doi.org/10.3390/books978-3-7258-8922-8

© 2026 by the authors. Articles in this reprint are Open Access and distributed under the Creative Commons Attribution (CC BY) license. The reprint as a whole is distributed by MDPI under the terms and conditions of the Creative Commons Attribution-NonCommercial-NoDerivs (CC BY-NC-ND) license (https://creativecommons.org/licenses/by-nc-nd/4.0/).

Contents

Hongze Gao, Jiajie Chen, Lei Mo, Genqiang Wei, Kaixuan Li, Yijuan Wu and Lili Wang
U-Pb Dating and Geochemical Characteristics of Zircon and Apatite from Ore-Bearing Porphyry of Huxu Au-Dominated Polymetallic Deposit in Dongxiang Volcanic Basin, South China
Reprinted from: *Minerals* **2026**, *16*, 103, https://doi.org/10.3390/min16010103 . . . . . **1**

Wei Zhang, Mao-Xue Chen, Mei-Li Yang, Wen-Hui Yang and Xing-Chun Zhang
Zircon U-Pb Geochronology and Hf Isotopes of the Granitoids from Cahanwusu Cu Deposit in Awulale Mountain, Western Tianshan: Implication for Regional Mineralization
Reprinted from: *Minerals* **2025**, *15*, 380, https://doi.org/10.3390/min15040380 . . . . . **20**

Yutong Song, Gongzheng Chen, Guang Wu, Tiegang Li, Tong Zhang, Jinfang Wang, et al.
Petrogenesis of the Chamuhan Intrusion in the Southern Great Xing'an Range: Constraints from Zircon U-Pb Dating and Petrogeochemistry
Reprinted from: *Minerals* **2025**, *15*, 1085, https://doi.org/10.3390/min15101085 . . . . . **36**

Valeria Krutikova, Nikolai Berdnikov and Pavel Kepezhinskas
Microminerals as Complimentary Guides into Metallogeny and the Ore-Forming Potential of Igneous Rocks: Evidence from the Stanovoy Superterrane (Russian Far East)
Reprinted from: *Minerals* **2025**, *15*, 504, https://doi.org/10.3390/min15050504 . . . . . **61**

Mariam Ferraq, Saïd Belkacim, Li-Zhen Cheng, Joshua H. F. L. Davies, Morgann G. Perrot, Abdelhay Ben-Tami and Mohammed Bouabdellah
New Geochemical and Geochronological Constraints on the Genesis of the Imourkhssen Cu±Mo±Au±Ag Porphyry Deposit (Ouzellagh-Siroua Salient, Anti-Atlas, Morocco): Geodynamic and Metallogenic Implications
Reprinted from: *Minerals* **2024**, *14*, 832, https://doi.org/10.3390/min14080832 . . . . . **81**

Mohammad Goudarzi, Hassan Zamanian, Urs Klötzli, Alireza Almasi, Sara Houshmand-Manavi and Jiranan Homnan
Mineral Geochemistry of Sulfides and Oxides and Its Implications for Ore-Forming Mechanisms in the Northeast Saveh Epithermal System, Central Urumieh–Dokhtar Magmatic Arc, Iran
Reprinted from: *Minerals* **2026**, *16*, 212, https://doi.org/10.3390/min16020212 . . . . . **120**

Danial M. Fathy, Faris A. Abanumay, Shehata Ali, Esam S. Farahat, Andrey Bekker and Mokhles K. Azer
An Occurrence of Pyroxmangite in the NYF Granitic Pegmatite of the Gabal El-Bakriya Intrusion, Arabian–Nubian Shield
Reprinted from: *Minerals* **2025**, *15*, 1027, https://doi.org/10.3390/min15101027 . . . . . **149**

Ştefan Marincea, Delia-Georgeta Dumitraş, Cristina Sava Ghineț, George Dincă, Aurora-Mărușa Iancu, Frédéric Hatert, et al.
Hydrothermal Scheelite Associated with Upper Cretaceous Intrusions in Romania: A Mineralogical Insight to the W Metallogeny
Reprinted from: *Minerals* **2025**, *15*, 854, https://doi.org/10.3390/min15080854 . . . . . **178**

Emmanuel Daanoba Sunkari and Abdurrahman Lermi
Geological, Mineralogical, Geochemical, and Petrogenetic Characteristics of Plutonic Rocks in Çiftehan (Ulukışla-Niğde) Area, South-Central Türkiye: Implication for Genetic Link with Fe-Zn Skarn Mineralization
Reprinted from: *Minerals* **2025**, *15*, 578, https://doi.org/10.3390/min15060578 . . . . . **205**

Rongfang Zhang, Chong Cao, Yanbo Zhang, Shuzhi Wang, Yang Zhang, Zhaokang Yuan, et al.
Advances in Distribution Pattern and Enrichment Mechanism of Associated Cobalt Resources in Skarn-Type Deposits, China
Reprinted from: *Minerals* **2025**, *15*, 913, https://doi.org/10.3390/min15090913 . . . . . **242**

minerals

MDPI

Article

U-Pb Dating and Geochemical Characteristics of Zircon and Apatite from Ore-Bearing Porphyry of Huxu Au-Dominated Polymetallic Deposit in Dongxiang Volcanic Basin, South China

Hongze Gao [1], Jiajie Chen [1,*], Lei Mo [1], Genqiang Wei [1], Kaixuan Li [1], Yijuan Wu [1] and Lili Wang [2]

[1] School of Earth and Planetary Sciences, East China University of Technology, Nanchang 330013, China; 18170409040@163.com (H.G.); 2025010085@ecut.edu.cn (L.M.); yqrs_wei@163.com (G.W.); likaixuan191016@ecut.edu.cn (K.L.); 17807002280@163.com (Y.W.)

[2] Geological and Mineral Resources Center Laboratory of Ningxia, Ningxia Fundamental Geological Survey Institute, Yinchuan 750021, China; liliwang2580@163.com

* Correspondence: chenjiajie03@126.com; Tel.: +86-18579123095

Abstract

The Huxu Au-dominated deposit is a representative intermediate sulfidation epithermal deposit in the middle section of the Gan-Hang belt. The formation of such deposits is commonly closely related to deep magmatism. However, the specific relationship between the formation of the Huxu deposit and the magmatic rocks, and the tectonic setting of the related magmatism and mineralization in this deposit still remains unclear. In this study, we present the results of U-Pb dating, major and trace element analysis, and Nd isotope analysis of the magmatic zircon and apatite from the ore-bearing quartz diorite porphyry in the Huxu deposit. The results show that the U-Pb ages of zircon and apatite from the quartz diorite porphyry are 137.9 ± 1.3 Ma and 130 ± 16 Ma, respectively; the total content of rare earth elements (ΣREEs) in the zircons ranges from 446.66 to 2752.92 ppm, exhibiting enrichment in heavy REE and depletion in light REE, with a slightly negative Eu anomaly and a slightly positive Ce anomaly; the ΣREEs in the apatite is relatively high, ranging from 3252.02 to 13,155.92 ppm, averaged 5604.16 ppm, and exhibits a right-leaning mode with light REE enrichment and heavy REE depletion, with a moderate degree of negative Eu anomaly; the distribution of $^{143}Nd/^{144}Nd$ ratios of the apatite is rather concentrated (0.512145–0.512271), and the εNd(t) value calculated based on the U-Pb age of apatite ranges from −8.31 to 5.79. By combining the geological characteristics and the geochemical data of the deposit and the ore-bearing magmatic rocks, we propose that the ore-bearing quartz diorite porphyry of the Huxu Au-dominated polymetallic deposit belongs to I-type granite; the parental magma is the mixture of juvenile and ancient crustal melts; the tectonic setting of the intrusion and mineralization is the continental margin arc related to the subduction of the ancient Pacific Ocean Plate in the Early Cretaceous Epoch; and the ore-forming fluids and metals are provided by deep magma.

Keywords: Huxu deposit; quartz diorite porphyry; zircon; apatite; Nd isotope

1. Introduction

The Huxu Au-dominated polymetallic deposit is located in the middle section of the Gan-Hang tectonic belt, and is the most representative deposit within the Mesozoic volcanic basin in Dongxiang County. A series of studies on this deposit have been conducted previously, involving basic geology, fluid inclusion, trace element of sulfide and

isotope geochemistry [1–5], and it has been believed that the ore-forming materials mainly originate from magma, and the deposit is the intermediate sulfidation type epithermal deposit [4,5], but the deep source of the fluids and materials, the age of mineralization, and the tectonic setting of mineralization are not fully understood presently. The previous study has revealed that the epithermal deposit is closely related in genesis to its host volcano-subvolcanic rock [6–10]. Therefore, the study of the igneous rocks may reveal the deep source of ore-forming materials, the age of mineralization and the mineralization tectonic setting.

As the main sub-volcanic rock in the basin and the host rock of the Huxu Au-dominated polymetallic deposit, the quartz diorite porphyry in the study area has received only scarce research overall. Only a small amount of research has been conducted on the whole-rock major elements and REEs previously, from which it is inferred that the quartz diorite porphyry is a product of the concurrent and homologous calc-alkaline volcanic activity which also produced the volcanic rock strata in the study area [2,11]. However, the formation era and the source area characteristics of the quartz diorite porphyry have not been explored, which may be due to the relatively intense alteration of the quartz diorite porphyry and thus obstruct the understanding of the genesis of the gold deposit. Accessory minerals, trace minerals in the igneous rocks, can effectively record information about the source area, diagenetic age, and even the diagenetic process of the igneous rocks [12–17]. Although the whole-rock composition of altered igneous rocks associated with ore formation has changed, some of their accessory minerals may retain a record of the original rock due to their strong chemical stability. In recent years, the quantitative analytical technology for the accessory minerals has experienced rapid development and has been widely applied in related geochemical studies. For example, laser ablation single-zircon and apatite U-Pb dating, along with trace element and isotopic analysis of associated accessory minerals (e.g., zircon, apatite), has been widely applied in research on diagenesis and mineralization, yielding significant results [18–29].

In this paper, we focus on zircon and apatite from the ore-bearing quartz diorite porphyry of the Huxu Au-dominated polymetallic deposit. To this end, we conducted U-Pb dating and trace element analysis on zircon, alongside major-trace element analysis and Nd isotope testing on apatite. These analyses aim to constrain the diagenetic and mineralization ages, tectonic setting, and the deep sources of the ore-forming fluids and materials.

2. Geological Setting

2.1. Regional Geology

The Huxu Au-dominated polymetallic deposit lies in the orogenic belt caused by the collision of the Yangtze Block and the Cathaysia Block in the Proterozoic era (the middle section of the Gan-Hang tectonic belt; Figure 1). Studies have shown that the Pacific Plate has undergone multiple transitions in subduction direction during the Jurassic-Cretaceous (Yanshanian) and retreated during the Late Jurassic-Early Cretaceous. The intense tectonic and complex volcanic activities extended throughout the South China area in the Jurassic-Cretaceous period, forming a series of volcanic basins and related hydrothermal metallic deposits (occurrences) [6,11,30–32].

2.2. Deposit Geology

The Dongxiang basin is one of the numerous volcanic basins in the Gan-Hang tectonic belt (Figure 1). The basement of the basin comprises the Mesoproterozoic Shuangqiaoshan Group. This unit is primarily composed of quartzite, tuffite, and blastopsammite, interbedded with phyllite. The overlying exposed strata are Jurassic-Cretaceous in age and dominated by intermediate-acidic volcanic rocks (e.g., dacite and andesite) from multiple

https://doi.org/10.3390/min16010103

eruption cycles, along with pyroclastic rocks such as tuffite and agglomerate. Additionally, subordinate terrigenous clastic sedimentary rocks occur sporadically in the northwestern part of the basin (Figure 2). The magmatic activity in the area is relatively intensive. The intrusive rocks are mainly Mesozoic intermediate-acidic shallow intrusions such as dacite-porphyry, diorite porphyry, and andesite-porphyry, with a small amount of Mesozoic diabase and Caledonian granite. The main structures of this volcanic basin mainly include the northeast-trending faults, folds and volcanic-related structures [34,35]. The mineral resources in the basin are mainly gold, lead, zinc, silver and copper, with the major deposits including the Fenglin copper deposit, the Huxu Au-dominated polymetallic deposit, the Yinfengjian gold deposit, the Huxingshan gold deposit and many other mesothermal and epithermal metalliferous deposits (occurrences). However, the understanding of the genesis of these deposits in the basin is poor, and only a small amount of research has been carried out on the Huxu Au-dominated polymetallic deposit and the Fenglin copper deposit [1,2,36,37].

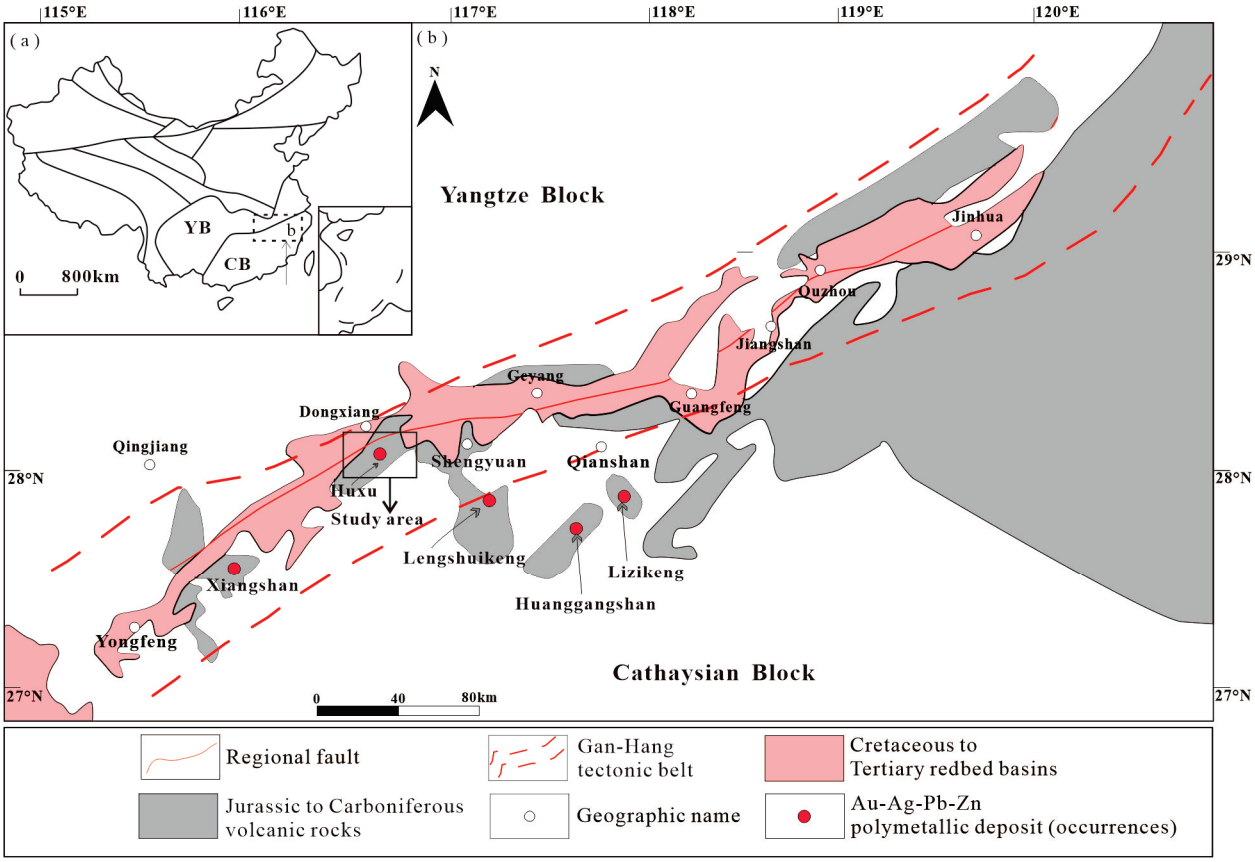


Figure 1. (**a**) Main terrains in China showing the location of the study area (after Yuan et al., 2009 [33]); (**b**) Geological sketch of the middle section of the Gan-Hang tectonic belt (after Yuan et al., 2009 [33]).

The strata of the mining area are relatively simple, mainly consisting of the Late Cretaceous Hekou Formation and the Early Cretaceous Daguding Formation (Figure 2b). The Late Cretaceous Hekou Formation is mainly composed of red sandstone, calcareous sandstone and siltstone, and is mainly distributed in the northwest of the mining area, whereas the Early Cretaceous Daguding Formation is mainly composed of rhyolitic tuff, dacitic ignimbrite and a small amount of andesite (Figure 3). The faults in the area are highly developed, mainly including the NE-trending fault (F13) in the northern part of the mining area and the NW-trending faults in the middle (Figure 2b). The rock involved in the NE-trending F13 fault shows a strong crushing phenomenon, indicating multi-stage

activation of the faults. The F13 fault is the major rock-controlling fault in the area and controls the distribution of the quartz diorite porphyry and the ore body. The NW-trending fault is the major ore-bearing fault in the area. The ore body is relatively steep and can extend up to several hundred meters deep. It mainly occurs within the faults occurring in the quartz diorite porphyry and is locally in contact between porphyry and pyroclastic rocks (Figure 2b,c) [2,38,39].

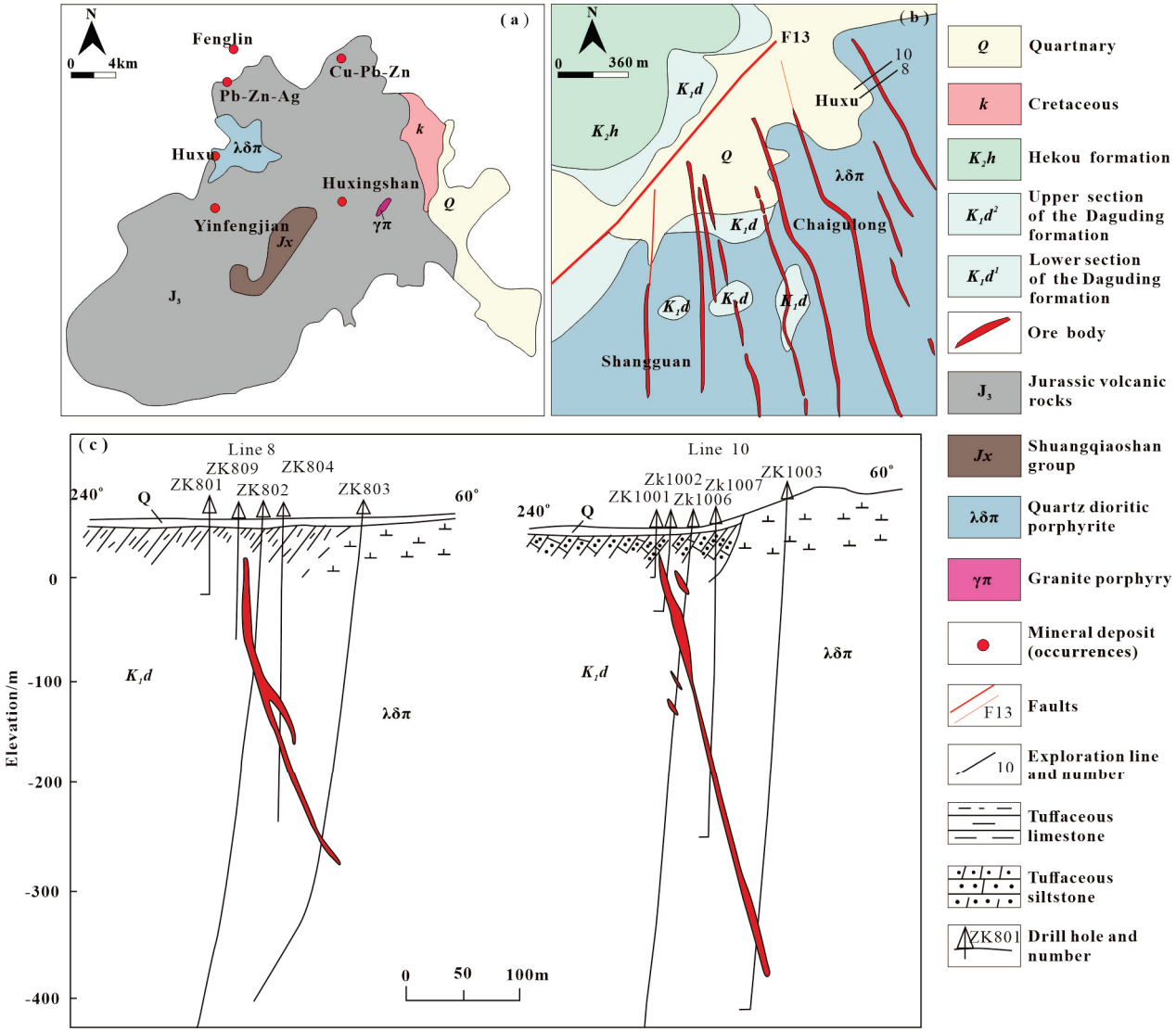


Figure 2. Geological diagram and the ore body section of the Huxu mining area. (**a**) Geological sketch of the Dongxiang basin (after Yan, et al., 2012 [34]); (**b**) geological map of the Huxu Au-dominated polymetallic deposit (after Zhou, et al. 2019 [38]); (**c**) sectional view of ore body 10 (after Zhou, et al., 2019 [38]).

The wall rocks in the study area have suffered relatively strong alteration under the influence of mineralization, the main alteration types are silicification, hematitization, sericitization, chloritization, carbonatization and pyritization (Figure 4).

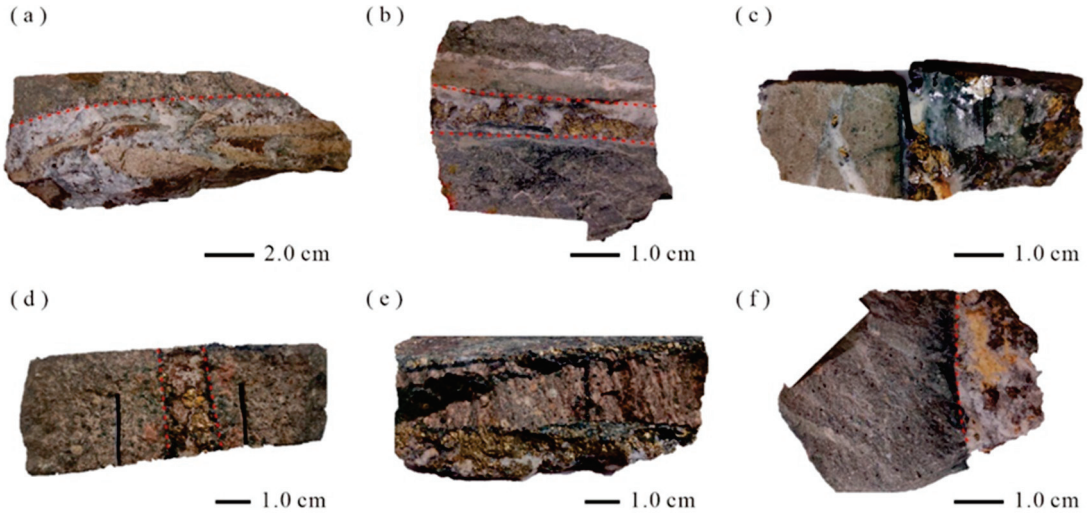


Figure 3. Characteristics of typical magmatic rocks in the mining area. (**a**,**b**) Quartz pyrite veins interlacing the altered quartz diorite porphyry; (**c**) Quartz polymetallic veins interlacing the altered quartz diorite porphyry; (**d**,**e**) Altered quartz diorite porphyry; (**f**) Altered rhyolite pyroclastic rock.

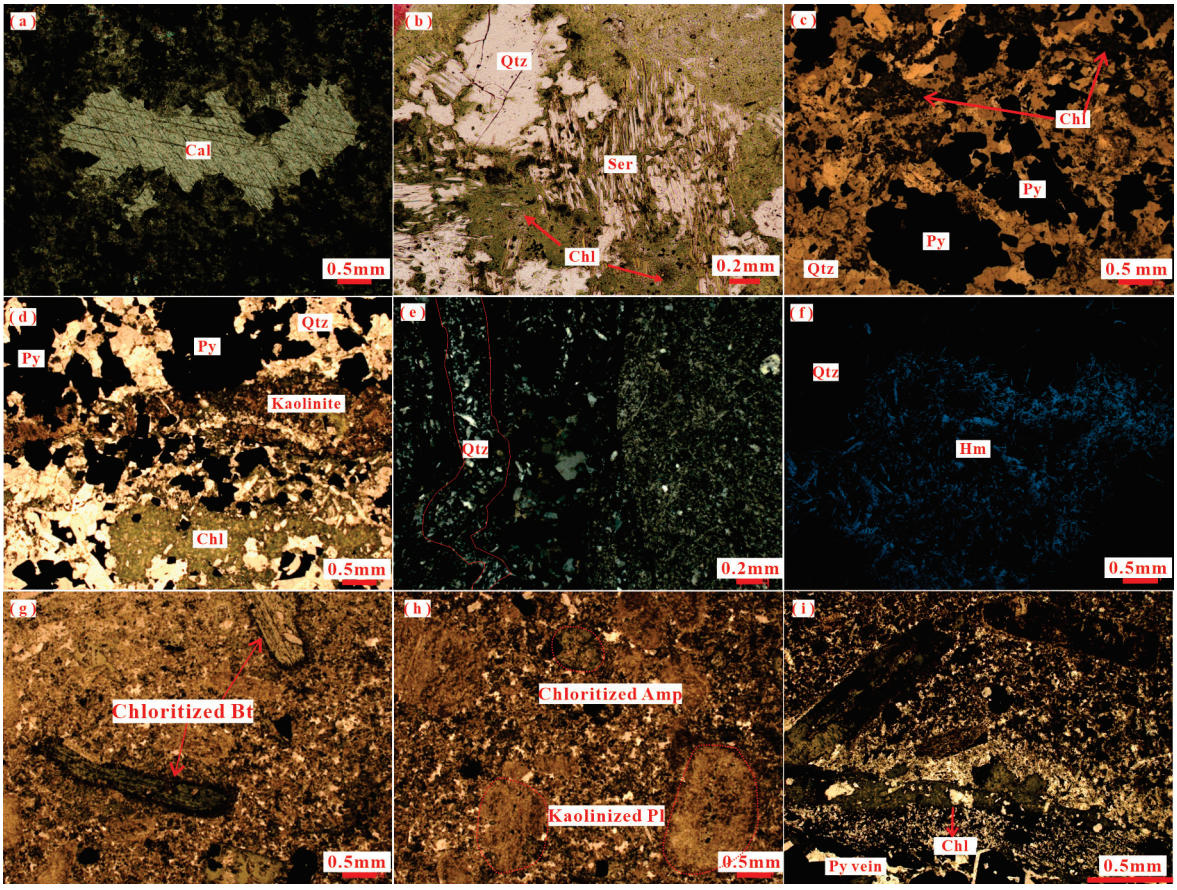


Figure 4. Alteration characteristics of the Huxu gold polymetallic deposit. (**a**) Carbonatization; (**b**) sericitization and chloritization; (**c**) Pyritization and chloritization; (**d**) Kaolinization and chloritization; (**e**) Silicification; (**f**) Hematitization; (**g**) Chloritized biotite; (**h**) Alteration of amphibole and feldspar; (**i**) Chloritization. Qtz—Quartz; Hm—Hematite; Py—Pyrite; Cal—Calcite; Ser—Sericite; Chl—Chlorite; Amp—Amphibole.

3. Analytical Methods

A total of 27 samples were collected for this study, 24 of which were made into thin sections for petrographic and mineralogic analysis, and their approximate sampling locations are marked in Figure 2b based on field records, as further explained in this section. In addition, zircon and apatite were separated from one representative quartz diorite porphyry sample for in-situ U-Th-Pb isotopic and elemental analysis. Whole-rock geochemical analysis was not performed on this sample due to its severe alteration. All samples were obtained from underground workings in the Huxu mining area. The zircon and apatite separation from the quartz diorite porphyry and the mineral grain mounting in the epoxy resin were carried out at Guangzhou Tuoyan Testing Technology Co., Ltd. (Guangzhou, China). The quartz diorite porphyry samples were first crushed to an appropriate particle size; then shaken, washed, and separated by electromagnetic force and gravity; and, finally, the zircon and apatite grains were obtained. These mineral grains were further selected under a binocular, and the selected zircon and apatite grains were mounted in ring resin, which were then ground and polished for microscopic observation and geochemical analysis.

The U-Pb dating and trace element analysis of zircons, and the U-Pb isotope and trace element analysis of apatite, were conducted at the State Key Laboratory of Nuclear Resources and Environment, East China University of Technology (Nanchang, China). The instrument used during the analysis is a Laser Ablation Inductively Coupled Plasma Mass Spectrometer (LA-ICP-MS). The laser ablation system employed was a GeoLasHD 193 nm ArF excimer laser (wavelength 193 nm) manufactured by Coherent (Gilching, Germany). The mass spectrometer used was an Agilent 7900 quadrupole inductively coupled plasma mass spectrometer (ICP-MS) manufactured by Agilent Technologies (Santa Clara, CA, USA). The laser beam with a diameter of 50 μm was used in the U-Pb dating and trace element testing of zircon. The standard zircon 91500 was used as the external standard for isotope ratio correction, and the synthetic silicate glass NIST SRM 610 was used as the external standard. Si was used as the internal standard for the quantitative calculation of zircon trace element content. The offline processing of the analysis data was conducted by using the software ICPMSDataCal 11.0 (including the selection of samples and blank signals, the correction of instrument sensitivity drift, and the calculation of elemental mass fraction, U-Th-Pb isotope ratio, and age). The U-Pb concordia diagram was created and the calculation of the weighted average age of the samples was performed by using the lsoplot/Ex ver 3 software [40].

The laser beam with a diameter of 30 μm, laser energy of 4.6 mJ/cm^2, and frequency of 4 Hz was used for ablation in the U-Th-Pb isotope and trace element analysis of apatite, with helium gas as the carrier gas. NIST SRM 610 and NIST SRM 612 were used as external standards. The Ca content of each ablation spot, as determined by electron probe microanalysis (EPMA), served as the internal standard for quantitative calibration of trace element concentrations. The original data obtained were processed by using Iolite 4 software, and the uncertainty of most trace element analyses was less than 5%.

The JEOLJXA8100 electron probe (EPMA) was used for testing the major elements in apatite, and a 20nA beam current, 15kV acceleration voltage, and 5 μm diameter electron beam were applied for quantitative analysis. In the testing process, F and Cl were analyzed first in order to avoid migration loss. The analysis accuracy was ±2% to ±5%. All original data were corrected by the internal ZAF procedure. For specific procedures, please refer to Xing et al. (2017) [41].

The Nd isotope testing of apatite was carried out at Wuhan Sample Solution Analysis Technology Co., Ltd. using Laser Ablation Multi-Receiving Cup Inductively Coupled Plasma Mass Spectrometry (LA-MC-ICP-MS). The laser ablation system used is Geolas

HD (Coherent, Gilching, Germany), and the MC-ICP-MS used is Neptune Plus mass spectrometer (Thermo Fisher Scientific, Bremen, Germany). Helium was used as a carrier gas in the laser ablation system, and a small amount of nitrogen was added to the ICP to enhance the test signal of the Nd isotope [42]. The analysis was conducted in a single-point mode, with the laser spot size being 90 μm in diameter, the ablation frequency being 8Hz, and the laser energy density being fixed at approximately ~8.0 J/cm^2. A signal smoothing device was used in the analysis process, which could improve signal stability and the testing precision of the isotope ratio [42]. The NeptunePlus mass spectrometer was equipped with 9 Faraday cups and could simultaneously receive the signals of ^{142}Nd, ^{143}Nd, ^{144}Nd, ^{145}Nd, ^{146}Nd, ^{147}Sm, ^{148}Nd, and ^{149}Sm statically. The instrumental mass fractionation of the ^{143}Nd/^{144}Nd isotope was corrected by the exponential rule, with the correction factor being estimated by using ^{146}Nd/^{144}Nd = 0.7219. The correction of the interference of ^{144}Sm on ^{144}Nd was achieved by monitoring the signal of ^{149}Sm and using the ^{144}Sm/^{149}Sm ratio of 0.22332. The instrumental mass fractionation of ^{144}Sm/^{149}Sm was corrected by normalizing the ^{144}Sm/^{149}Sm ratio to the interference-free value and using the ^{147}Sm/^{149}Sm ratio of 1.08680. For a detailed description of the analysis method correction, please refer to Xu et al. (2015) [42]. All analytical data were processed using the professional isotope data processing software Iso-Compass [43]. Two natural apatite standard samples, Durango and MAD, were used to monitor the reliability of the apatite Nd isotope correction method. The chemical composition and Nd isotope composition of Durango and MAD can be found in the paper by Xu et al. (2015) [42].

4. Results

4.1. Morphological Characteristics of Zircon and Apatite

The cathodoluminescence (CL) image of zircon shows that it is mainly columnar (Figure 5), with a long axis of about 50 to 100 μm and a short axis of about 40 μm. The zircons are colorless and transparent, with euhedral-subhedral texture and oscillatory zoning, indicating their magmatic origin.

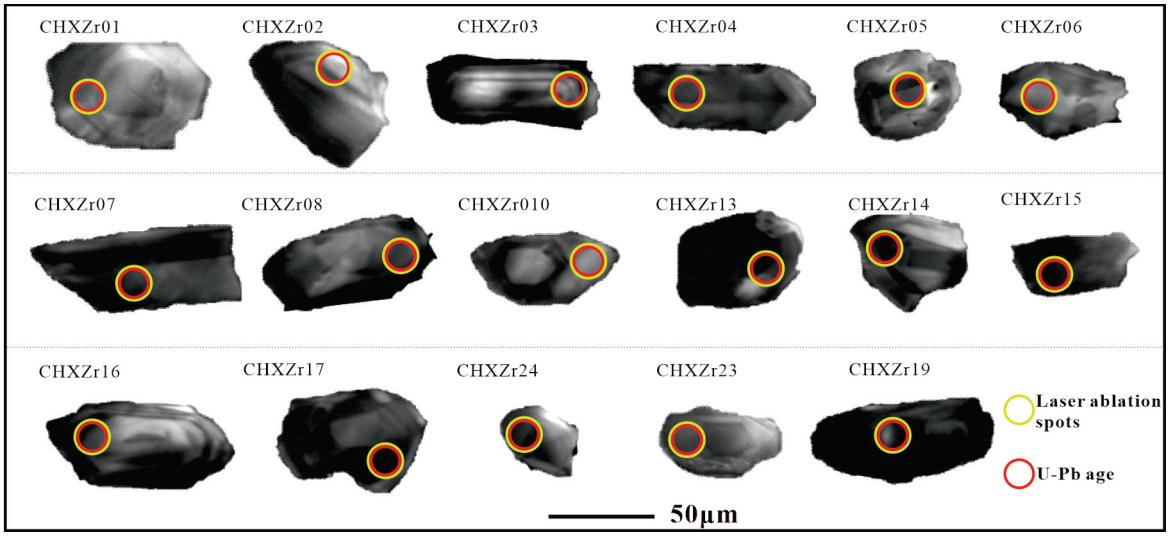


Figure 5. Typical CL image of zircon from quartz diorite porphyry and distribution of test points.

The backscattering (BSE) image of apatite shows that the apatite grains are mainly euhedral-subhedral (Figure 6); the grain diameters generally exceed 100 μm, with relatively uniform particle size. For some apatite grains, the intragranular fractures can be observed. In addition, pyrite inclusions are also observed in some apatite samples. Overall, the BSE image of apatite indicates the characterization of magmatic apatite.

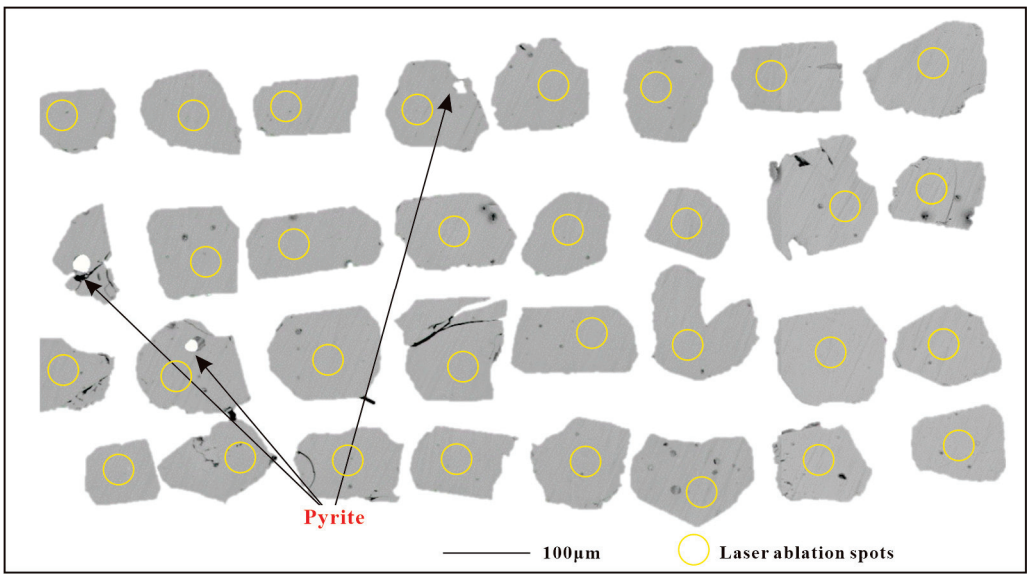


Figure 6. Typical backscattered (BSE) image of apatite from quartz diorite porphyry and distribution of test points.

4.2. U-Pb Dating and Trace Element Analysis of Zircon and Apatite

The isotopic compositions and geochronologic data of zircon are listed in Table S1 and shown in Figure 7. It can be seen that the concordance of the model ages is relatively low due to the loss of lead. Thus, the zircon Tera-Wasserburg diagram has been plotted (Figure 7a). The lower intersection point indicates the age of 137.9 ± 1.3 Ma (MSWD = 0.62), belonging to the Early Cretaceous, and similar with the formation age of the other volcanic rocks in the region (142–134 Ma [35]).

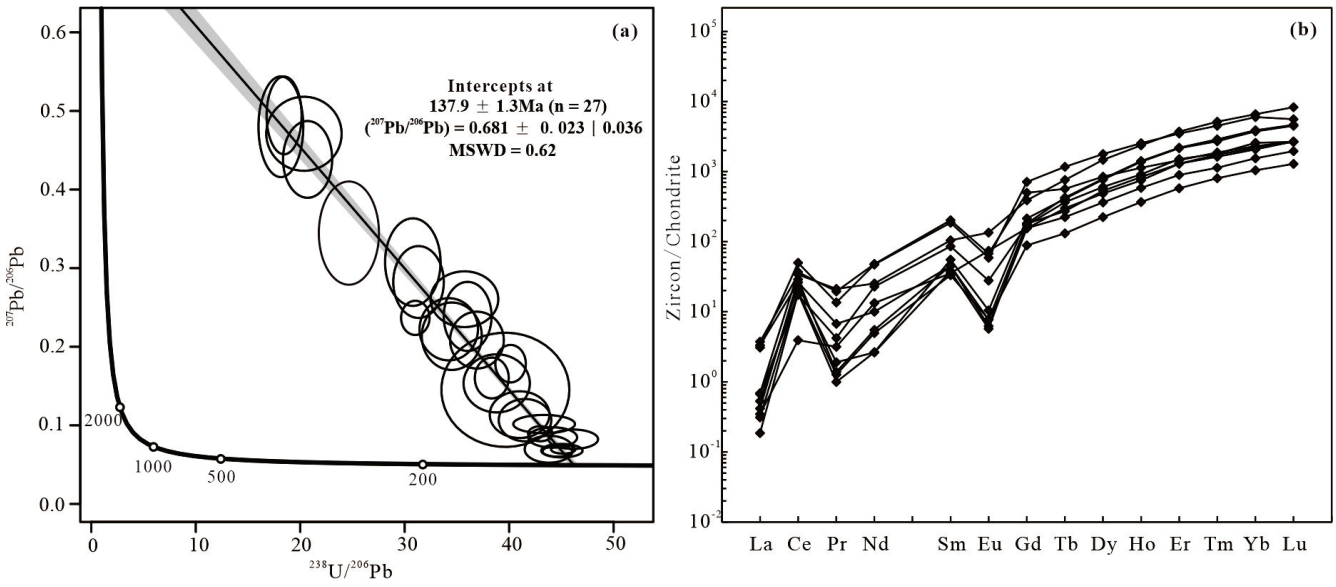


Figure 7. (**a**) Tera-Wasserburg diagram for zircon; (**b**) chondrite-normalized REE distribution pattern for zircon (after Sun and Donough, 1989 [44]).

The rare earth elements (REEs) in zircon can be easily affected by inclusions, leading to errors in the analysis results. Data with La > 1 × 10^{-6} and Ti > 50 × 10^{-6} need to be excluded from the analysis results in order to remove the interference of the tiny inclusions [45]. The data of the trace elements in zircon are shown in Table S2. It can be seen that the Th/U values of zircon from the quartz diorite porphyry range from 0.41 to

1.23, showing the characteristics of magmatic zircon (Th/U > 0.4). The total content of the REEs (ΣREE) in zircon ranges from 446.66 to 2752.92 ppm. In the chondrite-normalized REEs distribution diagrams (Figure 7b), all REE distribution curves show the characteristics of heavy REE enrichment and light REE depletion, with a slightly negative Eu anomaly and a slightly positive Ce anomaly. The Eu/Eu* ratio ranges from 0.069 to 1.00 (avg. 0.27), while the Ce/Ce* ratio ranges from 3.77 to 42.77 (avg. 17.66).

The isotopic compositions and geochronologic data of apatite by using LA-ICP-MS are shown in Table S3 and illustrated in Figure 8. After applying the common lead correction using the Stacey and Kramers (1975; [46]) model to the apatite U-Pb data, the resulting age (~410 Ma) was found to be inconsistent with the generally accepted ages in the region. Therefore, we did not adopt this method. The apatite U-Pb dating results, as displayed on the Tera-Wasserburg concordia diagram, yield a lower intercept age of 130 ± 16 Ma (MSWD = 1.7, n = 61), which is relatively consistent with the zircon age

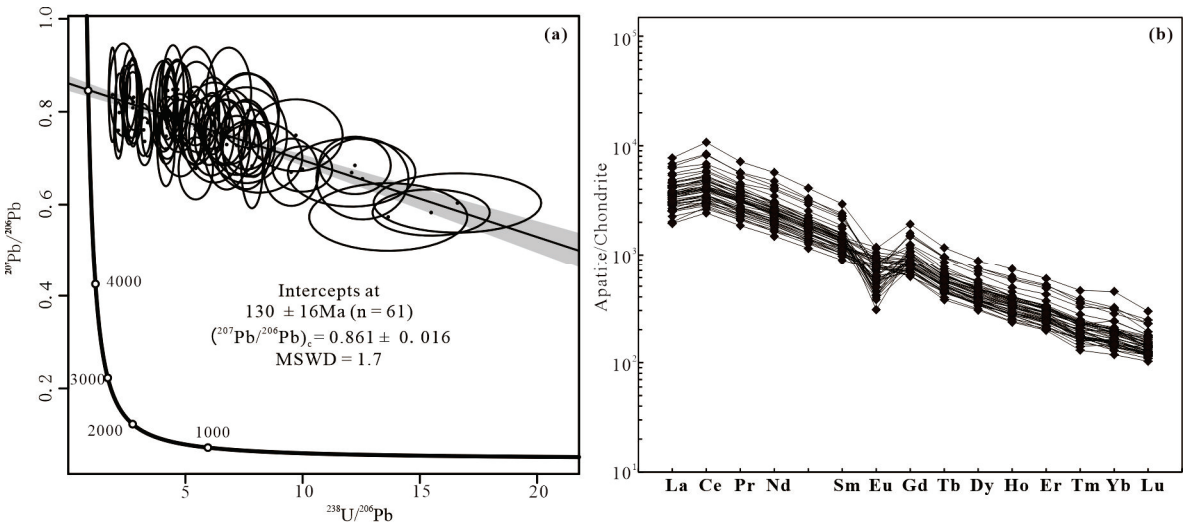


Figure 8. (**a**) Tera-Wasserburg diagram for apatite ("c" represents the distinguishing character); (**b**) chondrite-normalized REE distribution pattern for apatite (after Sun and Donough, 1989 [44]).

The trace element data in apatite are shown in Table S4. The results show that the content of REEs in the apatite samples is relatively high, with the ΣREE content ranging from 3252.02 × 10^{-6} to 13,155.92 × 10^{-6}, averaged 5604.16 × 10^{-6}. The REE distribution pattern (Figure 8b) shows a right-leaning mode with enrichment of light REEs and depletion of heavy REEs, and a moderate degree of negative Eu anomaly.

The major element data of apatite from the quartz diorite porphyry are presented in Table S5. The results show that the apatite is primarily composed of CaO, P_2O_5, and F, while the contents of SO_3, SrO, Al_2O_3, Cl, MnO, Na_2O, and MgO are all extremely low (<1%). The CaO content ranges from 51.87% to 55.48% with an average of 53.04%, the P_2O_5 content ranges from 40.26% to 43.55% with an average of 42.35%, and the F content ranges from 2.23% to 5.27% with an average of 4.24%. All analyzed apatite grains are fluorapatite.

The Nd isotopic compositions of 23 apatite spots are listed in Table S6. The results show that the $^{143}Nd/^{144}Nd$ ratios of apatite from the quartz diorite porphyry are relatively concentrated, ranging from 0.512145 to 0.512271. This indicates that the apatite crystallized in a relatively closed system and can reflect the source characteristics of the host rock. The calculated εNd(t) values, based on the zircon U-Pb age of 137.9 Ma, range from −8.31 to −5.79.

https://doi.org/10.3390/min16010103

5. Discussion

5.1. Genetic Type and Source Region

Previous studies have revealed that zircon trace element compositions (e.g., Hf, U, Th, Y) can discriminate their parent rock types [47]. In the Y-U diagram (Figure 9a), nearly all zircon samples from the Huxu quartz diorite porphyry plot within the field for granitoids. Granitoids are genetically classified into I-, S-, and A-types. I-type granites are typically characterized by minerals such as hornblende, S-types by peraluminous minerals (e.g., garnet, muscovite), and A-types by abundant alkali minerals. The quartz diorite porphyry samples collected from the Huxu area in this study have undergone intense alteration overall, as they were obtained in proximity to the ore body, resulting in the alteration of most phenocrysts. However, based on unpublished geological reports and previous studies, it has been observed that the quartz diorite porphyry in this area contains minor biotite and hornblende phenocrysts [2]. These mineralogical characteristics generally resemble those of I-type granites. This mineralogical signature is generally consistent with an I-type affinity.

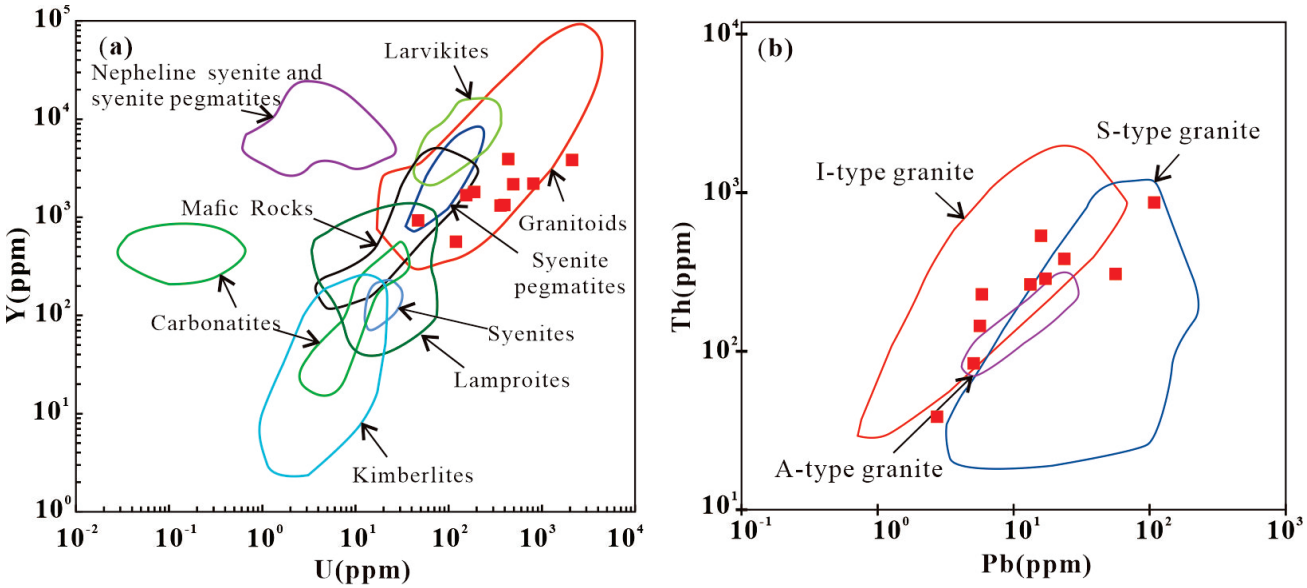


Figure 9. Diagram of rock type discrimination based on zircon trace elements. (**a**) Zircon Y-U discrimination of different rock types (after Belousova, et al., 2002a [47]); (**b**) Zircon Th-Pb discrimination of I-, S-, and A- type granites (after Wang, et al., 2012 [48]).

This interpretation is further supported by zircon trace element discriminants. Belousova et al. [47] demonstrated that zircon chemistry can indicate protolith. Specifically, the Th and Pb contents in zircon vary systematically among different granite types [48]. In the Th-Pb diagram (Figure 9b), data from the Huxu porphyry predominantly fall within the I-type granite field, providing independent geochemical evidence that it belongs to the I-type granite series.

The geochemical characteristics of apatite have also been widely applied in discriminating between the rock genetic types. Zhu et al. (2004) [49] found that the REE distribution patterns of apatite from different types of rocks are significantly different by comparing the REE compositions of apatite from rocks with different genetic types. The REE composition of apatite from the Huxu quartz diorite porphyry shows a high REE content, a moderately sloping right-leaning mode and a moderately negative Eu anomaly. These characteristics are consistent with the REE distribution curve of apatite from I-type granite, but significantly different from the REE distribution characteristics of apatite from S- and A-type granites (Figure 10). Moreover, in the apatite Y-Ce and Th/U-La/Sm discrimination

diagrams for discriminating the I-type and S-type granites [17], most data fall into the I-type granite area (Figure 11). Furthermore, to enhance the robustness of our conclusions, we applied a previously established machine learning model that discriminates granite types based on apatite trace element compositions [50]. This model also classifies the rock as I-type granite (Table S7).

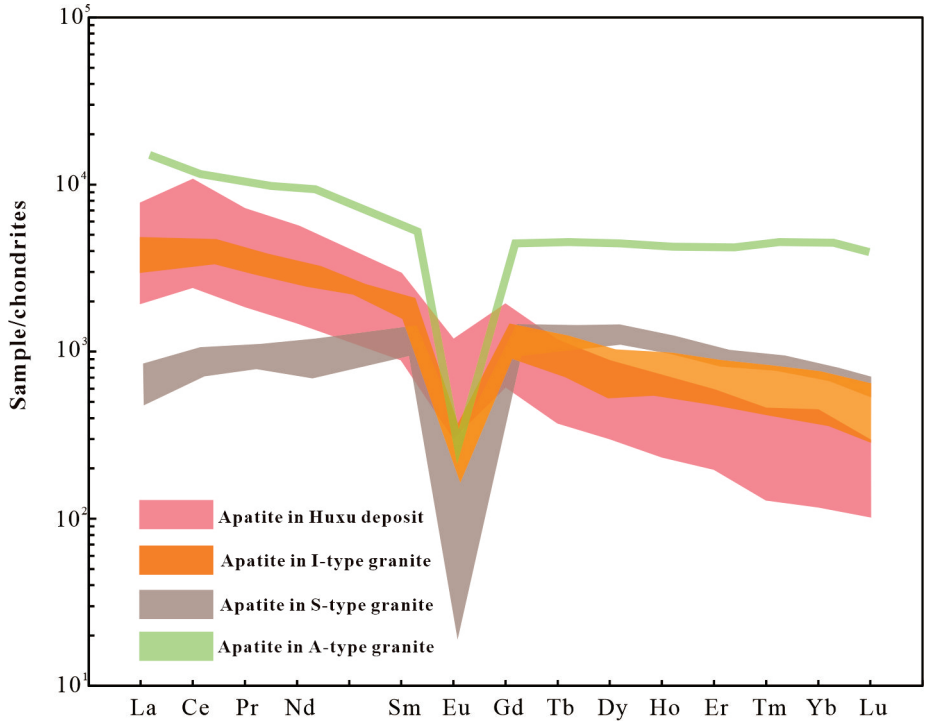


Figure 10. Diagram of I-, S-, and A-type granite discrimination based on the distribution pattern of REEs in apatite (after Zhu et al., 2004 [49]).

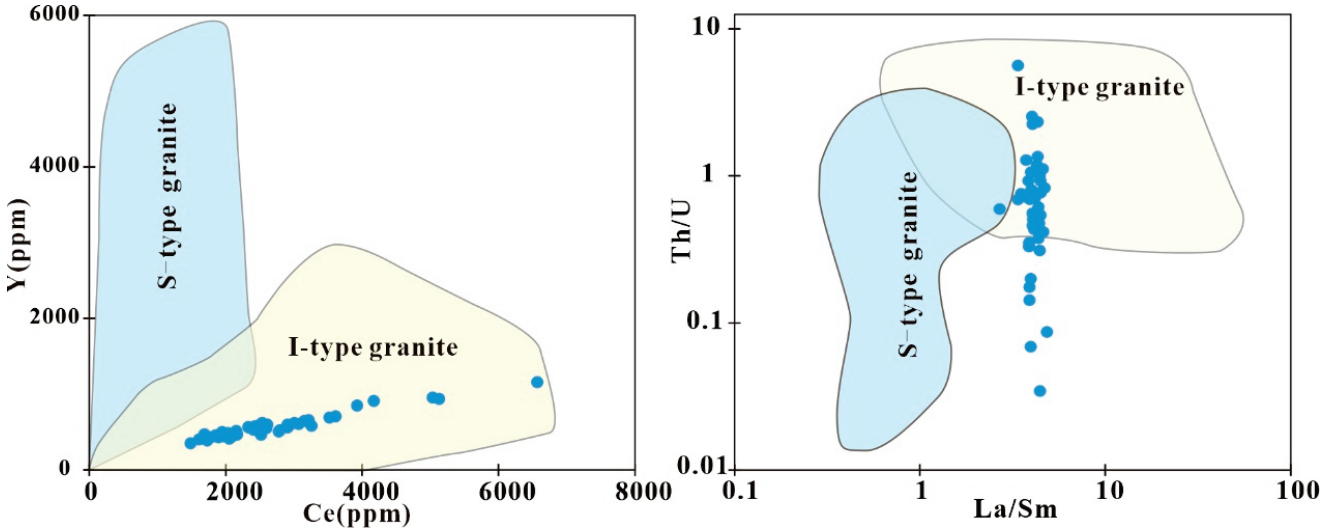


Figure 11. Diagram of granite genesis type discrimination based on trace elements in apatite (after Chen et al., 2021 [17]).

Apatite geochemistry provides key constraints on the magma source. The rare earth element (REE) composition of apatite can indicate the provenance of diagenetic materials [48]. In the apatite ΣLa~Nd-ΣSm~Ho-ΣEr~Lu ternary diagram, all data from the Huxu quartz diorite porphyry plot within the crust-mantle mixing field (Figure 12a). More definitively, the Nd isotopes of apatite offer direct evidence for the source. In the εNd(t)-t

diagram (Figure 12b), the data predominantly fall within the field of Late Jurassic–Early Cretaceous mafic magmas derived from an enriched mantle, with only a minor trend towards the Proterozoic crust of South China. This indicates that the sedimentary rock is unlikely to be the primary source and points strongly to a source involving the enriched mantle or melts derived from it. Currently, there are four main genetic models proposed for the origin of granite. To contextualize this evidence within current petrogenetic frameworks, we evaluate the four primary genetic models for granitoids: (1) differentiation of mantle-derived magmas [51,52]; (2) mixing between mantle-derived and crust-derived magmas [53]; (3) melting of subducted slabs [54]; and (4) evolution of purely crustal magmas [55]. Several lines of evidence argue against models (1), (3), and (4) for the Huxu porphyry. First, direct differentiation of mantle-derived magma typically yields rocks with very high Mg# values, inconsistent with the low Mg# of the Huxu samples (28.19–31.72, according to an unpublished geological report). The regional scale of coeval felsic magmatism in the Dongxiang Basin would also require an immense, yet unobserved, volume of parental mafic magma. Second, slab-derived melts are characterized by high Sr/Yb ratios, a feature absent in the contemporaneous magmatic rocks of the basin. Third, while crustal melting can produce quartz diorite, the relatively high εNd(t) values observed (Figure 12b) are difficult to reconcile with a pure ancient crustal source. Therefore, the combined evidence from apatite (REE and Nd isotopes) and the exclusion of alternative models converge to support the process of magma generation involving crust-mantle interaction. The mantle component could be contributed via juvenile crust or direct mantle melts. Although direct magma mixing might erase textural evidence like mafic enclaves through thorough hybridization, the geochemical signature remains definitive.

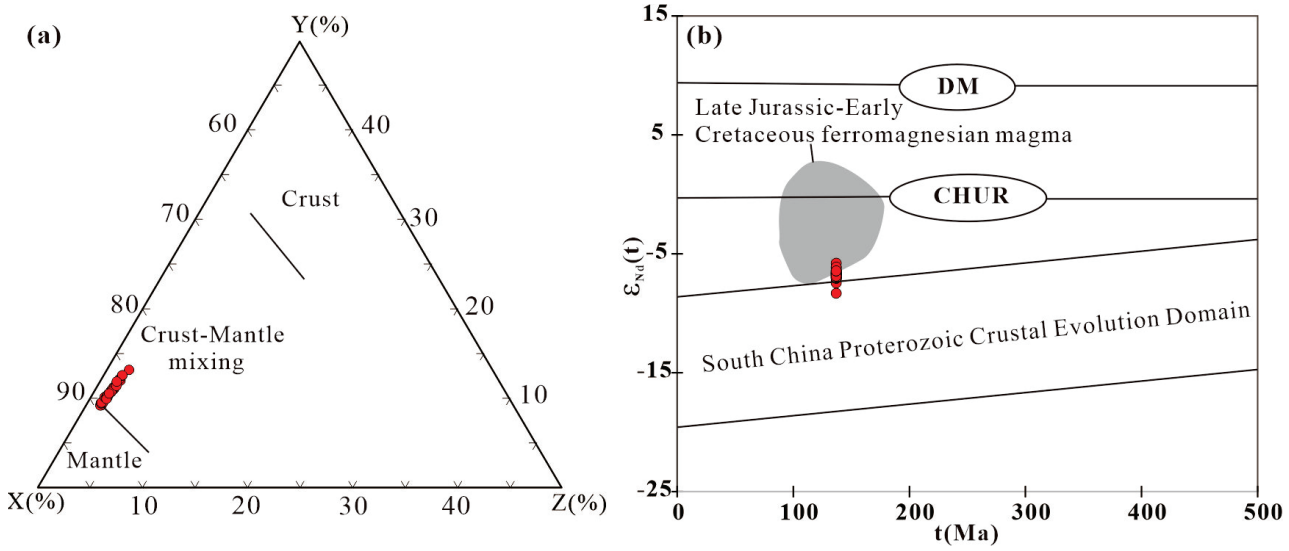


Figure 12. Diagram for source area discrimination based on REE and Nd isotope in apatite (**a**) Apatite ΣLa~Nd-ΣSm~Ho-ΣEr~Lu ternary diagram (after Zhu et al., 2004 [49]); (**b**) Apatite εNd(t)-t diagram (after Xiong, 2017 [56]).

Based on the above evidence, we conclude that the quartz diorite porphyry in the Huxu deposit is I-type granite, derived from the mixing between juvenile and ancient crustal melts.

5.2. Extensive Cretaceous Magmatism and Tectonic Setting

The ages of zircon and apatite from the quartz diorite porphyry of the Huxu Au-dominated polymetallic deposit are determined as 137.9 ± 1.3 Ma, and 130 ± 16 Ma respectively (Figures 7a and 8a). Since zircon and apatite show magmatic origin (Figures 5 and 6),

their ages can represent the magma emplacement time. Critically, the overlap of these two ages within analytical uncertainty, despite the large difference in U-Th-Pb system closure temperatures between zircon (>750 °C) and apatite (~350 °C), indicates a rapid post-emplacement cooling history for the porphyry. Such rapid cooling is characteristic of porphyry systems emplaced at shallow crustal depths [57,58]. Therefore, both mineral systems robustly record the same primary magmatic event.

Therefore, it is believed that the quartz diorite porphyry in the study area is the product of the Early Cretaceous magmatism. It should be noted that the Early Cretaceous volcanic-subvolcanic rocks are widely distributed in the Dongxiang basin. A series of zircon U-Pb isotope dating studies on some of these volcanic rocks have been carried out previously, and the results obtained show that the andesite (135.5 ± 2.1, 137.3 ± 2.3 and 141.7 ± 3.4 Ma), trachyandesite (142.0 ± 2.7 Ma), granite porphyry (139.4 ± 3.9 Ma), and rhyolite pyroclastic rocks (134.14 ± 0.6, 137.44 ± 0.67 and 141.35 ± 0.67 Ma) have similar ages with the Huxu quartz diorite porphyry [35], indicating that an intense magmatic activity event occurred in the Early Cretaceous. In South China, porphyry-related mineralization predominantly occurred during the Middle to Late Jurassic [59]. Although Cretaceous porphyry-related mineralization is less common, a review of its spatial distribution reveals that deposits of this age, while not as numerous as those from the Middle to Late Jurassic, are widely distributed across the region [60–66]. This likely represents an extensive magmatic-hydrothermal mineralization event in South China.

Magmatic rocks with different tectonic settings and source regions often have different whole-rock or mineral geochemical characteristics. Therefore, the whole-rock or mineral geochemical characteristics of magmatic rocks can be used to explore the tectonic setting of diagenesis. The quartz diorite porphyry samples from the Huxu area have undergone quite strong alteration overall, and the whole-rock composition has changed significantly. In this situation, the trace elements from the accessory mineral (e.g., zircon) less affected by alteration are chosen to discriminate the source rock type and tectonic environment. Grimes et al. (2007) [13] found that zircons crystallized in different environments have certain differences in the contents of elements such as U, Yb, Hf and Y after statistically analyzing a large amount of trace element and the REE data in zircon from the Indian Ocean ridge, the Atlantic Ocean ridge, the Talkeetna island arc in Alaska, and the continental areas. They constructed the U/Yb-Hf and U/Yb-Y diagrams to distinguish the source area characteristics of zircon. In the U/Yb-Hf diagram (Figure 13a), most zircon data of the Huxu quartz diorite porphyry fall into the continental crust zircon area; whereas in the lg(U/Yb)-lg(Sc/Yb) tectonic background discrimination diagram (Figure 13b), most zircon data fall into the continental arc environment area [2,35]. These observations combinedly suggest that the Huxu quartz diorite porphyry was formed in a continental arc environment.

Since the activities of the contemporaneous magmas with similar compositions occurred widely in South China, the magmatic rocks may have similar tectonic settings. Previous studies on the Early Cretaceous magmatic rocks in South China suggest that the Gan-Hang tectonic belt has undergone significant tectonic transitions during the late Yanshanian period, mainly manifesting as multiple changes in the subduction angle of the Paleo-Pacific Plate. In the early Cretaceous period, the Pacific Plate experienced subduction and retreated, leading to a local extensional environment and the upwelling of mantle-derived magma in the area [29,67,68]. It can be seen that the tectonic environments determined by the Huxu quartz diorite porphyry and the regional magmatic rocks are consistent. Therefore, in conclusion, we believe that the Huxu quartz diorite porphyry was formed in the marginal arc environment related to the subduction of the ancient Pacific Ocean Plate.

https://doi.org/10.3390/min16010103

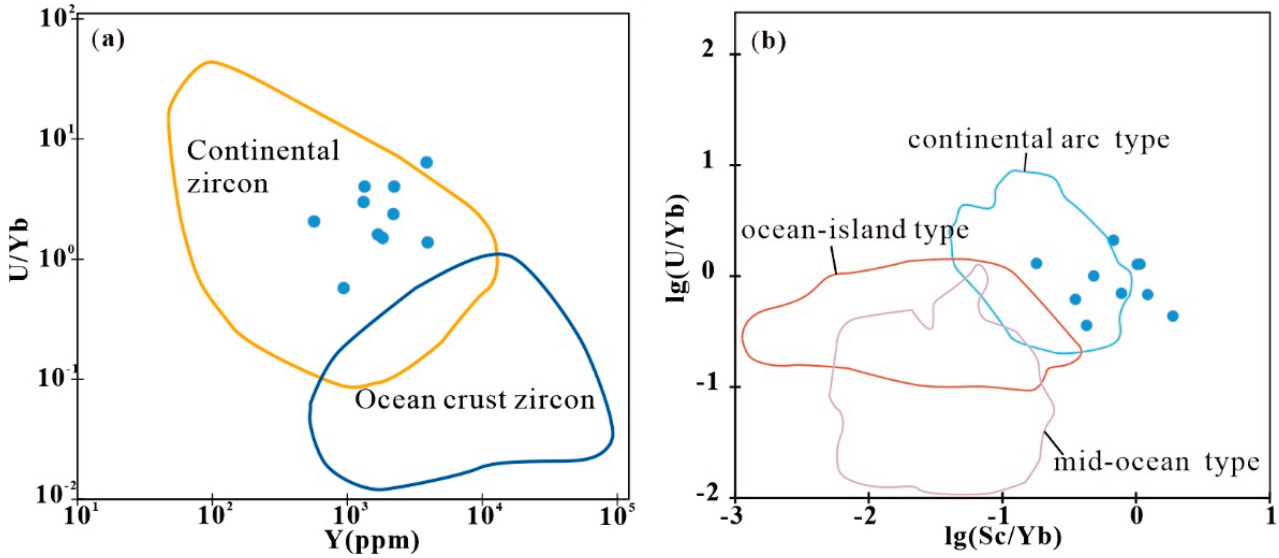


Figure 13. Diagram of tectonic environment discrimination based on zircon trace elements. (**a**) U/Yb-Y discrimination map of zircon from continental area and oceanic crust (after Grimes et al., 2007 [13]); (**b**) Log (U-Yb)-log (Sc/Yb) discrimination map of zircon from different tectonic settings (after Grimes et al., 2015 [14]).

5.3. Implication for Mineralization

Previous studies have identified the Huxu gold-polymetallic deposit as an intermediate-sulfidation epithermal deposit [4,5]. For this type of deposit, the ore-forming fluids and materials are typically derived from magmatic systems coeval with the host volcanic-subvolcanic rocks [6–10]. H-O isotope analysis of quartz veins by Wang et al. (1998) [2] revealed that the ore-forming fluids exhibited characteristics of a mixture between magmatic water and meteoric water. This is further corroborated by in-situ S-Pb isotopic analyses of pyrite from the Huxu deposit: the sulfur isotopic composition ($\delta^{34}S \approx 1.72‰$) indicates a magmatic sulfur source, while the lead isotopic signatures are highly consistent with those of the regional magmatic rocks and collectively suggest an orogenic belt/island arc setting [2,5]. These lines of evidence together suggest that the ore-forming magma and the magmas that formed the contemporaneous intrusive rocks in the area were likely derived from the same source. Furthermore, the presence of sulfide inclusions within apatite from the host quartz diorite porphyry (Figure 5) provides direct evidence for sulfide saturation in the parental magma, indicating its significant ore-forming potential. Integrating these geochemical constraints with the close spatial association between the ore bodies and the intrusive rocks, we propose that the ore-forming materials of the Huxu deposit were most likely derived from the same source as the volcanic-subvolcanic rocks in the area and that mineralization occurred concurrently with or shortly after the emplacement of the quartz diorite porphyry. Moreover, the ore-forming porphyries of both the Dongxiang copper deposit within the same basin and the neighboring Dexing copper deposit are characterized by crust-mantle magma mixing. This further indicates that such mixing played a significant role in the Yanshanian Cu-Au mineralization within the region [5,69,70].

Combining the above analysis with previous research, we propose the following genetic model for the Huxu Au-dominated polymetallic deposit (Figure 14). The continuous southwestward subduction of the Pacific Plate during the Early Cretaceous induced the upwelling of mafic magma from a mantle source. This mantle-derived magma triggered the melting of juvenile crust, and the resultant melts assimilated ancient crustal materials during ascent, forming a hybrid magma. This hybrid magma ascended, underwent crystallization and differentiation, and finally emplaced as the quartz diorite porphyry

at shallow crustal levels. Subsequent intense regional tectonism created faults within the porphyry, providing favorable conduits and space for ore deposition. During the late magmatic to hydrothermal transition, ore-forming fluids exsolved from the cooling magma and rose along these pre-existing faults. During their ascent, the fluids underwent boiling, water-rock interaction, and mixing with meteoric water. These processes changed the physicochemical properties of the fluids, leading to the precipitation of gold, lead, and zinc within the fault zones [5].

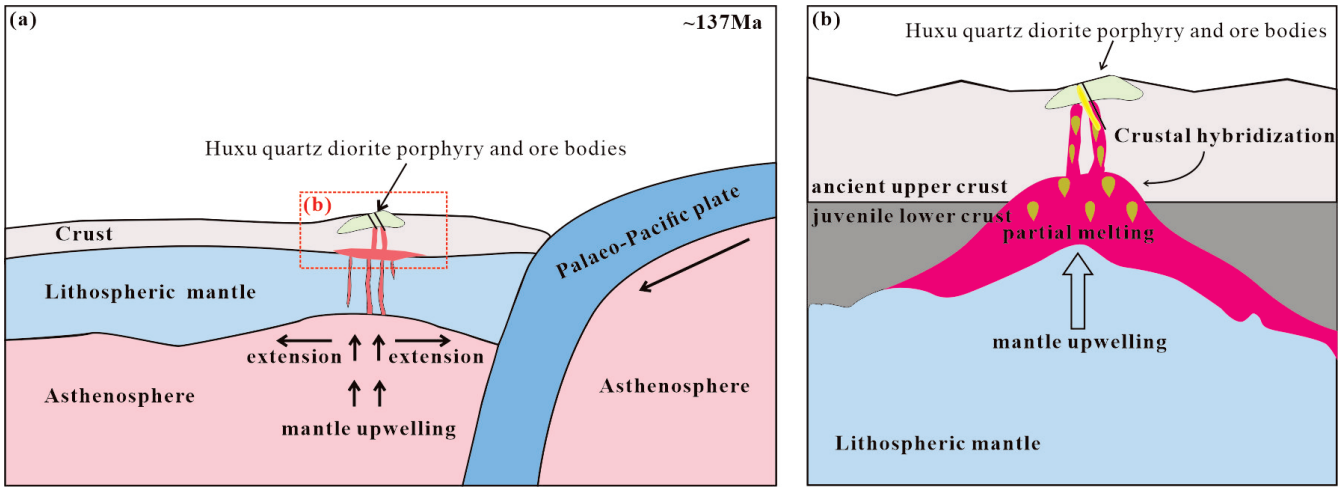


Figure 14. (**a**) Paleo-Pacific Plate roll-back-induced emplacement of the Huxu Quartz Diorite Porphyry (~137 Ma) and (**b**) shallow magmatic-hydrothermal processes controlling the formation of the Huxu Gold Deposit.

6. Conclusions

(1) Zircon and apatite U-Pb dating results indicate that the quartz diorite porphyry formed during the Early Cretaceous period, with zircon and apatite U-Pb ages of 137.9 ± 1.3 Ma and 130 ± 16 Ma, respectively. These two ages, consistent within analytical uncer-tainty, record rapid post-emplacement cooling of the intrusion and jointly constrain its crystallization age.

(2) The trace element characteristics of zircon (e.g., Y-U and Th-Pb discrimination diagrams) and its typical magmatic oscillatory zoning, combined with the rare earth ele-ment (REE) patterns of apatite (enriched in light REEs with moderate negative Eu anoma-lies), consistently indicate that the rock belongs to the I-type granite series.

(3) The Nd isotopic composition of apatite ($\varepsilon Nd(t)$ = –8.31 to –5.79) suggests that the parental magma was derived from mixing of juvenile crustal material and ancient crustal melts. Zircon trace element tectonic discrimination diagrams (e.g., U/Yb-Y and U/Yb-Sc/Yb) further reveal that the intrusion formed in a continental margin arc setting related to southwestward subduction of the Paleo-Pacific Plate during the Early Cretaceous peri-od.

(4) The presence of sulfide inclusions in apatite, together with published S-Pb isotopic data from the ores, indicates that the ore-bearing porphyry magma reached sulfide saturation and that the ore-forming materials were predominantly derived from the magmatic system. This study proposes that the ore-forming fluids and metal components of the Huxu deposit were mainly sourced from a magmatic–hydrothermal system cogeneric with the quartz diorite porphyry and that mineralization occurred during the magmatic–hydrothermal transition stage following porphyry emplacement.

Supplementary Materials: The following supporting information can be downloaded at: https://www.mdpi.com/article/10.3390/min16010103/s1, Table S1: U-Pb dating results of zircon from quartz diorite porphyry by using LA-ICP-MS; Table S2: Trace element content of zircon in Huxu

quartz diorite porphyry (ppm); Table S3: U-Pb dating results of apatite from quartz diorite porphyry by using LA-ICP-MS; Table S4: In situ trace element analysis results (ppm) of Apatiten in Huxu quartz diorite porphyry; Table S5: Electronic microprobe analysis results (%) of Apatite in Huxu quartz diorite porphyry; Table S6: In situ Nd isotopic analysis results of Apatite; Table S7: Machine learning method for discriminating granite genetic types based on trace element composition of apatite.

Author Contributions: Conceptualization, J.C.; writing—original draft preparation, H.G. and J.C.; writing—review and editing, J.C., H.G., L.M., K.L., Y.W. and L.W.; sample preparation, H.G. and J.C.; data curation, H.G. and G.W.; funding acquisition, J.C. All authors have read and agreed to the published version of the manuscript.

Funding: This research was funded by Jiangxi Provincial Natural Science Foundation (20232BAB213064) and the National Natural Science Foundation of China (No. 42102088).

Data Availability Statement: The original contributions presented in the study are included in the article/Supplementary Material.

Acknowledgments: We are grateful to the 1st Team of Jiangxi Nonferrous Metals Geological Exploration Bureau and Wei-Wei Chao, Bo Yuan, Jun-Feng Dai, Feng Lai, and Jian Zhang from East China University of Technology for their assistance during field geological surveys and the sample collection process.

Conflicts of Interest: The authors declare no conflict of interest.

References

1. Tiegeng, L.; Lin, Y. The Relationship between Mineralogical Characteristics and Isotopic Composition of Sphalerite, as Exemplified by The Huxu deposit, China. *Chin. J. Geochem.* **1995**, *14*, 160–167. [CrossRef]
2. Wang, K.Y.; Lu, Z.X.; Zhang, X.G. The Geological and Mineralization Feature of Huxu Gold Deposit and Study on Its Origin. *Gold* **1998**, *5*, 7–12, (In Chinese with English Abstract).
3. Chao, W.W.; Xu, D.R.; Li, Z.H.; Chen, L.Q.; Zhou, X.J.; Yuan, B.; Yang, L.F.; Chen, J.J.; Zhang, J. Characteristics and Geological Implications of Mineral Chemistry and Fluid Inclusions in Huxu Au-Pb-Zn Ore Deposit, Jiangxi Province. *Earth Sci.* **2024**, *49*, 1292–1306, (In Chinese with English Abstract). [CrossRef]
4. Chen, J.J.; Li, Z.H.; Xu, D.R.; Deng, T.; Chen, L.Q.; Zhou, X.J.; Chao, W.W.; Yuan, B.; Yang, L.F.; Liao, J. Metal Precipitation Mechanism of Huxu Au-dominated Deposit in Dongxiang Basin: Constraints from Mineral Paragenesis and Trace Elements. *Geotecton. Et Metallog.* **2024**, *48*, 737–753. (In Chinese with English Abstract)
5. Gao, H.Z.; Chen, J.J.; Leng, C.B.; Hu, Y.H.; Xie, H.D.; Li, Z.H. Ore-forming mechanism of Huxu Au-dominated polymetallic deposit in the Dongxiang Basin, South China: Constraints from in-situ trace elements and S–Pb isotopes of pyrite. *Acta Geochim.* **2024**, *43*, 1223–1240. [CrossRef]
6. Mao, J.W.; Chen, M.H.; Yuan, S.D.; Guo, C.L. Geological Characteristics of the Qinhang (or Shihang) Metallogenic Belt in South China and Spatial-Temporal Distribution Requlority of Mineral Deposits. *Acta Geol. Sin.* **2011**, *85*, 636–658. (In Chinese with English Abstract)
7. Song, G.X.; Qin, K.Z.; Li, G.M.; Wang, L. Basic characteristics and research progresses of intermediate sulfidation type epithermal gold poly-metallic deposits, and prospects. *Acta Petrol. Sin.* **2018**, *34*, 748–762, (In Chinese with English Abstract).
8. Wang, L.; Qin, K.Z.; Song, G.X.; Li, G.M. A Review of Intermediate Sulfidation Epithermal Deposits and Subclassification. *Ore Geol. Rev.* **2019**, *107*, 434–456. [CrossRef]
9. Wang, L.; Percival, J.B.; Hedenquist, J.W.; Hattori, K.; Qin, K.Z. Alteration mineralogy of the Zhengguang epithermal Au-Zn Deposit, Northeast China: Interpretation of shortwave infrared analyses during mineral exploration and assessment. *Econ. Geol.* **2021**, *116*, 389–406. [CrossRef]
10. Wang, L.; Chiaradia, M.; Qin, K.Z.; Hui, K.X.; Li, Z.Z.; Cao, M.J.; Song, G.X.; Pang, X.Y.; Shan, P.F.; Li, G.M. Magmatic Controls on Au- and Ag-Rich Intermediate-Sulfidation Epithermal Deposits from Northeast China. *Econ. Geol.* **2024**, *119*, 1913–1936. [CrossRef]
11. Wu, Z.R. Metallogenetic Character and Prospeeting of Gold Deposit in Dongxiang Volcanic Basin. *Miner. Resour. Geol.* **2003**, *17*, 410–413, (In Chinese with English Abstract).
12. Ballard, J.R.; Palin, J.M.; Campbell, I.H. Relative oxidation states of magmas inferred from Ce (IV)/Ce (III) in zircon: Application to porphyry copper deposits of northern Chile. *Contrib. Mineral. Petrol.* **2002**, *144*, 347–364. [CrossRef]

13. Grimes, C.B.; John, B.E.; Kelemen, P.B.; Mazdab, F.K.; Wooden, J.L.; Cheadle, M.J.; Hanghøj, K.; Schwartz, J.J. Trace element chemistry of zircons from oceanic crust: A method for distinguishing detrital zircon provenance. *Geology* **2007**, *35*, 643–646. [CrossRef]
14. Grimes, C.B.; Wooden, J.L.; Cheadle, M.J.; John, B.E. "Fingerprinting" tectono-magmatic provenance using trace elements in igneous zircon. *Contrib. Mineral. Petrol.* **2015**, *170*, 46. [CrossRef]
15. Leng, C.B.; Chen, X.L.; Zhang, J.J.; Ma, X.H.; Tian, F.; Guo, J.H.; Zhang, L.J. Lithogeochemical and mineral chemical footprints of porphyry Cu±Mo±Au deposits: A review. *Acta Geol. Sin.* **2020**, *94*, 3189–3212. (In Chinese with English Abstract) [CrossRef]
16. Sun, J.F.; Yang, J.H.; Zhang, J.H.; Yang, Y.H.; Zhu, Y.S. Apatite geochemical and Sr-Nd isotopic insights into granitoid petrogenesis. *Chem. Geol.* **2021**, *566*, 120104. [CrossRef]
17. Chen, X.L.; Leng, C.B.; Zou, S.H.; Li, K.X.; Zhang, L.J. Geochemical compositions of apatites from the Xuejiping and Disuga porphyries in Zhongdian arc: Implications for porphyry Cu mineralization. *Ore Geol. Rev.* **2021**, *130*, 103954. [CrossRef]
18. Gao, X.; Yang, L.Q.; Meng, J.Y.; Zhang, L.J. Zircon U-Pb, molybdenite Re-Os geochronology and Sr-Nd-Pb-Hf-O-S isotopic constraints on the genesis of Relin Cu-Mo deposit in Zhongdian, Northwest Yunnan, China. *Ore Geol. Rev.* **2017**, *91*, 945–962. [CrossRef]
19. Zou, X.Y.; Jiang, J.L.; Qin, K.Z.; Zhang, Y.G.; Yang, W.; Li, X.H. Progress in the principle and application of zircon trace element. *Acta Petrol. Sin.* **2021**, *37*, 985–999. (In Chinese with English Abstract) [CrossRef]
20. Cao, K.; Yang, Z.M.; Hou, Z.Q.; White, N.C.; Yu, C. Contrasting porphyry Cu fertilities in the Yidun Arc, eastern Tibet: Insights from zircon and apatite compositions and implications for exploration. *SEG Spec. Publ.* **2021**, *24*, 231–255.
21. Watson, E.B.; Wark, D.A.; Thomas, J.B. Crystallization thermometers for zircon and rutile. *Contrib. Mineral. Petrol.* **2006**, *151*, 413–433. [CrossRef]
22. Chew, D.M.; Spikings, R.A. Apatite U-Pb Thermochronology: A Review. *Minerals* **2021**, *11*, 1095. [CrossRef]
23. Trail, D.; Watson, E.B.; Tailby, N.D. Ce and Eu anomalies in zircon as proxies for the oxidation state of magmas. *Geochim. Cosmochim. Acta* **2012**, *97*, 70–87. [CrossRef]
24. Wang, R.; Richards, J.P.; Hou, Z.Q.; Yang, Z.M.; DuFrane, S.A. Increased magmatic water content-the key to oligo-miocene porphyry Cu-Mo ± Au formation in the eastern Gangdese Belt, Tibet. *Econ. Geol.* **2014**, *109*, 1315–1339. [CrossRef]
25. Wang, R.; Richards, J.P.; Hou, Z.Q.; Yang, Z.M.; Gou, Z.B.; DuFrane, S.A. Increasing magmatic oxidation state from Paleocene to Miocene in the eastern Gangdese Belt, Tibet: Implication for collision-related porphyry Cu-Mo ± Au mineralization. *Econ. Geol.* **2014**, *109*, 1943–1965. [CrossRef]
26. Chen, H.J.; Sun, X.M.; Li, D.F.; Yin, R.; Tong, Z.D.; Wu, Z.W.; Fu, Y.; Liu, Q.F.; Chen, X.; Yi, J.Z.; et al. In situ apatite U-Pb dating for the ophiolite-hosted Nianzha orogenic gold deposit, Southern Tibet. *Ore Geol. Rev.* **2022**, *144*, 104811. [CrossRef]
27. Loucks, R.R.; Fiorentini, M.L.; Henríquez, G.J. New magmatic oxybarometer using trace elements in zircon. *J. Petrol.* **2020**, *61*, egaa034. [CrossRef]
28. Mo, L.; Leng, C.B.; Chen, X.L.; Li, K.X. Zircon trace elements and Hf-O isotopes of porphyries in the Zhongdian area of Yunnan Province and their implications for petrogenesis and mineralization. *Acta Petrol. Sin.* **2024**, *40*, 1163–1184. (In Chinese with English Abstract) [CrossRef]
29. Li, Y.; Yuan, F.; Jowitt, S.M.; Li, X.L.; Zhou, T.F.; Wang, F.Y.; Deng, Y.F. Combined garnet, scheelite and apatite U–Pb dating of mineralizing events in the Qiaomaishan Cu–W skarn deposit, eastern China. *Geosci. Front.* **2023**, *14*, 101459. [CrossRef]
30. Sun, W.D.; Ling, M.X.; Wang, F.Y.; Ding, X.; Hu, Y.H.; Zhou, J.B.; Yang, X.Y. Pacific Plate Mesozoic Geological Event in Easten China. *Bull. Mineral. Petrol. Geochem.* **2008**, *27*, 218–225. (In Chinese with English Abstract)
31. Su, H.M.; Mao, J.W.; He, X.R.; Lu, R. Timing of The Formation of The Tianhuashan Basin in Northem Wuyi as Constrained by Geochronology of Volcanic and Plutonic Rocks. *Sci. China Earth Sci.* **2013**, *56*, 940–955. (In Chinese with English Abstract) [CrossRef]
32. Qin, X.F. *A Preliminary Framework for The Sequence of Volcanic-Intrusive Magma of Relation to Mineralization in The North Wuyi Yanshanian Area*; China University of Geosciences: Beijing, China, 2014. (In Chinese with English Abstract)
33. Yuan, M.W.; Li, S.R.; Li, C.L.; Santosh, M.; Alam, M.; Zeng, Y.J. Geochemical and Isotopic Composition of Auriferous Pyrite from The Yongxin Gold Deposit, Central Asian Orogenic Belt: Implication for Ore Genesis. *Ore Geol. Rev.* **2018**, *93*, 255–267. [CrossRef]
34. Yan, J.L.; Jiang, J.J.; Zhang, J.; Zhang, J.; Wu, Z.C.; Zhu, X.P. Metallogenic Geological and Geochemical Characteristics and Ore-Prospecting Potential of Dongxiang Volcanic Area, Jiangxi Province. *Geophys. Geochem. Explor.* **2012**, *36*, 534–538. [CrossRef]
35. Yang, Q. *Age and Attribution of Volcanic Rocks in The Dongxiang Volcanic Basin in The North Wuyi*; China University of Geosciences: Beijing, China, 2015; pp. 43–56. (In Chinese with English Abstract)
36. Cai, Y.T.; Ni, P.; Shen, K.; Zhu, X.T.; Huang, S.J.; Zhang, X.C.; Xu, J.H. Study on The Fluid Inclusion from Dongxian Copper Deposit Jiangxi Province China. *Acta Petrol. Sin.* **2011**, *27*, 1375–1386. (In Chinese with English Abstract) [CrossRef]
37. Ouyang, X.C. Geological and Geochemical Characteristics and Its Genesis of the Dongxiang Copper Deposit, Jiangxi Province. Ph.D. Thesis, China University of Geosciences, Beijing, China, 2015; p. 68, (In Chinese with English Abstract).

38. Zhou, X.J.; Li, S.Q.; Chen, L.Q. Discussion of Metallogenic Regularity and Prospecting Direction of Dongxiang Volcanic Basin in Jiangxi province. *J. East China Univ. Technol. (Nat. Sci.)* **2019**, *42*, 45–51. (In Chinese with English Abstract)
39. Wan, L.; Zhou, T.; Dai, W.; Chang, T. Metallogenic Geological Characteristics and Prospecting Prediction in The South of Dongxiang, Jiangxi Province. *World Nonferrous Met.* **2020**, *9*, 89–90. (In Chinese with English Abstract)
40. Ludwig, K.R. ISOPLOT 3.00: A Geochronological Toolkit for Microsoft Excel. Berkeley Geochronology Center, California, Berkeley. *Nat. Sci.* **2003**, *5*, 39.
41. Xing, C.M.; Wang, C.Y. Cathodoluminescence images and trace element compositions of fluorapatite from the Hong ge layered intrusion in SW China: A record of prolonged crystallization and overprinted fluid metasomatism. *Am. Mineral. J. Earth Planet. Mater.* **2017**, *102*, 1390–1401. [CrossRef]
42. Xu, L.; Hu, Z.C.; Zhang, W.; Yang, L.; Liu, Y.S.; Gao, S. In situ Nd isotope analyses in geological materials with signal enhancement and non-linear mass dependent fractionation reduction using laser ablation MC-ICP-MS. *J. Anal. Spectrom.* **2015**, *30*, 232–244. [CrossRef]
43. Zhang, W.; Hu, Z.C.; Liu, Y.S. Iso-Compass: New freeware software for isotopic data reduction of LA-MC-ICP-MS. *J. Anal. At. Spectrom.* **2020**, *35*, 1087–1096. [CrossRef]
44. Sun, S.; McDonough, W.F. Chemical and Isotopic Systematics of Oceanic Basalts: Implications for Mantle Composition and Processes. *Geol. Soc. Lond. Spec. Publ.* **1989**, *42*, 313–345. [CrossRef]
45. Chen, X.L.; Liang, H.Y.; Zhang, J.; Sotiriou, P.; Huang, W.T.; Ren, L.; Zhang, L.; Zou, Y.O. Geochemical characteristics and magma fertility for the Jurassic arc rocks in the Gangdese belt, Tibet. *Ore Geol. Rev.* **2019**, *115*, 103169. [CrossRef]
46. Stacey, J.S.; Kramers, J.D. Approximation of terrestrial lead isotope evolution by a two-stage model. *Earth Planet. Sci. Lett.* **1975**, *26*, 207–221. [CrossRef]
47. Belousova, E.A.; Griffin, W.L.; O'Reilly, S.Y.; Fishe, N. Igneous zircon: Trace element composition as an indicator osource rock type. *Contrib. Mineral.* **2002**, *143*, 601–622. [CrossRef]
48. Wang, Q.; Zhu, D.C.; Zhao, Z.D.; Guan, Q.; Zhang, X.Q.; Sui, Q.L.; Hu, Z.C.; Mo, X.X. Magmatic zirconsfrom I, S-and A-type granitoids in Tibet: Trace elementcharacteristics and their application to detrital zircon provenancestudy. *J. Asian Earth Sci.* **2012**, *53*, 59–66. [CrossRef]
49. Zhu, X.Q.; Wang, Z.G.; Huang, Y.; Wang, G.L. REE Content and Distribution in Apatite and Its Geological Tracing Significance. *Chin. Rare Earths* **2004**, *25*, 41–45. (In Chinese with English Abstract)
50. Han, F.G.; Leng, C.B.; Chen, J.J.; Zou, S.H.; Wang, D.Z. Machine learning method for discriminating granite genetic types based on trace element composition of apatite. *Acta Petrol. Sin.* **2025**, *41*, 737–750. [CrossRef]
51. Sisson, T.W.; Ratajeski, K.; Hankins, W.B.; Glazner, A.F. Voluminous granitic magmas from common basaltic sources. *Contrib. Mineral. Petrol.* **2005**, *148*, 635–661. [CrossRef]
52. Whitaker, M.L.; Nekvasil, H.; Lindsley, D.H.; McCurry, M. Can crystallization of olivine tholeiite give rise to potassic rhyolites? —An experimental investigation. *Bull. Volcanol.* **2008**, *70*, 417–434. [CrossRef]
53. Chen, J.; Wei, J.; Fu, L.; Li, H.; Zhou, H.; Zhao, X.; Zhan, X.; Tan, J. Multiple sources of the Early Mesozoic Gouli batholith, Eastern Kunlun Orogenic Belt, northern Tibetan Plateau: Linking continental crustal growth with oceanic subduction. *Lithos* **2017**, *292*, 161–178. [CrossRef]
54. Martin, H. Adakitic magmas: Modern analogues of Archaean granitoids. *Lithos* **1999**, *46*, 411–429. [CrossRef]
55. Carvalho, B.B.; Bartoli, O.; Cesare, B.; Satish-Kumar, M.; Petrelli, M.; Kawakami, T.; Hokada, T.; Gilio, M. Revealing the link between A-type granites and hottest melts from residual metasedimentary crust. *Geology* **2023**, *51*, 845–849. [CrossRef]
56. Xiong, L. *Petrologic Characteristics and Petrogenetic Study of Intrusive Rocks in TangLi Mining Area, North Wuyishan Area*; China University of Geosciences: Beijing, China, 2017; p. 45, (In Chinese with English Abstract).
57. Zhao, J.X.; Qin, K.Z.; Xiao, B.; McInnes, B.; Li, G.; Evans, N.; Cao, M.J.; Li, J.X. Thermal history of the giant Qulong Cu–Mo deposit, Gangdese metallogenic belt, Tibet: Constraints on magmatic–hydrothermal evolution and exhumation. *Gondwana Res.* **2016**, *36*, 390–409. [CrossRef]
58. Cernuschi, F.; Dilles, J.H.; Grocke, S.B.; Valley, J.W.; Kitajima, K.; Tepley, F.J. Rapid formation of porphyry copper deposits evidenced by diffusion of oxygen and titanium in quartz. *Geology* **2018**, *46*, 611–614. [CrossRef]
59. Mao, J.W.; Zheng, W.; Xie, G.; Lehmann, B.; Goldfarb, R. Recognition of a Middle—Late Jurassic arc-related porphyry copper belt along the southeast China coast: Geological characteristics and metallogenic implications. *Geology* **2021**, *49*, 592–596. [CrossRef]
60. Chen, F.W.; Li, H.Q.; Mei, Y.P. Zircon SHRIMP U–Pb chronology of diagenetic mineralization of the Longtoushan porphyry gold orefield, Gui County, Guangxi. *Acta Geol. Sin.* **2008**, *82*, 921–926. (In Chinese with English Abstract)
61. Chen, X.H.; Zheng, S.H. New prospecting discovery in Yongping Shizitou molybdenum mineralized zone. *Jiangxi Nonferrous Met.* **2008**, *22*, 7–9, (In Chinese with English Abstract).
62. Liang, Q.L.; Jiang, S.H.; Wang, S.H.; Li, C.; Zeng, F.G. Re–Os dating of molybdenite from the Luoboling porphyry Cu–Mo deposit in the Zijinshan ore field of Fujian province and its geological significance. *Acta Geol. Sin.* **2012**, *86*, 113–1118. (In Chinese with English Abstract)

63. Xu, C.; Chen, H.Y.; Huang, W.; Qi, J.; Duan, G.; Zhang, L.; Wu, C.; Zhang, S.; Zhong, W. Mesozoic multiphase magmatism at the Xinan Cu–Mo ore deposit (Zijinshan Orefield): Geodynamic setting and metallogenic implications. *Ore Geol. Rev.* **2017**, *88*, 768–790. [CrossRef]
64. Duan, G.; Chen, H.Y.; Hollings, P.; Qi, J.P.; Xu, C.; Zhang, S.; Xiao, B.; Liu, G.Y.; Liu, J.M. The Mesozoic magmatic sources and tectonic setting of the Zijinshan mineral field, South China: Constraints from geochronology and geo chemistry of igneous rocks in the Southeastern Ore Segment. *Ore Geol. Rev.* **2017**, *80*, 800–827. [CrossRef]
65. Zheng, W.; Zhao, H.J.; Ouyang, H.G.; Zhao, C.S.; Yu, X.F.; Luo, D.L.; Huang, H.G.; Ouyang, Z.X. Re-Os dating for the molybdenite from the Xiping Mo-Cu polymetallic deposit in Guangdong Province and its geological signifi cance. *Acta Petrol. Sin.* **2017**, *33*, 843–858. (In Chinese with English Abstract)
66. Shen, H.J.; Zhang, Y.; Pan, Z.; Shao, Y.J.; Brzozowski, M.J.; Zhao, L.J.; Liu, G.Q.; Liu, Q.Q.; Shi, J.; Wang, X.; et al. Newly discovered Early Cretaceous Au mineralization overprinting Late Jurassic Pb-Zn-Ag mineralization in the Qin-Hang metallogenic belt (South China). *GSA Bull.* **2024**, *137*, 1021–1036. [CrossRef]
67. Li, S.Z.; Zang, Y.B.; Wang, P.C.; Suo, Y.H.; Li, X.Y.; Liu, X.; Zhou, Z.Z.; Liu, X.G.; Wang, Q. Mesozoie tectonie transition in South China and initiation of Palaeo-Pacific subduction. *Earth Sci. Front.* **2017**, *24*, 213–225.
68. Mao, J.R.; Li, Z.L.; Ye, H.M. Mesozoic tectono-magmatic activities in South China: Retrospect and prospect. *Sci. China Earth Sci.* **2014**, *57*, 2853–2877. [CrossRef]
69. Ouyang, X.C.; Di, Y.J.; Zhang, D.; Xu, Y.; Yang, Q.; Wang, S.Y.; Wang, S.Y.; Chen, J. Geochemical features and LA-ICP-MS zircon U Pb ages of the granite porphyry in the Dongxiang copper deposit of Jiangxi Province and their geological significance. *Geol. Bull. China* **2016**, *35*, 1869–1883. (In Chinese with English Abstract)
70. Wang, G.G.; Ni, P.; Yao, J.; Yao, J.; Wang, X.L.; Zhao, K.D.; Zhu, R.Z.; Xu, Y.F.; Pan, J.Y.; Zhang, Y.H. The link between subduction modified lithosphere and the giant Dexing porphyry copper deposit, South China: Constraints from high-Mg adakitic rocks. *Ore Geol. Rev.* **2015**, *67*, 109–126. [CrossRef]

Disclaimer/Publisher's Note: The statements, opinions and data contained in all publications are solely those of the individual author(s) and contributor(s) and not of MDPI and/or the editor(s). MDPI and/or the editor(s) disclaim responsibility for any injury to people or property resulting from any ideas, methods, instructions or products referred to in the content.

minerals

MDPI

Article

Zircon U-Pb Geochronology and Hf Isotopes of the Granitoids from Cahanwusu Cu Deposit in Awulale Mountain, Western Tianshan: Implication for Regional Mineralization

Wei Zhang [1,2], Mao-Xue Chen [1], Mei-Li Yang [1], Wen-Hui Yang [3] and Xing-Chun Zhang [4,*]

[1] School of Earth Sciences, Yunnan University, Kunming 650500, China; zhangwei1988@ynu.edu.cn (W.Z.)
[2] Yunnan International Joint Laboratory of Critical Mineral Resource, Kunming 650500, China
[3] Henan Nuclear Technology Application Center, Zhengzhou 450044, China
[4] State Key Laboratory of Ore Deposit Geochemistry, Institute of Geochemistry Chinese Academy of Sciences, Guiyang 550081, China
* Correspondence: zhangxingchun@mail.gyig.ac.cn

Abstract: Awulale Mountain is one of the most important Fe-Cu concentration areas situated in the eastern part of Western Tianshan. The Cu deposits in the belt are genetically associated with the Permian intermediate and felsic intrusions. However, the precise age and magma source of the causative intrusions are currently not confirmed, constraining our understanding of regional mineralization. The Cahanwusu porphyry Cu deposit is located in the western part of Awulale Mountain. Field investigations have shown that the mineralization in the deposit is genetically associated with granitic porphyry and diorite porphyry. In this paper, we provide detailed zircon U-Pb ages and in-situ Hf isotopic compositions of the granitic porphyry and diorite porphyry. The granitic porphyry and diorite porphyry have zircon U-Pb ages of 328.6 ± 2.6 Ma (MSWD = 0.52; n = 23) and 331 ± 2.8 Ma (MSWD = 0.95; n = 21), respectively. This indicates that the Cahanwusu deposit was formed in the Carboniferous in a subduction setting. This is distinguishable from other porphyry Cu deposits in the belt, which were generally formed in the Permian in the post-collision extensional setting. The granitic porphyry and diorite porphyry exhibit positive $\varepsilon_{Hf}(t)$ values varying from +2.8 to +5.4 (average of +4.1) and +2.0 to +5.1 (average of +4.1), respectively. The magmas of these causative intrusions were interpreted to be derived from the partial melting of the juvenile lower crust which originated from cooling of mantle-derived magmas related to the subduction process. Our new results highlight that the Cahanwusu deposit represents a new episode of Cu mineralization in the belt and the Carboniferous granitoids in Awulale Mountain are potential candidates for Cu exploration.

Keywords: Awulale Mountain; zircon U-Pb age; Hf isotope; regional mineralization; Cahanwusu deposit

1. Introduction

Awulale Mountain is located in the eastern segment of the Western Tianshan orogeny. It hosts numerous Fe and Cu (Au) polymetallic deposits, defining the so-called Awulale Fe-Cu Metallogenetic Belt [1–6]. Typical Fe deposits in the belt include the Zhibo, Dunde, Chagangnuoer, and Beizhan deposits. They are hosted by volcanic and volcanic-clastic rocks, especially the Carboniferous Dahalajunshan formation [1,5,7]. On the other hand, the Cu deposits, including the Nulasai, 109, Qunji, and Qunjisayi deposits, are generally genetically associated with the Permian intermediate and felsic intrusions [4,8,9]. Over the past decade, most research in the Awulale Fe-Cu metallogenetic belt has focused on

Fe mineralization, and the genesis of these volcanic-related Fe deposits has been well established [6,10–15]. However, the Cu mineralization in the belt is rarely investigated. The precise age and magma source of the causative intrusions are currently not confirmed, constraining our understanding of regional mineralization.

The newly discovered Cahanwusu Cu deposit is located in the western part of Awulale Mountain. Filed investigations have shown that the mineralization in the deposit is genetically associated with granitic porphyry and diorite porphyry. However, the age and background of the mineralization is still ambiguous. In this paper, we provide detailed zircon U-Pb ages and in-situ Hf isotopic compositions of the granitic porphyry and diorite porphyry. Our new results not only well constrain the age and magma source of causative rocks in the Cahanwusu deposit, but also have important implications for the regional mineralization of the Awulale metallogenetic belt.

2. Geologic Background

The Tianshan orogenic belt is located in the southern part of the Central Asian Orogenic Belt (CAOB) (Figure 1a) and is divided into the Western and Eastern Tianshan belts. The Western Tianshan belt, which hosts Awulale Mountain, is sandwiched between the Junggar Block to the north and Tarim block to the south (Figure 1a). Tectonically, the Western Tianshan belt comprises four segments, including the North Tianshan arc accretionary complex in the north, the Yili block and the central Tianshan arc terrane in the middle and the northern margin of the Tarim block in the south [16–19]. The Western Tianshan belt has undergone a complex tectonic evolution [17–19]. The Paleozoic oceans, including the Terskey, North Tianshan, and South Tianshan Oceans, were closed in the Paleozoic, resulting in the amalgamations of a large amount of micro-continents in this period [17,18].

Awulale Mountain is located in the eastern part of the central Tianshan arc terrane in the Western Tianshan orogenic belt (Figure 1a). The Precambrian basement is located in the western part of Awulale Mountain and is composed of Meso- to Neo-Proterozoic gneisses, marble, migmatite and clastic rocks [20,21]. Volcanic sedimentary rocks and volcaniclastic sedimentary rocks with Silurian and Devonian ages are outcropped along the northern and southern margins of Awulale Mountain. Silurian and Devonian limestone are developed well, especially in the region around the Cahanwusu deposit. The carboniferous volcanic and volcaniclastic rocks, which are closely associated with Fe mineralization in the region, are widely distributed as a result of slab subduction. The Permian, Triassic and Jurassic strata consist mainly of conglomerate, sandstone, mudstone and shale and are locally present in the western part of Awulale Mountain.

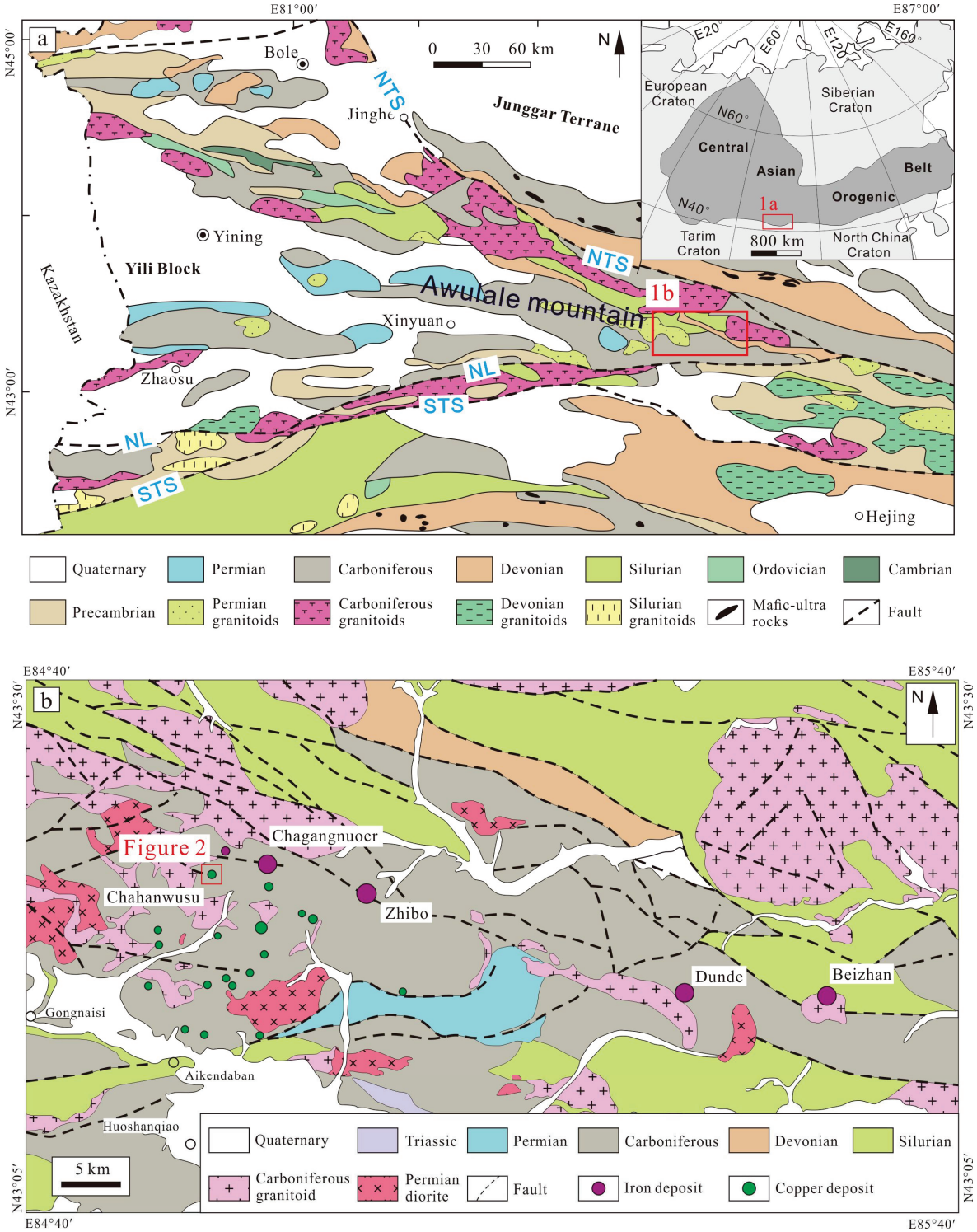


Figure 1. (**a**) Regional geological map of the Western Tianshan and the location of Awulale Mountain. Modified from Zhang et al. 2014 [5]. Inset map showing the location of the Western Tianshan within the Central Asian Orogenic Belt. (**b**) Simplified geological map of the Awulale Fe-Cu Metallogenetic Belt and the location of some Cu and Fe deposits. Modified from Hong et al. 2020 [11]. NTS = North Tianshan Suture, NL = Nikolaev Line, STS = South Tianshan Suture.

3. Geology of the Cahanwusu Cu Deposit

The Cahanwusu Cu deposit is located in the eastern segment of Awulale Mountain (Figure 1b). The strata in the deposit are predominantly composed of Carboniferous volcano-sedimentary rocks and carbonate, which are locally overlain by the Quaternary

alluvial and glacial–fluvial sediments (Figure 2). The volcano-sedimentary rocks are located in the northern part and are composed of andesites, tuffs and breccias. The intrusions include granitic porphyry and diorite porphyry, both of which are closely associated with mineralization (Figure 2). The granitic porphyry occurs as intrusions intruding both the volcano-sedimentary rocks and carbonate. It is composed of quartz, K-feldspar, plagioclase, and biotite with accessory minerals of apatite, zircon, allanite, and magnetite (Figure 3a). On the other hand, the diorite porphyry intrudes the volcano-sedimentary rocks and is composed dominantly of quartz, hornblende, plagioclase, and biotite, with minor zircon, apatite, titanite, and magnetite (Figure 3b).

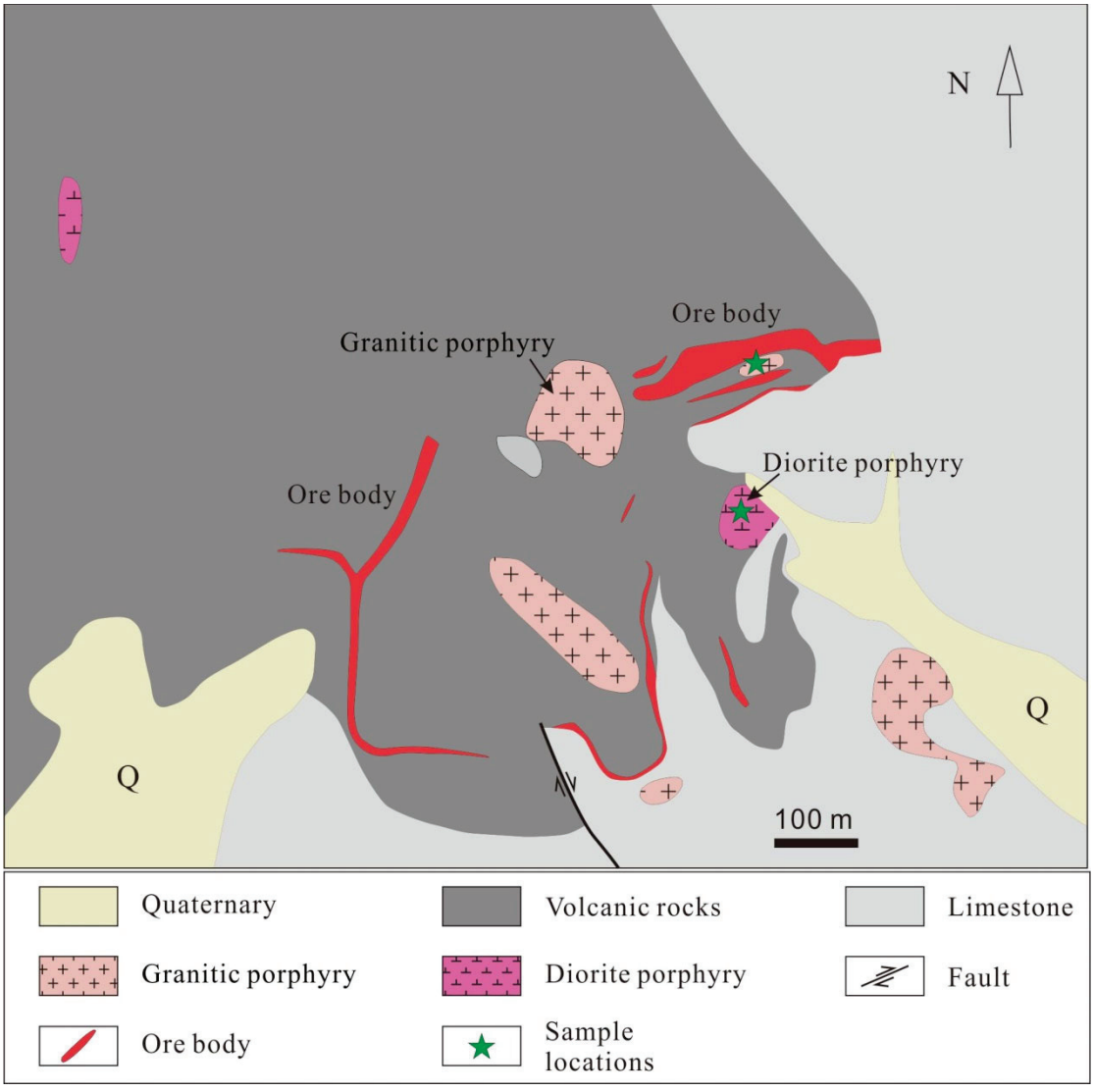


Figure 2. Simplified geological map of the Cahanwusu Cu deposit (after Central South Geo-Exploration Institute, unpublished internal report).

The orebodies in the Cahanwusu deposit are typically lenticular in shape and are hosted in the volcano-sedimentary rocks (Figure 2). They have lengths of 100 to 500 m thickness of 10 to 50 m. The mineralization in the deposit occurs mainly as veins/veinlets. The veins (veinlets) have thicknesses ranging from one to several centimeters and are filled by granular quartz with abundant sulfides including bornite, chalcopyrite, molybdenite, pyrrhotite and pyrite (Figure 3c). Bornite is present as anhedral crystal and typically replaced by chalcopyrite. Chalcopyrite is widespread in the veins and occurs as subhedral

to anhedral crystal or as disseminations (Figure 3c). The bornite and chalcopyrite at the surface are generally oxidized to malachite (Figure 3d). Molybdenite occurs in the form of flakes and small aggregates. In addition, disseminated molybdenite is also observed in the porphyries. Locally, the skarn-type mineralization, which consists of garnet, pyroxene, epidote, chlorite, quartz, calcite, chalcopyrite, bornite, molybdenite, and pyrite, is observed in the carbonate.

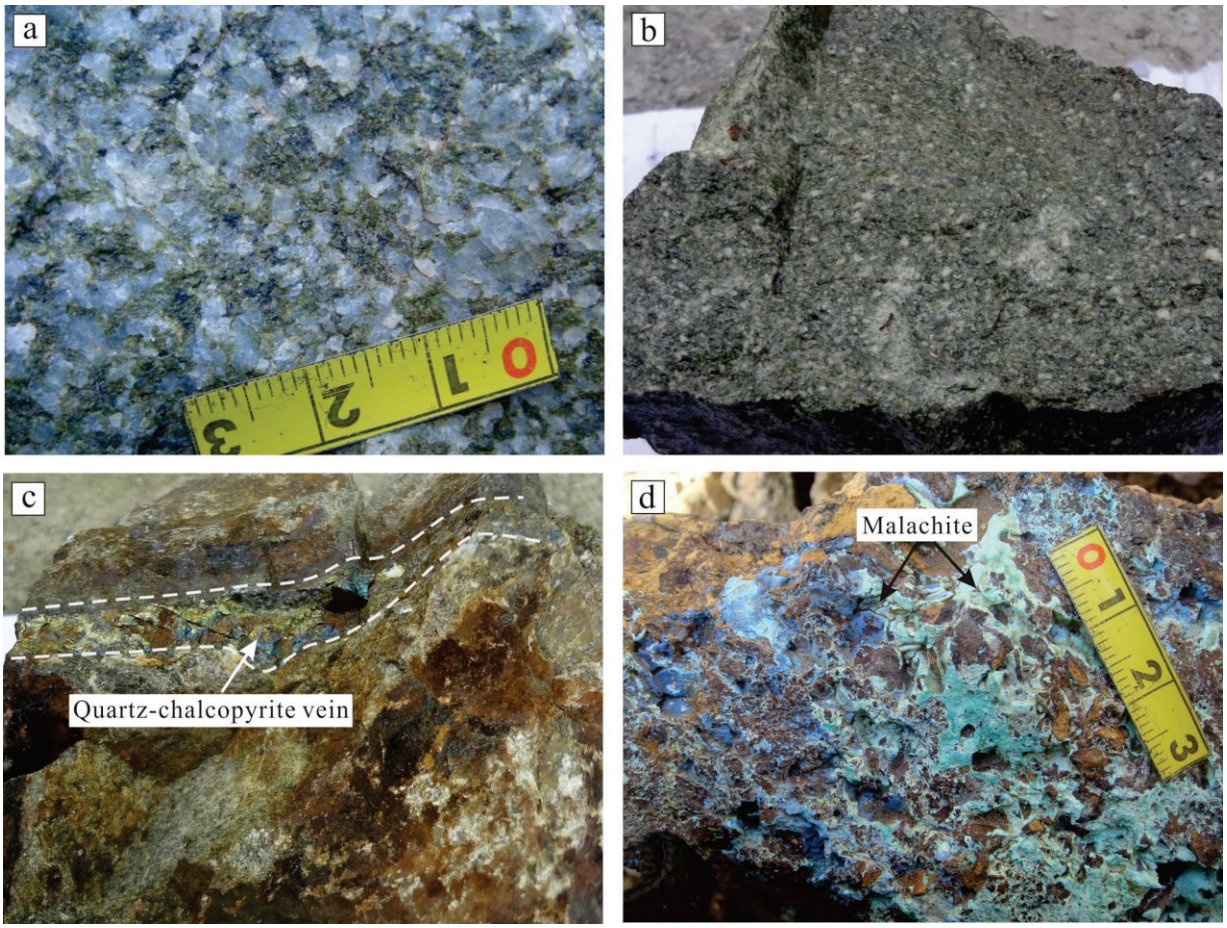


Figure 3. (**a**) Photograph of the granitic porphyry. Note that the biotite and hornblende are intensively replaced by epidote. (**b**) Photograph of the diorite porphyry. (**c**) Quartz-chalcopyrite vein crosscut the volcanic rock. (**d**) Chalcopyrite is oxidized to malachite at the surface.

Propylitic alteration is intensive and pervasively developed in the volcano-sedimentary rocks and porphyries. It forms an alteration halo with a diameter of 2 km, enveloping the orebodies. The propylitic alteration is characterized by the development of widespread epidote and chlorite with minor sericite, actinolite, calcite, pyrite and chalcopyrite. In the volcano-sedimentary rocks and porphyries adjacent to the orebodies, the mafic minerals (e.g., biotite and hornblende) are almost completely replaced by the epidote and chlorite (Figure 3a). In addition to propylitic alteration, the quartz-sericite alteration, which is dominated by quartz, sericite, muscovite, pyrite, chlorite, bornite, chalcopyrite, pyrrhotite and molybdenite, is locally presented.

4. Analytical Methods

Representative granitic porphyry and diorite porphyry samples from the Cahanwusu deposit were collected for zircon LA-ICP-MS U-Pb dating and in-situ Hf isotopic analyses. The fresh porphyry samples were powdered into 80 meshes and deslimed in the purified water. This was followed by density separation and magnetic separation. After hand-

picking, the zircon grains were mounted in epoxy and polished to nearly a half section to expose internal structures. Prior to U-Pb and Hf isotopic analyses, all the zircon grains were investigated in optical microscopy and cathodoluminescent (CL) images to make sure that all the analyses were performed on the least fractured, inclusion-free zones.

4.1. Zircon U-Pb Dating

Zircon U-Pb analyses were performed using ELAN DRC-e ICP-MS equipped with a 193 nm Excimer laser at the State Key Laboratory of Ore Deposit Geochemistry (SKLODG), Institute of Geochemistry, Chinese Academy of Sciences. The measurement procedures and analytical conditions were similar to those described by Zhang et al. 2016 [22]. During the analyses, the spot sizes were 32 μm, whereas the laser repetition rates of the laser ablation system were 8 Hz. Helium and Argon were applied as carrier gas and make-up gas, respectively. The U-Pb fractionation and instrumental mass discrimination of zircon were normalized using the matrix-matched external zircon standard 91,500 ($^{206}Pb/^{208}U$ age = 1062 Ma; Supplementary Materials Table S1) [23]. Two standard analyses were measured after every ten unknown spots. The data acquisition of each U-Pb analysis includes 20 s of gas blank, which is followed by 50 s of data acquisition. Off-line selection, integration of background and analytic signals, and mass bias calibrations were performed using ICPMSDataCal [24]. Age calculations and Concordia diagrams were conducted using the software Isoplot 3.0 [25].

4.2. Zircon Hf Isotope Analyses

In situ zircon Hf isotopic measurements were carried out using a Neptune MC-ICPMS equipped with a 193 nm ArF excimer laser ablation system at the SKLODG. The detailed operating conditions and analytical procedures are similar to those reported by Zhang et al. 2016 [22]. The analyses of zircon Lu-Hf isotopes were carried out on the same spots of U-Pb dating, using a laser beam diameter of 60 μm, a laser repetition rate of 10 Hz, and a laser beam energy density of 2.64–3.52 J/cm^2. Helium was used as a carrier gas to transport the ablated material from the laser-ablation cell to the ICPMS torch. Each measurement consisted of 20 s of background signal acquisition followed by 50 s of ablation signal acquisition. Zircon standard 91500 was used for external standard calibration to further optimize the analysis and test results. Two analyses of the standard were measured after every ten unknown spots. The standard zircons of 91500 yielded average $^{176}Hf/^{177}Hf$ values of 0.282298 ± 0.000012 (Supplementary Materials Table S2), in agreement with their recommended values (0.282297 ± 0.000044) [26,27]. Off-line selection and integration were also performed by using ICPMSDataCal.

5. Results

5.1. Zircon U-Pb Ages

Zircon grains from the granitic porphyry are generally colorless or transparent, euhedral to subhedral, and elongate to stubby in shape (Figure 4a). They have length varies from 100 to 200 μm with length-to-width ratios of 2:1 to 3:1. Most zircon grains exhibit typical magmatic oscillatory zonation and few contain inherited cores (Figure 4a). The detailed U-Pb results are reported in Table 1 and the U-Pb concordia diagram and weighted mean $^{206}Pb/^{238}U$ ages are shown in Figure 5. Zircon grains from the granitic porphyry have Th/U ratios varying between 0.35 and 0.93 (average 0.52; Table 1), which is consistent with a magmatic origin [28,29]. On the U-Pb Wetherill concordia diagram, the analyses yield a concordia age of 328.8 ± 3.5 Ma (Figure 5a). This age is consistent with the weighted mean $^{206}Pb/^{238}U$ ages of 328.6 ± 2.6 Ma (MSWD = 0.52; n = 23) (Figure 5b).

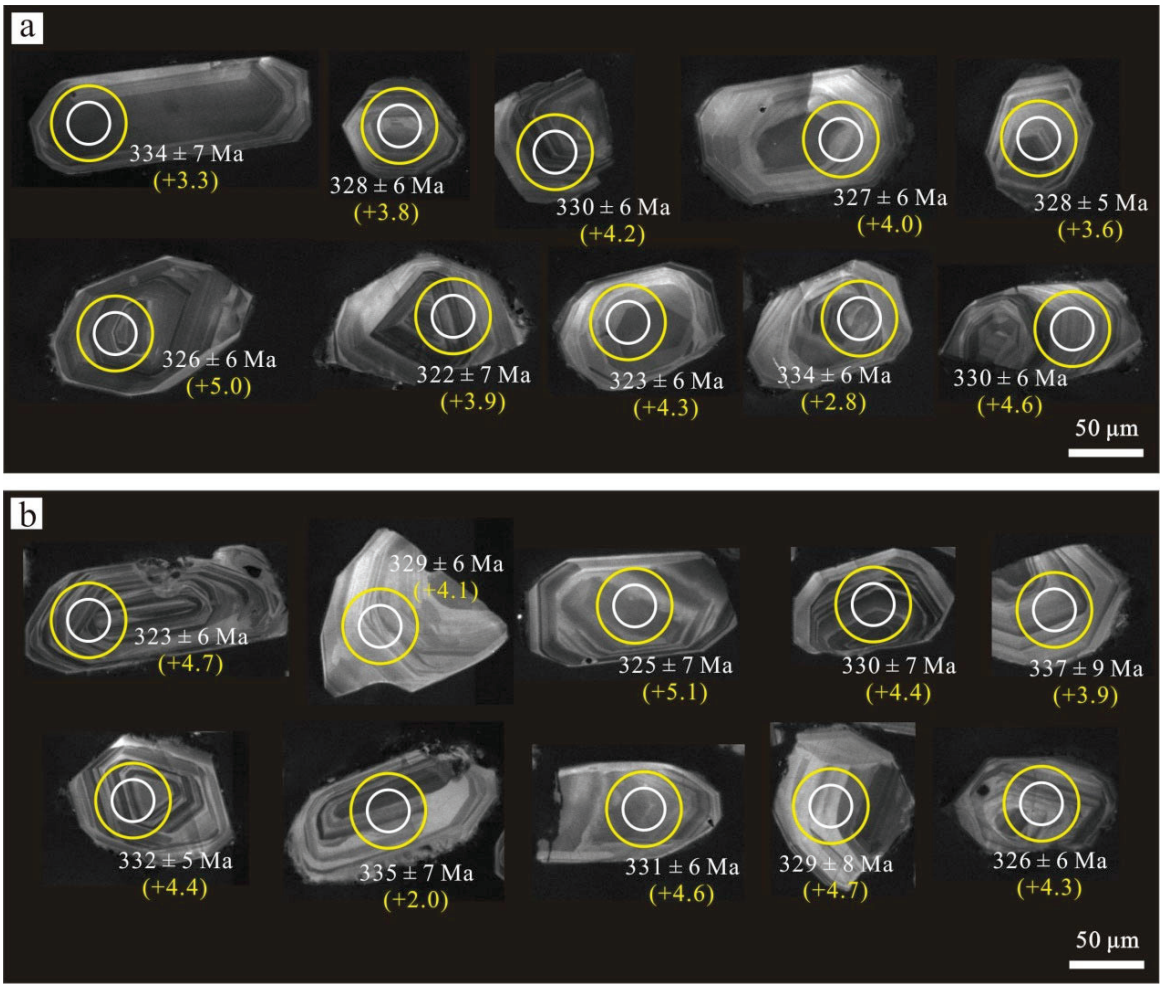


Figure 4. Representative cathodoluminescence images of zircon grains in the granitic porphyry (**a**) and diorite porphyry (**b**). The U-Pb dating spots are denoted by white circles and the Lu-Hf isotopic spots are denoted by yellow circles.

Table 1. Zircon LA-ICP-MS U-Pb ages of granitic porphyry and diorite porphyry in the Cahanwusu deposit.

Spots	Th (ppm)	U (ppm)	Th/U	$^{207}Pb/^{206}Pb$		$^{207}Pb/^{235}U$		$^{206}Pb/^{238}U$		$^{207}Pb/^{206}Pb$		$^{207}Pb/^{235}U$		$^{206}Pb/^{238}U$		Concordance
				Ratio	1sigma	Ratio	1sigma	Ratio	1sigma	Age	1sigma	Age	1sigma	Age	1sigma	
Granitic Porphyry																
CH12-01	325	693	0.47	0.0597	0.0036	0.4496	0.0251	0.0532	0.0011	594	131	377	17.5	334	6.83	97%
CH12-02	355	611	0.58	0.0570	0.0034	0.4218	0.0228	0.0531	0.0011	500	131	357	16.3	334	6.47	95%
CH12-03	350	751	0.47	0.0528	0.0028	0.3832	0.0178	0.0522	0.0009	320	122	329	13.1	328	5.77	99%
CH12-04	244	518	0.47	0.0555	0.0032	0.4116	0.0247	0.0524	0.0010	435	134	350	17.8	330	6.16	98%
CH12-05	234	673	0.35	0.0540	0.0026	0.3957	0.0187	0.0521	0.0009	369	109	339	13.6	327	5.66	96%
CH12-06	179	321	0.56	0.0531	0.0036	0.3920	0.0252	0.0537	0.0013	332	154	336	18.4	337	7.73	99%
CH12-07	560	916	0.61	0.0569	0.0027	0.4080	0.0179	0.0514	0.0008	487	99.1	347	12.9	323	5.15	96%
CH12-09	283	634	0.45	0.0551	0.0032	0.4059	0.0239	0.0520	0.0009	417	128	346	17.3	327	5.71	94%
CH12-10	562	914	0.61	0.0546	0.0025	0.4003	0.0180	0.0521	0.0008	394	97.2	342	13.1	328	5.15	95%
CH12-11	125	257	0.48	0.0589	0.0056	0.4146	0.0328	0.0535	0.0014	565	208	352	23.5	336	8.37	95%
CH12-12	381	722	0.53	0.0577	0.0027	0.4175	0.0185	0.0519	0.0010	517	102	354	13.3	326	6.09	97%
CH12-14	264	504	0.52	0.0647	0.0043	0.4583	0.0293	0.0512	0.0012	765	142	383	20.4	322	7.10	96%
CH12-15	168	382	0.44	0.0601	0.0037	0.4503	0.0282	0.0530	0.0013	606	140	377	19.7	333	7.77	97%
CH12-16	208	470	0.44	0.0538	0.0033	0.3864	0.0217	0.0515	0.0010	365	141	332	15.9	323	6.40	97%
CH12-17	279	593	0.47	0.0564	0.0029	0.4108	0.0197	0.0519	0.0010	465	113	349	14.2	326	5.90	93%
CH12-18	292	648	0.45	0.0537	0.0026	0.4058	0.0191	0.0532	0.0009	367	105	346	13.8	334	5.62	96%
CH12-19	349	641	0.55	0.0531	0.0029	0.4017	0.0205	0.0537	0.0011	332	121	343	14.9	337	6.81	98%
CH12-20	104	272	0.38	0.0518	0.0038	0.3886	0.0281	0.0530	0.0014	280	167	333	20.6	333	8.56	99%
CH12-22	427	555	0.77	0.0565	0.0032	0.4103	0.0227	0.0512	0.0011	472	124	349	16.3	322	6.46	93%
CH12-23	367	554	0.66	0.0583	0.0031	0.4340	0.0222	0.0525	0.0010	543	110	366	15.7	330	5.91	98%
CH12-24	685	734	0.93	0.0546	0.0027	0.4066	0.0185	0.0527	0.0010	394	109	346	13.4	331	5.94	95%
CH12-25	374	763	0.49	0.0536	0.0026	0.3915	0.0177	0.0517	0.0009	354	107	335	12.9	325	5.82	96%
CH12-26	135	362	0.37	0.0624	0.0038	0.4533	0.0267	0.0517	0.0013	687	130	380	18.7	325	7.70	95%

Table 1. *Cont.*

Spots	Th (ppm)	U (ppm)	Th/U	$^{207}Pb/^{206}Pb$		$^{207}Pb/^{235}U$		$^{206}Pb/^{238}U$		$^{207}Pb/^{206}Pb$		$^{207}Pb/^{235}U$		$^{206}Pb/^{238}U$		Concordance
				Ratio	1sigma	Ratio	1sigma	Ratio	1sigma	Age	1sigma	Age	1sigma	Age	1sigma	
Diorite porphyry																
CH15-01	180	278	0.6467	0.0541	0.0031	0.3928	0.0209	0.0514	0.0010	376	128	336	15.2	323	6.3	97%
CH15-02	313	422	0.7413	0.0543	0.0026	0.3916	0.0182	0.0524	0.0009	383	107	336	13.3	329	5.5	98%
CH15-03	157	318	0.4950	0.0568	0.0032	0.4050	0.0217	0.0523	0.0010	483	129	345	15.7	329	6.2	96%
CH15-04	364	490	0.7425	0.0513	0.0022	0.3702	0.0155	0.0522	0.0009	254	100	320	11.5	328	5.3	97%
CH15-05	116	181	0.6377	0.0556	0.0036	0.3949	0.0247	0.0517	0.0011	435	146	338	18.0	325	6.6	96%
CH15-06	97.3	195	0.4984	0.0541	0.0032	0.3825	0.0218	0.0511	0.0012	376	135	329	16.0	321	7.2	97%
CH15-08	600	644	0.9308	0.0513	0.0022	0.3795	0.0158	0.0520	0.0009	254	98.1	327	11.6	327	5.3	99%
CH15-09	151	240	0.6264	0.0533	0.0036	0.3836	0.0236	0.0519	0.0010	339	147	330	17.3	326	6.2	98%
CH15-10	190	318	0.5965	0.0553	0.0028	0.4041	0.0198	0.0525	0.0011	433	147	345	14.3	330	6.7	95%
CH15-11	57.2	125	0.4573	0.0573	0.0049	0.4066	0.0287	0.0537	0.0014	502	189	346	20.7	337	8.8	97%
CH15-13	406	510	0.7964	0.0533	0.0023	0.3941	0.0159	0.0529	0.0008	339	98.1	337	11.6	332	4.9	98%
CH15-14	87.8	174	0.5054	0.0550	0.0036	0.4185	0.0267	0.0545	0.0012	413	146	355	19.1	342	7.4	96%
CH15-15	142	255	0.5559	0.0577	0.0036	0.4273	0.0239	0.0545	0.0011	520	137	361	17.0	342	6.8	94%
CH15-16	130	235	0.5544	0.0557	0.0037	0.4079	0.0248	0.0533	0.0012	443	148	347	17.9	335	7.1	96%
CH15-17	94.4	183	0.5165	0.0593	0.0041	0.4371	0.0272	0.0541	0.0014	589	145	368	19.2	340	8.4	98%
CH15-19	177	285	0.6213	0.0590	0.0034	0.4206	0.0216	0.0527	0.0010	565	126	356	15.4	331	6.1	97%
CH15-20	76.1	146	0.5193	0.0578	0.0045	0.4238	0.0301	0.0550	0.0014	524	174	359	21.5	345	8.6	96%
CH15-21	67.3	127	0.5303	0.0657	0.0054	0.4391	0.0296	0.0523	0.0013	798	174	370	20.9	329	7.8	98%
CH15-22	119	182	0.6542	0.0531	0.0037	0.3948	0.0261	0.0540	0.0012	345	157	338	19.0	339	7.1	99%
CH15-23	237	488	0.4860	0.0555	0.0025	0.3978	0.0167	0.0518	0.0009	432	98.1	340	12.1	326	5.6	95%
CH15-24	193	360	0.5366	0.0540	0.0028	0.4038	0.0201	0.0540	0.0011	372	119	344	14.6	339	6.7	98%

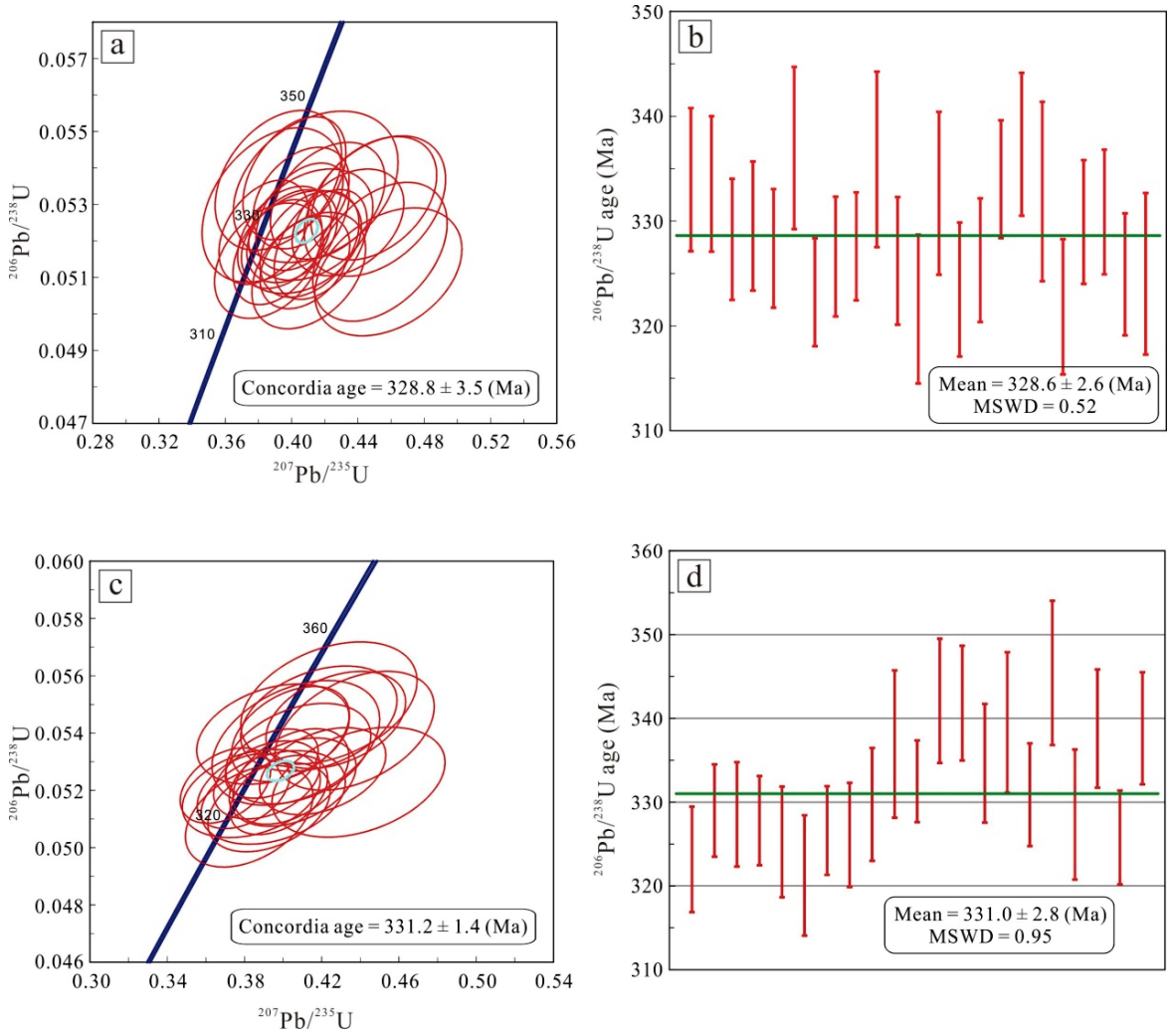


Figure 5. LA-ICP-MS U-Pb ages of zircon from the granitic porphyry and diorite porphyry in the Cahanwusu deposit. (**a**) Wetherill concordia diagram and (**b**) weighted average $^{206}Pb/^{238}U$ ages of zircon from the granitic porphyry. (**c**) Wetherill concordia diagram and (**d**) weighted average $^{206}Pb/^{238}U$ ages of zircon from the diorite porphyry.

Zircon grains from the diorite porphyry have a morphology similar to that in the granitic porphyry (Figure 4b). They have Th/U ratios varying from 0.45 and 0.92 (average 0.58; Table 1), indicating they are magmatic in origin [28,29]. On the U-Pb Wetherill concordia diagram, the analyses yield a concordia age of 331.2 ± 1.4 Ma (Figure 5c). The weighted mean $^{206}Pb/^{238}U$ ages is 331.0 ± 2.8 Ma (MSWD = 0.95; n = 21) (Figure 5d). These ages are consistent with that of zircon grains in the granitic porphyry (Figure 5).

5.2. Zircon Hf Isotopes

Detailed in-situ Lu-Hf isotopic data of zircon from the granitic porphyry and diorite porphyry are presented in Table 2. Zircon grains from the granitic porphyry have $^{176}Hf/^{177}Hf$ ratios of 0.282659 to 0.282727 (average of 0.282692; Table 2). The calculated $\varepsilon_{Hf}(t)$ values (age-corrected using the U-Pb age of individual grains) are similar, ranging from +2.83 to +5.42 with an average value of +4.09 (Table 2). All the analyses fall between the chondrite uniform reservoir reference line and the depleted mantle evolution line (Figure 6). The corresponding two-stage Hf model ages (T_{DM2}) vary from 992 to 1155 Ma (average of 1075 Ma) (Table 2). On the other hand, zircon grains from the diorite porphyry have $^{176}Hf/^{177}Hf$ ratios of 0.282637 to 0.282725 (average of 0.282690). The calculated $\varepsilon_{Hf}(t)$ values (age-corrected using the U-Pb age of individual grains) are similar to that of zircon in the granitic porphyry, varying from +2.0 to +5.1 (average of +4.1; Figure 6). The T_{DM2} ages vary from 1013 to 1208 Ma (average of 1079 Ma), also consistent with that of zircon grains in the granitic porphyry (Table 2).

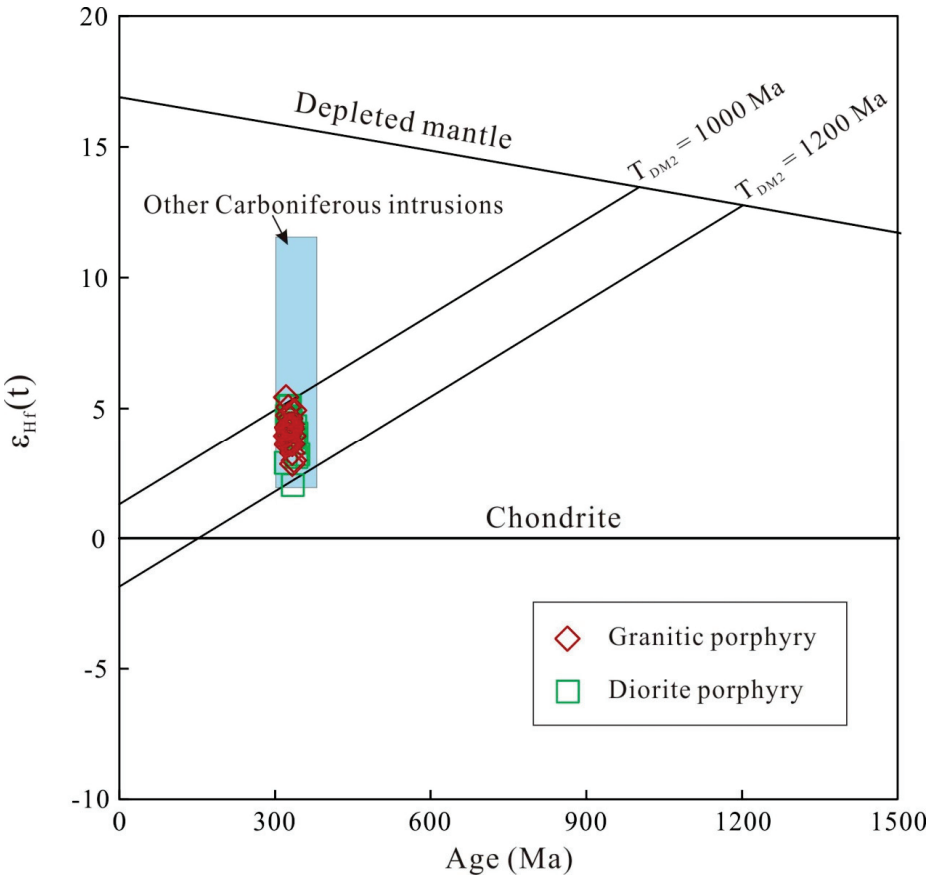


Figure 6. The $\varepsilon_{Hf}(t)$ vs. U-Pb age (Ma) diagram of the granitic porphyry and diorite porphyry in the Cahanwusu deposit. The area of other Carboniferous intrusions in Awulale Mountain is plotted by Tang et al. (2014) [30], Yan et al. (2015) [31], and Sun et al. (2021, 2022) [32,33].

Table 2. Hf isotopes of zircons from the granitic porphyry and diorite porphyry in the Cahanwusu deposit.

Spots	$^{176}Lu/^{177}Hf$	1σ	$^{176}Hf/^{177}Hf$	1σ	$\varepsilon_{Hf}(t)$	1σ	T_{DM1}	1σ	T_{DM2}	1σ
Granitic Porphyry										
CH12-01	0.001403	0.000010	0.282669	0.000018	3.26	0.64	835	25.7	1128	40.4
CH12-02	0.001606	0.000087	0.282680	0.000017	3.60	0.60	824	24.5	1106	38.2
CH12-03	0.001168	0.000016	0.282682	0.000018	3.77	0.64	812	25.5	1096	40.4
CH12-04	0.001018	0.000010	0.282694	0.000016	4.23	0.57	792	22.6	1067	35.9
CH12-05	0.001135	0.000003	0.282699	0.000016	4.38	0.57	787	22.7	1057	35.9
CH12-06	0.001293	0.000034	0.282660	0.000011	2.96	0.39	846	15.7	1147	24.7
CH12-07	0.001359	0.000013	0.282678	0.000018	3.59	0.64	822	25.7	1107	40.4
CH12-09	0.001334	0.000022	0.282689	0.000017	3.98	0.60	805	24.2	1082	38.2
CH12-10	0.001491	0.000018	0.282679	0.000019	3.59	0.67	823	27.2	1107	42.6
CH12-11	0.001388	0.000011	0.282688	0.000018	3.94	0.64	808	25.7	1085	40.4
CH12-12	0.001535	0.000025	0.282720	0.000021	5.04	0.74	765	30.1	1015	47.2
CH12-14	0.001058	0.000017	0.282686	0.000019	3.94	0.67	804	26.9	1085	42.7
CH12-15	0.001384	0.000056	0.282696	0.000018	4.22	0.64	797	25.7	1067	40.4
CH12-16	0.000990	0.000026	0.282695	0.000012	4.27	0.42	790	17.0	1064	27.0
CH12-17	0.001237	0.000009	0.282687	0.000022	3.95	0.78	806	31.3	1085	49.4
CH12-18	0.001832	0.000035	0.282659	0.000018	2.83	0.64	860	26.0	1156	40.4
CH12-19	0.001041	0.000002	0.282713	0.000019	4.92	0.67	765	26.9	1024	42.7
CH12-20	0.001347	0.000075	0.282700	0.000015	4.39	0.53	790	21.4	1057	33.7
CH12-22	0.001003	0.000038	0.282727	0.000014	5.42	0.50	745	19.8	992	31.5
CH12-23	0.001152	0.000012	0.282705	0.000018	4.61	0.64	779	25.5	1043	40.5
CH12-24	0.001255	0.000012	0.282697	0.000016	4.30	0.57	792	22.8	1063	35.9
CH12-25	0.001733	0.000030	0.282712	0.000017	4.73	0.60	781	24.5	1036	38.2
CH12-26	0.001641	0.000063	0.282696	0.000019	4.18	0.67	802	27.3	1070	42.7
Diorite Porphyry										
CH15-01	0.001253	0.000005	0.282707	0.000019	4.70	0.67	778	27.0	1039	42.7
CH15-02	0.002497	0.000180	0.282725	0.000016	5.07	0.57	778	23.9	1016	36.1
CH15-03	0.001476	0.000026	0.282692	0.000018	4.12	0.64	804	25.8	1076	40.4
CH15-04	0.001392	0.000006	0.282695	0.000020	4.25	0.71	798	28.5	1068	44.9
CH15-05	0.001217	0.000004	0.282718	0.000014	5.10	0.50	762	19.9	1014	31.5
CH15-06	0.001352	0.000043	0.282656	0.000016	2.87	0.57	853	22.8	1155	35.9
CH15-08	0.002171	0.000140	0.282699	0.000016	4.22	0.57	809	23.5	1070	36.0
CH15-09	0.001465	0.000020	0.282706	0.000012	4.62	0.42	784	17.2	1044	27.0
CH15-10	0.001126	0.000003	0.282697	0.000020	4.37	0.71	790	28.3	1060	44.9
CH15-11	0.001149	0.000004	0.282683	0.000014	3.87	0.50	810	19.8	1092	31.4
CH15-13	0.001150	0.000004	0.282699	0.000013	4.44	0.46	787	18.4	1056	29.2
CH15-14	0.001118	0.000006	0.282661	0.000019	3.10	0.67	840	26.9	1140	42.6
CH15-15	0.001203	0.000018	0.282688	0.000015	4.04	0.53	804	21.3	1081	33.7
CH15-16	0.002177	0.000065	0.282637	0.000018	2.02	0.64	900	26.3	1209	40.3
CH15-17	0.001253	0.000012	0.282696	0.000018	4.31	0.64	794	25.6	1064	40.4
CH15-19	0.000946	0.000006	0.282701	0.000019	4.56	0.67	780	26.8	1048	42.7
CH15-20	0.000825	0.000010	0.282662	0.000017	3.20	0.60	833	23.9	1134	38.1
CH15-21	0.001016	0.000013	0.282705	0.000024	4.68	0.85	776	33.9	1040	53.9
CH15-22	0.001241	0.000006	0.282677	0.000014	3.64	0.50	821	19.9	1106	31.4
CH15-23	0.001360	0.000021	0.282695	0.000013	4.25	0.46	797	18.5	1068	29.2
CH15-24	0.001603	0.000030	0.282685	0.000016	3.85	0.57	817	23.0	1093	35.9

ε_{Hf} (t) = $(((^{176}Hf/^{177}Hf)_S - (^{176}Lu/^{177}Hf)_S \times (e^{\lambda t} - 1))/((^{176}Hf/^{177}Hf)_{CHUR,0} - (^{176}Lu/^{177}Hf)_{CHUR} \times (e^{\lambda t} - 1) - 1) \times 10{,}000$; $T_{DM1} = 1/\lambda \times \ln(1 + ((^{176}Hf/^{177}Hf)_S - (^{176}Hf/^{177}Hf)_{DM})/((^{176}Lu/^{177}Hf)_S - (^{176}Lu/^{177}Hf)_{DM}))$; $T_{DM2} = T_{Hf1} - (T_{Hf1} - t)((f_{cc} - f_s)/(f_{cc} - f_{DM}))$. Note: the $\varepsilon_{Hf}(t)$ ratios were calculated with the age in Table 1.

6. Discussion

6.1. New Episode of Cu Mineralization in Awulale Mountain

The granitic porphyry and diorite porphyry are the exclusive intrusions in the Cahanwusu Cu deposit (Figure 2). The two pluses of porphyryies occur as plugs and host abundant quartz-chalcopyrite veins. In addition, they are strongly overprinted by propylitic alteration, where mafic minerals such as biotite and hornblende are mostly replaced by epidote and chlorite (Figure 3a). These features fit well with the causative intrusions in the porphyry Cu deposits [34,35]. This indicates that the mineralization is genetically associated with the granitic porphyry and diorite porphyry in the Cahanwusu deposit.

Previous studies have shown that the Cu mineralization in the Awulale Fe-Cu Metallogenetic Belt mostly occurred in the Permian. For example, the mineralization associated albite porphyry in the 109 deposit yields zircon U-Pb ages of 300 ± 4 Ma [8], the diabase, which hosts Cu mineralization in the Qunjsai deposit, has zircon U-Pb ages of 289.9 ± 1.4 Ma [9], and the granite porphyry in the Nulasai Cu deposit has zircon U-Pb ages of 288.3 ± 3.0 Ma. On the other hand, the sulfides in the deposit yield Re-Os ages of 283.5 ± 5.8 Ma [36]. However, our new results show that the mineralization-associated granitic porphyry and diorite porphyry in the Cahanwusu deposit have zircon U-Pb ages of 328.6 ± 2.6 Ma and 331 ± 2.8 Ma, respectively (Figure 5). This indicates that mineralization in the Cahanwusu deposit occurred at ca. 330 Ma, significantly older than that of other Cu deposits in Awulale Mountain. On this basis, we suggest that the Cahanwusu deposit represents an old episode of Cu mineralization in Awulale Mountain.

6.2. Tectonic Setting and Magma Sources

Detailed zircon U-Pb ages demonstrate that the Cahanwusu deposit was generated in the Carboniferous (Figure 5). The tectonic evolution of Awulale Mountain in the Late Paleozoic is still controversial. Two main models have been proposed, including (1) intra-continental rifting and post-collisional mantle plume activity in the extension setting [37–39], and (2) active continental arc setting related to the northward subduction of the South Tianshan Ocean [17,40–44]. The Carboniferous granitoids in Awulale Mountain are all calc-alkaline I-type granites with subduction-related features, e.g., enrichment in large ion lithophile elements (LILEs) relative to high field strength elements (HFSEs), and depletion of Nb and Ta [15,43–45]. In addition, the widely distributed Dahalajunshan Formation, which consisted of volcanic rocks with Early Devonian to Late Carboniferous ages (417 Ma to 304 Ma), also displays arc type signatures [1,40,46,47]. These observations indicate that the South Tianshan Ocean had been subducting northward under the Yili block during the Carboniferous (Figure 7a). Therefore, we suggest that the Cahanwusu deposit was formed in the continental arc setting related to the northward subduction of the South Tianshan Ocean. However, Permian shoshonitic rocks and underplating adakite with post-subduction signatures have widely been reported in Awulale Mountain [32,44,48–50]. This implies that the subduction of the South Tianshan Ocean had ceased and Awulale Mountains entered a post-collisional extensional setting since the Permian (Figure 7b).

The granitic porphyry and diorite porphyry in the Cahanwusu deposit have similar zircon U-Pb ages and Hf isotopic compositions (Figures 5 and 6). This indicates that the two pluses of porphyries share similar magma sources. The granitic porphyry and diorite porphyry have positive $\varepsilon_{Hf}(t)$ values varying from +2.83 to +5.42 (average of +4.09) and +2.0 to +5.1 (average of +4.1), respectively (Figure 6), which is inconsistent with granitoids derived from renewed melting or deep melting of ancient crust. However, this positive $\varepsilon_{Hf}(t)$ value is similar to other Carboniferous intrusions in Awulale Mountain (Figure 6), such as the Wuling hornblende gabbro [31] and Zhongyangchang granitoids [30]. Actually, Paleozoic granitoids with positive $\varepsilon_{Nd}(t)$ and/or $\varepsilon_{Hf}(t)$ values have been widely reported in the CAOB [22,30,32,50–55]. This isotopic anomaly was interpreted to have resulted from the involvement of juvenile materials in their mantle source.

The juvenile crust has played an important role in the generation of the Phanerozoic granitoids in the CAOB [16,55–58]. During the Neoproterozoic to Mesozoic orogeny, large amounts of juvenile materials were incorporated into the crust, representing the most important crustal growth event in the Phanerozoic [16,57–59]. Most juvenile crusts in the CAOB were related to the accretion of arc complexes that were derived from the cooling of mantle-derived magmas in the course of the subduction process [58]. However, mantle underplating in post-collisional settings also played an important role in the crustal growth

of juvenile crusts in the CAOB [55,57]. It is proposed that the voluminous A-type granites with positive $\varepsilon_{Nd}(t)$ and $\varepsilon_{Hf}(t)$ values in the post-collision setting were derived from the partial melting of the underplated basaltic magmas and subsequent extensive fractional crystallization [55]. However, A-type granites contemporary with the granitic porphyry and diorite porphyry in the Cahanwusu deposit have not been documented in Awulale Mountain. Therefore, the crustal growth model that involves mantle underplating in post-collisional settings can be excluded. As mentioned earlier, the Carboniferous granitoids in Awulale Mountain generally exhibit subduction-related features, i.e., enrichment in LILEs relative to HFSEs, and depletion of Nb and Ta [15,43–45]. On this basis, we suggest that the magmas of granitic porphyry and diorite porphyry could be derived from the partial melting of the juvenile lower crust which originated from cooling of mantle-derived magmas related to the subduction process.

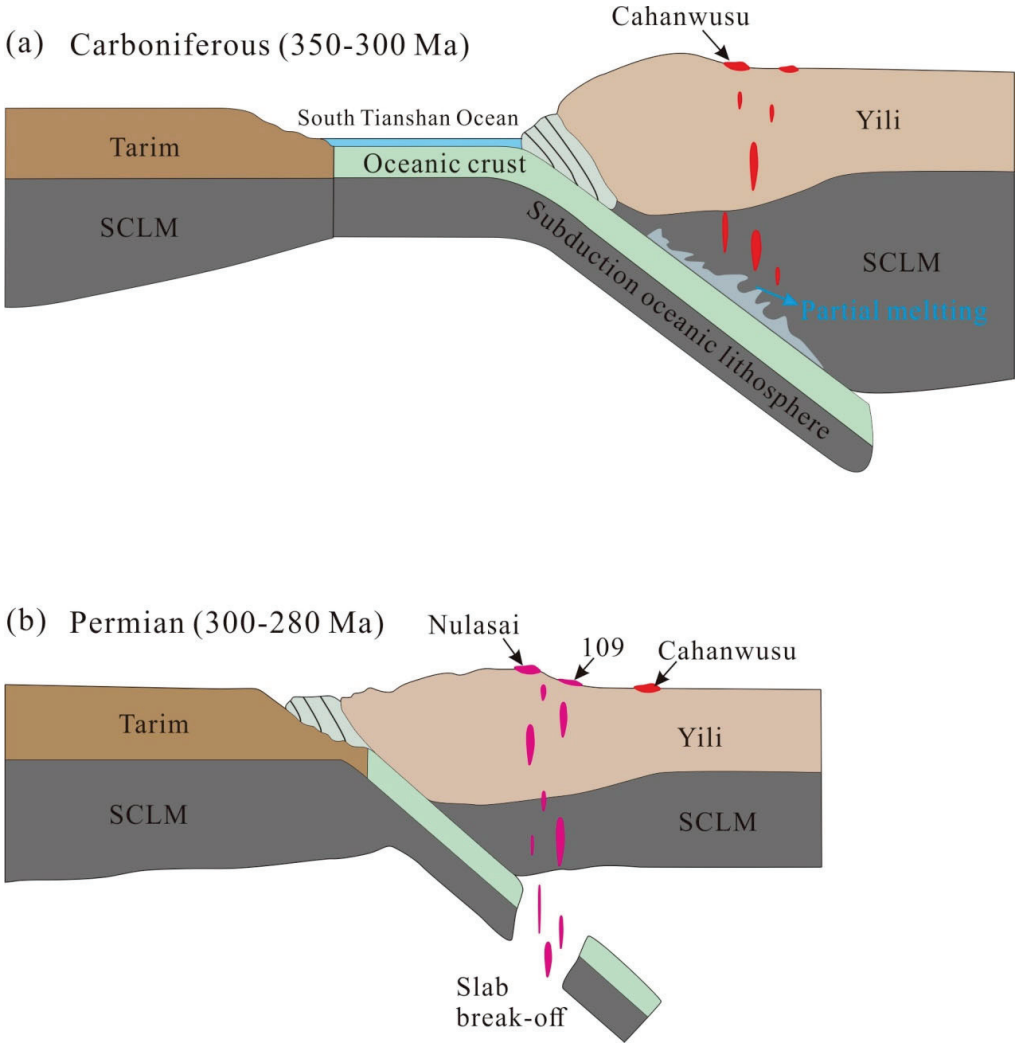


Figure 7. Sketch model showing the tectonic evolution of Awulale Mountain and the corresponding Cu mineralization in the Late Paleozoic. (**a**) In the Carboniferous, the South Tianshan Oceanic Crust subducted beneath the Yili-central Tianshan, resulting in the formation of Cahanwusu Cu deposit. (**b**) In the Permian, break-off of the subducted slab in the post-collisional setting triggered the upwelling of the depleted asthenospheric mantle and produced the Nalusai and 109 deposits. SCLM = subcontinental lithospheric mantle.

6.3. Implication for Regional Mineralization

Our new results show that the Cahanwusu deposit represents a new episode of Cu mineralization in the Awulale metallogenetic belt formed in the subduction setting

(Figure 7a). This has important implications for regional exploration of porphyry Cu deposits in the belt. Porphyry Cu deposits can be formed in both subduction and post-collision settings [60–62]. Most porphyry Cu deposits in the Awulale metallogenetic belt are clustered in the Permian [2,4,8,9,63,64]. Some causative intrusions in these deposits show an affinity of A-type granitic rocks which were generally related to extensional settings, such as the 109 and Qunjisayi deposits [8,65]. Therefore, these porphyry Cu deposits were interpreted to be formed in a post-collision extensional setting (Figure 7b). In contrast, the Cahanwusu deposit was formed in the Carboniferous during the subduction of the South Tianshan Ocean. Actually, the subduction of the South Tianshan Ocean in the Carboniferous has resulted in a variety of calc-alkaline I-type granitoids in Awulale Mountain [15,43–45]. The calc-alkaline I-type granitoids formed in the subduction setting are generally potential targets for porphyry-type Cu mining [35,66,67]. Therefore, although Cu mineralization associated with these Carboniferous granitoids has rarely been documented currently, our new results of the Cahanwusu deposit indicate that these Carboniferous granitoids are also potential candidates for Cu exploration in Awulale Mountain.

7. Conclusions

The granitic porphyry and diorite porphyry in the Cahanwusu deposit have zircon U-Pb ages of 328.6 ± 2.6 Ma and 331 ± 2.8 Ma, respectively. These ages are significantly older than that of other Cu deposits in the Awulale metallogenetic belt, indicating that the Cahanwusu deposit represents a new episode of Cu mineralization in the belt. The Cahanwusu deposit was formed in a subduction setting, distinguishable from other Cu deposits in the belt which were generally formed in the post-collision extensional setting. The granitic porphyry and diorite porphyry exhibit positive $\varepsilon_{Hf}(t)$ values, and the magmas of these causative intrusions were derived from partial melting of the juvenile lower crust which originated from the cooling of mantle-derived magmas related to the subduction process. Our new results highlight that the Carboniferous granitoids in Awulale Mountain are potential candidates for Cu exploration.

Supplementary Materials: The following supporting information can be downloaded at: https://www.mdpi.com/article/10.3390/min15040380/s1, Table S1: LA-ICP-MS U-Pb results of zircon standard 91500; Table S2: LA-MC-ICP-MS Hf isotopes of zircon standard 91500.

Author Contributions: Conceptualization, W.Z. and X.-C.Z.; methodology, M.-X.C. and M.-L.Y.; software, W.-H.Y.; validation, W.Z. and X.-C.Z.; investigation, W.Z., W.-H.Y. and X.-C.Z.; data curation, M.-X.C. and M.-L.Y.; writing—original draft preparation, W.Z.; writing—review and editing, W.Z. and X.-C.Z.; supervision, X.-C.Z.; project administration, W.Z. and X.-C.Z.; funding acquisition, W.Z. and X.-C.Z. All authors have read and agreed to the published version of the manuscript.

Funding: This study was supported by the National Natural Science Foundation of China (41872097) and Yunnan Fundamental Research Projects (202301AU070004). Additional support was provided by the Yunnan Key Research and Development Plan Program (Grant NO. 202303AP140020).

Data Availability Statement: Data is contained within the article and Supplementary Materials.

Acknowledgments: We are grateful to Zhi-Hui Dai and Hong-Feng Tang for their help with the analyses. Ding-Jin Wu and Jing-Liang Cao are thanked for their assistance in the field.

Conflicts of Interest: The authors declare no conflicts of interest.

References

1. Ge, S.; Zhai, M.; Safonova, I.; Li, D.; Zhu, X.; Zuo, P.; Shan, H. Whole-rock geochemistry and Sr–Nd–Pb isotope systematics of the Late Carboniferous volcanic rocks of the Awulale metallogenic belt in the western Tianshan Mountains (NW China): Petrogenesis and geodynamical implications. *Lithos* **2015**, *228–229*, 62–77. [CrossRef]

2. Liu, R.; Chen, G. Characteristics of rare earth elements, Zr, and Hf in ore-bearing porphyries from the Western Awulale Metallogenic Belt, Northwestern China and their application in determining metal fertility of granitic magma. *Resour. Geol.* **2018**, *69*, 193–210.
3. Shan, Q.; Zhang, B.; Luo, Y.; Zhou, C.P.; Yu, X.Y.; Zeng, Q.S.; Yang, W.B.; Niu, H.C. Characteristics and trace element geochemistry of pyrite from the Songhu iron deposit, Nilek County, Xinjiang, China. *Acta Petrol. Sinica* **2009**, *25*, 1456–1464.
4. Wang, R.; Zhao, X.; Xue, C.; Chu, H.; Zhao, Y.; Sun, Q.; Zhu, W. Fluid evolution of the Nulasai Cu deposit, Xinjiang, NW China: Evidence from fluid inclusions and O-H-C isotopes. *Ore Geol. Rev.* **2024**, *173*, 106220.
5. Zhang, Z.; Hong, W.; Jiang, Z.; Duan, S.; Li, F.; Shi, F. Geological characteristics and metallogenesis of iron deposits in western Tianshan, China. *Ore Geol. Rev.* **2014**, *57*, 425–440.
6. Sun, W.; Niu, Y.; Ma, Y.; Liu, Y.; Zhang, G.; Hu, Z.; Zhang, Z.; Chen, S.; Li, J.; Wang, X.; et al. Petrogenesis of the Chagangnuoer deposit, NW China: A general model for submarine volcanic-hosted skarn iron deposits. *Sci. Bull.* **2015**, *60*, 363–379.
7. Feng, J.X.; Shi, F.P.; Wang, B.Y.; Hu, J.M.; Wang, J.T.; Tian, J.Q. *The Syngenetic Volcanogenic Iron ore Deposits in Awulale Metallogenetic Belt, Western Tianshan Mountains*; Geological Publishing House: Beijing, China, 2010; p. 132. (In Chinese)
8. Liu, R.; Chen, G. The 109 porphyry Cu deposit in the western Tianshan orogenic belt, NW China: An example of Cu mineralization in a reduced magmatichydrothermal system in an extensional setting. *Ore Geol. Rev.* **2019**, *112*, 102989.
9. Zhao, X.; Xue, C.; Chi, G.; Zhao, J.; Yan, Y. Diabase-hosted copper mineralization in the Qunjsai deposit, West Tianshan, NW China: Geological, geochemical and geochronological characteristics and mineralization mechanism. *Ore Geol. Rev.* **2018**, *92*, 430–448.
10. Duan, S.; Zhang, Z.; Jiang, Z.; Zhao, J.; Zhang, Y.; Li, F.; Tian, J. Geology, geochemistry, and geochronology of the Dunde iron-zinc ore deposit in western Tianshan, China. *Ore Geol. Rev.* **2014**, *57*, 441–446. [CrossRef]
11. Hong, W.; Zhang, Z.; Baker, M.J.; Jiang, Z.; Duan, S. Zircon U-Pb dating and stable isotopic compositions for constraining the genesis of the Chagangnuoer magnetite deposit in western Tianshan, NW China. *Ore Geol. Rev.* **2020**, *121*, 103478.
12. Jiang, Z.; Zhang, Z.; Wang, Z.; Duan, S.; Li, F.; Tian, J. Geology, geochemistry, and geochronology of the Zhibo iron deposit in the Western Tianshan, NW China: Constraints on metallogenesis and tectonic setting. *Ore Geol. Rev.* **2014**, *57*, 406–424.
13. Wang, X.S.; Zhang, X.; Gao, J.; Li, J.L.; Jiang, T.; Xue, S.C. A slab break-off model for the submarine volcanic-hosted iron mineralization in the Chinese Western Tianshan: Insights from Paleozoic subduction-related to post-collisional magmatism. *Ore Geol. Rev.* **2018**, *92*, 144–160.
14. Zhang, X.; Klemd, R.; Gao, J.; Dong, L.H.; Wang, X.S.; Haase, K.; Jiang, T.; Qian, Q. Metallogenesis of the Zhibo and Chagangnuoer volcanic iron oxide deposits in the Awulale Iron Metallogenic Belt, Western Tianshan orogen, China. *J. Asian Earth Sci.* **2015**, *113*, 151–172. [CrossRef]
15. Zhang, X.; Tian, J.Q.; Gao, J.; Klemd, R.; Dong, L.H.; Fan, J.J.; Jiang, T.; Hu, C.J.; Qian, Q. Geochronology and geochemistry of granitoid rocks from the Zhibo syngenetic volcanogenic iron ore deposit in the Western Tianshan Mountains (NW-China): Constraints on the age of mineralization and tectonic setting. *Gondwana Res.* **2012**, *22*, 585–596.
16. Windley, B.F.; Alexeiev, D.; Xiao, W.J.; Kröner, A.; Badarch, G. Tectonicmodels for accretion of the Central Asian Orogenic Belt. *J. Geol. Soc.* **2007**, *164*, 31–47.
17. Gao, J.; Long, L.L.; Klemd, R.; Qian, Q.; Liu, D.Y.; Xiong, X.M.; Sun, W.; Liu, W.; Wang, Y.T.; Wang, F.Y. Tectonic evolution of the South Tianshan orogen and adjacent regions, NW China: Geochemical and age constraints of granitoid rocks. *Int. J. Earth Sci.* **2009**, *98*, 1221–1238.
18. Charvet, J.; Shu, L.S.; Laurent-Charvet, S.; Wang, B.; Faure, M.; Cluzel, D.; Chen, Y.; De Jong, K. Palaeozoic tectonic evolution of the Tianshan belt, NW China. *Sci. China Earth Sci.* **2011**, *54*, 166–184.
19. Xiao, W.J.; Windley, B.F.; Allen, M.B.; Han, C.M. Paleozoic multiple accretionary and collisional tectonics of the Chinese Tianshan orogenic collage. *Gondwana Res.* **2013**, *23*, 1316–1341.
20. Gao, J.; Li, M.S.; Xiao, X.C.; Tang, Y.Q.; He, G.Q. Paleozoic tectonic evolution of the Tianshan Orogen northwestern China. *Tectonophysics* **1998**, *287*, 212–231.
21. Li, J.L.; Su, W.; Zhang, X. Zircon Cameca U–Pb dating and its significance for granulite-facies granitic gneisses from the west Awulale Mountains, West Tianshan. *Geol. Bull Chin.* **2009**, *28*, 1852–1862. (In Chinese with English Abstract).
22. Zhang, W.; Leng, C.B.; Zhang, X.C.; Su, W.C.; Tang, H.F.; Yan, J.H.; Cao, J.L. Petrogenesis of the Seleteguole granitoids from Jinhe county in Xinjiang (West China): Implications for the tectonic transformation of Northwest Tianshan. *Lithos* **2016**, *256–257*, 148–164. [CrossRef]
23. Wiedenbeck, M.; Allé, P.; Corfu, F.; Griffin, W.L.; Meier, M.; Oberli, F.; Quadt, A.V.; Roddick, J.C.; Spiegel, W. Three natural zircon standards for U-Th-Pb, Lu-Hf, trace element and REE analyses. *Geostand. Geoanal. Res.* **1995**, *19*, 1–23. [CrossRef]
24. Liu, Y.S.; Gao, S.; Hu, Z.C.; Gao, C.G.; Zong, K.Q.; Wang, D.B. Continental and oceanic crust recycling-induced melt-peridotite interactions in the Trans-North China orogen: U-Pb dating, Hf isotopes and trace elements in zircons of mantle xenoliths. *J. Petrol.* **2010**, *51*, 537–571. [CrossRef]
25. Ludwig, K.R. *User's Manual for Isoplot 3.0: A Geochronological Toolkit for Microsoft Excel*; Special Publication No 4; Berkeley Geochronology Center: Berkeley, CA, USA, 2003.

26. Griffin, W.L.; Pearson, N.J.; Belousova, E.; Jackson, S.E.; van Achterbergh, E.; O'Reilly, S.Y.; Shee, S.R. The Hf isotope composition of cratonic mantle: LAM-MC-ICPMS analysis of zircon megacrysts in kimberlites. *Geochim. Cosmochim. Acta* **2000**, *64*, 133–147. [CrossRef]
27. Griffin, W.L.; Wang, X.; Jackson, S.E.; Pearson, N.J.; O'Reilly, S.Y.; Xu, X.; Zhou, X. Zircon chemistry and magma mixing, SE China: In-situ analysis of Hf isotopes. Tonglu and Pingtan igneous complexes. *Lithos* **2002**, *61*, 237–269. [CrossRef]
28. Belousova, E.A.; Griffin, W.L.; O'Reilly, S.Y.; Fisher, N.I. Igneous zircon, trace element composition as an indicator of source rock type. *Contrib. Mineral. Petr.* **2002**, *143*, 602–622. [CrossRef]
29. Rubatto, D. Zircon trace element geochemistry: Partitioning with garnet and the link between U-Pb ages and metamorphism. *Chem. Geol.* **2002**, *184*, 123–138. [CrossRef]
30. Tang, G.J.; Chung, S.L.; Wang, Q.; Wyman, D.A.; Dan, W.; Chen, H.Y.; Zhao, Z.H. Petrogenesis of a Late Carboniferous mafic dike-granitoid association in the western Tianshan: Response to the geodynamics of oceanic subduction. *Lithos* **2014**, *202–203*, 85–99. [CrossRef]
31. Yan, S.; Shan, Q.; Niu, H.C.; Yang, W.B.; Li, N.B.; Zeng, L.J.; Jiang, Y.H. Petrology and geochemistry of late Carboniferous hornblende gabbro from the Awulale Mountains, western Tianshan (NW China): Implication for an arc–nascent back-arc environment. *J. Asian Earth Sci.* **2015**, *113*, 218–237. [CrossRef]
32. Sun, Q.; Zhao, X.; Xue, C.; Seltmann, R.; Symons, D.T. Late Carboniferous –Early Permian mafic dikes and granitoids in the heart of the Western Tianshan Orogen, NW China: Implications for a tectonic transition from a syn- to post-collisional setting. *Lithos* **2021**, *400–401*, 106417. [CrossRef]
33. Sun, Q.; Zhao, X.; Xue, C.; Seltmann, R.; McClenaghan, S.H.; Chu, H.; Wang, M. Two episodes of Late Paleozoic mafic magmatism in the western Tianshan Orogen: From Carboniferous subduction to Permian post-collisional extension. *Gondwana Res.* **2022**, *109*, 518–535.
34. Seedorff, E.; Dilles, J.H.; Proffett, J.M., Jr.; Einaudi, M.T.; Zurcher, L.; Stavast, W.J.A.; Johnson, D.A.; Barton, M.D. *Porphyry Deposits: Characteristics and Origin of Hypogene Features*; Society of Economic Geologists: Littleton, CO, USA, 2005; pp. 251–298.
35. Sillitoe, R.H. Porphyry copper systems. *Econ. Geol.* **2010**, *105*, 3–41.
36. Luo, H. Geological, Geochemical Characteristics of the Nulasai Copper Deposit, Western Tian Shan, Xinjiang. Master's Thesis, China University of Geosciences (Beijing), Beijing, China, 2016; 63p. (In Chinese with English Abstract).
37. Che, Z.C.; Liu, L.; Liu, H.F.; Luo, J.H. Review on the ancient Yili rift, Xinjiang, China. *Acta Petrol. Sinica* **1996**, *12*, 478–490. (In Chinese with English Abstract).
38. Gu, L.X.; Hu, S.X.; Yu, C.S.; Wu, C.Z.; Yan, Z.F. Initiation and evolution of the Bogda subduction-tore-type rift. *Acta Petrologica Sinica* **2001**, *17*, 585–597. (In Chinese with English Abstract).
39. Xia, L.Q.; Xu, X.Y.; Xia, Z.C.; Li, X.; Ma, Z.P.; Wang, L.S. Petrogenesis of Carboniferous rift-related volcanic rocks in the Tianshan, northwestern China. *Geol. Soc Am. Bull.* **2004**, *116*, 419–433.
40. An, F.; Zhu, Y.F.; Wei, S.N.; Lai, S.C. An Early Devonian to Early Carboniferous volcanic arc in North Tianshan, NW China: Geochronological and geochemical evidence from volcanic rocks. *J. Asian Earth Sci.* **2013**, *78*, 100–113.
41. Feng, W.; Zhu, Y. Petrogenesis and tectonic implications of the late Carboniferous calc-alkaline and shoshonitic magmatic rocks in the Awulale mountain, western Tianshan. *Gondwana Res.* **2019**, *76*, 44–61.
42. Gao, J.; Klemd, R. Formation of HP-LT rocks and their tectonic implications in the western Tianshan Orogen, NW China: Geochemical and age constraints. *Lithos* **2003**, *66*, 1–22.
43. Long, L.; Gao, J.; Klemd, R.; Beier, C.; Qian, Q.; Zhang, X.; Wang, J.; Jiang, T. Geochemical and geochronological studies of granitoid rocks from the Western Tianshan Orogen: Implications for continental growth in the southwestern Central Asian Orogenic Belt. *Lithos.* **2011**, *126*, 321–340.
44. Yang, W.B.; Niu, H.C.; Shan, Q.; Luo, Y.; Sun, W.D.; Li, C.Y.; Li, N.B.; Yu, X.Y. Late Paleozoic calc-alkaline to shoshonitic magmatism and its geodynamic implications, Yuximolegai area, western Tianshan, Xinjiang. *Gondwana Res.* **2012**, *22*, 325–340.
45. Wang, M.; Zhang, J.; Zhang, B.; Liu, K.; Chen, Y.; Zheng, Y. Geochronology and geochemistry of the Borohoro pluton in the northern Yili Block, NW China: Implication for the tectonic evolution of the northern West Tianshan orogen. *J. Asian Earth Sci.* **2018**, *153*, 154–169. [CrossRef]
46. Zhu, Y.F.; Zhang, L.F.; Gu, L.B.; Guo, X.; Zhou, J. The zircon SHRIMP chronology and trace element geochemistry of the Carboniferous volcanic rocks in western Tianshan Mountains. *Chin. Sci. Bull.* **2005**, *50*, 2201–2212. [CrossRef]
47. Zhu, Y.F.; Guo, X.; Song, B.; Zhang, L.F.; Gu, L. Petrology, Sr-Nd-Hf isotopic geochemistry and zircon chronology of the Late Palaeozoic volcanic rocks in the southwestern Tianshan Mountains, Xinjiang, NW China. *J. Geol. Soc.* **2009**, *166*, 1085–1099. [CrossRef]
48. Xiong, X.L.; Zhao, Z.H.; Bai, Z.H.; Mei, H.J.; Xu, J.F.; Wang, Q. Origin of Awulale adakitic sodium-rich rocks in western Tianshan: Constraints for Nd and Sr isotopic compositions. *Acta Petrol. Sinica* **2001**, *17*, 514–522.
49. Zhao, Z.H.; Guo, Z.J.; Han, B.F.; Wang, Y. The geochemical characteristics and tectonic-magmatic implications of the latest-Paleozoic volcanic rocks from Santanghu basin, eastern Xinjiang, northwest China. *Acta Petrol. Sinica* **2006**, *22*, 199–214.

50. Zhao, Z.; Xiong, X.; Wang, Q.; Bai, Z.; Qiao, Y. Late Paleozoic underplating in North Xinjiang: Evidence from shoshonites and adakites. *Gondwana Res.* **2009**, *16*, 216–226. [CrossRef]
51. Cao, R.; Bagas, L.; Chen, B.; Wang, Z.; Gao, Y. Geochronology and petrogenesis of the composite Zuluhong Granite, North Xinjiang Province of China: Implications for the crust-mantle interaction and continental crustal growth in Western Tianshan Orogen. *Lithos* **2021**, *380–381*, 105837. [CrossRef]
52. Chen, J.; Zhou, T.; Xie, Z.; Zhang, X.; Guo, X. Formation of positive 1 Nd(T) granitoids from the Alataw Mountains, Xinjiang, China, by mixing and fractional crystallization: Implication for Phanerozoic crustal growth. *Tectonophysics* **2000**, *328*, 53–67. [CrossRef]
53. Feng, W.; Zheng, J.; Shen, P. Petrology, mineralogy, and geochemistry of the Carboniferous Katbasu Au-Cu deposit, western Tianshan, Northwest China: Implications for petrogenesis, ore genesis, and tectonic setting. *Ore Geol. Rev.* **2023**, *161*, 105659. [CrossRef]
54. Han, B.; Wang, S.; Jahn, B.; Hong, D.; Kagami, H.; Sun, Y. Depleted-mantle source for the Ulungur River A-type granites from North Xinjiang, China: Geochemistry and Nd–Sr isotopic evidence, and implications for Phanerozoic crustal growth. *Chem. Geol.* **1997**, *138*, 135–159. [CrossRef]
55. Jahn, B.M.; Wu, F.Y.; Hong, D.W. Important crustal growth in the Phanerozoic: Isotopic evidence of granitoids from east-central Asia. *Acad. Proc. Earth Planet. Sci.* **2000**, *109*, 5–20. [CrossRef]
56. Hu, A.Q.; Jahn, B.M.; Zhang, G.X.; Zhang, Q.F. Crustal evolution and Phanerozoic crustal growth in northern Xinjiang: Nd–Sr isotopic evidence. Part I: Isotopic characterisation of basement rock. *Tectonophysics* **2000**, *328*, 15–51.
57. Jahn, B.M.; Windley, B.; Natal'in, B.; Dobretsov, N. Phanerozoic continental growth in Central Asia. *J. Asian Earth Sci.* **2004**, *23*, 599–603.
58. Sengör, A.M.C.; Natal'in, B.A.; Burtman, V.S. Evolution of the Altaid tectonic collage and Palaeozoic crustal growth in Eurasia. *Nature* **1993**, *364*, 298–307.
59. Kröner, A.; Kovach, V.; Belousova, E.; Hegner, E.; Armstrong, R.; Dolgopolova, A.; Seltmann, R.; Alexeiev, D.V.; Hoffmann, J.E.; Wong, J.; et al. Reassessment of continental growth during the accretionary history of the Central Asian Orogenic Belt. *Gondwana Res.* **2014**, *25*, 103–125. [CrossRef]
60. Hou, Z.; Yang, Z.; Qu, X.; Meng, X.; Li, Z.; Beaudoin, G.; Rui, Z.; Gao, Y.; Zaw, K. The Miocene Gangdese porphyry copper belt generated during post-collisional extension in the Tibetan Orogen. *Ore Geol. Rev.* **2009**, *36*, 25–51. [CrossRef]
61. Hou, Z.Q.; Yang, Z.M.; Lu, Y.J.; Kemp, A.; Zheng, Y.C.; Li, Q.Y.; Tang, J.X.; Yang, Z.S.; Duan, L.F. A genetic linkage between subduction-continental collision-related porphyry Cu deposits in Tibet. *Geology* **2015**, *43*, 247–250.
62. Richards, J.P. Magmatic to hydrothermal metal fluxes in convergent and collided margins. *Ore Geol. Rev.* **2011**, *40*, 1–26. [CrossRef]
63. Liu, R.; Wang, L.X.; Chen, G.W. Genesis, geological significance and metallogentic potentiality of A-type granites in the Awulale area of the western Tianshan, Xinjiang. *Acta Petrol. Sinica* **2017**, *33*, 1741–1751. (In Chinese with English Abstract).
64. Zhao, Z.H.; Xiong, X.L.; Wang, Q.; Bai, Z.H.; Mei, H.J. A case study on porphyry Cu deposit related with adakitic quartz albite porphyry in Mosizaote, Western Tianshan, Xinjiang, China. *Acta Petrol. Sinica* **2004**, *20*, 249–258. (In Chinese with English Abstract).
65. Li, N.B.; Niu, H.C.; Shan, Q.; Yang, W.B. Two episodes of Late Paleozoic A-type magmatism in the Qunjisayi area, western Tianshan: Petrogenesis and tectonic implications. *J. Asian Earth Sci.* **2015**, *113*, 238–253. [CrossRef]
66. Cooke, D.R.; Hollings, P.; Walshe, J.L. Giant porphyry deposits: Characteristics, distribution, and tectonic Controls. *Econ. Geol.* **2005**, *100*, 801–818. [CrossRef]
67. Candela, P.A.; Piccoli, P.M. *Magmatic Processes in the Development of Porphyry-Type Ore Systems*; Society of Economic Geologists: Littleton, CO, USA, 2005; pp. 25–37.

Disclaimer/Publisher's Note: The statements, opinions and data contained in all publications are solely those of the individual author(s) and contributor(s) and not of MDPI and/or the editor(s). MDPI and/or the editor(s) disclaim responsibility for any injury to people or property resulting from any ideas, methods, instructions or products referred to in the content.

minerals

MDPI

Article

Petrogenesis of the Chamuhan Intrusion in the Southern Great Xing'an Range: Constraints from Zircon U-Pb Dating and Petrogeochemistry

Yutong Song [1], Gongzheng Chen [1,2,3,*], Guang Wu [3], Tiegang Li [3,*], Tong Zhang [2], Jinfang Wang [1], Yingjie Li [1,4], Chenyu Liu [1], Yuze Li [1] and Yinlong Wang [1]

[1] Hebei Province Collaborative Innovation Center for Strategic Critical Mineral Research, Hebei GEO University, Shijiazhuang 050031, China
[2] Inner Mongolia Research Institute of Geological Survey, Hohhot 010020, China
[3] MNR Key Laboratory of Metallogeny and Mineral Assessment, Institute of Mineral Resources, Chinese Academy of Geological Sciences, Beijing 100037, China
[4] School of the Earth Sciences and Resources, China University of Geosciences, Beijing 100083, China
* Correspondence: gzchen@hgu.edu.cn (G.C.); 19171534274@163.com (T.L.)

Abstract

The Southern Great Xing'an Range (SGXR), an important W–Sn polymetallic metallogenic belt in northern China, hosts multiphase magmatism and has witnessed recent discoveries of multiple tungsten–tin polymetallic deposits. The W–Sn mineralization in this area is intimately associated with Early Cretaceous highly fractionated granites. The Chamuhan deposit, a small-sized W–Mo polymetallic deposit in SGXR, is genetically linked to a concealed fine-grained porphyritic alkali feldspar granite intrusion. In this study, we present the LA-ICP-MS zircon U-Pb ages, whole-rock geochemical, and electron probe microanalysis (EPMA) mineral chemistry to constrain the petrogenesis and metallogenic implications of this granite. Zircon U–Pb dating yields a crystallization age of 141.3 ± 1.2 Ma, consistent with molybdenite Re–Os ages. The granite is characterized by elevated SiO_2 (76.9–79.1 wt%) and total alkalis (7.3–8.5 wt%), and exhibits peraluminous high-K calc-alkaline affinity (A/CNK = 1.37–1.57). Geochemical signatures reveal enrichment in large ion lithophile elements (LILEs, e.g., Rb, Th, U) coupled with depletion in high-field strength elements (HFSEs, e.g., Ba, Sr, P, Eu, Ti, Nb, Ta), and are accompanied by right-sloping REE patterns with LREE enrichment and HREE depletion. EPMA data indicate that the mica in the intrusion is primarily zinnwaldite and Li-rich phengite, whereas the plagioclase occurs as albite. The feldspar thermobarometry yields crystallization temperatures of 689–778 °C and 313 MPa–454 MPa, while the melt H_2O content and oxygen fugacity are 8.61–11.1 wt% and −22.58–−14.48, respectively. These geochemical signatures indicate that the granites are highly fractionated I-type granites with extensive fractional crystallization of various minerals like plagioclase, K-feldspar, and apatite, etc. From the Late Jurassic to the Early Cretaceous, the subduction and rollback of the Paleo-Pacific Ocean plate resulted in extensional tectonic environments in eastern China. Asthenospheric upwelling and lower crustal melting generated parental magmas, wherein progressive fractional crystallization during ascent concentrated ore-forming elements and volatiles within residual melts. This process played a key role in the formation of the Chamuhan deposit, exemplifying the metallogenic potential of highly evolved granitic systems in the SGXR.

Keywords: zircon U–Pb dating; the Chamuhan intrusion; highly differentiated I-type granite; Southern Great Xing'an Range

1. Introduction

The Southern Great Xing'an Range (SGXR) is situated at the intersection of the Paleo-Asian, Mongolia-Okhotsk, and Paleo-Pacific tectonic regimes. With intense tectonic–magmatic activity and favorable metallogenic conditions, this region is a significant non-ferrous metallogenic area in northern China [1–5]. The traditional dominant ore types in this region are Pb–Zn–Ag. In recent years, exploration has discovered multiple tin–polymetallic deposits in the peripheral and deep zones of Pb–Zn–Ag deposits. The Sn-polymetallic and Pb–Zn–Ag mineralization share the same mineralization ages, with ore-forming fluids exhibiting continuous evolutionary characteristics that represent distinct mineralization stages in a unified metallogenic system, as demonstrated by: the Baiyinchagan Sn–Ag–Cu–Pb–Zn deposit [6], Huaaobaote Sn–Cu–Pb–Zn–Ag deposit [7], and Dajing Sn–Cu–Pb–Zn–Ag deposit [8]. The Pb–Zn–Ag deposits and the W–Sn polymetallic deposits in SGXR, both formed during the Early Cretaceous (~140 Ma) peak metallogenic episode, share a common extensional tectonic setting driven by Paleo-Pacific slab rollback. The metallogenic intrusions of W–Sn polymetallic deposits in the SGXR are primarily hidden at depth, complicating their identification and leading to controversy regarding some deposits' petrogenetic and mineralization ages [9,10]. Moreover, the W–Sn polymetallic deposits in the SGXR are mainly Sn-dominated, with relatively few W-rich deposits, and W–Sn enrichment varies by an order of magnitude. Currently, the mechanisms responsible for the differential enrichment of W and Sn remain poorly understood; petrogenetic studies of ore-forming intrusions associated with W-rich deposits would elucidate the geochemical disparities between W ore-forming intrusions and Sn ore-forming intrusions, advancing our comprehension of the regional W-Sn metallogenic regularity and the mechanisms of differential W–Sn enrichment in this region [11,12].

W–Sn mineralization in South China is commonly associated with a granitic complex [13–15]. Traditionally, the supplementary intrusion has been interpreted as representing residual magmas derived from fractional crystallization of the predominant intrusion. However, recent studies suggest that supplementary intrusion formation may be linked to underplated mafic magmatic activity. The residual magma composition gradually approaches the cotectic point of the granite system due to intense fractional crystallization induced by magmatic activity. At this stage, magma is primarily stored as crystal mush, but minor external heating (e.g., mantle-derived magma) can trigger its remobilization [16]. As magma ascends in multiple phases, it facilitates the extraction of residual magma, driving fractional crystallization and forming highly differentiated granites and W–Sn deposits. The Chamuhan deposit, a small-sized W–Mo polymetallic deposit located in the SGXR, is associated with the Chamuhan granitic complex. This intrusion comprises shallow-level predominant intrusion of white medium-grained biotite monzogranite (WMG), pinkish medium-grained biotite monzogranite (PMG), and a deep-seated supplementary intrusion of fine-grained porphyritic alkali feldspar granite (FAG). Geochronological and geochemical analyses of WMG and PMG, which were intruded by ore-bearing veins, yield crystallization ages of 144 $\pm$ 2 Ma, which predate the mineralization age of 139.3 $\pm$ 1.5 Ma. [17]. Geochemical data reveal high W and Mo contents in WMG, but depletion of the same elements in FAG, indicating these elements were leached out during the interaction of the parental magma with hydrothermal fluid. WMG served as structurally controlled conduits for ore-forming fluids, with mineralization finally formed at the upper part of the intrusion [18]. This paper reports the petrography, LA-ICP-MS zircon U-Pb age, geochemistry, and EPMA data for mica and feldspar minerals from FAG. Our objectives are to: (1) constrain the emplacement chronology and petrogenetic classification of the intrusion, (2) decipher its magmatic evolutionary processes, and (3) elucidate the genetic relationships between highly fractionated granites and W-polymetallic mineralization in the SGXR.

2. Regional Geology

The SGXR is situated within the suture zone that separates the Siberian Craton from the North China Craton (Figure 1a). This region is bounded by major tectonic belts: the Erenhot–Hegenshan suture zone to the north, the Xar Moron fault to the south (which delineates the northern margin of the North China Craton), and the Nenjiang–Balihan fault to the east. Its western boundary is generally located in the Xilinhot–East Ujimqin Banner area [19]. Geodynamically, the SGXR records the Paleozoic subduction and closure of the Paleo-Asian Ocean, as evidenced by the development of EW-trending fold-thrust systems (Figure 1b). These include prominent anticlinoria and synclinoria, such as the Mishengmiao anticlinoria and the Linxi synclinoria, as well as deep faults (e.g., Erenhot–Hegenshan and Xar Moron deep faults). During the Mesozoic, the SGXR experienced significant tectonic reworking due to the far-field effects of Paleo-Pacific subduction, resulting in the formation of NE–NNE-trending faults, including the Nenjiang–Balihan fault, and NNE-trending faults, including the main ridge and western slope faults of the Great Xing'an Range [20]. The superposition of Mesozoic structures onto pre-existing Paleozoic frameworks created a complex grid-like structural architecture, which subsequently controlled the spatial–temporal distribution of granitic complexes and deposits throughout the region [21] (Figure 1b).

The exposed strata in the SGXR include Proterozoic, Paleozoic, Mesozoic, and Cenozoic (Figure 1b). The Proterozoic strata are dominated by the Xilin Gol Complex, which is distributed in Xilinhot and the southern regions of West Ujimqin Banner [22]. The Paleozoic strata include the Lower Paleozoic and Upper Paleozoic, which are extensively distributed in this region. The Lower Paleozoic strata mainly consist of marine volcanic and terrigenous clastic rock, including andesite, dacite, metamorphic sandstone, and siltstone. The Upper Paleozoic strata are mainly comprised of marine-terrigenous sandstone, siltstone, slate, carbonate rock, and intermediate-acid volcanic rock. The Mesozoic strata are widely distributed in this region and include a volcano-sedimentary sequence consisting of terrestrial clastic rocks, volcanic clastic rocks, and continental volcanic rocks. The Cenozoic strata are primarily distributed in the western part of SGXR and comprise Quaternary sediments. Magmatic activity in the SGXR occurred primarily during the Late Paleozoic and Mesozoic, with the latter being predominant. Influenced by the Mesozoic subduction of the Paleo-Pacific plate, this region experienced large-scale magmatism, which peaked in the Late Jurassic to Early Cretaceous and produced a lithological assemblage dominated by syenogranite, monzogranite, and alkaline granite. In contrast, Paleozoic magmatism, triggered by subduction of the Paleo-Asian Ocean, was extensive during the Carboniferous and Permian. Carboniferous diorites and granodiorites exhibit low-K tholeiitic to calc-alkaline geochemical signatures, while Early–Middle Permian granites are characteristically high-K calc-alkaline. Collectively, these magmatic records imply slab break-off following the closure of the Paleo-Asian Ocean [23].

The Chamuhan area, located in the SGXR, exposed strata comprising Permian, Jurassic, Cretaceous, and Quaternary units. The Permian comprises the Dashizhai Formation (volcanoclastic and siltstone), Shoushangou Formation (siltstone), Zhesi Formation (shale, sandstone, and slate), and Linxi Formation (sandstone, slate, and shale). The Jurassic includes the Manketouebo Formation (felsic volcanic and pyroclastic rocks), Manitu Formation (intermediate volcanic rocks-pyroclastic rock), and Xinmin Formation (rhyolite and rhyolitic volcaniclastic rocks). The Cretaceous includes the Baiyangaolao Formation, comprised of felsic volcanic rock and pyroclastic rock, while the Quaternary features regionally extensive heterogeneous sediments, dominated by eluvial–deluvial materials with minor surface humic soils [24,25].

The NE-trending Chamuhan fault traverses the eastern sector of the Chamuhan deposit, controlling the spatial distribution and alteration of granitic rocks in the area.

Magmatic activity occurred in two principal episodes: Carboniferous-Permian and Jurassic-Cretaceous. Carboniferous-Permian intrusions, comprising sparsely distributed diorite porphyry, are localized in the northwestern part of the Chamuhan area. Jurassic-Cretaceous intrusions evolved in two phases: an initial emplacement of granite porphyry and rhyolite porphyry in the southeast, followed by biotite syenogranite and biotite monzogranite concentrically distributed around the Chamuhan deposit.

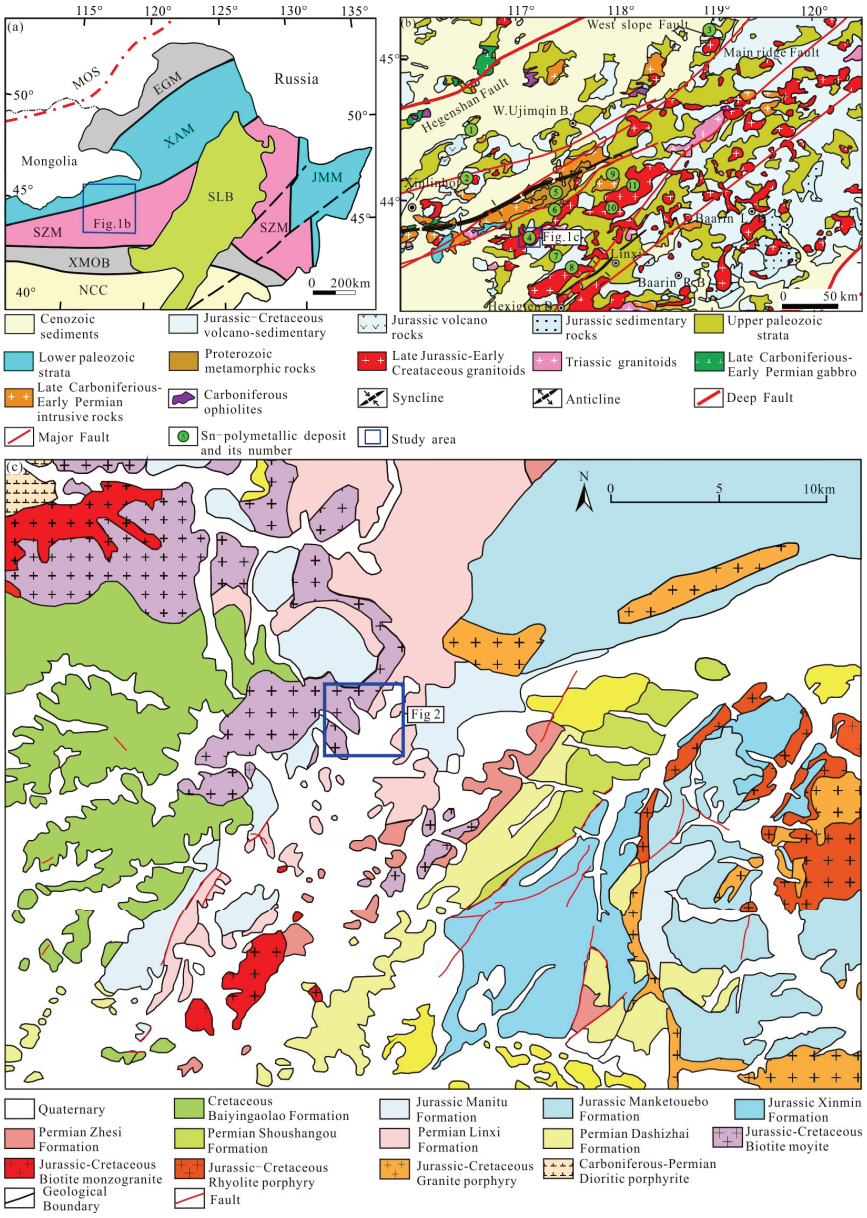


Figure 1. The geotectonic units of the southern section of the Great Xing'an Range ((**a**). modified after [26]). The regional geological map of the southern section of the Great Xing'an Range ((**b**). modified after [27]), and the geological map of the Chamuhan area ((**c**). modified after [28]). Names of numbered Sn-polymetallic deposits: 1 = Bayan Qagan Dongshan giant-sized Sn–Ag–Pb–Zn–Cu–Sb deposit; 2 = Maodeng-Xiaogushan medium-sized Sn–Cu deposit; 3 = Huaaobaote giant-sized Pb–Zn–Ag–Sn–Cu deposit; 4 = Chamuhan small-sized W–Mo polymetallic deposit; 5 = Weilasituo large-sized Sn–Li–Rb–Nb–Ta–Cu–Zn deposit; 6 = Anle medium-size Sn–Cu deposit; 7 = Huanggang giant-sized Sn–Fe deposit; 8 = Laopandaobeihou medium-sized Sn–Pb–Zn–Ag deposit; 9 = Daolundaba medium-sized Cu–W–Sn–Ag deposit; 10 = Dongshanwan small-sized Sn–Ag–Pb–Zn deposit; 11 = Baogaigou small-sized Sn deposit.

3. Deposit Geology and Characteristics of Related Rock Bodies

3.1. Ore Deposit Geology

The Chamuhan deposit is a small-sized W–Mo polymetallic deposit dominated by W, located in the Huanggang–Ganzhuermiao metallogenic belt, SGXR. The deposit contains proven reserves of 3102.44 tons WO_3 and 45.2 tons Sn, with corresponding average grades of 0.2% WO_3 and 0.2% Sn. Geographically, the deposit falls under the administrative jurisdiction of Hexigten Banner, Chifeng city, Inner Mongolia Autonomous Region, approximately 300 km northwest of Chifeng city. Coordinate referencing identifies the deposit at 117°27′49″ E longitude and 43°43′30″ N latitude.

The exposed strata in the Chamuhan ore district include the Upper Permian Linxi Formation, the Upper Jurassic Manitu Formation, and the Lower Cretaceous Baiyingaolao Formation (Figure 2a). The Upper Permian Linxi Formation is distributed on both sides of medium-grained granite; it consists of black slate with different degrees of sericitization and chloritization near the ore body. The Manitu Formation is distributed as an NE-trending belt in the western part of the ore district, consisting of basalt, andesite, and andesitic breccia-bearing tuff. The Baiyingaolao Formation is sparsely exposed in the northern part of the ore district, consisting of felsic volcanic rocks and pyroclastic rocks. The Quaternary sediments in the ore area are relatively thin, primarily composed of grayish-black humus soil, with interlayers of gravel-bearing red soil beneath the humus soil layer. The intrusive rocks developed in the ore district mainly comprise WMG, covering an area of approximately 0.15 km^2. The intrusion is emplaced into the Linxi Formation slate along the southeast direction. The structural setting in the ore district is dominated by two sets: NNE-trending faults and NW-trending faults. The NNE-trending faults are the primary ore-controlling structures within the ore district. The NW-trending faults are oblique thrust faults, with fault gouge and schistosity developed on both sides of the fault plane.

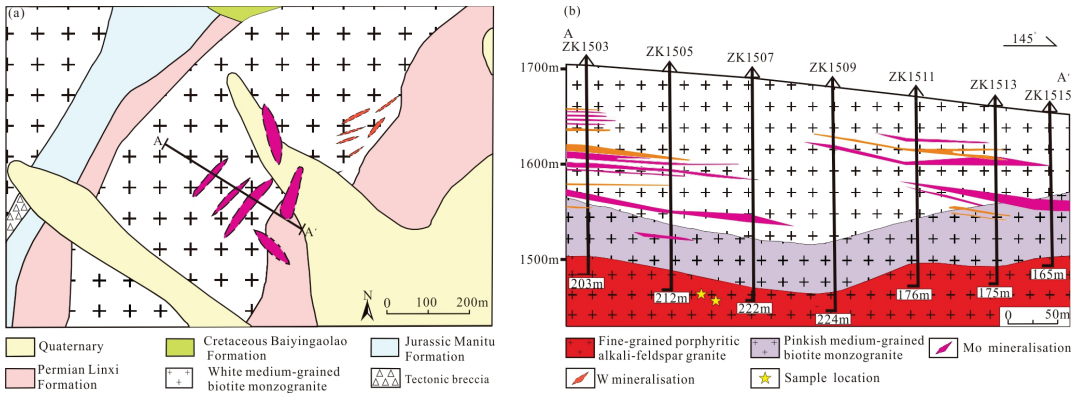


Figure 2. Geological map of the Chamuhan ore deposit ((**a**), modified after [24]) exploration line profile ((**b**), modified after [24]).

The Chamuhan deposit hosts over 50 predominantly low-grade and small-scale veins, with 12 economically viable ore bodies delineated. W-Mo mineralization is present in the Chamuhan granite, specifically hosted within the WMG phase of the Chamuhan intrusion. These ore bodies, measuring up to 150 m in length and 1–2 m in width, are primarily NE-trending veins (Figure 2b). The ore minerals in tungsten ore bodies (WO_3 up to 5.92%) are mainly wolframite and cassiterite, followed by minor bismuthinite, arsenopyrite, and scheelite. Gangue minerals primarily include quartz, fluorite, muscovite, topaz, and tourmaline. Disseminated tin mineralization occurs near the tungsten ore bodies, with a maximum grade of tin reaching 0.97%. The molybdenum ore bodies are located to the west of the tungsten ore bodies, with an average grade of 0.08%. The primary ore minerals are molybdenite and pyrite, accompanied by minor cassiterite and chalcopyrite.

Gangue minerals mainly consist of quartz and feldspar, with accessory minerals including muscovite, fluorite, and tourmaline.

3.2. Geology and Petrography of the Chamuhan Intrusions

The Chamuhan intrusion is composed of WMG, PMG, and FAG (Figure 2b). The contact relationship between the WMG and PMG is characterized by intrusive emplacement into the Upper Permian Linxi Formation slate. Contextual evidence suggests they are contemporaneous phases of the same granitic complex emplaced at ~144 ± 2 Ma, exhibiting either gradational intrusive contacts without significant tectonic disruption; meanwhile, the FAG remains concealed but structurally connected as the source intrusion. The tungsten–tin and molybdenum ore veins in the Chamuhan deposit are predominantly hosted within WMG, exhibiting progressive greisenization, albitization, and silicification that diminishes with distance from the ore veins. The surface of the FAG exhibits a light red color with a massive structure and porphyritic texture (Figure 3a,b). It is composed of k-feldspar (50%–60%), quartz (30%–40%), and plagioclase (5%–10%). Accessory minerals, constituting approximately 2% of the total rock volume, include muscovite, monazite, zircon, and apatite. The porphyritic texture of the FAG is characterized by phenocrysts of perthite and quartz, with grain sizes ranging from 0.8 to 1 mm. The perthite phenocrysts occur as euhedral–subhedral lath-shaped with well-developed perthitic textures, while quartz phenocrysts display xenomorphic-granular textures. The groundmass consists of interlocking quartz, muscovite, and plagioclase grains (Figure 3c,d). Some perthite phenocrysts within the FAG present with minor kaolinization, while the groundmass shows slight sericitization.

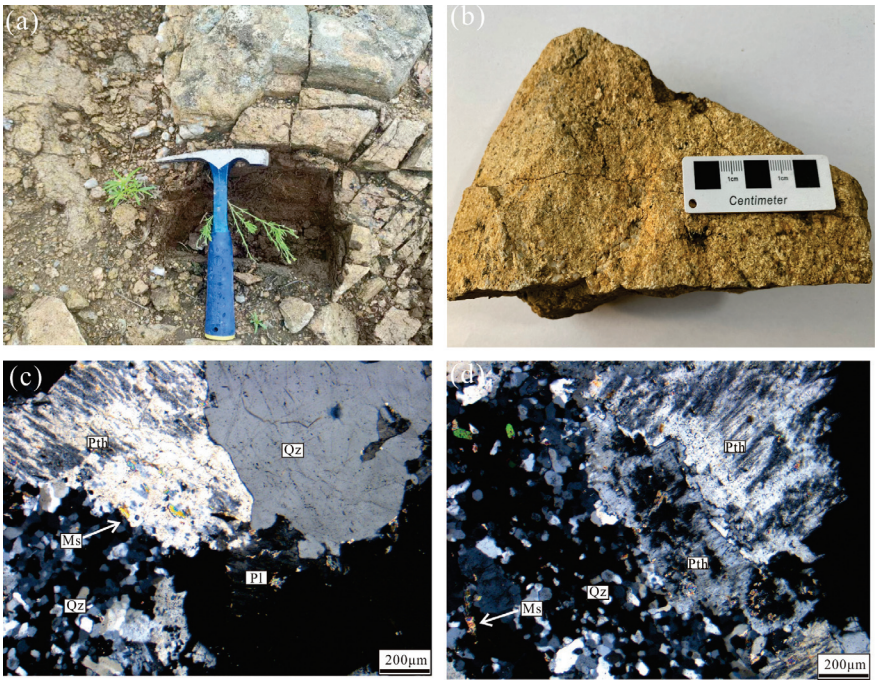


Figure 3. Field photograph, hand specimens, and photomicrographs of FAG in the Chamuhan intrusion: (**a**) Field photograph showing a typical outcrop of FAG in the Chamuhan intrusion; (**b**) FAG hand specimens, primarily composed of K-feldspar, plagioclase, and quartz; (**c**) FAG exhibiting perthitic K-feldspar development. Plagioclase displays subhedral–euhedral tabular morphology. Phenocrysts comprise perthite and quartz, while the matrix consists of plagioclase, quartz, and muscovite. Slight sericitization occurs in interstitial spaces between plagioclase and quartz; (**d**) Porphyritic-like texture observed in fine-grained alkali-feldspar granite, with perthite phenocrysts and fine-grained quartz-muscovite matrix. Prominent perthitic texture developed in K-feldspar.; Ms = muscovite; Pl = plagioclase; Pth = perthite; Qz = quartz.

4. Sampling and Analytical Methods

4.1. Sampling

Nine FAG samples were collected from the Chamuhan intrusion. Zircon was collected from one sample (CY1), eight samples (CY10–CY17) were analyzed for major and trace elements, and two samples (CY12 and CY13) for mica and feldspar EPMA analysis.

4.2. Zircon U-Pb Dating

One sample was crushed and elutriated, and then separated using conventional heavy liquid (sodium polytungstate) and magnetic separation at Tuoxuan Geological Exploration Technology Co., Ltd., Langfang, China. Large, crack-free, transparent zircon crystals were selected under a binocular microscope. These zircon crystals were mounted in epoxy resin discs and polished to expose the ablation surface for scanning electron microscope–cathodoluminescence (SEM-CL) imaging and zircon LA-ICP-MS U-Pb dating. The SEM-CL imaging and zircon LA-ICP-MS U-Pb analyses were performed at Beijing Yanduzhongshi Geological Analysis Laboratories Co., Ltd. (Beijing, China) Analyses were conducted using an Analytik Jena PlasmaQuant MC-ICP-MS(manufactured by Analytik Ltd. in Jena, Germany) and a 193 nm NWR ArF excimer laser(manufactured by Analytik Ltd. in Jena, Germany); each acquisition incorporated 15 s background (gas blank), followed by 40 s laser ablation. Ablation parameters were: 35 μm spot size, 6 Hz frequency, and 4.0 J/cm^2 energy density. Uncertainties for the weighted mean age are reported at the 2σ confidence level. The U-Pb concordia ages and weighted mean age calculations were made using Isoplot software (version 4.15) [29].

4.3. Major and Trace Element Analyses

The Beijing Yanduzhongshi Geological Analysis Laboratories Co., Ltd. analyzed major and trace elements. For major elements analyses, using a Leeman Prodigy inductively (manufactured by Leeman Labs in Hudson, NH, USA) coupled plasma optical emission spectroscopy (ICP-OES) with a high dispersion grating system, the standard samples were the US Geological Survey rock standards BCR-1 and AVG-2. An Agilent-7500a ICP–MS was used for the trace elements, with the standard samples GSR1 and BCR-1 from the US Geological Survey. The analytical uncertainties for major element oxides were around 1%, and for trace elements, they were better than 5%. The detailed analytical process was introduced by Pei [30].

4.4. Electron Probe Microanalysis

The rock probe samples were prepared in Langfang Tuoxuan Geological Exploration Technology Co., Ltd. The EMPA of feldspar and mica was completed at the Institute of Regional Geological Survey, Langfang, Hebei Province, using a JEOL JXA-8230 microprobe (manufactured by JEOL Ltd. in Tokyo, Japan) with an accelerating voltage of 15 kV, a beam current of 10 nA, and a beam spot of 1–5 μm. The background counting time was 20 s, and the analysis accuracy was around 0.01%.

5. Results

5.1. Zircon U-Pb Age

Eleven zircon grains were selected from one FAG sample (CY1) for LA-ICP-MS U-Pb dating. CL images (Figure 4) reveal that the zircon grains are subhedral, with no magmatic oscillatory zoning. The intense blackness in zircon cathodoluminescence (CL) images from the FAG results from extreme uranium enrichment (U = 9923–24,946 ppm), which suppresses luminescence. The length/width ratio of zircon grains was 1:1 to 1:2, and particle sizes are 50–60 μm. Zircon exhibits high Th (517 ppm–25,022 ppm) and U

(9923 ppm–24,946 ppm) contents. The Th/U ratios of zircon grains indicate a magmatic origin. Magmatic zircons typically exhibit Th/U values of 0.2–1.0, whereas metamorphic zircons generally show values less than 0.1 [31]. The FAG zircons yield Th/U ratios ranging from 0.44 to 1.00 (average 0.77), consistent with a magmatic origin. The LA-ICP-MS zircon U-Pb dating results are reported in Table 1. Eleven spots from the eleven zircon grains show that $^{206}Pb/^{238}U$ age data are plotted within the field on the diagram between 137.5 and 153.4 Ma (Figure 5a), defining a weighted mean $^{206}Pb/^{238}U$ age of 141.3 ± 1.2Ma (MSWD = 0.39, Figure 5b). The 141 Ma age is interpreted as the crystallization age of the FAG in the Chamuhan intrusion.

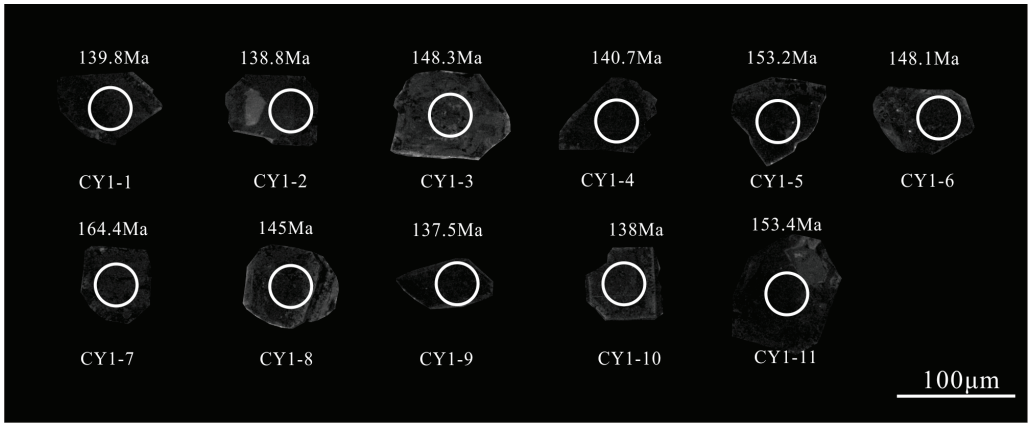


Figure 4. Zircon cathodoluminescence images of FAG, indicating the location of analytical points and $^{206}Pb/^{238}U$ corresponding ages.

Table 1. Zircon U-Pb LA-ICP-MS results of the FAG from the Chamuhan intrusion.

Spot no	Th	U	Th/U	Isotopic Ratios						Ages/Ma					
	ppm			$^{207}Pb/^{206}Pb$	2σ	$^{207}Pb/^{235}U$	2σ	$^{206}Pb/^{238}U$	2σ	$^{207}Pb/^{206}Pb$	2σ	$^{207}Pb/^{235}U$	2σ	$^{206}Pb/^{238}U$	2σ
1	17,943	20,851	0.86	0.05009	0.00143	0.15124	0.00424	0.02194	0.00073	194.2	65	142.9	3	139.8	4
2	10,980	18,028	0.61	0.05141	0.00520	0.15372	0.01734	0.02177	0.00088	233.7	204	144.9	15	138.8	5
3	517	1183	0.44	0.04854	0.00294	0.15701	0.01229	0.02327	0.00091	99.9	141	147.8	10	148.3	5
4	19,905	22,280	0.89	0.04890	0.00168	0.14996	0.00624	0.02207	0.00052	133.9	76	141.8	5	140.7	3
5	20,491	20,521	1.00	0.10715	0.01627	0.36604	0.06512	0.02406	0.00100	142.6	6	311.8	48	153.2	6
6	5794	9923	0.58	0.10375	0.00743	0.33923	0.02593	0.02325	0.00072	138.4	4	306.9	29	148.1	4
7	9450	12,379	0.76	0.16725	0.01708	0.60814	0.06224	0.02584	0.00041	141.2	6	479.7	37	164.4	2
8	23,602	24,131	0.98	0.07229	0.00612	0.23114	0.01995	0.02275	0.00050	140.9	3	210.6	16	145.0	3
9	10,398	15,640	0.66	0.04796	0.00102	0.14508	0.00425	0.02157	0.00074	93.0	49	137.5	3	137.5	4
10	25,022	24,946	1.00	0.05026	0.00133	0.15159	0.00434	0.02165	0.00049	201.3	58	143.2	3	138.0	3
11	11,080	15,595	0.71	0.10658	0.01431	0.35909	0.05592	0.02409	0.00106	142.9	7	308.1	39	153.4	6

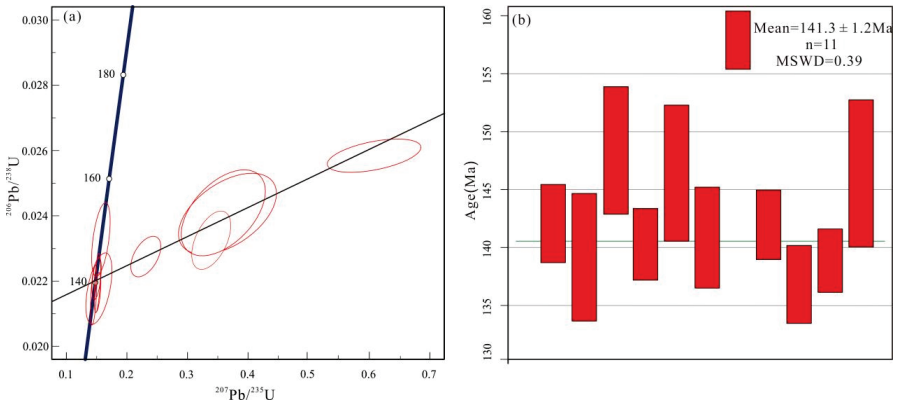


Figure 5. (**a**) Concordance diagram and (**b**) weighted mean plot of zircon $^{206}Pb/^{238}U$ corresponding age of FAG.

5.2. EPMA of Mica and Feldspar

The EPMA data for mica from the FAG are presented in Table 2, with those for plagioclase and K-feldspar in Tables 3 and 4, respectively. The types of mica samples are the zinnwaldite and Li-rich phengite (Figure 6a). The SiO_2 content of mica is 42.3%–46.3%, the TiO_2 content is 0.01%–0.4%, the Al_2O_3 content is 31.1%–35.8%, the FeO content is 2.75%–6.65%, and the F content is 1.92%–2.94%. The plagioclase samples have high Ab values (96.0–98.5) and low An values (0.84–3.20) and Or values (0.66–0.89), classifying them as albite. The K-feldspar samples have high Or values (92.9–98.0) and low An values (0.01–0.05) and Ab values (1.96–7.10), suggesting they are orthoclase (Figure 6b).

Table 2. The EPMA data for mica samples from FAG in the Chamuhan intrusion.

Sample	CY12-M1	CY12-M2	CY12-M3	CY12-M4	CY12-M5	CY13-M1	CY13-M2	CY13-M3
SiO_2	44.2	45.4	43.9	42.3	46.3	45.23	45.1	45.4
TiO_2	0.11	0.25	0.13	0.40	0.14	0.29	0.23	0.01
Al_2O_3	34.2	31.1	33.1	31.2	32.5	35.8	32.1	34.6
FeO	5.05	4.50	4.58	6.65	3.58	2.75	4.55	4.50
MnO	0.11	0.09	0.08	0.17	0.12	0.08	0.08	0.18
MgO	0.76	3.02	1.24	1.95	2.00	1.18	2.11	0.97
CaO	0.01	0.01	0.08	0.02	0.02	0.01	0.02	0.00
Na_2O	0.20	0.14	0.10	0.13	0.16	0.16	0.18	0.10
K_2O	10.8	10.7	8.5	9.8	10.3	10.6	10.6	10.8
Cr_2O_3	0.01	0.02	0.00	0.05	0.00	0.00	0.02	0.02
F	2.35	2.94	2.08	2.75	2.55	1.92	2.37	2.24
Cl	0.00	0.01	0.00	0.06	0.02	0.02	0.01	0.00
Total	96.8	96.9	93.0	94.2	96.6	97.2	96.4	97.9
Number of cations calculated on the basis of 11 oxygen atoms								
Si	2.94	3.00	2.99	2.91	3.04	2.95	3.00	2.97
Al^{IV}	1.05	0.99	1.00	1.08	0.95	1.04	0.99	1.02
Al^{VI}	1.62	1.43	1.65	1.44	1.56	1.71	1.52	1.64
Ti	0.01	0.01	0.01	0.02	0.006	0.01	0.01	0.01
Fe^{3+}	0.28	0.24	0.26	0.38	0.19	0.15	0.25	0.24
Mn	0.010	0.005	0.004	0.009	0.006	0.004	0.004	0.010
Mg	0.07	0.29	0.12	0.20	0.19	0.11	0.20	0.09
Ca	0.001	0.001	0.005	0.001	0.001	0.001	0.001	0.000
Na	0.02	0.01	0.01	0.01	0.02	0.02	0.02	0.01
K	0.91	0.90	0.74	0.86	0.86	0.88	0.90	0.90
Total	6.93	6.92	6.81	6.93	6.86	6.90	6.93	6.91
MF	0.20	0.53	0.32	0.33	0.49	0.42	0.44	0.26
$Al^{VI} + Fe^{3+} + Ti$	1.91	1.69	1.92	1.84	1.77	1.87	1.79	1.89
$Fe^{2+} + Mn$	0.006	0.005	0.004	0.009	0.006	0.004	0.004	0.010
Ti/(Mg + Fe + Ti + Mn)	0.01	0.02	0.01	0.03	0.01	0.05	0.02	0.01
Al/(Al + Mg + Fe + Ti + Mn + Si)	0.44	0.40	0.43	0.41	0.42	0.45	0.41	0.44
Li	1.44	1.60	1.40	1.19	1.72	1.58	1.56	1.60
Li_2O	3.11	3.40	3.02	2.56	3.72	3.41	3.37	3.46
Mg − Li	−1.37	−1.31	−1.28	−0.99	−1.53	−1.47	−1.35	−1.51
$Fe + Mn + Ti - Al^{IV}$	−1.33	−1.16	−1.38	−1.03	−1.35	−1.54	−1.25	−1.38

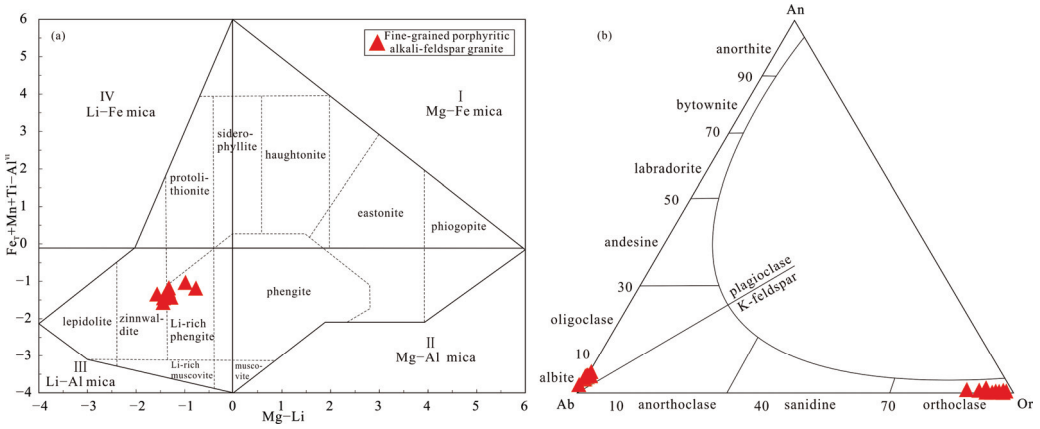


Figure 6. (**a**) Diagram of $Fe^T + Mn + Ti - Al^{VI}$ versus Mg–Li for mica minerals [32] and (**b**) An-Ab-Or diagram for feldspar minerals [33].

Table 3. The EPMA data for plagioclase samples from FAG in the Chamuhan intrusion.

Sample	CY12-P1	CY12-P2	CY12-P3	CY12-M4	CY13-P1	CY13-P2	CY13-P3	CY13-P4	CY13-P5
SiO_2	70.1	69.0	68.9	69.7	66.7	67.6	69.3	69.5	69.3
Al_2O_3	20.3	19.3	19.8	20.4	20.7	20.2	19.8	19.7	20.1
CaO	0.49	0.18	0.41	0.66	0.42	0.70	0.38	0.27	0.48
Na_2O	11.3	11.7	11.3	11.3	11.1	11.6	10.8	11.7	11.4
K_2O	0.13	0.12	0.16	0.16	0.15	0.14	0.12	0.14	0.15
TiO_2	0.00	0.00	0.00	0.00	0.00	0.00	0.00	0.00	0.01
FeO	0.01	0.00	0.01	0.03	0.06	0.01	0.01	0.01	0.01
MgO	0.00	0.01	0.00	0.01	0.00	0.00	0.01	0.01	0.00
Total	102.4	100.4	100.6	102.2	99.1	100.3	100.4	101.3	101.4
Number of cations calculated on the basis of 8 oxygen atoms									
Si	2.98	3.00	2.99	2.97	2.94	2.95	3.00	2.99	2.98
Al	1.02	0.99	1.01	1.02	1.07	1.04	1.01	1.00	1.02
Ca	0.02	0.01	0.01	0.03	0.01	0.03	0.01	0.01	0.02
Na	0.93	0.98	0.95	0.93	0.94	0.98	0.90	0.97	0.95
K	0.007	0.006	0.008	0.008	0.008	0.007	0.006	0.007	0.008
An	2.32	0.84	1.95	3.10	2.03	3.20	1.89	1.25	2.25
Ab	96.9	98.5	97.1	96.0	97.1	96.0	97.3	97.9	96.9
Or	0.73	0.66	0.91	0.89	0.86	0.76	0.71	0.77	0.84
X_{An}	0.02	0.008	0.02	0.03	0.02	0.03	0.02	0.01	0.02
X_{Ab}	0.97	0.99	0.97	0.96	0.97	0.96	0.97	0.98	0.97
$\omega(H_2O)$/%	9.57	10.1	9.01	8.61	11.1	8.12	10.3	10.5	9.44
t(°C)	725	698	739	763	689	778	705	691	729
P(MPa)	382	347	400	435	321	454	353	313	392

Table 4. The EPMA data for K-feldspar samples from FAG in the Chamuhan intrusion.

Sample	CY12-K1	CY12-K2	CY12-K3	CY12-K4	CY12-K5	CY13-K1	CY13-K2	CY13-K3	CY13-K4	CY13-K5
SiO_2	64.5	64.4	64.7	64.4	64.3	64.6	64.9	64.6	64.4	64.9
Al_2O_3	18.1	18.3	18.1	18.0	18.2	18.3	18.4	18.2	18.2	18.3
CaO	0.01	0.01	0.00	0.00	0.00	0.00	0.00	0.00	0.00	0.01
Na_2O	0.41	0.22	0.27	0.27	0.23	0.55	0.38	0.34	0.47	0.81
K_2O	15.9	16.7	16.7	16.4	16.2	16.1	16.6	16.6	16.3	16.1
TiO_2	0.00	0.01	0.01	0.00	0.01	0.00	0.00	0.03	0.00	0.00
FeO	0.02	0.02	0.01	0.02	0.04	0.02	0.04	0.02	0.03	0.03
MgO	0.00	0.01	0.00	0.00	0.00	0.00	0.00	0.00	0.02	0.00
Total	98.9	99.6	99.9	99.2	99.0	99.6	100.3	99.8	99.5	100.1
Number of cations calculated on the basis of 8 oxygen atoms										
Si	3.00	2.99	3.00	3.00	3.00	2.99	2.99	2.99	2.99	2.99
Al	0.99	1.00	0.99	0.99	1.00	1.00	1.00	0.99	0.99	0.99
Ca	0.0005	0.0005	0.00	0.00	0.00	0.00	0.00	0.00	0.00	0.0005
Na	0.03	0.01	0.02	0.02	0.02	0.04	0.03	0.03	0.04	0.07
K	0.94	0.99	0.98	0.97	0.96	0.95	0.97	0.98	0.96	0.94
An	0.05	0.05	0.00	0.00	0.00	0.00	0.00	0.00	0.00	0.05
Ab	3.77	1.96	2.40	2.44	2.11	4.94	3.36	3.02	4.20	7.10
Or	96.1	97.9	97.6	97.5	97.8	95.0	96.6	96.9	95.8	92.8

5.3. Whole-Rock Geochemistry

The whole-rock major elements and trace elements of the FAG in the Chamuhan intrusion are listed in Table 5. All sample LOI values are less than 1 wt%, indicating that the samples exhibit minimal effects of alteration and weathering processes. The FAG shows high SiO_2 (76.95%–79.14%), Al_2O_3 (11.9%–12.6%), and Na_2O + K_2O (7.3%–8.5%) contents; Na_2O and K_2O values are 3.36%–4.60% and 3.89%–4.86%, respectively. The FAG has low FeO^T (0.20%–0.74%), CaO (0.22%–0.66%), MgO (0.03%–0.09%), TiO_2 (0.04%–0.06%), and P_2O_5 contents (0.01%–0.02%). The Differentiation Index (DI) and Solidification Index (SI) are 95.49–97.75 and 0.44–1.16, respectively. All samples plot within the alkali granite field of the R_1–R_2 diagram (Figure 7a). In the TAS diagram, samples are concentrated in the granite field (Figure 7b), and in the SiO_2-K_2O diagram, samples fall into the high-K calc-alkaline series field (Figure 7c). As evidenced in the A/CNK-A/NK diagram (Figure 7d), the samples are strongly peraluminous, with A/CNK values between 1.37 and 1.57. The FAG samples have low ΣREE values (65.57 ppm–102.06 ppm). LREE values and HREE values are 46.80 ppm–95.25 ppm and 6.79 ppm–15.62 ppm, respectively. The LREE/HREE ratio ranges from 4.97 to 10.91, and the La_N/Yb_N ratio ranges from 5.05 to 14.86. The FAG samples exhibit negative Eu anomalies, as indicated by δEu values ($\delta Eu = \frac{Eu_N}{\sqrt{Sm_N \times Gd_N}}$) ranging from 0.08 to 0.19. The primitive mantle-normalized trace spider diagram (Figure 8a) shows that

they are enriched in Rb, Th, and U and depleted in Sr, Ba, Zr, and Nb. The chondrite-normalized rare earth element distribution diagram indicates that the REE patterns are right-leaning shapes (Figure 8b).

Table 5. Analysis results of major elements (wt%) and trace elements (ppm) of FAG in the Chamuhan intrusion.

Sample No.	CY10	CY11	CY12	CY13	CY14	CY15	CY16	CY17
SiO_2	77.1	76.9	77.9	78.7	79.1	77.8	76.9	77.1
Al_2O_3	12.4	12.6	11.9	12.2	12.2	12.1	12.3	12.2
FeO^T	0.22	0.31	0.74	0.20	0.41	0.42	0.51	0.40
Na_2O	3.55	4.60	3.74	3.91	3.36	3.90	4.09	3.78
MgO	0.05	0.05	0.09	0.03	0.08	0.05	0.05	0.06
P_2O_5	0.01	0.01	0.01	0.01	0.01	0.02	0.01	0.01
K_2O	4.86	3.98	3.89	4.40	3.99	4.33	4.22	4.44
CaO	0.66	0.49	0.45	0.25	0.43	0.22	0.35	0.30
TiO_2	0.05	0.04	0.05	0.06	0.05	0.05	0.04	0.04
MnO	0.01	0.01	0.02	0.01	0.02	0.01	0.01	0.01
LOI	0.71	0.59	0.77	0.51	0.62	0.61	0.49	0.64
Total	99.7	99.7	99.8	100.6	100.5	99.6	99.3	99.3
A/NK	1.48	1.47	1.56	1.48	1.66	1.46	1.49	1.49
A/CNK	1.37	1.39	1.47	1.43	1.57	1.42	1.43	1.44
T_{Zr}(°C)	788	760	753	795	814	843	768	854
Rb	262.5	176.8	186.4	234.4	278.1	161.2	236.1	194.3
Sr	11.3	5.90	11.7	9.00	9.41	7.02	10.8	5.58
Ba	109.4	88.9	86.4	154.5	145.1	46.4	105.5	57.2
Th	19.9	7.00	11.6	15.3	20.2	26.2	17.8	25.9
U	4.12	3.48	1.60	3.12	2.86	7.20	3.20	6.79
Nb	23.8	12.9	8.80	18.8	18.3	13.7	12.9	16.4
Ta	3.08	1.74	1.13	2.35	2.43	2.05	1.52	2.02
Zr	158.8	118.8	97.3	162.2	179.9	273.3	122.3	302.1
Hf	9.70	6.07	4.57	8.76	9.51	12.7	7.08	13.8
Co	1.01	2.06	5.32	0.66	0.45	1.09	1.58	0.44
Ni	0.92	1.66	3.23	2.50	0.98	1.09	0.74	0.99
V	1.26	0.86	2.38	1.81	1.42	1.53	1.29	1.29
Sc	2.49	2.05	4.42	1.85	2.84	4.16	3.78	2.44
Cu	2.46	1.78	12.0	2.88	1.93	5.12	5.67	3.28
Pb	11.9	12.2	13.8	10.8	5.88	20.0	14.1	31.4
La	12.6	11.4	20.6	15.4	17.4	16.1	22.5	19.3
Ce	21.6	18.5	40.8	23.2	26.4	25.9	34.3	27.2
Pr	4.33	3.60	7.47	5.07	5.47	5.64	7.30	6.53
Nd	13.3	11.0	22.3	15.8	15.4	17.1	22.0	20.0
Sm	2.74	2.14	3.81	2.98	3.09	3.56	4.43	4.43
Eu	0.12	0.08	0.14	0.17	0.18	0.08	0.15	0.11
Gd	2.69	1.95	3.45	2.60	2.85	3.17	3.90	4.06
Tb	0.52	0.34	0.49	0.41	0.49	0.57	0.63	0.79
Dy	2.60	1.54	1.90	1.64	2.17	2.51	2.65	3.80
Ho	0.68	0.38	0.43	0.39	0.52	0.60	0.61	0.94
Er	1.77	1.03	1.07	0.97	1.33	1.51	1.48	2.46
Tm	0.31	0.19	0.18	0.16	0.24	0.27	0.25	0.46
Yb	1.78	1.11	0.99	0.93	1.42	1.45	1.42	2.57
Lu	0.34	0.21	0.18	0.18	0.28	0.28	0.27	0.51
DI	96.1	97.2	95.7	97.7	95.4	97.6	96.9	97.0
SI	0.63	0.59	1.16	0.44	1.03	0.62	0.65	0.72
ΣREE	65.6	53.5	103.9	70.0	77.3	78.8	102.1	93.3
LREE	54.8	46.8	95.3	62.7	68.0	68.4	90.8	77.6
HREE	10.7	6.79	8.73	7.32	9.34	10.3	11.2	15.6
LREE/HREE	5.11	6.90	10.9	8.58	7.29	6.59	8.08	4.97
Eu/Eu*	0.14	0.13	0.12	0.19	0.19	0.08	0.12	0.08
La_N/Yb_N	5.06	7.35	14.8	11.8	8.77	7.96	11.3	5.38
$TE_{1,3}$	0.95	0.95	0.90	0.92	0.95	0.95	0.93	0.97

Note: $TE_{1,3} = \sqrt{\sqrt{\frac{Ce_{cn}}{La_{cn}^{\frac{2}{3}} \times Nd_{cn}^{\frac{1}{3}}} \times \frac{Pr_{cn}}{La_{cn}^{\frac{1}{3}} \times Nd_{cn}^{\frac{2}{3}}}} \times \sqrt{\frac{Tb_{cn}}{Gd_{cn}^{\frac{2}{3}} \times Ho_{cn}^{\frac{1}{3}}} \times \frac{Dy_{cn}}{Gd_{cn}^{\frac{1}{3}} \times Ho_{cn}^{\frac{2}{3}}}}}$, Ln_{cn} = chondrite-normalized lanthanide concentration.

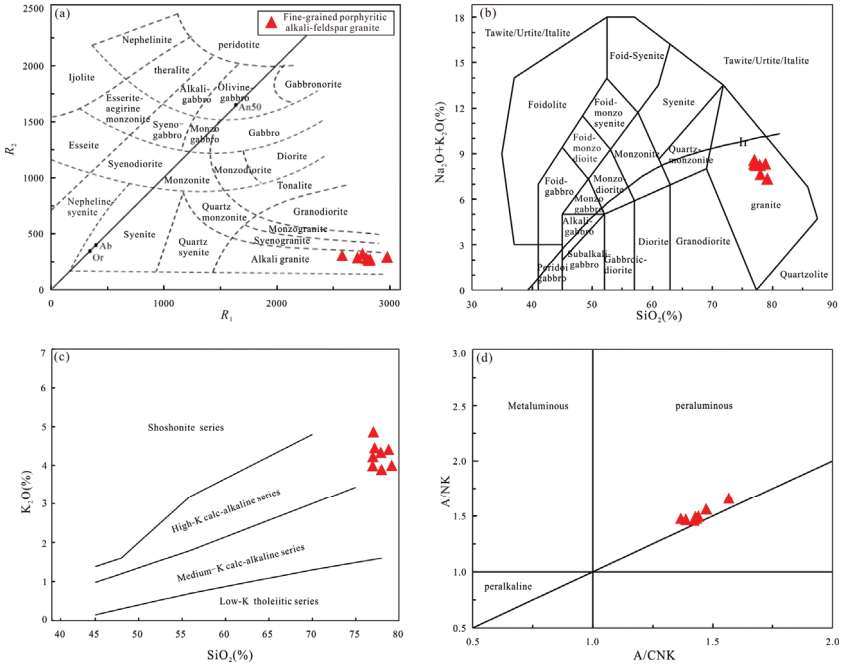


Figure 7. Classification diagrams of the FAG in the Chamuhan intrusion. (**a**) R_1-R_2 diagram [34]; (**b**) TAS diagram [35]; (**c**) SiO_2-K_2O diagram [36]; (**d**) A/CNK-A/NK diagram [37].

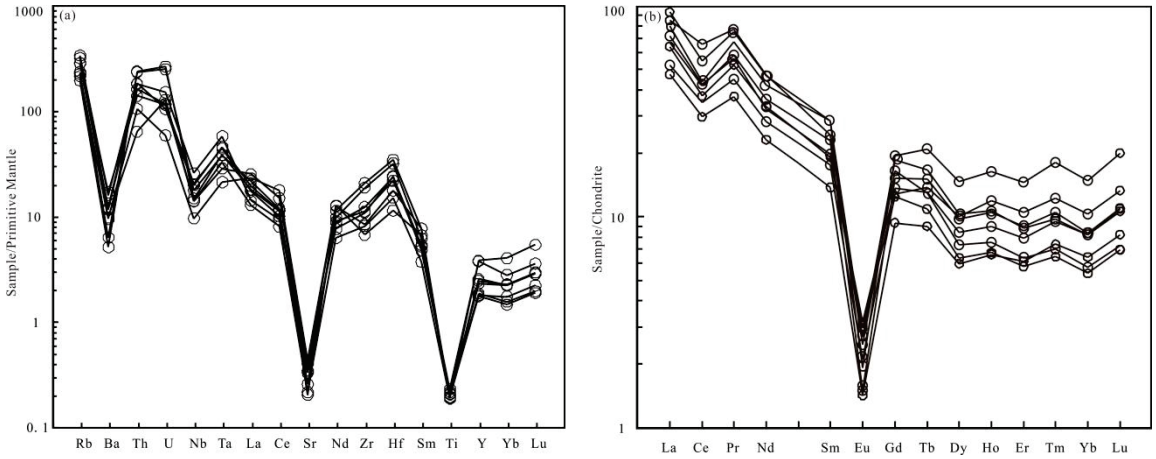


Figure 8. Primitive mantle-normalized trace spider diagram (**a**) and chondrite-normalized rare earth element distribution diagram (**b**) of FAG in the Chamuhan intrusion.

6. Discussion

6.1. Petrogenic Age

The mineralization age of the Chamuhan W–Mo polymetallic deposit has been extensively studied, with Re–Os isotope dating of molybdenite yielding ages of 140.5 ± 1.1 Ma and 139.5 ± 1.5 Ma [28,38], indicating an Early Cretaceous formation. However, the crystallization age of the ore-forming intrusion remains unclear. Zhang et al. [18] conducted a detailed geochronological and geochemical study on the WMG, PMG, and FAG within the Chamuhan intrusion, and their data, including geochemical and $\delta^{18}O$ isotopes, indicate that the FAG represents a more evolved melt compared to the WMG and PMG. Zircon and monazite U-Pb dating by Zhang et al. [18] yielded consistent ages of 143–144 Ma for the WMG and PMG. However, determining a reliable age for the FAG proved challenging due to intense hydrothermal alteration, which resulted in porous, metamorphic zircons. Among fourteen analytical spots, only three yielded ages consistent with the WMG and PMG (143 ± 2 Ma, 145 ± 2 Ma, 143 ± 1 Ma), while the remainder showed significant

scatter down to 100 ± 1 Ma, rendering the dataset inconclusive. Furthermore, monazite grains exhibited complex hydrothermal age zoning [39], preventing them from reliably recording the magmatic crystallization age. In this study, we targeted pristine, magmatic zircon grains from the FAG with uniform internal textures and obtained a robust weighted mean $^{206}Pb/^{238}U$ age of 141.3 ± 1.2 Ma, which we interpret as the crystallization age of the FAG. This new age is consistent with the mineralization age of the Chamuhan deposit, confirming a genetic link between the granite emplacement and ore formation.

In comparison, the crystallization ages of the ore-forming intrusions and the mineralization ages of numerous recently discovered tungsten–tin polymetallic deposits within the SGXR—including the Daolundaba Cu–W–Sn–Ag deposit, the Weilasituo Sn deposit, the Huanggang Fe–Sn deposit, the Baiyinhan W–Mo deposit, and the Dongshanwan W–Mo–Sn deposit—are predominantly Early Cretaceous (Table 6). This concentration of ages strongly suggests a genetic link between tungsten–tin mineralization and the emplacement of highly fractionated granites during the Early Cretaceous in this region. Molybdenite Re–Os dating from the Chamuhan deposit is consistent with the zircon U–Pb dating results within analytical uncertainties, indicating that both the intrusion and the deposit formed during the Early Cretaceous. The age data combined with geological characteristics and chronological studies support that FAG is the ore-forming intrusion for the Chamuhan W–Mo polymetallic deposit.

Table 6. The crystallization and mineralization ages of the major W–Sn polymetallic deposits in the SGXR.

Deposit	Metal Assemblage	Ore-Causative Intrusion (Ma)	Mineralization (Ma)	References
Daolundaba	Cu–W–Sn–Ag	Zircon U–Pb 134–136Ma	Cassiterite U-Pb 134.7 ± 2.8Ma	Chen et al. [40]; Wu et al. [41]
Weilasituo	Sn–Li–Rb–Cu–Zn	Zircon U–Pb 137–138Ma	Cassiterite U-Pb 135 ± 6Ma	Wang et al. [42]
Huangganliang	Sn–Fe	Zircon U–Pb 136.8 ± 0.57Ma	Molybdenite Re-Os 134.9 ± 5.2Ma	Zhai et al. [43]; Zhou et al. [44]
Baiyinhan	W–Mo	Zircon U–Pb 139.1 ± 2.5Ma	Molybdenite Re-Os 139.6 ± 7.6Ma	Wang et al. [45]
Dongshanwan	Sn–Ag–Pb–Zn	Zircon U–Pb 142.2 ± 0.9 Ma	Molybdenite Re-Os 141.3 ± 2.7Ma	Zeng et al. [46]; Zhang et al. [47]

6.2. Petrogenesis

6.2.1. Petrogenetic Type

The genetic classification of granites encompasses I-, S-, M-, and A-types, reflecting distinct magmatic origins and petrogenetic processes [48,49]. The FAG is peraluminous (A/CNK = 1.36–1.56), depleted in Ba, Sr, Ti, and P, and exhibits a pronounced negative Eu anomaly. Although both S-type and highly fractionated I-type granites can be peraluminous, their origins differ: S-types derive from partial melting of aluminous metasedimentary protoliths, which typically contain minerals such as cordierite, garnet, or corundum [50], whereas highly fractionated I-types acquire their composition through extreme fractional crystallization of metaluminous magmas. This distinction is further reflected geochemically: S-type granites typically show depletion in Th and Y with negative Rb–Th–Y correlations due to early monazite crystallization, whereas highly fractionated I-types display elevated Th and Y with positive Rb–Th and Rb–Y correlations [51,52]. Petrographic observations reveal that the FAG lacks typical peraluminous minerals (e.g., cordierite, garnet) except for minor muscovite (Figure 3). Geochemically, it shows a positive

Rb–Th/Y correlation (Figure 9), supporting its classification as a highly fractionated I-type rather than S-type granite [53,54].

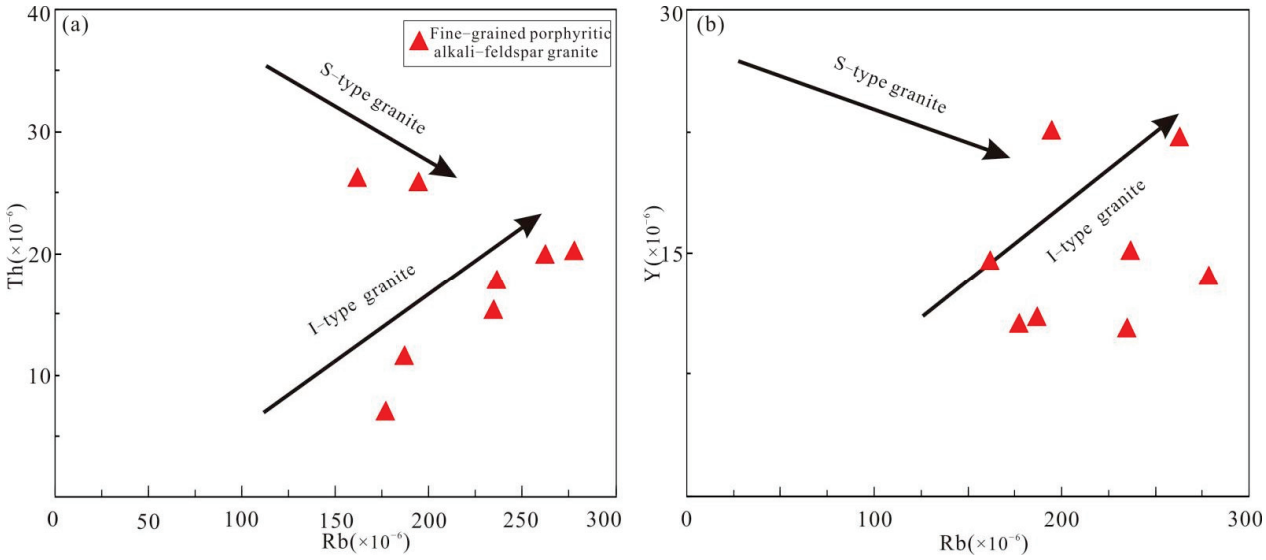


Figure 9. Rb vs. Th (**a**) and Rb vs. Y (**b**) diagrams of FAG in the Chamuhan intrusion.

In the $(Na_2O + K_2O)/CaO$ vs. Zr + Nb + Ce + Y discrimination diagram, the FAG plots within the field of fractionated granites (Figure 10a). In the 10,000 × Ga/Al vs. Zr diagram, data fall near the boundary between A-type and I-/S-type fields (Figure 10b). The A-type signatures in some diagrams are acquired through extensive fractional crystallization of an original I-type melt, which can drive the residual magma into compositional fields that overlap with A-type granites. The granite shows characteristic features of high fractionation, including low ratios of geochemically coherent elements (Zr/Hf = 16–21; Nb/Ta = 6.6–8.5), low total REE contents, LREE enrichment with low LREE/HREE ratios (avg. 7.3), and significant negative Eu anomalies [49,55]. These features collectively indicate that the Chamuhan granite underwent high-degree magmatic differentiation.

Highly fractionated I-type and A-type granites exhibit highly similar geochemical characteristics and are often difficult to distinguish [56]. Due to advanced differentiation, highly fractionated granites possess chemical and mineral compositions similar to those of low eutectic granite, resulting in comparable geochemical features. As a result, conventional petrogenetic discrimination diagrams often fail in distinguishing highly fractionated I-type and A-type granites. However, according to Wang et al. [57], A-type granites are characterized by higher total iron contents (>1%) and higher emplacement temperatures (average 840 °C). The FAG displayed a considerably lower total iron content (average 0.4%), far below that of typical A-type granites [58]. Calculations using ternary feldspar geothermobarometry [59,60] yield emplacement pressures ranging from 313 MPa to 454 MPa and temperatures between 689 °C and 778 °C. These values are consistent with the average temperature of 796 °C obtained from whole-rock zircon saturation thermometry, and all are lower than the mean temperature of 840 °C for A-type granites [58]. In addition, the average 10,000 Ga/Al ratio of Chamuhan granite is 2.9, which is lower than the average 10,000 × Ga/Al ratio (3.75) proposed for A-type granite by Whalen et al. [61]. The total Zr + Nb + Ce + Y values (average 234.86 ppm) of the granites are also significantly lower than the minimum threshold of 350 ppm for A-type granites proposed by Whalen et al. [61]. In summary, based on the comprehensive evidence—including the absence of Al-rich minerals, a positive Rb-Th/Y correlation, low iron content, moderate emplacement temperatures,

and low Ga/Al ratios and Zr + Nb + Ce + Y values—the FAG intrusion is more likely to be the highly differentiated I-type granite.

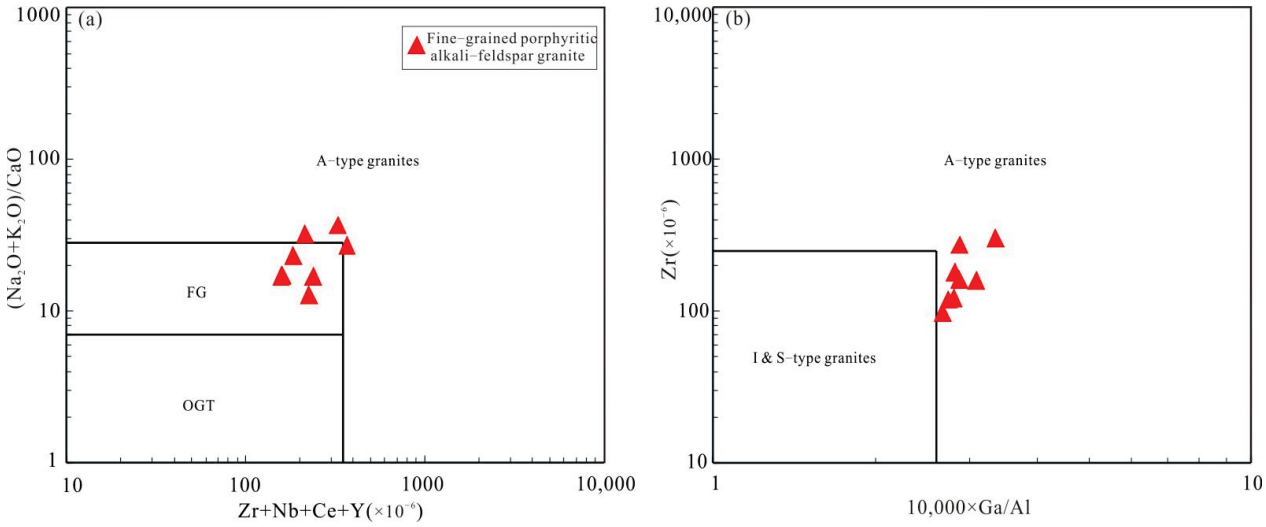


Figure 10. Discriminant diagram of granite type (**a**) $(Na_2O + K_2O)/CaO$ vs. Zr + Nb + Ce + Y discrimination diagram [51]; (**b**) 10,000 × Ga/Al vs. Zr diagram [59].

6.2.2. Magmatic Evolution and Metallogenesis

To simulate the mineral phases produced during crystallization differentiation, the fractional crystallization process of the FAG was modeled based on Rayleigh fractionation, and the thermodynamic software GeoPS in conjunction with the melt model of Holland et al. [62]. Combined with its crystallization conditions, the magmatic evolution was simulated over a pressure of 500 MPa and a temperature range of 600 to 1200 °C. As shown in the separating crystallization trend diagram and thermodynamic phase diagram, the fractional crystallization of plagioclase results in depletion of Sr and Eu in the residual melt and an increase in the Rb/Sr ratio (Figure 11a). Similarly, crystallization of K-feldspar led to Ba depletion, while crystallization of Ti-bearing minerals (e.g., titanite, ilmenite, and rutile) caused Ti depletion (Figure 11a). The crystallization of accessory minerals (e.g., muscovite, biotite, garnet) reduced the total REE content and Zr/Hf ratios (Figure 11b). In summary, these diagrams reflected the magma experienced crystallization of quartz, plagioclase, K-feldspar, muscovite, biotite, albite, garnet, ilmenite, and rutile.

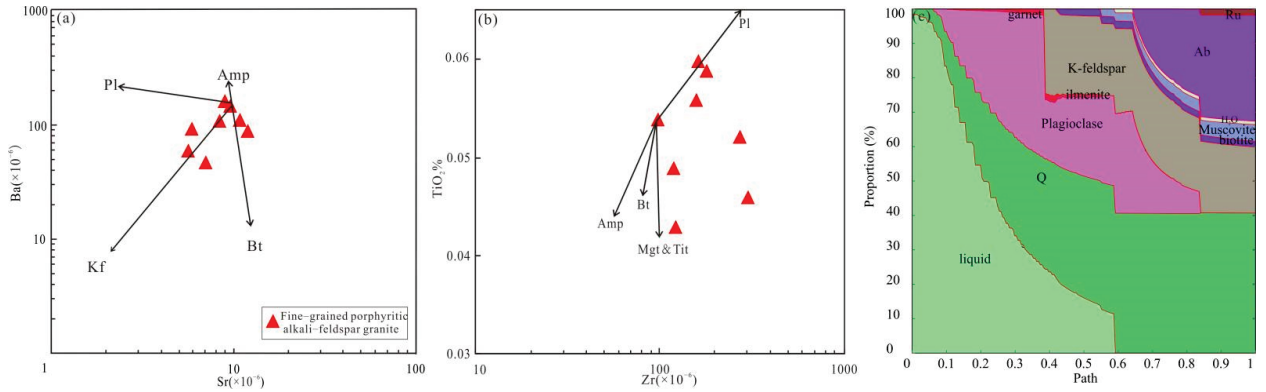


Figure 11. Separating crystallization trend diagram (**a**,**b**) and the thermodynamic phase diagram of mineral and melt phases (**c**) of the Chamuhan intrusion [63,64]. Ab = albite; Amp = hornblende; Bt = biotite; Kf = K-feldspar; Mgt = magnetite; Pl = plagioclase; Q = quartz; Ru = rutile; Tit = titanite.

In geochemistry, Zr/Hf and Nb/Ta are termed "twin elements" due to their similar ionic properties, leading to CHARAC behavior. During magmatic differentiation, ligand complexation in evolved melts causes their ratios to decrease [65,66], making these ratios key indicators of magma evolution. Ballouard et al. [67] proposed Nb/Ta < 5 as a threshold for fluid-altered granites, helping distinguish magmatic–hydrothermal from fractionation-dominated systems, while Zr/Hf = 26 and Y/Ho < 24 denote hydrothermal input (Figure 12a) [68,69]. Instead of following CHARAC behavior, evolved and volatile-rich systems (enriched in H_2O, F, and B) commonly exhibit non-CHARAC signatures, as fluid–melt interactions preferentially fractionate high-field-strength element pairs [70,71]. This results in systematically lowered ratios such as Zr/Hf (16–21) and Nb/Ta (6.68–8.53) (Figure 12b), as well as Y/Ho (23–32, avg. 26) in the FAG (Figure 12c). Low Zr/Hf, Nb/Ta, and Y/Ho ratios and high Cs concentration reflect a high degree of fractionation [72], and the tetrad effect values can reflect the evolution degree of granite. High tetrad effect values in FAG ($TE_{1,3}$ = 0.93–0.99) further confirm evolved melt conditions (Figure 12d). All ratios deviate from chondritic values and decrease systematically, supporting extensive fractional crystallization with minimal magmatic–hydrothermal influence in the FAG.

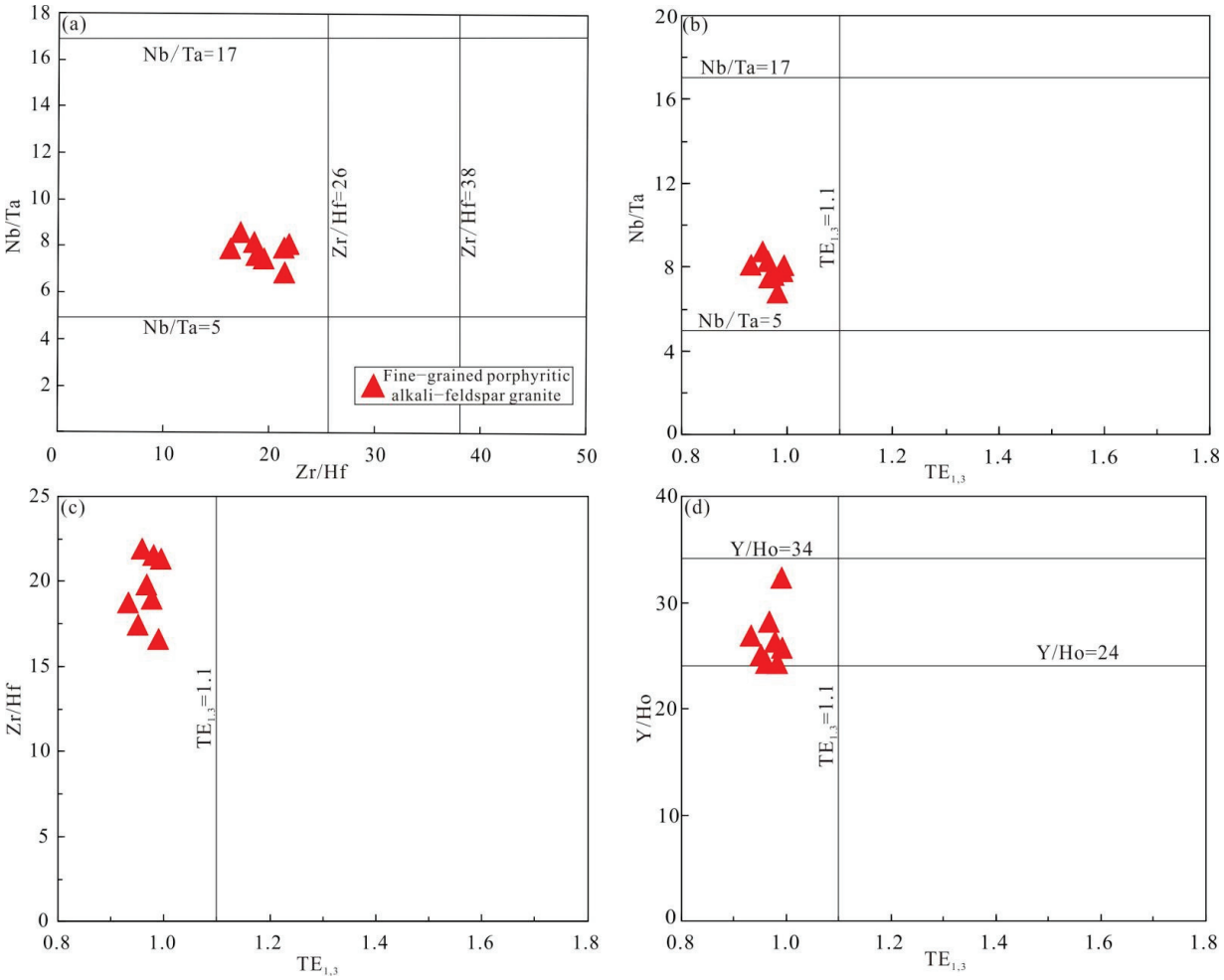


Figure 12. Discrimination diagrams for evolution degree of granites [73]. (**a**) Zr/Hf vs. Nb/Ta diagram; (**b**) Nb/Ta vs. TE1,3 diagram; (**c**) Zr/Hf vs. TE1,3 diagram; (**d**) Y/Ho vs. TE1,3 diagram.

The water content of the FAG, calculated using the plagioclase hygrometer of Waters and Lange [74], ranges from 8.61% to 11.1%. EMPA data reveal that fluorine (F) content in muscovite ranges from 1.92% to 2.94%, and lithium (Li) content ranges from 1.19% to 1.72%, suggesting that the parental magma was a volatile-rich system. When granitic magmas

are enriched in volatiles such as H_2O, F, and Li, the solidus temperature of the magma is significantly reduced [75,76], resulting in prolonged fractional crystallization and more extensive magmatic evolution. The type of mica in granite can reflect its evolutionary degree. The transition from muscovite to zinnwaldite represents a progressive increase in the evolutionary degree of granitic magma [77]. The FAG contains zinnwaldite and Li-rich phengite, indicating that the FAG has undergone a high degree of evolution.

Candela et al. [78] emphasized that tungsten deposit formation is associated with reduced magmas, as the partitioning of tungsten during fractional crystallization is influenced by magma oxygen fugacity. Under reducing conditions, tungsten behaves as an incompatible element during crystal-melt distribution and becomes enriched in the residual melt through magmatic crystallization differentiation. This study estimates the oxygen fugacity of the magma using Ce and Eu in zircon [79], yielding $\log fO_2$ values of −22.58 to −14.48 (average −18.1) for the FAG, indicating that the magma was characterized by low oxygen fugacity. Thompson et al. [80] summarized the occurrence relationship between Cu, Cu–Mo, Mo, W, and Sn mineralization and alkaline–calc-alkaline magmatic rocks with different oxidation states in several typical deposits around the world. They concluded that different metal combinations are distributed based on magma fractionation degree and oxidation state [81]. The magmatic oxygen fugacity $\log fO_2$ of FAG falls within the range of W-Mo mineralization (−22–−12). From the perspective of magmatic evolution, the magma experienced continuous fractional crystallization of minerals such as plagioclase and K-feldspar (Figure 11), leading to further enrichment of ore-forming elements (including W, Sn, Mo) and volatiles (F, Cl) in the residual melt. The accumulation of volatiles reduces magma viscosity and solidus temperature, resulting in further magma evolution [82]. During the late stage of magmatic evolution, volatile-rich fluids are exsolved and separated from the melt [83]. The experimental petrological results show that the $D_W^{fluid/melt}$ in a peraluminous melt with high H_2O content (10 wt%) is ninefold higher than those with low H_2O content (2 wt%) [84]. Thermodynamic experiments demonstrate that when $m_{HF} > 2$, $D_W^{fluid/melt}$ increases linearly with the molar concentration of HF in the medium [85]. At 800 °C and 100 MPa, $D_W^{fluid/melt} = 0.37$ in 1 mol/L NaCl, $D_{Mo}^{fluid/melt} = 1.70$, in aqueous solution, $D_W^{fluid/melt} = 0.07$, $D_{Mo}^{fluid/melt} = 0.13$. The distribution coefficients of Mo and W show a positive linear correlation with the chloride (Cl^-) concentration, indicating that high Cl^- systems enhance the mobility of Mo and W into the fluid phase [86,87]. Furthermore, the addition of F to the melt significantly increases the non-bridging oxygen (NBO) content, thereby promoting the solubility of WO_4^{2-} in the melt [88,89]. In summary, the melt with high H_2O, F, and Cl contents facilitates the enrichment of W–Mo in the magmatic–hydrothermal system. The plagioclase hygrometer results indicate that the H_2O contents of the FAG range from 8.61% to 11.1% (average 9.64%). EPMA data of mica show F contents between 1.92% and 2.94%, indicating that high water and F contents enhanced the enrichment of ore-forming elements.

Thermodynamic experiments demonstrate that temperature and pH influence tungsten (W) speciation during migration [90]. Acidic solutions promote the formation of polymeric tungstate species (e.g., HW_6O_{5-21} and W_6O_{2-19}), the stability of which increases at temperatures above 200 °C. In neutral/alkaline solutions at temperatures exceeding 300 °C, monomeric tungstate species (e.g., WO, HWO_4^-, H_2WO_4, and alkali metal tungstate complexes) become the dominant forms of W [91]. Molybdenum may migrate as MoO_2Cl^+ in Cl-rich fluids [92]. Han [28] concluded, based on fluid inclusion studies of the Chamuhan deposit, that the ore-forming fluids were characterized by high temperature, high salinity, and CO_2-rich compositions. The close association of tungsten ore bodies with fluorite indicates the ore-forming fluid was rich in F^- and Cl^-. The Chamuhan deposit contains pervasive greisenization. During the late magmatic stage, fluids exsolved from residual

melts migrated upward, triggering greisenization at the top of the granite. Reaction (1) consumes H^+ to form mica and quartz, which increases the pH of the fluid and consequently destabilizes polymeric tungstate species, converting them into monomeric forms. CO_2 plays a dual role in high-temperature, high-pressure hydrothermal fluids by enhancing the solubility of tungsten (W) and stabilizing precipitating cations (e.g., Fe^{2+}, Mn^{2+}, Ca^{2+}) [91]. Decompression during the upward migration of fluids caused boiling and CO_2 degassing, destabilizing $WO_4{}^{2-}$ along with cations such as Fe^{2+} and Mn^{2+}. The ensuing Reaction (2) was responsible for the precipitation of wolframite ([Fe,Mn]WO_4) from the reaction of $WO_4{}^{2-}$ with Fe^{2+} and Mn^{2+} [88,93,94]. The paragenesis of pyrrhotite and arsenopyrite indicates a reducing environment, which reduced Mo^{6+} to Mo^{4+} and $SO_4{}^{2-}$ to S^{2-}, leading to the precipitation of molybdenite (MoS_2) [95]. Fluid–melt interaction is the critical trigger for ore deposition, where exsolution of late-stage F-Cl-rich hydrothermal fluids—facilitated by the high melt H_2O content (8.6–11.1 wt%) and reduced conditions (logfO_2 = 22.6 to −14.5)—efficiently scavenge W-Mo from the melt (enhanced by F-complexation) and precipitate them via pH shifts (greisenization) into the vein system. Fractional crystallization removes Sr, Eu, and Ca from the melt, suppressing scheelite ($CaWO_4$) formation. In the F-rich hydrothermal system, Ca^{2+} preferentially forms fluorite with F^-. Scheelite precipitation occurs only under high Ca^{2+} and low F^- conditions. This selective mineralization accounts for the common paragenesis of wolframite with fluorite and the predominance of wolframite over scheelite in the Chamuhan deposit.

$$2Na[AlSi_3O_8] + K[AlSi_3O_8] + 2H^+ = KAl_2[AlSi_3O_{10}](OH)_2 + 6SiO_2 + 2Na^+ \quad (1)$$

$$HWO_4^- + FeCl_2(aq) = FeWO_4 + 2Cl^- + H^+ \quad (2)$$

6.3. Tectonic Setting

The SGXR is characterized by a complex tectonic setting situated at the confluence of the Paleo-Asian and Paleo-Pacific metallogenic domains, which was also influenced by the subduction and closure of the Mongol-Okhotsk Ocean. The genesis and tectonic setting of Mesozoic magmatic rocks in the SGXR remain debated, primarily between two viewpoints: (1) Paleo-Pacific subduction accompanied by slab rollback processes [70,96], or (2) post-collisional extension triggered by the closure of the Mongol-Okhotsk oceanic basin [97,98].

Mao et al. [99] proposed that multiple large-scale metallogenic events occurred during the Mesozoic in northern China, with three high-intensity metallogenic episodes (160–200 Ma, ~140 Ma, and ~120 Ma) identified along the Northern margin of the North China Craton and the Southern Great Xing'an Range. These episodes correspond to three major geodynamic events: (1) collisional orogeny, (2) tectonic regime transition, and (3) large-scale lithospheric delamination. The geodynamic framework in northern China at ~140 Ma corresponds to a period of tectonic regime transition, which transformed from a compressional environment to an extensional environment driven by complex tectonic interactions. Combined with the Yb vs. Ta-Rb tectonic discrimination diagram, most data points fall in the fields of syn-collision and post-orogenic granites [100] (Figure 13a,b). Data points on the R_1-R_2 diagram are concentrated in the post-orogenic granites (Figure 13c), while SiO_2-log[$CaO/(K_2O + Na_2O)$] diagrams exhibit data points that fall in the extensional area (Figure 13d). These geochemical indicators collectively suggest that previous studies widely supported the SGXR in a fully extensional environment in the Mesozoic [101–103]. Therefore, the Chamuhan intrusion was formed under the background of an extensional environment. The formation mechanism of the extensional environment in the study area is influenced by the subduction of the Paleo-Pacific plate, the subduction and closure of the Mongolia-Okhotsk Ocean, or the combined control of the two, though this remains a controversial issue.

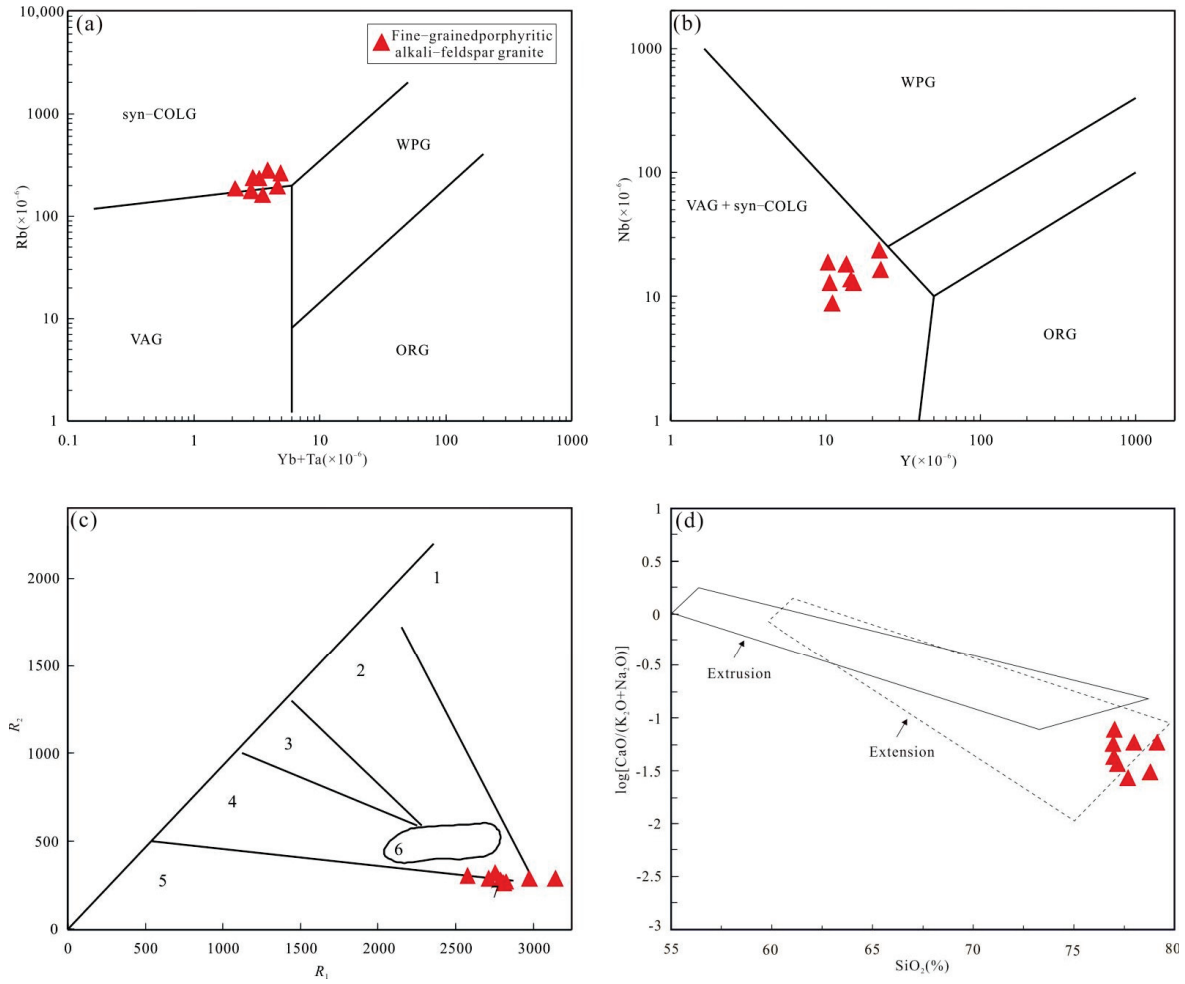


Figure 13. The tectonic setting discrimination diagrams of the Chamuhan intrusion. (**a**) Yb vs. Ta-Rb diagram [104]; (**b**) Y vs. Nb diagram [104]; (**c**) R_1 vs. R_2 diagram [105]; (**d**) SiO_2 vs. log[$CaO/K_2O + Na_2O$] [105]. ORG = oceanic ridge granites; syn-COLG = syn-collisional granites; VAG = volcanic arc granites; WPG = within-plate granites. 1 = mantle differentiated granites; 2 = pre-collisional granites; 3 = post-collisional uplifting granites; 4 = late-orogenic granites; 5 = anorogenic granites; 6 = syn-collisional granites; 7 = post-orogenic granites.

The Mongol-Okhotsk Ocean underwent scissor-like closure from west to east during the Triassic, leading to the collision between the Siberian Craton and the North China-Amur Block. This collision formed the Mongol-Okhotsk Orogen, the youngest major orogenic belt in Northeast Asia. Following this orogeny, the assembly of continental blocks in Northeast Asia was completed, marking a transition to intraplate tectonic evolution. However, the precise timing of the final closure of the Mongol-Okhotsk Ocean remains controversial [106–108]. Middle Jurassic paleomagnetic data from the northern margin of the North China Craton indicate a paleolatitude of 61.7° ± 9.1°, consistent with contemporaneous positions of the Siberian Craton [109]. Sorokin et al. [110] conducted zircon U-Pb dating of metasedimentary rocks from the Mongol-Okhotsk basin, which revealed an absence of ages younger than 171 Ma. Based on this geochronological evidence, they proposed that the final closure of the Mongol-Okhotsk Ocean occurred at the Early–Middle Jurassic (Figure 14a). Wang et al. [111] used the extensive data analysis to reconstruct the regional paleogeographic structure and evolution history. By constructing a zircon age database and applying digital mapping techniques, they traced the migration of major magmatic provinces across Asia. Their results, based on the spatial distribution of Jurassic–Cretaceous igneous rocks, suggest that the influence of the Mongol-Okhotsk

tectonic system is confined to central and northern Mongolia–Transbaikalia and eastern Mongolia–Great Xing'an Ranges. Wu et al. [39] proposed that the Late Jurassic to Early Cretaceous igneous rocks in the SGXR are predominantly aligned in a NNE orientation. This orientation is oblique relative to the Mongol-Okhotsk orogenic belt but generally parallel to the Pacific-Eurasian plate boundary, implying that the Early Cretaceous magmatism in this region was likely associated with the subduction of the Paleo-Pacific Plate. This evidence collectively suggests that the Mongol-Okhotsk Ocean closed by the Early–Middle Jurassic and that its subsequent tectonic influence did not extend to the SGXR. There is no consistent spatiotemporal correlation between the Chamuhan intrusion and the subduction or closure of the Mongolia-Okhotsk Ocean. Instead, the Middle Jurassic calc-alkaline volcanic associations in eastern Jilin–Heilongjiang and bimodal igneous rock suites in the Lesser Xing'an–Zhangguangcai Range signal the onset of the Paleo-Pacific tectonic influence [112,113]. By the Early Cretaceous, rollback of the Paleo-Pacific slab induced an extensional regime in the SGXR (Figure 14a). Asthenosphere upwelling triggered partial melting of the lower crust, generating magma that subsequently underwent high-degree fractional crystallization, ultimately forming the W–Sn polymetallic deposits in this region (Figure 14b).

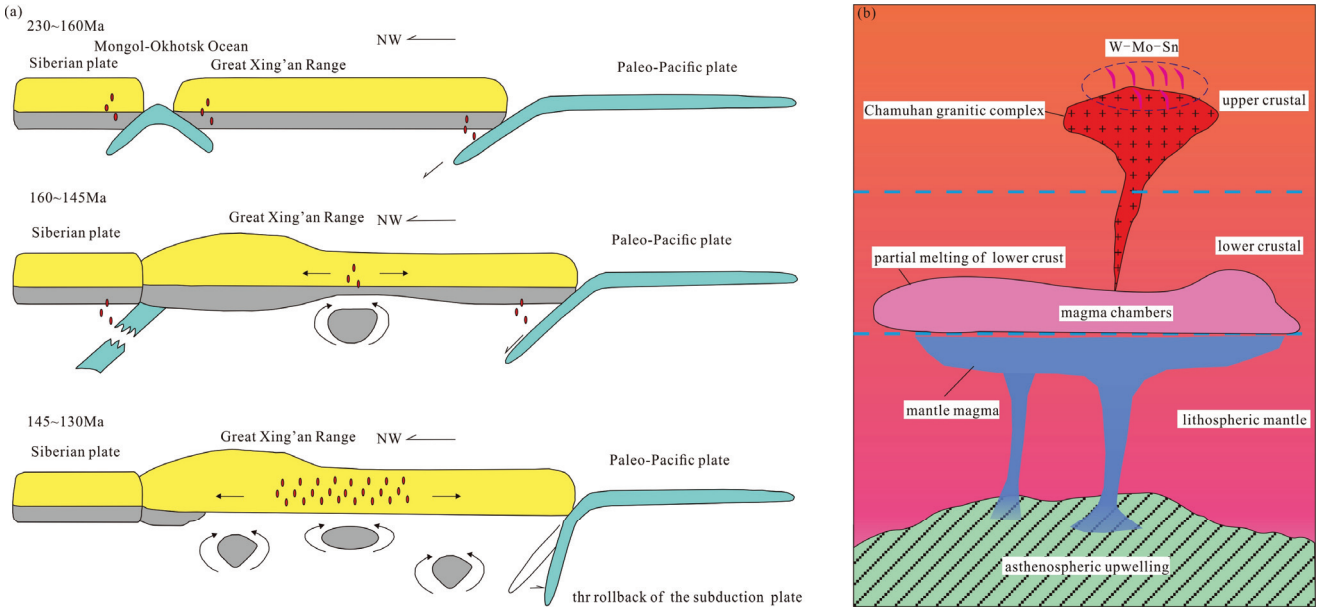


Figure 14. Mesozoic Tectonic Evolution Diagram of the Great Xing'an Range (**a**) Magmatic Evolution and Mineralization Model of the Chamuhan Granitic Complex (**b**).

7. Conclusions

1. LA-ICP-MS zircon U-Pb dating of the Chamuhan FAG yields an age of 141.3 ± 1.2 Ma, indicating that the Chamuhan intrusion formed during the Early Cretaceous.

2. The Chamuhan FAG shows high SiO_2 and total alkali contents, with enrichments in Rb, Th, and U, and depletions in Sr, Ba, Ti, and P. Its petrogenetic classification corresponds to a highly fractionated I-type granite.

3. The formation of the Chamuhan FAG involved fractional crystallization of quartz, plagioclase, K-feldspar, muscovite, biotite, albite, garnet, ilmenite, and rutile.

4. The Chamuhan FAG crystallized within an extensional regime triggered by Paleo-Pacific subduction. Extensive fractional crystallization enriched the magma in trace elements and volatiles, which were later transported by hydrothermal fluids to form vein-type W polymetallic ore bodies in the upper part of the intrusion.

Author Contributions: Conceptualization, Y.S. and G.C.; methodology, Y.S.; software, Y.S., T.L., Y.L. (Yuze Li). and Y.S.; validation, G.C., T.L. and G.W.; formal analysis, Y.S., T.Z., J.W. and Y.L. (Yingjie Li); writing—Y.S.; writing—review and editing: G.C., T.L. and G.W.; investigation, Y.S., G.C., G.W., C.L., Y.L. (Yingjie Li) and Y.W.; resources, G.C., G.W. and T.L.; data collection, G.C. and G.W.; data curation: G.C. and G.W.; visualization, Y.S., T.L. and Y.W.; supervision, G.C., G.W. and Y.S.; project administration and funding acquisition, G.C. All authors have read and agreed to the published version of the manuscript.

Funding: This research was funded by the National Natural Science Foundation of China (Grant No. 42202080), the Open Project Program of Hebei Province Collaborative Innovation Center for Strategic Critical Mineral Research, Hebei GEO University, China (Grant No. HGUXT2025-3), the Doctoral Research Initiation Fund Project of Hebei GEO University (Grant No. BQ2024017), and the Project of China Chemicalgeology and Mine Bureau Inner Mongolia S-Pb-Zn Polymetallic Ore Deep Prospecting Technology Innovation Team (No. ZHTD202402).

Data Availability Statement: Data are contained within the article.

Acknowledgments: We thank the anonymous reviewers and the Managing Editor, for their valuable and constructive comments, which have helped to improve our manuscript.

Conflicts of Interest: The authors declare no conflicts of interest.

References

1. Ying, J.F.; Zhou, X.H.; Zhang, L.C.; Wang, F. Geochronological Framework of Mesozoic Volcanic Rocks in the Great Xing'an Range, NE China, and Their Geodynamic Implications. *J. Asian Earth Sci.* **2010**, *39*, 786–793. [CrossRef]
2. Li, S.; Chung, S.; Wang, T.; Wilde, S.A.; Chu, M.; Guo, Q. Tectonic Significance and Geodynamic Processes of Large-scale Early Cretaceous Granitoid Magmatic Events in the Southern Great Xing'an Range, North China. *Tectonics* **2017**, *36*, 615–633. [CrossRef]
3. Zhou, Z.; Mao, J.; Stuart, F.M.; Chen, X.; Wilde, S.A.; Ouyang, H.; Gao, X.; Zhao, J. The Role of Mantle Melting in Granite-Associated Hydrothermal Systems: He–Ar Isotopes in Fluids Responsible for Sn–Ag–Pb–Zn Mineralization in Northeast China. *Min. Depos.* **2023**, *58*, 1421–1443. [CrossRef]
4. Mi, K.; Lü, Z.; Yan, T.; Yao, X.; Ma, Y.; Lin, C. Zircon Geochronological and Geochemical Study of the Baogaigou Tin Deposits, Southern Great Xing'an Range, Northeast China: Implications for the Timing of Mineralization and Ore Genesis. *Geol. J.* **2020**, *55*, 5062–5081. [CrossRef]
5. Zhao, P.; Chu, X.; Williams-Jones, A.E.; Mao, J.; Yuan, S. The role of phyllosilicate partial melting in segregating W and Sn deposits in W-Sn metallogenic provinces. *Geology* **2022**, *50*, 783–792. [CrossRef]
6. Shang, Z.; Chen, Y.; Guo, X. Felsic Igneous Rocks in the Hua'aobaote Pb–Zn–Ag Polymetallic Orefield, Southern Great Xing'an Range: Genesis, Metallogenetic and Tectonic Significance. *Acta Geol. Sin.* **2022**, *96*, 221–239. [CrossRef]
7. Li, S.; Li, Z.; Chen, G.; Yi, H.; Yang, F.; Lü, X.; Shi, J.; Dou, H.; Wu, G. Age, Fluid Inclusion, and H–O–S–Pb Isotope Geochemistry of the Superlarge Huaaobaote Ag–Pb–Zn Deposit in the Southern Great Xing'an Range, NE China. *Minerals* **2023**, *13*, 939. [CrossRef]
8. Liu, Y.; Jiang, B.; Chen, Y.; Wu, L.; Zuo, Y.; Liu, Z. Genesis of Cu-Sn Mineralization in the Shuangjianzishan Super-Large Silver Deposit, Inner Mongolia: Trace Element Constraints from Chalcopyrite and Cassiterite. *Appl. Sci.* **2024**, *14*, 3822. [CrossRef]
9. Zeng, Q.; Liu, J.; Zhang, Z.; Jia, C.; Yu, C.; Ye, J.; Liu, H. Geology and Lead-Isotope Study of the Baiyinnuoer Zn-Pb-Ag Deposit, South Segment of the Da Hinggan Mountains, Northeastern China. *Resour. Geol.* **2009**, *59*, 170–180. [CrossRef]
10. Zhao, Q.; Xiao, R.; Zhang, D.; Wang, J.; Zhang, Y.; Li, P. Petrogenesis and Tectonic Setting of Ore-Associated Intrusive Rocks in the Baiyinnuoer Zn–Pb Deposit, Southern Great Xing'an Range (NE China): Constraints from Zircon U–Pb Dating, Geochemistry, and Sr–Nd–Pb Isotopes. *Minerals* **2019**, *10*, 19. [CrossRef]
11. Yuan, S.; Williams-Jones, A.E.; Romer, R.L.; Zhao, P.; Mao, J. Protolith-Related Thermal Controls on the Decoupling of Sn and W in Sn-W Metallogenic Provinces: Insights from the Nanling Region, China. *Econ. Geol.* **2019**, *114*, 1005–1012. [CrossRef]
12. Zhao, P.; Yuan, S.; Williams-Jones, A.E.; Romer, R.L.; Yan, C.; Song, S.; Mao, J. Temporal Separation of W and Sn Mineralization by Temperature-Controlled Incongruent Melting of a Single Protolith: Evidence from the Wangxianling Area, Nanling Region, South China. *Econ. Geol.* **2022**, *117*, 667–682. [CrossRef]
13. Xie, W.; Zeng, Q.D.; Wang, R.L.; Wu, J.J.; Zhang, Z.M.; Li, F.C.; Zhang, Z. Spatial-Temporal Distribution and Tectonic Setting of Mesozoic W-Mineralized Granitoids in the Xing-Meng Orogenic Belt, NE China. *Int. Geol. Rev.* **2022**, *64*, 1845–1884. [CrossRef]
14. Yuan, S.; Peng, J.; Hu, R.; Li, H.; Shen, N.; Zhang, D. A Precise U–Pb Age on Cassiterite from the Xianghualing Tin-Polymetallic Deposit (Hunan, South China). *Min. Depos.* **2008**, *43*, 375–382. [CrossRef]

15. Yuan, S.; Williams-Jones, A.E.; Mao, J.; Zhao, P.; Yan, C.; Zhang, D. The origin of the zhangjialong tungsten deposit, South China: Implications for W-Sn mineralization in large granite batholiths. *Econ. Geol.* **2018**, *113*, 1193–1208. [CrossRef]
16. Huber, C.; Bachmann, O.; Manga, M. Homogenization Processes in Silicic Magma Chambers by Stirring and Mushification (Latent Heat Buffering). *Earth Planet. Sci. Lett.* **2009**, *283*, 38–47. [CrossRef]
17. Zhai, D.; Liu, J.; Cook, N.J.; Wang, X.; Yang, Y.; Zhang, A.; Jiao, Y. Mineralogical, Textural, Sulfur and Lead Isotope Constraints on the Origin of Ag-Pb-Zn Mineralization at Bianjiadayuan, Inner Mongolia, NE China. *Min. Depos.* **2019**, *54*, 47–66. [CrossRef]
18. Zhang, L.; Jiang, S.; Bagas, L.; Han, N.; Liu, Y.; Liu, Y. Element Behaviour during Interaction of Magma and Fluid: A Case Study of Chamuhan Granite, and Implications on the Genesis of W–Mo Mineralisation. *Lithos* **2019**, *343*, 31–44. [CrossRef]
19. Li, Y.; Zhou, H.; Brouwer, F.M.; Wijbrans, J.R.; Zhong, Z.; Liu, H. Tectonic Significance of the Xilin Gol Complex, Inner Mongolia, China: Petrological, Geochemical and U–Pb Zircon Age Constraints. *J. Asian Earth Sci.* **2011**, *42*, 1018–1029. [CrossRef]
20. Wu, H.-R.; Yang, H.; Zhu, Y.-S.; Santosh, M.; Chen, Z.-Y.; Ji, Z.; Zhang, Z.-C.; Ge, W.-C. Zircon and Apatite as Tracers of Physicochemical Differences between Barren and Rare Metal Plutons in Granite-Pegmatite Systems. *Geol. Soc. Am. Bull.* **2025**, *137*, 2982–2998. [CrossRef]
21. Zhu, X.; Lu, M. Fault Structures and Magmatic Intrusions Inferred from Magnetic Data for the Southern Great Xing'an Range, Northern China. *Ore Geol. Rev.* **2021**, *135*, 104206. [CrossRef]
22. Zhang, P.; Fang, H.; Zhong, Q.; Zhang, X.; Yuan, Y.; Liu, J. Structural Features and Tectonic Evolution of the Nenjiang–Balihan Fault in the Western Margin of the Songliao Basin, NE China, Inferred from 2D Inversion of Magnetotelluric Data. *J. Asian Earth Sci.* **2021**, *206*, 104628. [CrossRef]
23. Ouyang, H.; Mao, J.; Zhou, Z.; Su, H. Late Mesozoic Metallogeny and Intracontinental Magmatism, Southern Great Xing'an Range, Northeastern China. *Gondwana Res.* **2015**, *27*, 1153–1172. [CrossRef]
24. Zhang, J.H.; Gao, S.; Ge, W.C.; Wu, F.Y.; Yang, J.H.; Wilde, S.A.; Li, M. Geochronology of the Mesozoic Volcanic Rocks in the Great Xing'an Range, Northeastern China: Implications for Subduction-Induced Delamination. *Chem. Geol.* **2010**, *276*, 144–165. [CrossRef]
25. Zhang, H.; Zhang, H.; Shen, S.; Zhao, Z.; Qiu, L.; Chen, S.; Zhang, J.; Gong, F.; Li, Y.; Zheng, Y.; et al. Volcanic Age and Geochemistry of the Permian Linxi Formation in Northeast China: Implications for the Tectonic Evolution of the Paleo-Asian Ocean. *Lithosphere* **2023**, *2023*, 1–20. [CrossRef]
26. Ge, W.; Wu, F.; Zhou, C.; Zhang, J. Porphyry Cu-Mo Deposits in the Eastern Xing'an-Mongolian Orogenic Belt: Mineralization Ages and Their Geodynamic Implications. *Chin. Sci. Bull.* **2007**, *52*, 3416–3427. [CrossRef]
27. Xu, Z.G.; Chen, M.C.; Wang, D.H.; Chen, Z.H.; Li, H.M. *China Metallogenic Belt Division Scheme*; Geology Press: Beijing, China, 1989; pp. 1–103. (In Chinese)
28. Han, N. The Study on the Metallogenesis of the Chamuhan W-Mo Deposit, Hexigten Banner, Inner Mongolia. Ph.D. Thesis, Chinese Academy of Geological Sciences, Beijing, China, 2022. (In Chinese)
29. Vermeesch, P. IsoplotR: A Free and Open Toolbox for Geochronology. *Geosci. Front.* **2018**, *9*, 1479–1493. [CrossRef]
30. Pei, Q.-M.; Zhang, S.-T.; Hayashi, K.; Cao, H.-W.; Li, D.; Tang, L.; Hu, X.-K.; Li, H.-X.; Fang, D.-R. Permo–Triassic Granitoids of the Xing'an–Mongolia Segment of the Central Asian Orogenic Belt, Northeast China: Age, Composition, and Tectonic Implications. *Int. Geol. Rev.* **2018**, *60*, 1172–1194. [CrossRef]
31. Rubatto, D. Zircon Trace Element Geochemistry: Partitioning with Garnet and the Link between U–Pb Ages and Metamorphism. *Chem. Geol.* **2002**, *184*, 123–138. [CrossRef]
32. De La Roche, H.; Leterrier, J.; Grandclaude, P.; Marchal, M. A Classification of Volcanic and Plutonic Rocks Using R_1-R_2 Diagram and Major-Element Analyses—Its Relationships with Current Nomenclature. *Chem. Geol.* **1980**, *29*, 183–210. [CrossRef]
33. Tischendorf, G.; Gottesmann, B.; Förster, H.-J.; Trumbull, R.B. On Li-Bearing Micas: Estimating Li from Electron Microprobe Analyses and an Improved Diagram for Graphical Representation. *Mineral. Mag.* **1997**, *61*, 809–834. [CrossRef]
34. Deer, W.A.; Howie, R.A.; Zussman, J. *An Introduction to the Rock-Forming Minerals*, 3rd ed.; The Minerological Society: London, UK, 2013; pp. 1–492.
35. Middlemost, E.A.K. Naming Materials in the Magma/Igneous Rock System. *Earth-Sci. Rev.* **1994**, *37*, 215–224. [CrossRef]
36. Peccerillo, A.; Taylor, S.R. Geochemistry of Eocene Calc-Alkaline Volcanic Rocks from the Kastamonu Area, Northern Turkey. *Contrib. Mineral. Petrol.* **1976**, *58*, 63–81. [CrossRef]
37. Maniar, P.D.; Piccoli, P.M. Tectonic Discrimination of Granitoids. *Geol. Soc. Am. Bull.* **1989**, *101*, 635–643. [CrossRef]
38. Sun, Y.; Li, B.; Sun, F.; Ding, Q.; Wang, B.; Li, Y.; Wang, K. Mineralization Events in the Xiaokele Porphyry Cu (–Mo) Deposit, NE China: Evidence from Zircon U–Pb and K-feldspar Ar–Ar Geochronology and Petrochemistry. *Resour. Geol.* **2020**, *70*, 254–272. [CrossRef]
39. Bergemann, C.A.; Gnos, E.; Berger, A.; Janots, E.; Whitehouse, M.J. Dating Tectonic Activity in the Lepontine Dome and Rhone-Simplon Fault Regions through Hydrothermal Monazite-(Ce). *Solid Earth* **2020**, *11*, 199–222. [CrossRef]

40. Chen, G.; Wu, G.; Li, T.; Liu, R.; Li, R.; Li, Y.; Yang, F. Mineralization of the Daolundaba Cu–Sn–W–Ag Deposit in the Southern Great Xing'an Range, China: Constraints from Geochronology, Geochemistry, and Hf Isotope. *Ore Geol. Rev.* **2021**, *133*, 104117. [CrossRef]
41. Wu, G.; Liu, R.L.; Chen, G.Z.; Li, T.G.; Li, R.H.; Li, Y.L.; Yang, F.; Zhang, T. Mineralization of the Weilasituo rare metaltin-polymetallic ore deposit in Inner Mongolia: Insights from fractional crystallization of granitic magmas. *Acta Petrol. Sin.* **2021**, *37*, 637–664. (In Chinese)
42. Wang, F.; Bagas, L.; Jiang, S.; Liu, Y. Geological, Geochemical, and Geochronological Characteristics of Weilasituo Sn-Polymetal Deposit, Inner Mongolia, China. *Ore Geol. Rev.* **2017**, *80*, 1206–1229. [CrossRef]
43. Wang, C.; Shao, Y.; Zhang, X.; Dick, J.; Liu, Z. Trace Element Geochemistry of Magnetite: Implications for Ore Genesis of the Huanggangliang Sn-Fe Deposit, Inner Mongolia, Northeastern China. *Minerals* **2018**, *8*, 195. [CrossRef]
44. Zhou, Z.H.; Mao, J.W.; Lyckberg, P. Geochronology and Isotopic Geochemistry of the A-Type Granites from the Huanggang Sn–Fe Deposit, Southern Great Hinggan Range, NE China: Implication for Their Origin and Tectonic Setting. *J. Asian Earth Sci.* **2012**, *49*, 272–286. [CrossRef]
45. Wang, R.; Zeng, Q.; Zhang, Z.; Guo, Y.; Lu, J. Fluid Evolution, H-O Isotope and Re-Os Age of Molybdenite from the Baiyinhan Tungsten Deposit in the Eastern Central Asian Orogenic Belt, NE China, and Its Geological Significance. *Minerals* **2020**, *10*, 664. [CrossRef]
46. Zeng, Q.D.; Sun, Y.; Chu, S.X.; Duan, X.X.; Liu, J. Geochemistry and Geochronology of the Dongshanwan Porphyry Mo–W Deposit, Northeast China: Implications for the Late Jurassic Tectonic Setting. *J. Asian Earth Sci.* **2015**, *97*, 472–485. [CrossRef]
47. Zhang, Z.; Ji, Z.; Ge, W.; Yang, H.; Wu, H.; Wang, Y. Contribution Discrepancy of Two Distinct Wall Rocks to Wolframite Mineralization from Dongshanwan Quartz-Vein Tungsten Deposit, Southern Great Xing'an Range, China. *Ore Geol. Rev.* **2023**, *163*, 105800. [CrossRef]
48. Azman, A.G. The Western Belt Granite of Peninsular Malaysia: Some Emergent Problems on Granite Classification and Its Implication. *Geosci. J.* **2000**, *4*, 283–293. [CrossRef]
49. Bucher, K.; Seelig, U. Bristen Granite: A Highly Differentiated, Fluorite-Bearing A-Type Granite from the Aar Massif, Central Alps, Switzerland. *Swiss J. Geosci.* **2018**, *111*, 317–340. [CrossRef]
50. Chappell, B.W.; White, A.J.R. Two Contrasting Granite Types: 25 Years Later. *Aust. J. Earth Sci.* **2001**, *48*, 489–499. [CrossRef]
51. Sylvester, P.J. Post-Collisional Alkaline Granites. *J. Geol.* **1989**, *97*, 261–280.
52. Wu, F.; Jahn, B.; Wilde, S.A.; Lo, C.H.; Yui, T.F.; Lin, Q.; Ge, W.; Sun, D. Highly Fractionated I-Type Granites in NE China (I): Geochronology and Petrogenesis. *Lithos* **2003**, *66*, 241–273. [CrossRef]
53. King, P.L.; White, A.J.R.; Chappell, B.W.; Allen, C.M. Characterization and Origin of Aluminous A-Type Granites from the Lachlan Fold Belt, Southeastern Australia. *J. Petrol.* **1997**, *38*, 371–391. [CrossRef]
54. Sardinha, A.S.; Barros, C.E.D.M.; Krymsky, R. Geology, Geochemistry, and U–Pb Geochronology of the Archean (2.74Ga) Serra Do Rabo Granite Stocks, Carajás Metallogenetic Province, Northern Brazil. *J. S. Am. Earth Sci.* **2006**, *20*, 327–339. [CrossRef]
55. Gelman, S.E.; Deering, C.D.; Bachmann, O.; Huber, C.; Gutiérrez, F.J. Identifying the Crystal Graveyards Remaining after Large Silicic Eruptions. *Earth Planet. Sci. Lett.* **2014**, *403*, 299–306. [CrossRef]
56. Zhao, X.-F.; Zhou, M.-F.; Li, J.-W.; Wu, F.-Y. Association of Neoproterozoic A- and I-Type Granites in South China: Implications for Generation of A-Type Granites in a Subduction-Related Environment. *Chem. Geol.* **2008**, *257*, 1–15. [CrossRef]
57. Aspinall, W.P.; Woo, G.; Voight, B.; Baxter, P.J. Evidence-Based Volcanology: Application to Eruption Crises. *J. Volcanol. Geotherm. Res.* **2003**, *128*, 273–285. [CrossRef]
58. KEby, G.N. The A-Type Granitoids: A Review of Their Occurrence and Chemical Characteristics and Speculations on Their Petrogenesis. *Lithos* **1990**, *26*, 115–134. [CrossRef]
59. Green, N.L.; Usdansky, S.I. Ternary feldspar mixing relations and thermobarometry. *Am. Mineral.* **1986**, *71*, 1101–1108.
60. Benisek, A.; Dachs, E.; Kroll, H. A Ternary Feldspar-Mixing Model Based on Calorimetric Data: Development and Application. *Am. Mineral.* **2004**, *89*, 1496–1504. [CrossRef]
61. Whalen, J.B.; Currie, K.L.; Chappell, B.W. A-Type Granites: Geochemical Characteristics, Discrimination and Petrogenesis. *Contrib Miner. Petrol.* **1987**, *95*, 407–419. [CrossRef]
62. Holland, T.J.B.; Green, E.C.R.; Powell, R. Melting of Peridotites through to Granites: A Simple Thermodynamic Model in the System KNCFMASHTOCr. *J. Petrol.* **2018**, *59*, 881–900. [CrossRef]
63. Xiang, H.; Connolly, J.A.D. GeoPS: An Interactive Visual Computing Tool for Thermodynamic Modelling of Phase Equilibria. *J. Metamorph. Geol.* **2022**, *40*, 243–255. [CrossRef]
64. Li, X.-H.; Klyukin, Y.I.; Steele-MacInnis, M.; Fan, H.-R.; Yang, K.-F.; Zoheir, B. Phase Equilibria, Thermodynamic Properties, and Solubility of Quartz in Saline-Aqueous-Carbonic Fluids: Application to Orogenic and Intrusion-Related Gold Deposits. *Geochim. Cosmochim. Acta* **2020**, *283*, 201–221. [CrossRef]
65. Jochum, K.P.; Seufert, H.M.; Spettel, B.; Palme, H. The Solar-System Abundances of Nb, Ta, and Y, and the Relative Abundances of Refractory Lithophile Elements in Differentiated Planetary Bodies. *Geochim. Cosmochim. Acta* **1986**, *50*, 1173–1183. [CrossRef]

66. Deering, C.D. Trace Element Indicators of Crystal Accumulation in Silicic Igneous Rocks. *Earth Planet. Sci. Lett.* **2010**, *297*, 324–331. [CrossRef]
67. Ballouard, C.; Poujol, M.; Boulvais, P.; Branquet, Y.; Tartèse, R.; Vigneresse, J.-L. Nb-Ta Fractionation in Peraluminous Granites: A Marker of the Magmatic-Hydrothermal Transition. *Geology* **2016**, *44*, 231–234. [CrossRef]
68. Ke, L.; Zhang, H.; Liu, J.; Zhai, D.; Guo, D.; Yang, J.; Tan, Q.; Xu, Y.; Zhang, M.; Wang, S. Fluid Inclusion, H-O, S, Pb and Noble Gas Isotope Studies of the Aerhada Pb–Zn–Ag Deposit, Inner Mongolia, NE China. *Ore Geol. Rev.* **2017**, *88*, 304–316. [CrossRef]
69. Dong, Y.; Ge, W.; Tian, D.; Ji, Z.; Yang, H.; Bi, J.; Wu, H.; Hao, Y. Geochronology and Geochemistry of Early Cretaceous Granitic Plutons in the Xing'an Massif, Great Xing'an Range, NE China: Petrogenesis and Tectonic Implications. *Acta Geol. Sin.* **2019**, *93*, 1500–1521. [CrossRef]
70. Bau, M. Controls on the Fractionation of Isovalent Trace Elements in Magmatic and Aqueous Systems: Evidence from Y/Ho, Zr/Hf, and Lanthanide Tetrad Effect. *Chem. Geol.* **1985**, *48*, 43–55. [CrossRef]
71. Lehmann, B. Formation of Tin Ore Deposits: A Reassessment. *Lithos* **2021**, *402–403*, 105756. [CrossRef]
72. Wen, C.M.; Zhao, P.L.; Grondahl, C.; Tsay, A.; Zajacz, Z.; Yuan, S.D. Cesium partitioning between granitic melts and aqueous fluids: Is Cs in hydrothermal fluids an accurate proxy of the degree of fractionation of parental magmas? *Geochim. Cosmochim. Acta* **2025**, *396*, 159–169. [CrossRef]
73. Irber, W. The Lanthanide Tetrad Effect and Its Correlation with K/Rb, Eu/Eu*, Sr/Eu, Y/Ho, and Zr/Hf of Evolving Peraluminous Granite Suites. *Geochim. Cosmochim. Acta* **1999**, *63*, 489–508. [CrossRef]
74. Waters, L.E.; Lange, R.A. An Updated Calibration of the Plagioclase-Liquid Hygrometer-Thermometer Applicable to Basalts through Rhyolites. *Am. Mineral.* **2015**, *100*, 2172–2184. [CrossRef]
75. Giordano, D.; Dingwell, D.B.; Romano, C. Viscosity of a Teide phonolite in the welding interval. *J. Volcanol. Geotherm. Res.* **2000**, *103*, 239–245. [CrossRef]
76. Thomas, R.; Förster, H.J.; Heinrich, W. The behaviour of boron in a peraluminous granite-pegmatite system and associated hydrothermal solutions: A melt and fluid-inclusion study. *Contrib. Mineral. Petrol.* **2003**, *144*, 457–472. [CrossRef]
77. Roda, E.; Keller, P.; Pesquera, A.; Fontan, F. Micas of the Muscovite–Lepidolite Series from Karibib Pegmatites, Namibia. *Mineral. mag.* **2007**, *71*, 41–62. [CrossRef]
78. Candela, P.A. Controls on Ore Metal Ratios in Granite-Related Ore Systems: An Experimental and Computational Approach. *Trans. R. Soc. Edinb. Earth Sci.* **1992**, *83*, 317–326.
79. Trail, D. Ce and Eu Anomalies in Zircon as Proxies for the Oxidation State of Magmas. *Geochim. Cosmochim. Acta* **2012**, *97*, 70–87. [CrossRef]
80. Thompson, J.F.H.; Sillitoe, R.H.; Baker, T.; Lang, J.R.; Mortensen, J.K. Intrusion-Related Gold Deposits Associated with Tungsten-Tin Provinces. *Min. Depos.* **1999**, *34*, 323–334. [CrossRef]
81. Yuan, S.; Williams-Jones, A.E.; Bodnar, R.J.; Zhao, P.; Zajacz, Z.; Chou, I.-M.; Mao, J. The Role of Magma Differentiation in Optimizing the Fluid-Assisted Extraction of Copper to Generate Large Porphyry-Type Deposits. *Sci. Adv.* **2025**, *11*, 927–933. [CrossRef]
82. Li, J.; Huang, X.-L.; Fu, Q.; Li, W.-X. Tungsten Mineralization during the Evolution of a Magmatic-Hydrothermal System: Mineralogical Evidence from the Xihuashan Rare-Metal Granite in South China. *Am. Mineral.* **2021**, *106*, 443–460. [CrossRef]
83. Zhao, P.; Zajacz, Z.; Tsay, A.; Yuan, S. Magmatic-Hydrothermal Tin Deposits Form in Response to Efficient Tin Extraction upon Magma Degassing. *Geochim. Cosmochim. Acta* **2022**, *316*, 331–346. [CrossRef]
84. Qiu, Y.; Wang, X.; Lu, J.; Chou, I.-M.; Wan, Y.; Zhang, R.; Zhang, W.; Sun, R. In Situ Observations of Tungsten Speciation and Partitioning Behavior during Fluid Exsolution from Granitic Melt. *Sci. Bulletin.* **2022**, *67*, 2358–2368. [CrossRef]
85. Chen, Z.L.; Peng, S.L. The experimental Result of W and Sn flow-melting distribution and its genetic significance. *Geol. Rev.* **1994**, *40*, 284–294. (In Chinese)
86. Guan, S.J.; Zhang, H.; Tang, Y.; Zhang, J.Y. An experimental study on the partitioning of molybdenum and tungsten between granitic melt and coexisting aqueous fluid at 100 MPa and 800 °C. *Geo Chim.* **2011**, *40*, 516–524. (In Chinese)
87. Zhao, P.; Zajacz, Z.; Tsay, A.; Chu, X.; Cheng, Q.M.; Yuan, S.D. The partitioning behavior of Mo during magmatic fluid exsolution and its implications for Mo mineralization. *Geochim. Cosmochim. Acta* **2022**, *339*, 115–126. [CrossRef]
88. Mysen, B. Relationships between Silicate Melt Structure and Petrologic Processes. *Earth-Sci. Rev.* **1990**, *27*, 281–365. [CrossRef]
89. Keppler, H.; Wyllie, P.J. Partitioning of Cu, Sn, Mo, W, U, and Th between Melt and Aqueous Fluid in the Systems Haplogranite-H/O-HCl and Haplogranite-H_2O-HF. *Contrib. Miner. Petrol.* **1991**, *109*, 139–150.
90. Carocci, E.; Truche, L.; Cathelineau, M.; Caumon, M.-C.; Bazarkina, E.F. Tungsten (VI) Speciation in Hydrothermal Solutions up to 400 °C as Revealed by in-Situ Raman Spectroscopy. *Geochim. Cosmochim. Acta* **2022**, *317*, 306–324. [CrossRef]
91. Wang, X.; Qiu, Y.; Lu, J.; Chou, I.-M.; Zhang, W.; Li, G.; Hu, W.; Li, Z.; Zhong, R. In Situ Raman Spectroscopic Investigation of the Hydrothermal Speciation of Tungsten: Implications for the Ore-Forming Process. *Chem. Geol.* **2020**, *532*, 119299. [CrossRef]
92. Ulrich, T.; Mavrogenes, J. An Experimental Study of the Solubility of Molybdenum in H_2O and KCl–H_2O Solutions from 500 °C to 800 °C, and 150 to 300 MPa. *Geochim. Cosmochim. Acta.* **2008**, *72*, 2316–2330. [CrossRef]

93. Gibert, F.; Moine, B.; Schott, J.; Dandurand, J.-L. Modeling of the Transport and Deposition of Tungsten in the Scheelite-Bearing Calc-Silicate Gneisses of the Montagne Noire, France. *Contrib. Mineral. Petrol.* **1992**, *112*, 371–384. [CrossRef]
94. Wood, S.A.; Samson, I.M. The Hydrothermal Geochemistry of Tungsten in Granitoid Environments: I. Relative Solubilities of Ferberite and Scheelite as a Function of T, P, pH, and mNaCl. *Econ. Geol.* **2000**, *95*, 143–182. [CrossRef]
95. Jin, C.; Gao, X.-Y.; Chen, W.T.; Zhao, T.-P. Magmatic-Hydrothermal Evolution of the Donggou Porphyry Mo Deposit at the Southern Margin of the North China Craton: Evidence from Chemistry of Biotite. *Ore Geol. Rev.* **2018**, *92*, 84–96. [CrossRef]
96. Ruan, B.; Lv, X.; Yang, W.; Liu, S.; Yu, Y.; Wu, C.; Adam, M.M.A. Geology, Geochemistry and Fluid Inclusions of the Bianjiadayuan Pb–Zn–Ag Deposit, Inner Mongolia, NE China: Implications for Tectonic Setting and Metallogeny. *Ore Geol. Rev.* **2015**, *71*, 121–137. [CrossRef]
97. Ouyang, H.G. Metallogenesis of Bairendaba-Weilasituo Silver-Polytmetallic Deposit and Its Geodynamic Setting, in the Southern Segment of Great Xing'an Range, NE China. Ph.D. Thesis, China University of Geosciences, Beijing, China, 2013. (In Chinese)
98. Li, Y.; Liu, Z.; Shao, Y.; Liu, L.; Chen, K.; Zhao, H.; You, S.; He, M. Garnet Geochronology, Major and Trace Element Geochemistry of the Huangganglіang Fe-Sn Polymetallic Deposit, NE China. *Ore Geol. Rev.* **2024**, *168*, 106048. [CrossRef]
99. Mao, J.W.; Xie, G.Q.; Zhang, Z.H.; Li, X.F.; Wang, X.T.; Zhang, C.Q.; Li, Y.F. Mesozoic large-scale metallogenic pulses in North China and corresponding gcadynalllie settings. *Acta Petrol. Sin.* **2005**, *21*, 171–190. (In Chinese)
100. Bonin, B.; Azzouni-Sekkal, A.; Bussy, F.; Ferrag, S. Alkali-Calcic and Alkaline Post-Orogenic (PO) Granite Magmatism: Petrologic Constraints and Geodynamic Settings. *Lithos* **1998**, *45*, 45–70. [CrossRef]
101. Wang, J.F.; Li, Y.J.; Li, H.Y.; Dong, P.P. Zircon U-Pb dating of the Shijiangshan Late Jurassic-Early Cretaceous A-type granite in Xi Ujimqin Banner of Inner Mongolia and its tectonic setting. *Geol. Bull. China* **2018**, *37*, 382–396. (In Chinese)
102. Deng, C.; Sun, D.; Han, J.; Chen, H.; Li, G.; Xiao, B.; Li, R.; Feng, Y.; Li, C.; Lu, S. Late-Stage Southwards Subduction of the Mongol-Okhotsk Oceanic Slab and Implications for Porphyry Cu Mo Mineralization: Constraints from Igneous Rocks Associated with the Fukeshan Deposit, NE China. *Lithos* **2019**, *326*, 341–357. [CrossRef]
103. Deng, C.; Sun, D.; Ping, X.; Huang, H.; Zhang, L.; Lu, S. Geochemistry of Early Cretaceous Volcanic Rocks in the Northeastern Great Xing'an Range, Northeast China and Implication for Geodynamic Setting. *Int. Geol. Rev.* **2019**, *61*, 1594–1612. [CrossRef]
104. Pearce, J.A.; Harris, N.B.W.; Tindle, A.G. Trace Element Discrimination Diagrams for the Tectonic Interpretation of Granitic Rocks. *J. Petrol.* **1984**, *25*, 957–983. [CrossRef]
105. Batchelor, R.A.; Bowden, P. Petrogenetic Interpretation of Granitoid Rock Series Using Multicationic parameters. *Chem. Geol.* **1985**, *48*, 43–55. [CrossRef]
106. Mo, S.G.; Han, M.L.; Li, J.T. Compositions and Orogenic Processes of Mongolia-Okhotsk Orogen. *J. Shandong Univ. Sci. Technol.* **2005**, *24*, 50–52+64. (In Chinese)
107. Zhao, P.; Xue, B.; Chen, Y. Mongolia-Okhotsk Ocean: Evolution and final closure. *Sci. Sin. Terrae* **2023**, *53*, 2541–2559. (In Chinese)
108. Kong, J.G.; Zhang, G.B.; Zhang, W.D.; Wang, Q.L.; Dong, J.S.; Chen, X.K.; He, Y.L. Geochronology and geochemistry of Late Jurassic granodiorite in Huma area of northern segment of Da Hinggan Ling (Mts): Constraints on tectonic evolution of Mongolia-Okhotsk Ocean. *World Geol.* **2024**, *43*, 171–192. (In Chinese)
109. Zhao, P.; Xu, B.; Chen, Y. Evolution and Final Closure of the Mongol-Okhotsk Ocean. *Sci. China Earth Sci.* **2023**, *66*, 2497–2513. [CrossRef]
110. Sorokin, A.A.; Zaika, V.A.; Kovach, V.P.; Kotov, A.B.; Xu, W.; Yang, H. Timing of Closure of the Eastern Mongol–Okhotsk Ocean: Constraints from U–Pb and Hf Isotopic Data of Detrital Zircons from Metasediments along the Dzhagdy Transect. *Gondwana Res.* **2020**, *81*, 58–78. [CrossRef]
111. Wang, T. Granitic Record of the Assembly of the Asian Continent. *Earth-Sci. Rev.* **2023**, *237*, 104298. [CrossRef]
112. Zhang, G.; Xie, W.; Wen, S.; Gong, E.; Guo, R.; Tang, T. Petrogenesis and Tectonic Implications of Late Mesozoic Volcanic Rocks in the Northern and Central Great Xing'an Range, NE China: Constraints from Geochronology and Geochemistry. *Geol. J.* **2020**, *55*, 8282–8308. [CrossRef]
113. Feng, Z.; Sun, D.; Yue, Y.; Mao, A.; Tian, L.; Sun, C.; Gou, J. Petrogenesis of Highly Differentiated I-type Volcanic Rocks: Reinjection of High-temperature Magma—An Example from Suolun Silicic Volcanic Rocks, Central Great Xing'an Range, China. *Geol. J.* **2020**, *55*, 6677–6695. [CrossRef]

Disclaimer/Publisher's Note: The statements, opinions and data contained in all publications are solely those of the individual author(s) and contributor(s) and not of MDPI and/or the editor(s). MDPI and/or the editor(s) disclaim responsibility for any injury to people or property resulting from any ideas, methods, instructions or products referred to in the content.

minerals

MDPI

Article

Microminerals as Complimentary Guides into Metallogeny and the Ore-Forming Potential of Igneous Rocks: Evidence from the Stanovoy Superterrane (Russian Far East)

Valeria Krutikova, Nikolai Berdnikov and Pavel Kepezhinskas *

Institute of Tectonics and Geophysics, Russian Academy of Sciences, Khabarovsk 680000, Russia; nm32697@gmail.ru (V.K.); nick@itig.as.khb.ru (N.B.)
* Correspondence: pavel_k7@yahoo.com

Abstract: Numerous mineral microinclusions discovered in the Triassic Ildeus mafic–ultramafic intrusion are dominated by base metal sulfides, gold, silver, and their alloys, as well as rare earth element (REE) minerals. These mineral microinclusions were formed through both the magmatic differentiation of the Ildeus intrusion and the multi-stage interaction of intrusive rocks with late-magmatic, post-magmatic and post-collisional fluids. A comparison of the results of our microinclusions study with ore mineralization discovered within the Ildeus intrusion suggests that microinclusion assemblages in igneous rocks are, in some cases, precursors of potentially economic mineralization. In the case of the Ildeus rocks, sulfide microinclusions correspond to potentially economic disseminated nickel–cobalt sulfide ores, while microinclusions of gold and its alloys correlate with intrusion-hosted, erratic gold mineralization. The occurrence of silver and rare earth element minerals in Ildeus plutonic rocks indicates the possible presence of silver and REE mineralization, which is supported by sub-economic whole-rock silver and REE grades in parts of the Ildeus intrusion. The results of our investigation suggest that studies of mineral microinclusions in magmatic rocks may be useful in the evaluation of their metallogenic specialization and ore-forming potential and could possibly be utilized as an additional prospecting tool in the regional exploration for precious, base, and rare metals.

Keywords: Stanovoy superterrane; Ildeus intrusion; base metal sulfides; Au, Ag, and REE microminerals; ore-forming potential of igneous rocks

1. Introduction

Igneous rocks associated with ore deposits carry important information about the metal sources, the composition of mineralizing melts and fluids, as well as the conditions of fluid exsolution and the transport of critical ore metals into the upper crust [1–10]. Typical criteria for recognizing the ore-bearing potential of igneous rocks include their trace element and isotopic characteristics [11–16], chemical variations in rock-forming [17–26] and accessory [27–31] minerals, as well as the composition of the melt and fluid inclusions [32–36]. Some magmatic rocks display close geologic and (possibly) genetic affinities to certain ore deposits and are successfully used as exploration guides across different tectonic terranes and geodynamic environments [11,13,37–40]. The widely recognized examples include Phanerozoic adakites (high Sr/Y felsic rocks [41–44]); Precambrian komatiites [45–49]; potassic alkaline rocks, such as shoshonites [50–53], kimberlites [54–56], carbonatites [57–60], alkaline granites, and rhyolites [61–66]; and some other rock associations.

Some plutonic and volcanic rocks contain associations of metal and mineral microinclusions (usually up to 50 μm in size), hereafter termed microminerals, in rock-forming silicates, accessory minerals, and, in the case of volcanic rocks, groundmass glass [67–71]. Occasionally, these micromineral assemblages directly correlate with the mineralogy of ores hosted by the micromineral-bearing igneous rock formations. For example, platinum-group metal (PGM)- and Cu-Ag-Au alloy-bearing microinclusions in explosive volcanic rocks in the Lesser Khingan mineral province record the early stages of the formation of spatially associated PGM-Au-bearing iron–manganese ore deposits [72–76]. The iron titanium oxide–apatite–sulfide–sulfate (ITOASS) microinclusions in magmatic rocks from the Stanovoy superterrane are linked to the early magmatic and metasomatic stages of the formation of iron oxide–copper–gold (IOCG)/iron oxide–apatite (IOA) mineralization, providing a conceptual basis for the refined prospecting for these valuable mineral deposits throughout the Stanovoy cratonic superterrane [77,78]. Thus, comprehensive studies of micromineral assemblages in igneous rocks can provide new insights into regional metallogenic patterns in addition to the currently used economic geology and exploration approaches.

In this paper, we report new data on the micromineral assemblages in the Triassic Ildeus mafic–ultramafic intrusion from the Stanovoy superterrane at the southern edge of the Siberian craton. We document several associations of microminerals and compare them with ore-grade mineralization recently discovered within the Ildeus intrusion. We then further explore the potential usage of microminerals as a complimentary guide to the regional metallogeny and ore-forming potential of igneous rocks in accreted terranes and orogenic belts at plate edges.

2. Geologic and Petrologic Background

The Stanovoy cratonic superterrane is located at the southern edge of the Siberian craton (Figure 1) and is composed of Precambrian high-grade (granulite) metamorphic complexes, amphibolite facies and greenschist facies metavolcanic and metasedimentary rocks, and Mesozoic subduction (248–203 Ma)- and collision (145–127 Ma)-related mafic to felsic plutonic and volcanic rocks [79,80]. The Precambrian to Mesozoic metamorphic, magmatic, and sedimentary rock units are intruded by post-collisional Early Cretaceous (122–117 Ma) diorites, monzonites, and granites with distinct adakite geochemistry [80–83], as well as high-Nb lamprophyric dikes [84]. The Stanovoy superterrane records the protracted tectonic history of the Mesozoic subduction of the Mongol-Okhotsk oceanic basin along the southern active convergent margin of the Siberian craton, followed by the Jurassic collision of the Siberian craton with the Amur microcontinent and Early Cretaceous post-collisional rifting and granitic magmatism [80].

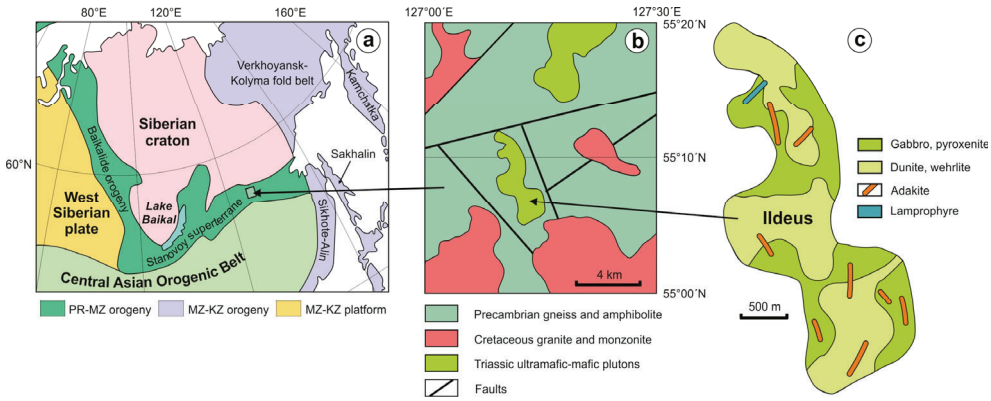


Figure 1. (**a**) Tectonic setting of the Stanovoy superterrane at the southern edge of the Siberian craton. (**b**) Simplified geologic map of the central part of the Stanovoy superterrane. (**c**) Simplified map of the Ildeus mafic–ultramafic intrusion. Modified after [77].

Precambrian granulite and amphibolite complexes (the Stanovoy series) are intruded on by several Triassic mafic–ultramafic bodies, which are typically viewed as arc root plutonic complexes of the Mesozoic active margin at the southern edge of the Siberian craton [80–82,84]. The Ildeus mafic–ultramafic massif is located within the eastern part of the Stanovoy superterrane (Figure 1) and is characterized by a core of coarsely layered plagioclase- and amphibole-bearing peridotites, olivine websterites, wehrlites, and gabbronorites, surrounded by a thin (<100 m) rim composed of two-pyroxene gabbros and gabbroic anorthosites [82,84,85]. Both peridotites and gabbros are frequently crosscut by numerous clinopyroxenite and orthopyroxenite dikes [84]. The Ildeus complex experienced several episodes of the later-stage ultramafic (serpentine + talc + chlorite ± carbonate) and felsic (quartz + albite + K-feldspar + biotite ± calcite) metasomatism and the emplacement of low- and high-sulfidation quartz–carbonate–adularia veins [81,82]. Abundant adakite veinlets, veins, and dikes intrude on all earlier plutonic and metasomatic rocks throughout the Ildeus intrusion [82–84].

Ultramafic rocks in the Ildeus intrusion's core commonly display meso- and adcumulate textures composed of olivine, orthopyroxene, and minor clinopyroxene with inter-cumulus, high-Al amphibole and plagioclase (Figure 2a). Pyroxenites (mostly olivine websterites) in the core also have a cumulate texture, while pyroxenite veins and dikes are characterized by a granular texture [82,84]. Gabbroic rocks contain varying amounts of plagioclase, orthopyroxene, and clinopyroxene (Figure 2b), as well as amphibole with minor olivine and biotite, displaying a range of poikilitic, granular and hypidiomorphic textures [82]. Accessory minerals include Cr-Al-Fe spinel, magnetite (with varying amounts of Ti, V, and Cr), ilmenite, rutile, titanite, apatite, zircon, and baddeleyite.

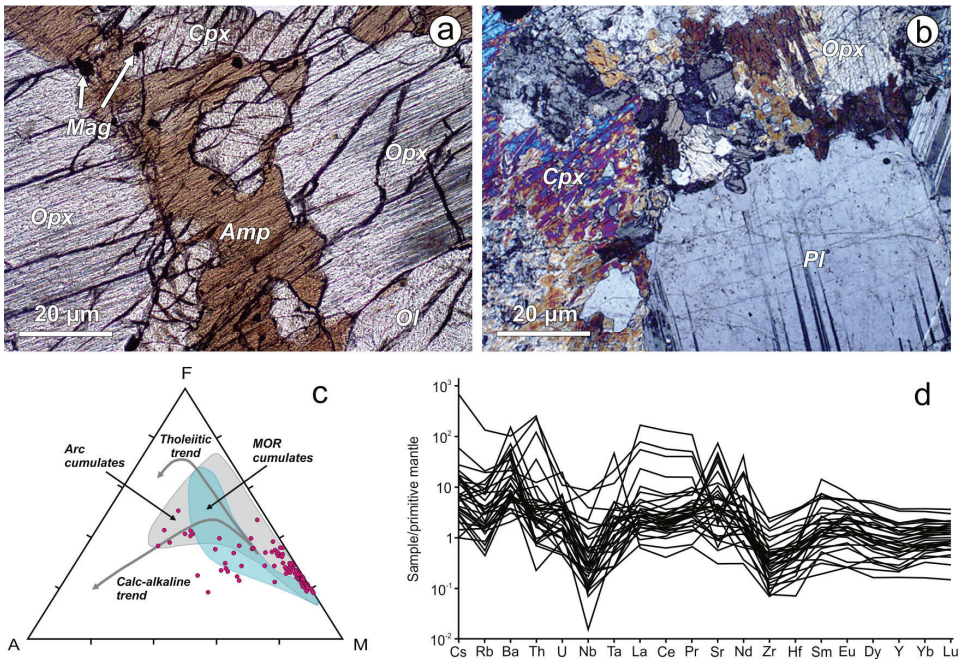


Figure 2. Petrographic (**a**,**b**) and geochemical (**c**,**d**) characteristics of plutonic rocks from the Ildeus intrusion. (**a**) Amphibole-bearing peridotite mesocumulate from the ultramafic core. (**b**) Two-pyroxene gabbro from the mafic rim. (**c**) A (Na_2O+K_2O)–F (total FeO)–M (MgO) diagram for Ildeus mafic–ultramafic rocks (solid red dots) modified from [86]. (**d**) Primitive mantle-normalized trace element patterns for mafic–ultramafic plutonic rocks from the Ildeus intrusion. Normalizing values are from [87]. Ildeus data in (**c**,**d**) are from [77,82,84,85]. Mineral abbreviations: Cpx—clinopyroxene; Opx—orthopyroxene; Amp—amphibole; Pl—plagioclase; Mag—magnetite. Mineral abbreviations in this figure as well as all other figures with BSE images follow the nomenclature of [88].

Major and trace element variations in mafic–ultramafic rocks from the Ildeus intrusion indicate their subduction-related origin [81,82,84,85]. Peridotites, pyroxenites, and gabbros plot into the field of arc cumulates or the area of compositional overlap between the arc and mid-ocean ridge (MOR) cumulates in the AFM (Na_2O+K_2O–total FeO–MgO) diagram (Figure 2c). Although a substantial data point scatter is observed in the AFM space, the bulk of the Ildeus rock compositions tend to follow calc-alkaline differentiation trend defined by the gradual decrease in MgO and increase in total alkali contents (Figure 2c). The subduction-related character of the Ildeus intrusion is further confirmed by primitive mantle-normalized trace element patterns (Figure 2d). Ildeus mafic–ultramafic rocks exhibit an enrichment in large-ion lithophile and depletion in high-field strength elements, coupled with a moderate enrichment of light over heavy rare earth elements typical of convergent zone magmas [89].

3. Materials and Methods

Samples for this study were obtained during a 2022 exploration drilling of the Ildeus intrusion by the Oslo-based Khingan Minerals AS (Norway) [81,82]. All analytical work was carried out at the Khabarovosk Innovation-Analytical Center (KhIAC) of the Institute of Tectonics and Geophysics (Far East Branch of the Russian Academy of Science, Khabarovsk, Russian Federation).

A petrographic study of plutonic rocks from the Ildeus intrusion was carried out using the Imager A2m microscope (Carl Zeiss, Jena, Germany). Investigation of the morphology and chemical composition of the minerals, mineral microinclusions, native metals, and their alloys was conducted using a Vega 3 LMH (Tescan, Brno, Czech Republic) scanning electron microscope (SEM) equipped with an X-Max 80 (Oxford Instruments, Abingdon, UK) energy dispersive spectrometer (EDS) with the following operating conditions: accelerating voltage of 20 kV, beam current of ~500 nA, and beam diameter of 0.2 μm. An extensive database of reference samples for all of the chemical elements incorporated into the Aztec Version 4.0 software and the Co-standard Oxford Instruments № 6864-15 were used as standards during our SEM study. Accuracy of the EDS analysis was estimated to be ±0.1 wt.%. X-ray spectra of microinclusions of less than 5 μm in size, besides the spectral response from the inclusion itself, typically include some excitation spectra from a host mineral. The correction method proposed in [90] was used to interpret mixed spectra from ultra-small metal and mineral microinclusions. Selected SEM-EDS spectra are listed in Figure S1 (Supplementary Materials).

4. Results

Mafic to ultramafic rocks from the Ildeus intrusion contain abundant primary (magmatic) and secondary (metasomatic) metal and mineral microinclusions in silicate and oxide minerals [77,80–82,84,85,90,91]. We have previously used various assemblages of microinclusions to reconstruct magmatic–hydrothermal evolution and metal transport at arc plutonic roots [81,82,85]. Microinclusions in the Ildeus intrusion can be subdivided into the following principal groups: (1) sulfides, (2) Au and Au-bearing alloys, (3) Ag and Ag-bearing minerals and alloys, and (4) REE-bearing minerals.

4.1. Sulfide Microinclusions

Sulfide microinclusions are by far the most common and are observed in all studied samples of plutonic rocks from the Ildeus intrusion. Microinclusions of Co-Cu-Ni-Fe sulfides are frequently spatially associated with larger (>50 μm) sulfide grains (Figure 3a–c). Sulfide populations are typically dominated by primary magmatic pyrrhotite, Ni-bearing (Ni = 0.7–7.3 wt.%) pyrrhotite, pentlandite, Co-enriched (Co = 1.7–21.0 wt.%) pentlandite,

and chalcopyrite included in cumulate clinopyroxene, orthopyroxene, and interstitial high-Al amphibole (Figure 3d–g, Figure S1a,b). Interstitial amphibole contains microinclusion of chalcocite and millerite (Figure 3h). A single microinclusion of composite Co-Ni-Fe-Zn sulfide is observed in primary magmatic orthopyroxene (Figure 3i, Figure S1c). In addition, microinclusions of chalcopyrite and galena are present in secondary chlorite and orthoclase [82].

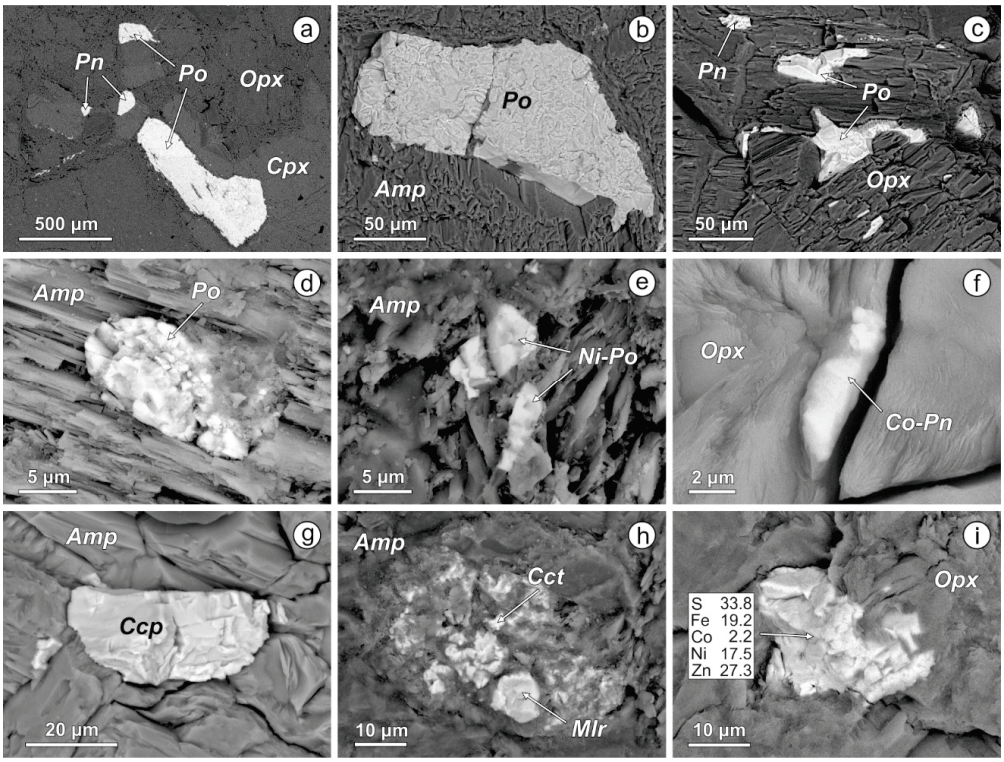


Figure 3. BSE images of sulfide microinclusions in rocks of the Ildeus intrusion. (**a**) Pyrrhotite and pentlandite in association with clinopyroxene and orthopyroxene. (**b**) Pyrrhotite inclusion in amphibole. (**c**) Pyrrhotite and pentlandite inclusions in orthopyroxene. (**d**) Pyrrhotite microinclusion in amphibole. (**e**) Ni-bearing pyrrhotite microinclusion in amphibole. (**f**) Cobalt-enriched pentlandite microinclusion in orthopyroxene. (**g**) Chalcopyrite inclusion in amphibole. (**h**) Intergrowth of millerite with chalcocite in amphibole. (**i**) Composite Co-Ni-Fe-Zn sulfide microinclusion (or intergrowth of several sulfides) in orthopyroxene. Mineral abbreviations: Cpx—clinopyroxene; Opx—orthopyroxene; Amp—amphibole; Po—pyrrhotite; Pn—pentlandite; Ni-Po—Ni-bearing pyrrhotite; Co-Pn—Co-enriched pentlandite; Ccp—chalcopyrite; Cct—chalcocite; Mlr—millerite.

4.2. Microinclusions of Au and Au-Bearing Alloys

Gold-bearing microinclusions are represented by native gold, two-component Ag-Au, and three-component Cu-Ag-Au alloys, as well as multi-component alloys of gold with some other chalcophile (Cu, Zn, Ag, etc.) and siderophile (Ni, Co) metals. Polycrystalline grains of almost pure gold are observed as microinclusions in clinopyroxene (Figure 4a, Figure S1d) and the magnetite–calcite matrix (Figure 4b). Ag-Au alloys are typically present in magmatic orthopyroxene (Figure 4c, Figure S1e) and secondary interstitial albite (Figure 4d). Clinopyroxene in ultramafic cumulates frequently contains microinclusions of Cu-Ag-Au alloys (Figure 4e, Figure S1f). A microinclusion of the multi-component Ni-Zn-Ag-Cu-Au alloy is observed in interstitial amphibole from the ultramafic Ildeus cumulate (Figure 4f, Figure S1g).

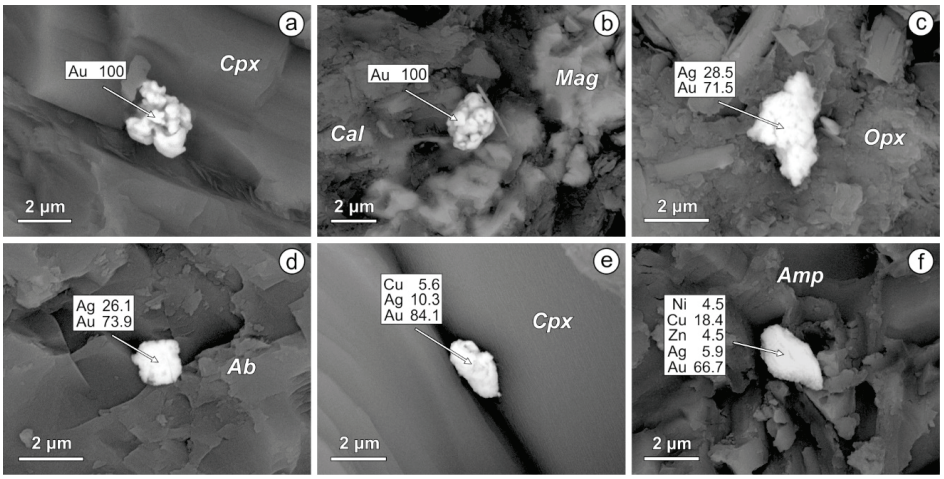


Figure 4. BSE images of microinclusions of Au and Au-bearing alloys in rocks of the Ildeus intrusion. Native gold microinclusion in clinopyroxene (**a**) and in association with calcite and magnetite (**b**). (**c**,**d**) Microinclusion of Ag-Au alloy in orthopyroxene (**c**) and albite (**d**). (**e**) Microinclusion of Cu-Ag-Au alloys in clinopyroxene. (**f**) Microinclusion of Ni-Zn-Ag-Cu-Au alloy in amphibole. Mineral abbreviations: Ab—albite; Amp—amphibole; Cal—calcite; Cpx—clinopyroxene; Mag—magnetite; Opx—orthopyroxene.

4.3. Microinclusions of Ag-Bearing Minerals

Silver microinclusions in Ildeus rocks occur as native metal, alloys with Cu, Zn, and Au, as well as chlorides and sulfides in association with various rock-forming silicate minerals. An elongated native silver particle is present in orthopyroxene (Figure 5a). Serpentine in Figure 5b contains an inclusion of a Ag-Au alloy (Figure S1h). Microinclusions of cupriferous silver (Figure 5c) and silver with minor zinc and copper (Figure 5d, Figure S1i) are observed in orthopyroxene. Serpentine in Figure 5e contains an inclusion of porous chlorargyrite (Figure S1k). Acanthite, frequently with an admixture of some chalcocite, is present in olivine from the Ildeus intrusion (Figure 5f, Figure S1l).

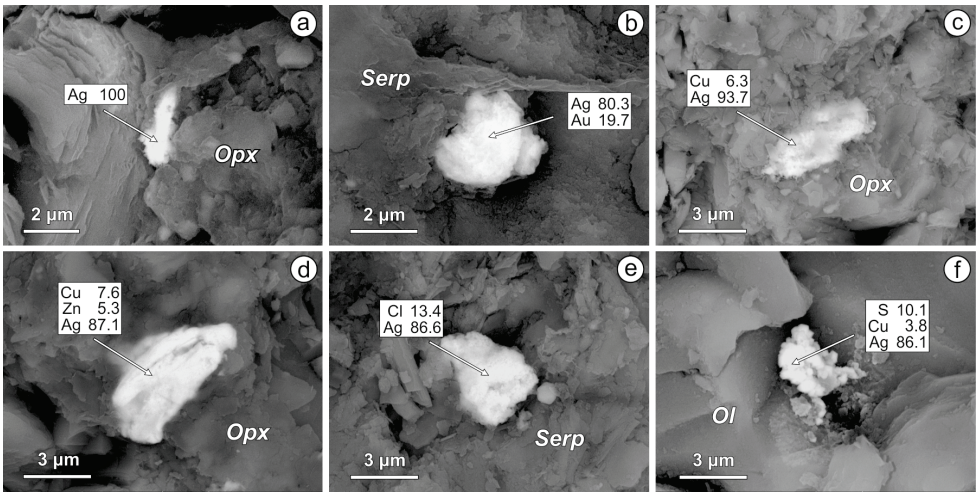


Figure 5. BSE images of microinclusions of Ag-bearing minerals in rocks of the Ildeus intrusion. (**a**) Native silver microinclusion in orthopyroxene. (**b**) Microinclusion of Au-Ag alloys in serpentine. (**c**) Cupriferous silver microinclusion in orthopyroxene. (**d**) Microinclusion of Zn-Cu-Ag alloy in orthopyroxene. (**e**) Chlorargyrite microinclusion in serpentine. (**f**) Microinclusion of acanthite with minor chalcocite in olivine. Mineral abbreviations: Serp—amphibole; Ol—olivine; Opx—orthopyroxene.

4.4. Microinclusions of REE-Bearing Minerals

Monazite and xenotime are the most common among the REE-bearing microminerals present in the intrusive rocks of the Ildeus intrusion. Monazite frequently forms monazite-orthopyroxene aggregates in association with apatite (Figure 6a). Individual micrograins of euhedral to subhedral and anhedral monazite are observed in albite (Figure 6b, Figure S1m), serpentine (Figure 6c), secondary orthoclase, and primary orthopyroxene [80]. Xenotime is frequently associated with titanite and albite (Figure 6d, Figure S1n). Microinclusions of REE-bearing oxides are observed in chlorite (Figure 6e, Figure S1o). Some sodic feldspars contain botryoidal aggregates of bastnaesite (Figure 6f, Figure S1p). Microinclusions of REE oxides and carbonates are also present in some olivines and orthopyroxenes from the Ildeus ultramafic rocks [80].

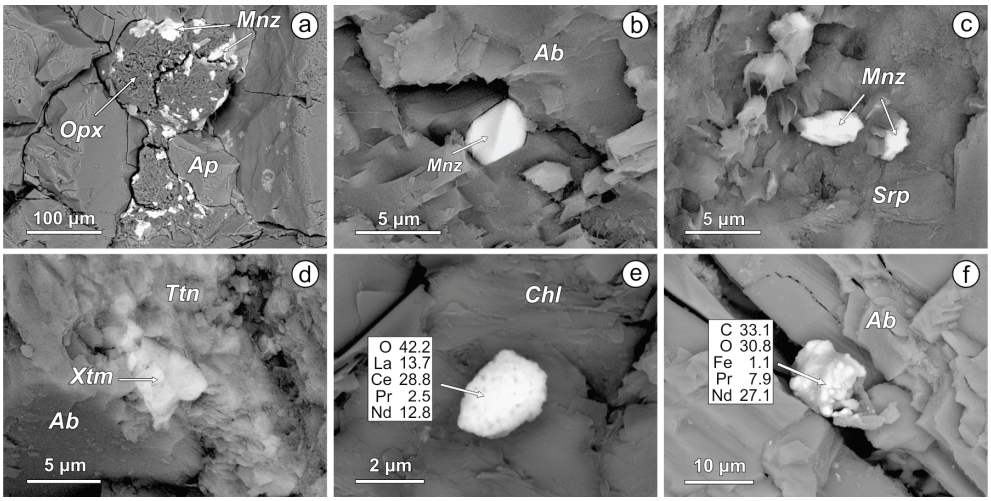


Figure 6. BSE images of microinclusions of REE-bearing minerals in rocks of the Ildeus intrusion. (**a**) Monazite-orthopyroxene aggregate in association with apatite. (**b**,**c**) Monazite microinclusions in albite (**b**) and serpentine (**c**). (**d**) Xenotime microinclusion in association with titanite in albite. (**e**) Microinclusion of REE oxide in chlorite. (**f**) Bastnaesite microinclusion in albite. Mineral abbreviations: Ab—albite; Ap—apatite; Chl—chlorite; Mnz—monazite; Opx—orthopyroxene; Srp—serpentine; Ttn—titanite; Xtm—xenotime.

5. Discussion

Ore mineral microinclusions in igneous rocks crystallize as individual mineral phases during magmatic differentiation and are also formed during the later-stage metasomatic alteration of their magmatic hosts [2,26,92–98]. The results of the current study suggest that associations of ore microminerals can potentially be used as complementary exploration tools in a variety of mineralized terranes across different tectonic settings.

5.1. Base Metal Sulfides

Previous exploration within the Ildeus intrusion established the presence of disseminated nickel, cobalt, and copper mineralization, commonly associated with peridotites and pyroxenites in the Ildeus core (Table 1). This disseminated sulfide mineralization is principally composed of pentlandite, Co-enriched pentlandite, pyrrhotite (occasionally with some Co and Ni), chalcopyrite, and bornite, with minor (possibly late-stage) galena and sphalerite (Table 1 (see also Table 6 in [82])). Pentlandite and pyrrhotite, in most cases, occur as large anhedral-to-subhedral grains in variably altered olivine-rich cumulates (Figure 7). Occasionally, interstitial pentlandite forms a sulfide matrix, effectively "cementing" altered olivine grains (Figure 7b). In some cases, pentlandite is observed via inclusions in cumulate olivine (Figure 7a), orthopyroxene, and clinopyroxene (for example, Figure 14e

in [82]), suggesting the presence of two generations of nickel–iron–sulfides in the Ildeus intrusion (Table 2; [82,84]). Surface grab samples yielded Ni values of up to 0.55 wt.%, while limited data from the 2022 drill core indicate Ni grades of 0.05 to 0.2 wt.% in core intervals with disseminated sulfide mineralization (Table 1). Although grades of up to 0.34% Cu and 0.1% Co were reported by previous Russian exploration parties [84], our limited core analysis resulted in substantially lower cobalt and copper grades (Table 1), suggesting that the drill-indicated sulfide mineralization is dominated by pentlandite and pyrrhotite. Moreover, pentlandite and pyrrhotite are not only the most abundant microinclusions in the Ildeus ultramafic rocks (Table 2); they also dominate the disseminated sulfide mineralization, emphasizing direct correlation between sulfide microinclusions and the macromineralization of the same composition within the Ildeus intrusion (Table 1). The assemblages of sulfide microinclusions, the mineralogy of ores, and the observed nickel, cobalt, and copper grades in the Ildeus intrusion are broadly similar to magmatic sulfide deposits in convergent margin settings such as the Late Paleozoic mafic–ultramafic intrusions in NW China (Kalatongke, Baishiquan, Pobei, Yueyawan, etc. [99–101]), the Mesoproterozoic Kabanga ultramafic massif in Tanzania [102,103], and the Carboniferous Aguablanca mafic plutonic complex in SW Spain [104,105].

Table 1. Principal associations of microminerals compared to the observed mineralization and metal grades in the Ildeus intrusion.

Mineral Associations	Microminerals	Known Disseminated Mineralization	Metal Grades [(1)]
Sulfides	Pentlandite, Co-enriched pentlandite, pyrrhotite, Ni-pyrrhotite, chalcopyrite, chalcocite, Co-Ni-Fe-Zn sulfide	Pentlandite, Co-enriched pentlandite, pyrrhotite, chalcopyrite, bornite with minor sphalerite and galena	Up to 0.55% Ni, 0.1% Co and 0.34% Cu in individual grab samples; typically, 0.05–0.2% Ni, 0.01–0.02% Co, and 0.005–0.08% Cu in the drill core
Au and Au alloys	Native Au, Ag-Au and Cu-Ag-Au alloys	Mostly Cu-Ag-Au (±Ni and Zn) alloys	Up to 596 g/t Au in individual grab samples; typically, 0.01–2.5 g/t in the drill core
Ag-bearing minerals	Cupriferous silver, acanthite, silver halides	Currently unknown	Up to 163 g/t in select drill core samples; typically, 0.1–1 g/t over widths of several m in the core
REE-bearing minerals	Monazite, xenotyme, REE oxides and carbonates	Currently unknown	Total REE content of 330–890 g/t in individual samples; one sample has a total REE content of 1938 g/t

[(1)] Refers to mineralized intervals as defined by the Russian exploration standards and based on core logging during the 2022 drilling campaign by Khingan Minerals AS. Data for the disseminated mineralization and metal grades in the Ildeus intrusion are from [80–82,84,85].

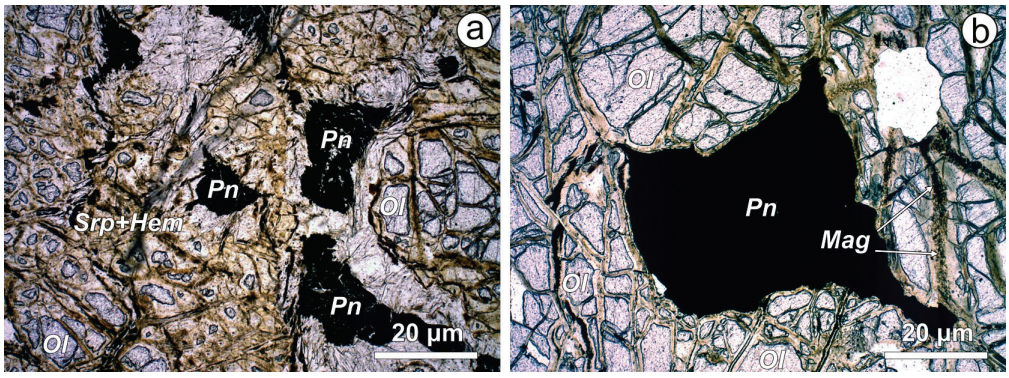


Figure 7. (**a**,**b**) Disseminated pentlandite mineralization in variably altered dunnites from the central part of the Ildeus intrusion. Mineral abbreviations: Ol—olivine; Srp—serpentine; Mag—magnetite; Hem—hematite; Pn—pentlandite.

Table 2. Distribution of main associations of microinclusions in the principal types of plutonic lithologies in the Ildeus mafic–ultramafic intrusion.

Principal Intrusive Lithologies	Base Metal Sulfides	Au-Bearing Microinclusions	Ag-Bearing Microinclusions	REE-Bearing Microinclusions
Dunite, plagioclase-bearing dunite	Abundant	Present	Present	Present
Harzburgite, lherzolite	Abundant	Present	Present	Absent
Wehrlite, websterite	Abundant	Abundant	Abundant	Present
Pyroxenite dikes and veins	Present	Abundant	Abundant	Absent
Gabbro-norite and gabbro-anorthosite	Present *	Absent	Present	Absent

Notes: Abundant: >10 microinclusions per SEM sample (~2 cm^2 in area); Present: 1–10 microinclusions per SEM sample; Absent: Not detected by SEM-EDS. *—almost exclusively Cu-sulfides, sometimes as ITOASS (iron titanium oxide–apatite–sulfide–sulfate)-type segregations [77].

Textural evidence suggests a magmatic origin for pentlandite + pyrrhotite mineralization, although some pyrrhotite, selected Cu-sulfides, and additional pyrite, sphalerite, and galena could have been formed during later-stage metasomatic transformations of ultramafic rocks from the Ildeus intrusion [82,84]. Sulfur isotope data for the Ildeus massif and its satellite Lucha intrusion (located to the north of Ildeus) (Figure 1b) reported in [106] support the case for the magmatic origins of nickel sulfide mineralization, which is consistent with the available textural, mineralogical, and geochemical data [82,84]. The Ildeus $\delta^{34}S$ value of 4.7 substantially differs from the typical mid-ocean ridge basalt (MORB) $\delta^{34}S$ range of -0.18 to -1.91 and trends towards the average $\delta^{34}S$ of ~8 characteristic of the slab-derived sulfur (Figure 8).

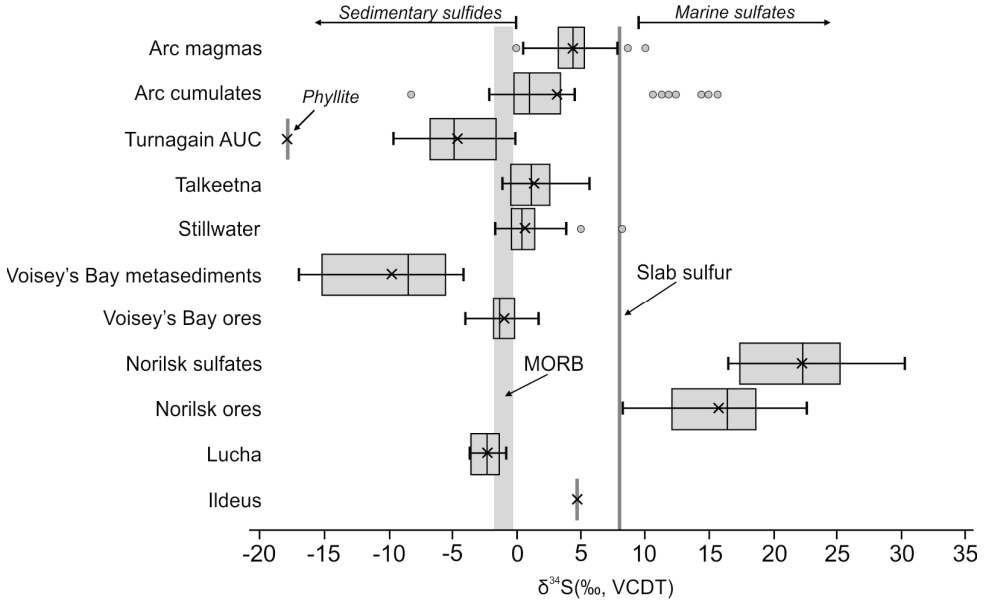


Figure 8. Variations of sulfur isotopes in Ildeus and Lucha mafic–ultramafic intrusions from the Stanovoi superterrane (Russia) [106] compared with selected magmatic sulfide ores and associated sediments from Norilsk (Russia) [107], Voisey's Bay (Canada) [108], Stillwater (USA) [109], Talkeetna ultramafic arc (Alaska, USA) [110], Turnagain Alaskan–Uralian-type plutonic complex and host graphite phyllite [111], arc cumulates [112], and arc magmas from the Marianas, Japan, and Indonesia [113–115]. Data for MORB are from [116], those for slab sulfur are from [117], those for sedimentary sulfides are from [110], and those for marine sulfates are from [118].

Interestingly, the satellite Lucha intrusion exhibits mantle (e.g., MORB-like) $\delta^{34}S$, which is comparable to the sulfur isotopic variations in magmatic sulfide ores in non-convergent margin mafic–ultramafic intrusions such as Voisey's Bay and Stillwater, as well

as the convergent margin Alaskan–Uralian-type complexes exemplified in Figure 8 by the Turnagain intrusion in British Columbia. The latter shows some variations towards host pyrite-bearing graphite phyllite, suggesting possible contamination by sedimentary sulfide [111]. Norilsk sulfide ores exhibit strongly positive $\delta^{34}S$ values, partially overlapping with host Permian evaporates (Figure 8). Abundant geological, petrological and geochemical data suggest that Norilsk sulfide-bearing intrusions have undergone extensive contamination by the Paleozoic anhydrite, rock salt, and dolostone [119,120]. The ultramafic lower crustal section of the Talkeetna arc in Alaska, mafic cumulates from the Lesser Antilles arc, and lavas from modern volcanic arcs display some enrichment in heavy sulfur isotopes, with a tendency towards slab-derived sulfates (Figure 8) indicating the potential recycling of marine sulfate-bearing sediments into arc magma sources [115,121,122]. The Ildeus $\delta^{34}S$ value of +4.7 falls within the range of various arc igneous rocks, which suggests derivation from subduction-related magma sources, with the possible involvement of recycled oceanic sediments.

5.2. Gold-Bearing Minerals

Alongside the disseminated Ni-Fe-sulfide mineralization, mafic and ultramafic rocks from the Ildeus intrusion contain potentially economic gold mineralization with erratic Au grade distribution (Tables 1 and 2). Gold grades of up to 0.19 g/t in the Ildeus intrusion were first reported in [106], together with some silver (up to 6 g/t) and palladium (up to 0.04 g/t). Some of the first surface grab samples collected by us along the western margin of the Ildeus intrusion returned some lode-type grades of 596 g/t, along with many samples in the range of 0.05 to 0.5 g/t [84,85]. Gold mineralization at the Ildeus intrusion is represented by flattened gold micronuggets (Figure 9a), typically accompanied by various sulfides and other metal alloys (Pd-Pt, Fe-Pt, Ni-Rd-Pt, Fe-W, Ti-Co-W, Pb-Sb, Sn-Zn-Cu, etc. [82,84,85,89,90]). Alongside gold, these micronuggets contain some minor nickel, silver, and copper (Figure 9b). In addition to the uniform flattened textural appearance (Figure 9a), these gold grains show uniform chemical compositions in a Cu-Ag-Au ternary diagram (Figure 9b), suggesting their formation under similar petrological conditions and, probably, through a uniform ore-forming process. The spatial association of gold with ultramafic cumulates in the Ildeus intrusion (Table 2 [84,85]) suggests potential magmatic origin, which is consistent with gold's flattened appearance, possibly caused by their growing from residual metal-rich magmatic liquids in interstitial spaces between the expanding cumulate olivine, orthopyroxene, and clinopyroxene grains [89,90]. The constant presence of minor nickel admixture (Figure 9b) may also reflect crystallization from the Ni-rich parental melt that gave birth to the Ni-sulfides, which are frequently found together with gold micronuggets in the Ildeus intrusion. At the same time, we cannot exclude the re-deposition of primary magmatic gold matter as texturally similar flattened particles in microfractures and inter-granular spaces under the influence of the late- and/or post-magmatic fluids.

Alongside nickel, gold micronuggets occasionally contain small amounts of zinc (Figure 10a) and show some surface sculpturing features that might be attributable to later-stage interaction with metasomatic fluids (Figure 10b).

Abundance of gold micronuggets in individual rock samples from the Ildeus intrusion show a strong correlation with the Au contents in these rocks (Figure 10c), with the highest gold microparticle counts being associated with the lode-type Au grades of up to 596 g/t [85, 86]. It is worth mentioning here that placer gold is being intermittently mined on a small scale by local alluvial miners from multiple creeks draining the Ildeus intrusion. The gold-bearing particle association is the second most abundant after the sulfide microinclusions in the studied ultramafic rocks (Table 2). The Au-bearing microinclusions in ultramafic cumulates

and the later-stage pyroxenite dikes (Table 2) clearly indicate the existence of potentially economic gold mineralization associated with the Ildeus intrusion (Table 1). The true scale of this erratic bulk gold mineralization is a subject for future exploration efforts in this part of the Stanovoy superterrane.

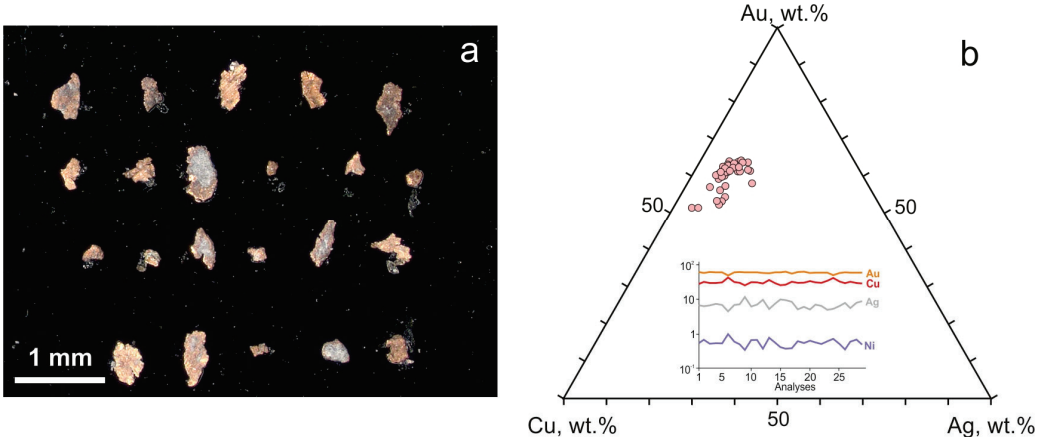


Figure 9. Flattened gold micronuggets from the Ildeus ultramafic rocks (**a**) and their composition (total of 46 grains) in the Cu-Au-Ag ternary plot (**b**). The inset shows the distribution of Au, Cu, Ag, and Ni contents in the individual micronuggets (a total of 29 grains) determined by the SEM-EDS.

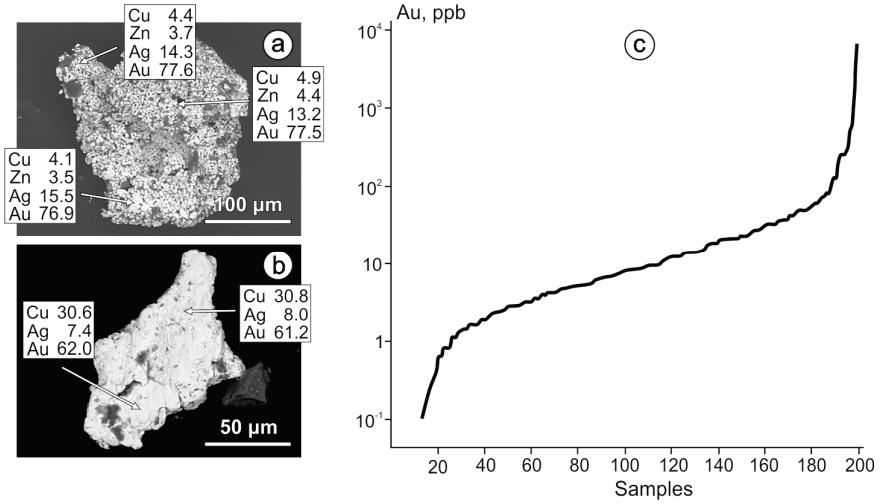


Figure 10. (**a**,**b**) BSE images of large particles of an Au-bearing alloy extracted from the Ildeus intrusion. (**c**) Variation of bulk Au content in the Ildeus intrusion sorted according to the ascending Au values in samples #1 to #200, modified from [85].

5.3. Silver-Bearing Minerals

Silver-bearing microinclusions in the Ildeus intrusion are represented by native and cupriferous silver, chlorargyrite, and acanthite, with small amounts of copper (Figure 5). Based on the abundance of Ag-bearing microinclusions in certain Ildeus igneous lithologies (Table 2) and the relationships between microinclusion assemblages and visibly disseminated nickel sulfide and gold mineralization, as described above, one can expect that separate silver mineralization might exist within the Ildeus mafic–ultramafic intrusion [81,82]. Several drill holes within the northern part of the Ildeus intrusion contain intervals composed of various mafic–ultramafic rocks assayed at 0.1 to 1 g/t Ag (Table 1), which represent drill-supported silver geochemical anomalies. A single one-meter section of websterites at the bottom of one of the holes was assayed at 162.2 g/t Ag [81,82], which is comparable to the silver content in low-grade hydrothermal deposits [123]. In

the volcanogenic massive sulfide (VMS) and sedimentary exhalative (SEDEX)-type deposits, where silver is a byproduct of polymetallic ores, its grades are around 30–50 g/t, while in the vein type, hydrothermal silver mineralization Ag grades in excess of 500 g/t are common [123]. With the exception of a single drill core sample with a Ag grade of 162.2 g/t, all of the silver contents detected in the Ildeus samples so far are interpreted as geochemically anomalous [81,82], and no silver ore has been discovered in this part of the Stanovoy superterrane as of yet. The abundance of silver-bearing microinclusions in the Ildeus mafic–ultramafic rocks (Table 2) suggests high exploration potential for large-scale, low-to-medium-grade silver mineralization at the Ildeus intrusion. The presence of microinclusions of silver chlorides (Figure 5e) and iodides (Figure 13c,d in [82]) may indicate the late-magmatic or, possibly, later-stage metasomatic nature (Figure 9b) of these silver mineral assemblages [124], possibly linked to the Lower Cretaceous post-collisional tectonic processes in the Stanovoy superterrane [81]. Alternatively, at least some silver could be of primary magmatic origin, as suggested by the presence of abundant microinclusions of native and cupriferous silver, Ag sulfides, and Ag chlorides in Quaternary lavas from the Kamchatka volcanic arc [125].

5.4. REE-Bearing Minerals

The recent discovery of rare earth element (REE) mineral microinclusions in the Ildeus intrusion has been reported in [80]. The REE microminerals include monazite (Figure 6a–c) and xenotime (Figure 6d), as well as REE oxides (Figure 6e) and carbonates (Figure 6f). Ultramafic rocks with abundant REE microinclusions (Table 2) are associated with total REE contents ranging from 330 to 890 ppm (Table 1 [80]). One microinclusion-rich sample yielded total REE content of 1938 ppm, which is comparable with the REE grades in some low-grade disseminated rare earth deposits (total REE $\geq$ 0.2% [126]). While monazite and xenotime are commonly considered as magmatic minerals in alkaline complexes and associated REE mineralization [126–128], REE-enriched carbonates such as bastnaesite are usually interpreted as precipitates from post-collisional metasomatic fluids exsolved from REE-enriched alkaline magmas and carbonatites [129–131]. In the case of the Ildeus intrusion, we interpret microinclusions of REE minerals as indicators of possible metasomatic rare earth element mineralization caused by the interaction with metal-rich trans-lithospheric fluids linked to the widespread post-collisional processes in the Stanovoy cratonic superterrane [80].

5.5. Relationship Between Microminerals and Ore Mineralization

The results of our investigation into the microinclusions in the Ildeus intrusive rocks indicate a link between various microinclusion assemblages and the formation of potentially economic mineralization within the Ildeus intrusion. For example, sulfide microinclusions correspond to the disseminated Ni-Co sulfide mineralization confirmed by drilling within the northern part of the Ildeus intrusion [82]. Microinclusions of gold and its alloys correlate with the erratic bulk gold mineralization in wehrlites, websterites, and pyroxenites (Table 2, Figure 9a [82]). The presence of silver- and REE-bearing microminerals in several Ildeus rocks suggests that the Ildeus intrusion may potentially host large-scale silver and REE mineralization, which is consistent with the sub-economic grades of these metals in some intrusive lithologies (Table 1).

The general hypothetical model for the formation of such complex polymetallic mineralization within the Ildeus intrusion is presented in Figure 11. Textural and mineralogical data support the formation of magmatic sulfide mineralization—possibly the earliest—in the Ildeus mafic–utramafic intrusion through crystal fractionation and accumulation (Figure 11a) under mantle and crustal conditions similar to those of continental layered

igneous complexes worldwide [5,38,132,133]. The late magmatic crystallization processes and late- and post-magmatic, metal-rich fluids appear to be responsible for the gold mineralization and, possibly, for the not yet discovered bulk silver mineralization (Figure 11b). This later-stage precious metals deposition might be similar to the later-stage hydrothermal gold and platinum-group metal mineralization formed through a high-salinity hydrous fluid infiltration in such layered intrusions as the Bushveld complex in South Africa [134] and the Stillwater complex in Montana, USA [135,136]. Experimental data suggest the elevated mobility of gold and silver in hydrothermal fluids associated with mafic–ultramafic intrusive systems controlled by such physicochemical parameters as oxygen fugacity, acidity, and chlorinity [137].

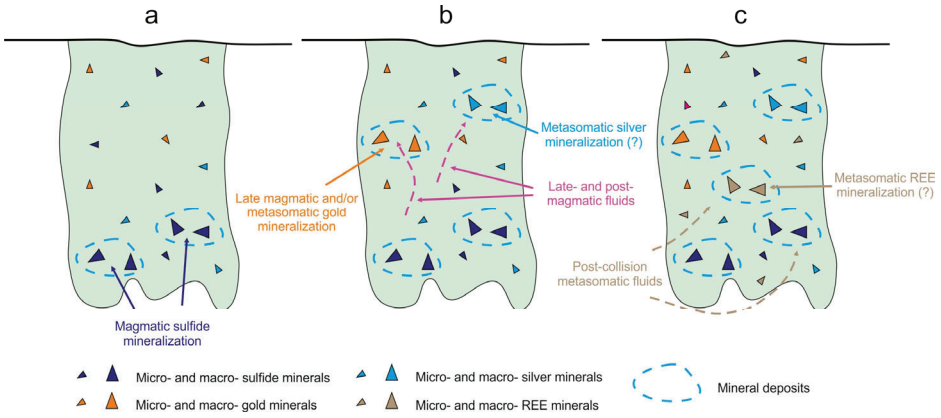


Figure 11. A schematic conceptual diagram showing possible models of formation of magmatic sulfide (**a**), gold and silver (**b**), and REE (**c**) mineralization in the Ildeus mafic–ultramafic intrusion.

This interpretation is consistent with presence of the abundant chlorine-bearing microinclusions associated with gold- and silver-bearing minerals in the Ildeus intrusive rocks (Figure 5e [82,84,85]). Finally, low-grade REE mineralization in some Ildeus intrusive lithologies can be linked to the metal-rich, post-collisional fluids associated with Early Cretaceous slab tear and break-off under the Stanovoy superterrane [80].

The exact role of microminerals in the formation of potentially economic macromineralization is yet to be fully understood and clarified. Based on the available petrological and geochemical information for the Ildeus intrusion and other igneous suites, it appears that the observed micromineral assemblages may reflect initial elevated contents of certain metals in primary magmas and their volcanic and plutonic differences [36,38,72,75,77,89,90,97]. Alternatively, microminerals can possibly be later reassembled and accumulated into metal macromineralization through the common processes of magma differentiation, fluid-induced precipitation, and fluid–rock interaction under the upper crustal conditions [2,4,8,12]. Oxygen fugacity, fluid composition (especially salinity), and sulfur activity will play additional and important roles in the transformation of micromineral assemblages in igneous rocks into related economic ore deposits and showings [19,30,34,44,47,48,132,137,138].

6. Conclusions

Mafic–ultramafic rocks from the subduction-related Triassic mafic–ultramafic Ildeus intrusion in the Stanovoy superterrane of the Russian Far East contain four distinct assemblages of mineral microinclusions, namely, (1) base metal sulfides, (2) Au and Au-bearing alloys, (3) Ag and Ag-bearing minerals, and (4) REE-bearing minerals. We interpret these microinclusions as records of the early stages of the development of the Ildeus crustal magmatic–hydrothermal system, linked to its general mineralizing potential. The Ildeus

intrusion contains disseminated nickel–cobalt sulfide and gold mineralization, which is compositionally similar to the sulfide- and Au-rich microminerals observed in the Ildeus peridotites and pyroxenites. Silver-bearing and REE-bearing minerals have, so far, been found only as microinclusions, but some grab and drill core samples are characterized by anomalous silver and total REE contents comparable to metal grades in low-grade ore deposits.

Our results suggest that a genetic link may exist between assemblages of ore mineral microinclusions of certain compositions and the ore macromineralization present in magmatic rocks. If this is the case, future investigations into microminerals in igneous rocks can be used as complimentary guides for (1) deciphering of metallogenic evolution of their primary magmas and (2) prospecting and exploring the ore mineralization potentially associated with micromineral-bearing magmatic complexes.

Supplementary Materials: The following supporting information can be downloaded at: https://www.mdpi.com/article/10.3390/min15050504/s1, Figure S1. Selected SEM-EDA spectra for microminerals from intrusive rocks of the Ildeus intrusion. (a–p) BSE images: a—Figure 3e; b—Figure 3f; c—Figure 3i d—Figure 4a; e—Figure 4c; f—Figure 4e; g—Figure 4f; h—Figure 5b; i—Figure 5d; k—Figure 5e; l—Figure 5f; m—Figure 6b; n—Figure 6d; o—Figure 6e; p—Figure 6f.

Author Contributions: Conceptualization, V.K., N.B. and P.K.; methodology, V.K. and N.B.; software, V.K.; validation, V.K.; formal analysis, V.K.; investigation, V.K., N.B. and P.K.; resources, V.K. and N.B.; data curation, V.K. and N.B.; writing—original draft preparation, V.K., N.B. and P.K.; writing—review and editing, V.K., N.B. and P.K.; visualization, V.K. and N.B.; supervision, N.B.; project administration, N.B.; funding acquisition, N.B. All authors have read and agreed to the published version of the manuscript.

Funding: This research was funded through the state assignment of the Institute of Tectonics and Geophysics, Far Eastern Branch, Russian Academy of Sciences (topic no. 124042300007-3, youth laboratory), using scientific equipment of the Khabarovsk Innovation and Analytical Center.

Data Availability Statement: Data are available upon request from the corresponding author.

Acknowledgments: We greatly appreciate the highly constructive reviews from four anonymous reviewers that significantly improved this manuscript. This study would not have been possible without the long-term support from the personnel of Khingan Minerals AS (Oslo, Norway) and Khingan LLC (Khabarovsk, Russia). We specifically thank Oleg Alekseenko for his support during our fieldwork in the Stanovoy superterrane (Russian Far East).

Conflicts of Interest: The authors declare no conflicts of interest.

References

1. Dilles, J.H. Petrology of the Yerington Batholith, Nevada—Evidence for evolution of porphyry copper ore fluids. *Econ. Geol.* **1987**, *82*, 1750–1789. [CrossRef]
2. Hedenquist, J.W.; Lowenstern, J.B. The role of magmas in the formation of hydrothermal ore deposits. *Nature* **1994**, *370*, 519–527. [CrossRef]
3. Hattori, K.H.; Keith, J.D. Contribution of mafic melt to porphyry copper mineralization: Evidence from Mount Pinatubo, Philippines, and Bingham Canyon, Utah, USA. *Miner. Depos.* **2001**, *36*, 799–806. [CrossRef]
4. Williams, P.J.; Barton, M.D.; Johnson, D.A.; Fontboté, L.; Antoine, M.; Geordie, O.; Marschik, R. Iron oxide copper-gold deposits: Geology, space-time distribution, and possible modes of origin. *Econ. Geol.* **2005**, *100*, 371–405.
5. Simon, A.C.; Ripley, E.M. The role of magmatic sulfur in the formation of ore deposits. *Rev. Mineral. Geochem.* **2011**, *73*, 513–578. [CrossRef]
6. Groves, D.I.; Bierlein, F.P.; Meinert, L.D.; Hitzman, M.W. Iron oxide copper-gold (IOCG) deposits through Earth history: Implications for origin, lithospheric setting, and distinction from other epigenetic iron oxide deposits. *Econ. Geol.* **2010**, *105*, 641–654. [CrossRef]
7. Pang, K.-N.; Zhou, M.-F.; Qi, L.; Shelnutt, J.G.; Wang, C.Y.; Zhao, D. Magmatic Fe-Ti-V oxide deposits in the Emeishan large igneous province, SW China. *Lithos* **2010**, *119*, 123–136. [CrossRef]

8. Sillitoe, R.H. Porphyry copper systems. *Econ. Geol.* **2010**, *105*, 3–41. [CrossRef]
9. Bain, W.M.; Steele-MacInnis, M.; Li, K.; Mazdab, F.K.; Marsh, E.E. A fundamental role of carbonate-sulfate melts in the formation of iron oxide-apatite deposits. *Nat. Geosci.* **2020**, *13*, 751–757. [CrossRef]
10. Yan, S.C.; Wan, B.; Anenburg, M.; Mavrogenes, J.A. Silicate and iron phosphate melt immiscibility promotes REE enrichment. *Geochem. Perspect. Lett.* **2024**, *32*, 14–20. [CrossRef]
11. Pearce, J.A.; Gale, G.H. Identification of ore-deposition environment from trace-element geochemistry of associated igneous host rocks. *Geol. Soc. Lond. Spec. Publ.* **1977**, *7*, 14–24. [CrossRef]
12. Richards, J.P.; McCulloch, M.T.; Chappell, B.W.; Kerrich, R. Sources of metals in the Porgera gold deposit, Papua New Guinea: Evidence from alteration, isotope, and noble metal geochemistry. *Geochim. Cosmochim. Acta* **1991**, *55*, 565–580. [CrossRef]
13. Du Bray, E.A. Geochemical characteristics of igneous rocks associated with epithermal mineral deposits—A review. *Ore Geol. Rev.* **2017**, *80*, 767–783. [CrossRef]
14. Wang, P.; Dong, G.; Santosh, M.; Liu, K.; Li, X. Copper isotopes trace the evolution of skarn ores: A case study from the Hongshan-Hongniu Cu deposit, southwest China. *Ore Geol. Rev.* **2017**, *88*, 822–831. [CrossRef]
15. Zhao, Q.; Xiao, R.; Zhang, D.; Wang, J.; Zhang, Y.; Li, P. Petrogenesis and tectonic setting of ore-associated intrusive rocks in the Baiyinnuoer Zn-Pb deposit, Southern Great Xing'an (NE China): Constraints from zircon U-Pb dating, geochemistry, and Sr-Nd-Pb isotopes. *Minerals* **2020**, *10*, 19. [CrossRef]
16. Chen, X.; Brzozowski, M.J.; Zou, S.; Qi, L.; Li, K.; Leng, C.-B. Platinum-group element geochemistry of igneous rocks in the Chongjiang Cu-Mo_Au deposit, southern Tibet: Implications for the formation of post-collision porphyry Cu deposits. *J. Petrol.* **2024**, *65*, egae025. [CrossRef]
17. Streck, M.J. Mineral textures and zoning as evidence for open system processes. *Rev. Mineral. Geochem.* **2008**, *69*, 595–622. [CrossRef]
18. Williamson, B.J.; Herrington, R.J.; Morris, A. Porphyry copper enrichment linked to excess aluminium in plagioclase. *Nat. Geosci.* **2016**, *9*, 237–241. [CrossRef]
19. Chelle-Michou, C.; Chiaradia, M. Amphibole and apatite insights into the evolution and mass balance of Cl and S in magmas associated with porphyry copper deposits. *Contrib. Mineral. Petrol.* **2017**, *172*, 105. [CrossRef]
20. Vigneresse, J.-L. Addressing ore formation and exploration. *Geosci. Front.* **2019**, *10*, 1613–1622. [CrossRef]
21. Li, J.-X.; Fan, W.-M.; Zhang, L.-Y.; Ding, L.; Yue, Y.-H.; Xie, J.; Cai, F.-L.; Quan, Q.-Y.; Sein, K. Biotite geochemistry deciphers magma evolution of Sn-bearing granite, southern Myanmar. *Ore Geol. Rev.* **2020**, *121*, 103565. [CrossRef]
22. Taghavi, A.; Maanijou, M.; Lentz, D.R.; Sepahi-Gerow, A.A.; Maruoka, T.; Fujisaki, W.; Suzuki, K. Biotite compositions and geochemistry of porphyry-related systems from the central Urumieh Dokhtar Magmatic Belt, western Yazd, Iran: Insights into mineralization potential. *Lithos* **2022**, *412–413*, 106593. [CrossRef]
23. Lee, W.-S.; Kontak, D.J.; Petts, D.C.; Jackson, S.E. Mineral chemistry-driven protocol to unravel the complex paragenesis of the Klaza (Yukon, Canada) superimposed porphyry-epithermal system. *Ore Geol. Rev.* **2022**, *143*, 104761. [CrossRef]
24. Tatnell, L.; Anenburg, M.; Loucks, R. Porphyry copper deposit formation: Identifying garnet and amphibole fractionation with REE apttern curvature modeling. *Geophys. Res. Lett.* **2023**, *50*, e2023GL103525. [CrossRef]
25. Fan, Y.; Deng, Y.; Xia, Z.; Ren, M.; Huang, J. Petrogenesis of the Dalaku'an mafic-ultramafic intrusion in the East Kunlun, Xinjiang: Constraints from the mineralogy of amphiboles. *Minerals* **2024**, *14*, 651. [CrossRef]
26. Simpson, B.; Ubide, T.; Spandler, C. Drivers of critical metal enrichment in peralkaline magmas recorded by clinopyroxene zoning. *Commun. Earth Environ.* **2025**, *6*, 89. [CrossRef]
27. Belousova, E.A.; Griffin, W.L.; O'Reilly, S.Y.; Fisher, N.I. Apatite as an indicator mineral for mineral exploration: Trace-element compositions and their relationship to host rock type. *J. Geochem. Explor.* **2002**, *76*, 45–69. [CrossRef]
28. Dare, S.A.S.; Barnes, S.-J.; Beaudoin, G.; Méric, J.; Boutroy, E.; Potvin-Doucet, C. Trace elements in magnetite as petrogenetic indicators. *Mineral. Depos.* **2014**, *49*, 785–796. [CrossRef]
29. Mao, M.; Rukhlov, A.S.; Rowins, S.M.; Spence, J.; Coogan, L.A. Apatite trace element compositions: A robust new tool for mineral exploration. *Econ. Geol.* **2016**, *111*, 1187–1222. [CrossRef]
30. Nathwani, C.; Blundy, J.; Wilkinson, J.J.; Buret, Y.; Loader, M.A.; Tavazzani, L.; Chelle-Michou, C. A zircon case for super-wet arc magmas. *Nat. Commun.* **2024**, *15*, 8982. [CrossRef]
31. Wen, Z.-H.; Kirkland, C.L.; Li, S.-R.; Sun, X.-J.; Lei, J.-L.; Xu, B.; Hou, Z.-O. A machine learning approach to discrimination of igneous rocks and ore deposits by zircon trace elements. *Am. Mineral.* **2024**, *109*, 1129–1142. [CrossRef]
32. Wilkinson, J.J. Fluid inclusions in hydrothermal ore deposits. *Lithos* **2001**, *55*, 229–272. [CrossRef]
33. Student, J.J.; Bodnar, R.J. Silicate melt inclusions in porphyry copper deposits: Identification and homogenization behavior. *Can. Mineral.* **2004**, *42*, 1583–1599. [CrossRef]
34. Audétat, A.; Pettke, T.; Heinrich, C.; Bodnar, R.J. The composition of magmatic-hydrothermal fluids in barren and mineralized intrusions. *Econ. Geol.* **2008**, *103*, 877–908. [CrossRef]

35. Pettke, T.; Oberli, F.; Heinrich, C.A. The magma and metal source of giant porphyry-type ore deposits, based on lead isotope microanalysis of individual fluid inclusions. *Earth Planet. Sci. Lett.* **2010**, *296*, 267–277. [CrossRef]
36. Halter, W.; Heinrich, C.A.; Pettke, T. Magma evolution and the formation of porphyry Cu-Au ore fluids: Evidence from silicate and sulfide melt inclusions. *Miner. Depos.* **2005**, *39*, 845–863. [CrossRef]
37. Candela, P. A review of shallow, ore-related granites: Textures, volatiles, and ore metals. *J. Petrol.* **1997**, *38*, 1619–1633. [CrossRef]
38. Arndt, N.T.; Lesher, C.M.; Czamanske, G.K. Mantle-derived magmas and magmatic Ni-Cu-(PGE) deposits. *Econ. Geol.* **2005**, *100*, 5–24.
39. Cerny, P.; Blevin, P.L.; Cuney, M.; London, D. Granite-related ore deposits. *Econ. Geol.* **2005**, *100*, 337–370.
40. Peck, D.C.; Huminicki, M.A.E. Value of mineral deposits associated with mafic and ultramafic magmatism. *Ore Geol. Rev.* **2016**, *72*, 269–298. [CrossRef]
41. Sajona, F.G.; Maury, R. Association of adakites with gold and copper mineralization in the Phillippines. *C. R. Acad. Sci. Ser. IIA Earth Planet. Sci.* **1988**, *326*, 27–34.
42. Defant, M.J.; Kepezhinskas, P. Evidence suggests slab melting in arc magmas. *EOS Trans. Am. Geophys. Union* **2001**, *82*, 65–69. [CrossRef]
43. Kepezhinskas, P.; Berdnikov, N.; Kepezhinskas, N.; Konovalova, N. Adakites, high-Nb basalts and copper-gold deposits in magmatic arcs and collisional orogens: An overview. *Geosciences* **2022**, *12*, 29. [CrossRef]
44. Leong, T.S.J.; Mavrogenes, J.A.; Arculus, R.J. Water-sulfur-rich, oxidized adakite magmas are likely porphyry copper progenitors. *Sci. Rep.* **2023**, *13*, 5078. [CrossRef]
45. Naldrett, A.J. Nickel sulfide deposits: Classification, composition, and genesis. *Econ. Geol.* **1981**, *75*, 628–685.
46. Lesher, C.M. Komatiite-associated nickel sulfide deposits. *Rev. Econ. Geol.* **1989**, *4*, 45–101.
47. Keays, R.R. The role of komatiitic and picritic magmas and S-saturation. *Lithos* **1995**, *34*, 1–18. [CrossRef]
48. Barnes, S.-J.; Lightfoot, P.C. Formation of magmatic nickel sulfide ores and processes affecting their copper and platinum group element contents. *Econ. Geol.* **2005**, *100*, 179–214.
49. Barnes, S.J.; Fiorentini, M.L. Komatiite magmas and sulfide nickel deposits: A comparison of variably endowed Archean terranes. *Econ. Geol.* **2012**, *107*, 755–780. [CrossRef]
50. Müller, D.; Groves, D.I. Direct and indirect associations between potassic igneous rocks, shoshonites and gold-copper deposits. *Ore Geol. Rev.* **1993**, *8*, 383–406. [CrossRef]
51. Soloviev, S.G.; Kryazhev, S.G.; Semenova, D.V.; Kalinin, Y.A.; Dvurechenskaya, S.S.; Sidorova, N.V. Geology, mineralization, igneous geochemistry, and zircon U-Pb geochronology of the Early Paleozoic shoshonite-related Julia skarn deposit, SW Siberia, Russia: Toward a diversity of Cu-Au-Mo skarn to porphyry mineralization in the Altai-Sayan orogenic system. *Ore Geol. Rev.* **2022**, *142*, 104706. [CrossRef]
52. Schaarschmidt, A.; Klemd, R.; Regelous, M.; Voudouris, P.C.; Melfos, V.; Haase, K.M. The formation of shoshonitic magma and its relationship to porphyry-type mineralization: The Maronia pluton in NE Greece. *Lithos* **2021**, *380–381*, 105911. [CrossRef]
53. Kepezhinskas, P.; Berdnikov, N.; Kepezhinskas, N.; Konovalova, N.; Krutikova, V.; Astapov, I. Nature of Paleozoic basement of the Catalan Coastal Ranges (Spain) and tectonic setting of the Priorat DOQ wine terroir: Evidence from volcanic and sedimentary rocks. *Geosciences* **2023**, *13*, 31. [CrossRef]
54. Guiliani, A.; Pearson, D.G. Kimberlites: From deep Earth to diamond mines. *Elements* **2019**, *15*, 377–380. [CrossRef]
55. Kjarsgaard, B.A.; de Wit, M.; Heaman, L.M.; Pearson, D.G.; Stiefenhofer, J.; Janusczcak, N.; Shirey, S.B. A review of the geology of global diamond mines and deposits. *Rev. Mineral. Geochem.* **2022**, *88*, 1–117. [CrossRef]
56. Kepezhinskas, N.; Kjarsgaard, B.A.; Sarkar, C.; Luo, Y.; Locock, A.J.; Pearson, D.G. Petrology, geochemistry, and geochronology of the Mel kimberlites, Nunavut, Canada and their relationship to Neoproterozoic to Cambrian magmatism in North America. In *Mineralogy and Petrology*; Springer: Berlin/Heidelberg, Germany, 2024. [CrossRef]
57. Jones, A.P.; Genge, M.; Carmody, L. Carbonate melts and carbonatites. *Rev. Mineral. Geochem.* **2013**, *75*, 289–322. [CrossRef]
58. Wang, Z.-Y.; Fan, H.-R.; Zhou, L.; Yang, K.-F.; She, H.-D. Carbonatite-realted REE deposits: An overview. *Minerals* **2020**, *10*, 965. [CrossRef]
59. Anenburg, M.; Broom-Fendley, S.; Chen, W. Formation of rare earth deposits in carbonatites. *Elements* **2021**, *17*, 327–332. [CrossRef]
60. Simandl, G.J.; Paradis, S. Carbonatites: Related ore deposits, resources, footprint, and exploration methods. *Appl. Earth Sci.* **2018**, *127*, 123–152. [CrossRef]
61. Bowden, P.; Kinnaird, J.A. The petrology and geochemistry of alkaline granites from Nigeria. *Phys. Earth Planet. Inter.* **1984**, *35*, 199–211. [CrossRef]
62. Kogarko, L.N.; Williams, C.T.; Wooley, A.R. Chemical evolution and petrogenetic implications of loparite in the layered, agpaitic Lovozero complex, Kola Peninsula, Russia. *Mineral. Petrol.* **2002**, *74*, 1–24.
63. Chakhmouradian, A.R.; Zaitsev, A.N. Rare earth mineralization in igneous rocks: Sources and processes. *Elements* **2012**, *8*, 347–353. [CrossRef]

64. Sheard, E.R.; Williams-Jones, A.E.; Helligmann, M.; Pederson, C.; Trueman, D.L. Controls on the concentration of zirconium, niobium, and the rare earth elements in the Thor Lake rare metal deposit, Northwest Territories, Canada. *Econ. Geol.* **2012**, *107*, 81–104. [CrossRef]
65. Benson, T.R.; Coble, M.A.; Rytuba, J.J.; Mahood, G.A. Lithium enrichment in intracontinental rhyolitic magmas leads to Li deposits in caldera basins. *Nat. Commun.* **2017**, *8*, 270. [CrossRef]
66. Jowitt, S.M.; Medlin, C.C.; Cas, R.A.F. The rare earth element (REE) mineralization potential of highly fractionated rhyolites: A potential low-grade, bulk tonnage source of critical metals. *Ore Geol. Rev.* **2017**, *86*, 548–562. [CrossRef]
67. Farrow, C.E.G.; Watkinson, D. Diversity of precious-metal mineralization in footwall Cu-Ni-PGE deposits, Sudbury, Ontario: Implications for hydrothermal models of formation. *Can. Mineral.* **1997**, *35*, 817–839.
68. Jennings, E.S.; Marschall, H.R.; Hawkesworth, C.J.; Storey, C.D. Characterization of magma from inclusions in zircon: Apatite and biotite work well, feldspar less so. *Geology* **2011**, *39*, 863–866. [CrossRef]
69. Anenburg, M.; Mavrogenes, J.A. Experimental observations on noble metal nanonuggets and Fe-Ti oxides, and the transport of platinum group elements in silicate melts. *Geochim. Cosmochim. Acta* **2016**, *192*, 258–278. [CrossRef]
70. Bell, E.A.; Kirkpatrick, H.M.; Harrison, T.M. Crystallization order effect on inclusion assemblages in magmatic accessory mineral and implications for the detrital record. *Chem. Geol.* **2022**, *613*, 121143. [CrossRef]
71. Schneider, P.; Balen, D. Inclusions in magmatic zircon from Slavonian mountains (eastern Croatia): Anatase, kumdykolite and kokchetavite and implications for the magmatic evolution. *Eur. J. Mineral.* **2024**, *36*, 209–223. [CrossRef]
72. Berdnikov, N.V.; Nevstruev, V.G.; Kepezhinskas, P.K.; Mochalov, A.G.; Yakubovich, O.V. PGE mineralization in andesite explosive breccias associated with the Poperechny iron-manganese deposit (Lesser Khingan, Far East Russia): Whole-rock geochemical, $^{190}Pt/^{4}He$ isotopic, and mineralogical evidence. *Ore Geol. Rev.* **2020**, *118*, 103352. [CrossRef]
73. Berdnikov, N.; Nevstruev, V.; Kepezhinskas, P.; Astapov, I.; Konovalova, N. Gold in mineralized volcanic systems from the Lesser Khingan Range (Russian Far East): Textural types, composition and possible origins. *Geosciences* **2021**, *11*, 103. [CrossRef]
74. Berdnikov, N.V.; Nevstruev, V.G.; Kepezhinskas, P.K.; Krutikova, V.O.; Konovalova, N.S.; Astapov, I.A. Silicate, Fe-oxide, and Au-Cu-Ag microspherules in ores and pyroclastic rocks of the Kostenga iron deposit, in the Far East of Russia. *Russ. J. Pac. Geol.* **2021**, *15*, 236–251. [CrossRef]
75. Mochalov, A.G.; Berdnikov, N.V.; Galankina, O.L.; Kepezhinskas, P.K.; Liu, J.; Krutikova, V.O. PGE mineralogy in explosive breccias of the Poperechnoe Deposit (the Lesser Khingan Range, Russia). *Russ. J. Pac. Geol.* **2022**, *16*, 544–559. [CrossRef]
76. Berdnikov, N.; Kepezhinskas, P.; Nevstruev, V.; Krutikova, V.; Konovalova, N.; Savatenkov, V. Magmatic-hydrothermal origin of Fe-Mn deposits in the Lesser Khingan Range (Russian Far East). *Minerals* **2023**, *13*, 1366. [CrossRef]
77. Kepezhinskas, P.; Berdnikov, N.; Krutikova, V.O.; Kozhemyako, N. Iron-titanium oxide-apatite-sulfide-sulfate microinclusions in gabbro and adakite from the Russian Far East indicate possible magmagtic links to iron oxide-apatite and iron oxide-copper-gold deposits. *Minerals* **2024**, *14*, 188. [CrossRef]
78. Kepezhinskas, P.K.; Berdnikov, N.V.; Krutikova, V.O.; Kozhemiako, N.V. Assemblages of microinclisions of Fe-Ti oxides, apatite, sulfates and sulfides in pyroxenites, gabbroids, and adakitic granitoids from the Gabbrovy Massif as precursors of iron oxide-copper-gold and iron oxide-apatite mineralization in the Stanovoy superterrane (Russian Far East). *Russ. J. Pac. Geol.* **2024**, *18*, 621–636.
79. Glebovitsky, V.A.; Kotov, A.B.; Sal'nikova, E.B.; Larin, A.M.; Velikoslavinsky, S.D. Granulite complexes of the Dzhugdzhur-Stanovoi fold region and the Peristanovoi belt: Age, formation conditions, and geodynamic settings of metamorphism. *Geotectonics* **2009**, *43*, 253–263. [CrossRef]
80. Kepezhinskas, P.K.; Khanchuk, A.I.; Berdnikov, N.V.; Krutikova, V.O. Rare-earth minerals in ultrabasites of the Ildeus massif (Stanovoy cratonic terrane): Influence of post-collision processes on deep ore-magmatic systems of convergent plate boundaries. *Russ. J. Pac. Geol.* **2024**, *18*, 601–620. [CrossRef]
81. Kepezhinskas, P.K.; Berdnikov, N.V.; Krutikova, V.O.; Kepezhinskas, P.K.; Astapov, I.A.; Kirichenko, E.A. Silver mineralization in deep magmatogenic systems of ancient island arcs: The Ildeus ultrabasic massif, Stanovoy mobile belt (Russian Far East). *Russ. J. Pac. Geol.* **2023**, *17*, 322–349. [CrossRef]
82. Kepezhinskas, P.; Berdnikov, N.; Kepezhinskas, N.; Krutikova, V.; Astapov, I. Magmatic-hydrothermal transport of metals at arc plutonic roots: Insights from the Ildeus mafic-ultramafic complex, Stanovoy Suture Zone (Russian Far East). *Minerals* **2023**, *13*, 878. [CrossRef]
83. Kepezhinskas, P.K.; Berdnikov, N.V.; Krutikova, V.O. Metal and mineral microinclusions in adakites from the framing of the Utanak massif (Stanovoy superterrane, Russian Far East) as evidence for metal enrichment in adakitic magmas. *Russ. Geol. Geophys.* **2025**, *66*, 127–141. [CrossRef]
84. Kepezhinskas, P.; Kepezhinskas, N.P.; Berdnikov, N.V.; Krutikova, V.O. Native metals and intermetallic compounds in subduction-related ultramafic rocks from the Stanovoy mobile belt (Russian Far East): Implications for redox heterogeneity in subduction zones. *Ore Geol. Rev.* **2020**, *127*, 103800. [CrossRef]

85. Berdnikov, N.; Kepezhinskas, P.; Konovalova, N.; Kepezhinskas, N. Formation of gold alloys during crustal differentiation of convergent zone magmas: Constraints from an Au-rich websterite in the Stanovoy suture zone (Russian Far East). *Geosciences* **2022**, *12*, 126. [CrossRef]
86. Tassara, S.; Ague, J.J.; Keller, D.S.; Rooney, A.D.; Wostbrock, J.A.G.; Axler, J.A.; Tardani, D. Osmium and oxygen isotope constraints on magma-crust interactions and the transport of copper at the roots of arcs. *Chem. Geol.* **2024**, *664*, 122301. [CrossRef]
87. McDonough, W.F.; Sun, S.-S. The composition of the Earth. *Chem. Geol.* **1995**, *120*, 223–253. [CrossRef]
88. Whitney, D.L.; Evans, B.W. Abbreviations for names of rock—Forming minerals. *Amer. Mineral.* **2010**, *95*, 185–187. [CrossRef]
89. McCulloch, M.T.; Gamble, J.A. Geochemical and geodynamical constraints on subduction zone magmatism. *Earth Planet. Sci. Lett.* **1991**, *102*, 358–374. [CrossRef]
90. Krutikova, V.O.; Berdnikov, N.V.; Kepezhinskas, P.K. Metal and mineral microinclusions in rocks: Research finding interpretation and application to the study of magmatic systems of Kamchatka and Stanovoi fold belt. *Russ. J. Pac. Geol.* **2024**, *18*, 37–49. [CrossRef]
91. Berdnikov, N.V.; Kepezhinskas, P.K.; Nevstruev, V.G.; Krutikova, V.O.; Konovalova, N.S. Magmatic native gold: Composition, texture, genesis, and evolution in the Earth's crust. *Russ. Geol. Geophys.* **2024**, *65*, 388–403. [CrossRef]
92. Huber, C.; Bachmann, O.; Vigneresse, J.-L.; Dufek, J.; Parmigianim, A. A physical model for metal extraction and transport in shallow magmatic systems. *Geochem. Geophys. Geosyst.* **2012**, *13*, 1–18. [CrossRef]
93. Costa, S.; Fulignati, P.; Gioncada, A.; Pistolesi, M.; Bosch, D.; Bruguier, O. Tracking metal evolution in arc magmas: Insights from the active volcano of La Fossa, Italy. *Lithos* **2021**, *180–181*, 105851. [CrossRef]
94. Brandl, P.A.; Portnyagin, M.; Zeppenfeld, H.; Tepley, F.J., III; de Ronde, C.E.J.; Timm, C.; Hauff, F.; Garbe-Schönberg, D.; Bousquet, R. The origin of magmas and metals at the submarine Brothers volcano, Kermadec arc, New Zealand. *Econ. Geol.* **2023**, *118*, 1577–1604. [CrossRef]
95. Kogarko, L.N. Ore-forming potential of alkaline magmas. *Lithos* **1990**, *26*, 167–175. [CrossRef]
96. Naumov, V.B.; Dorofeeva, V.A.; Girnis, A.V.; Kovalenker, V.A. Volatile, trace, and ore elements in magmatic melts and natural fluids: Evidence from mineral-hosted inclusions. I. Mean concentrations of 45 elements in the main geodynamic settings of the Earth. *Geochem. Int.* **2022**, *60*, 325–344. [CrossRef]
97. Kepezhinskas, P.; Berdnikov, N.; Konovalova, N.; Kepezhinskas, N.; Krutikova, V.; Kirichenko, E. Native metals and alloys in trachytes and shoshonite from the continental United States and high-K dacite from the Bolivian Andes: Magmatic origins of ore metals in convergent and within-plate tectonic settings. *Russ. J. Pac. Geol.* **2022**, *16*, 405–426. [CrossRef]
98. Gao, X.; Zhou, Z.; Breiter, K.; Mao, J.; Romer, R.L.; Cook, N.J.; Holtz, F. Magmatic-hydrothermal fluid evolution of the tin-polymetallic metallogenic systems from the Weilasituo ore district, Northeast China. *Sci. Rep.* **2024**, *14*, 3006. [CrossRef]
99. Zhang, Z.; Mao, J.; Chai, F.; Yan, S.; Chen, B.; Pirajno, F. Geochemistry of the Permian Kalatongke mafic intrusions, Northern Xinjiang, Northwest China: Implications for the genesis of magmatic Ni-Cu sulfide deposits. *Econ. Geol.* **2009**, *104*, 185–203. [CrossRef]
100. Su, B.-X.; Qin, K.-Z.; Tang, D.-M.; Sakyi, P.A.; Liu, P.-P.; Sun, H.; Xiao, Q.-H. Late Paleozoic mafic-ultramafic intrusions in southern Central Asian Orogenic Belt (NW China): Insight into magmatic Ni-Cu sulfide mineralization in orogenic setting. *Ore Geol. Rev.* **2013**, *51*, 57–73. [CrossRef]
101. Gao, J.-F.; Wang, H.H. Permian mafic-ultramafic magmatism and sulfide mineralization in the Central Asian Orogenic Belt: A review. *J. Asian Earth Sci.* **2024**, *264*, 106071. [CrossRef]
102. Evans, D.M.; Boadi, I.; Byemelwa, L.; Gilligan, J.; Kabete, J.; Marcet, P. Kabanga magmatic sulfide deposits, Tanzania: Morphology and geochemistry of associated intrusions. *J. Afr. Earth Sci.* **2000**, *30*, 651–674. [CrossRef]
103. Maier, W.D.; Barnes, S.-J.; Sarkar, A.; Ripley, E.; Li, C.; Livesey, T. The Kabanga Ni sulfide deposit, Tanzania: I. Geology, petrography, silicate rock geochemistry, and sulfur and oxygen isotopes. *Miner. Depos.* **2010**, *45*, 419–441. [CrossRef]
104. Tornos, F.; Galindo, C.; Casquet, C.; Pevida, L.R.; Martínez, C.; Martínez, E.; Velasco, F.; Iriondo, A. The Aguablanca Ni-(Cu) sulfide deposit, SW Spain: Geologic and geochemical controls and the relationship with a midcrustal layered mafic complex. *Miner. Depos.* **2006**, *41*, 737–769. [CrossRef]
105. Piña, R.; Romeo, I.; Ortega, L.; Lunar, R.; Capote, R.; Gervilla, F.; Tejero, R.; Quesada, C. Origin and emplacement of the Aguablanca magmatic Ni-Cu-(PGE) sulfide deposit, SW Iberia: A multidisciplinary approach. *Geol. Soc. Am. Bull.* **2010**, *122*, 915–925. [CrossRef]
106. Buchko, I.V.; Izokh, A.E.; Nosyrev, M.Y. Sulfide mineralization of ultramafic-mafic rocks of the Stanovoy megablock. *Pac. Geol.* **2002**, *21*, 56–68.
107. Ryabov, V.V.; Smirnov, O.N.; Snisar, S.G.; Borovikova, A.A. The source of sulfur deposits in the Siberian Platfrom traps (from isotope data). *Russ. Geol. Geophys.* **2018**, *59*, 945–961. [CrossRef]
108. Ripley, E.M.; Park, Y.-R.; Li, C.; Naldrett, A.J. Sulfur and oxygen isotopic evidence of country rock contamination in the Voisey's Bay Ni-Cu-Co deposit, Labrador, Canada. *Lithos* **1999**, *47*, 53–68. [CrossRef]

109. Ripley, E.M.; Wernette, B.W.; Ayre, A.; Li, C.; Smith, J.M.; Underwood, B.S.; Keyas, R.R. Multiple S isotope studies of the Stillwater complex and country rocks. *Geochim. Cosmochim. Acta* **2017**, *214*, 226–245. [CrossRef]
110. Rezeau, H.; Jagoutz, O.; Beaudry, P.; Izon, G.; Kelemen, P.; Ono, S. The role of immiscible sulfides for sulfur isotope fractionation in arc magmas: Insights from the Talkeetna island arc crustal section, south-central Alaska. *Chem. Geol.* **2023**, *619*, 121325. [CrossRef]
111. Scheel, J.E. Age and Origin of the Turnagain Alaskan-Type Intrusion and Associated Ni-Sulphide Mineralization, North-Central British Columbia, Canada. Master's Thesis, University of British Columbia, Vancouver, BC, Canada, 2007.
112. Pollock, T. Sulfur Isotope Composition of Sulfides in Mafic Cumulates, Lesser Antilles Arc. Master's Thesis, University of Maine, Orono, ME, USA, 2021.
113. Ueda, A.; Sakai, H. Sulfur isotope study of Quaternary volcanic rocks from the Japanese Island Arc. *Geochim. Cosmochim. Acta* **1984**, *48*, 1837–1848. [CrossRef]
114. Alt, J.C.; Shanks, W.C., III; Jackson, M.C. Cycling of sulfur in subduction zones: The geochemistry of sulfur in the Mariana island arc and back-arc trough. *Earth Planet. Sci. Lett.* **1993**, *119*, 477–494. [CrossRef]
115. De Hoog, J.C.M.; Taylor, B.E.; van Bergen, M.J. Sulfur isotope systematics of basaltic lavas from Indonesia: Implications for the sulfur cycle in subduction zones. *Earth Planet. Sci. Lett.* **2001**, *189*, 237–252. [CrossRef]
116. Labidi, J.; Cartigny, P.; Birck, J.L.; Assayag, N.; Bourrand, J.J. Determination of multiple sulfur isotopes in glass: A reapprasisal of the MORB δ^{34}S. *Chem. Geol.* **2012**, *334*, 189–198. [CrossRef]
117. De Moor, J.M.; Fisher, T.P.; Plank, T. Constraints on the sulfur subduction cycle in Central America from sulfur isotope compositions of volcanic gases. *Chem. Geol.* **2022**, *588*, 120627. [CrossRef]
118. Rielli, A.; Tomkins, A.G.; Nebel, O.; Raveggi, M.; Jeon, H.; Martin, L.; Àvila, J.N. Sulfur isotope and PGE systematics of metasomatized mantle wedge. *Earth Planet. Sci. Lett.* **2018**, *497*, 181–192. [CrossRef]
119. Arndt, N.T.; Czamanske, G.K.; Walker, R.J.; Chauvel, C.; Fedorenko, V.A. Geochemistry and origin of the intrusive hosts of the Norilsk-Talnakh Cu-Ni-PGE sulfide deposits. *Econ. Geol.* **2003**, *98*, 495–515.
120. Pang, K.-N.; Arndt, N.; Svensen, E.; Planke, S.; Polozov, A.; Polteau, S.; Iizuka, Y.; Chung, S.-L. A petrologic, geochemical and Sr-Md isotopic study on contact metamorphism and degassing of Devonian evaporates in the Norilsk aureoles, Siberia. *Contrib. Mineral. Petrol.* **2013**, *165*, 683–704. [CrossRef]
121. Muth, M.J.; Wallace, P.J. Sulfur recycling in subduction zones and the oxygen fugacity of mafic arc magmas. *Earth Planet. Sci. Lett.* **2022**, *599*, 117836. [CrossRef]
122. Milidragovic, D.; Nott, J.A.; Spence, D.W.; Schumann, D.; Scoates, J.S.; Nixon, G.T.; Stern, R.A. Sulfate recycling at subduction zones indicated by sulfur isotope systematics of Mesozoic ultramafic island arc cumulates in the North America Cordillera. *Earth Planet. Sci. Lett.* **2023**, *620*, 118337. [CrossRef]
123. Graybeal, F.T.; Vikre, P.G. A review of silver-rich mineral deposits and their metallogeny. In *The Challenge of Finding New Mineral Resources: Global Metallogeny, Innovative Exploration, and New Discoveries*; Goldfarb, R.J., Marsh, E.E., Monecke, T., Eds.; Society of Economic Geologists: Littleton, CO, USA, 2010; Volume 15, pp. 85–117. [CrossRef]
124. Arribas, A.; Mathur, R.; Megaw, P.; Arribas, I. The isotopic composition of silver in ore minerals. *Geochim. Geophys. Geosyst.* **2020**, *21*, e2020GC009097. [CrossRef]
125. Kozhemyako, N.; Kepezhinskas, P.; Berdnikov, N.; Krutikova, V. Fingerprints of S-Cl-rich fluids in Kamchatka lavas: Evidence from mineral microinclusions and ore metal geochemistry. In Proceedings of the Goldschmidt 2024 Conference Abstracts, Chicago, IL, USA, 18–23 August 2024. [CrossRef]
126. Dostal, J. Rare earth element deposits of alkaline igneous rocks. *Resources* **2017**, *6*, 34. [CrossRef]
127. Gao, L.-G.; Hu, R.-Z.; Chen, Y.-W.; Bi, X.-W.; Gao, J.-F.; Dong, S.-H.; Luo, J.-C. Formation of Huayangchuan (Central China) carbonatite-associated REE-Nb-U polymetallic deposit constrained from monazite mineral chemistry and isotope systematics: HREE enrichment in late-stage monazite. *Ore Geol. Rev.* **2023**, *157*, 105450. [CrossRef]
128. Benson, E.K.; Watts, K.E. Apatite and monazite geochemistry record magmatic and metasomatic processes in rare earth element mineralization at Mountain Pass, California. *Econ. Geol.* **2024**, *119*, 1611–1642. [CrossRef]
129. Beland, C.M.J.; Williams-Jones, A.E. The genesis of the Ashram REE deposit, Quebec: Insights from bulk-rock geochemistry, apatite-monazite-bastnäsite replacement reactions and mineral chemistry. *Chem. Geol.* **2021**, *578*, 120298. [CrossRef]
130. Yuan, X.; Yang, Z.; Mayanovic, R.A.; Hou, Z. Experimental evidence reveals the mobilization and mineralization processes of rare earth elements in carbonatites. *Sci. Adv.* **2024**, *10*, eadm9118. [CrossRef]
131. Wang, J.; Li, L.; Santosh, M.; Yan, G.-Y.; Shen, J.-F.; Yuan, M.-W.; Alam, M.; Li, R.-S. Multistage ore formation in the world's largest REE-Nb-Fe deposit of Bayan Obo, North China Craton: New insights and implications. *Ore Geol. Rev.* **2024**, *164*, 105817. [CrossRef]
132. Naldrett, A.J. *Magmatic Sulfide Deposits: Geology, Geochemistry, Exploration*; Springer: Berlin/Heidelberg, Germany, 2004; pp. 1–743.
133. Barnes, S.J.; Holwell, D.A.; Vaillant, M. Magmatic sulfide ore deposits. *Elements* **2017**, *13*, 89–95. [CrossRef]

134. Smith, J.W.; Holwell, D.A.; McDonald, I. Precious and base metal geochemistry and mineralogy of thee Grasvally norite-pyroxenite-anorthosite (GNPA) member, northern Bushveld Complex, South Africa: Implications for a multistage emplacement. *Miner. Depos.* **2014**, *49*, 667–692. [CrossRef]
135. Cabri, L.J.; LaFlammer, J.H.G. Rhodium, platinum, and gold alloys from the Stillwater Complex. *Can. Mineral.* **1974**, *12*, 399–403.
136. Gupta, A.R.; Boudreau, A.E. The role of hydrothermal processes and the formation of the J-M reef and associated rocks of olivine-bearing zone I of the Stillwater Complex, Montana. *Miner. Depos.* **2025**, *60*, 351–374. [CrossRef]
137. Sullivan, N.A.; Zajacz, Z.; Brenan, J.M.; Hinder, J.C.; Tsay, A.; Yin, Y. The solubility of gold and palladium in magmatic brines: Implications for PGE enrichment in mafic-ultramafic and porphyry environments. *Geochim. Cosmochim. Acta* **2022**, *316*, 230–252. [CrossRef]
138. Kesler, S.E. Ore-forming fluids. *Elements* **2005**, *1*, 13–18. [CrossRef]

Disclaimer/Publisher's Note: The statements, opinions and data contained in all publications are solely those of the individual author(s) and contributor(s) and not of MDPI and/or the editor(s). MDPI and/or the editor(s) disclaim responsibility for any injury to people or property resulting from any ideas, methods, instructions or products referred to in the content.

minerals

MDPI

Article

New Geochemical and Geochronological Constraints on the Genesis of the Imourkhssen Cu±Mo±Au±Ag Porphyry Deposit (Ouzellagh-Siroua Salient, Anti-Atlas, Morocco): Geodynamic and Metallogenic Implications

Mariam Ferraq [1,2,*], Saïd Belkacim [1,2], Li-Zhen Cheng [2], Joshua H. F. L. Davies [3], Morgann G. Perrot [3], Abdelhay Ben-Tami [1] and Mohammed Bouabdellah [4,5]

[1] Laboratory of Applied Geology and Geo-Environment (LAGAGE), Department of Earth Sciences, Faculty of Sciences, Ibn Zohr University, Agadir 80000, Morocco; s.belkacim@uiz.ac.ma (S.B.); abdelhaybentami@gmail.com (A.B.-T.)
[2] Mining and Environmental Research Institute, University of Quebec in Abitibi-Timiskaming, Rouyn-Noranda, QC J9X 5E4, Canada; lizhen.cheng@uqat.ca
[3] Department of Earth and Atmosphere Sciences, University of Quebec in Montreal, Montreal, QC H3C 3P8, Canada; davies.joshua@uqam.ca (J.H.F.L.D.); perrot.morgann@uqam.ca (M.G.P.)
[4] Department of Earth Sciences, Faculty of Sciences, Mohammed First University, Oujda 60000, Morocco; mbouabdellah2002@yahoo.fr
[5] Geology and Sustainable Mining Institute, Mohammed VI Polytechnic University, Benguerir 43150, Morocco
* Correspondence: mariam.ferraq@edu.uiz.ac.ma

Abstract: The Imourkhssen porphyry Cu±Mo±Au±Ag deposit is located at the Ouzellagh-Siroua Salient (OSS) straddling the boundary between the central Anti-Atlas and the central High Atlas. It is characterized by a typical porphyry-style mineralization. The volcanic rocks are intruded by numerous magmatic rocks of the Ouarzazate Group (580–539 Ma), referred to as the Late Ediacaran magmatic suites (LEMS). Of these, the Askaoun, Imourkhssen, and Imourgane granites are the most significant as they are related to the porphyry mineralization. The entire set is intruded by the Zaghar mafic dyke swarms. Zircon U-Pb dating of the Imourkhssen granite and the ore-bearing granite porphyry shows that these intrusive rocks were emplaced at 558 ± 1 and 550 ± 2 Ma, respectively. Moreover, the whole-rock major and trace element geochemistry reveal a high-K calc-alkaline I-type composition, consistent with an emplacement in a post-collisional setting under a trans-tensional tectonic regime. Ore bodies are hosted by the Askaoun granodiorite as well as the Imourgane granite. The mineralization occurs as fine-grained dissemination and infills of hydrothermally altered NNE–SSW to N–S trending veins and veinlets. Ore-related hydrothermal alteration consists of potassic, chlorite-sericite, serecitic, and propylitic mineral assemblages along with pervasive silicification and pyritization, providing a porphyry-style alteration pattern. The ore periods comprise supergene and magmatic-hydrothermal periods. The latter includes primary dissemination and secondary NNE–SSW to N–S ore-bearing system stages. The occurrence of molybdenite is either restricted to the potassic and chlorite-sericite alteration zones of the ore-bearing granite as fine disseminations or alternatively as veinlet infills within the propylitic halos. The molybdenite occurrences along with pyrite, chalcopyrite, galena, and tennantite dissemination are assigned to the primary ore stage, while the NNE–SSW to N–S ore-bearing system is related to the secondary ore stage. It consists of pyrite, chalcopyrite, bornite, covellite, diagenite, sphalerite, hematite, galena, gold, and chenguodaite. The predominance of cockade and crack-and-seal textures suggest multiple episodes of ore-forming fluid circulations under epithermal conditions. The supergene stage is achieved by subordinate malachite, azurite, barite, hematite, epsomite, and chrysocolla. From the descriptions above, we argue that the Imourkhssen Cu±Mo±Au±Ag mineralization shares many mineralogical and paragenetic attributes of porphyry-copper deposits.

Keywords: Ediacaran; Imourkhssen; porphyry-copper

1. Introduction

Porphyry deposits are a critical type of magmatic-hydrothermal ore deposit, known for their large tonnage and significant contribution to the production of copper, gold, and molybdenum, encouraging current research and exploration [1,2]. These deposit types are widely documented, but their origin and evolution are in many cases still poorly constrained due to: (i) the diversity of their geodynamic settings, (ii) the variability of the host rocks, and (iii) the zoning in both paragenetic succession and alteration assemblage [1,3]. Indeed, porphyry copper deposits are commonly associated with medium to high potassic calc-alkaline (shoshonitic) or alkaline I-type magnetite series [4]. This type of magmatism is frequently associated with subduction zones in continental arc settings [5], as well as with orogenic collapse zones linked to post-collisional events [6].

Porphyry copper deposits range in age from Archean to Holocene, although the most productive are Jurassic or younger [3]. A large number of these deposits occur along the peri-pacific belt (Figure 1), particularly in the Andean (Chili, Peru) and North American Cordillera (Colorado belt), where the three largest molybdenum porphyry deposits occur (e.g., Climax, Urad-Henderson, and Emmons Mounts [7]).

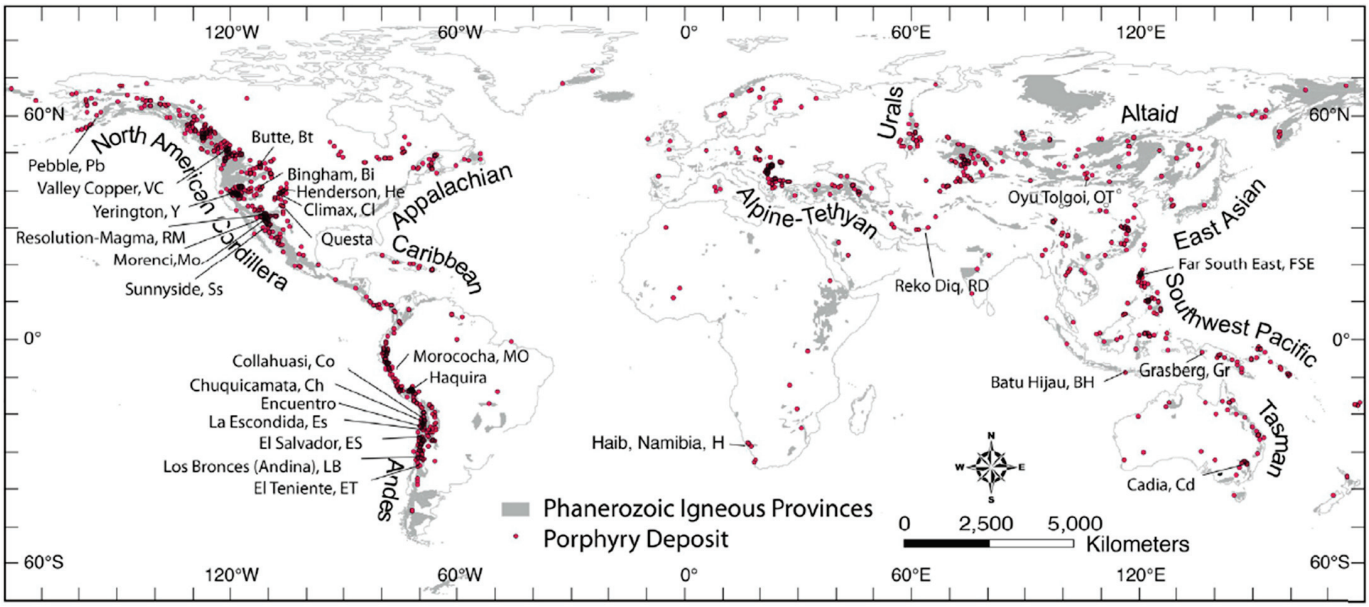


Figure 1. Global distribution of porphyry deposits (from [8]).

Porphyry ore deposits display a distinctive, broad-scale alteration-mineralization zoning pattern that includes from the core to the periphery, sodic-calcic, potassic, chlorite-sericite, serecitic, advanced argillic, and propylitic mineral assemblages [1,7]. Potassic alteration is usually the innermost alteration, which grades irregularly into propylitic alteration patterns [9]. The chlorite-sericite zone is considered as the early stage of the phyllic alteration overprinting the previous potassic mineral assemblage [9]. Phyllic (or serecitic) alteration is observed in the field as bleached outcrops [10]. It is a pyrite-dominated shell and also contains quartz and sericite minerals [1]. The extreme, distal, and shallowest part of the alteration zone is the propylitic alteration, which consists of chlorite, carbonate, epidote, adularia, and albite [1,11]. These widespread and distinctive hydrothermal zones provide a useful footprint for porphyry copper exploration [4].

In the Anti-Atlas belt of Morocco, many examples of deposits seem to exhibit some of the characteristics that are indicative of porphyry copper systems, such as Tiouit [12,13], the "Patte d'Oie" part of Bouskour [6,14], and Ismlal Au stockwork deposits [15]. Here,

we describe the geological features of the Imourkhssen deposit, which is thought to be the first example of a Neoproterozoic porphyry Cu±Mo±Au deposit in Morocco [16]. This study provides new geological, geochemical, geochronological, and ore features on the Imourkhssen Cu±Mo±Au±Ag porphyry deposit. The timing of the ore emplacement is discussed in the framework of a multi-pulse featuring Ouarzazate Silicic Large Igneous Province (SLIP) during the concluding stages of the Pan-African orogeny, within the context of an extensional regime along the northern metacratonic border of the West African craton (WAC).

2. Regional Geology

2.1. The Anti-Atlas

The Anti-Atlas Mountains of Morocco are a WSW–ENE oriented belt formed by the Precambrian basement unconformably overlain by slightly folded Paleozoic sedimentary formations (Figure 2B). The orogen records the effects of two main periods of tectono-magmatic activities linked to the Paleoproterozoic Eburnean (2.07–2.20 Ga) and Neoproterozoic Pan-African (885–539 Ma) orogenies [17,18].

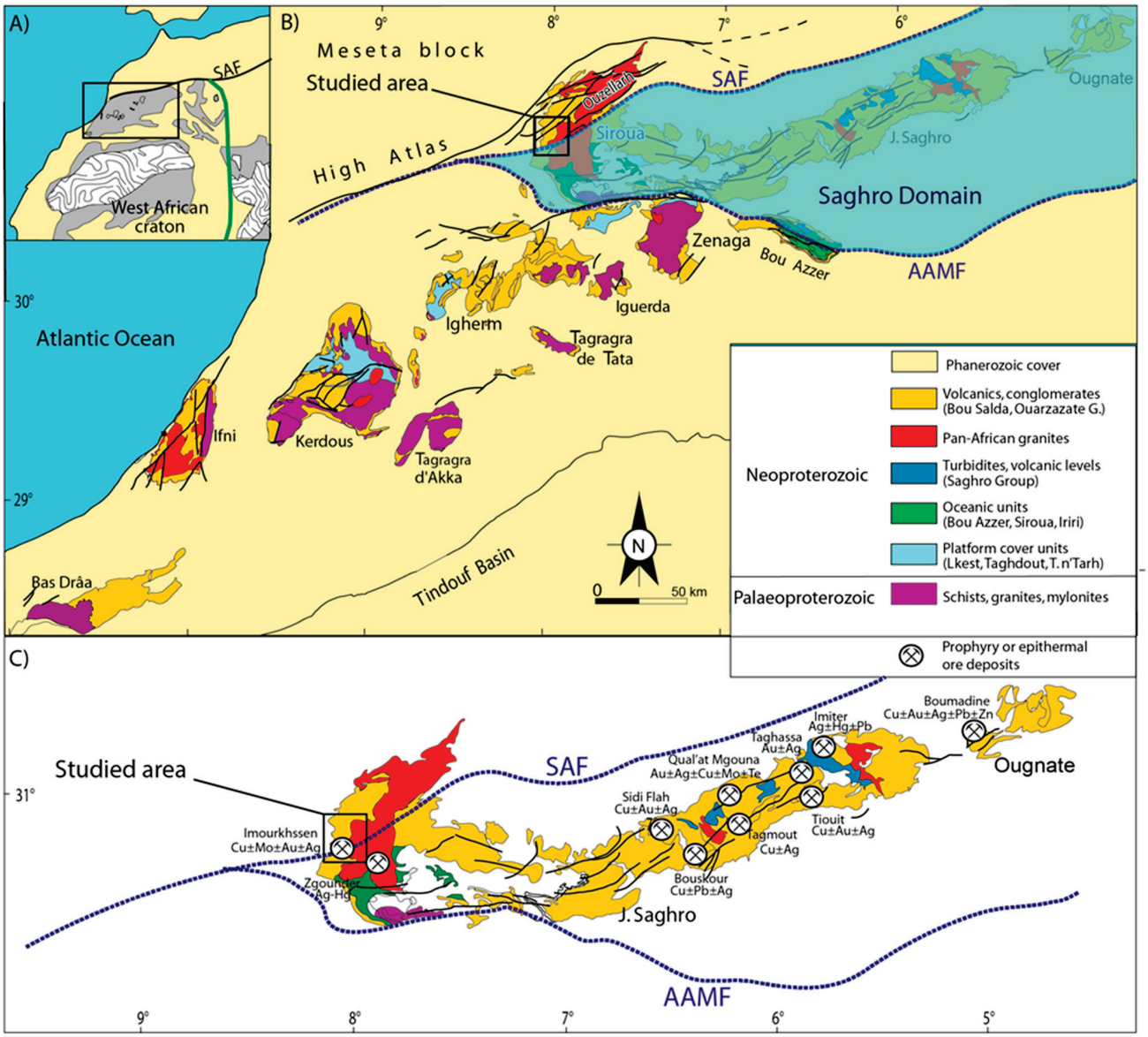


Figure 2. (**A**) Location of the Anti-Atlas domain and its relationship to the West African craton. (**B**) Location of the studied area modified after [19]. The geology of the studied area is detailed in Figure 3. (**C**) Simplified geological map of the Saghro domain showing the location of major porphyry and epithermal ore deposits [15]. Abbreviations: SAF: South Atlas fault, AAMF: Anti-Atlas major fault.

The Eburnean terranes form the crystalline basement into which some Neoproterozoic Pan-African successions were deposited and subsequently deformed in four stages, which likely correspond to a Wilson cycle: (1) Rifting and break-up (>800 Ma) of an unknown continent to which belonged the WAC coincident with rift-related magmatism activity [20]. (2) Formation of island arcs at 770–720 Ma [21]. (3) Ocean closure (720–630 Ma), highlighted by a polyphase accretion of oceanic rocks, as a diverse amphibolite to greenschist facies metamorphosed assemblage of ophiolitic complexes [22–25]. (4) Post-collisional period (630–539 Ma), which evolved from a transpressive to a transtensive tectonic setting, with the emplacement of huge high potassic calc-alkaline to shoshonitic volcano-plutonic rocks, accompanied by sedimentary successions deposited into pull-apart basins [17,26,27]. This final stage consists of the deposition of:

(i) The Saghro Group (620–600 Ma), which consists of volcanic and volcano-sedimentary rocks of andesite-basaltic and andesitic to trachytic compositions, with rare sedimentary intercalations [19,25].
(ii) The Bou Salda Group successions (600–580 Ma), which are characterized by poorly sorted sediments and abundant high-K calc-alkaline volcanic and intrusive rocks [20,28].
(iii) The Ouarzazate Group (580–539 Ma), which is composed mainly of high potassic calc-alkaline volcanic, volcanoclastic and plutonic rocks [27,29,30]. This Late Neoproterozoic magmatism is also widespread in the High Atlas and Meseta [18,30].

In the Anti-Atlas, Late Ediacaran magmatic activity coupled with strong extensional trans-tensional tectonic structures are invoked to explain the pervasive hydrothermal activity at the origin of the genesis of some of the world-class precious metal, base metal, and SEDEX-type deposits that have been documented through the central and eastern parts of the Anti-Atlas [15,27,28] and have recently been defined as the Saghro domain (Figure 2B,C) [30].

2.2. Deposit-Scale Geology

The Cu±Mo±Au±Ag Imourkhssen deposit is hosted by granitic intrusions (Figure 3) stratigraphically assigned to the Ouarzazate (580–539 Ma) Group and belongs to the Ouzellagh-Siroua Salient (OSS) [31]. These intrusions intrude the rocks of the Saghro Group (630–610 Ma; [26]) and comprise a wide spectrum of igneous rocks spanning from volcanic to plutonic bodies. These rocks belong to the Late Ediacaran magmatic suites (LEMS), comprising the Assarag, Amassine, and Ougougane suites.

In the Imourkhssen area, the Assarag suite includes the large Askaoun batholith, which consists of the Askaoun granodiorite and quartz diorite. This batholith covers 800 km^2 in the NW part of the OSS [21]. The Amassine suite is represented by the star-shaped Imourkhssen granite. This suite was previously interpreted to encompass an ore-bearing granite porphyry. In this study, the latter lithotype is referred to as "the Imourgane granite" since it is actually related the Ougougane suite (see geochronology section). This porphyritic intrusion consists of a succession of rhyolite, microgranite, and granite, all of which are crosscut by the Zaghar mafic dyke swarms (Figure 4).

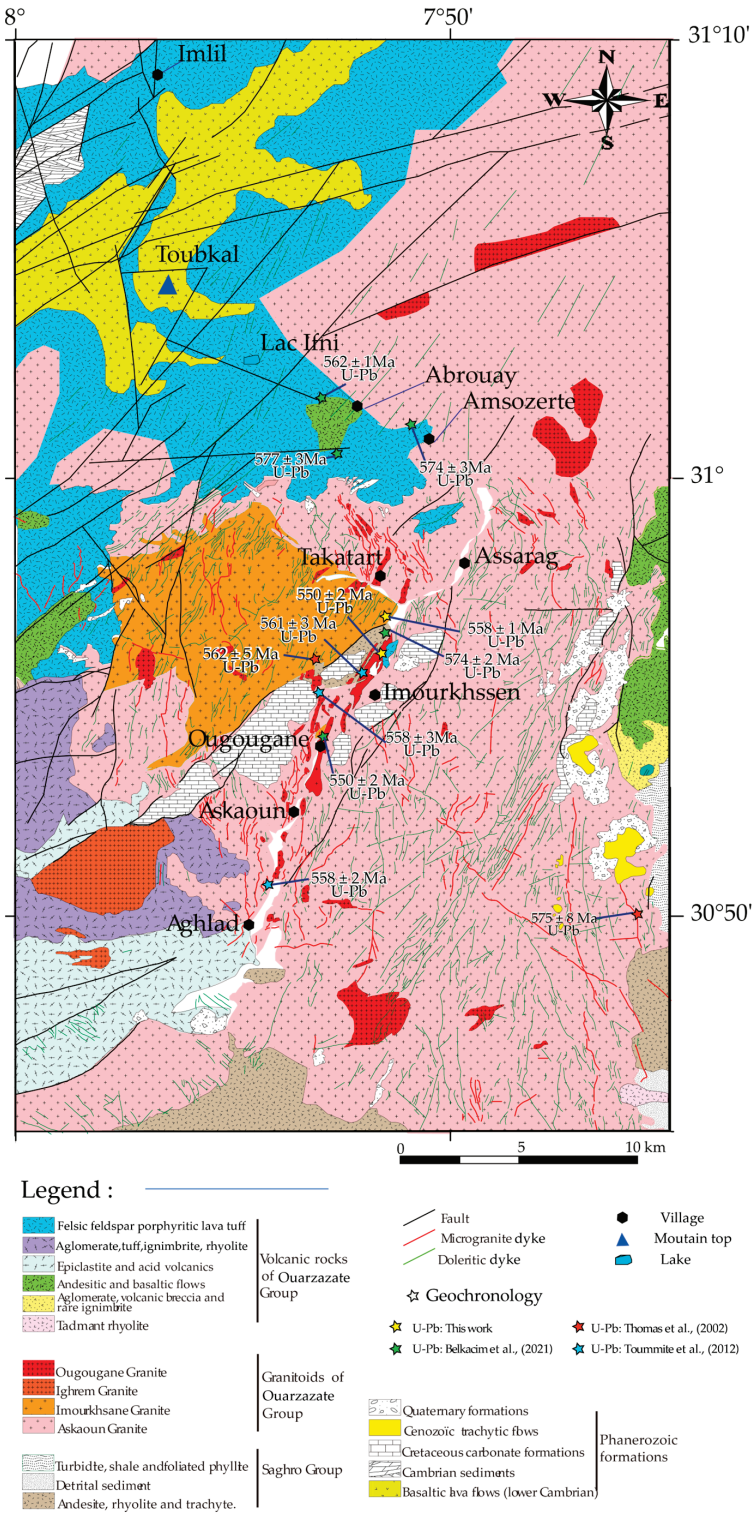


Figure 3. Geological map of the studied area. Modified from [21,29,32].

The emplacement of the LEMS is related to the development of many base and precious metal deposits in the OSS, including the Ag-Hg Zgounder ore deposit [33] and the Cu-Co-Mo Inki mineralization [21]. Nonetheless, the Imourkhssen deposit has been identified as a Cu±Mo±Au porphyry mineralization associated with Imourkhssen and Askaoun granitoids [16].

This study focuses on the ore feature of the Cu±Mo±Au±Ag Imourkhssen ore deposit and discusses the emplacement of the LEMS in the framework of a long-lived Ouarzazate Silicic large igneous province (see discussion section).



Figure 4. The Zaghar dykes crosscut the Ougougane granite.

3. Sampling and Analytical Methods

Sampling was carried out on both fresh and altered rocks from the Imourkhssen area, including the abandoned Talat nl'bour galleries. More than seventy samples were collected. The representative samples were selected for petrographic, mineralogical, geochemical, and geochronological studies (Appendix A, Table A1).

Polished thin sections representing different alteration assemblages and mineralized veins were examined using plane-polarized and reflected-light microscopy. For phase identification, and for the local quantitative mineralogical and elementary compositions, more than nine thin sections were analyzed at the research center of the Faculty of Sciences of Agadir, Ibn Zohr University using a JEOL JSM IT-100 scanning electron microscope. The resolution was at most 100 nm, where both backscattered electron and energy-dispersive spectroscopy were used.

Six samples were also analyzed for mineral composition using a D8 ADVANCE Twin X-ray diffractometer (XRD). The diffractometer has a two-theta geometry with a copper sealed tube x-ray source, producing Cu Kα1 radiation at a wavelength of 1.5406 Å. The x-rays are issued from a generator operating at 40 kV and 25 mA and its operating energy is 100 W. XRD data were collected from 5 to 100° ± 0.05 θ. The diffraction patterns obtained were used for mineral identification and semi-quantitative assessment of mineral content, indexed using X'Pert HighScore Plus v. 3. software.

For whole-rock geochemistry, the major and trace elements of seventeen samples were analyzed by ICP–OES/ICP–MS (fusion of inductively-coupled plasma–optical emission spectrometry and inductively-coupled plasma–mass spectrometry) methods at Actlabs laboratory, Canada (Appendix A, Table A2).

Moreover, two powdered molybdenite samples from Imourgane granite were analyzed at the Robert M. MacKay electron microprobe laboratory, located in the Department of Earth Sciences, Dalhousie University, Halifax. The analyses were carried out with a JXA-8200 electron microprobe, using the internal standards for quality control (Appendix A, Table A3).

For geochronological purposes, two granite samples were dated by LA–ICP–MS U-Pb on zircon at the Geotop Research Center, University of Quebec in Montreal (UQAM). Each sample was crushed and sieved to obtain a uniform grain size fraction of 50–250 μm. The

resulting fraction was then introduced over a Wilfley table to separate the smaller and denser minerals. The fine dense fraction was collected and then processed with heavy liquids (methylene diodide) and a Franz isodynamic separator using a current up to 1 ampere to concentrate zircon grains.

Hundreds of clear, well-formed zircon grains were hand-picked from each sample under a binocular microscope, avoiding inclusions and fractures. Selected grains were then mannealed in a muffle furnace at 1000 degrees for 48 hours before being mounted in epoxy resin on a standard 1-inch round mount, polished, and imaged on a Hitachi S-3400 Variable Pressure SEM at an accelerating voltage of 20 kV using a Centaurus Cathodoluminescence (CL) detector to outline the growth zoning, rims, and inherited cores within individual grains and guide the spot selection for in situ laser ablation analysis. The U-Pb analysis was performed using a Nu Atom single collector mass spectrometer coupled with a photon machine G2 193 nm excimer laser, following a modified procedure reported in [34], adding 3 ml/min N2 before the torch to reduce oxide formation in the plasma. The sensitivity of the mass spectrometer was optimized using U from a NIST610 glass, and the gas flow was adjusted by to ensure a U/Th of 1 and Th/ThO of 1×10^{-3} for the NIST glass. We used a laser energy of 4.54 J/cm^2, a repetition rate of 6 Hz, and a 30 μm ablation spot. Measurements were conducted using a sample reference material bracketing approach, with sets of 15 unknown samples bracketed by two primary reference samples and at least one secondary reference grain analysis for quality control purposes.

The 91500 (1065 Ma, [35]) and Plešovice [36] were used respectively as primary and secondary reference materials. The two samples were analyzed over one analytical session. The individual analyses were processed and corrected for down-hole fractionation using Iolite v4 software with the U-Pb geochronology data reduction scheme (DRS) [35]. Analyses with detectable ^{204}Pb were excluded prior to data reduction, and no general Pb correction was applied. The repeated analyses of Plešovice produced a weighted mean ^{206}Pb/^{238}U age of 337 ± 1 Ma, in agreement within error with its known age ([36]; see Appendix A, Tables A4 and A5). After processing the raw data and generating U-Pb ratios, Isoplot R 1.0 [37] was used to generate U-Pb ages, draw concordia diagrams, and calculate the discordance distance and ^{206}Pb/^{238}U weighted mean ages. All error bars and reported errors in the text are at the 2σ level.

4. Results

4.1. Petrography of the Host Rocks

The host rocks comprise the Late Ediacaran magmatic suites (LEMS) of the Ouarzazate Group (580–539 Ma), which intrude the volcanic and volcanoclastic rocks of the Saghro Group (620–600 Ma) [16,29,38]. Considering their absolute ages, the LEMS in the Tifnoute Valley area comprise the Assarag, Amassine, and Ougougane suites.

4.1.1. The Assarag Magmatic Suite

The Assarag magmatic suite is represented by the Askaoun quartz diorite and amphibole-biotite granodiorite. The granodiorite is pink-colored and medium-grained rock. The primary mineral paragenesis consists of various proportions of euhedral plagioclase, quartz, and K-feldspar locally developing mermekitic and graphic textures, while biotite and amphibole occur as anhedral megacrysts (Figure 5A). Accessory minerals consist of apatite, zircon, titanite, and magnetite. Secondary minerals consist of sericite, chlorite, epidote, and kaolinite. The quartz diorite is dark grey-colored, medium to coarse-grained, and heavily altered, and its mineral paragenesis consists of mm-sized sericitized plagioclase, epidotized amphibole, chloritized biotite, and abundant quartz and opaque minerals.

4.1.2. The Amassine Magmatic Suite

This suite is represented by the large Imourkhssen granite that occurs as a star-shaped barren batholith intruded into the granodiorite of the Assarag suite. Macroscopically, the Imourkhssen granite is pinkish and coarse-grained rock. The primary mineral paragenesis

comprises perthitic K-feldspar (≃30%), albite-oligoclase (≃30%), along with quartz (≃35%) and chloritized biotite (<5%) (Figure 5B). Accessory minerals contain magnetite, apatite, and zircon, while the secondary mineral assemblage consists of sericite, chlorite, and kaolinite.

4.1.3. The Ougougane Magmatic Suite

This suite consists of a series of rhyolitic, microgranitic, and granitic intrusions cutting across both the Amassine and Assarag suites. The rhyolite exhibits pyromerides in the form of radiant fibers of orthoclase surrounding a quartz nucleus and displaying a distinguishable hyaline spherulitic texture. Accessory minerals consist of zircon, rare apatite, and Fe-oxides, while sericite and chlorite are the secondary minerals.

The microgranite occurs as pink-colored and fine-grained dykes. Its mineralogy consists of a significant proportion of interstitial quartz, perthitic K-feldspar, and albite-oligoclase displaying locally a well-developed mermekitic texture. Biotite and opaque minerals are observed as accessory minerals within the microgranite.

The granite of the Ougougane suite, including the nearby Imourgane intrusion, occurs as a pinkish and coarse-grained to porphyritic granite (Figure 5C). The mineral paragenesis consists of quartz and K-feldspar displaying a graphic texture. The feldspars are commonly hydrothermally altered to sericite and/or kaolinite. Muscovite is rarely observed, whereas biotite is ubiquitous. The latter is commonly altered to chlorite and exhibits numerous inclusions of apatite, zircon, and opaque minerals.

4.1.4. The Zaghar Mafic Dykes

The Zaghar mafic dykes consist of a swarm of doleritic dykes (2 to 15 m thick) that intrude the LEMS. These dykes are fine to medium-grained, olive green in color, and have intersertal ophitic textures. The primary mineralogy of some dykes consists of plagioclase laths, while the Fe-Mg minerals are often transformed to chlorite and epidote. Nevertheless, some dykes contain many phenocrysts of clinopyroxene exhibiting the glomeroporphyritic texture (Figure 5D).

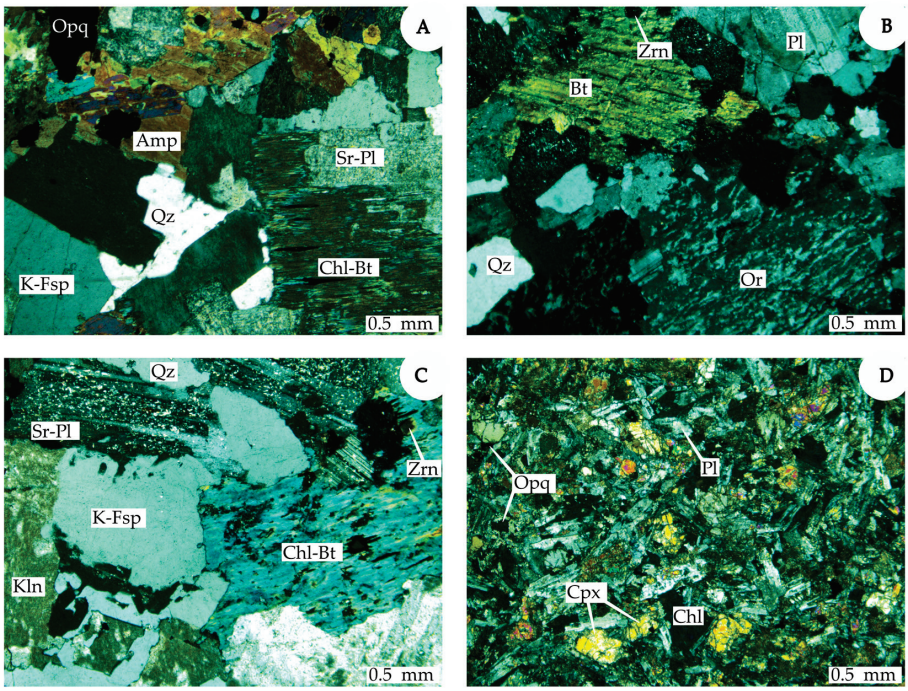


Figure 5. Selected photomicrographs of the LEMS at XPL (cross-polarized light) with the Askaoun granodiorite in (**A**), the Imourkhssen granite in (**B**), the Imourgane granite in (**C**) and the Zaghar mafic dyke in (**D**). Mineral abbreviations: Opq: opaque, Amp: amphibole, Qz: quartz, Chl: chlorite, Bt: biotite, Kln: kaolinite, K-Fsp: K-feldspar, Or: orthoclase, Cpx: clinopyroxene, Sr: sericite, Pl: plagioclase, Zrn: zircon.

Locally, the Zaghar dyke swarm shows co-mingling magmatic textures at contact with the Askaoun granodiorite of the Assarag suite (Figure 6), suggesting their simultaneous emplacement. Similar textures have also been documented in the Zaghar mafic dyke swarms located in Douar Eç-çour, north of the studied area [39]. Geochronological dates have not been reported in the Imourkhssen area. However, a zircon/apatite/rutile U-Pb age of 554 ± 6 Ma was documented from a dolerite dyke in the Douar Eç-çour [39].

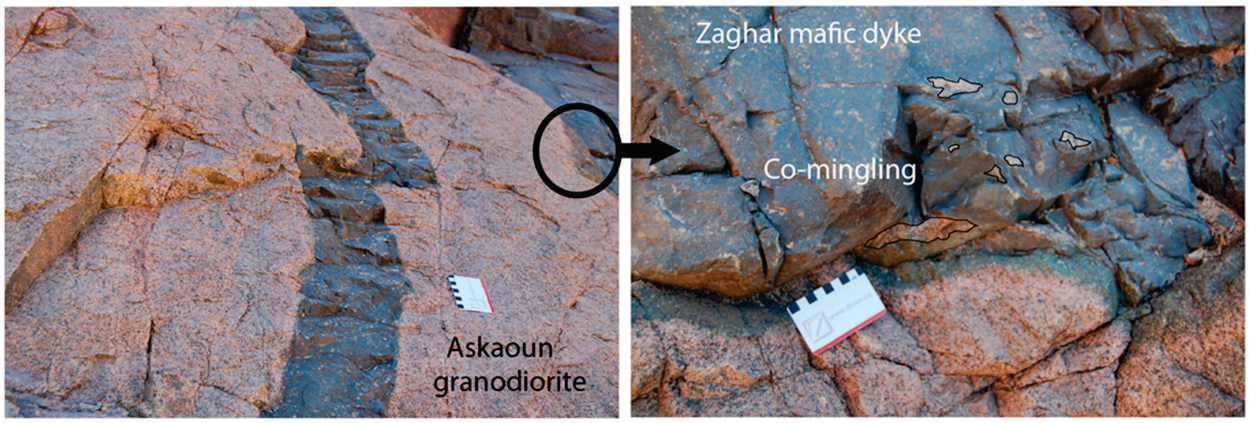


Figure 6. Co-mingling textures between the Askaoun granodiorite and Zaghar mafic dyke in Talat nl'bour area. The transition between the two magmatic bodies is progressive and outlined by the incorporated granodioritic fragments within the mafic dyke.

4.2. Whole-Rock Geochemistry

Seventeen representative samples of the LEMS were analyzed for major and trace elements, as shown in Appendix A, Table A2.

The rocks of the Ougougane suite, including the Imourgane granite, exhibit high SiO_2 content (72.39–77.02 wt%) and medium total alkali content (K_2O+Na_2O) within the range of 8.27 wt%. They fall into the granite field on the total alkalis versus SiO_2 diagram (Figure 7A). The A/CNK values [Al_2O_3/(CaO+Na_2O+K_2O)] of these samples are from 1.34 to 1.67, whereas the A/NK values [Al_2O_3/(Na_2O+K_2O)] range from 1.38 to 1.72, indicating a peraluminous composition (Figure 7B).

The spidergrams (Figure 7E) of these rocks are generally parallel and typical to calc-alkali series with enrichments in LILEs (large ion lithophile elements, K to Th), in addition to large Sr, Ba, P, and Ti negative anomalies. These anomalies can be explained by feldspar (Sr and Ba) and accessory mineral fractionation and accumulation in the source as apatite (P) and titanite (Ti), whilst the Nb anomaly is likely to be characteristic of the melt source (See discussion section). Their chondrite-normalized REE (rare earth element) patterns (Figure 7F) also show calc-alkali trends alongside a slight Pr negative anomaly in many samples. The rocks display a fractionated LREE and flat HREE patterns in addition to a notable Eu anomaly.

The Askaoun batholiths of the Assarag suite are distinctive due to their high Fe_2O_3(T) contents, oscillating between 7.76 and 9.01 wt% and between 4.1 and 5.57 wt% for the quartz diorite and the granodiorite, respectively. The silica contents vary from 57.4 to 66.54 wt%. The A/CNK ratios of 1.37–2.90 indicate a peraluminous characteristic (Figure 7B). Their spidergrams and REE patterns are close to those of the Ougougane suite, with less pronounced Sr, Ba, P, Nb, Ti, and Eu negative anomalies.

Though their Nb-Ta arc signature, the LEMS samples straddle the post-orogenic field in the Rb versus (Y+Nb) tectonic discrimination diagram (Figure 7D). Their Harker diagrams show negative correlations between SiO_2 and MgO, FeO, CaO, TiO_2, Sr, and V, and positive correlations with K_2O, Rb, and Th (Figure 8). Such compositional variations of the rocks could be produced by different amounts of crystal fractionation [40].

The LEMS of the Tifnoute Valley area plot in the high potassic calc-alkaline series in the K_2O versus SiO_2 diagram (Figure 7C), as already mentionned in [29]. They exhibit a peraluminous composition and lack Al-rich minerals (e.g., muscovite, cordierite, and garnet). This geochemical feature is consistent with an I-type affinity [29], which is portrayed as well by the Nd and Sr isotope values (εNd − 560 Ma + 0.8 and + 3.5 with ($^{87}Sr/^{86}Sr$)i between 0.7034 and 0.7065 [29]) (Figure 9B), pointing to a mainly juvenile source (mantle or young lower crust) [29].

The negative correlation between SiO_2 and P_2O_5 (Figure 9A) also suggests an I-type granite trend [41] for the LEMS. Those authors suggest that this I-type granite evolution implies the potential origin of the magma through the partial melting of metaigneous rocks.

The entire geochemical characteristics of the LEMS is typical of post-collisional magmas [42]. Those magmas have been emplaced in the framework of the Late Ediacaran collapse of the Pan-African orogen [21,28].

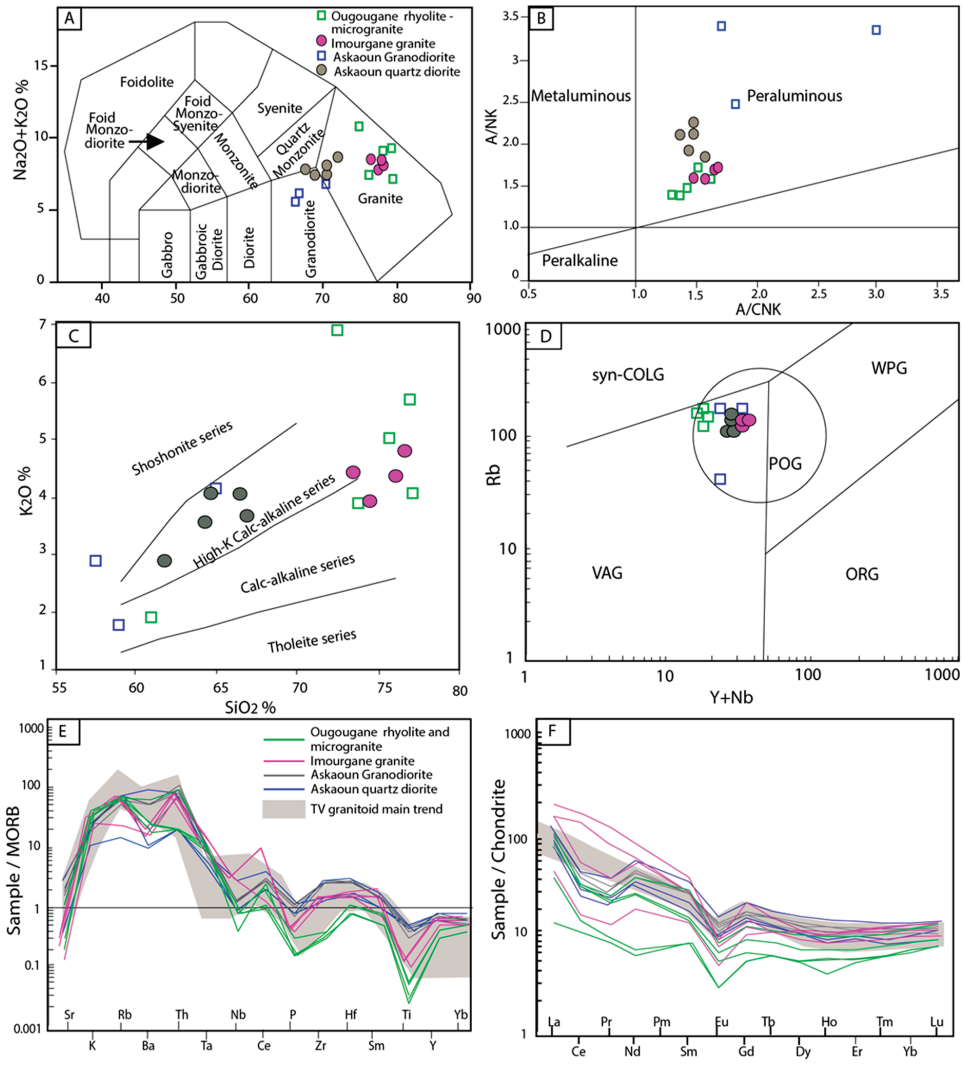


Figure 7. Whole-rock geochemistry of the Late Ediacaran granites of the TV area. (**A**) Total alkali ($Na_2O + K_2O$) (wt%) versus SiO_2 (wt%) diagram after [43]. (**B**) A/NK versus A/CNK diagram of [44]. (**C**) SiO_2 vs. K_2O diagram after [45]. (**D**) Tectonic discrimination Rb vs. Y+Nb diagram after [46,47]. Abbreviations: syn-COLG: syn-collisional granite, WPG: within plate granite, POG: post-collisional granite, VAG: volcanic arc granite, ORG: oceanic ridge granite. (**E**,**F**) Primitive mantle-normalized trace-element spidergram and chondrite-normalized REE distribution diagrams of TV magmatic rocks compared to previous trends in [29], shown as grey trends. The MORB values are from [48], and the chondrite values are from [45].

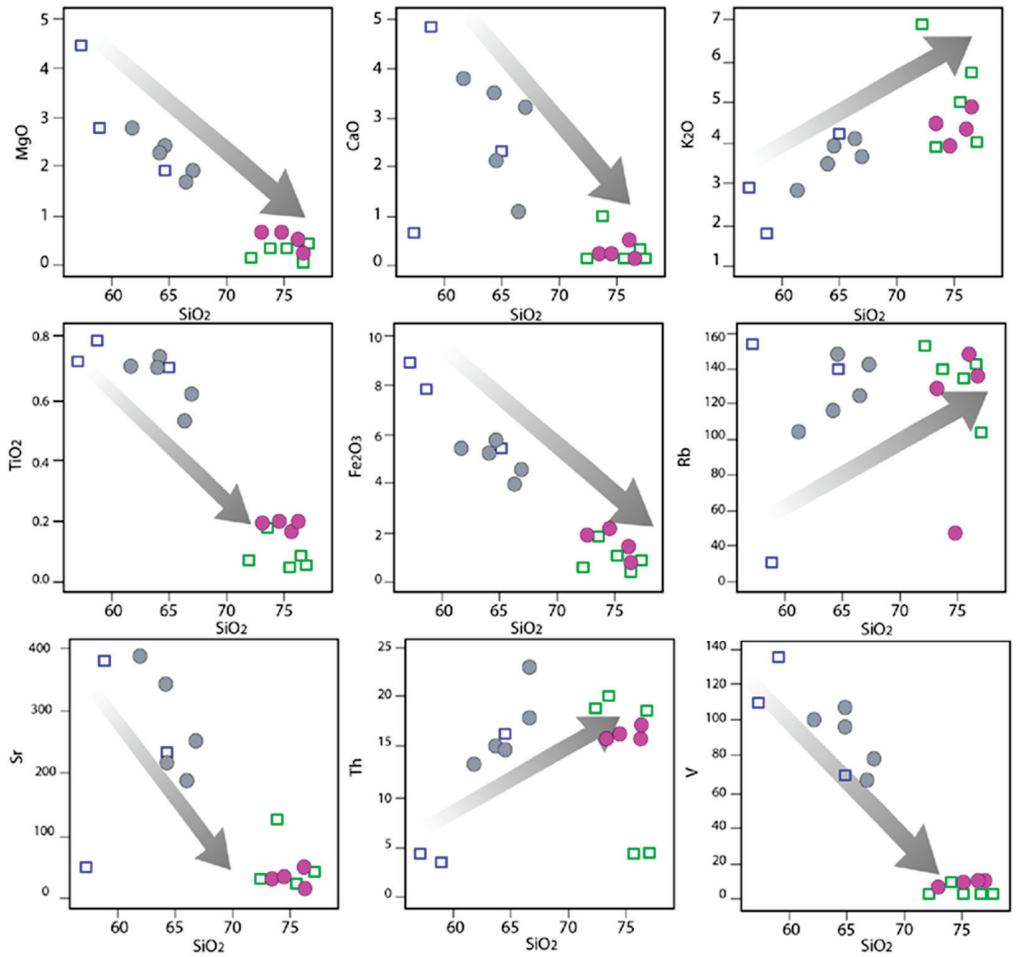


Figure 8. Harker diagrams of selected major oxide and trace elements content of the Late Ediacaran granites of the TV area. The proximal evolutionary trends are highlighted by the grey arrows.

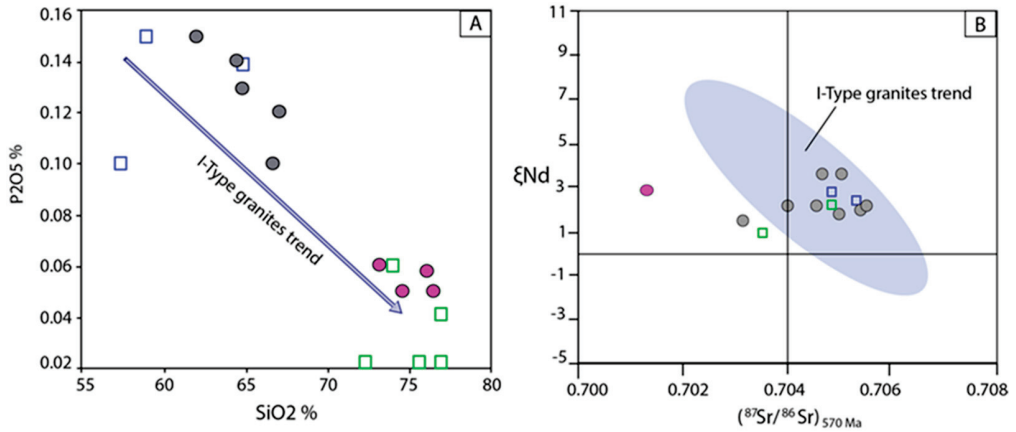


Figure 9. (**A**) P_2O_5 vs. SiO_2 classification diagram after [49]. Data for geochemical trend are from this study. (**B**) Sr and Nd isotopic initial ratios (εNd vs. ($^{87}Sr/^{86}Sr$)i at 570 Ma for the TV magmatic rocks from [29], I-type granite values from [50].

4.3. X-ray Data

XRD analyses were carried out for the identification of various primary and secondary mineral assemblages in several samples, especially those related to alteration zones (Figure 10). Indeed, the serecitic mineral assemblages (i.e., 22im05) is composed mainly of quartz and sericitized feldspars. The Imourgane granite (i.e., 22im02) is composed

of quartz, feldspar, biotite, and muscovite. Furthermore, X-ray primary investigations delineate the quartz-chlorite-sulfide assemblages (i.e., 22im17 and 22im13C), which form the ore-bearing structures (see mineralization section). The pervasive silica enrichment within the Imourgane granite is also outlined (i.e., 22im20). It impacts the outcrops near the galleries, where epsomite ($MgSO_4 \cdot 7H_2O$) encrustations can be found (i.e., T1). This mineral was recently discovered to be useful for geochemical classification [51].

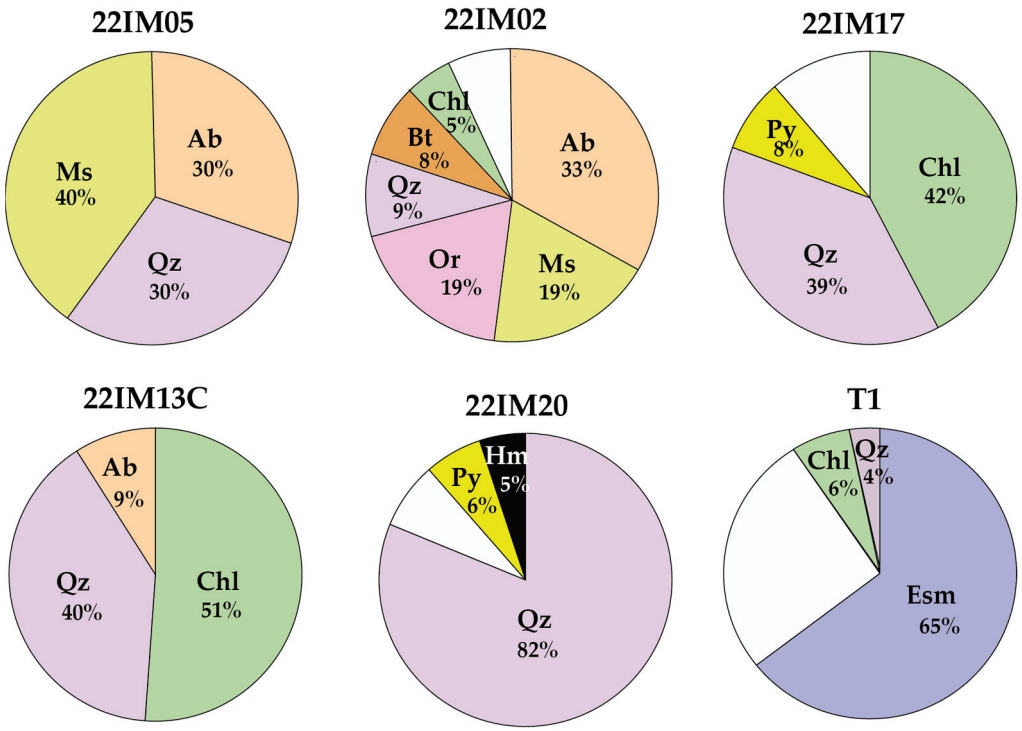


Figure 10. Mineralogy of the Imourkhssen deposit determined after XRD analysis. Abbreviations: Qz: quartz, Ab: albite, Chl: chlorite, Pl: plagioclase, Ms: muscovite, Or: orthoclase, Py: pyrite, Hm: hematite, Bt: biotite, Esm: epsomite. Mineral abbreviations from [52,53].

4.4. Hydrothermal Alteration and Veining System

4.4.1. Hydrothermal Alteration

Field observations and petrographic examination allowed us to identify several hydrothermal alteration assemblages, including (i) potassic, (ii) chlorite-sericite, (iii) serecitic, and (iv) propylitic alteration.

(i) The potassic alteration affects the Imourgane granite and exhibits disseminated molybdenite and molybdenite veinlets (Figure 11A). This alteration is highlighted by the characteristic brick red color of secondary K-feldspars, locally crossed by stockworks of chlorite. The altered feldspar to clay minerals (kaolinite), along with quartz, chlorite, and altered biotite, make up the potassic alteration mineral assemblage.

(ii) The chlorite-sericite alteration surrounds the potassic alteration zone. It occurs as grey dark halos surrounding disseminated molybdenite (Figure 11B). This alteration consists of chloritized biotite crystals along with quartz and sericitized plagioclase.

(iii) The serecitic or phyllic alteration overprints a large area of the Imourgane granite, as evidenced by the large, bleached zones (Figure 11C) extending over tens of square meters. It consists of quartz and sericite along with pervasive pyritization and silicification.

(iv) The propylitic alteration consists of chlorite alteration halos along with epidote and local calcite (Figure 11D).

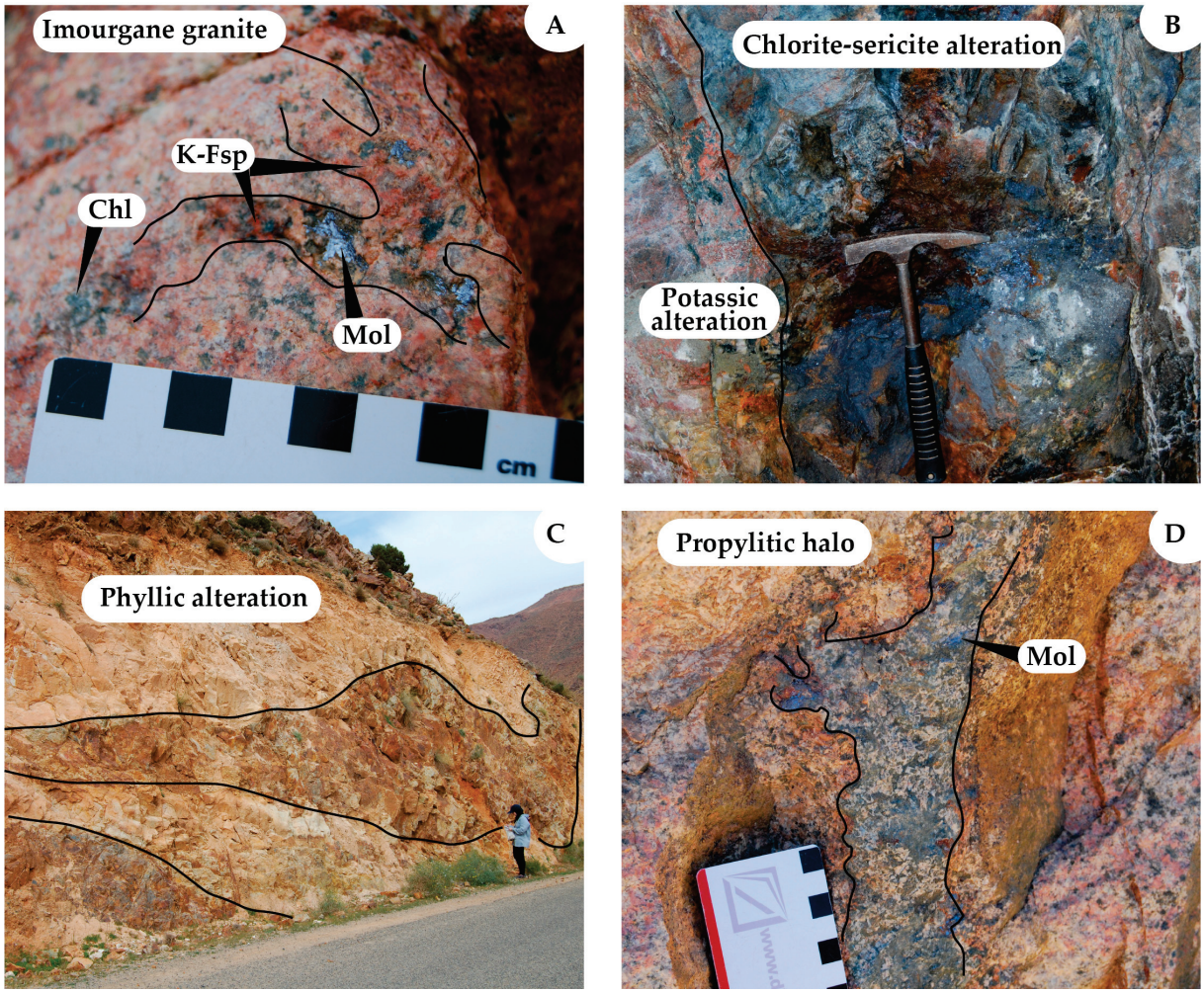


Figure 11. Photomicrographs of the hydrothermal alteration mineral assemblages with associated samples. (**A**) Potassic alteration highlighted by brick red-colored K-feldspar and molybdenite (Mol) dissemination within the Imourgane granite. (**B**) Chlorite-sericite alteration with molybdenite dissemination. (**C**) Phyllic or sericitic alteration highlighted by bleached outcrops. (**D**) Propylitic halo within the Imourgane granite along with molybdenite dissemination. Mineral abbreviations: K-Fsp: K-feldspar, Chl: chlorite, Mol: molybdenite.

4.4.2. Veining System

The predominant strike orientation of veins and their controlling faults are of NNE–SSW to N–S directions. In the studied area, several vein types are recognized and can be categorized into four types: (i) Aplitic mega lenses, (ii) stockwork-type quartz veins, (iii) quartz-hematite-barite veins, and (iv) quartz-chlorite-sulfide lenses.

(i) The aplitic mega lenses occur as N–S oriented structures within the Imourgane granite (Figure 12A). These structures consist mainly of quartz, sericitized k-feldspars, and plagioclase with minor disseminated pyrite. The aplitic lenses extend for several meters, especially in the sericitized areas.

(ii) Stockwork-type quartz veins are shown in Figure 12B and are characterized by anastomosing quartz networks affecting the Imourgane granite. These veins occur more frequently within the altered potassic and serecitic bleached zones.

(iii) Quartz-hematite veins manifest as decimetric veins (Figure 12C) that evolve to barite-hematite veins exclusively in the Imourgane granite (Figure 12D). The evolution from quartz-hematite to baryte-hematite assemblages could be the result of quartz transformation to baryte during cooling of the hydrothermal solutions, if the fluid's composition and the

physical conditions (T, P) allow it (see [54]). The barite-hematite vein zonation is observed on the small scale, creating a centimetric-sized cockade texture. Thus, an active pulsating process during ore deposition is suspected [55].

(iv) Quartz-chlorite-sulfide lenses occur as NNE–SSW to N–S trending ore-related structures (Figure 12E,F), which affect mainly the Askaoun granodiorite and the Imourgane granite. These structures exhibit crack-and-seal and cockade textures (Figure 13A) along with hydrothermal breccia (Figure 13B), highlighting multiple episodes of fluid circulation [6].

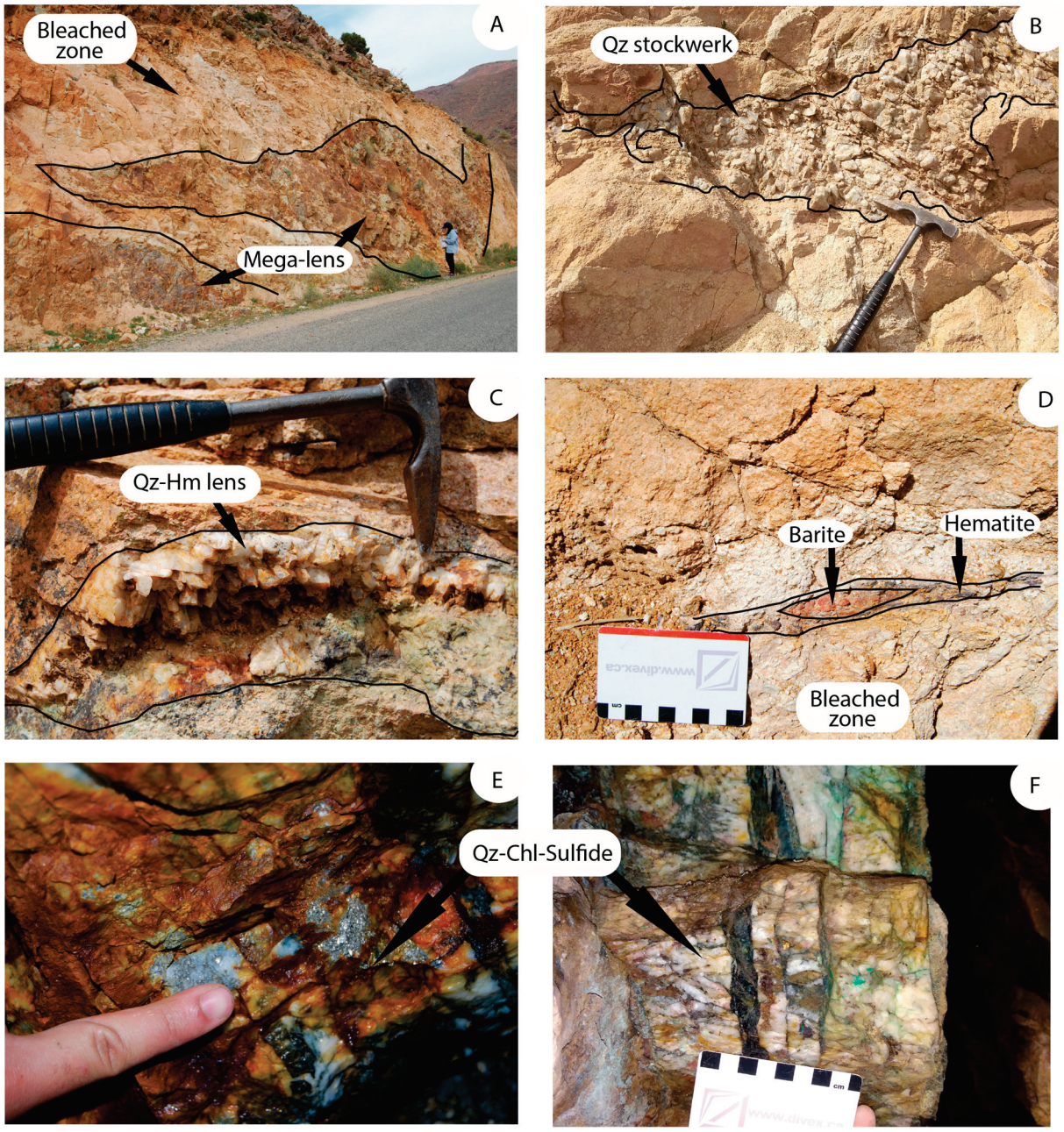


Figure 12. The different hydrothermal vein types observed in the studied area: (**A**) Aplite mega-lens surrounded by the bleached zone. (**B**) Quartz stockworks. (**C**) Quartz-hematite lens. (**D**) Barite-hematite lens out crops in phyllic alteration zone. (**E**,**F**) Quartz-chlorite sulfide lenses.

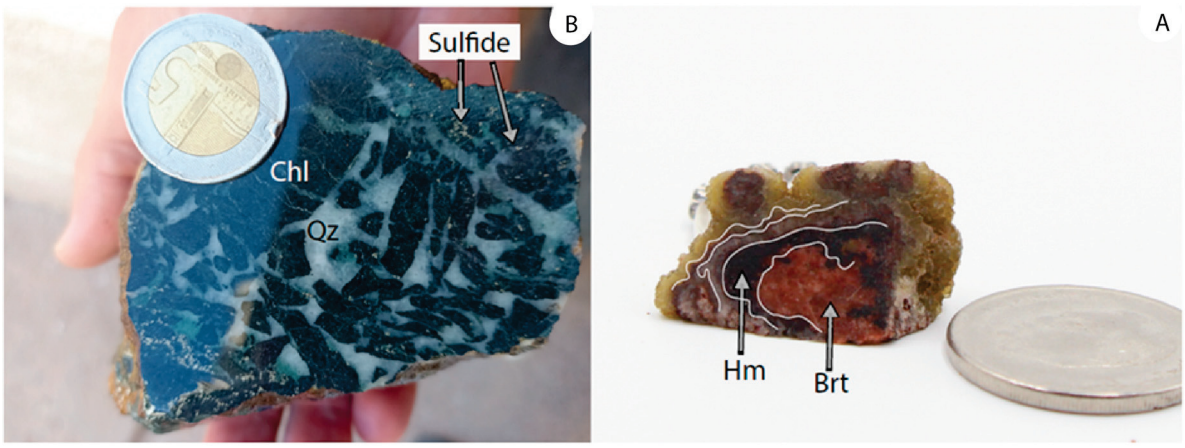


Figure 13. (**A**) Cockade texture in a centimetric barite-hematite vein observed within the Imourgane granitic intrusion. (**B**) Hydrothermal breccia affecting the quartz-chlorite-sulfide lens in a gallery of the Talat nl'bour area. Mineral abbreviations: Chl: chlorite, Qz: quartz, Hm: hematite, Brt: barite.

4.5. The Imourkhssen Porphyry-Style Mineralization

The ore genesis of the Imourkhssen Cu±Mo±Au±Ag deposit can be divided into supergene and magmatic-hydrothermal periods, comprising primary dissemination and secondary NNE–SSW to N–S ore-bearing system stages (Figure 14). The molybdenite occurrences and Fe-Cu disseminated sulfides belong to the primary ore stage, while the NNE–SSW to N–S quartz-chlorite-sulfide-bearing system is assigned to the secondary ore stage (Figure 15).

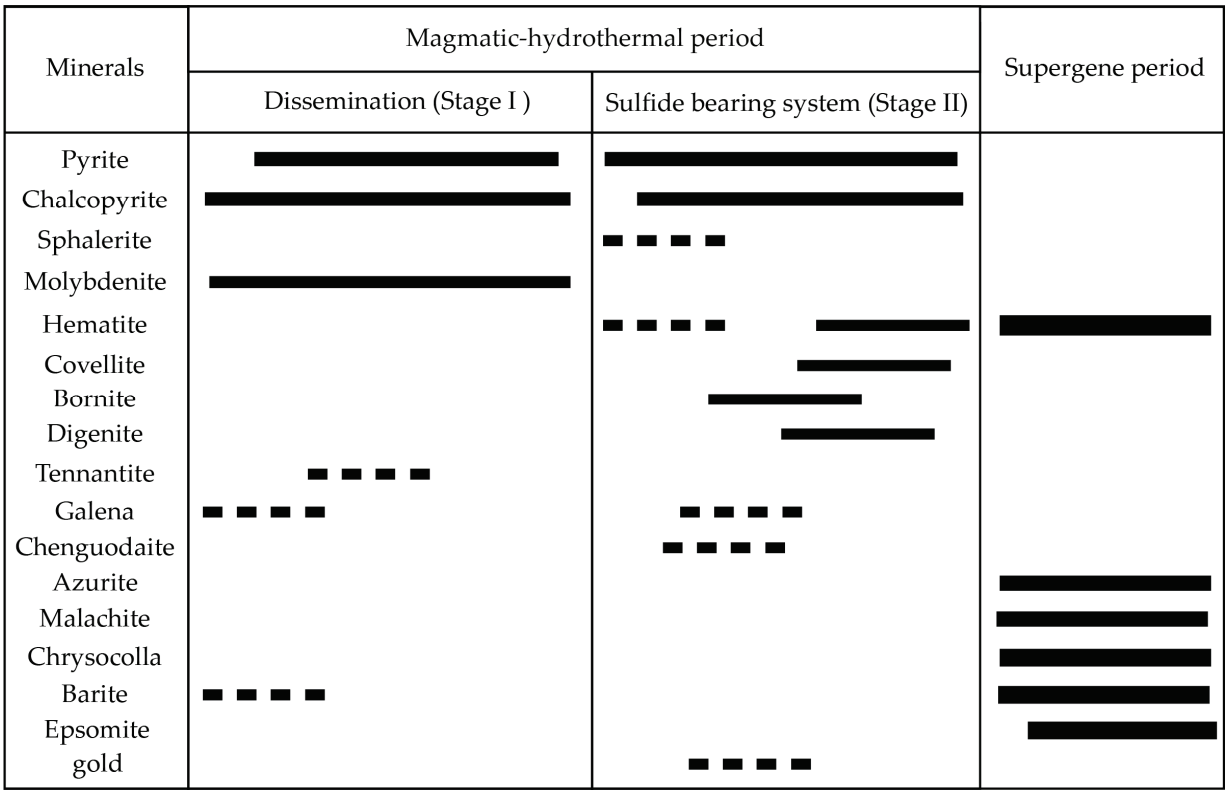


Figure 14. Inferred paragenetic sequence of the Imourkhssen Cu±Mo±Au±Ag deposit (modified from [16]).

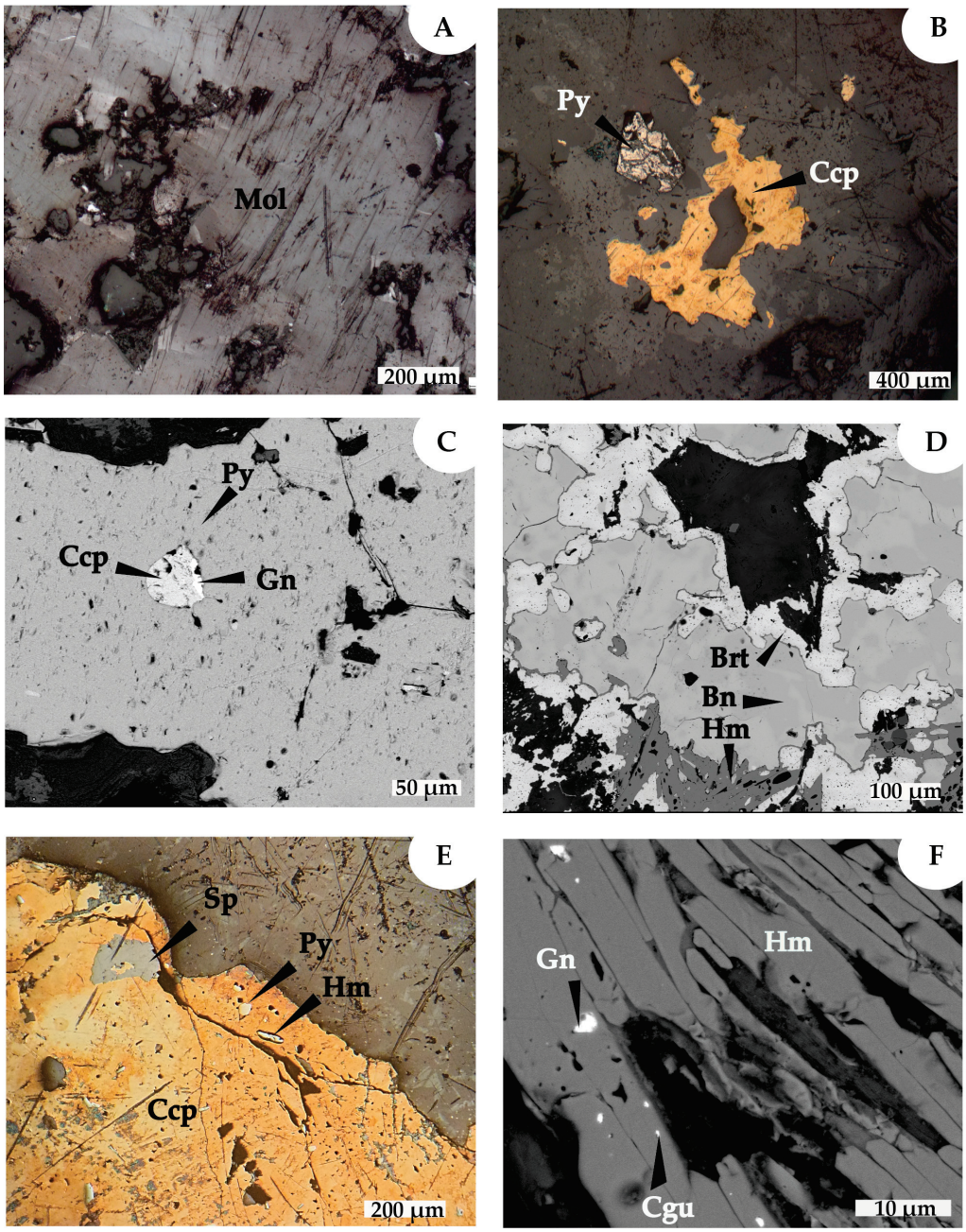


Figure 15. Reflected light (RL) photomicrographs and scanning electron microscopy (SEM) of: (**A**) Molybdenite (Mol) flake in the Imourgane granite. (**B**) Pyrite (Py) and chalcopyrite (Ccp) dissemination in the Askaoun granodiorite. (**C**) Galena (Gn) inclusion surrounded by chalcopyrite, which is itself enclosed by pyrite. (**D**) Barite (Brt), bornite (Bn), and hematite assemblages within the Zaghar dyke sample. (**E**) Sphalerite (Sp), hematite (Hm), and pyrite inclusions within the chalcopyrite. (**F**) Hematite displaying chenguodaite (Cgu) and galena inclusions. Mineral abbreviations from [52,53].

(i) The molybdenite is exclusively enclosed by the small elongated Imourgane granite. It occurs as fine-grained disseminations or fine flake aggregates in the potassic and the chlorite-sericite alteration zones (Figures 15A and 16A) or even as centimetric veinlets within the propylitic halos (Figure 16B). Microprobe analysis of the two molybdenite types shows different geochemical compositions (Figure 17, Appendix A, Table A3), suggesting that the molybdenite was remobilized during multiple fluid circulation events.

(ii) Fe-Cu sulfide disseminations occur as patchy pyrite, chalcopyrite, galena, and tennantite mineralization in the Askaoun granodiorite (Figure 15B) and the Imourgane granite. The chalcopyrite is encased by pyrite, and exhibits itself galena inclusions (Figure 15C). The tennantite is enclosed by calcite veins, while scarce barite and bornite crystals are evidenced by scanning electron microscopy within a Zaghar doleritic dyke sample (Figure 15D).

(iii) The NNE–SSW to N–S quartz-chlorite-sulfide-bearing system is well developed in the Talat nl'bour area, where it is hosted mainly by the Askaoun granodiorite. It affects less strongly the Imourgane granite, for which scarce traces of silver have been imaged by scanning electron microscopy analysis in thin chenguodaite minerals (Figure 15F). Overall, the post mineral assemblage is formed by secondary chalcopyrite exhibiting sphalerite and pyrite inclusions (Figure 15E). The bornite, digenite, and covellite occur as replacement phases as small veinlets, filling thin fractures or around the primary minerals, while gold traces have been previously documented in [16]. Those ore-related systems displaying crack-and-seal and cockade textures and a hydrothermal breccia along NNE–SSW to N–S trends suggest multiple episodes of fluid circulation (see veining system section). The supergene stage is achieved by the mineral assemblage composed of hematite, azurite, malachite, barite, chrysocolla, and epsomite.

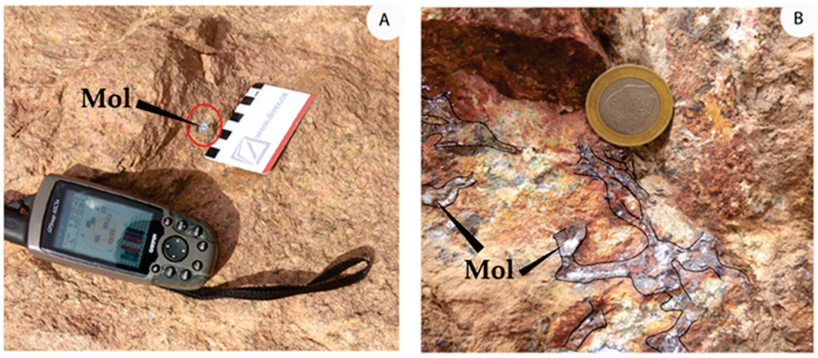


Figure 16. (**A**) Molybdenite dissemination within the Imourgane granite. (**B**) Molybdenite veinlets within a propylitic halo. Abbreviation: Mol: molybdenite.

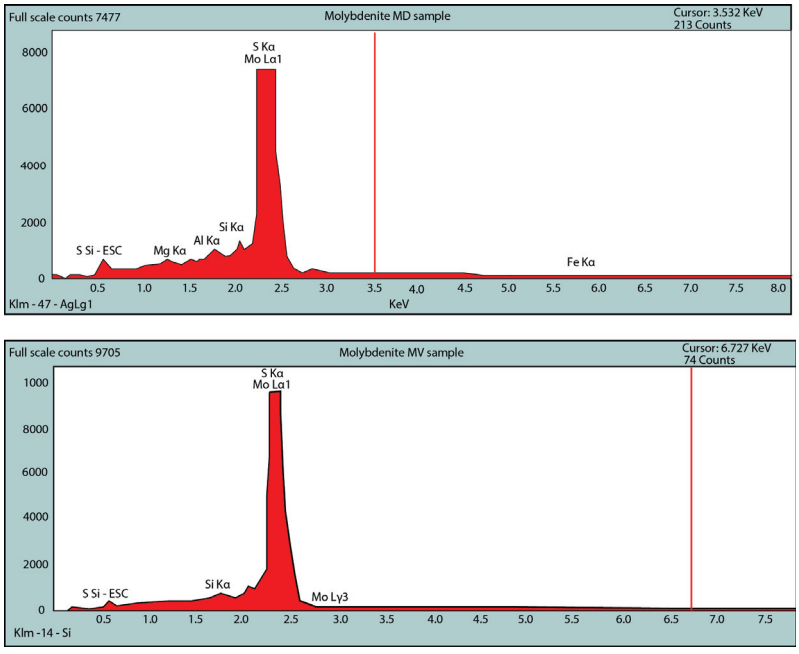


Figure 17. Quantitative results for molybdenite dissemination (MD) and molybdenite veinlet (MV) powdered samples.

4.6. LA–ICP–MS U/Pb Zircon Dating

The ore-bearing Imourgane granite was previously thought to be part of the star-shaped barren Imourkhssen granite. To clarify the ages and the timing of the associated porphyry mineralization, U-Pb geochronology was conducted on both granites. The J23IM09 sample represents the Imourgane granite, while the J23IM13 sample was collected from the star-shaped barren granitic intrusion of the TV area (the Imourkhssen granite). One hundred and two zircon grains were collected for LA–ICP–MS (laser ablation–inductively-coupled plasma–mass spectrometry) U-Pb dating. Most of the zircons were euhedral and prismatic, with rare elliptic ones. CL images show mostly a homogeneous texture with some oscillatory zoning (Figure 18). Many zircon grains exhibit titanite inclusions along with sharp edges.

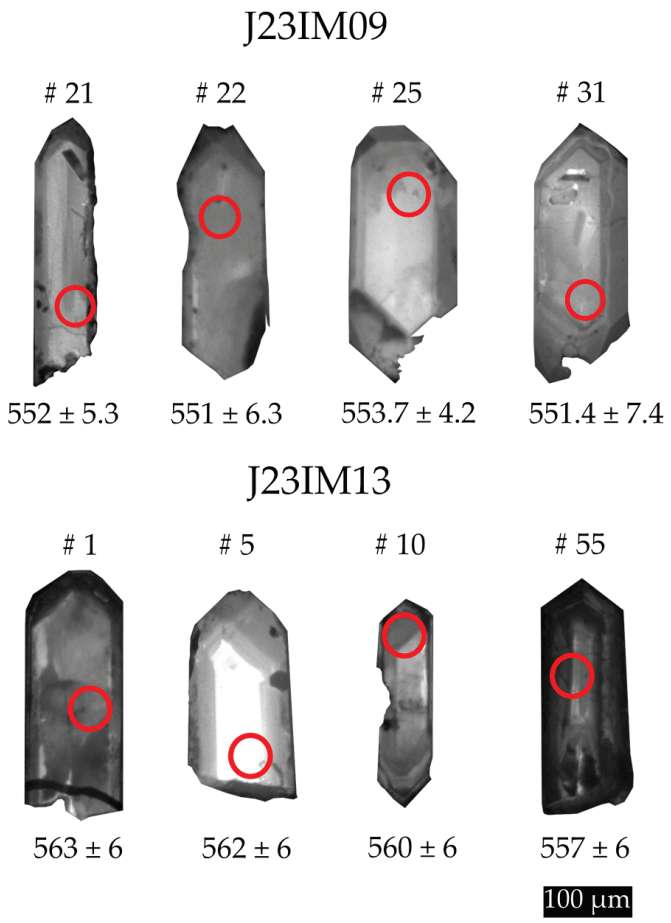


Figure 18. Cathodoluminiscence images of the dated zircon from the J23IM09 and J23IM13 samples.

The age interpretations and calculations are performed using all of the zircons that are concordant within error (Appendix A, Table A4; Figure 19). The ages of the Imourkhssen and the Imourgane granites show a homogeneous distribution and can be subdivided into three classes: (i) An older generation with ages over ca. 580 Ma. These ages are considered to be inherited from the superimposed Saghro Group and older formations. (ii) A younger generation yielding scattered ages less than 550 Ma, which we interpret as resulting from Pb loss and likely due to the hydrothermal alteration recognized in the Imourkhssen area. (iii) The remaining concordant analyses are used for the concordia and weighted mean $^{206}Pb/^{238}U$ age calculations. Nineteen zircons for the Imourgane granite (J23IM09) yielded an age of 550 ± 2 Ma, while thirty-nine zircons from the Imourkhssen granite (J23IM13) yielded an age of 558 ± 1 Ma.

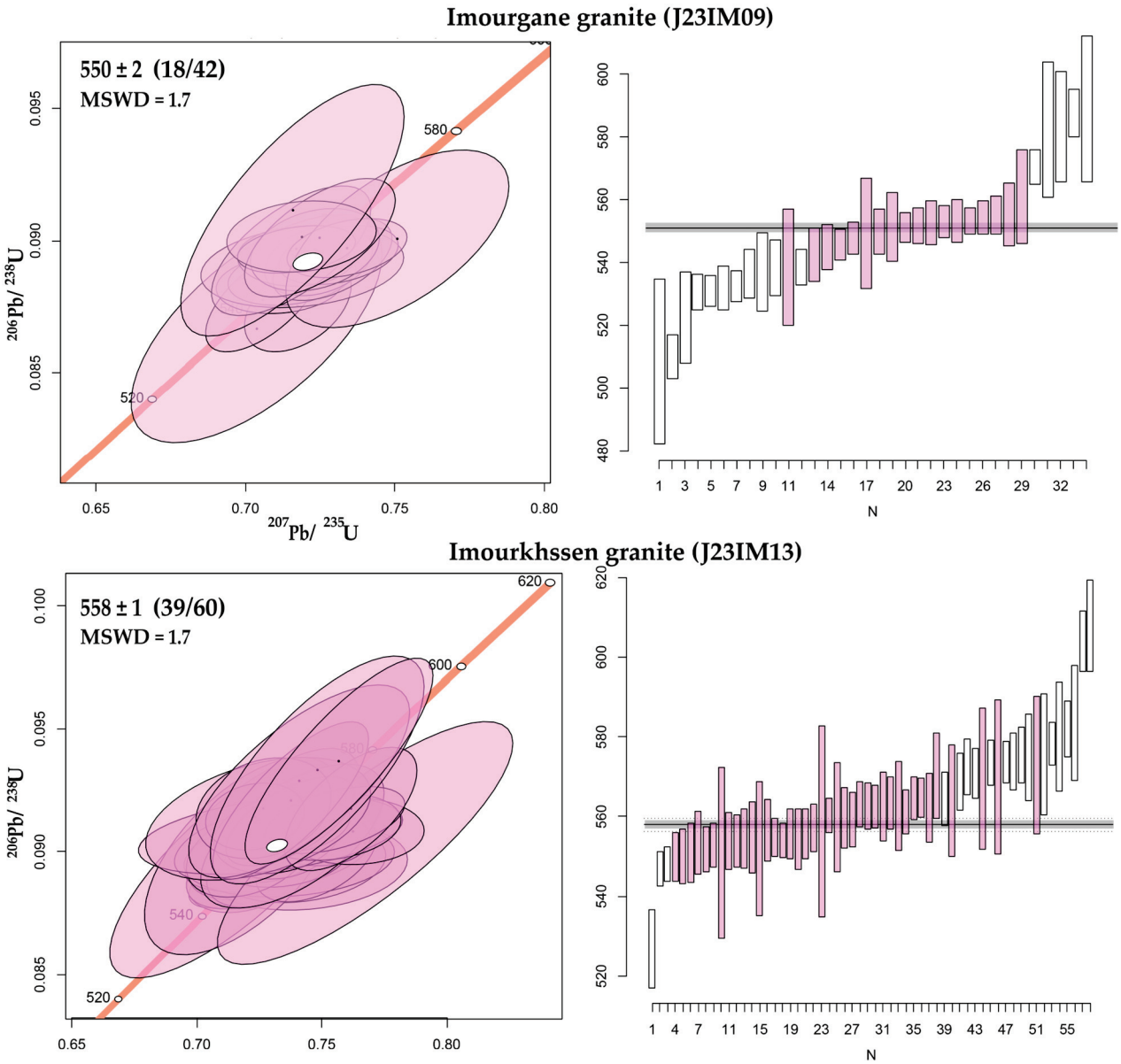


Figure 19. U-Pb concordia and Pb^{206}/U^{238} weighted mean diagrams showing LA–ICP–MS zircon ages of 550 ± 2 Ma and 558 ± 1 Ma for the J23IM09 and J23IM13 samples, respectively. Error ellipses are given at the 2σ level. Ages were calculated using Isoplot R 1.0 [37].

5. Discussion

5.1. Timing of the Plutonic Magmatism

The previous geochronological data reveal the existence of at least three granitoid intrusions corresponding to three magmatic pulses during the Late Ediacaran, one of which contains the Cu±Mo±Au±Ag Imourkhssen deposit [29,33,38]. The time sequence of this magmatism is described below.

5.1.1. The Askaoun Granodiorite

The Askaoun granodiorite is dated at 575 ± 8 Ma (SHRIMP method) [21], with a similar age of 575 ± 2 Ma reported in [32]. LA–ICP–MS zircon U-Pb dating in [29] yielded younger ages of 558 ± 2 Ma and 558 ± 6 Ma. On the other hand, an additional SHRIMP U-Pb zircon study provided both an older age of 579 ± 7 Ma and a zircon/apatite/rutile U-Pb younger age of 554 ± 6 Ma for the same granodiorite outcropping in the douar

Eç-çour area [39] (the northeastern part of the studied area). These ages provide evidence of the multi-stage feature of the Askaoun granodiorite.

Based on a geochronological compilation of ages published throughout the Saghro domain, as defined in [30], the Ouarzazate Group (OG) seems to have been emplaced over three pulses [32]. In this paper, we propose that the initial magmatic pulse (1st flare-up) of the OG took place around ca. 575 Ma. This age announces the beginning of the deposition of the OG and the minimum age of the collision event [32,38]. In the TV area, [32] documented the same age within error from a rhyodacitic ignimbrite (577 ± 3) and a rhyolitic flow (574 ± 3 Ma) at the bottom of the volcanic series. Similar U-Pb ages within error have been measured from the Bas Drâs inlier for the Taourgha granite (575 ± 2 Ma; [56]). In the Saghro massif, this age was reported for a rhyolitic tuff and for the Wizergane granodiorite (574 ± 7 Ma and 577 ± 6 Ma, respectively; [57]), as well as for the Igoudrane granodiorite (575 ± 10 Ma; [58]) and Bou Teglimt granite (576 ± 4 Ma; [59]). In the Siroua massif, a similar age was reported in [33] for a rhyolitic plug (578 ± 4 Ma) and in [21] for the Tourcht diorite (579 ± 7 Ma), a rhyolite from the Tikhfist Formation (571 ± 8 Ma), the Aguins member (577 ± 8 Ma), and the Tilsakht granite (579 ± 7 Ma). In the Zenaga inlier, a rhyolitic ignimbrite and the Tilsakht granite have been dated at 575 ± 3 Ma and 579 ± 7 Ma in [60] and [21], respectively. In the Sidi Ifni Inlier, it has been considered that the earliest magmatic event occurred at ca. 590 Ma [30]. This was evidenced by the emplacement of the Taoulecht and Tirhite intrusions.

5.1.2. The Imourkhssen Granite

A SHRIMP U-Pb zircon study of the Imourkhssen granite produced an age of 562 ± 5 Ma [21]. In addition, an age of 561 ± 3 Ma was obtained using LA–ICP–MS U-Pb dating of zircon [29]. The LA–ICP–MS U-Pb zircon dating conducted in this study yielded an age of 558 ± 1 Ma for the Imourkhssen granitic intrusion of the TV area.

This age of approximately 560 Ma could correspond to the 2nd pulse of the OG magmatism that is also reported in many inliers of the Anti-Atlas belt. In the Sirwa inlier, an andesitic tuff is dated at ca. 562 ± 1 Ma [32]. This tuff contains inherited zircons exclusively from the Saghro Group (<610 Ma), as is the case with the Imourkhssen granite. The ignimbrite of Sirwa had also been dated in [61] at 563 ± 5 Ma. The ages of 558 ± 2 Ma and 558 ± 6 Ma obtained for the Askaoun in [29] could be assigned to the second pulse of the OG. A nearly synchronous age of ca. 560 Ma is reported in the Bas Draâ inlier in [56] for the Tarçouate gabbro-diorite (560 ± 2 Ma). In the Ighrem inlier, the Ighrem tuff, Minount rhyodacite, and Houssi El Gah rhyolitic are dated at 564.6 ± 3.2 Ma, 562.89 ± 0.49 Ma, and 560.0 ± 2.1, respectively [62]. A rhyolitic ignimbrite in Tagragra of Tata yielded the same average age (565 ± 7 Ma; [63]). Similar ages are reported in the Agadir-Melloul inlier, with many rhyolitic domes yielding an age bracket between 567 Ma and 564 Ma [64]. In the Saghro inlier, the age of 560 ± 5 Ma was reported for a mineralized halo of the Imiter deposit [65]. Geochronological dating in [66] yielded an age of 566 ± 20 Ma for the Isk-n-Alla granite, while dating in [57] yielded an age of 559 ± 5 Ma for the same granite. The Ikniwn pluton records an age of 564 ± 6 Ma [67]. Similar ages are reported in [30] for the volcanic and plutonic rocks in the Ifni inlier (e.g., the Mesti monzogranite at 567 ± 4 Ma and the Ifni syeno-granite at 566 ± 4 Ma).

5.1.3. The Ougougane Granite

The Ougougane granite yielded a LA–ICP–MS zircon U-Pb age of 550 ± 1.5 Ma [32]. This age had been interpreted as the zircon crystallization age. In this study, geochronological dating was performed on the ore-bearing granite that had been formerly assigned to the Amassine suite. LA–ICP–MS U-Pb dating on zircon yielded an age of 550 ± 2 Ma for the mineralized granite, leading to its affiliation being constrained within the Ougougane suite, and it was subsequently renamed as the Imourgane granite.

Similar ages are documented in many inliers of the Anti-Atlas (ca. 550 Ma) and could correspond to the 3rd pulse of the OG. In the Ougnat inlier, the Bou Madine rhyolitic

has been dated at 552 ± 5 Ma in [28] and at 553 ± 16 Ma in [65]. In the Saghro inlier, the Takhatert and Tachkakacht rhyolites have been dated at 550 ± 3 Ma and 547 ± 8 Ma, respectively [65]. This period could be correlated with regional events that occurred through the whole Anti-Atlas, mainly the transition from a transpressive to transtensive tectonic regime by the orogenic collapse [65].

5.2. Ore Genesis and Source in the Framework of the Geodynamic Context of the Anti-Atlas

To reconstruct the magmatic-hydrothermal processes responsible for the Imourkhssen Cu±Mo±Au±Ag ore deposit, the regional geodynamic context has to be considered. As clearly reported in [16], the ore genesis of the Imourkhssen deposit is linked to the emplacement of the LEMS. This period is clearly correlated with the huge metallogenic activity associated with the highly silicic magmatism of the Ouarzazate Group. During this epoch, a large volume of juvenile material, precious metals, and chalcophile elements was added to the continental crust all over the Pan-African Anti-Atlas belt system [28,68,69]. Therefore, numerous deposits in the Moroccan Anti-Atlas, particularly in the Saghro domain, as defined in [30], seem to be affected by this magmatic event. This magmatic manifestation triggered pervasive hydrothermal activity and gave rise to world-class epithermal mineralization and base metal porphyry deposits (e.g., Imiter and Zgounder (Ag-Hg), Bou-Azzer (Co-Ni-As-Ag-Au), Iourirn (Au), and Bou Ma-dine (Cu-Pb-Zn-Au-Ag) [27,28].

In the OSS, the LEMS shows a high potassic calc-alkaline I-type granite affinity, with enrichment in LILE, relative depletion in HFSE, and a pronounced Nb-Ta anomaly. These geochemical features are akin to rocks derived from subduction-related sources [70]. Nevertheless, this signature is considered to be an inherited signature, transferred to the igneous rocks during the remelting of the subduction-related lithosphere [71]. Therefore, the emplacement of the LEMS invokes the contribution of a recycled subduction-related component [27,29]. This component could be involved in the ore enrichment, as indicated by several studies, especially for Mo and Au mineralization [72]. Its significant role is due to the H_2O, CO_2, and Cl provided from the subducted material, which ultimately contributes to the enhancement of associated hydrothermal systems [1].

In general, the ore source for porphyry copper deposits is still debated. However, a crustal component is widely invoked for the genesis of fertile sulfide rich magmas. The authors of [73] suggested that the Gattar fertile magmas originated from an underplated crustal source that was fertilized by metasomatized underplating mantle derived melts. This magmatism was responsible for the molybdenite bearing granitic intrusions in the northern Eastern Desert of Egypt. The authors of [74] assumed that the mineralization of the fertile Yulong porphyry copper deposit (eastern Tibet) originated from an eclogitized sulfide-rich juvenile lower crust melt. These melts were fueled by the injection of an ultrapotassic subduction-related metasomatized subcontinental lithospheric mantle-derived melt. The authors of [75] presumed the melting of the lower crust for the Mo enrichment, whilst the copper was suggested to be sourced from mantle melts, including subducted slab. Nevertheless, the authors of [76] assumed that Mo is more enriched in reduced sediment. In this regard, the authors of [77] associated the Mo enrichment of the porphyry Mo-Cu Pınarbaşı system (Western Turkey) with the melting of terrigenous sediment, or at least the melting of the lower crust and metasomatized mantle by subducted sediment-derived fluids.

Analogous with the observations made in [77], the Imourkhssen porphyry mineralization seems to contains a terrigenous component. The chondritic Zr/Hf ratios of the Assarag suite are scattered within the range of crustal material (32–37), while the rocks of the Ougougane suite show low Zr/Hf ratios (26–32). This feature highlights its fractionated origin [78]. Chondritic values of Zr/Hf are from [78]. Moreover, the ages of many inherited zircons (ca. 720–630 Ma) of the Imourkhssen and Imourgane granites correspond with the subduction episode that occurred in the Anti-Atlas during the Pan-African orogeny. Therefore, the LEMS could have originated from melts that include recycled subducted sediments.

The emplacement of the LEMS is contemporaneous with the widespread and huge volcanic Ouarzazate Group and its subsequent intense hydrothermal activity. This thermo-magmatic event occurred in a trans-tensional tectonic regime, corresponding with the post-collisional stage of the Pan-African orogeny that evolved toward extension during the Cambrian [27,28]. In this context, the uprising of the asthenospheric mantle close to the Moho generated a high regional heat flow that fueled the melting of the lithospheric or even the asthenospheric mantle itself [29], in addition to the lower crust with the incorporated recycled juvenile sulfide rich subduction components.

The contribution of mafic components could also be discussed for enabling sulfur and metal element enrichment to the parental magma [1]. We can assess the likely involvement of the Zaghar mafic dykes on Imourkhssen ore genesis using the following observations: (i) Many porphyry ore deposits record the associations of rhyolites of bimodal basalt-rhyolite suites [79]. (ii) The Zaghar mafic dykes of the studied area have a coeval magmatic feature with the Late Ediacaran granitoids elucidated by co-mingling structures. (iii) Disseminated mineralization is observed within the Zaghar dykes in the Imourkhssen area. These observations lead us to assume the possible contribution of this mafic component in the evolution of the Cu±Mo±Au±Ag Imourkhssen porphyry mineralization.

The multi-pulse character of the Askaoun pluton, evidenced by older and younger ages, by new geophysical data interpretations [80], and the proximity of the dated samples in [29] to the studied area, lead us to constrain the age of the mineralized granodioritic rocks of the Askaoun pluton at ca. 558 Ma. Consequently, the Imourkhssen Cu±Mo±Au±Ag porphyry-style mineralization is considered to be associated with the emplacement of the Askaoun granodiorite (ca. 558 Ma) and the Imourgane granite (ca. 550 Ma), which are coeval with the 2nd and 3rd magmatic pulses of the Ouarzazate SLIP (see Section 5.3). Field observations and detailed analysis of the Imourkhssen mineralization led us take into account the following issues:

- All the Late Ediacaran granitoids follow the same trend as mentioned in Section 4.2. Thus, these rocks belong to a single parental magma that evolved progressively and gave rise to multiple pulses and became more fractionated and differentiated over time (i.e., Ougougane suite).
- Secondly, we should contemplate the specific mineralization style of the Imourkhssen district. The Cu sulfide mineralization occurs mainly within the Askaoun granodiorite. This pluton contains a high metal grade of 0.30% and 22 g/t for Cu and Au, respectively [16]. In this framework, the probable contribution of the Zaghar mafic dykes to the Cu and Au mineralization could be envisaged because of their co-magmatic feature with the Askaoun pluton.
- Likewise, we should note that the molybdenite occurrences are restricted to the more felsic Imourgane granite, which is widely known for porphyry mineralization (e.g., similar to Mamut, East Malaysia) [81]. These observations imply not only late molybdenite precipitation but also a spatial shift from the Cu-Au bulk [1]. This feature is ideally portrayed by the Mo occurrences in the Imourgane granite and the well-developed Askaoun Cu-Au mineralization. The described shift between Mo and Cu-Au mineralizations could be related to the increasing Mo/Cu ratio in the residual parental melt, as proposed in [82].
- The importance of scarce silver is mitigated due to the lack of information. More insights could be drawn from Pb-S-O-C isotopic analysis, Re content in molybdenite, as well as from the gaseous and aqueous compositions of fluid inclusions in quartz. These analyses would be very helpful to understand the low silver concentrations here.

5.3. Late Ediacaran Ouarzazate SLIP and Implications for the Anti-Atlas Mineralization

Large igneous provinces (LIPs) are defined as large volume (>0.1 million km^3) encompassing mafic rocks, with their plumbing systems, emplaced within an intraplate setting in a single pulse of short duration (<5 Ma) [83]. Nonetheless, LIPs may contain multi-pulses of magmatism that extend over a period of less than 50 Ma [84]. In continental margins,

LIPs can also be associated with silicic magmatism and, in these cases, they are referred to as silicic large igneous provinces (SLIPs) [85].

During the Late Ediacaran episode, huge silicic magmatic activity took place in the Anti-Alas belt of Morocco [28]. This magmatism has been more recently bracketed between 575 and 540 Ma and gathered under a litho-structural unit referred to as the Upper Complex in [15]. Those authors assume that throughout this timeframe (575–540 Ma), the whole Anti-Atlas belt witnessed a long-lived tectono-magmatic event evolving from high-K calc-alkaline (575–550 Ma) to alkaline (550–540 Ma) affinity, which is also reported in [86,87] in the Saghro inlier. This magmatism is thought to belong to a continental silicic large igneous province (SLIP), defined in [30] as the Ouarzazate SLIP, and emplaced over multiple pulses at ca. 575 Ma, ca. 560 Ma, and ca. 550 Ma [33] (Figure 20).

Various studies have outlined the significant role of LIPs for several metallogenic systems. LIPs are commonly related to a wide variety of metal deposits [84] and could represent the source of metals and energy for hydrothermal systems [83]. The emplacement of LIPs could provide copper and other metals for several ore deposit types, including iron-oxide-copper-gold (IOCG) and volcanogenic massive sulfide (VMS), potentially with Au deposits [84]. Nevertheless, the epithermal Au- and Carlin-type mineralizations appear to be more related to SLIPs [88].

In this regard, the authors of [28] assumed that the long-lived silicic magmatic activity of the Ouarzazate SLIP was accompanied by a pervasive hydrothermal and metallogenic manifestations. Additionally, the authors of [15] suggested possible relationships between many ore deposits and magmatic systems with multiple magmatic pulses (flare-ups) and their associated hydrothermal systems, such as Qal'at MGouna district Au-Ag (Cu, Mo, Bi, Te), including the Ismlal Au(-Cu-Mo) porphyry, Zone des Dykes Au-base metal, Thaghassa Au-Ag, Imiter Ag-Hg-Pb, Bouskour Ag-base metal, Tiouit Au-Ag-Cu, Sidi Flah Cu-Au-Ag, Tagmout Cu-Ag, and Bou Madine Au-Ag-base metal deposits (Figure 21).

In the TV area, we suggest an earlier emplacement of the first magmatic pulse generating the Askaoun granodiorite at 575 Ma (Figure 19). The age obtained in [29] (ca. 558 Ma) for this pluton outlines its extended emplacement until the second magmatic pulse (ca. 560 Ma), during which the large barren Imourkhssen intrusion was formed. The third magmatic pulse is considered to be the last manifestation of the Ouarzazate magmatic activity [32]. It spans around 550 Ma and corresponds with the emplacement of the Ougougane suite, including the Imourgane ore-bearing porphyry granite. These intrusions developed a spherulitic texture, highlighting fast cooling under low-temperature conditions [89].

The Imourkhssen Cu±Mo±Au±Ag porphyry-style mineralization is considered to be associated with the emplacement of the Askaoun granodiorite (ca. 558 Ma) and the Imourgane granite (ca. 551 Ma) that are coeval, respectively, with the 2nd and 3rd flare-ups reported in [15]. These two flare-ups correspond with the 2nd and 3rd magmatic pulses of the Ouarzazate SLIP (560 Ma and 550 Ma, respectively) [32]. The 3rd magmatic pulse could be also responsible for the occurrence of the Zgounder Ag-Hg epithermal ore deposit in the southwestern part of the studied area. In this regard, the potential relationship between the Imourkhssen porphyry and the Zgounder epithermal mineralization could be discussed.

Overall, this period could be correlated with regional events, highlighted by the transition from a transpressive to transtensive tectonic regime by the orogenic collapse [65]. In the framework of this extensional regime, leached hydrothermal fluids are inferred to have flowed along faults, developing the porphyry and epithermal deposits [15].

Consequently, the Ouarzazate SLIP could be potentially invoked as the metal source and hydrothermal energy that fueled the Late Ediacaran porphyry and epithermal hydrothermal and metallogenic activities in the central and eastern Anti-Atlas, namely, the Saghro domain of Morocco (see Section 5.4).

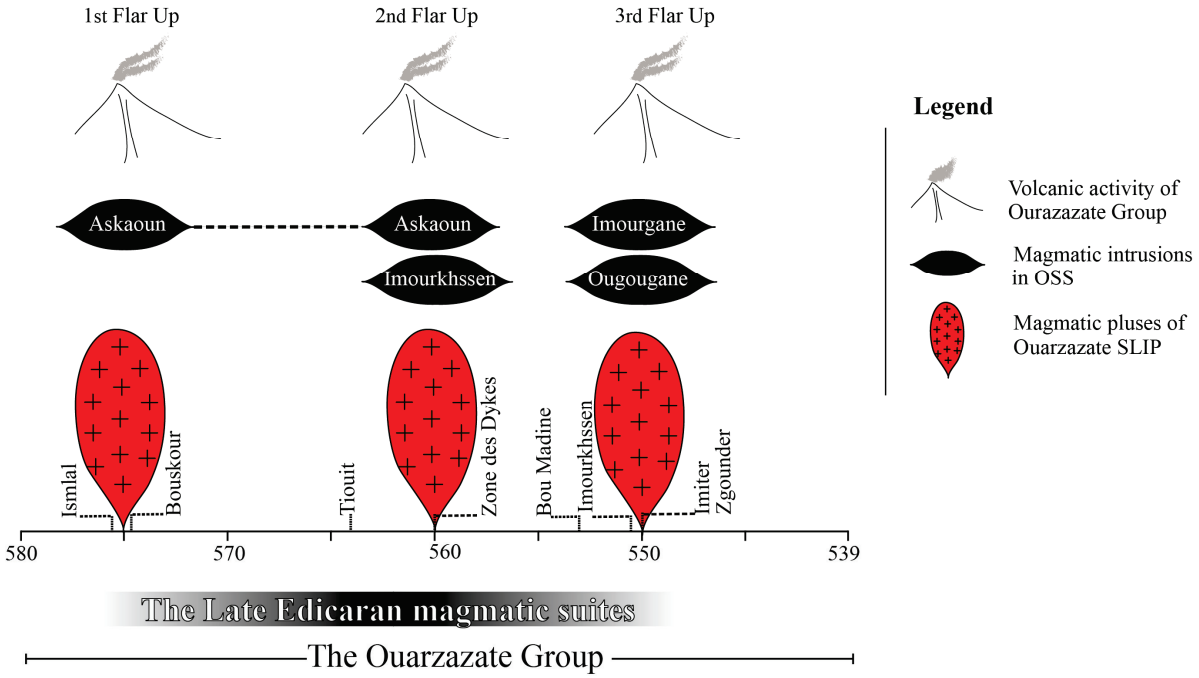


Figure 20. The emplacement of the Late Ediacaran magmatic suites (LEMS) related to the three magmatic pulses of the Ouarzazate SLIP [15,33] and the position of the Imourkhssen and many ore deposits of the Anti-Atlas.

5.4. A Probable Late Ediacaran Porphyry-Epithermal Province in the Anti-Atlas

The post-collisional period in the Pan-African Anti-Atlas belt system involved the transition to a passive continental margin with a strong extensional tectonic regime and subsequent orogenic collapse [21,28]. In the framework of this extensional regime, intense metallogenic activity occurred, giving rise to numerous world-class precious metal epithermal deposits (Imiter and Zgounder), base metal porphyry, and SEDEX-type occurrences (Bou Madine; [28]) within outcrops formed mainly by highly silicic magmatism. This magmatism was speculated to be the Ouarzazate SLIP [28,30].

The consistency of the geological, geochemical, and metallogenic features of several precious and base metal occurrences occurring in the central and the eastern part of the Anti-Atlas are remarkable. This part of the Anti-Atlas chain delimited by the southern High Atlas fault (SAF) and the Anti-Atlas major fault (AAMF) was recently considered as a single terrane, referred to as the Saghro domain [30]. On the other hand, numerous ore deposits show a spatial and probably a temporal link with Late Ediacaran silicic magmatism of the Ouarzazate SLIP within the Saghro domain

In the framework of the extensional tectonic regime and the long-lived magmatic activity of the Ouarzazate SLIP [32,33], the authors of [15] proposed that Jbel Saghro constitutes a large mineralized provin6ce regarding pervasive hydrothermal activity and several metallogenic manifestations. In this paper, we propose that the Saghro domain should be considered as a Late Ediacaran porphyry-epithermal province englobing the entirety of porphyry and epithermal ore deposits linked to the post-orogenic collapse episode of the Pan-African orogen (Figure 21).

This system was powered by the injection of silicic magmatic pulses of the Ouarzazate SLIP. In three epochs, the incorporated juvenile sulfide-rich related subduction component of the melted magma allowed to the emplacement of fertile intrusions. These intrusions developed porphyry and epithermal mineralizations under a single porphyry–epithermal system. This system, with the associated SLIP magmatism, occurred during the latest post-collisional episodes of the Pan-Africain orogeny, corresponding with the metacratonic evolution of the northern edge of the West African craton (WAC) [90,91].

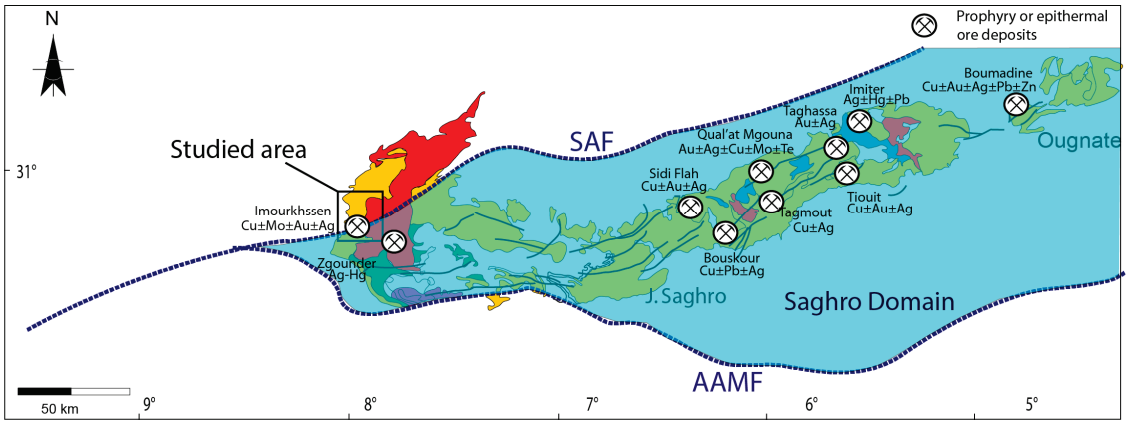


Figure 21. The emplacement of many ore porphyry and epithermal deposits within the Saghro domain, creating a Late Ediacaran porphyry epithermal province in the Anti-Atlas of Morocco [15]. Abbreviations: SAF: south Atlas fault, AAMF: Anti-Atlas major fault.

5.5. Similarities with Porphyry and Epithermal Ore Deposits in the World

The mineralization style of the porphyry and epithermal ore deposits and related magmatic activity occurring in the Saghro domain are widely recognized in several ore deposits around the world.

Before debating the porphyry–epithermal relationship, we can discuss the multi-pulse feature of the hydrothermal-magmatic activity responsible for the huge metallogenic activity during the Late Ediacaran times. Indeed, this multi-pulse character is broadly recognized in the development of several ore deposits, such as the Cu-Pb-Zn polymetallic deposit in Jiangxi Province. The latter is considered to be tied to three main magmatic-hydrothermal events (ca. Middle-Late Triassic, Late Jurassic, and Early Cretaceous) that are responsible for the metallogenic activity in the North Wuyi area of China [92].

In Jiangxi province, East China, the porphyry Cu-Au-Mo mineralizations and the Ag-Pb-Zn epithermal occurrences are related to five magmatic phases recognized in the Dexing area [75]. Based on the geochronogical and geochemical features of both mineralization styles, those authors reasonably assumed a link between the Dexing Cu-Au-Mo porphyry and Ag-Pb-Zn epithermal ore deposits in Jiangxi province.

The connection between the porphyry and epithermal deposits envisaged in the Saghro domain is observed in several ore deposits worldwide. Indeed, numerous epithermal ore deposits are underlain by porphyry-type mineralization, often rooted in their advanced argillic alteration lithocaps [1,93]. In China, several porphyry and epithermal deposits are suggested to be genetically related. Namely, the Yinshan Ag-Pb-Zn epithermal and Cu-Au porphyry ore deposits [94].

Moreover, the epithermal deposits can also be grounded within the serecitic alteration zone (e.g., the Far Southeast-Lepanto (FSEL) Cu-Au porphyry and epithermal deposits; [95]). In this example, the examination of fluid inclusions and δO and δD compositions led the researchers to conclude that gradational alteration patterns from advanced argillic alteration, through phyllic and K-silicate alterations, could be used to outline the spatial evolution of a single hydrothermal fluid during the formation of the FSEL porphyry and the epithermal district in the Philippines [95].

On the other hand, discussing the relationship between porphyry and epithermal ore deposits involves understanding the metal source [1]. For this reason, the authors of [95] assumed a common magmatic metal source for the entire FSEL porphyry-epithermal mineralization stages based on similar metal associations. Therefore, the identical magmatic fluid sources for both porphyry and epithermal systems is the best evidence for their genetic connection.

In the Baguio mineral district, the Philippines, two (I and II) porphyry vein stages are superimposed by four (III to V) paragenetic stages of the Acupan epithermal mineraliza-

tions [96]. Fluid-inclusion studies revealed that the porphyry vein stages were sourced from hot and hypersaline magmatic fluids exsolved during the crystallization of the subvolcanic porphyry dacite, while the co-existing magmatic vapor generated gold and silver epithermal mineralizations alongside gang and alteration patterns. This mineralization style was also guided by structures associated with the emplacement of the Balatoc diatreme [96].

A further example in the Apuseni Mountains, Romania, is reported in [97]. Those authors demonstrated using 3D structural measurements that there is a spatial link between the Bolcana Cu-porphyry and three epithermal deposits (e.g., Troita, Trestia, and Magura). This study was based on studding in 3D the spatial dispersion of metal contents around the Bolcana Cu-porphyry, revealing a specific distribution that could not result from a telescoped system. Thus, a strong relationship between porphyry copper and epithermal ore deposits occurs within the Apuseni Mountains.

5.6. Spatial Correlation with the Avalon Epithermal Ore Deposits

During the Late Ediacaran period, as Gondwana was nearing its final amalgamation, the West African craton (WAC) was surrounded by Pan-African terranes (Figure 22), which included island arcs or continental active margins. In this context, the WAC assumed the role of a passive margin amidst these geological features ([91] and references therein). During the Paleozoic era, terranes adjacent to the northwestern edge of Gondwana separated, resulting in the formation of the Rheic Ocean [98]. Hence, specific peri-Gondwanan terranes exhibit significant similarities in age, tectonic evolution, metallogenic history, and facies progression to the Pan-African belts found in the West African craton, including the Anti-Atlas. Here, we mainly focus on the metallogenic aspect as a tool for global correlation.

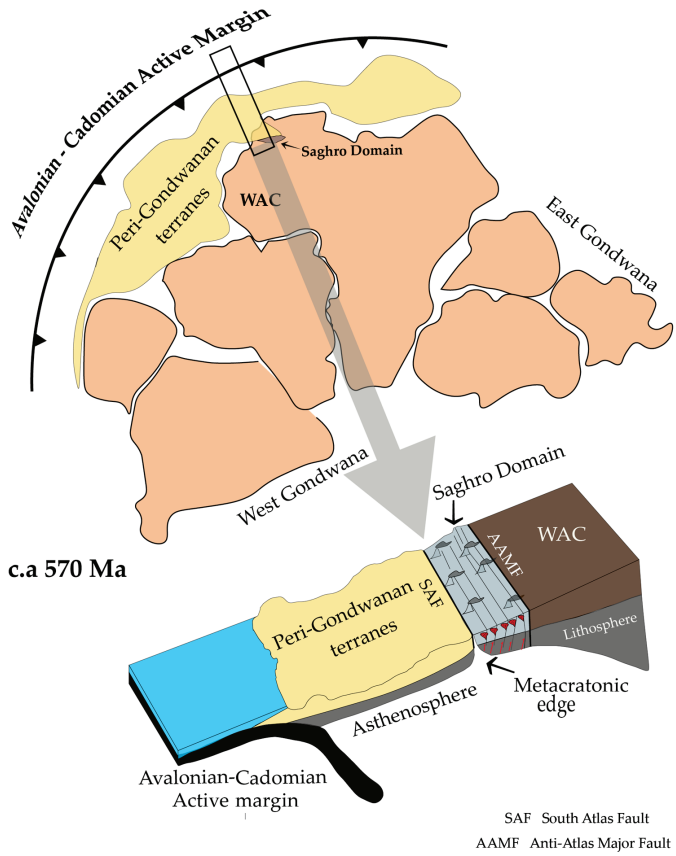


Figure 22. Paleogeographic location and geotectonic cross section of the Saghro domain through the Peri-Gondwanan terranes and the West African craton (WAC) and at ca. 570 Ma. Modified from [90,99].

Indeed, most of the epithermal alterations and related mineralizations identified in the Avalon zone occurring from 590 to 550 Ma are also associated with potential buried porphyry deposits [100]. In this regard, the Late Neoproterozoic epithermal mineralization of the Saghro porphyry-epithermal province portrays a link with the west Avalon zone's epithermal deposits.

Indeed, the Hickey's Pond, Big Easy, Long Harbour, Hope Brook, and Heritage epithermal deposits occur in the Newfoundland area of the west Avalon zone. The Hickey's Pond high-sulfidation deposits [101] have an age of 586 ± 3 Ma from the advanced argillic alteration [102]. A reinterpretation of the age from the host rocks provides a younger age of 572.5 ± 1.5 Ma [103]. Further studies of the Hope Brook high-sulfidation deposits bracketed the age of the alteration and the mineralization between 578 and 574 Ma [104]. The Big Easy epithermal deposit has a Late Neoproterozoic age (ca. 573 Ma; [103]), while the Long Harbour prospect, a mineralized rhyolite, constrains the age of this low epithermal deposit at 566.5 ± 1.9 Ma and has been used to indicate its alkaline affinity and potential relationship with late arc-extension [103]

On the other hand, the correlation between the WAC edge and the boundary of North America is currently debated. Based on geochemical and geochronological data, the authors of [30] proposed potential correlations between the magmatic rocks of the Ouarzazate Group outcropping in the Ifni inlier and the magmatic rocks of west Avalonia, including the Newfoundland area. The authors of [105] interpreted the Late Ediacaran magmatism in the El Jadida region as an example of a Moroccan peri-Gondwanan (Avalonian?) remnant, while the authors of [106] described many fossils found in the Anti-Atlas of Morocco (e.g., Aspidella) that are ubiquitous in the Avalon zone. These fossils point to the Ediacaran period and underscore a similar deposit style.

Here, we suggest a spatial link between the northern boundary of the West African craton (WAC), namely the Saghro domain, and the west Avalon zone during the Late Ediacaran times.

6. Conclusions

This study allows us to draw several conclusions, which we summarize below:

(1) We support the hypothesis of porphyry-type mineralization for the Imourkhssen deposit (central Anti-Atlas, Morocco), which was previously suggested in [32]. We argue this based on the following points: (i) the geochemical nature of the host rocks and multi-phase magmatic (Assarag, Amassine, and Ougougane suites) and hydrothermal activities, (ii) the style and the zonation of hydrothermal alteration and mineralization, (iii) the mineral assemblage and paragenetic sequence, and (iv) the post-collisional geodynamic setting of the host rocks.

(2) The model envisaged in this study for the Imourkhssen Cu±Mo±Au±Ag mineralization could be related to the 2nd and the 3rd flare-ups reported in [15], which are coeval with the 2nd and the 3rd magmatic pulses of the Ouarzazate SLIP, as evidenced in [33].

(3) The ore genesis potentially involves the Zaghar mafic dykes during the magma evolution, which is corroborated by their co-mingling textures.

(4) The concordia and $^{206}Pb/^{238}U$ ages and averages of the barren Imourkhssen and the ore-bearing granite from the TV area allow us to constrain the age of the Imourkhssen intrusion at 558 ± 1 Ma.

(5) The ore-bearing granite is newly identified as the "Imourgane granite". The concordia age of 550 ± 2 Ma indicates that it belongs to the Ougougane suite, and this allows us to constrain the age of the porphyry–epithermal system in the OSS beneath the 2nd and 3rd magmatic pulses of the Ouarzazate SLIP.

(6) Several ore deposits in the whole Anti-Atlas seem to belong to a Late Ediacaran porphyry–epithermal system linked to the emplacement of a multi-pulse continental silicic large igneous province, namely, the Ouarzazate SLIP (580–539 Ma). This SLIP was generated during the post-collisional period of the Pan-African orogen.

(7) The average ages of the epithermal ore deposits of the west Avalon zone and the porphyry-epithermal province entail their potential spatial link during the Late Neoproterozoic times, corresponding with the metacratonic evolution of the northern boundary of the West African craton.

Author Contributions: Conceptualization, M.F. and S.B.; Data curation, M.F., J.H.F.L.D., M.G.P. and A.B.-T.; Investigation, M.F., S.B., L.-Z.C., J.H.F.L.D., M.G.P. and M.B.; Methodology, M.F. and S.B.; Resources, L.-Z.C.; Software, M.F., S.B., J.H.F.L.D., M.G.P. and A.B.-T.; Supervision, S.B. and L.-Z.C.; Validation, S.B., L.-Z.C. and M.B.; Visualization, M.F., J.H.F.L.D., M.G.P., A.B.-T. and M.B.; Writing—original draft, M.F. and S.B.; Writing—review & editing, M.F., S.B., L.-Z.C., J.H.F.L.D., M.G.P. and M.B. All authors have read and agreed to the published version of the manuscript.

Funding: Part of this work has been undertaken with the help of the Natural Sciences and Engineering Research Council of Canada "CRSNG" subventions awarded to Professor Li-Zhen Cheng.

Data Availability Statement: The data used for the research are presented in the article.

Acknowledgments: Most of this work was carried out at the Faculty of Sciences of Agadir, Ibn Zohr University, and at the University of Quebec in Abitibi-Timiskaming, Canada. We gratefully acknowledge the technical staff of the laboratory of the Applied Geosciences and Geo-Environment (LAGAGE), the research center of the Faculty of Sciences of Agadir, as well as the research center of geochronology and isotopic geochemistry (GEOTOP) of the University of Quebec in Montreal who contributed in this work. We also appreciate the support provided by the National Centre for Scientific and Technological Research (CNRST) and their encouragement to succeed in this work. We further thank to journal's anonymous referees for their constructive reviews and edits, as well as to the entire editorial staff of *Minerals* for their handling of the manuscript, which significantly enhanced this work.

Conflicts of Interest: The authors declare no conflicts of interest.

Appendix A

Table A1. Characteristics and localization of the samples used for different studies.

ID sample	Suite	Rock	Analysis	Location	Characteristics
23IM27	Assarag	Askaoun granodiorite	Petrography Geochemistry	N 30°55,13′/W 007°52,05′	The sample is collected near the Talat nl'bour galleries
J23IM13	Amassine	Imourkhssen granite	Petrography Geochronology	N 30° 56,72′/W007° 51,57′	Fresh sample collected from the star-shaped intrusion
23IM13	Ougougane	Imourgane granite	Petrography Geochemistry	N30° 55,36′/W007° 52,28′	The sample exhibits molybdenite dissemination
J23IM09	Ougougane	Imourgane granite	Geochronology	N30° 55,91′/W007° 51,71′	The sample exhibits a molybdenite vein
23IM20		Zaghar dyke	Petrography Metallogeny	N30° 57,65′/W007° 52,22′	The dyke (50 cm thick) cut across the Imourgane granite. This dyke exhibit sulfide dissemination (Figure 15D)
23IM07A	Ougougane	Ougougane microgranite dyke	Geochemistry	N30° 56,04′/W007° 51,70′	The dyke (30 cm thick) cut across the quartz-diorite
23IM09	Ougougane	Ougougane microgranite dyke	Geochemistry	N30° 56,02′/W007° 51,80′	N175-oriented dyke, with a thickness of about 50 cm
23IM19	Ougougane	Imourgane	Geochemistry	N30° 57,70′/W007° 52,51′	Fresh sample
23IM22	Ougougane	Ougougane rhyolite	Geochemistry	N30° 53,80′/W007° 53,03′	The sample is cut by a N130 Qz-Hm vein
23IM24	Ougougane	Ougougane microgranite dyke	Geochemistry	N30° 52,51′/W007° 53,62′	This dyke is cut by a Zaghar mafic dyke
23IM26B	Ougougane	Imourgane	Geochemistry	N30° 55,35′/W007° 52,20′	Fresh sample
23IM26C	Ougougane	Imourgane	Geochemistry	N30° 55,38′/W007° 52,11′	The intrusion is cut by a N70 hematite lens
23IM26D	Ougougane	Imourgane	Geochemistry	N30° 55,52′/W007° 51,98′	Fresh sample near molybdenite veinlets
23IM17A	Assarag	Askaoun granodiorite	Geochemistry	N30° 56,15′/W007° 51,57′	This sample is near sulfide dissemination
23IM23	Assarag	Askaoun granodiorite	Geochemistry	N30° 53,81′/W007° 53,05′	Fresh sample
23IM25	Assarag	Askaoun granodiorite	Geochemistry	N30° 53,95′/W007° 53,23′	The intrusion is cut by the N130 doleritic dyke
23IM26A	Assarag	Askaoun granodiorite	Geochemistry	N30° 52,27′/W007° 52,00′	The sample is collected near the Talat nl'bour galleries
23IM27	Assarag	Askaoun granodiorite	Geochemistry Metallogeny	N30° 55,13′/W007° 52,05′	The sample displays sulfide disseminations
23IM07B	Assarag	Askaoun quartz-diorite	Geochemistry	N30° 56,03′/W007° 51,71′	Fresh sample
23IM14A	Assarag	Askaoun quartz-diorite	Geochemistry	N30° 55,34′/W007° 52,39′	The intrusion is cut by the Ougougane dyke

Table A1. *Cont.*

ID sample	Suite	Rock	Analysis	Location	Characteristics
23IM28	Assarag	Askaoun quartz-diorite	Geochemistry	N30° 55,57′/W007° 51,92′	Fresh sample
22IM05	Ougougane	Imourgane	X-Ray Diffraction	N30° 55,57′/W007° 51,92′	Altered sample collected from serecitic alteration zone
22IM02	Ougougane	Imourgane	X-Ray Diffraction	N30° 55,22′/W007° 52,05′	Fresh sample from the Imourgane granite
22IM17	Assarag	Askaoun granodiorite	X-Ray Diffraction Metallogeny	N30°54,97′/W007°51,97′	The sample is collected from a quartz-chlorite sulfide vein cutting across the granodiorite. Sulfides are shown in Figure 15E
23IM13C	Assarag	Askaoun granodiorite	X-Ray Diffraction	N30°54,99′/W007°51,96′	The sample is collected from a quartz-chlorite sulfide vein cutting across the granodiorite
22IM20	Ougougane	Imourgane	X-Ray Diffraction	N30°55,32′/W007°51,93′	The sample is collected from a silicic alteration zone
T1	Ougougane	Imourgane	X-Ray Diffraction	N30°55,21′/W007°52,20′	The sample is collected from the wall's galleries
J23IM08	Assarag	Askaoun granodiorite	Metallogeny	N30°55,57′/W007°51,80′	Sulfide dissemination (Figure 15C)
J23IM10	Ougougane	Imourgane	Metallogeny	N30°55,91′/W007°51,71′	Sulfide dissemination (Figure 15F)

Table A2. Whole-rock major and trace element geochemical data of the Late Ediacaran granite of the TV area (in percent "%" for major elements and part-per-million "ppm" for trace elements).

	23IM7A	23IM09	23IM19	23IM22	23IM24	23IM7B	23IM14	23IM28	23IM13	23IM26	23IM26′	23IM26″	23IM17	23IM23	23IM25	23IM26‴	23IM27
SiO_2	72.39	76.68	73.72	77.02	75.54	57.4	64.75	58.91	73.25	74.53	76.49	75.99	66.54	64.64	64.31	66.99	61.83
Al_2O_3	14.11	11.98	13.21	12.27	12.26	17.43	15.55	16.57	13.1	13.16	13.24	12.95	14.47	14.17	15.52	14.96	14.88
FeO	0.54	0.4	1.93	0.76	0.95	9.01	5.49	7.76	1.9	2.29	0.66	1.66	4.1	5.57	5.25	4.57	5.49
MnO	0.009	0.013	0.034	0.007	0.024	0.115	0.08	0.132	0.019	0.063	0.007	0.032	0.074	0.107	0.091	0.085	0.135
MgO	0.12	0.12	0.29	0.36	0.38	4.46	1.9	2.76	0.62	0.62	0.24	0.42	1.64	2.34	2.21	1.77	2.74
CaO	0.14	0.23	0.96	0.14	0.12	0.64	2.29	4.81	0.23	0.2	0.15	0.48	1.15	2.22	3.43	3.18	3.77
Na_2O	3.35	2.93	3.78	3.52	3.47	2.31	2.21	3.09	3.68	3.79	3.26	3.66	3.9	3.4	3.49	3.41	4.18
K_2O	6.87	5.72	3.9	4.05	5	2.9	4.11	1.77	4.44	3.88	4.81	4.32	4.04	4.08	3.58	3.66	2.9
TiO_2	0.067	0.083	0.179	0.049	0.043	0.712	0.71	0.778	0.191	0.181	0.203	0.179	0.527	0.721	0.697	0.615	0.71
P_2O_5	0.02	0.04	0.06	0.02	0.02	0.1	0.14	0.15	0.06	0.05	0.05	0.06	0.1	0.13	0.14	0.12	0.15
LOI	0.26	0.64	0.79	0.89	3.15	4.15	1.86	2.52	1.1	0.3	0.71	1.02	1.58	1.58	0.9	0.8	2.07
Total	97.86	98.84	98.85	99.07	101	99.22	99.09	99.25	98.59	99.06	99.83	100.8	97.97	98.95	99.62	100.2	98.84
Sc	1	2	3	2	2	14	13	16	3	2	3	2	9	14	13	11	14
Be	1	1	2	1	<1	2	2	1	1	2	2	2	2	1	1	1	1
V	<5	<5	9	<5	<5	108	69	135	7	8	9	9	65	105	96	77	78
Ba	1812	1313	815	674	971	376	1946	437	674	645	500	771	844	1068	1055	1006	797
Sr	62	78	123	53	47	93	231	376	54	56	34	87	187	220	342	256	386
Y	11	14	24	12	10	18	27	18	23	20	23	17	22	25	22	22	21
Zr	75	71	136	58	52	144	261	142	147	145	141	126	274	246	242	254	258
Cr	<20	<20	<20	<20	<20	40	30	30	<20	<20	20	<20	<20	30	30	30	30
Co	76	80	63	72	84	34	59	42	129	54	56	68	53	77	69	65	52
Ni	<20	<20	<20	<20	<20	30	<20	30	<20	<20	<20	<20	<20	<20	<20	<20	<20
Cu	<10	10	<10	<10	30	40	10	70	<10	<10	<10	<10	20	50	40	50	140
Zn	<30	60	<30	<30	<30	90	70	110	<30	<30	<30	<30	120	90	70	70	110
Ga	15	12	17	14	15	25	20	23	17	17	17	17	19	18	19	19	20
Ge	1	1	2	<1	<1	1	1	1	1	1	1	1	1	1	1	1	1
As	<5	<5	<5	<5	<5	<5	5	17	<5	<5	<5	<5	9	8	10	15	9
Rb	153	141	140	104	133	154	140	63	129	95	137	147	126	147	116	144	105
Nb	3	7	9	6	6	8	10	7	11	12	11	10	9	9	9	9	9
Mo	<2	<2	<2	<2	<2	<2	<2	<2	> 100	18	5	63	3	<2	2	<2	<2
Ag	<0.5	<0.5	<0.5	<0.5	<0.5	<0.5	<0.5	<0.5	<0.5	<0.5	<0.5	<0.5	0.5	<0.5	<0.5	<0.5	<0.5
La	24.3	28.2	30.3	11.6	8.4	22.9	35.8	22.7	60.6	47.3	13.1	45.5	23.9	29.7	29.1	32.4	30.3
Ce	61.9	49.9	58.3	23.1	17.7	38.8	72.7	43.7	126	101	26.6	86.9	54.1	60.8	58.8	63.4	61.4
Pr	4.79	5.62	6.66	2.51	2.08	4.76	8.49	5.25	14.1	10.1	3.11	9.28	5.83	7.14	6.79	7.11	6.85
Nd	15.9	18.9	23.4	8.6	7.3	17.7	31.6	20.8	48.2	33.5	11.4	31.9	22.2	26.2	25.2	26.3	26
Sm	2.5	3.2	4.1	1.7	1.6	3.4	6.2	4.2	7.5	5.3	2.5	4.8	4.8	5.1	4.8	5	5
Eu	0.41	0.5	0.56	0.21	0.22	0.69	1.08	1.1	0.6	0.7	0.37	0.57	0.83	0.85	0.91	0.84	0.96
Gd	1.8	2.5	3.7	1.5	1.5	3.2	5.4	3.6	4.9	3.7	2.7	3.2	4.3	4.6	4	4.1	4.2
Yb	1.4	1.8	2.9	1.4	1.5	2.2	2.8	1.9	2.7	2.5	2.6	2	2.5	2.3	2.1	2.2	2.3
Lu	0.25	0.31	0.47	0.25	0.25	0.36	0.43	0.29	0.43	0.43	0.41	0.34	0.38	0.39	0.35	0.37	0.35
Hf	2.7	2.7	4.2	2.1	2	4.3	7.4	3.9	4.2	4.5	4.2	3.7	7.5	6.6	6.5	7.2	7
Ta	1.8	2.3	2.2	1.9	2	0.9	1.6	1	2.9	1.9	2.2	2.1	1.5	1.6	1.5	1.4	1.4
Tb	0.3	0.4	0.6	0.3	0.3	0.5	0.8	0.6	0.7	0.6	0.5	0.5	0.7	0.7	0.6	0.6	0.7
Dy	1.7	2.3	3.9	1.8	1.8	3.5	4.9	3.3	3.9	3.5	3.5	2.9	4.1	4.2	3.8	4.2	4
Ho	0.3	0.5	0.8	0.4	0.4	0.7	1	0.6	0.8	0.7	0.7	0.6	0.9	0.8	0.7	0.8	0.8
Er	1.1	1.5	2.4	1.2	1.2	2.1	2.8	1.9	2.3	2.3	2.4	1.8	2.4	2.5	2.2	2.4	2.3
Tm	0.19	0.25	0.38	0.21	0.2	0.31	0.42	0.27	0.37	0.35	0.37	0.29	0.36	0.37	0.32	0.33	0.34
W	616	666	548	561	620	151	457	249	1020	455	540	670	393	536	479	429	402
Tl	0.6	0.7	0.4	0.4	0.6	0.5	0.4	0.2	0.5	0.4	0.4	0.5	0.5	0.6	0.4	0.6	0.4
Bi	<0.4	<0.4	<0.4	<0.4	<0.4	<0.4	<0.4	<0.4	<0.4	<0.4	<0.4	<0.4	<0.4	<0.4	<0.4	<0.4	<0.4
Th	18.8	18.4	19.7	8.7	8.8	8.1	16.1	6.6	15.8	15.9	17	15.9	23.1	15	15.2	18	13.2
U	4.2	5.2	6.5	4.2	5.1	3.4	8.5	4.2	4.5	8.5	12	8	14.3	4.6	8.4	5.8	8.3
In	<0.2	<0.2	<0.2	<0.2	<0.2	<0.2	<0.2	<0.2	<0.2	<0.2	<0.2	<0.2	<0.2	<0.2	<0.2	<0.2	<0.2
Sn	<1	<1	<1	<1	1	1	1	1	2	5	2	1	2	1	1	1	1
Sb	<0.5	<0.5	<0.5	<0.5	<0.5	0.9	1.3	2	<0.5	<0.5	<0.5	<0.5	1.7	2.1	2	3.5	3.5
Cs	0.9	0.7	0.7	0.9	0.5	2.2	2.3	0.9	1.2	1	1.2	0.8	0.8	1.8	0.9	1	0.7
Pb	<5	14	9	<5	6	<5	20	7	<5	7	<5	7	25	24	14	24	18

Table A3. Quantitative results for the molybdenite dissemination (MD) and the molybdenite veinlet (MV) samples.

Element Line	Net Counts	Weight %	Weight % Error	Atom %	Atom % Error	Compnd %
MD sample						
Si K	1550	0.32	± 0.06	0.60	± 0.11	0.32
Si L	0	---	---	---	---	---
S K	168319	41.59	± 1.59	67.77	± 2.59	41.59
S L	0	---	---	---	---	---
Mo L	177420	58.09	± 2.30	31.63	± 1.25	58.09
Mo M	1229	---	---	---	---	---
Total		100.00		100.00		100.00
MV sample						
Mg K	827	0.16	± 0.02	0.33	± 0.05	0.16
Al K	439	0.08	± 0.03	0.16	± 0.05	0.08
Si K	3130	0.59	± 0.05	1.07	± 0.10	0.59
Si L	0	---	---	---	---	---
S K	194626	43.51	± 0.65	68.85	± 1.03	43.51
S L	0	---	---	---	---	---
Fe K	418	0.45	± 0.11	0.41	± 0.10	0.45
Fe L	0	---	---	---	---	---
Mo L	186335	55.21	± 1.13	29.19	± 0.60	55.21
Mo M	1586	---	---	---	---	---
Total		100.00		100.00		100.00

Table A4. LA–ICP–MS U-Pb data for the J23IM09 and J23IM13 samples of the Imourgane and Imourkhssen granites, respectively.

					Data for Tera–Wasserburg Plot								Data for Wetherill Plot					Dates						Conc -Age	2s	% Conc
Sample	f206c	^{206}Pb	Uppm	Th/U	^{206}Pb/^{204}Pb	1s%	^{238}U/^{206}Pb	1s%	^{207}Pb/^{206}Pb	1s%	^{208}Pb/^{206}Pb	1s%	^{207}Pb/^{235}U	1s%	^{206}Pb/^{238}U	1s%	Rho	^{207}Pb/^{235}U	2s	^{206}Pb/^{238}U	2s	^{207}Pb/^{206}Pb	2s			
J23IM09																										
IM09_42	1.82	113,465.01	1856	0.22	1628.79	32.76	22.04	2.0	0.06581	2.26	0.101656532	1.542769	0.4116	2.8	0.04538	2.1	0.60	350.0	16.4	286.1	11.8	799.4	94.6	291.6	12.0	36.3
IM09_13	2.06	161,550.20	2640	0.22	994.70	36.67	20.04	1.2	0.07010	1.33	0.118650273	1.143269	0.4821	1.5	0.04990	1.1	0.51	399.5	10.2	313.9	6.9	930.5	56.1	322.6	7.0	34.0
IM09_50	0.78	130,894.92	1530	0.60	−10,479.33	−55.20	17.08	1.7	0.06632	1.44	0.114750055	1.084423	0.5352	2.6	0.05856	1.8	0.85	435.3	18.2	366.9	12.6	815.6	59.5	336.3	12.1	45.9
IM09_8	−0.47	136,017.00	1340	0.20	2367.08	44.04	13.80	1.9	0.05827	1.18	0.068617945	2.542060	0.5821	2.5	0.07249	2.1	0.86	465.8	18.3	451.1	18.7	539.0	55.0	459.2	18.3	86.6
IM09_30	−0.04	162,532.62	1901	0.22	−302.55	−203.07	12.22	0.8	0.05836	0.90	0.055314891	1.154858	0.6581	1.0	0.08182	0.8	0.53	513.5	8.2	507.0	7.5	542.5	39.3	509.6	6.9	95.7
IM09_28	−0.09	115,708.43	1276	0.28	3101.82	41.18	12.00	2.6	0.06029	2.27	0.063703567	1.698743	0.6923	4.2	0.08333	2.7	0.88	534.2	34.8	515.9	27.1	613.0	96.4	509.3	26.8	89.0
IM09_29	−0.28	148,949.72	1918	0.43	231.34	599.99	11.81	1.6	0.05738	1.77	0.106412593	2.185354	0.6695	2.1	0.08466	1.6	0.55	520.4	17.1	523.9	16.5	505.2	80.2	522.3	14.8	107.4
IM09_36	0.09	165,969.27	1000	0.31	1162.37	100.19	11.74	1.6	0.05969	1.20	0.080819076	1.358081	0.7007	1.5	0.08518	1.5	0.71	539.2	12.9	527.0	15.4	591.3	50.4	536.6	12.8	91.0
IM09_38	−0.10	97,428.57	583	0.28	185.45	204.35	11.67	0.5	0.05898	1.32	0.078596684	2.589182	0.6964	1.3	0.08568	0.5	0.18	536.7	10.9	529.9	5.2	565.4	57.4	530.8	5.0	98.2
IM09_47	0.28	99,263.60	937	0.33	−2107.03	−29.71	11.66	0.6	0.05814	1.34	0.083235690	1.769080	0.6874	1.3	0.08579	0.6	0.20	531.2	11.0	530.6	5.9	534.1	58.6	530.7	5.6	102.3
IM09_18	0.71	128,793.30	1105	0.23	−17.07	−6060.72	11.64	0.7	0.05913	2.02	0.067701160	2.391053	0.6998	2.0	0.08588	0.7	0.22	538.7	17.1	531.1	7.3	570.8	87.6	531.8	7.2	93.2
IM09_33	−0.05	126,750.48	688	0.30	4346.80	34.68	11.64	0.5	0.05920	0.96	0.076141230	1.083022	0.7009	1.0	0.08590	0.5	0.34	539.3	8.5	531.2	4.7	573.6	42.0	532.2	4.6	95.8
IM09_15	−0.32	137,915.60	1182	0.26	583.68	93.37	11.59	0.8	0.06018	1.59	0.064202238	1.395470	0.7157	1.6	0.08629	0.8	0.25	548.1	13.5	533.5	8.2	609.3	68.9	536.5	7.7	89.3
IM09_27	0.35	177,923.11	1987	0.21	4040.33	32.73	11.54	0.9	0.05922	0.91	0.056072724	0.776586	0.7069	1.2	0.08662	0.9	0.67	542.9	10.4	535.5	9.3	574.0	40.0	537.9	9.0	95.4
IM09_49	0.29	115,149.47	956	0.34	−1373.76	−98.54	11.54	2.1	0.05892	1.84	0.092323916	2.197912	0.7038	2.4	0.08667	2.0	0.65	541.1	20.4	535.8	20.5	563.3	82.8	538.4	18.6	97.7
IM09_24	−0.54	68,982.24	628	0.42	−5165.33	−322.65	11.52	0.6	0.05965	1.37	0.102088125	1.580077	0.7135	1.3	0.08680	0.6	0.14	546.8	11.1	536.6	5.9	589.8	58.9	538.4	5.5	94.4
IM09_37	0.15	145,672.41	814	0.30	788.66	88.77	11.42	0.8	0.05946	0.96	0.077821272	1.931281	0.7174	1.0	0.08754	0.8	0.43	549.1	8.5	541.0	8.0	582.9	42.0	544.6	7.0	95.4
IM09_41	−0.05	147,896.77	1350	0.36	273.42	198.16	11.40	0.8	0.05835	0.89	0.091891479	1.362570	0.7058	1.1	0.08776	0.9	0.64	542.2	9.4	542.3	8.9	542.1	38.3	542.2	8.3	102.5
IM09_9	−0.01	99,319.66	725	0.27	1085.33	49.34	11.32	0.5	0.05841	1.18	0.068986597	1.371982	0.7113	1.2	0.08836	0.5	0.14	545.5	9.7	545.8	4.9	544.4	51.6	545.8	4.6	102.9
IM09_23	−0.55	100,882.77	851	0.45	−3659.90	−38.32	11.28	0.5	0.05854	1.18	0.120289034	3.089733	0.7155	1.2	0.08868	0.5	0.26	548.0	10.4	547.7	4.9	549.1	52.2	547.8	4.8	103.6
IM09_12	0.61	37,544.25	358	0.23	−81.17	−154.45	11.23	0.7	0.05857	1.93	0.059050253	1.809297	0.7188	1.9	0.08904	0.7	0.22	549.9	16.5	549.9	7.9	550.2	83.7	549.9	7.6	107.7
IM09_22	−0.28	128,486.91	1012	0.27	−5413.91	−26.57	11.21	0.6	0.05893	1.03	0.068883865	2.037317	0.7246	1.0	0.08923	0.6	0.30	553.4	8.9	551.0	6.3	563.4	45.2	551.6	5.8	100.0
IM09_31	0.31	153,624.47	904	0.26	−13,357.62	−30.23	11.20	0.6	0.05922	1.00	0.065719123	1.417447	0.7289	1.1	0.08930	0.7	0.51	555.9	9.8	551.4	7.2	574.3	43.0	552.3	7.0	99.4
IM09_21	0.19	105,753.52	790	0.36	−3438.12	−28.15	11.19	0.5	0.05820	1.19	0.088292712	1.228585	0.7170	1.1	0.08940	0.5	0.02	548.9	9.2	552.0	5.6	536.3	52.3	551.2	4.8	105.9
IM09_40	−0.40	116,156.81	733	0.34	−472.08	−81.88	11.18	0.5	0.05932	1.07	0.086265604	1.564234	0.7312	1.1	0.08945	0.5	0.34	557.3	9.6	552.3	5.7	577.8	46.4	553.1	5.5	98.9
IM09_19	−0.48	123,754.99	945	0.29	−530.61	−88.81	11.16	1.1	0.05791	1.14	0.072851558	1.851605	0.7153	1.5	0.08962	1.1	0.65	547.9	12.8	553.3	12.0	525.4	50.4	551.0	11.2	107.4
IM09_43	0.25	85,408.40	819	0.27	−572.00	−57.53	11.15	0.7	0.05852	1.21	0.070307712	1.586753	0.7232	1.2	0.08966	0.7	0.28	552.5	10.4	553.5	7.2	548.5	53.1	553.2	6.6	104.8
IM09_25	−0.22	117,840.94	1126	0.26	7043.18	41.79	11.15	0.4	0.05801	1.04	0.064470472	1.181541	0.7170	1.1	0.08969	0.4	0.32	548.9	9.3	553.7	4.4	529.1	45.5	553.3	4.3	108.0
IM09_32	0.45	137,655.95	753	0.24	25,790.67	30.01	11.15	0.5	0.05936	1.02	0.064902098	2.617898	0.7340	1.1	0.08972	0.5	0.37	558.9	9.4	553.9	5.4	579.4	44.7	554.5	5.3	99.0
IM09_1	0.28	76,280.36	566	0.35	−633.43	−63.69	11.10	1.4	0.06049	1.70	0.096842375	1.944924	0.7508	2.0	0.09007	1.5	0.59	568.7	17.6	555.9	15.9	620.2	71.7	560.6	15.0	92.9
IM09_17	13.53	6411.62	52	2.44	−1.72	−1273.33	11.09	1.6	0.18980	2.76	0.858867869	1.438672	2.3580	2.5	0.09014	1.6	0.16	1230.0	35.7	556.4	17.4	2739.7	90.7	579.0	17.7	20.5
IM09_7	−0.07	298,971.72	2201	0.27	13,274.24	35.64	11.10	1.0	0.05836	1.06	0.072648344	1.134184	0.7248	1.4	0.09011	1.0	0.63	553.5	11.7	556.2	11.1	542.4	47.6	555.1	10.3	104.0
IM09_20	−0.27	92,546.02	665	0.24	−71.33	−417.68	11.09	0.6	0.05787	1.42	0.061718028	1.576752	0.7189	1.4	0.09014	0.6	0.16	550.0	11.7	556.3	6.5	523.8	62.2	555.1	6.0	109.7
IM09_51	0.44	139,636.21	980	0.20	1402.05	56.65	10.97	2.1	0.05699	1.54	0.059687397	2.018009	0.7159	2.1	0.09115	2.1	0.74	548.2	18.0	562.3	22.6	490.1	67.7	549.7	17.8	116.2
IM09_5	−0.97	32,809.19	225	0.24	1992.02	928.31	10.79	0.6	0.05852	2.25	0.061926834	1.715075	0.7472	2.1	0.09265	0.6	−0.24	566.6	17.9	571.2	6.0	548.5	98.4	570.5	5.2	114.0
IM09_14	0.09	188,290.70	1901	0.34	1501.70	61.13	10.56	1.5	0.05940	2.04	0.088092270	2.132788	0.7754	2.7	0.09472	1.6	0.63	582.9	24.3	583.4	17.8	580.8	92.7	583.3	17.7	104.7
IM09_45	0.53	130,358.05	1097	0.31	−1153.73	−85.19	10.47	2.1	0.05862	1.58	0.078505954	1.819150	0.7715	2.5	0.09549	2.2	0.77	580.6	21.8	587.9	24.7	552.1	70.2	582.3	21.4	108.7
IM09_48	0.24	80,335.21	696	0.33	−1348.49	−37.90	10.47	0.7	0.05958	1.42	0.086234864	2.048943	0.7840	1.5	0.09547	0.7	0.29	587.7	13.0	587.8	7.7	587.5	61.5	587.8	7.3	103.6
IM09_16	9.41	8501.25	67	2.54	−23.84	−124.06	10.35	1.1	0.18396	2.22	0.854025101	1.320554	2.4485	2.1	0.09657	1.1	0.21	1257.0	30.9	594.3	12.2	2688.2	72.3	593.2	12.4	22.3
IM09_35	0.76	102,677.26	466	0.21	1088.03	58.95	10.25	2.1	0.05802	1.49	0.055250821	2.185268	0.7801	2.7	0.09755	2.3	0.82	585.5	23.6	600.0	25.9	529.6	66.1	588.9	23.0	118.7
IM09_2	17.04	5455.27	33	2.25	−102.27	−48.47	9.24	1.7	0.22251	3.64	0.912762464	1.977918	3.3177	2.9	0.10819	1.5	−0.07	1485.2	46.0	662.2	19.5	2998.2	110.3	722.8	18.9	22.4
IM09_34	25.20	2733.39	9	1.77	35.23	58.44	7.50	2.3	0.36833	3.54	1.054242935	2.695861	6.7716	4.7	0.13340	2.5	0.67	2082.0	83.4	807.2	37.5	3783.9	107.7	588.7	31.2	21.7
J23IM13																										
IM13_15	0.53	147,533.31	1119	0.40	−450.29	−98.48	12.53	1.4	0.05924	1.21	0.078222216	1.249097	0.6518	1.8	0.07984	1.4	0.72	509.6	14.6	495.1	13.6	574.8	55.5	500.4	13.2	88.2
IM13_49	0.64	110,748.18	935	0.23	−331.89	−119.70	12.00	0.7	0.06165	1.08	0.069503892	1.566091	0.7081	1.3	0.08334	0.7	0.54	543.6	10.8	516.0	7.2	661.1	46.4	518.8	7.2	81.2
IM13_34	0.80	139,589.03	1709	0.33	−4450.49	−38.85	11.75	1.0	0.05905	1.87	0.076412682	1.368866	0.6925	2.1	0.08510	1.0	0.47	534.3	17.6	526.5	9.8	567.8	81.8	526.9	9.8	96.9
IM13_35	−0.54	105,941.95	1020	0.35	−3270.66	−39.08	11.31	0.4	0.05911	1.66	0.086070256	1.822950	0.7205	1.6	0.08845	0.4	0.00	551.0	13.6	546.3	4.6	570.2	72.3	546.8	4.3	100.0
IM13_26	0.44	133,027.24	1054	0.26	−1611.77	−45.20	11.23	0.5	0.05751	1.19	0.064977190	1.306250	0.7057	1.1	0.08904	0.5	0.00	542.2	8.9	549.9	4.9	510.2	50.7	548.1	4.3	109.5
IM13_41	−0.24	160,436.72	1274	0.39	2326.15	56.42	11.23	0.6	0.05854	0.95	0.094449391	1.611378	0.7184	1.2	0.08905	0.6	0.60	549.7	10.1	549.9	6.2	548.9	42.3	549.9	6.2	104.3
IM13_54	−0.18	104,782.17	868	0.27	888.64	60.09	11.23	0.7	0.05858	1.31	0.071699025	2.290324	0.7191	1.3	0.08908	0.7	0.27	550.2	11.2	550.1	7.3	550.5	57.2	550.1	6.8	104.8
IM13_16	0.49	127,901.11	854	0.38	−379.70	−127.15	11.21	0.8	0.05860	1.28	0.096080793	1.117857	0.7207	1.4	0.08923	0.7	0.39	551.1	11.6	551.0	7.8	551.3	55.7	551.0	7.4	102.4
IM13_48	0.03	122,383.66	961	0.24	731.00	103.46	11.19	0.8	0.06035	2.20	0.061771237	1.989648	0.7436	2.2	0.08940	0.8	0.16	564.5	18.7	552.0	8.2	615.3	94.3	553.4	7.9	92.7
IM13_42	−0.67	100,111.59	810	0.27	774.08	70.18	11.18	0.5	0.05826	1.21	0.069183336	2.188661	0.7181	1.2	0.08942	0.6	0.27	549.5	10.4	552.1	5.9	538.7	52.5	551.7	5.7	107.7
IM13_44	−0.03	115,836.08	852	0.41	1432.47	65.84	11.17	0.6	0.05882	1.40	0.094624155	1.457772	0.7254	1.3	0.08949	0.6	0.08	553.9	11.3	552.5	6.1	559.5	61.0	552.8	5.5	102.8
IM13_23	0.22	132,400.68	1237	0.35	−779.71	−77.94	11.17	2.0	0.05792	1.77	0.078672272	2.986619	0.7148	2.8	0.08954	2.1	0.78	547.6	23.9	552.8	22.1	525.8	78.3	551.0	21.4	107.9
IM13_6	0.42	89,477.78	947	0.31	1395.99	62.19	11.17	0.7	0.06017	1.78	0.063985802	2.649602	0.7423	1.8	0.08951	0.7	0.24	563.7	15.6	552.6	7.4	608.9	76.4	553.8	7.2	94.4
IM13_9	0.40	65,994.37	621	0.24	−1965.39	−42.32	11.15	0.6	0.05919	1.83	0.064447794	4.362465	0.7319	2.0	0.08972	0.6	0.43	557.7	17.5	553.9	6.6	573.1	80.8	553.8	6.6	100.4
IM13_53	−0.26	49,261.05	418	0.32	834.03	44.95	11.14	0.7	0.05958	2.27	0.082380675	2.488174	0.7370	2.3	0.08975	0.7	0.17	560.6	19.6	554.0	7.6	587.5	98.2	554.6	7.4	104.1
IM13_17	1.38	87,767.81	578	0.38	240.40	131.51	11.14	0.9	0.05911	1.33	0.101777241	2.334647	0.7311	1.5	0.08976	0.9	0.48	557.2	13.0	554.1	9.2	570.0	58.0	554.7	8.9	99.7
IM13_36	−0.06	54,280.28	538	0.48	−731.14	−53.58	11.13	1.6	0.05801	1.84	0.120337029	2.034620	0.7182	2.2	0.08983	1.8	0.60	549.6	18.9	554.5	18.9	529.3	80.5	552.0	16.9	111.0
IM13_11	−0.23	163,860.51	1282	0.35	−3922.11	−28.20	11.14	0.7	0.06043	1.17	0.090428852	1.170878	0.7477	1.3	0.08977	0.8	0.47	566.9	11.4	554.2	8.0	618.2	50.5	556.6	7.8	90.6
IM13_20	0.41	112,039.04	723	0.40	−1102.63	−50.89	11.13	0.5	0.05873	1.18	0.103191626	1.141426	0.7273	1.2	0.08985	0.5	0.18	555.0	10.1	554.7	5.0	556.2	51.9	554.7	4.8	101.8

Table A4. *Cont.*

		Data for Tera–Wasserburg Plot									Data for Wetherill Plot						Dates						Conc -Age	2s	% Conc
Sample	f206c	^{206}Pb	U$_{ppm}$	Th/U	^{206}Pb/^{204}Pb	1s%	^{238}U/^{206}Pb	1s%	^{207}Pb/^{206}Pb	1s%	^{208}Pb/^{206}Pb	1s%	^{207}Pb/^{235}U	1s%	^{206}Pb/^{238}U	1s%	Rho	^{207}Pb/^{235}U	2s	^{206}Pb/^{238}U	2s	^{207}Pb/^{206}Pb	2s			
IM13_12	0.34	93,512.91	681	0.26	59.05	577.72	11.13	0.4	0.05798	1.23	0.065409197	1.451185	0.7183	1.2	0.08988	0.4	0.07	549.6	10.0	554.9	4.6	528.1	53.8	554.0	4.3	107.0
IM13_3	−0.13	148,766.49	1500	0.34	1503.88	64.08	11.12	0.6	0.05923	1.48	0.081113927	1.368830	0.7338	1.5	0.08990	0.6	0.19	558.8	12.6	554.9	6.6	574.5	64.1	555.6	6.2	97.3
IM13_43	−0.20	89,308.87	740	0.42	817.54	72.34	11.12	0.7	0.05818	1.37	0.107712452	1.852263	0.7211	1.4	0.08994	0.8	0.34	551.3	12.2	555.2	8.1	535.4	60.6	554.4	7.6	110.1
IM13_25	0.33	96,562.84	782	0.44	−451.12	−90.23	11.09	0.6	0.05746	1.17	0.106879351	1.328882	0.7142	1.3	0.09019	0.6	0.44	547.2	11.1	556.6	6.4	508.3	51.9	555.7	6.3	113.3
IM13_55	−0.23	90,481.69	734	0.46	526.49	67.63	11.08	0.7	0.05884	1.30	0.107549014	1.279030	0.7317	1.2	0.09023	0.6	0.09	557.6	10.4	556.9	6.8	560.2	57.4	557.1	5.9	103.9
IM13_50	0.59	113,672.47	846	0.39	−337.24	−143.96	11.07	1.8	0.06161	1.78	0.108557100	1.498952	0.7672	3.1	0.09036	2.2	0.82	578.2	27.3	557.6	23.4	659.6	76.7	558.6	23.9	90.6
IM13_7	0.11	102,662.94	983	0.29	8291.72	222.96	11.04	0.4	0.05999	1.23	0.073550934	1.271346	0.7487	1.1	0.09055	0.5	0.01	567.4	9.9	558.8	4.8	602.4	53.0	560.4	4.4	94.6
IM13_24	−0.08	160,638.02	1383	0.33	745.50	119.38	11.03	1.4	0.05910	1.58	0.084129965	1.708132	0.7382	2.0	0.09064	1.3	0.60	561.4	17.0	559.3	14.2	569.7	68.8	559.9	13.7	99.2
IM13_27	1.15	99,831.71	714	0.43	−2017.12	−79.95	11.03	0.7	0.05834	2.74	0.108375047	2.255178	0.7292	2.9	0.09069	0.7	0.39	556.1	24.9	559.6	7.7	541.6	118.7	559.7	7.6	106.5
IM13_8	0.46	120,910.30	1211	0.38	−6090.48	−44.82	11.03	0.7	0.05860	1.41	0.091002477	1.054368	0.7325	1.4	0.09070	0.7	0.20	558.0	12.0	559.7	7.4	551.2	62.3	559.3	6.8	104.3
IM13_10	0.08	128,480.70	1209	0.38	−1535.32	−77.61	11.01	0.6	0.06091	1.59	0.093252216	1.419036	0.7625	1.5	0.09083	0.6	0.02	575.4	13.2	560.5	6.2	635.0	68.9	563.0	5.6	89.1
IM13_5	0.14	119,308.67	1225	0.35	2271.39	49.07	10.99	0.6	0.06008	1.44	0.087078501	0.902088	0.7536	1.5	0.09102	0.6	0.21	570.3	12.7	561.6	6.0	605.4	62.7	562.6	5.8	94.8
IM13_29	0.21	111,713.12	889	0.34	−383.84	−118.77	10.97	0.5	0.05901	1.08	0.079388664	0.988541	0.7411	1.1	0.09113	0.5	0.23	563.0	9.1	562.2	5.8	566.4	46.6	562.4	5.4	101.7
IM13_21	−0.40	161,314.06	1256	0.38	−2162.87	−32.48	10.96	0.8	0.05862	1.15	0.088702902	1.317675	0.7371	1.4	0.09124	0.8	0.62	560.7	12.3	562.9	8.7	552.0	49.1	562.6	8.7	103.8
IM13_1	0.57	86,884.00	776	0.30	82.95	338.19	10.95	0.6	0.06001	1.27	0.083938084	3.599114	0.7550	1.5	0.09129	0.6	0.48	571.1	12.9	563.2	6.6	602.9	56.0	563.3	6.6	97.4
IM13_31	0.26	144,575.99	1668	0.40	106.18	477.09	10.95	1.1	0.05757	2.21	0.093619397	2.073641	0.7247	2.5	0.09133	1.1	0.41	553.4	21.4	563.4	11.3	512.5	100.9	562.6	11.2	116.7
IM13_39	0.03	100,297.21	849	0.27	−7731.54	−27.24	10.94	0.6	0.05741	1.17	0.070715278	1.263577	0.7234	1.1	0.09142	0.6	0.17	552.7	9.7	563.9	6.1	506.5	52.2	561.2	5.5	116.2
IM13_58	−0.20	147,215.03	1215	0.32	596.25	92.72	10.92	0.5	0.05850	0.96	0.083069719	1.540365	0.7383	1.1	0.09157	0.5	0.50	561.4	9.5	564.8	5.4	547.7	41.8	564.6	5.4	107.0
IM13_52	−0.29	69,707.24	531	0.41	1468.18	46.09	10.90	0.5	0.05805	1.55	0.107016081	2.603264	0.7339	1.5	0.09173	0.5	0.00	558.8	12.6	565.7	5.3	530.8	67.9	564.7	4.9	113.1
IM13_56	1.10	87,406.21	740	0.30	886.20	44.52	10.90	0.9	0.05745	1.58	0.078624198	1.475047	0.7266	1.5	0.09177	0.9	0.24	554.5	13.1	566.0	9.8	507.9	69.7	562.3	8.7	117.6
IM13_22	0.31	156,323.77	1311	0.41	−1604.66	−58.22	10.90	1.1	0.06023	1.11	0.103068820	2.003954	0.7617	1.4	0.09176	1.1	0.62	575.0	11.9	565.9	11.6	610.9	47.1	570.1	10.7	91.7
IM13_37	−0.52	80,362.95	763	0.46	−1991.26	−44.33	10.89	0.6	0.05757	1.56	0.099873606	1.355422	0.7285	1.6	0.09183	0.6	0.20	555.7	13.3	566.3	7.0	512.4	68.4	564.6	6.7	118.3
IM13_51	−0.20	118,399.91	932	0.38	6100.86	33.01	10.86	1.3	0.05812	1.02	0.090155355	1.802596	0.7377	1.7	0.09209	1.4	0.78	561.0	14.6	567.9	15.1	533.4	46.5	563.9	13.9	111.4
IM13_18	−0.20	117,878.12	783	0.34	−126.24	−349.95	10.81	0.7	0.05846	1.61	0.084755922	1.805144	0.7451	1.4	0.09248	0.8	0.08	565.4	12.5	570.2	8.2	546.1	68.4	568.8	7.1	105.8
IM13_45	1.74	44,565.77	325	0.35	246.15	96.17	10.80	0.7	0.06105	2.31	0.097219699	1.756498	0.7787	2.2	0.09255	0.7	−0.03	584.8	19.4	570.6	7.6	640.1	99.6	572.6	7.0	96.1
IM13_19	0.33	130,761.47	814	0.40	−339.65	−124.23	10.80	0.5	0.05964	1.09	0.098772336	0.997957	0.7612	1.3	0.09261	0.6	0.54	574.7	11.4	571.0	6.3	589.6	47.8	571.0	6.3	98.8
IM13_38	−0.18	110,061.75	956	0.20	−2590.83	−56.77	10.77	1.7	0.05788	1.68	0.049271998	1.427632	0.7410	2.4	0.09289	1.7	0.72	563.0	20.5	572.6	18.4	524.3	72.6	569.5	17.7	114.9
IM13_47	−0.51	68,121.92	528	0.21	201.43	139.60	10.75	0.5	0.05971	1.39	0.057103024	2.027474	0.7652	1.5	0.09299	0.5	0.31	577.0	13.0	573.2	5.7	592.2	61.0	573.4	5.6	102.8
IM13_14	−0.31	124,210.46	765	0.37	−969.96	−57.81	10.72	1.8	0.05818	1.59	0.091099598	2.533829	0.7483	2.3	0.09333	2.0	0.73	567.2	20.2	575.2	21.9	535.5	70.1	569.9	19.3	109.6
IM13_46	−0.51	89,226.11	686	0.34	−49.52	−460.24	10.72	0.5	0.05770	1.27	0.086775141	1.888714	0.7421	1.3	0.09332	0.5	0.23	563.7	11.2	575.2	5.4	517.5	56.0	573.7	5.2	118.2
IM13_33	−0.06	89,593.37	978	0.36	−353.36	−115.38	10.71	0.7	0.05815	1.20	0.088873497	2.804020	0.7479	1.3	0.09333	0.7	0.39	567.0	11.5	575.2	7.4	534.3	53.8	573.7	7.1	113.1
IM13_30	0.41	52,307.02	376	0.20	−620.39	−73.43	10.71	0.7	0.05944	2.62	0.048122591	2.385948	0.7647	2.4	0.09334	0.7	−0.17	576.7	21.4	575.3	8.0	582.4	114.9	575.5	7.0	105.2
IM13_4	0.59	72,465.89	741	0.26	565.16	54.49	10.71	1.0	0.05886	2.21	0.066866732	1.775229	0.7576	2.1	0.09339	1.1	0.18	572.6	18.6	575.6	12.0	561.0	96.0	574.8	10.8	106.5
IM13_57	0.25	89,756.77	743	0.21	511.45	64.57	10.67	1.9	0.05861	1.17	0.052707283	1.772673	0.7568	2.0	0.09369	1.8	0.83	572.2	17.4	577.4	19.9	551.6	48.9	572.8	17.3	108.8
IM13_32	−0.34	104,143.31	1131	0.43	−2354.77	−27.97	10.67	1.4	0.05846	1.14	0.103238028	1.054163	0.7553	1.9	0.09375	1.4	0.79	571.3	17.0	577.7	15.7	546.0	52.1	575.6	15.2	110.2
IM13_59	−0.11	87,044.51	683	0.20	213.33	162.94	10.65	0.5	0.05838	1.38	0.050685443	1.866758	0.7554	1.5	0.09389	0.5	0.33	571.3	12.9	578.5	5.3	542.9	61.0	578.2	5.3	112.2
IM13_13	0.28	110,912.19	770	0.43	−699.05	−61.21	10.61	1.2	0.05924	1.32	0.105976791	1.501405	0.7693	1.8	0.09423	1.3	0.71	579.4	16.2	580.5	14.0	574.9	56.2	580.2	13.7	104.4
IM13_2	0.97	44,639.49	419	0.23	346.72	54.14	10.58	0.6	0.05952	1.89	0.056390584	2.796483	0.7751	2.0	0.09450	0.6	0.23	582.7	17.6	582.1	7.1	585.1	84.1	582.1	6.9	107.4
IM13_28	0.14	108,327.20	804	0.48	−1388.23	−42.88	10.45	1.4	0.05779	1.33	0.110251321	1.149506	0.7622	1.9	0.09570	1.4	0.70	575.3	16.3	589.2	15.3	520.9	57.8	583.4	14.4	116.3
IM13_40	0.34	25,969.57	191	0.29	−2437.47	−32.93	10.16	0.7	0.05847	2.39	0.078128186	2.595515	0.7934	2.4	0.09846	0.7	0.06	593.1	21.2	605.4	7.9	546.5	105.8	604.0	7.5	129.4
IM13_60	−0.21	41,358.80	287	0.57	−189.01	−101.40	10.12	1.0	0.06110	2.67	0.145046360	1.762176	0.8324	2.9	0.09886	1.0	0.36	615.0	26.7	607.7	11.5	641.6	116.4	608.0	11.5	103.2

Table A5. LA–ICP–MS U-Pb data for the Plešovice as a secondary reference material.

				Data for Wetherill plot						Data for Tera–Wasserburg plot						Dates				Uppm	%Conc
Identifier	**f206c**	**^{206}Pb**	**Th/U**	**^{206}Pb/^{204}Pb**	**1s%**	**^{207}Pb/^{235}U**	**1s%**	**^{206}Pb/^{238}U**	**1s%**	**Rho**	**^{238}U/^{206}Pb**	**1s%**	**^{207}Pb/^{206}Pb**	**1s%**	**^{208}Pb/^{206}Pb**	**1s%**	**^{207}Pb/^{206}Pb 2s**		**^{206}Pb/^{238}U 2s**		**^{207}Pb/^{235}U 2s**			
Ples_23	0.75	53,639.15	0.10	−475.66	−55.12	0.3910	1.9	0.05333	0.7	0.14	18.75	0.7	0.05320	1.91	0.026077042	2.334217	336.1	86.3	335	4.4	335.1	10.7	755	113.2
Ples_24	0.65	51,582.22	0.10	−333.03	−59.50	0.3930	1.6	0.05398	0.5	0.15	18.53	0.6	0.05283	1.58	0.026185734	2.417102	320.5	71.5	338.9	3.6	336.6	9	753	117.0
Ples_21	−0.16	54,056.98	0.10	−710.06	−44.95	0.3849	1.9	0.05355	0.6	0.18	18.68	0.6	0.05215	1.85	0.026301091	2.096167	291.1	84.6	336.3	3.9	330.6	10.5	756	132.3
Ples_22	0.50	56,947.94	0.10	−481.16	−58.94	0.4003	1.5	0.05406	0.6	0.35	18.50	0.6	0.05372	1.42	0.026484392	2.432624	358.4	63.7	339.4	3.9	341.8	8.7	756	100.5
Ples_19	0.34	64,492.82	0.10	−717.73	−42.90	0.3862	1.4	0.05306	0.5	−0.07	18.85	0.5	0.05282	1.54	0.026989844	2.255749	320	70.4	333.3	3.4	331.6	8.1	759	110.7
Ples_20	−0.68	60,841.23	0.10	−128.01	−151.71	0.3967	1.6	0.05380	0.5	0.15	18.59	0.5	0.05351	1.57	0.027760912	2.252616	349.3	71.1	337.8	3.1	339.2	9.1	749	103.6
Ples_17	−0.13	50,483.61	0.10	−538.81	−38.77	0.4027	1.7	0.05417	0.6	0.04	18.46	0.6	0.05394	1.76	0.024589258	2.786096	367.6	78.8	340.1	4.1	343.6	9.7	761	102.4
Ples_18	0.94	45,108.48	0.10	−145.53	−91.66	0.3929	1.9	0.05352	0.6	0.16	18.68	0.6	0.05326	1.90	0.025098741	2.681902	339	85.8	336.1	4	336.5	10.9	746	113.5
Ples_15	0.22	57,762.89	0.10	3293.35	38.95	0.3978	1.8	0.05339	0.7	0.16	18.73	0.7	0.05406	1.79	0.026339451	2.085549	372.7	81.5	335.3	4.6	340.1	10.3	759	102.5
Ples_16	−0.10	56,786.00	0.10	3399.06	30.13	0.4058	1.5	0.05379	0.6	0.08	18.59	0.6	0.05473	1.60	0.026293593	2.371205	400.3	72	337.8	3.9	345.8	9	751	92.9
Ples_13	0.38	58,465.39	0.10	−3269.51	−25.66	0.3986	1.6	0.05351	0.5	0.03	18.69	0.5	0.05406	1.65	0.025898016	2.310606	372.5	74.2	336	3.2	340.7	9.2	755	100.9
Ples_14	0.87	58,262.30	0.10	−7853.69	−40.70	0.3842	1.5	0.05413	0.5	0.05	18.48	0.5	0.05150	1.58	0.030559173	3.721279	262.2	72.9	339.8	3.6	330.1	8.6	754	152.0
Ples_12	−0.53	58,000.28	0.10	−412.24	−50.33	0.3962	1.5	0.05373	0.5	0.04	18.61	0.5	0.05350	1.62	0.027386150	2.289054	349.2	73	337.4	3.6	338.9	8.9	755	106.2
Ples_9	−0.87	55,100.71	0.10	−229.31	−86.58	0.3907	1.7	0.05361	0.6	−0.03	18.65	0.6	0.05288	1.84	0.026982504	2.353171	322.6	82.5	336.6	3.8	334.9	9.7	758	114.0
Ples_10	0.35	50,624.57	0.10	181.71	103.68	0.3932	1.6	0.05346	0.6	0.00	18.70	0.6	0.05337	1.66	0.026793920	2.393834	343.4	75.9	335.7	3.8	336.7	9	750	105.5
Ples_7	−0.54	65,704.87	0.10	−1017.31	−33.47	0.3838	2.0	0.05366	0.5	0.06	18.64	0.5	0.05190	2.03	0.027179428	2.478643	280	92.8	336.9	3.6	329.8	11.2	756	140.8
Ples_8	−0.08	64,016.75	0.10	−881.40	−36.59	0.3945	1.5	0.05359	0.4	0.21	18.66	0.4	0.05342	1.48	0.026915904	2.317759	345.5	66.6	336.5	2.8	337.7	8.6	755	104.6
Ples_5	1.06	57,925.43	0.10	−378.49	−78.35	0.3958	1.9	0.05341	0.7	0.10	18.72	0.7	0.05377	1.92	0.031027944	4.375674	360.2	88.7	335.4	4.5	338.6	11	746	104.3
Ples_6	−0.21	70,445.41	0.10	−2120.34	−32.08	0.3977	1.3	0.05407	0.4	−0.05	18.50	0.4	0.05337	1.43	0.026248336	2.105787	343.4	64.8	339.5	2.9	340	7.7	764	107.5
Ples_4	0.52	53,505.12	0.10	−311.05	−66.13	0.3899	1.7	0.05365	0.5	−0.08	18.64	0.5	0.05273	1.85	0.026213515	2.597983	316.1	84.4	336.9	3.5	334.3	9.9	753	121.1
Ples_2	0.55	61,258.80	0.10	344.80	81.34	0.3948	1.5	0.05357	0.5	0.15	18.67	0.5	0.05347	1.50	0.026234842	2.470396	347.9	67.7	336.4	3.6	337.9	8.5	756	102.4

References

1. Sillitoe, R.H. Porphyry Copper Systems. *Econ. Geol.* **2010**, *105*, 3–41. [CrossRef]
2. Sun, W.; Huang, R.F.; Li, H.; Hu, Y.B.; Zhang, C.C.; Sun, S.J.; Zhang, L.P.; Ding, X.; Li, C.Y.; Zartman, R.E.; et al. Porphyry Deposits and Oxidized Magmas. *Ore Geol. Rev.* **2015**, *65*, 97–131. [CrossRef]
3. Sinclair, W. Porphyry Deposits. In *Understanding Mineral Deposits*; Geological Association of Canada, Mineral Deposits Division: St. John's, NL, Canada, 2007; pp. 353–413.
4. Cooke, D.R.; Hollings, P.; Walshe, J. Giant Porphyry Deposits: Characteristics, Distribution, and Tectonic Controls. *Turk. J. Fish. Aquat. Sci.* **2005**, *18*, 539–546. [CrossRef]
5. Lee, C.T.A.; Tang, M. How to Make Porphyry Copper Deposits. *Earth Planet. Sci. Lett.* **2020**, *529*, 115868. [CrossRef]
6. Jébrak, M.; Marcoux, E. *Géologie des Ressources Minérales*; Association Géologique du Canada: St. John's, NL, Canada, 2008; Volume 33, ISBN 9782551237371.
7. Sillitoe, R.H. Special Paper: Major Gold Deposits and Belts of the North and South American Cordillera: Distribution, Tectonomagmatic Settings, and Metallogenic Considerations. *Econ. Geol.* **2008**, *103*, 663–687. [CrossRef]
8. Seedorff, E.; Dilles, J.H.; Proffett, J.M.; Einaudi, M.T.; Zurcher, L.; Stavast, W.J.; Johnson, D.A.; Barton, M.D. *Porphyry Deposits—Characteristics & Origin of Hypogene Features*; Society of Economic Geologists: Littleton, CO, USA, 2005.
9. Zhiming, Y.; Cooke, D.R. Chapter 5 Porphyry Copper Deposits in China. *Miner. Depos. China* **2019**, *22*, 133–187.
10. Di Tommaso, I.; Rubinstein, N. Hydrothermal Alteration Mapping Using ASTER Data in the Infiernillo Porphyry Deposit, Argentina. *Ore Geol. Rev.* **2007**, *32*, 275–290. [CrossRef]
11. Lowell, J.D.; Guilbert, J. Lateral and Vertical Alteration-Mineralization Zoning in Porphyry Ore Deposit. *Econ. Geol.* **1970**, *65*, 373–408. [CrossRef]
12. Mouttaqi, A.; Rjimati, E.; Maacha, L.; Michard, A.; Soulaimani, A.; Ibouh, H. Main Mines of Morocco. *N. Geol. Min. Guid. Morocco* **2011**, *564*, 3–376.
13. Bouabdellah, M.; Chekroun, F.; Alansari, A.; Margoum, D. The Granitoid-Related Tiouit Gold Deposit, Saghro Inlier, Eastern Anti-Atlas (Morocco): Neoproterozoic Mineralization by a Polyphase Late-Magmatic to Hydrothermal System. In *Mineral Deposits of North Africa*; Springer: Berlin/Heidelberg, Germany, 2016; pp. 405–414. [CrossRef]
14. El Azmi, D.; Aissa, M.; Ouguir, H.; Mahdoudi, M.L.; El Azmi, M.; Ouadjo, A.; Zouhair, M. Magmatic Context of Bou Skour Copper Deposit (Eastern Anti-Atlas, Morocco): Petrogrography, Geochemistry and Alterations. *J. Afr. Earth Sci.* **2014**, *97*, 40–55. [CrossRef]
15. Tuduri, J.; Chauvet, A.; Barbanson, L.; Bourdier, J.L.; Labriki, M.; Ennaciri, A.; Badra, L.; Dubois, M.; Ennaciri-Leloix, C.; Sizaret, S.; et al. The Jbel Saghro Au(–Ag, Cu) and Ag–Hg Metallogenetic Province: Product of a Long-Lived Ediacaran Tectono-Magmatic Evolution in the Moroccan Anti-Atlas. *Minerals* **2018**, *8*, 592. [CrossRef]
16. Belkacim, S. Pétrographie, Géochimie et Isotopes (Sr-Nd) Du Volcanisme Édiacarien et Des Dykes Doléritiques de La Vallée de Tifnoute et Caractérisation Des Indices de Cu-Mo±Au d'Imourkhssan (Siroua, Anti-Atlas Central, Maroc). Ph.D. Thesis, Department of Geology, Faculty of Sciences of Agadir, Ibn Zohr Univesity, Agadir, Morocco, 2014.
17. Ennih, N.; Liégeois, J.P. The Moroccan Anti-Atlas: The West African Craton Passive Margin with Limited Pan-African Activity. Implications for the Northern Limit of the Craton. *Precambrian Res.* **2001**, *112*, 289–302. [CrossRef]
18. Karaoui, B.; Breitkreuz, C.; Mahmoudi, A.; Youbi, N.; Hofmann, M.; Gärtner, A.; Linnemann, U. U-Pb Zircon Ages from Volcanic and Sedimentary Rocks of the Ediacaran Bas Draâ Inlier (Anti-Atlas Morocco): Chronostratigraphic and Provenance Implications. *Precambrian Res.* **2015**, *263*, 43–58. [CrossRef]
19. Gasquet, D.; Ennih, N.; Liégeois, J.P.; Soulaimani, A.; Michard, A. The Pan-African Belt. *Lect. Notes Earth Sci.* **2008**, *116*, 33–64. [CrossRef]
20. Álvaro, J.J.; Benziane, F.; Thomas, R.; Walsh, G.J.; Yazidi, A. Neoproterozoic-Cambrian Stratigraphic Framework of the Anti-Atlas and Ouzellagh Promontory (High Atlas), Morocco. *J. Afr. Earth Sci.* **2014**, *98*, 19–33. [CrossRef]
21. Thomas, R.J.; Chevallier, L.P.; Gresse, P.G.; Harmer, R.E.; Eglington, B.M.; Armstrong, R.A.; De Beer, C.H.; Martini, J.E.J.; De Kock, G.S.; Macey, P.H.; et al. Precambrian Evolution of the Sirwa Window, Anti-Atlas Orogen, Morocco. *Precambrian Res.* **2002**, *118*, 1–57. [CrossRef]
22. Triantafyllou, A.; Berger, J.; Baele, J.M.; Diot, H.; Ennih, N.; Plissart, G.; Monnier, C.; Watlet, A.; Bruguier, O.; Spagna, P.; et al. The Tachakoucht-Iriri-Tourtit Arc Complex (Moroccan Anti-Atlas): Neoproterozoic Records of Polyphased Subduction-Accretion Dynamics during the Pan-African Orogeny. *J. Geodyn.* **2016**, *96*, 81–103. [CrossRef]
23. Triantafyllou, A.; Berger, J.; Baele, J.M.; Mattielli, N.; Ducea, M.N.; Sterckx, S.; Samson, S.; Hodel, F.; Ennih, N. Episodic Magmatism during the Growth of a Neoproterozoic Oceanic Arc (Anti-Atlas, Morocco). *Precambrian Res.* **2020**, *339*, 105610. [CrossRef]
24. Samson, S.D.; Inglis, J.D.; D'Lemos, R.S.; Admou, H.; Blichert-Toft, J.; Hefferan, K. Geochronological, Geochemical, and Nd-Hf Isotopic Constraints on the Origin of Neoproterozoic Plagiogranites in the Tasriwine Ophiolite, Anti-Atlas Orogen, Morocco. *Precambrian Res.* **2004**, *135*, 133–147. [CrossRef]
25. D'Lemos, R.S.; Inglis, J.D.; Samson, S.D. A Newly Discovered Orogenic Event in Morocco: Neoproterozic Ages for Supposed Eburnean Basement of the Bou Azzer Inlier, Anti-Atlas Mountains. *Precambrian Res.* **2006**, *147*, 65–78. [CrossRef]
26. Samson, S.D. Isotopically Juvenile, yet Chemically Evolved Granites: A Neoproterozoic Example from the Anti-Atlas Mountains, Morocco. *Geochim. Cosmochim. Acta* **2006**, *70*, A553. [CrossRef]

27. Belkacim, S.; Gasquet, D.; Liégeois, J.P.; Arai, S.; Gahlan, H.A.; Ahmed, H.; Ishida, Y.; Ikenne, M. The Ediacaran Volcanic Rocks and Associated Mafic Dykes of the Ouarzazate Group (Anti-Atlas, Morocco): Clinopyroxene Composition, Whole-Rock Geochemistry and Sr-Nd Isotopes Constraints from the Ouzellarh-Siroua Salient (Tifnoute Valley). *J. Afr. Earth Sci.* **2017**, *127*, 113–135. [CrossRef]
28. Gasquet, D.; Levresse, G.; Cheilletz, A.; Azizi-Samir, M.R.; Mouttaqi, A. Contribution to a Geodynamic Reconstruction of the Anti-Atlas (Morocco) during Pan-African Times with the Emphasis on Inversion Tectonics and Metallogenic Activity at the Precambrian-Cambrian Transition. *Precambrian Res.* **2005**, *140*, 157–182. [CrossRef]
29. Toummite, A.; Liegeois, J.P.; Gasquet, D.; Bruguier, O.; Beraaouz, E.H.; Ikenne, M. Field, Geochemistry and Sr-Nd Isotopes of the Pan-African Granitoids from the Tifnoute Valley (Sirwa, Anti-Atlas, Morocco): A Post-Collisional Event in a Metacratonic Setting. *Mineral. Petrol.* **2012**, *107*, 739–763. [CrossRef]
30. Schulte, B.; Boger, S.D.; Benziane, F.; Yazidi, A.; Fanning, C.M. The Ouarzazate Supergroup and Its Plutonic Keel: The Relicts of an Ediacaran Silicic Large Igneous Province in North Africa. *J. Geol. Soc. Lond.* **2022**, *179*, 1–18. [CrossRef]
31. Hollard, H.; Suter, G.; Didon, J.; Guardia, P.; du Dresnay, R.; Medioni, R.; Choubert, G.; Faure-Muret, A. Carte Géologique Du Maroc Au 1/1,000,000. *Notes Mémoires Serv. Géologique Maroc Feuille Nord.* **1985**, *260*, 1–96.
32. Belkacim, S.; Perrot, M.; Davies, J.; Liégeois, J.P.; Ikenne, M. The Ediacaran Ouarzazate Group, a Metacratonic Silicic Large Igneous Province (SLIP): New U-Pb Zircon Ages from Ouzellarh-Siroua Salient (Tifnoute Valley, Morocco). In *Geological Society o f America Northeastern Section (NEGSA)*; The Geological Society of America: Boulder, CO, USA, 2021.
33. Ewan, P.; Alain, C.; Dominique, G.; Abdellah, M.; Mohammed, A.; Quentin, C.; Etienne, D.; Lofti, O.; Ouchtouban, L.; Bounjama, H. U/Pb Ages of Magmatism in the Zgounder Epithermal Ag–Hg Deposit, Sirwa Window, Anti-Atlas, Morocco. In *Mineral Deposits of North Africa*; Springer: Berlin/Heidelberg, Germany, 2016.
34. Perrot, M.; Tremblay, A.; David, J. Detrital Zircon U-Pb Geochronology of the Magog Group, Southern Quebec—Stratigraphic and Tectonic Implications for the Quebec Appalachians. *Am. J. Sci.* **2017**, *317*, 1049–1094. [CrossRef]
35. Wiedenbeck, M.; Allé, P.; Corfu, F.; Griffin, W.L.; Meier, M.; Oberli, F.; Von Quadt, A.; Roddick, J.C.; Spiegel, W. Three Natural Zircon Standards for U-Th-Pb, Lu-Hf, Trace Element and Ree Analyses. *Geostand. Geoanalytical Res.* **1995**, *19*, 1–23. [CrossRef]
36. Sláma, J.; Košler, J.; Condon, D.J.; Crowley, J.L.; Gerdes, A.; Hanchar, J.M.; Horstwood, M.S.A.; Morris, G.A.; Nasdala, L.; Norberg, N.; et al. Plešovice Zircon—A New Natural Reference Material for U-Pb and Hf Isotopic Microanalysis. *Chem. Geol.* **2008**, *249*, 1–35. [CrossRef]
37. Vermeesch, P. IsoplotR: A Free and Open Toolbox for Geochronology. *Geosci. Front.* **2018**, *9*, 1479–1493. [CrossRef]
38. Thomas, R.J.; Fekkak, A.; Ennih, N.; Errami, E.; Loughlin, S.C.; Gresse, P.G.; Chevallier, L.P.; Liégeois, J.P. A New Lithostratigraphic Framework for the Anti-Atlas Orogen, Morocco. *J. Afr. Earth Sci.* **2004**, *39*, 217–226. [CrossRef]
39. El Moume, W.; Youbi, N.; Marzoli, A.; Profile, S.; Bertrand, H.; Ikenne, M.; Ahmed Boumehdi, M.; Ernst, R.E.; El Hachimi, H.; Khalil Bensalah, M.; et al. Geochemistry of Mafic Dyke Swarms of Douar Eç-Çour (High Atlas, Morocco): The Farthest Record of the Central Iapetus Magmatic Province (CIMP) into West African Craton. *Assoc. Port. Geólogos* **2020**, *33*, 95–124.
40. Dabiri, R.; Akbari-Mogaddam, M.; Ghaffari, M. Geochemical Evolution and Petrogenesis of the Eocene Kashmar Granitoid Rocks, NE Iran: Implications for Fractional Crystallization and Crustal Contamination Processes. *Iran. J. Earth Sci.* **2018**, *10*, 68–77.
41. Chappell, B.W.; White, A.J.R. Two Contrasting Granite Types: 25 Years Later. *Aust. J. Earth Sci.* **2001**, *48*, 489–499. [CrossRef]
42. Liégeois, J.P.; Navez, J.; Hertogen, J.; Black, R. Contrasting Origin of Post-Collisional High-K Calc-Alkaline and Shoshonitic versus Alkaline and Peralkaline Granitoids. The Use of Sliding Normalization. *Lithos* **1998**, *45*, 1–28. [CrossRef]
43. Middlemost, E.A.K. Naming Materials in the Magma/Igneous Rock System. *Earth Sci. Rev.* **1994**, *37*, 215–224. [CrossRef]
44. Maniar, P.D.; Piccoli, P. Tectonic Discrimination of Granitoids. *Geol. Soc. Am. Bull.* **1989**, *101*, 635–643. [CrossRef]
45. Boynton, W.V. Cosmochemistry of the Rare Earth Elements: Meteorite Studies. *Rare Earth Elem. Geochem.* **1983**, *2*, 63–114. [CrossRef]
46. Pearce, J.A.; Harris, N.B.W.; Tindle, A.G. Trace Element Discrimination Diagrams for the Tectonic Interpretation of Granitic Rocks. *J. Petrol.* **1984**, *25*, 956–983. [CrossRef]
47. Pearce, J.A. Petrogenetic Implications of Ti, Zr, Y, and Nb Variations in Volcanic Rocks. *Contrib. to Mineral. Petrol.* **1996**, *69*, 33–47. [CrossRef]
48. Pearce, J.A. Role of the Sub-Continental Lithosphere in Magma Genesis at Active Continental Margins. In *Continental Basalts and Mantle Xenoliths*; Shiva Publications: Natwich, UK, 1983; pp. 230–249.
49. Sylvester, P.J. Archean Granite Plutons. *Dev. Precambrian Geol.* **1994**, *11*, 261–314. [CrossRef]
50. Raeisi, D.; Babazadeh, S.; Long, L.E.; Zhao, M.; Cottle, J.M.; Nayebi, N.; Modabberi, S. Geochemical and Isotopic Signatures, and Zircon U[Sbnd]Pb Ages of the Oldest Known Intrusive Rocks Associated with Porphyry Cu Deposits in the Central Urumieh–Dokhtar Magmatic Arc, Iran. *J. Geochem. Explor.* **2024**, *256*, 107366. [CrossRef]
51. Ferdous, S.; Podder, J. Growth and Characterization of Epsomite Single Crystals Doped with KCl from Low Temperature Aqueous Solutions. *J. Bangladesh Acad. Sci.* **1970**, *33*, 47–54. [CrossRef]
52. Whitney, D.L.; Evans, B.W. Abbreviations for Names of Rock-Forming Minerals. *Am. Mineral.* **2010**, *95*, 185–187. [CrossRef]
53. Warr, L. IMA–CNMNC Approved Mineral Symbols. *Mineral. Mag.* **2021**, *85*, 291–320. [CrossRef]
54. Burisch, M.; Walter, B.F.; Markl, G. Silicification of Hydrothermal Gangue Minerals in Pb-Zn-Cu-Fluoritequartz-Baryte Veins. *Can. Mineral.* **2017**, *55*, 501–514. [CrossRef]
55. Jébrak, M.; Marcoux, É.; Nasloubi, M.; Zaharaoui, M. From Sandstone- to Carbonate-Hosted Strata Bound Deposits: An Isotope Study of Galena in the Upper-Moulouya District (Morocco). *Miner. Depos.* **1998**, *33*, 406–415. [CrossRef]

56. Aït Malek, H.; Gasquet, D.; Bertrand, J.M.; Leterrier, J. Géochronologie U–Pb Sur Zircon de Granitoïdes Éburnéens et Panafricains Dans Les Boutonnières pro- Térozoïques d'Igherm, Du Kerdous et Du Bas Drâa (Anti-Atlas Occidental, Maroc). *Comptes Rendus L'académie Sci.-Ser. IIA-Earth Planet. Sci.* **1998**, *327*, 819–826.
57. Walsh, G.J.; Benziane, F.; Aleinikoff, J.N.; Harrison, R.W.; Yazidi, A.; Burton, W.C.; Quick, J.E.; Saadane, A. Neoproterozoic Tectonic Evolution of the Jebel Saghro and Bou Azzer-El Graara Inliers, Eastern and Central Anti-Atlas, Morocco. *Precambrian Res.* **2012**, *216–219*, 23–62. [CrossRef]
58. Baidada, B.; Ikenne, M.; Barbey, P.; Soulaimani, A.; Cousens, B.; Haissen, F.; Ilmen, S.; Alansari, A. SHRIMP U–Pb Zircon Geochronology of the Granitoids of the Imiter Inlier: Constraints on the Pan-African Events in the Saghro Massif, Anti-Atlas (Morocco). *J. Afr. Earth Sci.* **2019**, *150*, 799–810. [CrossRef]
59. Errami, E.; Bonin, B.; Laduron, D.; Lasri, L. Petrology and Geodynamic Significance of the Post-Collisional Pan-African Magmatism in the Eastern Saghro Area (Anti-Atlas, Morocco). *J. Afr. Earth Sci.* **2009**, *55*, 105–124. [CrossRef]
60. Letsch, D.; Large, S.J.; Buechi, M.W.; Winkler, W.; von Quadt, A. Ediacaran Glaciations of the West African Craton—Evidence from Morocco. *Precambrian Res.* **2018**, *310*, 17–18. [CrossRef]
61. Mifdal, A.; Peucat, J.J. Datation U/Pb et Rb/Sr Du Volcanisme Acide de l'Anti- Atlas Marocain et Du Socle Sous-Jacent Dans La Région de Ouarzazate; Apport Au Problème de La Limite Précambrien-Cambrien. *Sci. Géol.* **1985**, *38*, 185–200.
62. Maloof, A.C.; Schrag, D.P.; Crowley, J.L.; Bowring, S.A. An Expanded Record of Early Cambrian Carbon Cycling from the Anti-Atlas Margin, Morocco. *J. Earth Sci.* **2005**, *42*, 2195–2216. [CrossRef]
63. Walsh, G.J.; Aleiniko, J.N.; Benziane, F.; Yazidi, A.; Armstrong, T.R. U–Pb Zircon Geochronology of the Palaeoproterozoic Tagragra de Tata Inlier and Its Neoproterzoic Cover, Western Anti-Atlas, Morocco. *Precambr. Res* **2002**, *117*, 11–20. [CrossRef]
64. Blein, O.; Baudin, T.; Soulaimani, A.; Cocherie, A.; Chevremont, P.; Admou, H.; Ouanaimi, H.; Hafid, A.; Razin, P.; Bouabdelli, M.; et al. Geochemical, Geochronological and Structural Constraints on the Ediacaran Evolution of the South Sirwa, Agadir-Melloul and Iguerda Inliers, Anti-Atlas, Morocco. *Afr. Earth Sci.* **2014**, *98*, 47–71. [CrossRef]
65. Levresse, G. *Contribution to the Establishment of a Genetic Model of the Imiter (Ag-Hg), Bou Madine (Pb-Zn-Cu-Ag-Au), Bou Azzer (Co-Ni-As-Au-Ag) Deposits in the Moroccan Anti-Atlas*; Institut National Polytechnique de Lorraine: Nancy, France, 2001.
66. O'Connor, E.A. *Geology of the Drâa, Kerdous, and Boumalne Districts, Anti-Atlas, Morocco*; British Geological Survey: Nottingham, UK, 2010.
67. Tuduri, J.; Chauvet, A.; Barbanson, L.; Labriki, M.; Dubois, M.; Trapy, P.-H.; Lahfid, A.; Poujol, M.; Melleton, J.; Badra, L. Structural Control, Magmatic-Hydrothermal Evolution and Formation of Hornfels-Hosted, Intrusion-Related Gold Deposits: Insight from the Thaghassa Deposit in Eastern Anti-Atlas, Morocco. *Ore Geol.* **2018**, *97*, 171–198. [CrossRef]
68. Cheilletz, A.; Levresse, G.; Gasquet, D.; Azizi-Samir, M.; Zyadi, R.; Archibald, D.A.; Farrar, E. The Giant Imiter Silver Deposit: Neoproterozoic Epithermal Mineralization in the Anti-Atlas, Morocco. *Miner. Depos.* **2002**, *37*, 772–781. [CrossRef]
69. Levresse, G.; Cheilletz, A.; Gasquet, D.; Reisberg, L.; Deloule, E.; Marty, B.; Kyser, K. Osmium, Sulphur, and Helium Isotopic Results from the Giant Neoproterozoic Epithermal Imiter Silver Deposit, Morocco: Evidence for a Mantle Source. *Chem. Geol.* **2004**, *207*, 59–79. [CrossRef]
70. Green, T.H. Significance of Nb/Ta as an Indicator of Geochemical Processes in the Crust-Mantle System. *Chem. Geol.* **1995**, *120*, 347–359. [CrossRef]
71. Morris, G.A.; Larson, P.B.; Hooper, P.R. "Subduction Style" Magmatism in a Non-Subduction Setting: The Colville Igneous Complex, NE Washington State, USA. *J. Petrol.* **2000**, *41*, 43–67. [CrossRef]
72. Chen, Y.J.; Zhang, C.; Wang, P.; Pirajno, F.; Li, N. The Mo Deposits of Northeast China: A Powerful Indicator of Tectonic Settings and Associated Evolutionary Trends. *Ore Geol. Rev.* **2017**, *81*, 602–640. [CrossRef]
73. Feteha, B.F.E.; Lentz, D.R.; El Bouseily, A.M.; Khalil, K.I.; Khamis, H.A.; Moghazi, A.K.M. Petrogenesis of Neoproterozoic Mo-Bearing A-Type Granites in the Gattar Area, Northern Eastern Desert, Egypt: Implications for Magmatic Evolution and Mineralization Processes. *Ore Geol. Rev.* **2022**, *148*, 105007. [CrossRef]
74. Wang, X.Q.; Ji, F.B. Petrogenesis and Metallogenic Implications of Eocene–Oligocene Magmatism in the Yulong Porphyry Copper Belt, Eastern Tibet: A Review and Analysis of Geochronological, Geochemical, and Sr–Nd–Pb–Hf Isotopic Data. *Can. J. Earth Sci.* **2024**, *61*, 270–285. [CrossRef]
75. Mao, J.; Zhang, J.; Pirajno, F.; Ishiyama, D.; Su, H.; Guo, C.; Chen, Y. Porphyry Cu-Au-Mo-Epithermal Ag-Pb-Zn-Distal Hydrothermal Au Deposits in the Dexing Area, Jiangxi Province, East China-A Linked Ore System. *Ore Geol. Rev.* **2011**, *43*, 203–216. [CrossRef]
76. Crusius, J.; Calve, S.; Pedersen, T.; Sage, D. Rhenium and Molybdenum Enrichments in Sediments as Indicators of Oxic, Suboxic and Sulfidic Conditions of Deposition. *Earth Planet. Sci. Lett.* **1996**, *145*, 65–78. [CrossRef]
77. Delibaş, O.; Moritz, R.; Chiaradia, M.; Selby, D.; Ulianov, A.; Revan, M.K. Post-Collisional Magmatism and Ore-Forming Systems in the Menderes Massif: New Constraints from the Miocene Porphyry Mo–Cu Pınarbaşı System, Gediz–Kütahya, Western Turkey. *Miner. Depos.* **2017**, *52*, 1157–1178. [CrossRef]
78. Lowery Claiborne, L.; Miller, C.F.; Walker, B.A.; Wooden, J.L.; Mazdab, F.K.; Bea, F. Tracking Magmatic Processes through Zr/Hf Ratios in Rocks and Hf and Ti Zoning in Zircons: An Example from the Spirit Mountain Batholith, Nevada. *Mineral. Mag.* **2006**, *70*, 517–543. [CrossRef]
79. Carten, R.B.; White, W.H.; Stein, H. *High-Grade-Granite Related Molybdenium Systems: Classification and Origin*; Geological Association of Canada: St. John's, NS, Canada, 1993; pp. 521–544.

80. Ferraq, M.; Belkacim, S.; Cheng, L.Z.; Alansari, A. Le Porphyre-Épithermal à Cu-Mo-Au-Ag d'Imourkhssen, Anti-Atlas Central, Maroc: Aperçu Des Données Métallogéniques, Géochimiques et Aéromagnétiques et Implications Pour l'exploration Minière. In *Posted Communication*; Québec Mines et Energies: Québec, QC, Canada, 2023.
81. Kósaka, H.; Wakita, K. Some Geologic Features of the Mmnut Porphyry Copper Deposit, Sabah, Malaysia. *Econ. Geol.* **1978**, *73*, 618–627. [CrossRef]
82. Candela, P.A.; Holland, H.D. A Mass Transfer Model for Copper and Molybdenum in Magmatic Hydrothermal Systems: The Origin of Porphyry-Type Ore Deposits. *Econ. Geol.* **1986**, *81*, 1–19. [CrossRef]
83. Ernst, R.E.; Bond, D.P.G.; Zhang, S.H.; Buchan, K.L.; Grasby, S.E.; Youbi, N.; El Bilali, H.; Bekker, A.; Doucet, L.S. Large Igneous Province Record Through Time and Implications for Secular Environmental Changes and Geological Time-Scale Boundaries. *Am. Geophys. Union* **2021**, 1–26. [CrossRef]
84. Ernst, R.E.; Jowitt, M.; Thompson, J.F.H. Large Igneous Provinces (LIPs) and Metallogeny. In *Tectonics, Metallogeny, and Discovery: The North American Cordillera and Similar Accretionary Settings*; Society of Economic Geologists, Inc.: Littleton, CO, USA, 2013; pp. 17–51. [CrossRef]
85. Bryan, S.E.; Ferrari, L. Large Igneous Provinces and Silicic Large Igneous Provinces: Progress in Our Understanding over the Last 25 Years. *Bull. Geol. Soc. Am.* **2013**, *125*, 1053–1078. [CrossRef]
86. Abia, E.H.; Nachit, H.; Marignac, C.; Ibhi, A.; Saadi, S.A. The Polymetallic Au-Ag-Bearing Veins of Bou Madine (Jbel Ougnat, Eastern Anti-Atlas, Morocco): Tectonic Control and Evolution of a Neoproterozoic Epithermal Deposit. *J. Afr. Earth Sci.* **2003**, *36*, 251–271. [CrossRef]
87. Rachid Zahour, R.; Zahour, G.; El Hadi, H.; Zerhouni, Y.; Baroudi, Z.; Khoukhouchi, M. Petrology, Geochemistry, and Geodynamic Implications of the Ediacaran Volcanism of the Southwestern Edge of the Saghro Massif (Eastern Anti-Atlas, Morocco). *Turk. J. Earth Sci.* **2022**, *31*, 339–358.
88. Bryan, S.E.; Ferrari, L.; Reiners, P.W.; Allen, C.M.; Petrone, C.M.; Ramos-rosique, A.; Campbell, I.H. New Insights into Crustal Contributions to Large-Volume Rhyolite Generation in the Mid-Tertiary Sierra Madre Occidental Province, Mexico, Revealed by U-Pb Geochronology. *J. Petrol.* **2008**, *49*, 47–77. [CrossRef]
89. Bard, J. *Microtexture des Roches Magmatique et Métamorphiques*; Masson: Issy-les-Moulineaux, France, 1980.
90. Linnemann, U.; Gerdes, A.; Hofmann, M.; Marko, L. The Cadomian Orogen: Neoproterozoic to Early Cambrian Crustal Growth and Orogenic Zoning along the Periphery of the West African Craton-Constraints from U-Pb Zircon Ages and Hf Isotopes (Schwarzburg Antiform, Germany). *Precambrian Res.* **2014**, *244*, 236–278. [CrossRef]
91. Ennih, N.; Liégeois, J.P. The Boundaries of the West African Craton, with Special Reference to the Basement of the Moroccan Metacratonic Anti-Atlas Belt. *Geol. Soc. Spec. Publ.* **2008**, *297*, 1–17. [CrossRef]
92. Cao, M.Y.; Jiang, S.Y.; Su, H.M.; Liu, T. Indosinian Magmatic–Hydrothermal Metallogenic Event in the North Wuyi Area, Southeastern China: An Example from the Chenfang Skarn Deposit in Jiangxi Province. *Ore Geol. Rev.* **2021**, *138*, 104386. [CrossRef]
93. Voudouris, P.; Mavrogonatos, C.; Spry, P.G.; Baker, T.; Melfos, V.; Klemd, R.; Haase, K.; Repstock, A.; Djiba, A.; Bismayer, U.; et al. Porphyry and Epithermal Deposits in Greece: An Overview, New Discoveries, and Mineralogical Constraints on Their Genesis. *Ore Geol. Rev.* **2019**, *107*, 654–691. [CrossRef]
94. Simmons, S.F.; White, N.C.; John, D.A. Geological Characteristics of Epithermal Precious and Base Metal Deposits. *Econ. Geol.* **2005**, 485–522. [CrossRef]
95. Hedenquist, J.; Arribas, A. Evolution of an Intrusion-Centered Hydrothermal System: Far Southeast-Lepanto Porphyry and Epithermal Cu-Au Deposits, Philippine. *Econ. Geol.* **1998**, *93*, 373–404. [CrossRef]
96. Figueroa, A.J.T.; Gabo-Ratio, J.A.S.; Manalo, P.C.; Takahashi, R.; Sato, H.; Ramos, A.B. Breccia and Vein Mineralization of the Balatoc Diatreme, Acupan Gold Deposit, Baguio Mineral District: An Example of a Diatreme-Hosted Epithermal Deposit in the Philippines. *Ore Geol. Rev.* **2022**, *144*, 104826. [CrossRef]
97. Cardon, O.; André-Mayer, A.S.; Sausse, J.; Milu, V.; Chauvet, A.; Leroy, J.L.; Lespinasse, M.; Udubasa, S. The Link between Porphyry Copper and Low-Sulfidation Epithermal Deposit: Structural Study and 3D Representation of the Sector of Bolcana, Apuseni Mountains, Romania. *Comptes Rendus—Geosci.* **2004**, *337*, 824–831. [CrossRef]
98. Nance, R.D.; Guti Errez-Alonso, G.; Keppie, J.D.; Linnemann, U.; Murphy, J.B.; Quesada, C.; Strachan, R.A.; Woodcock, N.H. A Brief History of the Rheic Ocean. *Geosci. Front.* **2012**, *3*, 125–135. [CrossRef]
99. Ouabid, M.; Garrido, C.J. Widespread Cadomian–Pan-African Ediacaran Magmatism across the Moroccan Meseta: Implication for the Geodynamic Evolution of the NW Gondwana Margin. *Precambrian Res.* **2023**, *387*, 106992. [CrossRef]
100. Sparkes, G.W.; Dunning, G.R. Late Neoproterozoic Epithermal Alteration and Mineralization in the Western Avalon Zone: A Summary of Mineralogical Investigations and New U/Pb Geochronological Results. *Curr. Res.* **2014**, *Report 14-1*, 99–128.
101. Arbiol, C.; Layne, G.D.; Zanoni, G.; Šegvić, B. Characteristics and Genesis of Phyllosilicate Hydrothermal Assemblages from Neoproterozoic Epithermal Au-Ag Mineralization of the Avalon Zone of Newfoundland, Canada. *Appl. Clay Sci.* **2021**, *202*, 105960. [CrossRef]
102. Sparkes, G.W.; Ferguson, S.A.; Layne, G.D.; Dunning, G.R.; Brien, S.J.O.; Langille, A. The Nature and Timing of Neoproterozoic High-Sulphidation Gold Mineralization from the Newfoundland Avalon Zone: Insights from New U-Pb Ages, Ore Petrography and Spectral Data From The Hickey's Pond Prospect. *Curr. Res.* **2016**, 91–116.

103. Ferguson, S.A. Late Neoproterozoic Epithermal-Style Au Mineralization of the Burin Peninsula, Newfoundland: U-Pb Geochronology and Deposit Characteristics. Ph.D. Thesis, Memorial University of Newfoundland, St. John's, NL, Canada, 2017.
104. Dubé, B.; Dunning, G.; Lauzière, K. Geology of the Hope Brook Mine, Newfoundland, Canada: A Preserved Late Proterozoic High-Sulfidation Epithermal Gold Deposit and Its Implications for Exploration. *Econ. Geol.* **1998**, *93*, 405–436. [CrossRef]
105. El Haibi, H.; El Hadi, H.; Tahiri, A.; Martínez Poyatos, D.; Gasquet, D.; Pérez-Cáceres, I.; González Lodeiro, F.; Mehdioui, S. Geochronology and Isotopic Geochemistry of Ediacaran High-K Calc-Alkaline Felsic Volcanism: An Example of a Moroccan Perigondwanan (Avalonian?) Remnant in the El Jadida Horst (Mazagonia). *J. Afr. Earth Sci.* **2020**, *163*, 103669. [CrossRef]
106. Jamal, E.K. Geobiology and Lithostratigraphy of the Ediacaran Successions of the Eastern Anti-Atlas (Morocco): Implications for the Geobiological and Geodynamic Evolution of the Northern Margin of the West African Craton. Ph.D. Thesis, Departement of Geology, University of Chouaib Doukkali, El Jadida, Morocco, 2023.

Disclaimer/Publisher's Note: The statements, opinions and data contained in all publications are solely those of the individual author(s) and contributor(s) and not of MDPI and/or the editor(s). MDPI and/or the editor(s) disclaim responsibility for any injury to people or property resulting from any ideas, methods, instructions or products referred to in the content.

minerals

MDPI

Article

Mineral Geochemistry of Sulfides and Oxides and Its Implications for Ore-Forming Mechanisms in the Northeast Saveh Epithermal System, Central Urumieh–Dokhtar Magmatic Arc, Iran

Mohammad Goudarzi [1,2], Hassan Zamanian [3], Urs Klötzli [1,*], Alireza Almasi [2], Sara Houshmand-Manavi [4] and Jiranan Homnan [1]

[1] Department of Lithospheric Research, Faculty of Earth Sciences, Geography and Astronomy, University of Vienna, 1090 Vienna, Austria; goudarzim95@univie.ac.at (M.G.); homnanj94@univie.ac.at (J.H.)
[2] Department of Geology, Faculty of Basic Sciences, Lorestan University, Khorramabad 6815144316, Iran; almasi.al@lu.ac.ir
[3] School of Geology, College of Science, University of Tehran, Tehran 1417935840, Iran; hasanzamanian@ut.ac.ir
[4] Geological Survey and Mineral Exploration of Iran, Tehran 1387835841, Iran; sarahoushmand88@gmail.com
* Correspondence: urs.kloetzli@univie.ac.at

Abstract

We have investigated the major- and trace-element composition of hydrothermal pyrite, magnetite, and Ti-magnetite, and of the principal Cu-minerals chalcopyrite and chalcocite, to constrain ore-forming processes in the northeastern Saveh district (central Urumieh–Dokhtar magmatic arc, Iran). Our data provide new constraints on the magmatic–hydrothermal evolution and subsequent hydrothermal–supergene modification of the ore system. Ti-magnetites hosted in monzodioritic intrusions are enriched in Ti–V–Al, plot below the magnetite–ulvöspinel join and record high crystallization temperatures (<500 °C) under relatively low oxygen fugacity. By contrast, magnetite from silica-rich hydrothermal veins is Fe-rich with very low TiO_2; it formed at intermediate temperatures (~200–300 °C) under higher fO_2 and is markedly depleted in Ti and V compared with the intrusive oxides. Textures and oxide systematics (Al + Mn vs. Ti + V; V/Ti–Fe) document repeated hydrothermal pulses, Fe^{2+} leaching and element redistribution during cooling and fluid–rock interaction. Geochemical trends indicate progressive evolution from a magmatic fluid to later meteoric water overprint, with increasing As contents reflecting cooling and mixing with meteoric waters. Vertical elemental zoning suggests that most samples represent mid- to deep-level sections of the epithermal system. Elevated Cu contents (up to 0.95 wt.%) highlight pyrite as a significant Cu host. Co/Ni ratios between 1 and 10 further corroborate a magmatic–hydrothermal origin. Chalcopyrite is the principal economic Cu carrier at Northeast Saveh. Replacement follows a temperature- and fluid-controlled pathway (chalcopyrite → covellite → chalcocite). At lower temperatures (<~200 °C) replacement proceeds more slowly, producing chalcocite/digenite under prolonged reaction conditions. Chalcocite commonly occurs as thin replacement rims and fracture fills that concentrate remobilized copper. Collectively, the investigated oxide and sulfide proxies provide robust discriminants for separating magmatic versus hydrothermal domains and for vectoring toward higher-temperature feeders and zones of remobilized copper.

Keywords: pyrite trace elements; chalcopyrite; magnetite chemistry; mineral replacement; EPMA; copper mineralization; Urumieh–Dokhtar magmatic arc (UDMA)

1. Introduction

Trace-element concentrations in sulfide and oxide minerals (e.g., pyrite, chalcopyrite, chalcocite, and magnetite) in porphyry and epithermal systems mainly reflect fluid composition, physicochemical conditions, and the stability of the minerals during crystallization [1]. Variations in these factors often lead to significant changes in the trace element contents of these minerals, which serve as vital indicators of fluid evolution and ore formation processes.

Pyrite is the most abundant sulfide in the Earth's crust and a key host for trace elements in magmatic–hydrothermal systems [2,3]. Its chemical composition reflects conditions such as temperature, pH, and oxygen fugacity of the mineralizing fluids and plays a critical role in controlling the distribution of economically valuable elements like Au, Ag, As, and heavy metals [4,5]. Pyrite accommodates trace elements through mechanisms like lattice substitution (e.g., Co, Ni, Cu, As) and the incorporation of nanoparticles or microscale inclusions [3,6]. These features make pyrite an excellent tracer for the evolution of hydrothermal systems.

On the other hand, chalcopyrite ($CuFeS_2$) is the most abundant copper sulfide, contributing to about 70% of global copper production [7]. Its trace element composition varies widely depending on deposit type, reflecting the physicochemical environment during mineralization [8]. Chalcopyrite often coexists with other sulfides, such as chalcocite and bornite, and serves as a primary host for elements like Ag, Bi, Cd, Zn, and Sb. However, its trace element capacity may increase in the absence of other sulfides, making it a valuable tool for understanding ore-forming processes [5,8–10].

As well, magnetite (Fe_3O_4) and Ti-magnetite are ubiquitous in igneous and hydrothermal systems and serve as valuable indicators of mineralization. Magnetite, with its spinel structure, incorporates a range of trace elements that reflect the conditions of fluid or magma evolution [11,12]. Magnetite and members of the magnetite-ulvöspinel solid solution series (Ti-magnetite) can incorporate other elements into their structure. Their chemistry has been widely used to reconstruct physicochemical parameters such as temperature, oxygen fugacity, and sulfur fugacity during ore formation [13,14].

This study presents the first integrated geochemical investigation of sulfides (pyrite, chalcopyrite, chalcocite) and oxides (magnetite, Ti-magnetite) in the Northeast Saveh region to unravel the evolution of the epithermal mineralization system in the central Urumieh–Dokhtar magmatic arc (UDMA). The results offer new insights into the evolution of epithermal/mineralization and magmatic processes in this region, which has received limited research attention despite its significant potential for Cu-Au-Ag mineralization.

2. Geological Background

Magmatic activity in the UDMA began in the Late Cretaceous and persisted intermittently until the Miocene (Figure 1A). The subduction and subsequent rollback of the Neo-Tethys slab during this time led to significant magmatic flare-ups, especially during the Eocene-Oligocene. This period marked a critical tectonic transition from extensional to compressional regimes, which is reflected in the structural and magmatic patterns observed across the arc. The UDMA hosts diverse intrusive and extrusive igneous rocks ranging from basaltic and andesitic volcanic flows to plutonic rocks such as diorites, monzonites, and granites, indicating multiple phases of magmatic evolution [15–18].

https://doi.org/10.3390/min16020212

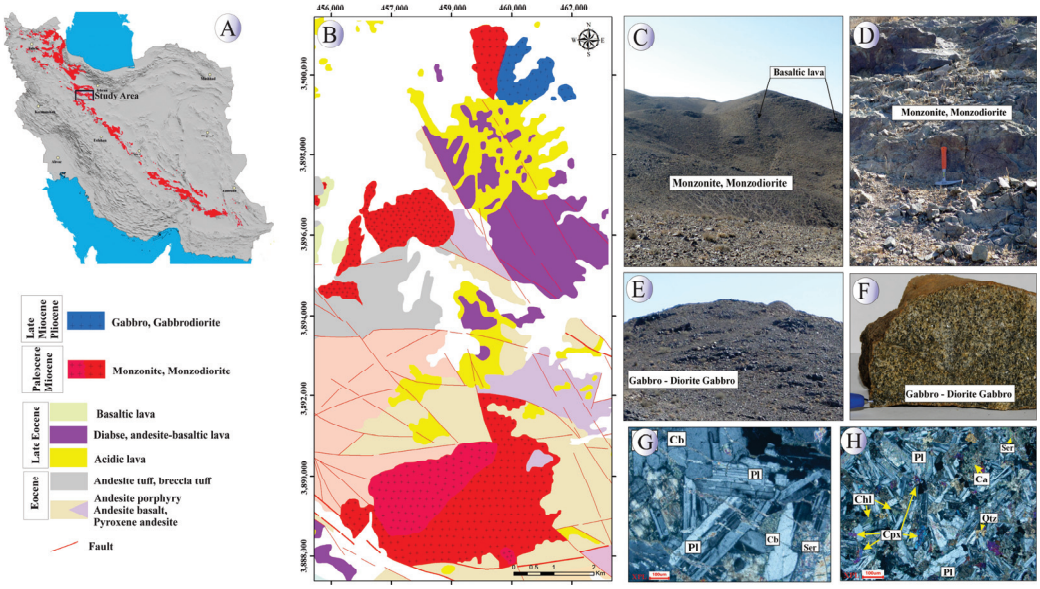


Figure 1. (**A**) Location of the study area in the UDMA (**B**) 1:20,000 geological map of the Northeast Saveh area [17]. (**C**) A view of monzonite–monzodiorite rocks. (**D**) Close-up view of monzonite, Monzo-diorite. (**E**) General view of gabbroic outcrops. (**F**) Close-up view of gabbroic rock. (**G**) Sericitization of plagioclase crystals along polysynthetic twining and fracture filling with carbonate in gabbro-diorite. (**H**) Coarse plagioclase crystals with small clinopyroxene crystal inclusions, where some minerals have been replaced by carbonate and chlorite.

Structurally, the region shows a transition from an extensional regime during the Eocene to a compressional regime in the late Eocene-Oligocene, marked by the development of dextral shear zones and strike-slip faults. This tectonic evolution facilitated the emplacement of plutonic bodies in transtensional settings, with later brittle deformation shaping the observed structural trends. Overall, the magmatic and structural characteristics of the study area reflect its dynamic evolution within the broader context of the Neo-Tethys subduction and the tectonic processes of the Alpine-Himalayan orogenic system.

The study area (Figure 1B), located northeast of Saveh in the central UDMA and approximately 100 km southwest of Tehran, highlights this complex geological history. Field and petrographic studies reveal the presence of two dominant intrusive rock units: monzonite-monzo-diorite and gabbro-gabbro-diorite. These intrusions have interacted with acidic to basic volcanic rocks and are structurally controlled by major west-northwest to east-southeast trending faults associated with the Alpine orogeny [17,18].

The monzonite-monzodiorite unit (Figure 1C,D), forming prominent topographic highs, includes quartz monzonite, monzonite, and monzodiorite compositions. These rocks exhibit granoblastic and porphyritic textures, with primary minerals such as plagioclase, potassium feldspar, hornblende, and clinopyroxene, alongside accessory minerals like apatite, zircon, and chlorite. Intense alteration features, including sericitization and carbonatization, are evident, particularly in plagioclase crystals.

The gabbro-gabbro-diorite unit (Figure 1E,F) is characterized by dark-grey outcrops with hetero-granular textures. These rocks consist of plagioclase, pyroxene, and hornblende, with secondary alteration minerals such as chlorite, epidote, and carbonate. The presence of anti-rapakivi textures and chloritized mafic minerals reflects the influence of hydrothermal fluids during emplacement.

3. Analytical Methods

Seventy polished thin sections were prepared from representative outcrops and drill cores across the mineralized zones for petrographic, mineralogical and micro-analytical

investigations. Twelve of these were selected for detailed textural study and BSE imaging of oxide and sulfide ore phases; all sections were carbon-coated prior to electron-beam work to ensure electrical conductivity.

Prior to quantitative microprobe work, samples were inspected by scanning electron microscopy (SEM) in back-scattered electron (BSE) mode to document textures, identify inclusions and intergrowths, and to guide microprobe spot selection. Quantitative wavelength-dispersive electron probe microanalysis (EPMA) was carried out on a CAMECA SX Five (field-emission cathode) at the Department of Lithospheric Research, University of Vienna. Operating conditions and analytical setup were as follows: an accelerating voltage of 20 kV, a beam current of 25 nA, and a focused electron beam (nominal diameter ≈ 0 μm) rastered over an area of ~60 μm to obtain representative average compositions of oxide-rich domains and coarse sulfide aggregates while minimizing beam damage and local heterogeneity effects. The instrumental configuration (spectrometers and analyzing crystals) and counting times were selected to optimize sensitivity for the targeted major and trace elements. WDS crystals used were LLIF, LTAP, PET and TAP as appropriate for each line.

Analyses were calibrated with certified/well-characterized standards matched to each analyte (e.g., FeS for Fe and S, GaAs for As, PbS for Pb, Zn metal/oxide for Zn, InSb for Sb, Sn metal for Sn, wollastonite for Si, etc.). Intensity-to-concentration calibrations were performed from these standards, and all compositions were corrected for matrix effects using the ZAF routine implemented in the probe software (version 6.2, Cameca)

Peak and background counting times were set individually for each element to maximize sensitivity while controlling analytical time. Repeat analyses of standards and internal consistency checks were performed routinely throughout each analytical run to monitor precision and accuracy; analytical drift was negligible after standard-normalization, and repeatability of matrix-matched standards was typically better than $\pm$2%–5% for majors and within acceptable limits for trace elements.

Because some reported trace concentrations are low, limits of detection were determined empirically for each element under the exact analytical conditions used. LODs were estimated following the commonly used 3σ criterion on background counts (i.e., LOD = 3·σbg, converted to concentration using the measured sensitivity from the corresponding standard), and take into account the peak/background counting times, spectrometer/crystal combination, and instrument sensitivity (cps per nA) logged for each line.

Where measured concentrations fell below the empirically determined LOD for a given element, they are reported as below detection (n.d.) in the data tables and were excluded from log-scale plots or any statistical computations that assume a measured value.

Microprobe spot analyses for the main mineral groups are summarized in Supplementary Tables S1–S5.

4. Mineralization and Mineralogy

4.1. Field Characteristics of Ore and Stages of Mineralization

Mineralization in the Northeast Saveh area primarily occurs within andesitic host rocks, with minor development in monzonitic and gabbroic units. The mineralized zones extend from several tens of meters up to approximately 1 km in length, with copper grades ranging from 0.1 to 5 wt.%. The predominant style of copper mineralization is of a vein and veinlet type, which is generally controlled by fault-related structures trending N–S and N40°W. Based on detailed field observations, six principal mineralized zones have been identified within the host rocks (Figure 2A).

Considering the structural and textural features of ore minerals, several distinct stages of mineralization can be recognized. During the pre-ore stage, pyrite and Ti-magnetite were

https://doi.org/10.3390/min16020212

formed as disseminated grains within the groundmass of the monzonitic and monzodioritic units. These minerals occur as euhedral to anhedral crystals and, to a lesser extent, as vein or veinlet fillings within open spaces. This early mineralization is interpreted to be related to the development of a magmatic–hydrothermal system associated with the emplacement of quartz monzonitic intrusions in the area [19].

Based on Goudarzi et al. 2024 [19], the main hypogene mineralization comprises an early magmatic–hydrothermal pre-ore event and a subsequent principal hydrothermal (ore) pulse. Field, textural and petrographic evidence indicate two generations of pyrite: an earlier, disseminated/hosting-phase pyrite and Fe–Ti oxide dissemination in the igneous host (pre-ore, magmatic–hydrothermal), and a later hydrothermal pyrite that occurs in veins, veinlets, stockworks and occasional xenocrysts within chalcopyrite. The principal hypogene (ore) stage is characterized by quartz ± sulfide ± oxide veinlets dominated by chalcopyrite (the main copper ore), locally accompanied by bornite and specular hematite; these veins display a range of morphologies (open-space, colloform, boxwork, breccia-cement) and crosscut earlier host textures, consistent with a distinct hydrothermal pulse responsible for emplacement of economic sulfide mineralization.

Subsequent supergene evolution is an exogenic process driven by descending meteoric, oxidizing fluids. Oxidation of the upper parts of the sulfide-bearing system produced an oxidation zone, and the resulting leaching and downward transport of copper led to a supergene enrichment horizon at the redox front. Here, secondary sulfides such as chalcocite and covellite (and locally native copper) precipitated by replacement of primary sulfides (e.g., chalcopyrite), while above the redox front continued weathering and oxidation gave rise to oxide–carbonate assemblages (malachite, azurite, cuprite, chrysocolla) and iron oxides/hydroxides (hematite, goethite, limonite) that occur as coatings, earthy masses, and veinlet infillings. Thus, supergene enrichment and the oxidation zone are conjugate near-surface processes. Oxidation creates the chemical gradients that drive Cu leaching and reprecipitation at the redox front and should be treated as linked, exogenic stages rather than as separate hydrothermal events.

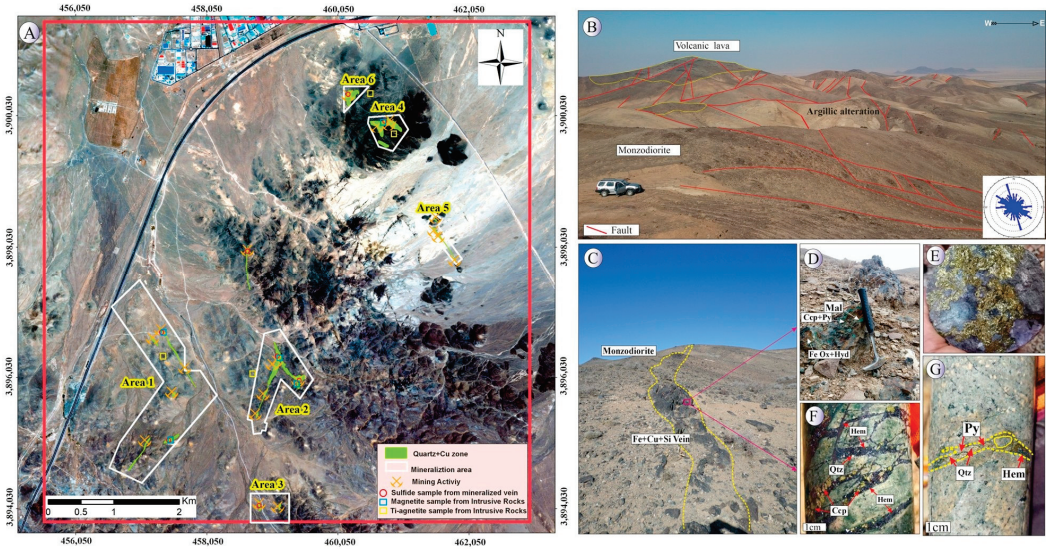


Figure 2. (**A**) Satellite image of the study area, and the location of the mineralization zones and samples. (**B**) General view of the Northeast Saveh area and intrusive-volcanic outcrops. (**C**) Mineralized silica vein containing Cu ore and magnetite. (**D**) A close view of the mineralized silica vein. (**E**) Core drilling sample containing chalcopyrite. (**F**) Core drilling sample containing chalcopyrite and Fe oxide (magnetite-hematite) veins. (**G**) Pyrite vein and Fe oxide in a core drilling sample. Mineral abbreviations after [20]: Py—Pyrite, Ccp—Chalcopyrite, Hem—hematite, Mal—malachite, Mag—magnetite, Qtz—Quartz.

https://doi.org/10.3390/min16020212

4.2. Mineralogy and Textural Characteristics of Sulfide Minerals (Pyrite, Chalcopyrite, Chalcocite)

Pyrite is the most abundant sulfide in the Northeast Saveh area. Detailed examination of hand specimens, reflected-light petrography, and BSE imaging shows two principal generations of pyrite plus a very limited subordinate occurrence of fine inclusions. The **first (early) generation** occurs as euhedral to subhedral grains, typically 100 µm–1 mm in size, disseminated throughout the host rocks and commonly associated with minor chalcopyrite (Figure 3A). These grains are interpreted as products of the early magmatic–hydrothermal (pre-ore) event. In places, the original pyrite morphology is partly preserved despite partial replacement by hematite and goethite, indicating later near-surface oxidation of this generation. The **second (ore-stage) generation** occurs predominantly as vein- and veinlet-filling crystals and as lattice/framework or framboidal textures, consistent with precipitation from later hydrothermal fluids that exploited existing fractures and pore space (Figure 3B,C). Finally, a **very limited subordinate occurrence** of fine-grained pyrite (≈5–20 µm) is observed as inclusions within chalcopyrite (Figure 3D); these micro-crystals are restricted in abundance and spatial extent and are therefore interpreted as a late, minor sub-generation or exsolution/recrystallization product during the final stages of sulfide crystallization. BSE images (Figure 4) illustrate these relationships, showing disseminated first-generation grains, vein-filling second-generation pyrite, and the occasional pyrite inclusions within chalcopyrite.

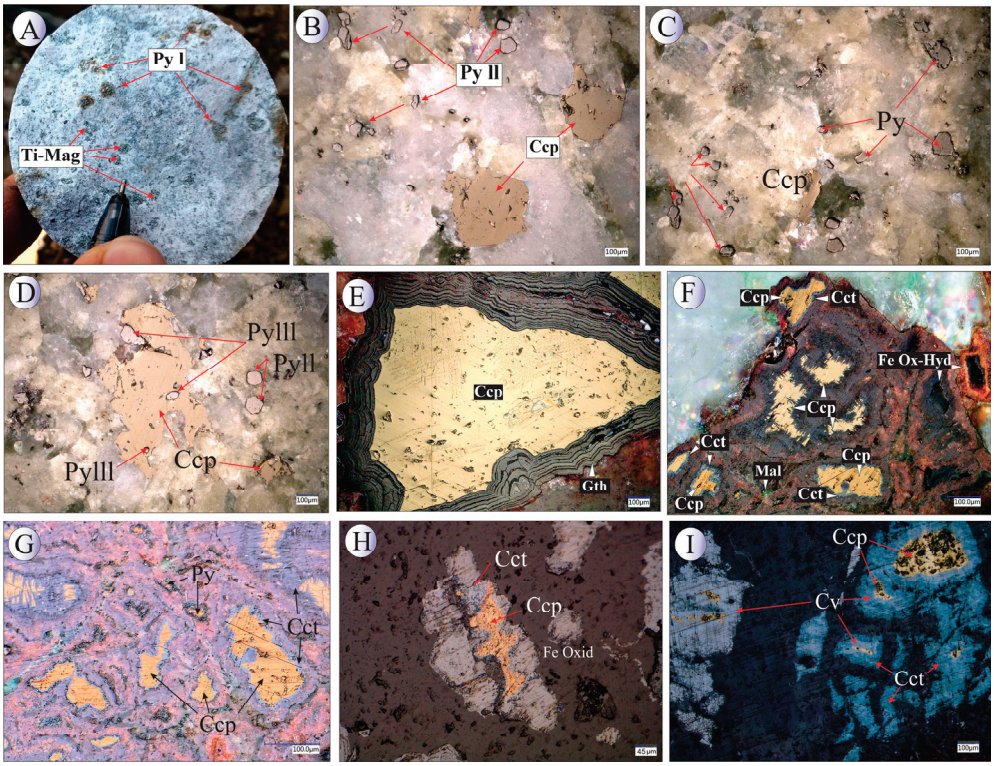


Figure 3. Photographs of sulfide mineralization at Northeast Saveh. (**A**) Disseminated first-generation pyrite and Ti-magnetite in the matrix of the rhyodacite unit. (**B**,**C**) Second-generation pyrite and chalcopyrite are disseminated in the matrix of a silica vein. (**D**) Second and third generations of disseminated pyrite and the second generation of pyrite in a chalcopyrite matrix. (**E**) Chalcopyrite, which has been altered to goethite at the rims due to weathering. (**F**–**I**) Chalcopyrite, which has been replaced by bands of blue chalcocite and covellite in its rim and supergene alteration products, including malachite and iron oxide-hydroxides in joints and fissures. Mineral abbreviations [20]: Ccp—chalcopyrite, Cct—chalcocite, Mal—malachite, Py—pyrite, Cv—covellite, Gth—goethite, Fe Ox-Hyd—iron oxides and hydroxides.

https://doi.org/10.3390/min16020212

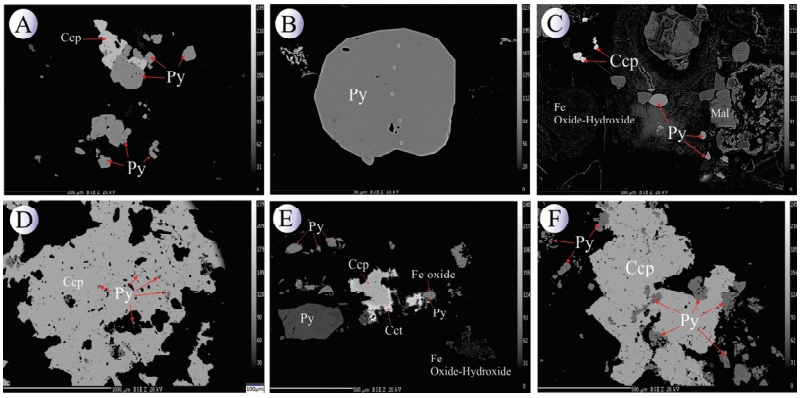


Figure 4. BSE images of hydrothermal pyrites associated with other oxide-sulfide minerals from the Northeast Saveh deposit. (**A**) Subhedral pyrite crystals alongside second-generation chalcopyrite. (**B**) Euhedral first-generation pyrite crystal. (**C**) Disseminated pyrite mineralization altered to iron oxides/hydroxides due to weathering. (**D**) Third-generation pyrites within a chalcopyrite matrix. (**E**) Second-generation well-faceted pyrites associated with chalcopyrite, covellite, and specularite. (**F**) Second- and third-generation pyrites embedded within a chalcopyrite matrix. Mineral abbreviations [20]: Ccp—chalcopyrite, Py—pyrite, Cct—Chalcocite, Mal—Malachite.

Chalcopyrite is the dominant primary copper sulfide in the Northeast Saveh and constitutes the main copper host. It occurs chiefly as anhedral to subhedral grains disseminated in the groundmass and as vein/veinlet fills (Figure 3B–I). Texturally, chalcopyrite is found both in the matrix and along structural conduits, where it often forms the core of composite sulfide aggregates. Supergene processes have extensively modified the primary chalcopyrite. Oxidation of the sulfide assemblage produced iron oxides/hydroxides (e.g., goethite, specular hematite) and released copper to solution; subsequently, secondary copper minerals (e.g., malachite) form by precipitation from Cu-bearing, carbonate-rich near-surface fluids and commonly occur as coatings, fillings, or botryoidal masses in fractures and pores (e.g., Figure 5E,F). In many samples, the original chalcopyrite grains are rimmed or partially pseudomorphosed by these secondary oxides, documenting progressive oxidation and leaching of copper from the primary sulfide phase.

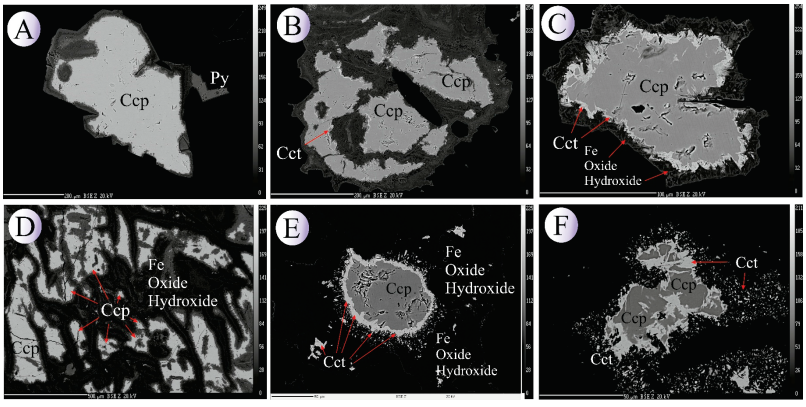


Figure 5. BSE images of chalcopyrite and chalcocite from the Northeast Saveh. (**A**) Primary chalcopyrite (Ccp) grain in contact with pyrite (Py); (**B**) chalcopyrite core showing initial stages of replacement by chalcocite (Cct) along the grain margins and internal fractures; (**C**) zonal replacement texture featuring a chalcopyrite core surrounded by a chalcocite rim, with an outermost layer of Fe-oxide/hydroxide; (**D**) advanced oxidation showing small, relict chalcopyrite grains preserved within a boxwork texture of Fe-oxide/hydroxide; (**E**) chalcopyrite grain with a distinct chalcocite reaction rim embedded within a porous matrix of Fe-oxide/hydroxide; (**F**) advanced replacement and fragmentation of chalcopyrite by chalcocite. Mineral abbreviations [20]: Ccp—chalcopyrite, Cct—Chalcocite, Cv—Covellite, Py—Pyrite.

https://doi.org/10.3390/min16020212

Chalcocite: Concomitant with oxidation, supergene enrichment produced a characteristic suite of secondary sulfides. Chalcocite is the most conspicuous product of this stage and defines the supergene sulfide zone in Northeast Saveh (Figure 3F–I). It commonly occurs as thin-rimmed replacements and fracture fillings around primary chalcopyrite and bornite, and locally as discrete aggregates in fractures and vein margins. Covellite and digenite, to a lesser extent, are also present as replacement phases, typically forming at the chalcopyrite margins or replacing thin rims of earlier-formed sulfides (Figure 3I). These textures indicate downward-percolating, oxidizing meteoric fluids mobilized copper from the upper parts of the system, followed by transport and reprecipitation as reduced Cu–S phases at or below the water table.

4.3. Mineralogy and Textural Characteristics of Oxide Ore Minerals (Magnetite-Ti-Magnetite)

Iron-oxide minerals in the Northeast Saveh area occur in two principal settings. In monzodioritic intrusive bodies, Ti-magnetite is the dominant syn-magmatic oxide, occurring mainly as disseminated grains within the groundmass (Figure 6A). In the silica veins that host or accompany Cu-sulfide mineralization, magnetite and specular hematite are predominant oxides, whereas Ti-magnetite appears less commonly (Figure 6B,C). Overall, hypogene oxide mineralization is relatively limited in volume and typically appears as scattered grains or vein infillings (Figure 6D–F).

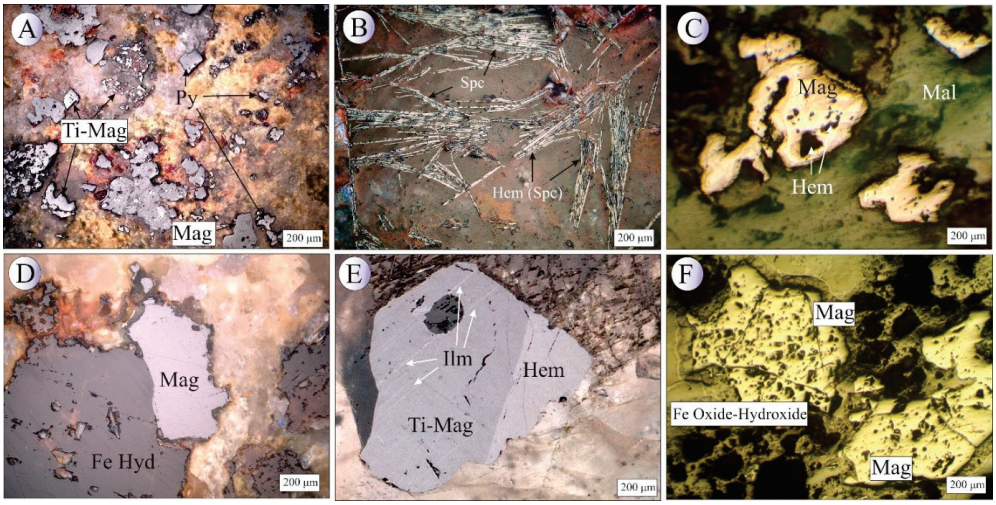


Figure 6. Photomicrographs of oxide minerals from the hypogene stage at Northeast Saveh. (**A**) Ti-magnetite and Pyrite disseminated Mineralization in the Monzonite matrix. (**B**) Bladed specular hematite in the silica vein. (**C**) Euhedral martitized magnetite crystals that are replaced by hematite due to alteration. (**D**) Euhedral magnetite crystals in the silica vein. (**E**) A Ti-magnetite crystal with stockwork texture that contains solid solution blades of ilmenite. (**F**) Euhedral martitized magnetite crystals that are replaced by hematite due to alteration. Mineral abbreviations [20]: Hem—hematite, Mal—malachite, Py—pyrite, Mag—magnetite, Ilm—ilmenite, Spc—Specularite.

Ti-magnetite in the intrusive units commonly occurs as euhedral to subhedral fine to coarse crystals, and locally shows intimate intergrowths with ilmenite. These intergrowths point to complex Ti–Fe oxide fractionation and exsolution histories during cooling (Figure 7B,E). In some crystals, blade-like hematite lamellae or exsolved hematite pockets are observed, indicating late-stage hematite separation that formed during the final cooling of the oxide phase (Figure 7E,F).

https://doi.org/10.3390/min16020212

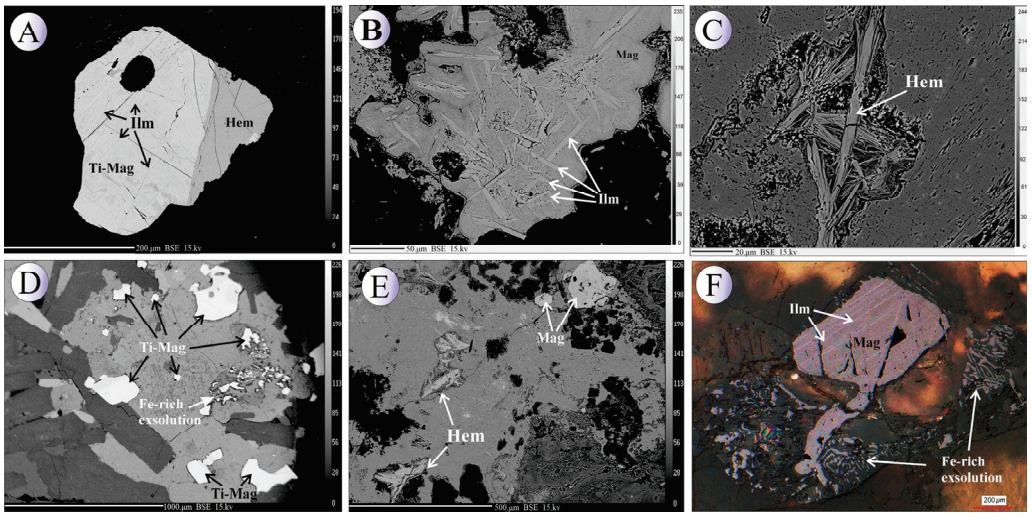


Figure 7. (**A**) BSE image of subhedral magnetite along with bladed hematite. (**B**) BSE image of magnetite along with solid solution blades of ilmenite. (**C**) BSE image of bladed hematite. (**D**) BSE image of subhedral homogenous Ti-magnetite crystals. (**E**) BSE image of Ti-magnetite crystal with stockwork texture that contains solid solution blades of ilmenite. (**F**) Photomicrograph in reflected light image of ilmenite exsolution in magnetite crystal. Mineral abbreviations [20]: Hem—hematite, Mag—magnetite, Ilm—Ilmenite.

Magnetite associated with the mineralized veins typically forms micron-sized crystals and occurs dominantly as veinlet infillings together with chalcopyrite or as disseminated crystals within the vein selvages (Figures 6A,D and 7A). Ti-magnetite is also observed as dissemination within the intrusive, commonly accompanied by subordinate pyrite and chalcopyrite.

5. Results

5.1. Mineral Chemistry of Pyrite

EPMA analyses were carried out on 43 points from 13 samples, exclusively targeting the fresh and well-preserved hydrothermal pyrite-II crystals (Figure 4). Although both pyrite-I and pyrite-II were examined petrographically, pyrite-I was not selected for quantitative analysis due to partial oxidation and replacement by hematite–goethite in many samples, which prevented obtaining reliable chemical data. In contrast, pyrite-II grains were texturally stable, unaltered, and suitable for accurate in situ EMPA measurements.

The analytical results are presented in Supplementary Table S1. The highest measured concentrations of trace elements in pyrite-II were: As (0.20 wt.%), Pb (0.26 wt.%), Cu (0.95 wt.%), Sb (0.23 wt.%), Ni (0.34 wt.%), and Co—the most abundant—at up to 1.12 wt.%. Gold was not detected in any of the analyzed points, and Ag contents were low, reaching a maximum of 0.05 wt.%. The strongest positive elemental correlations in pyrite-II were observed between Zn–Sn, Pb–As, and Pb–Mn, while the strongest negative correlations occurred between Fe–Co, S–Mn, Co–Zn, and S–Cu (Table 1)

Violin plots displaying the distribution of trace elements in pyrites are shown in Figure 8, and elemental variation diagrams are given in Figure 9. As observed, Fe and S contents do not exhibit significant variations with increasing As concentration, suggesting that As may be incorporated into pyrite through surface adsorption in the 3+ oxidation state. Cobalt content exhibits an increasing trend. Copper content in pyrite decreases as Fe concentration increases. The variation trends of Co and Ni are nearly constant when plotted against each other. Copper concentrations show an almost increasing trend with

rising Zn levels. Silver content decreases with increasing As and An concentrations but exhibits a positive correlation with Sn.

Table 1. Pearson's correlation matrix for elements measured in Northeast Saveh Pyrites.

	Fe	Mn	Co	Ni	Cu	Zn	As	S	Pb	Ag	Sb	Sn	Si
Fe	1												
Mn	−0.21	1											
Co	−0.52	0.2	1										
Ni	−0.25	0.34	−0.14	1									
Cu	−0.23	0.32	0.37	−0.19	1								
Zn	−0.05	0.14	−0.36	−0.04	−0.07	1							
As	0.05	0.06	−0.15	0.39	−0.20	0.48	1						
S	0.04	−0.54	−0.14	−0.07	−0.36	0.23	0.05	1					
Pb	−0.11	0.62	0.08	0.37	−0.01	0.49	0.76	−0.16	1				
Ag	0.12	0.51	0.03	−0.19	0.28	−0.20	−0.13	−0.17	−0.19	1			
Sb	−0.03	−0.31	0.08	0.24	0.08	0.28	−0.02	0.33	−0.20	−0.24	1		
Sn	−0.08	−0.25	0.09	−0.11	−0.13	0.83	0.16	0.29	0.12	−0.21	0.23	1	
Si	−0.20	−0.14	−0.07	−0.03	−0.12	−0.01	−0.18	−0.13	0.04	−0.10	−0.11	0.02	1

Low correlation — High correlation

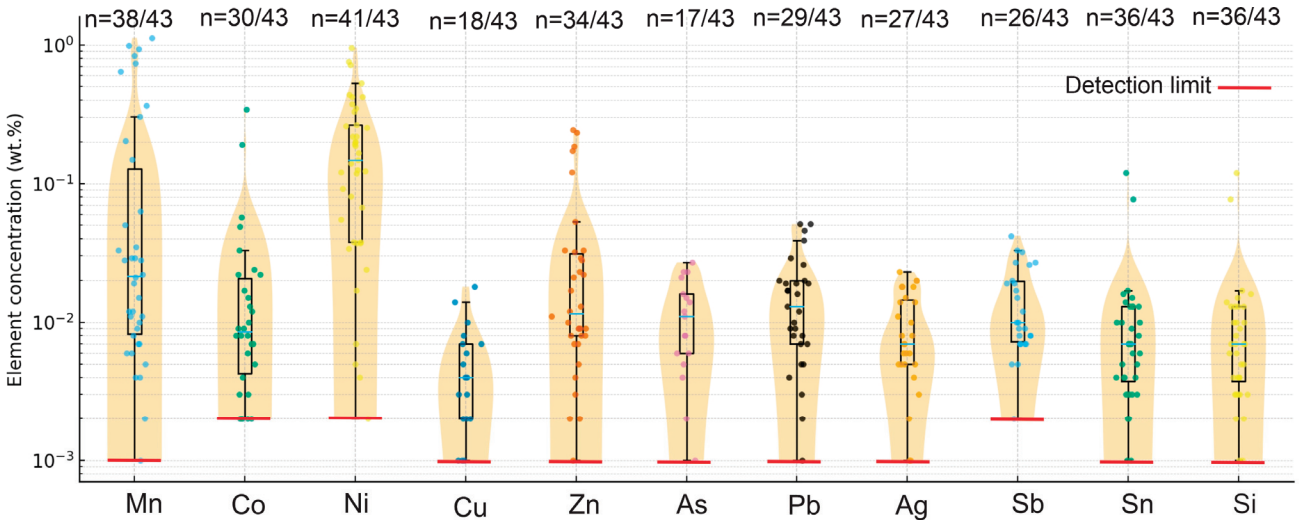


Figure 8. Violin plots showing the distribution of trace elements (wt.%) in the Northeast Saveh pyrites on a logarithmic scale and illustrating the data with kernel density distributions, highlighting the variability and skewness of elemental concentrations. Non-detected and zero values were excluded from the log-scale plots.

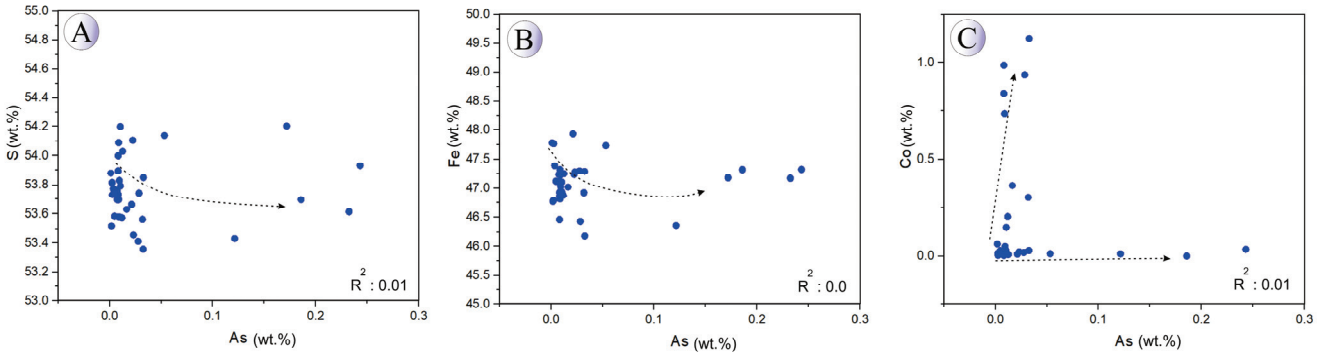


Figure 9. *Cont.*

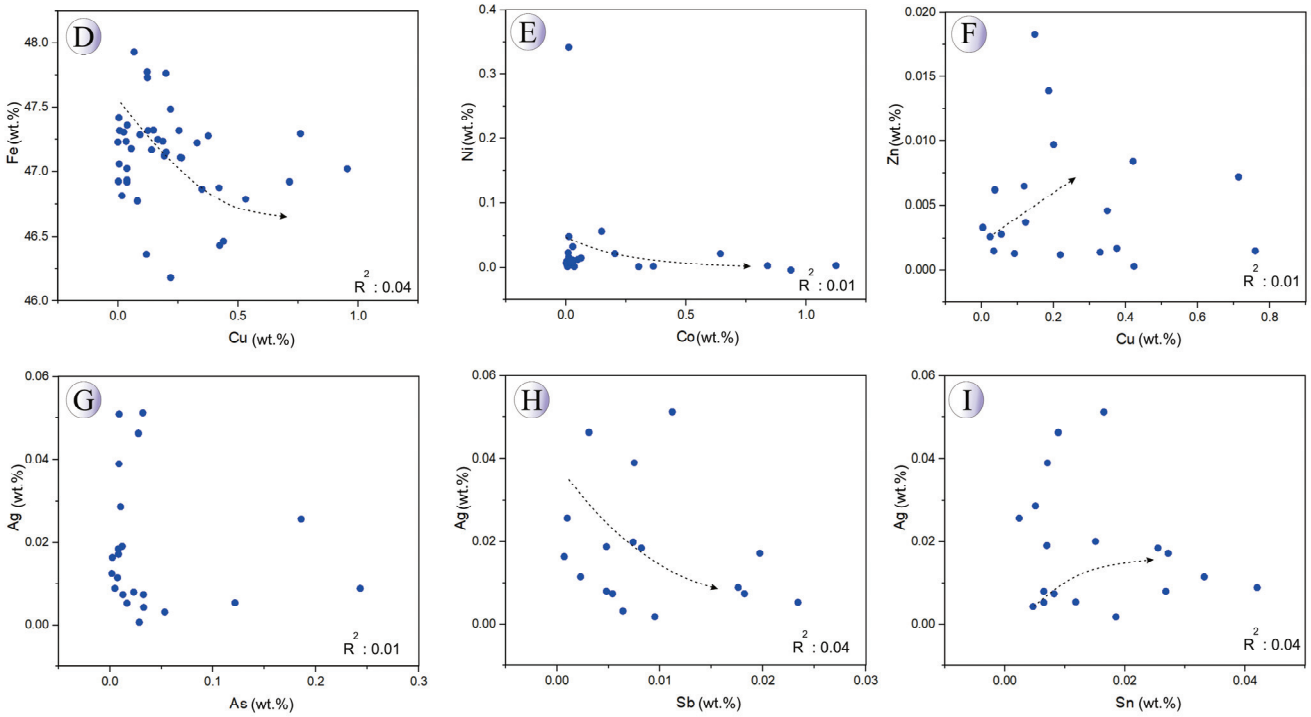


Figure 9. Binary plots of the variations in trace elements (in wt.%) in the Northeast Saveh pyrites. (**A**) As vs. S; (**B**) As vs. Fe; (**C**) As vs. Co; (**D**) Cu vs. Fe; (**E**) Co vs. Ni; (**F**) Cu vs. Zn; (**G**) As vs. Ag; (**H**) Sb vs. Ag; (**I**) Sn vs. Ag.

5.2. Mineral Chemistry of Chalcopyrite and Chalcocite

Chalcopyrite EPMA analysis was performed on 97 points (Supplementary Table S2). The chalcopyrite contains Fe ranging from 30.2 to 31 wt.%, sulfur from 34 to 35.5 wt.%, and copper from 33.2 to 35.1 wt.%. The concentrations of other trace elements are as follows: zinc up to 0.4 wt.%, lead up to 0.19 wt.%, silver up to 0.05 wt.%, antimony up to 0.02 wt.%, tin up to 0.05 wt.%, arsenic up to 0.02 wt.%, cobalt up to 0.01 wt.%, and nickel up to 0.02 wt.%. The strongest elemental correlations in chalcopyrite are observed between S and Fe, Fe and Cu, Sb and Ni, Cu and S, as well as Mn and As (Table 2).

Table 2. Pearson's correlation matrix for elements measured in Northeast Saveh Chalcopyrites.

	Fe	Mn	Co	Ni	Cu	Zn	As	S	Pb	Ag	Sb	Sn	Si
Fe	1												
Mn	−0.21	1											
Co	−0.19	−0.25	1										
Ni	−0.01	−0.04	0.25	1									
Cu	0.44	−0.15	−0.57	−0.11	1								
Zn	0.07	−0.05	−0.19	−0.25	0.01	1							
As	−0.11	0.35	0.25	0.14	−0.09	0.09	1						
S	0.53	0.03	−0.53	−0.07	0.43	0.11	0.02	1					
Pb	−0.14	0.04	−0.03	−0.07	0	−0.09	−0.01	0.02	1				
Ag	−0.10	0.07	−0.30	0.02	0.04	−0.30	−0.03	−0.19	−0.26	1			
Sb	0.1	0.09	0.09	0.39	−0.05	0.11	−0.15	−0.14	−0.11	−0.06	1		
Sn	0.01	−0.33	0.09	−0.32	−0.15	−0.31	−0.26	0.05	0.08	0.23	−0.16	1	
Si	−0.05	0.16	−0.16	0.27	−0.15	−0.02	0.36	0.15	−0.26	0.22	0.04	0.08	1

Low correlation — High correlation

Chalcocite EPMA analysis was conducted on 17 points (Supplementary Table S3). Chalcocite contains an average of 75.6 wt.% copper and 22.2 wt.% sulfur. The concentrations of other trace elements in chalcocite are as follows: zinc up to 0.58 wt.%, Pb up to 0.43 wt.%,

Ag up to 0.87 wt.%, Sb up to 0.02 wt.%, Sn up to 0.04 wt.% and Ni up to 0.01 wt.%. The strongest elemental correlations in Northeast Saveh chalcocite are observed between cobalt and nickel, nickel and copper, zinc and tin, silver and tin, antimony and cobalt, as well as sulfur with lead and cobalt (Table 3).

Table 3. Pearson's correlation matrix for elements measured in Northeast Saveh Chalcocite.

	Fe	Mn	Co	Ni	Cu	Zn	As	S	Pb	Ag	Sb	Sn	Si
Fe	1												
Mn	0.49	1											
Co	−0.17	0.34	1										
Ni	−0.21	−0.86	−0.72	1									
Cu	−0.09	−0.29	−0.47	0.65	1								
Zn	0.41	0.09	−0.30	0.62	0.13	1							
As	0.35	0.41	−0.22	−0.62	−0.02	−0.64	1						
S	−0.40	0	0.46	−0.53	−0.86	−0.32	−0.08	1					
Pb	−0.60	−0.31	−0.51	0.23	0.27	−0.51	−0.30	0.58	1				
Ag	−0.31	−0.51	0.32	−0.03	−0.11	−0.05	−0.40	0.18	−0.08	1			
Sb	0.34	0.2	0.83	−0.03	−0.40	0.68	0.25	−0.53	−0.70	−0.18	1		
Sn	0.04	−0.45	−0.27	0.61	0.41	0.63	−0.37	−0.44	−0.67	0.66	0.14	1	
Si	0.53	0.16	−0.67	0.32	−0.07	0.23	0.41	−0.23	0.29	−0.18	0.25	−0.21	1

Low correlation — High correlation

Overall, the distribution of trace elements in copper sulfides (chalcopyrite and chalcocite) does not show significant differences, with only minor variations. Zn, Pb, and Ag concentrations are slightly higher in chalcocite, whereas Sb, As, Co, and Ni are more enriched in chalcopyrite, suggesting that these elements preferentially incorporate into the chalcopyrite structure.

5.3. Mineral Chemistry of Magnetite and Ti-Magnetite

EMPA analyses were carried out on 44 points from primary Ti-magnetite grains within the intrusive units, including monzonite, monzodiorite, and gabbro (Supplementary Table S4), and on 44 points from hydrothermal magnetite associated with mineralized veins (Supplementary Table S5). The chemical composition and inter-element correlations of magnetite and Ti-magnetite indicate distinct geochemical signatures for intrusive rock and mineralized veins, respectively. The analytical results reveal that, in the intrusive rocks, Fe_2O_3 and TiO_2 contents range between 60 and 80 wt.% and 0–16.58 wt.%, respectively. In contrast, magnetite from the mineralized veins shows markedly higher Fe_2O_3 concentrations (80.6–91.4 wt.%) and significantly lower TiO_2 contents (0–0.12 wt.%) (Figures 10–13).

In the intrusive bodies, Fe_2O_3 correlates positively with Cr_2O_3 and V_2O_3 (Table 4), consistent with co-enrichment during magmatic crystallization under relatively oxidizing conditions. In hydrothermal magnetite, Fe_2O_3 correlates most strongly with MnO (Table 5). However, unlike the magmatic samples, trace elements such as Cr and V in the hydrothermal magnetite frequently approach or fall below the EPMA detection limits. Consequently, these elements do not exhibit statistically reliable correlation patterns in the mineralized veins, reflecting a significantly depleted signature compared to the intrusive oxides. This shift in chemical behavior may reflect either partial re-equilibration of the original magmatic magnetite by hydrothermal fluids or direct precipitation from compositionally distinct, evolved solutions.

https://doi.org/10.3390/min16020212

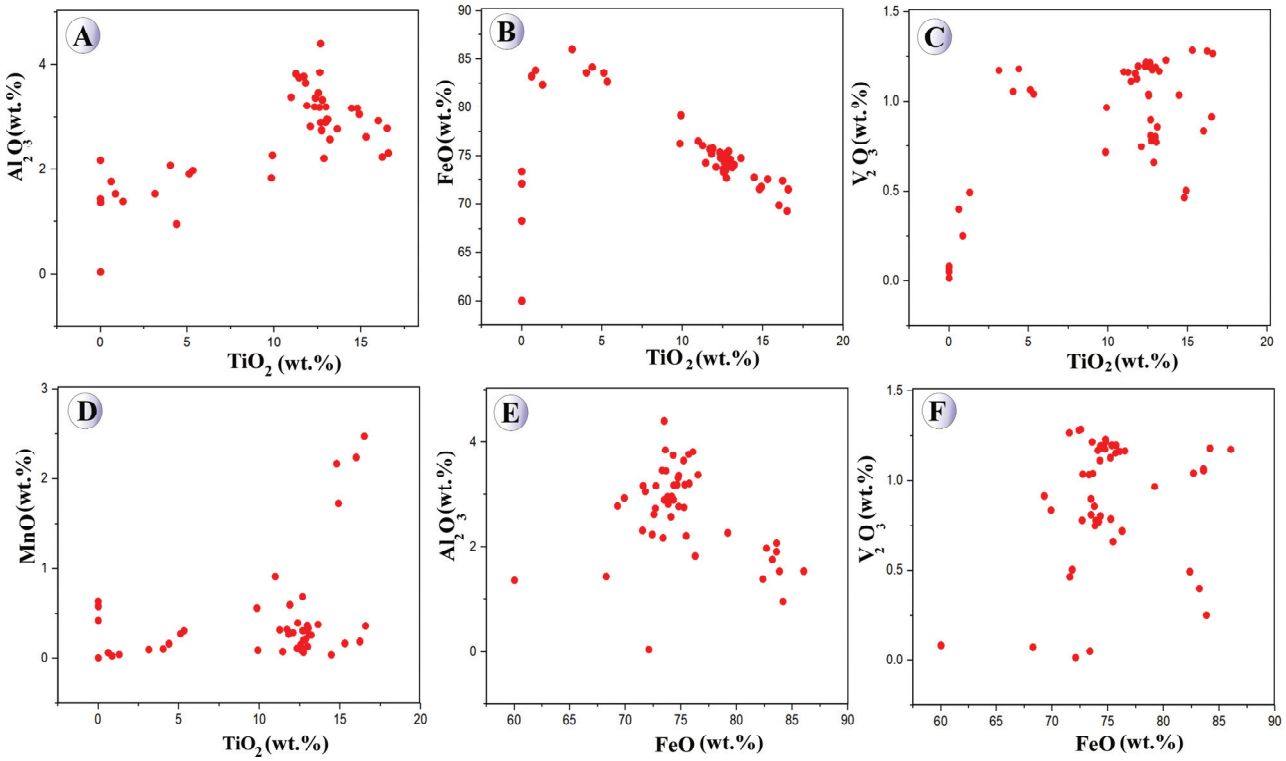


Figure 10. Major oxides (wt.%) vs. TiO_2 (wt.%) and FeO (wt.%) in Ti-magnetite related to intrusive rocks in Northeast Saveh. (**A**) TiO_2 vs. Al_2O_3. (**B**) TiO_2 vs. FeO. (**C**) TiO_2 vs. V_2O_3. (**D**) TiO_2 vs. MnO. (**E**) FeO vs. Al_2O_3. (**F**) FeO vs. V_2O_3.

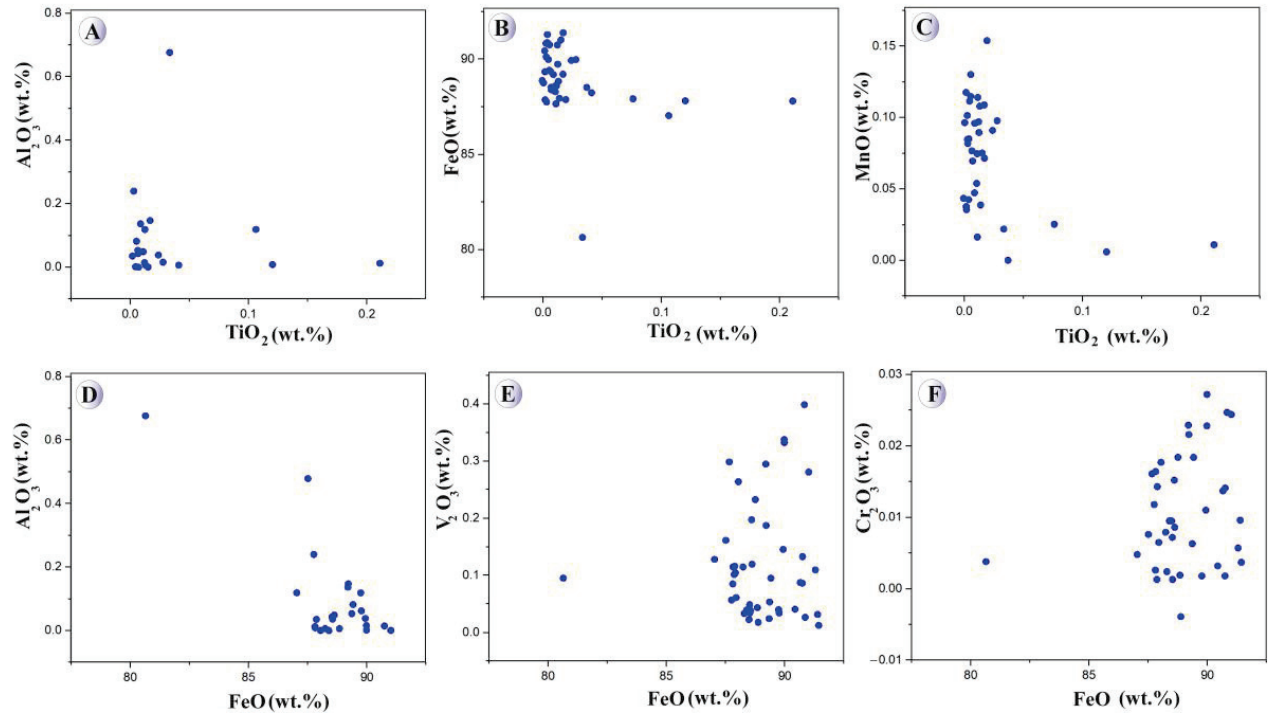


Figure 11. Major oxides (wt.%) versus TiO_2 (wt.%) and FeO (wt.%) in magnetites related to mineralized veins in Northeast Saveh. (**A**) TiO_2 vs. Al_2O_3. (**B**) TiO_2 vs. FeO. (**C**) TiO_2 vs. MnO. (**D**) FeO vs. Al_2O_3. (**E**) FeO vs. V_2O_3. (**F**) FeO vs. Cr_2O_3.

https://doi.org/10.3390/min16020212

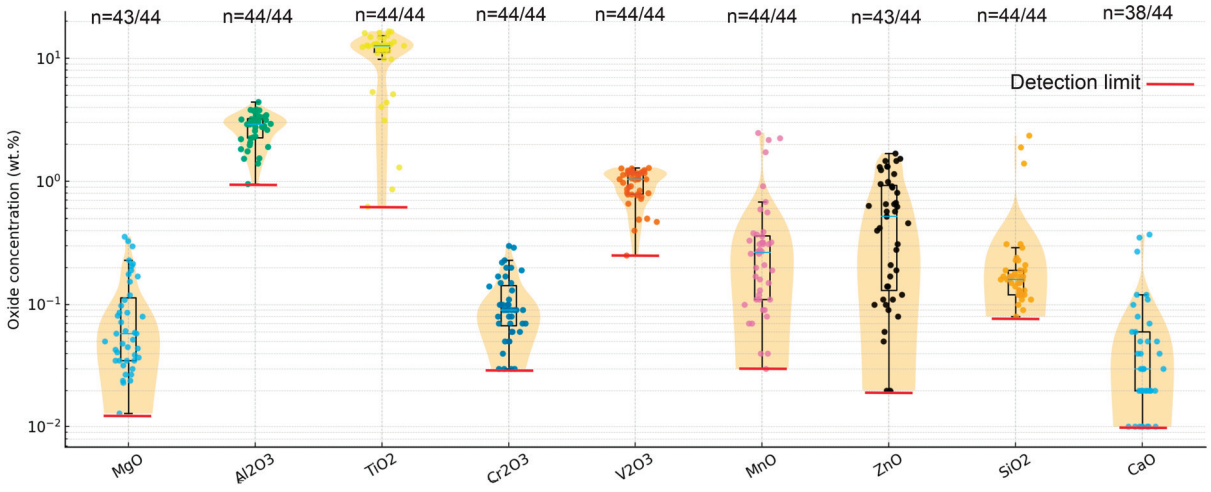


Figure 12. Violin plots showing the distribution of major oxides (wt.%)—except Fe_2O_3—in Ti-magnetite from intrusive rocks of NE Saveh on a logarithmic scale and showing kernel density distributions and compositional variability. Non-detected and zero values were excluded.

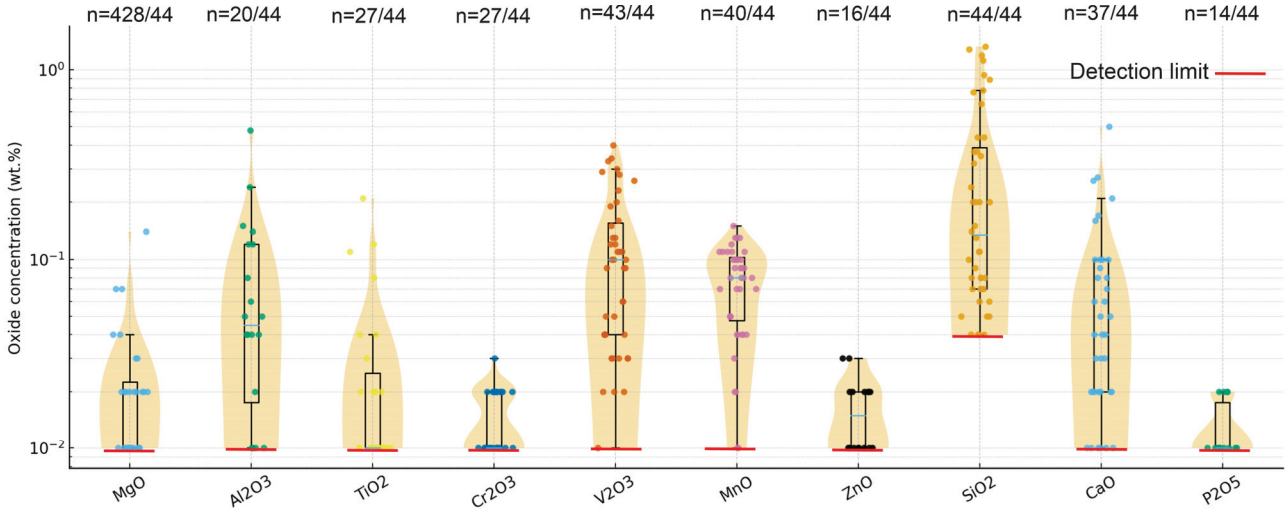


Figure 13. Violin plots showing the distribution of major oxides (wt.%)—except Fe_2O_3—in magnetite from intrusive rocks of NE Saveh on a logarithmic scale and showing kernel density distributions and compositional variability. Non-detected and zero values were excluded.

Table 4. Pearson Product correlation coefficient matrix for elements measured in magnetites and Ti-magnetite s in the Northeast Saveh intrusive rocks.

	MgO	Al_2O_3	TiO_2	Cr_2O_3	FeO	V_2O_3	MnO	ZnO	SiO_2	CaO	P_2O_5
MgO	1										
Al_2O_3	0.08	1									
TiO_2	−0.19	−0.07	1								
Cr_2O_3	0.24	−0.16	−0.14	1							
FeO	0.09	−0.76	−0.30	0.22	1						
V_2O_3	0.07	−0.08	−0.05	0.83	0.06	1					
MnO	0.31	−0.34	−0.47	0.37	0.42	0.26	1				
ZnO	−0.10	0.32	−0.14	−0.07	−0.26	0.15	0	1			
SiO_2	0.47	0.65	−0.08	0.05	−0.50	−0.04	0.2	−0.22	1		
CaO	0.52	0.04	−0.13	0.28	0.09	0.1	0.29	−0.34	0.54	1	
P_2O_5	0.02	0.77	−0.05	−0.24	−0.83	−0.11	−0.31	−0.56	0.8	0.24	1

Low correlation — High correlation

https://doi.org/10.3390/min16020212

Table 5. Pearson Product correlation coefficient matrix for elements measured in magnetites and Ti-magnetite s in mineralized veins.

	MgO	Al_2O_3	TiO_2	Cr_2O_3	FeO	V_2O_3	MnO	ZnO	SiO_2	CaO
MgO	1									
Al_2O_3	−0.39	1								
TiO_2	−0.60	0.71	1							
Cr_2O_3	0.29	0.16	0.1	1						
FeO	−0.11	−0.21	−0.32	0.33	1					
V_2O_3	−0.46	0.51	0.57	0.49	0.32	1				
MnO	−0.18	0.15	0.3	−0.37	−0.38	−0.21	1			
ZnO	−0.58	0.27	0.61	−0.45	−0.35	0.02	0.44	1		
SiO_2	0.56	−0.44	−0.62	−0.34	−0.50	−0.68	0.02	−0.30	1	
CaO	−0.03	−0.30	−0.33	−0.26	0.32	−0.21	−0.12	−0.16	0.03	1

Low correlation — High correlation

TiO_2 in the magmatic Ti-bearing magnetite correlates strongly with Al_2O_3, V_2O_3, and MnO, consistent with coupled high-temperature substitution mechanisms in the spinel lattice (e.g., incorporation of Ti4+ accompanied by trivalent cations such as Al3+ and V3+ to maintain charge balance) under magmatic crystallization conditions. By contrast, magnetite precipitated from hydrothermal fluids does not display the same Ti–Al–V coupling. This difference most likely reflects contrasting physico-chemical environments: hydrothermal formation at lower temperatures, different Al and V activities in the fluid, and kinetic limitations on cation diffusion. Therefore, the strong Ti–Al–V correlations observed in the intrusive samples are interpreted as primary magmatic signatures, whereas the low and scattered Ti contents in hydrothermal samples are controlled by different substitution pathways or secondary redistribution.

Due to the inability of EPMA to distinguish iron oxidation states, the concentrations of FeO and Fe_2O_3 in magnetite and Ti-bearing magnetite were calculated using the stoichiometric method of Zhao et al. (1999) [21], based on the assumption of 3 cations and 4 oxygens per formula unit. Variation diagrams of major oxides versus TiO_2 and FeO were constructed for Ti-bearing magnetite from the intrusive bodies (Figure 10) and for magnetite from oxide–sulfide mineralized veins (Figure 11). As illustrated in Figure 10, Al_2O_3, Cr_2O_3, and V_2O_3 contents in the intrusive Ti-bearing magnetite increase systematically with rising TiO_2 content, suggesting co-enrichment of these elements during fractional crystallization. Conversely, FeO and MgO display inverse trends, decreasing with increasing TiO_2.

Regarding the magnetite grains from the mineralized veins (Figure 11), TiO_2, Al_2O_3, and Cr_2O_3 concentrations remain consistently low, often clustering near the detection limit. While MnO and MgO exhibit some variability, the extremely low abundance of Cr and V in these samples precludes the identification of robust geochemical trends. With increasing Fe content, Al_2O_3 and V_2O_3 show scattered distributions rather than systematic correlations. These features collectively highlight a clear geochemical break between the magmatic and hydrothermal domains in the Northeast Saveh system.

6. Discussion

6.1. Pyrite Trace Element Behavior and Implications for Ore Genesis

Pyrite can incorporate significant amounts of copper [22], and, in the Northeast Saveh pyrites, Cu reaches up to ~0.95 wt.% in some samples. Copper in pyrite can occur either as true structural substitution or as fine-scale inclusions of Cu-bearing minerals (e.g., chalcopyrite). Cu substitution in the pyrite lattice is principally accommodated by the similarity in oxidation state and ionic radius between Cu^{2+} and Fe^{2+} in octahedral coordination ($Cu^{2+} \approx 0.73$ Å; $Fe^{2+} \approx 0.78$ Å), allowing limited substitution of Cu^{2+} for Fe^{2+} on the cation site. Copper does not substitute for sulfur (S^{2-}) on the anion site because

of the large difference in charge and coordination chemistry. This capacity of pyrite to sequester Cu implies that pyrite may act as a significant transient sink for copper during mineralization and supergene overprint.

Lead is unlikely to enter the pyrite lattice except as Pb^{2+}, due to its large ionic radius (~1.8 Å). Galena (PbS) precipitates from solution more rapidly than FeS [23,24], so galena typically forms early and, when present, is usually found as inclusions within pyrite [25]. However, no galena inclusions were observed in the Northeast Saveh pyrites. Pyrite can also trap certain chalcophile elements such as Ag, Sb and Sn during remobilization; in the Northeast Saveh samples, the maximum concentrations of these elements are low (≈500, 200 and 20 ppm, respectively).

The Co–Ni–As element suite in pyrite has long been recognized as a robust genetic indicator that reflects the geological setting and evolution of an ore system [26,27].

Plotting the Northeast Saveh pyrite data on Co–Ni–As discrimination diagrams (Figure 14; after [27,28]) reveals a predominant shift toward the Co-enriched endmember, consistent with magmatic–hydrothermal to epithermal affinities (Figure 14A). This pattern suggests a dominant magmatic water source during the early stages of mineralization, with progressive involvement of meteoric waters during later stages.

The degree of S → As substitution in pyrite is temperature-sensitive and generally increases at lower temperatures [29], so elevated As contents are commonly associated with cooler, more evolved fluids.

Nickel commonly concentrates in early, high-temperature phases formed during magmatic differentiation. As differentiation proceeds, Ni tends to decline while Co can become relatively enriched. Thus, the systematic shift in our samples toward higher Co/Ni ratios is compatible with cooling and evolution of the ore fluids. In addition, the relative abundance of As in pyrite is strongly influenced by the relative contributions of magmatic versus meteoric waters. Magmatic-dominated fluids tend to produce Co-rich pyrite compositions, whereas increasing meteoric-water input, typically associated with system cooling and fluid dilution, drives the signature toward higher As contents [27]. The Northeast Saveh pyrite data (Figure 14A) are therefore best interpreted as recording an evolution from an early magmatic-water dominated system to later stages with increased meteoric-water input.

Mixing of mineralizing fluids with high-fO_2 meteoric waters can also promote oxidation of arsenic species (As (0) → As^{3+}/As^{5+}, driving arsenic out of the pyrite lattice and into the fluid phase as oxide or oxyanion species (e.g., As_2O_3, As_2O_5). This process can reduce As concentrations in primary pyrite while increasing the mobility and redistribution of As within the evolving system, potentially causing As enrichment in other parts of the hydrothermal column or in secondary phases [30,31].

Complementary evidence from the magnetite chemistry (see Section 5.3) supports elevated fO_2 in the hydrothermal veins and a cooling trend during system evolution. Classic vertical zoning observed in epithermal systems—where the upper levels are enriched in As, Sb, Hg, Ba, and Ag, the mid-levels in Cu, Pb, Zn and Bi, and the deep levels in Co, Ni, Ti and Cr [32]—provides a useful framework for interpreting the Northeast Saveh pyrite data. As illustrated in Figure 14B, most Northeast Saveh pyrite samples plot within the middle to deeper sector of this zoning model, consistent with a predominantly mid-system hydrothermal character with some contribution from deeper, higher-temperature inputs.

The trace-element systematics of pyrite from Northeast Saveh reflect a multistage hydrothermal evolution, with an early, magmatic-fluid dominated stage (Co-rich signature) followed by progressive cooling and admixture of meteoric waters (increasing As signatures and oxidation).

https://doi.org/10.3390/min16020212

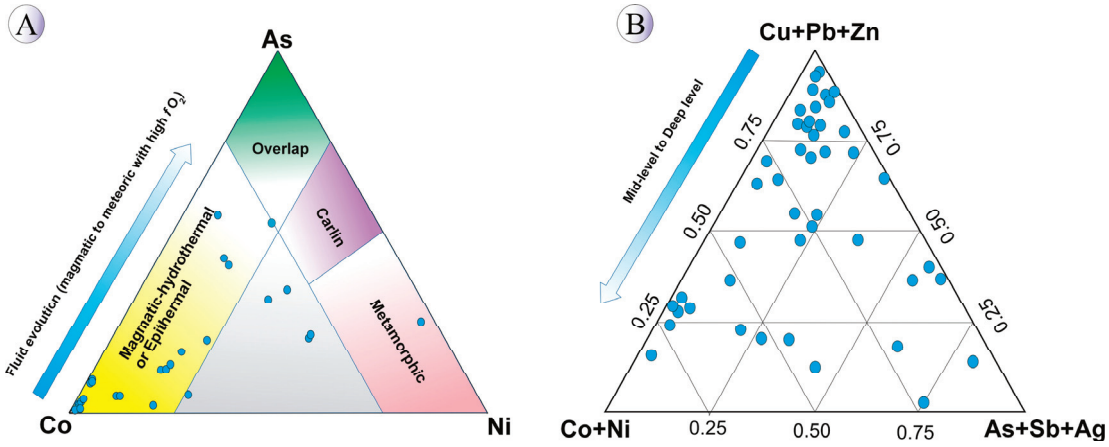


Figure 14. (**A**) Comparison of pyrite composition in metamorphic, Carlin, and magmatic–hydrothermal or epithermal deposits on the Co-Ni-As ternary diagram (modified from [27] and the position of the measured points of Northeast Saveh pyrites on it. (**B**) Ternary diagram of Cu + Pb + Zn, Co + Cr, and As + Sb + Ag based on [32] and the position of the measured points of Northeast Saveh pyrites on it.

Nickel readily substitutes into the pyrite crystal structure and, once incorporated, is relatively resistant to removal during later recrystallization [4,23,24,33]. Thus, pyrite Ni contents may record information about the source of the mineralizing fluid. Mantle- and mafic–ultramafic-related lithologies are typically Ni-rich, whereas felsic units have low Ni contents [25,34]. The Ni contents measured in the studied pyrites (up to ~0.34 wt.%) exceed typical continental-crust Ni concentrations (≈19–60 μg g^{-1}; [34]), suggesting a contribution from mafic–ultramafic or upper-mantle sources. Previous work in the region [17,18] using trace-element ratios (e.g., Ta, Nb, La) indicates a dominant mantle (spinel-lherzolitic) source modified by upper-crustal contamination, and Sr–Nd isotope ratios also point to a significant role for mantle metasomatism in the genesis of the intrusions [35,36].

Reported solubility limits suggest Ni can be accommodated in pyrite up to ~10 mol% NiS_2, whereas Co may achieve complete miscibility with pyrite at temperatures above ~700 °C [36]. This temperature dependence makes pyrite Co content a useful geothermometer [37]. Consequently, the Co/Ni ratio in pyrite is widely applied as a proxy for ore-forming conditions [25,38,39].

Empirically, low Co/Ni ratios (<1) characterize sedimentary/diagenetic pyrite [38], diagenetic pyrites commonly also show low Co/Ni (≤2), whereas hydrothermal pyrites typically display higher Co/Ni [4,40]. Co/Ni ratios between ~1 and 10 are diagnostic of magmatic–hydrothermal deposits [41,42]. The Co/Ni distribution for Northeast Saveh pyrites predominantly falls between 1 and 10 (Figure 15), consistent with a hydrothermal origin.

Given the similar geochemical behavior of Co and Ni, nickel solubility in hydrothermal fluids is primarily controlled by temperature [26]. Cooling of the hydrothermal fluid, therefore, tends to decrease the solubility of these trace metals and promotes their precipitation as discrete phases or their incorporation into sulfides (e.g., pyrite). Co and Ni are generally incorporated into the pyrite lattice by direct substitution for Fe^{2+}. In contrast, As incorporation occurs through charge-balanced, coupled-substitution mechanisms rather than simple one-for-one replacement. Specifically, As^{3+} may occupy Fe^{2+} sites with charge compensation achieved by Fe vacancies or complementary anion/cation substitutions, while reduced As^{1-} may substitute for S^{2-} with local charge balance adjustments [3,43,44]. Accordingly, Co, Ni, and As are likely present as solid-solution components in pyrites. Because of its relatively large ionic radius, although Pb commonly occurs as Pb^{2+} in aqueous

solution, Pb is not readily accommodated as a point defect in the pyrite lattice; minor Pb in pyrite samples most likely reflects nanoscale galena or other Pb-bearing inclusions, or surface/secondary Pb phases, rather than true lattice substitution [45,46].

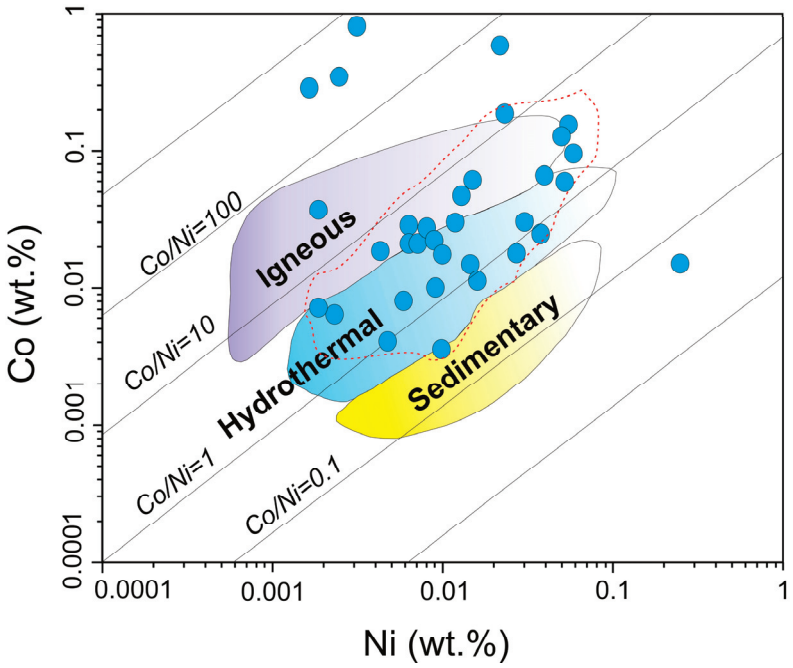


Figure 15. Diagram of Co variations versus Ni and the Co/Ni ratio in Northeast Saveh pyrites. The Co/Ni ratio of pyrite for most samples has a ratio between 1 and 10, which corresponds to pyrites of Igneous-hydrothermal origin [42]. Samples with a Co/Ni ratio of ~100 (as a result of cobalt enrichment rather than nickel depletion) reflect pyrite grains formed at shallower stratigraphic levels.

Hydrothermal pyrites with elevated Co/Ni ratios have been reported from a range of magmatic–hydrothermal deposits worldwide (for example, vein-type Ag–Pb–Zn deposits, [47]; IOCG systems, [48]; skarn Au–Cu deposits, [49]; and Pb–Zn skarns, [50], and are commonly attributed to intense fluid–rock interaction. On the basis of the evidence summarized above, pyrites from Northeast Saveh appear to be dominantly hydrothermal in origin and to have formed through interaction between magmatic–hydrothermal fluids and the plutonic host rocks.

6.2. Chalcopyrite-Chalcocite Trace Element Behavior and Implications for Ore Genesis

The evidence provided by the major and trace elements and textures confirms a fluid-driven replacement history in which primary chalcopyrite was the dominant magmatic–hydrothermal Cu reservoir that was subsequently dissolved and reprecipitated as Cu-rich sulfides along sharp reaction fronts (Figures 3 and 5). The major-element trends in chalcopyrite (Figure 16A; ≈33–35 wt.% Cu, 28–30 wt.% Fe, 33–35 wt.% S) versus chalcocite (≈74–77 wt.% Cu, 3–4 wt.% Fe, 22–25 wt.% S) demonstrate a classic Fe-depletion/Cu-enrichment trajectory consistent with fluid-controlled dissolution–reprecipitation [38,51]. The near-quantitative loss of Fe from the lattice and simultaneous increase in Cu/S ratio reflect interface-coupled dissolution of chalcopyrite and local precipitation of Cu-rich sulfides at the reaction front, rather than solid-state diffusion. This replacement style is supported by thin Cct/Cv rinds, fracture-controlled infills, and partial pseudomorphs, all pointing to an open, fluid-dominated system with sharp disequilibrium boundaries.

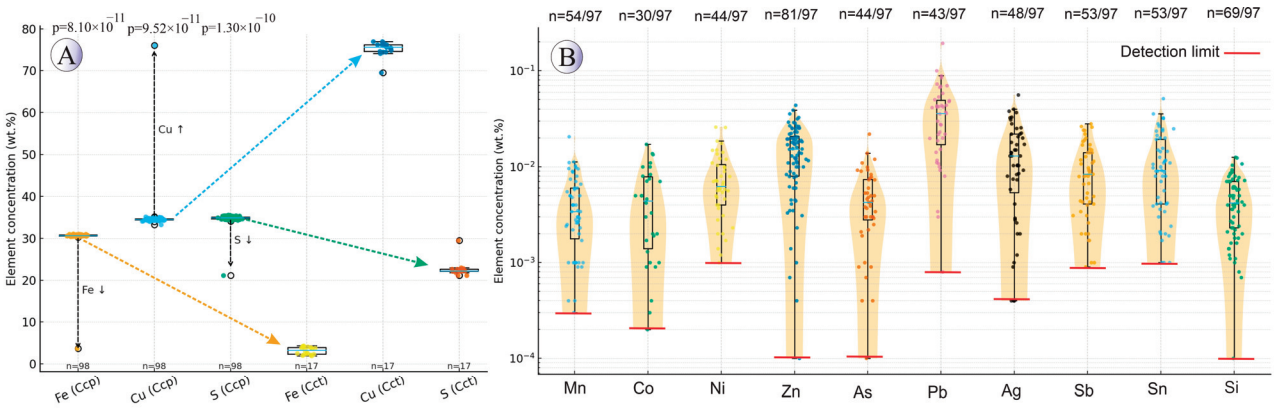


Figure 16. (**A**) Box plots showing variations in Fe, Cu, and S concentrations in chalcopyrite (Ccp) and chalcocite (Cct) from the Northeast Saveh area. Dashed arrows indicate compositional trends from chalcopyrite to chalcocite. (**B**) Violin plots showing the distribution of major oxides (wt.%) in chalcopyrite (except Fe, S, Cu) host rocks of NE Saveh on a logarithmic scale and showing kernel density distributions and compositional variability. Non-detected and zero values were excluded.

Trace-element patterns refine this genetic scenario (Figures 16B and 17). Chalcopyrite shows moderate Pb, Ag, Sb and Zn, with Pb having the broadest variability; chalcocite displays marked enrichment in Zn and Ag and retains variable Pb. This implies two complementary processes: (1) coupled lattice substitution (Pb–Bi, Sb–As, Sn–In type pairings) that reflects formation conditions and crystal-chemical accommodation [8,52], and (2) inclusion-entrainment or co-precipitation where micron/nano inclusions of sphalerite, bornite-derived phases or galena are reworked during replacement and become incorporated into secondary chalcocite [53,54]. The pronounced Zn signal in chalcocite, in particular, is best explained by remobilization of wall-rock or precursor sphalerite-derived Zn and local co-precipitation with chalcocite [8].

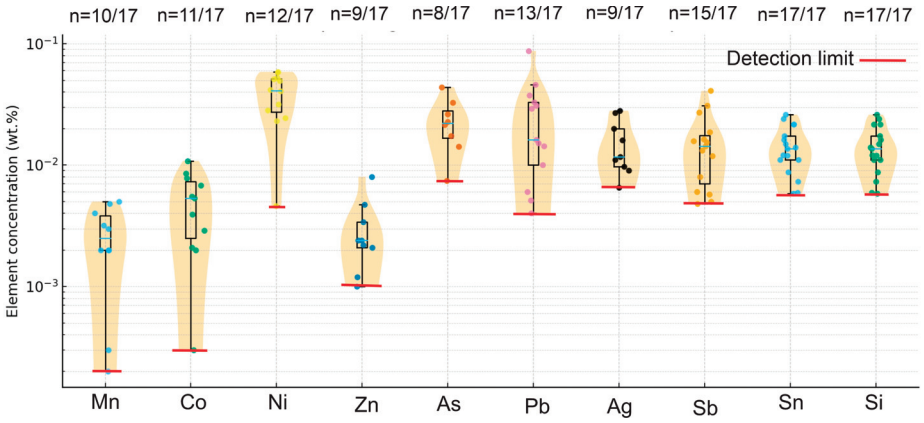


Figure 17. Violin plots showing the distribution of major oxides (wt.%) in chalcocite (except Fe, S, Cu) host rocks of NE Saveh on a logarithmic scale and showing kernel density distributions and compositional variability. Non-detected and zero values were excluded.

Redox, pH and temperature exert primary control on sequence and kinetics. Experimental and field work indicate that covellite commonly forms first, with chalcocite/digenite developing rapidly at intermediate temperatures (≈200–300 °C) or after a longer induction period at lower T (<~200 °C) [51]. However, the microtextural evidence in the Northeast Saveh samples indicates a predominantly supergene origin for the observed low-Fe copper sulfides. Specifically, rim-type replacement textures (thin chalcocite/covellite rinds around chalcopyrite and bornite), fracture-controlled infillings, partial pseudomorphism, and the close spatial association with oxidation textures and supergene oxides/carbonates point

to formation during oxidative weathering and downward Cu transport at the redox front (Figures 3 and 5). Microscopically, these processes produce sharp chemical zoning at grain boundaries, inclusion-bearing textures and occasional overgrowths, as documented in BSE imagery and EPMA spot analyses (Figure 5).

Sulfidic pulses in episodic, Cu-bearing near-surface fluids (or evolving ligand chemistry, e.g., chloride → sulfide complexes) would have promoted rapid local precipitation of low-Fe copper sulfides, while Fe was likely transported predominantly as Fe^{3+} (and possibly Fe^{2+}) species in the H_2O-rich, moderately oxidizing fluids [37].

While hydrothermal precipitation of chalcocite/covellite from deeper, high-temperature fluids is thermodynamically and experimentally possible, such a hydrothermal origin is not supported by the paragenetic, textural and field relations in our study area. We therefore interpret the dominant occurrences of chalcocite and covellite in the studied outcrops as products of supergene enrichment and oxidation-zone processes, while noting that rare hydrothermal occurrences cannot be fully excluded without targeted fluid-inclusion or isotopic analyses.

High-T conditions (>~500–600 °C) increase the capacity of chalcopyrite to host Ga, In, Sn, Zn, Mo and noble metals [8]. Studies demonstrate strong positive correlations between temperature and trace uptake (e.g., Zn solubility rises with T; [55,56]. Reported Au contents in chalcopyrite from porphyry systems decrease markedly with decreasing formation temperature [56], and it can be said that the lack of Au observation in the chalcopyrite s in northeastern Saveh is due to the decrease in system temperature and the onset of the epithermal system e.g., [19,57].

In many porphyry/epithermal systems, observed positive correlations (e.g., Pb–Bi, Pb–Mo, Zn–Cd, Sn–In, Sb–As, Sb–Ge) imply paired or linked substitutions and/or co-entrainment in inclusions, consistent with reports of Au, Ag, As, Te, In, Zn, Cd, Ge and Ga entering chalcopyrite via coupled mechanisms [52,58].

Cobalt and nickel are typically associated with fluids derived from mafic magmas or leached from rocks with a high background content of these elements [2,22,36]. The Co/Ni ratio in chalcopyrite from porphyry, skarn, and epithermal hydrothermal deposits is typically greater than 1, whereas in Cu-Ni sulfide deposits, it is less than 1 [59]. The Co/Ni ratio in Northeast Saveh chalcopyrites is predominantly above 1, aligning with the characteristics of chalcopyrite in hydrothermal deposits. The general immobility of Co–Ni during chalcopyrite → chalcocite replacement implies the replacement front selectively partitioned Fe and Cu while leaving Co–Ni distributions largely intact.

6.3. Magnetite-Ti-Magnetite Trace Element Behavior and Implications for Ore Genesis

The composition of Ti-magnetite s in the intrusive bodies and hydrothermal veins of Northeast Saveh lies below the magnetite-ulvöspinel join, with a tendency toward the wüstite (FeO) component (Figure 18). Martitized hematite observed in thin sections indicates that martitization of magnetite occurred during the final stages of oxidation, accompanied by decreasing temperature and increasing oxygen fugacity [60].

With increasing temperature, the Ti-magnetite solid solution separates into ulvöspinel and magnetite, with magnetite acting as the host for ulvöspinel lamellae along (111) planes, forming a Widmanstätten texture [60]. This texture is characterized by a distinctive trellis-like or geometric pattern of exsolution lamellae. It typically develops as thin, needle-like or plate-shaped crystals of a secondary mineral (e.g., ilmenite) oriented along the {111} octahedral planes of the host magnetite. Widmanstätten patterns are indicative of slow cooling rates from high magmatic temperatures, allowing sufficient time for solid-state diffusion and the separation of mineral phases as the solid solution becomes unstable. Subsequently,

ilmenite may form as ulvöspinel becomes unstable during cooling/oxidation. Two relevant pathways are: internal oxidation of ulvöspinel yielding magnetite plus ilmenite:

$$3\ Fe_2TiO_4 + 1/2\ O_2 \rightarrow Fe_3O_4 + 3\ FeTiO_3$$

(or equivalently $6\ Fe_2TiO_4 + O_2 \rightarrow 2\ Fe_3O_4 + 6\ FeTiO_3$), and reaction of ulvöspinel with available TiO_2 to produce ilmenite:

$$Fe_2TiO_4 + TiO_2 \rightarrow 2\ FeTiO_3.$$

The first reaction corresponds to oxidation-driven redistribution of Ti and conversion of Ti-magnetite/ulvöspinel to magnetite + ilmenite; the second requires an external TiO_2 phase (e.g., rutile or exsolved Ti-oxide). If rutile is present in samples (or TiO_2 is liberated by exsolution/dissolution), reaction (2) will promote ilmenite formation at lower temperatures.

These reactions indicate that the initial stage involved a Ti-magnetite solid solution, which, with increasing oxygen fugacity and decreasing temperature, led to the formation of ilmenite lamellae within Ti-magnetite. Thin ilmenite lamellae represent the instability of Ti-magnetite, whereas thicker lamellae result from internal exsolution after Ti-magnetite formation [61].

The degree of martitization varies among Ti-magnetite s in Northeast Saveh. Under high oxygen fugacity, strongly martitized crystals are occasionally observed. The presence of hematite lamellae within some ilmenites likely formed during the final oxidation stage and cooling of the mineralization system, with ilmenite decomposing according to:

$$FeTiO_3 + O_2 = 4TiO_2 + 2Fe_2O_3$$

Petrographic observations indicate disruption of the cubic structure of Ti-magnetite. Thin ilmenite lamellae appear to form during early oxidation of Ti-magnetite along planes enriched in Ti, whereas thicker lamellae developed gradually along the (111) and (100) planes due to progressive oxidation of ulvöspinel lamellae coupled with Ti enrichment along these planes. As noted by [62], thick ilmenite lamellae form under advanced oxidation conditions, while thin lamellae develop during initial oxidation stages.

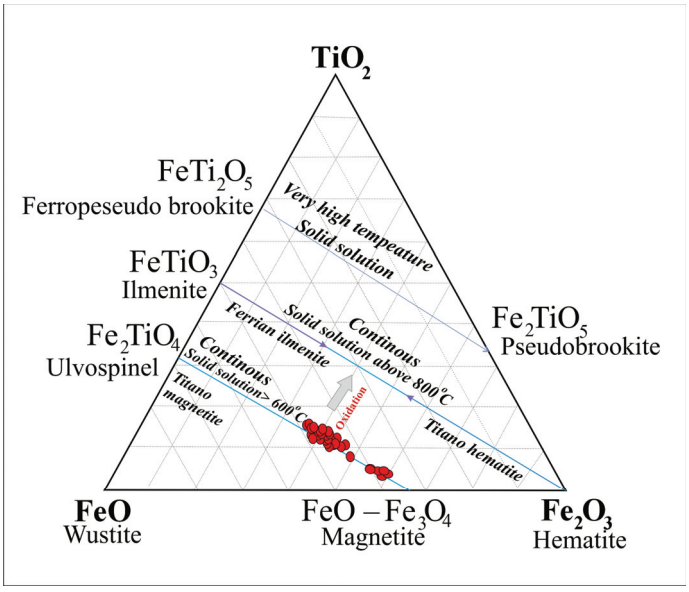


Figure 18. FeO–Fe_2O_3–TiO_2 ternary diagram [63], showing the locations of EPMA analysis results of magnetite and Ti-magnetite from intrusive rocks and hydrothermal veins.

6.3.1. Origin and Compositional Evolution of Ti-Magnetite–Magnetite

The chemistry of Fe–Ti oxides is controlled not only by temperature and oxygen fugacity but also by the compositions of the parental magmas and interacting hydrothermal fluids, and by the wall-rock chemistry that is leached during fluid–rock interaction [12,13,64]. Because cation mobility (e.g., Fe^{2+} and minor substituents) is limited during moderate-temperature martitization, hematite formed by oxidation commonly preserves much of the primary magnetite signature; however, dissolution of coexisting silicates can enrich hydrothermal fluids in elements such as Mg, Al and Ti, producing hematite that is locally enriched in those added elements compared with primary magnetite [12,64].

Oxidative overprinting and partial replacement of Fe–Ti oxides are widespread. Oxidation of magnetite to hematite—commonly expressed as martitization textures along grain margins and cleavage surfaces—is attributed to Fe^{2+} leaching under acidic, oxidizing conditions. This process may be represented stoichiometrically as, for example:

$$4\ Fe_3O_4 + O_2 \rightarrow 6\ Fe_2O_3,$$

and has been documented in comparable systems [65]. Such martitization is commonly observed along crystal boundaries and in alteration halos around oxide grains. Coexistence and textural relations between iron and titanium oxides—along with partial or complete replacement of magnetite and Ti-magnetite by hematite—suggest formation and subsequent modification under non-equilibrium thermodynamic conditions, with variable oxygen fugacity (fO_2) and temperature. The observed replacement textures are consistent with an increase in fO_2 during later stages, attributable to supergene weathering and/or late hydrothermal alteration [66–68]. Evidence of martitization within partly subhedral hematite crystals from Northeast Saveh further supports a hydrothermal-oxidative overprint on primary magnetite.

Comparison of intrusive Ti-magnetites and hydrothermal magnetites from the mineralized veins in Northeast Saveh demonstrates element redistribution during oxide phase transformations (Figure 19). Ti-magnetites from the intrusive bodies are enriched in Ti, Al and V, whereas magnetites from the silica-veins are depleted in those elements and show higher Fe contents—consistent with crystallization from a more mafic host for the intrusive and with later oxidation/repartitioning at elevated fO_2. Measured V_2O_5 in intrusive Ti-magnetite s ranges from ~0.016 to 1.28 wt.% (mean ≈ 0.88 wt.%), whereas V_2O_5 in vein magnetites ranges from ~0.012 to 0.39 wt.% (mean ≈ 0.12 wt.%)—confirming strong V and Cr enrichment in magmatic oxides relative to hydrothermal counterparts [12].

Vanadium partitioning is highly fO_2-sensitive: at low fO_2, V^{3+} (ionic radius ≈ 64 ppm) substitutes readily for Fe^{3+} (≈65 ppm), whereas at higher fO_2, V is oxidized to V^{5+} and becomes incompatible with the oxide lattice [69–71]. Thus, V (and Cr) concentrations in magnetite can record both the magmatic/hydrothermal redox path and fluid–rock reactions during magnetite growth [72,73].

Titanium incorporation into magnetite is likewise temperature-dependent. Higher crystallization temperatures favor greater Ti uptake into the Ti-magnetite solid solution, whereas cooling (and/or delayed increases in fO_2) promotes Ti exsolution (ilmenite/rutile) as lamellae or rims [74–76]. Petrographically, Northeast Saveh Ti-magnetite s display ilmenite lamellae of variable thickness (thin lamellae from early oxidation; thicker lamellae from exsolution), and martitization textures are common where repeated hydrothermal fluid pulses have leached Fe^{2+} and driven hematite replacement [61,62,77].

Chemical re-equilibration of magnetite during multi-phase hydrothermal activity can alter Ti, Al, Mg, Mn, Ca and Si contents [14,78]. A V/Ti versus Fe bivariate plot effectively discriminates magmatic Ti-magnetite s from hydrothermally re-equilibrated

https://doi.org/10.3390/min16020212

magnetites [76]. When our mineral data are plotted on this diagram, intrusive samples fall in the magmatic field while vein samples plot in the hydrothermal/re-equilibrated field (Figure 19), indicating the strong influence of hydrothermal fluids on oxide chemistry and the occurrence of repeated fluid release and Fe-leaching during system evolution.

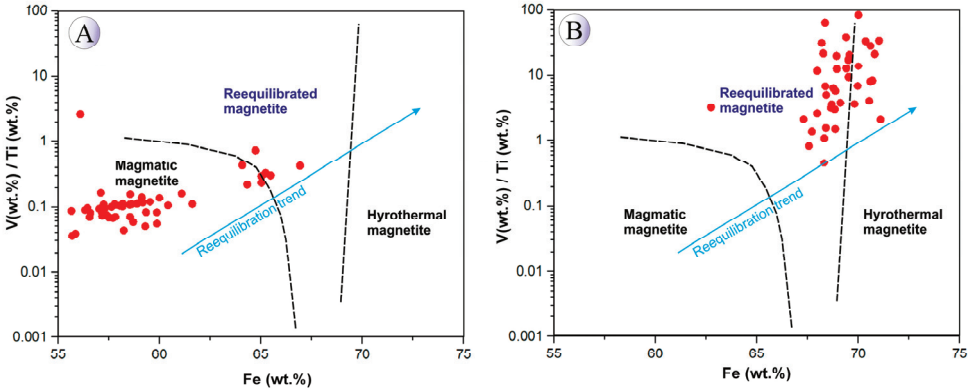


Figure 19. V (wt.%)/Ti (wt.%) versus Fe (wt.%) diagram to distinguish magmatic, hydrothermal and re-equilibrated magnetites [75]. (**A**) Samples related to intrusive bodies. (**B**) Samples related to mineralized veins.

6.3.2. Physicochemical Drivers of Magnetite Compositional Re-Equilibration During Ore Formation

These compositional differences clearly reflect the contrasting physicochemical conditions between magmatic and hydrothermal systems, particularly the relative oxidation state and temperature during mineral formation. To constrain the formation temperatures of Ti-magnetite –magnetite in Northeast Saveh, we plotted the element data on bivariate diagrams. An Al + Mn versus Ti + V (wt.%) plot (Figure 20) indicates that Ti-magnetite s from the intrusive bodies record high crystallization temperatures, whereas magnetites from silica-rich mineralized veins formed at intermediate temperatures (≈200–300 °C), consistent with fluid-inclusion constraints from quartz in the veins [19]. This trend is interpreted as cooling of the system coupled with progressive input of meteoric/oxidizing fluids during hydrothermal activity and subsequent magnetite precipitation at lower temperatures.

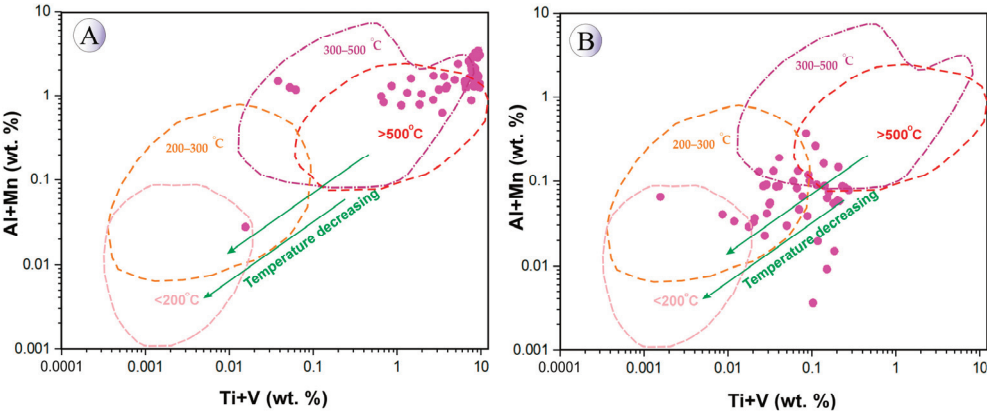


Figure 20. Bivariate plot of Ti + V (wt.%) versus Al + Mn (wt.%) [12,43] showing the temperature range of Northeast Saveh magnetites and Ti-magnetite s. (**A**) Samples related to intrusive bodies. (**B**) Samples related to mineralized veins.

A Ti (wt.%) vs. Mg + Al + Si (wt.%) diagram (after [74]; Figure 21A) further supports extensive fluid–rock interaction during vein magnetite formation. Likewise, plotting Ti (wt.%) versus V (wt.%) effectively discriminates magmatic from hydrothermal magnetites [12];

Northeast Saveh samples separate clearly into magmatic (intrusive) and hydrothermal (vein) groups on this diagram (Figure 21B).

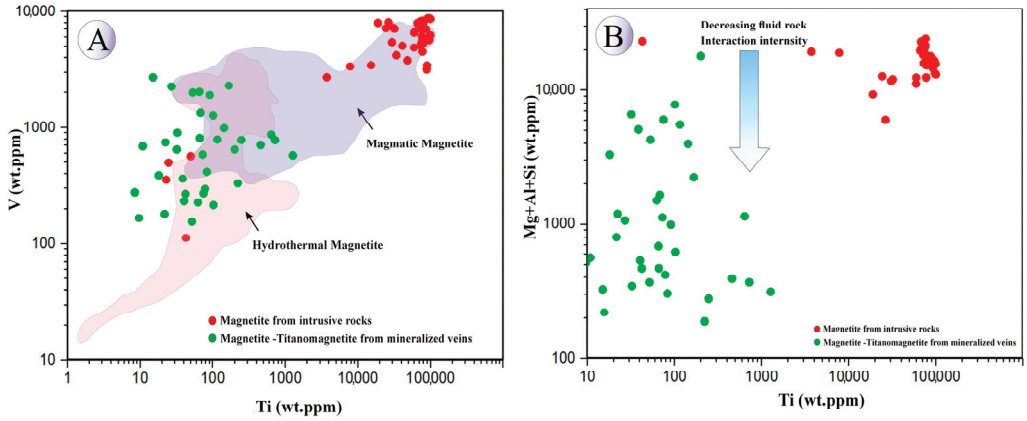


Figure 21. (**A**) Ti versus Mg + Al + Si diagram [73] for determining the reaction rate between fluid and wall rock in Northeast Saveh magnetites. The arrow indicates the direction of decreasing fluid-rock interaction rate. (**B**) Bivariate diagram of Ti versus V [12] showing the range of Northeast Saveh Ti-magnetite s in the magmatic field and Ti-magnetite s of mineralized veins in the hydrothermal field.

Vanadium and Ti distributions record redox and thermal evolution (Figure 22). Intrusive Ti-magnetites are relatively enriched in V and Ti compared with vein magnetites, consistent with crystallization from a lower-fO_2, higher-T magmatic environment [79,80]. Because V speciation and partitioning are highly oxygen-sensitive [69,81], the observed decrease in V and Cr from intrusive to vein magnetites indicates oxidation and element redistribution during hydrothermal re-equilibration. Plotting V (or V_2O_3) variations suggests a progressive increase in fluid fO_2 from the parental magma toward the mineralized veins, accompanied by cooling and crustal contamination, evidence for intense fluid–rock interaction during ore formation [82].

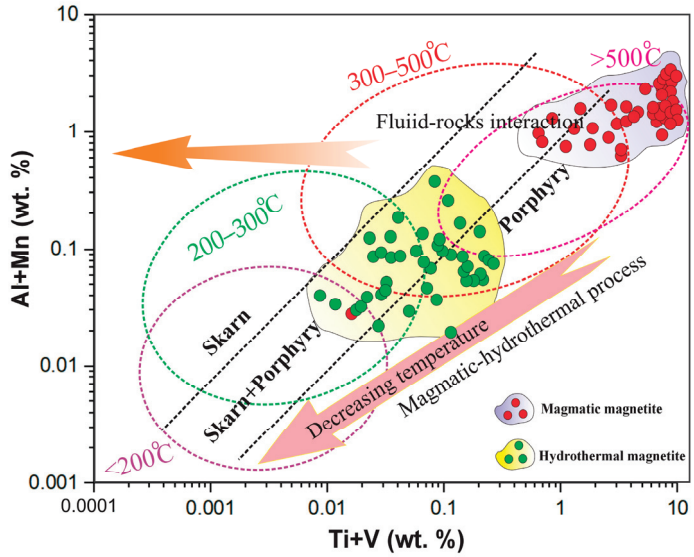


Figure 22. Diagram showing the relationship between magnetite composition and deposit type (temperature trends and boundaries from [12].

In sum, oxide geochemistry (Ti, V, Al, Mn) and mineral textures in Northeast Saveh record a high-T, low-fO_2 magmatic origin for intrusive Ti-magnetite s, followed by hydrothermal overprint at intermediate temperatures and higher fO_2 during vein magnetite

https://doi.org/10.3390/min16020212

formation. Multi-stage fluid release and Fe-leaching during hydrothermal events appear to have driven the observed compositional re-equilibration (Figures 11–14); [12,73,79].

7. Conclusions

This study integrates geology, back-scattered imaging and electron-microprobe analyses to constrain the origin and evolution of Cu–Fe sulfide–oxide mineralization in the Northeast Saveh district.

Mineralization is structurally controlled by fault corridors (N–S and N25°E–N50°W trends) with mineralized zones from tens of meters to ~1 km and Cu grades of ~0.1–5 wt.%. Combined oxide and sulfide geochemistry provides practical discriminants to separate magmatic vs. hydrothermal signatures and to vector toward higher-grade Cu domains.

Ti-magnetites in the shallow monzodiorite intrusions record a high-temperature, low-fO_2 magmatic signature (Ti, V, Al enrichment), whereas magnetites from silica-rich veins formed at lower, intermediate temperatures (~200–300 °C) and under higher fO_2. EPMA data plot the two groups in separate magmatic vs. hydrothermal fields, documenting oxide re-equilibration during hydrothermal overprint. Measured Fe_2O_3 and TiO_2 contents differ markedly between intrusive and vein oxides, reflecting crystallization from different parental fluids and subsequent element redistribution during oxidation and fluid–rock interaction.

Pyrite trace-element systematics (notably Co–Ni–As and dominant Co/Ni values ∼1–10) point to a principally magmatic–hydrothermal source with progressive cooling and increasing meteoric-water input. Pyrite chemistry thus records changes in temperature, ligand chemistry and redox during mineralization.

Chalcopyrite is the primary Cu-host. Replacement textures and micro-textures document a multi-stage evolution: early magmatic–hydrothermal chalcopyrite ± bornite, later hydrothermal reworking and sulfide replacement (covellite → chalcocite/digenite depending on T and fluid composition), and a pronounced supergene stage producing chalcocite, covellite and oxide-hydroxides (malachite, azurite, goethite).

The abundance and mode of incorporation of trace elements in chalcopyrite (solid solution vs. inclusions), and partitioning in Fe–Ti oxides (V, Cr, Ti) are controlled by temperature, fO_2/fS_2, fluid composition and competition among co-precipitating sulfides. Repeated hydrothermal pulses and Fe-leaching explain observed martitization and hematite replacement textures.

The Northeast Saveh Epithermal system is dominantly magmatic–hydrothermal in origin (early Fe–Ti oxides and primary sulfides), subsequently overprinted by lower-temperature hydrothermal re-equilibration and extensive supergene enrichment/oxidation that redistributed Cu and trace metals.

Supplementary Materials: The following supporting information can be downloaded at: https://www.mdpi.com/article/10.3390/min16020212/s1. Table S1: EPMA results of pyrite in the Northeast Saveh (wt.%). Table S2: EPMA results of chalcopyrite in the Northeast Saveh (wt.%), Table S3: EPMA results of chalcocite in the Northeast Saveh (wt.%), Table S4: EPMA results of magnetite in the Northeast Saveh (wt.%), Table S5: EPMA results of Ti-magnetite in the Northeast Saveh (wt.%).

Author Contributions: Conceptualization, M.G.; Methodology, M.G., H.Z. and U.K.; Software, M.G., A.A., S.H.-M. and J.H.; Validation, M.G., A.A. and S.H.-M.; Formal analysis, U.K.; Investigation, M.G.; Resources, M.G. and U.K.; Data curation, J.H.; Writing—original draft, M.G.; Writing—review and editing, H.Z., U.K. and A.A.; Supervision, H.Z.; Funding acquisition, M.G. and U.K. All authors have read and agreed to the published version of the manuscript.

Funding: This research was partly funded (without a specific grant number) by the Ministry of Sciences, Research and Technology, Tehran, Iran, and the University of Vienna, Austria (open Access Funding by the University of Vienna).

Data Availability Statement: The data presented in this study are available upon request from the corresponding author due to the ongoing research.

Acknowledgments: We sincerely appreciate the anonymous reviewers for their valuable time and insightful comments, which have significantly contributed to improving the quality of this manuscript.

Conflicts of Interest: The authors declare no conflicts of interest. The funders had no role in the design of the study; in the collection, analyses, or interpretation of data; in the writing of the manuscript; or in the decision to publish the results.

References

1. Zhu, Z.Y.; Cook, N.; Yang, T.; Ciobanu, C.; Zhao, K.D.; Jiang, S.Y. Mapping of sulfur isotopes and trace elements in sulfides by LA-(MC)-ICP-MS: Potential analytical problems, improvements and implications. *Minerals* **2016**, *6*, 110. [CrossRef]
2. Reich, M.; Deditius, A.; Chryssoulis, S.; Li, J.-W.; Ma, C.-Q.; Parada, M.A.; Barra, F.; Mittermayr, F. Pyrite as a record of hydrothermal fluid evolution in a porphyry copper system: A SIMS/EMPA trace element study. *Geochim. Cosmochim. Acta* **2013**, *104*, 42–62. [CrossRef]
3. Deditius, A.P.; Reich, M.; Kesler, S.E.; Utsunomiya, S.; Chryssoulis, S.L.; Walshe, J.; Ewing, R.C. The coupled geochemistry of Au and As in pyrite from hydrothermal ore deposits. *Geochim. Cosmochim. Acta* **2014**, *140*, 644–670. [CrossRef]
4. Large, R.R.; Danyushevsky, L.; Hollit, C.; Maslennikov, V.; Meffre, S.; Gilbert, S.; Bull, S.; Scott, R.; Emsbo, P.; Thomas, H.; et al. Gold and trace element zonation in pyrite using a laser imaging technique: Implications for the timing of gold in orogenic and Carlin-style sediment-hosted deposits. *Econ. Geol.* **2009**, *104*, 635–668. [CrossRef]
5. Cook, N.J.; Ciobanu, C.L.; Meria, D.; Silcock, D.; Wade, B. Arsenopyrite–Pyrite Association in an Orogenic Gold Ore: Tracing Mineralization History from Textures and Trace Elements. *Econ. Geol.* **2013**, *108*, 1273–1283. [CrossRef]
6. Sykora, S.; Cooke, D.R.; Meffre, S.; Stephanov, A.S.; Gardner, K.; Scott, R.; Selley, D.; Harris, A.C. Evolution of pyrite trace element compositions from porphyry-style and epithermal conditions at the Lihir Gold deposit: Implications for ore genesis and mineral processing. *Econ. Geol.* **2018**, *113*, 193–208. [CrossRef]
7. Córdoba, E.M.; Muñoz, J.A.; Blázquez, M.L.; González, F.; Ballester, A. Leaching of chalcopyrite with ferric ion. Part I: General aspects. *Hydrometallurgy* **2009**, *93*, 81–87. [CrossRef]
8. George, L.L.; Cook, N.J.; Crowe, B.B.P.; Ciobanu, C.L. Trace elements in hydrothermal chalcopyrite. *Mineral. Mag.* **2018**, *82*, 59–88. [CrossRef]
9. Caraballo, E.; Beaudoin, G.; Dare, S. Trace element composition of chalcopyrite as a tool for deposit type discrimination from magmatic and hydrothermal settings: A machine learning approach. *Miner. Deposita* **2025**, *61*, 299–326. [CrossRef]
10. Tang, Y.; Sun, D.; Gou, J.; Ni, X.; Zeng, X.; Zhang, X.; Liu, W.; Liang, S.; Deng, C. Chalcopyrite geochemistry: Advancements and implications in ore deposit research. *Ore Geol. Rev.* **2025**, *179*, 106528. [CrossRef]
11. Dupuis, C.; Beaudoin, G. Discriminant diagrams for iron oxide trace element fingerprinting of mineral deposit types. *Miner. Deposita* **2011**, *46*, 319–335. [CrossRef]
12. Nadoll, P.; Angerer, T.; Mauk, J.L.; French, D.; Walshe, J. The chemistry of hydrothermal magnetite: A review. *Ore Geol. Rev.* **2014**, *61*, 1–32. [CrossRef]
13. Dare, S.A.S.; Barnes, S.J.; Beaudoin, G.; Meric, J.; Boutroy, E.; Potvin-Doucet, C. Trace elements in magnetite as petrogenetic indicators. *Miner. Deposita* **2014**, *49*, 785–796. [CrossRef]
14. Hu, H.; Lentz, D.; Li, J.W.; McCarron, T.; Zhao, X.F.; Hall, D. Reequilibration processes in magnetite from iron skarn deposits. *Econ. Geol.* **2015**, *110*, 1–8. [CrossRef]
15. Verdel, C.; Wernicke, B.P.; Hassanzadeh, J.; Guest, B. A Paleogene extensional arc flare-up in Iran. *Tectonics* **2011**, *30*, 3008–3302. [CrossRef]
16. Babazadeh, S.; Haase, K.; Ghalamghash, J. Magmatic evolution of the migrating central Urumieh–Dokhtar arc, Iran: Implications for magma production. *Int. J. Earth Sci.* **2023**, *112*, 1577–1597. [CrossRef]
17. Goudarzi, M.; Zamanian, H.; Klötzli, U.; Sláma, J.; Míková, J.; Burda, J.; Lentz, D.R.; Ullah, M.; Homnan, J. Unraveling the Protracted Magmatic Evolution in the Central Urumieh–Dokhtar Magmatic Arc (Northeast Saveh, Iran): Zircon U-Pb Dating, Lu-Hf Isotopes, and Geochemical Constraints. *Minerals* **2025**, *15*, 375. [CrossRef]
18. Goudarzi, M.; Zamanian, H.; Klotzli, U. Geochemistry and tectono-magmatic setting of hypabyssal intrusive rocks in the south of Mamouniyeh, Urumieh–Dokhtar magmatic arc, Iran. *Sci. Q. J. Geosci.* **2025**, *35*, 129–148. [CrossRef]

19. Goudarzi, M.; Zamanian, H.; Klötzli, U.; Lentz, D.; Ullah, M. Genesis of the Mamuniyeh copper deposit in the central Urumieh–Dokhtar Magmatic Arc, Iran: Constraints from geology, geochemistry, fluid inclusions, and H–O–S isotopes. *Ore Geol. Rev.* **2024**, *175*, 106279. [CrossRef]
20. Whitney, D.L.; Evans, B.W. Abbreviations for names of rock-forming minerals. *Am. Mineral.* **2010**, *95*, 185–187. [CrossRef]
21. Zhao, D.; Essene, E.J.; Zhang, Y. An oxygen barometer for rutile–ilmenite assemblages: Oxidation state of metasomatic agents in the mantle. *Earth Planet. Sci. Lett.* **1999**, *166*, 127–137. [CrossRef]
22. Clark, C.; Grguric, B.; Schmidt, M.A. Genetic implications of pyrite chemistry from the Palaeoproterozoic Olary Domain and overlying neoproterozoic Adelaidean sequences, northeastern South Australia. *Ore Geol. Rev.* **2004**, *25*, 237–257. [CrossRef]
23. Huerta-Diaz, M.A.; Morse, J.W. Pyritization of Trace Metals in Anoxic Marine Sediments. *Geochim. Cosmochim. Acta* **1992**, *56*, 2681–2702. [CrossRef]
24. Koglin, N.; Frimmel, H.E.; Minter, W.E.L.; Brätz, H. Trace-Element Characteristics of Different Pyrite Types in Mesoarchaean to Palaeoproterozoic Placer Deposits. *Miner. Deposita* **2010**, *45*, 259–280. [CrossRef]
25. Zhao, H.X.; Frimmel, H.E.; Jiang, S.Y.; Dai, B.Z. LA-ICP-MS Trace Element Analysis of Pyrite from the Xiaoqinling Gold District, China: Implications for Ore Genesis. *Ore Geol. Rev.* **2011**, *43*, 142–153. [CrossRef]
26. Loftus-Hills, G.; Solomon, M. Cobalt, nickel and selenium in sulfides as indicators of ore genesis. *Miner. Deposita* **1967**, *2*, 228–242. [CrossRef]
27. Yan, Y.T.; Li, S.R.; Jia, B.J.; Zhang, N.; Yan, L.N. Composition typomorphic characteristics and statistical analysis of pyrite in gold deposits of different genetic types. *Adv. Mater. Res.* **2012**, *463–464*, 25–29. [CrossRef]
28. Niu, S.D.; Li, S.-R.; Santosh, M.; Zhang, D.-H.; Li, Z.-D.; Shan, M.-J.; Lan, Y.-X.; Gao, D.-R.; Zhao, W.-B. Mineralogical and Isotopic Studies of Base Metal Sulfides from the Jiawula Ag–Pb–Zn Deposit, Inner Mongolia, NE China. *J. Asian Earth Sci.* **2016**, *115*, 480–491. [CrossRef]
29. Kusebauch, C.; Oelze, M.; Gleeson, S.A. Partitioning of Arsenic between Hydrothermal Fluid and Pyrite during Experimental Siderite Replacement. *Chem. Geol.* **2018**, *500*, 136–147. [CrossRef]
30. Cook, N.J.; Chryssoulis, S.L. Concentrations of invisible gold in the common sulfides. *Can. Mineral.* **1990**, *28*, 1–16.
31. Liang, J.-L.; Sun, W.-D.; Li, Y.-L.; Zhu, S.-Y.; Li, H.; Liu, Y.-L.; Zhai, W. Study on the Valence States of Arsenic in Arsenian Pyrite: Implications for Au Deposition Mechanism of the Yangshan Carlin-Type Gold Deposit, Western Qinling Belt. *J. Asian Earth Sci.* **2013**, *62*, 363–372. [CrossRef]
32. Boyle, R.W. *The Geochemistry of Gold and Its Deposits*; Bulletin 280; Government of Canada, Energy, Mines and Resources: Ottawa, ON, Canada, 1979; p. 280.
33. Morse, J.W.; Luther, G.W. Chemical influences on trace metal-sulfide interactions in anoxic sediments. *Geochim. Cosmochim. Acta* **1999**, *63*, 19–20. [CrossRef]
34. Palme, H.; O'Neill, H.S.C. Cosmochemical Estimates of Mantle Composition. *Treatise Geochem.* **2003**, *2*, 1–38. [CrossRef]
35. Kahkhaei, M.R.; Esmaili, D.; Francisco, C.G. Geochemical and Isotopic (Nd and Sr) Constraints on Elucidating the Origin of Intrusions from Northwest Saveh, Central Iran. *Geopersia* **2014**, *4*, 103–123. [CrossRef]
36. Abraitis, P.K.; Pattrick, R.A.D.; Vaughan, D.J. Variations in the Compositional, Textural, and Electrical Properties of Natural Pyrite: A Review. *Int. J. Miner. Process.* **2004**, *74*, 41–59. [CrossRef]
37. Zhao, J.; Brugger, J.; Chen, G.; Ngothai, Y.; Pring, A. Experimental Study of the Formation of Chalcopyrite and Bornite via the Sulfidation of Hematite: Mineral Replacements with a Large Volume Increase. *Am. Mineral.* **2014**, *99*, 343–354. [CrossRef]
38. Bralia, A.; Sabatini, G.; Troja, F. A Revaluation of the Co/Ni Ratio in Pyrite as Geochemical Tool in Ore Genesis Problems. *Miner. Deposita* **1979**, *14*, 353–374. [CrossRef]
39. Yuan, Y.B.; Yuan, S.D.; Zhao, P.L.; Zhang, D.L. Properties and Evolution of Granitic Magma in the Huangshaping Polymetallic Deposit, Southern Hunan: Constraints on Mineralization Differences. *Acta Petrol. Sin.* **2018**, *34*, 2565–2580.
40. Gregory, D.D.; Large, R.R.; Halpin, J.A.; Baturina, L.; Lyons, T.W.; Wu, S.; Danyushevsky, L.; Sack, P.J.; Chappaz, A.; Maslennikov, V.V.; et al. Trace Element Content of Sedimentary Pyrite in Black Shales. *Econ. Geol.* **2015**, *110*, 1389–1410. [CrossRef]
41. Bajwah, Z.; Seccombe, P.; Offler, R.; Distribution, T.E. Co:Ni Ratios and Genesis of the Big Cadia Iron–Copper Deposit, New South Wales, Australia. *Miner. Deposita* **1987**, *22*, 292–300. [CrossRef]
42. Reich, M.; Simon, A.C.; Deditius, A.; Barra, F.; Chryssoulis, S.; Lagas, G.; Tardani, D.; Knipping, J.; Bilenker, L.; Sanchez-Alfaro, P.; et al. Trace Element Signature of Pyrite from the Los Colorados Iron Oxide–Apatite (IOA) Deposit, Chile: A Missing Link between Andean IOA and Iron Oxide Copper–Gold Systems? *Econ. Geol.* **2016**, *111*, 743–761. [CrossRef]
43. Deditius, A.P.; Utsunomiya, S.; Renock, D.; Ewing, R.C.; Ramana, C.V.; Becker, U.; Kesler, S.E. A Proposed New Type of Arsenian Pyrite: Composition, Nanostructure and Geological Significance. *Geochim. Cosmochim. Acta* **2008**, *72*, 2919–2933. [CrossRef]
44. Keith, M.; Smith, D.J.; Jenkin, G.R.T.; Holwell, D.A.; Dye, M.D. A Review of Te and Se Systematics in Hydrothermal Pyrite from Precious Metal Deposits: Insights into Ore-Forming Processes. *Ore Geol. Rev.* **2018**, *96*, 269–282. [CrossRef]
45. Feng, Y.Z.; Zhang, Y.; Xie, Y.L.; Shao, Y.J.; Lai, C.K. Pyrite Geochemistry and Metallogenic Implications of the Gutaishan Au Deposit in Jiangnan Orogen, South China. *Ore Geol. Rev.* **2020**, *117*, 103298. [CrossRef]

46. Cao, G.S.; Zhang, Y.; Zhao, H.; Cheng, J.; Hao, J.; Lei, J.; Song, S.; Wang, X. Trace Element Variations of Pyrite in Orogenic Gold Deposits: Constraints from Big Data and Machine Learning. *Ore Geol. Rev.* **2023**, *157*, 105447. [CrossRef]
47. Song, K.R.; Tang, L.; Zhang, S.-T.; Santosh, M.; Spencer, C.J.; Zhao, Y.; Li, H.-X.; Wang, L.; Zhang, A.-L.; Sun, Y.-Q. Genesis of the Bianjiadayuan Pb–Zn polymetallic deposit, Inner Mongolia, China: Constraints from in-situ sulfur isotope and trace element geochemistry of pyrite. *Geosci. Front.* **2019**, *10*, 1863–1877. [CrossRef]
48. Real, I.D.; Thompson, J.F.H.; Simon, A.C.; Reich, M. Geochemical and Isotopic Signature of Pyrite as a Proxy for Fluid Source and Evolution in the Candelaria–Punta del Cobre Iron Oxide Copper–Gold District, Chile. *Econ. Geol.* **2020**, *115*, 1493–1517. [CrossRef]
49. Zhang, J.K.; Shao, Y.J.; Liu, Z.F.; Chen, K. Sphalerite as a Record of Metallogenic Information Using Multivariate Statistical Analysis: Constraints from Trace Element Geochemistry. *J. Geochem. Explor.* **2022**, *232*, 106883. [CrossRef]
50. Zhao, Y.H.; Tian, H.; Li, J.; Chen, S.Y.; Zhao, J.N. Constraints on the Genesis of the Laochang Pb–Zn Ore, Gejiu District, Yunnan: Evidence from Sulfide Trace Element and Isotope Geochemistry. *Ore Geol. Rev.* **2022**, *150*, 105162. [CrossRef]
51. Chaudhari, A.K.; Webster, N.A.S.; Xia, F.; Friedrich, A.; Ram, R.; Etschmann, B.; Liu, W.; Wykes, J.; Brand, H.E.A.; Brugger, J. Anatomy of a Complex Mineral Replacement Reaction: Role of Aqueous Redox, Mineral Nucleation, and Ion Transport Properties Revealed by an In-Situ Study of the Replacement of Chalcopyrite by Copper Sulfides. *Chem. Geol.* **2021**, *581*, 120390. [CrossRef]
52. Torró, L.; Benites, D.; Vallance, J.; Laurent, O.; Ortz-Benavente, B.A.; Chelle-Michou, C.; Proenza, J.A.; Fontbote, L. Trace Element Geochemistry of Sphalerite and Chalcopyrite in Arc-Hosted VMS Deposits. *J. Geochem. Explor.* **2022**, *232*, 106882. [CrossRef]
53. Huston, D.L.; Sie, S.H.; Suter, G.F.; Cooke, D.R.; Both, R.A. Trace Elements in Sulfide Minerals from Eastern Australian Volcanic-Hosted Massive Sulfide Deposits. Part I: Proton Microprobe Analyses of Pyrite, Chalcopyrite, and Sphalerite; Part II: Selenium Levels in Pyrite—Comparison with δ34S Values and Implications for the Source of Sulfur in Volcanogenic Hydrothermal Systems. *Econ. Geol.* **1995**, *90*, 1167–1196. [CrossRef]
54. Aird, H.M.; Purcell, C.K.; DeWitt, N.; Matthews, J.; Capurro, T.; Claiborne, J.; Bermudez, J.; Meisel, Z. Gold- and silver-bearing assemblages in the Ann-Mason copper porphyry deposit, Yerington, Nevada. *Ore Geol. Rev.* **2021**, *138*, 104339. [CrossRef]
55. Kojima, S.; Sugaki, A. Phase Relations in the Cu–Fe–Zn–S System between 500° and 300 °C under Hydrothermal Conditions. *Econ. Geol.* **1985**, *80*, 158–171. [CrossRef]
56. Simon, G. Gold in Porphyry Copper Deposits: Experimental Determination of the Distribution of Gold in the Cu–Fe–S System at 400–700 °C. *Econ. Geol.* **2000**, *95*, 259–276. [CrossRef]
57. Goudarzi, M.; Zamanian, H.; Klötzli, U. Copper mineralization pattern based on mineralogy, alteration, geochemistry of intrusive rocks and fluid inclusion in the south of Mamuoniyeh, middle part of Urumieh–Dokhtar magmatic arc, Iran. *Sci. Q. J. Geosci.* **2024**, *34*, 35–62. [CrossRef]
58. Yang, C.; Beaudoin, G.; Tang, J.-X.; Song, Y.; Wang, L.-Q.; Huang, X.-W.; Mineralogy, C.-S. Texture, and Geochemistry in the Tiegelongnan Porphyry–Epithermal Copper System, Tibet, China. *Miner. Deposita* **2022**, *57*, 759–779. [CrossRef]
59. Chen, D.F. Characteristics of Main Metallic Minerals in Some Copper–Nickel Sulfide Deposits of China. *Acta Petrol. Mineral.* **1995**, *14*, 345–354.
60. Mondal, R.; Baidya, T.K. Titaniferous Magnetite Deposits Associated with Archean Greenstone Belt in the East Indian Shield. *Earth Sci.* **2015**, *4*, 15–30. [CrossRef]
61. Dunn, J.A.; Dey, A.K. Vanadium Bearing Titaniferous Magnetite Iron Ores in Singhbhum and Mayurbhanj, India. *Trans. Min. Geol. Metall. Inst. India* **1973**, *3*, 117–194. [CrossRef]
62. Pasteris, J.D. Relationships between Temperature and Oxygen Fugacity among Fe–Ti Oxides in Two Regions of the Duluth Complex. *Can. Mineral.* **1985**, *23*, 111–127.
63. Buddington, A.F.; Lindsley, D.H. Iron-titanium oxide minerals and synthetic equivalents. *J. Petrol.* **1964**, *5*, 310–357. [CrossRef]
64. Angerer, T.; Hagemann, S.G.; Danyushevsky, L.V. Geochemical Evolution of the Banded Iron Formation–Hosted High-Grade Iron Ore System in the Koolyanobbing Greenstone Belt, Western Australia. *Econ. Geol.* **2012**, *107*, 599–644. [CrossRef]
65. Mücke, A.; Cabral, A.R. Redox and Nonredox Reactions of Magnetite and Hematite in Rocks. *Geochemistry* **2005**, *65*, 271–278. [CrossRef]
66. Klein, C. Some Precambrian Banded Iron-Formations (BIFs) from around the World: Their Age, Geologic Setting, Mineralogy, Metamorphism, Geochemistry, and Origin. *Am. Mineral.* **2005**, *90*, 1473–1499. [CrossRef]
67. Makvandi, S.; Ghasemzadeh-Barvarz, M.; Beaudoin, G.; Grunsky, E.C.; McClenaghan, M.B.; Duchesne, C.; Boutroy, E. Partial Least Squares–Discriminant Analysis of Trace Element Compositions of Magnetite from Various VMS Deposit Subtypes: Application to Mineral Exploration. *Ore Geol. Rev.* **2016**, *78*, 388–408. [CrossRef]
68. Riegler, T.; Lescuyer, J.L.; Wollenberg, P.; Quirt, D.; Beaufort, D. Alteration Related to Uranium Deposits in the Kiggavik–Andrew Lake Structural Trend, 52, Nunavut, Canada: New Insights from Petrography and Clay Mineralogy. *Can. Mineral.* **2014**, *52*, 27–45. [CrossRef]
69. Bordage, A.; Balan, E.; Villiers, J.R.; Cromarty, R.; Juhin, A.; Carvallo, C. V Oxidation State in Fe–Ti Oxides by High-Energy Resolution Fluorescence-Detected X-Ray Absorption Spectroscopy. *Phys. Chem. Miner.* **2011**, *38*, 449–458. [CrossRef]

70. Toplis, M.J.; Carroll, M.R. An Experimental Study of the Influence of Oxygen Fugacity on Fe–Ti Oxide Stability, Phase Relations, and Mineral–Melt Equilibria in Ferro-Basaltic Systems. *J. Petrol.* **1995**, *36*, 1137–1170. [CrossRef]
71. Ahmadzadeh, G.; Jahangiri, A.; Lentz, D.; Mojtahedi, M. Petrogenesis of Plio-Quaternary post-collisional ultrapotassic volcanism in NW of Marand, NW Iran. *J. Asian Earth Sci.* **2010**, *39*, 37–50. [CrossRef]
72. Knipping, J.L.; Bilenker, L.D.; Simon, A.C.; Reich, M.; Barra, F.; Deditius, A.P.; Walle, M.; Heinrich, C.A.; Holtz, F.; Munizaga, R. Trace Elements in Magnetite from Massive Iron Oxide–Apatite Deposits Indicate a Combined Formation by Igneous and Magmatic–Hydrothermal Processes. *Geochim. Cosmochim. Acta* **2015**, *171*, 15–38. [CrossRef]
73. Tian, J.; Zhang, Y.; Gong, L.; Francisco, D.G.; Berador, A.G. Geochemical Evolution and Metallogenic Implications of Magnetite: Perspective from the Giant Cretaceous Atlas Porphyry Cu–Au Deposit (Cebu, Philippines). *Ore Geol. Rev.* **2021**, *133*, 104084. [CrossRef]
74. Craig, J.R.; Vaughan, D.J. *Ore Microscopy and Ore Petrography*; Wiley: New York, NY, USA, 1994.
75. Wen, G.; Li, J.W.; Hofstra, A.H.; Koenig, A.E.; Lowers, H.A.; Adams, D. Hydrothermal Reequilibration of Igneous Magnetite in Altered Granitic Plutons and Its Implications for Magnetite Classification Schemes: Insights from the Handan–Xingtai Iron District, North China Craton. *Geochim. Cosmochim. Acta* **2017**, *213*, 255–270. [CrossRef]
76. Zarasvandi, A.; Rezaei, M.; Sadeghi, M.; Lentz, D.; Adelpour, M.; Pourkaseb, H. Rare earth element signatures of economic and sub-economic porphyry copper systems in Urumieh–Dokhtar magmatic arc (UDMA). *Iran Ore Geol. Rev.* **2015**, *70*, 407–423. [CrossRef]
77. Yin, S.; Wirth, R.; He, H.; Ma, C.; Pan, J.; Xing, J.; Xu, J.; Fu, J.; Zhang, X.-N. Replacement of Magnetite by Hematite in Hydrothermal Systems: A Refined Redox-Independent Model. *Earth Planet. Sci. Lett.* **2022**, *577*, 117282. [CrossRef]
78. Hu, H.; Li, J.-W.; Lentz, D.; Ren, Z.; Zhao, X.-F.; Deng, X.-D.; Hall, D. Dissolution-reprecipitation process of magnetite from the Chengchao iron deposit: Insights into ore genesis and implication for in-situ chemical analysis of magnetite. *Ore Geol. Rev.* **2014**, *57*, 393–405. [CrossRef]
79. Sun, X.; Lin, H.; Fu, Y.; Li, D.; Hollings, P.; Yang, T.; Liu, Z. Trace Element Geochemistry of Magnetite from the Giant Beiya Gold–Polymetallic Deposit in Yunnan Province, Southwest China, and Its Implications for Ore-Forming Processes. *Ore Geol. Rev.* **2017**, *91*, 477–490. [CrossRef]
80. Valkama, M.; Sundblad, K.; Cook, N.J.; Ivashchenko, V.I. Geochemistry and Petrology of the Indium-Bearing Polymetallic Skarn Ores at Pitkäranta, Ladoga Karelia, Russia. *Miner. Deposita* **2016**, *51*, 823–839. [CrossRef]
81. Toplis, M.J.; Corgne, A. An Experimental Study of Element Partitioning between Magnetite, Clinopyroxene and Iron-Bearing Silicate Liquids with Particular Emphasis on Vanadium. *Contrib. Mineral. Petrol.* **2002**, *144*, 22–37. [CrossRef]
82. Wang, C.; Shao, Y.; Zhang, X.; Dick, J.; Liu, Z. Trace Element Geochemistry of Magnetite: Implications for Ore Genesis of the Huanggangliang Sn–Fe Deposit, Inner Mongolia, Northeastern China. *Minerals* **2018**, *8*, 195. [CrossRef]

Disclaimer/Publisher's Note: The statements, opinions and data contained in all publications are solely those of the individual author(s) and contributor(s) and not of MDPI and/or the editor(s). MDPI and/or the editor(s) disclaim responsibility for any injury to people or property resulting from any ideas, methods, instructions or products referred to in the content.

minerals

MDPI

Article

An Occurrence of Pyroxmangite in the NYF Granitic Pegmatite of the Gabal El-Bakriya Intrusion, Arabian–Nubian Shield

Danial M. Fathy [1], Faris A. Abanumay [2,*], Shehata Ali [1], Esam S. Farahat [1], Andrey Bekker [3,4] and Mokhles K. Azer [5]

[1] Geology Department, Faculty of Science, Minia University, El-Minia 61519, Egypt
[2] Department of Geology and Geophysics, King Saud University, Riyadh 11451, Saudi Arabia
[3] Department of Earth and Planetary Sciences, University of California, Riverside, Riverside, CA 92521, USA
[4] Department of Geology, University of Johannesburg, Auckland Park, P.O. Box 524, Johannesburg 2006, South Africa
[5] Geological Sciences Department, National Research Centre, Cairo 12622, Egypt
* Correspondence: fabannumay@ksu.edu.sa

Abstract

We report here, for the first time on the Nubian Shield, the western half of the Arabian–Nubian Shield (ANS), pegmatite-hosted pockets with a unique mineralogy, including pyroxmangite. It represents the second discovery on the ANS, where the first one was at Jabal Aja on the Arabian Shield, the eastern half of the ANS. One of the most remarkable aspects of pyroxmangite is its rarity and the potential economic value of its use in jewelry and decorative applications. Pegmatites are associated with A-type granites of the Gabal El-Bakriya intrusion (GEBI), Eastern Desert, Egypt. Mineralized pegmatites occur at the margin of the alkali-feldspar granite and exhibit gradational contacts with the host rocks. The pegmatites were emplaced as plugs and dikes within the intrusion and along its periphery. Pyroxmangite appears as coarse-grained, massive black aggregates or as disseminated crystals. The pegmatites are composed of K-feldspars and quartz, with subordinate amounts of albite, micas, and mafic minerals. Accessory phases include monazite-(Ce), zircon, fergusonite, xenotime, fluorite, pyrochlore, allanite, thorite, bastnäsite, samarskite, cassiterite, beryl, and pyrochlore. Pyroxmangite-bearing assemblages consist essentially of pyroxmangite and garnet, with accessory pyrochroite, quartz, zircon, magnetite, and fluorite. Geochemically, the pegmatites are highly evolved, with elevated SiO_2 content (76.51–80.69 wt.%) and variable concentrations of trace elements. They show significant enrichment in Nb (Nb > Ta), Y, REE, Zr, Th, U, and F, consistent with NYF-type pegmatites. REE contents range from 173.94 to 518.21 ppm, reflecting diverse accessory mineral assemblages. Tectonically, the pegmatites crystallized in a post-collisional setting, representing a late-stage differentiate of the A-type GEBI magma. Mineralization is concentrated in the apical and marginal zones of the granitic cupola and is dominated by barite, fluorite, Nb-Ta oxides, REE minerals, and uranium-bearing phases. The highly evolved granites, greisens, pegmatites, and quartz-fluorite veins of the GEBI have a high economic potential, deserving further exploration.

Keywords: Arabian–Nubian Shield; Eastern Desert; A-type granite; pegmatites; pyroxmangite; rare metals

1. Introduction

The Arabian–Nubian Shield (ANS), is one of the most significant, Neoproterozoic juvenile continental crust provinces on Earth. The ANS extends along both flanks of the Red Sea and was tectonically separated by Red Sea rifting ~25 Ma ago [1,2]. The ANS corresponds to the northern segment of the East African Orogen (EAO) and is largely composed of Neoproterozoic crystalline basement rocks that were assembled through arc–arc and arc–continent accretion between ca. 1000 and 640 Ma [3–8]. One of the most striking features of the ANS is the abundance of the post-collisional granites and associated pegmatites [9–12].

Post-collisional magmatism on the ANS is marked by widespread emplacement of evolved granitoids and associated pegmatites during the waning stage of the Pan-African orogeny (610–580 Ma). This magmatic transition reflects a shift from subduction-related calc-alkaline activity to anorogenic alkaline magmatism [13–16]. A temporal overlap between the final stages of arc magmatism and the onset of post-collisional, extensional activity is evident in many parts of the shield [17–20]. These late-stage granitoids commonly exhibit signs of post-magmatic alteration—such as albitization, greisenization, and silicification—which frequently result in enrichment in high-field strength elements (HFSEs) and rare metals of substantial economic significance (REEs; Nb, Ta, Zr, U, and Th) [21–27].

We investigated the petrology and geodynamic evolution of post-collisional Neoproterozoic pegmatites associated with A-type granites of the Gabal El-Bakriya intrusion (GEBI), Eastern Desert, Egypt. Although numerous studies have addressed the granitoids and associated rocks of the GEBI [28–34], their genetic interpretation remains controversial.

The investigated pegmatites are notable for containing pyroxmangite-rich pockets, reported here for the first time on the Nubian Shield, and host rare metal-bearing minerals similar to those recognized in other post-collisional systems. This is a report of detailed field observations, petrography, mineral chemistry, and whole-rock geochemical data for the pegmatite and associated pyroxmangite, based on classical methods and advanced techniques such as electron probe microanalyzer (EPMA) and scanning electron microscopy (SEM). The study, thus, sheds light on the magmatic sources and petrogenetic processes responsible for formation of the pegmatites and associated pyroxmangite. Further, it advances our understanding of the mechanisms responsible for rare-metal enrichment in pegmatites. We propose that late-stage magmatic evolution, involving crystallization of a residual melt and pegmatite formation, played a critical role for rare-metal mineralization.

2. Geologic Setting

The GEBI is among the most significant granitic complexes in the Eastern Desert of Egypt. It has garnered significant attention due to its unique geological features and potential economic mineralization. The intrusion is located in the southwestern part of the Central Eastern Desert (Figure 1), about 15 km north of the El-Barramiya gold mine. Geographically, it lies between longitudes 33°41′ and 33°43′ E and latitudes 25°15′ and 25°17′ N. The area is dissected by numerous structurally controlled dry valleys (wadis) filled with alluvial deposits such as the El-Bakriya wadi and its tributaries, which connect with the El-Miyah wadi at the southern part of the study area.

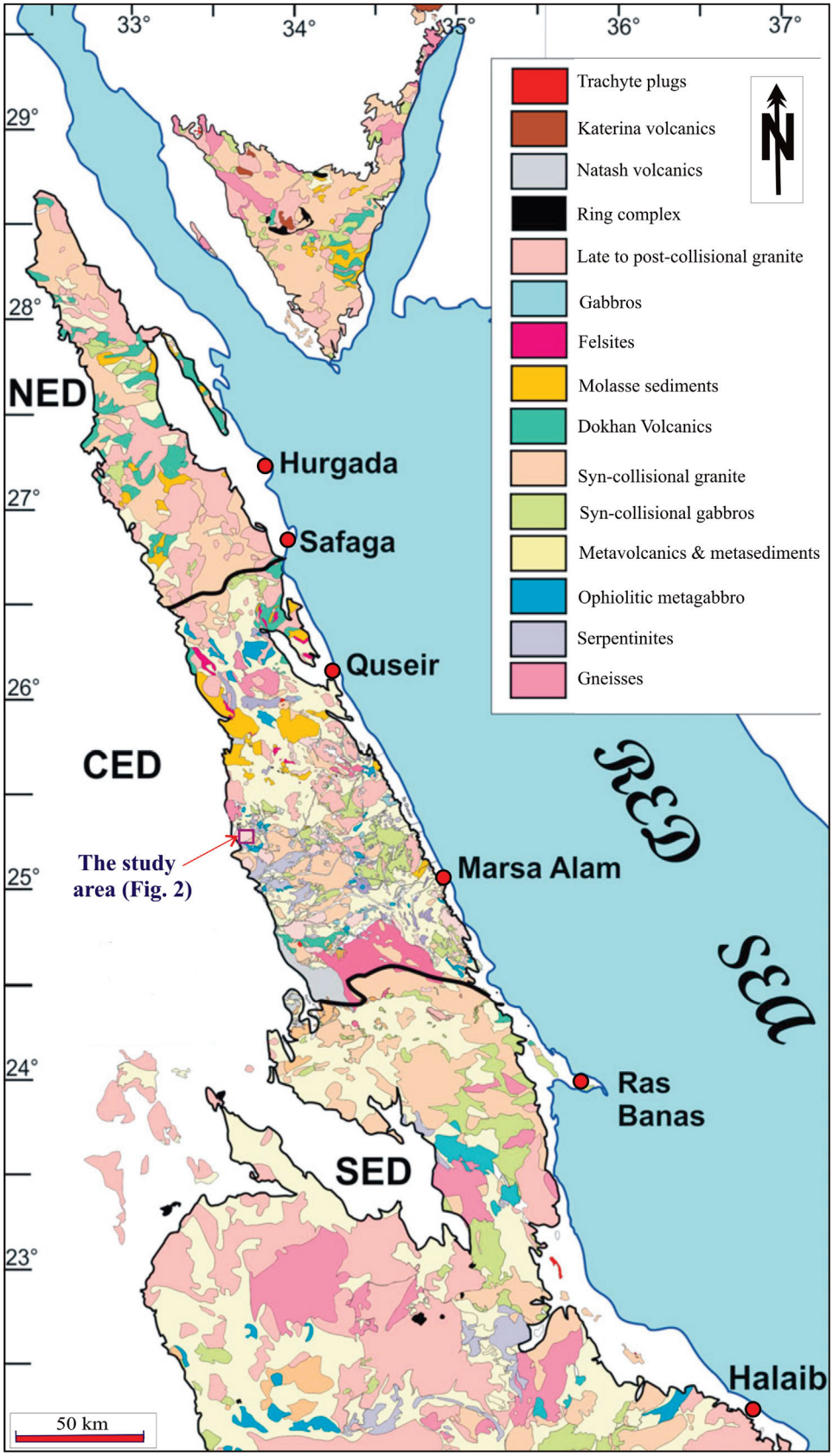


Figure 1. Geologic map of the Egyptian Nubian Shield showing three lithotectonic domains in the Eastern Desert of Egypt (Southern Eastern Desert (SED), Central Eastern Desert (CED), and Northern Eastern Desert (NED)) [35], with the location of the study area indicated. All units, except the tertiary trachyte plugs, are late Neoproterozoic in age.

The Gabal El-Bakriya region mostly consists of Neoproterozoic basement rocks, which are unconformably overlain by Cretaceous Nubian sandstone. The Neoproterozoic basement comprises granitoids, gabbros, and post-granitic dikes of diverse composition (Figure 2). The area displays a complex structural history characterized by faulting, joint formation, and subsequent exfoliation. Faults of various ages and orientations intersect the region, primarily going north–south, northwest–southeast, and northeast–southwest. The N–S faults are the most prevalent and are considered the youngest, whereas the NW–SE faults constitute the oldest fault series [36].

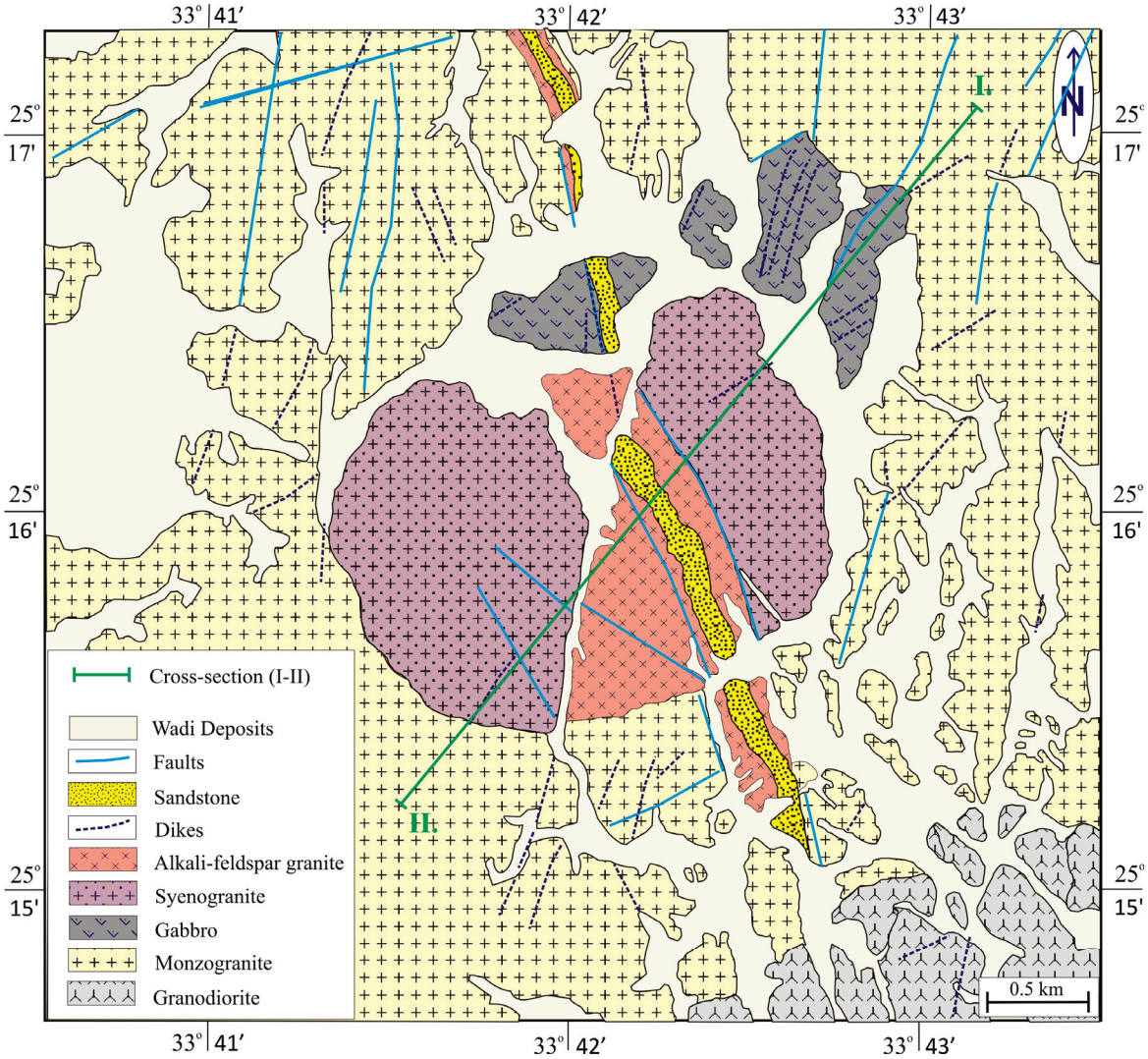


Figure 2. Detailed geologic map of the Gabal El-Bakriya area [22]. Location of the I-II cross-section (Figure 3) is indicated.

The granitoids of the Gabal El-Bakriya can be broadly categorized into syn-collisional and post-collisional varieties. The syn-collisional assemblage comprises diorite to granodiorite, whereas the post-collisional suite includes calc-alkaline monzogranite and A-type granites. The latter defines the GEBI, forming a ring complex with an inner core of alkali-feldspar granite and an outer rim of syenogranite. Although geochronological data are not available for the GEBI, relative age relationships among the rock units have been established from crosscutting relationships and are shown in the geological cross-section (Figure 3).

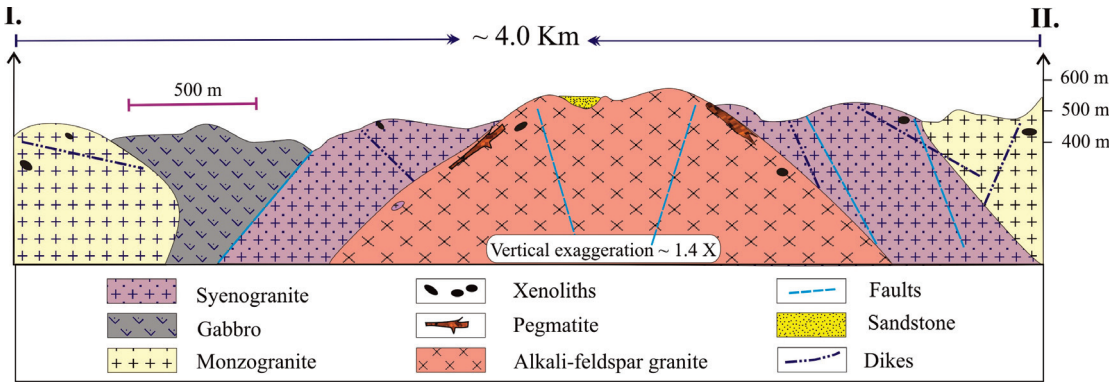


Figure 3. Schematic geologic cross-section showing the relationships among the different rock types in the Gabal El-Bakriya area.

In the field, the A-type granites are readily distinguished by their color and texture and intrude surrounding country rocks with sharp contacts (Figure 4a). Both sharp and gradational contacts between syenogranite and alkali-feldspar granite are observed (Figure 4b). Locally, shear zones transect the granites, particularly affecting the syenogranite and alkali-feldspar granite. These zones are fine-grained and exhibit a reddish to pinkish color. The outer zone of the alkali-feldspar granites is highly tectonized, displaying pervasive alteration and a distinctly dissected appearance. Alteration is characterized by intense sericitization and silicification. Evidence for brittle deformation, including mylonitization and cataclasis, is widespread, producing sheared and fractured granites. Conjugate fractures are common and often injected with thin quartz veinlets.

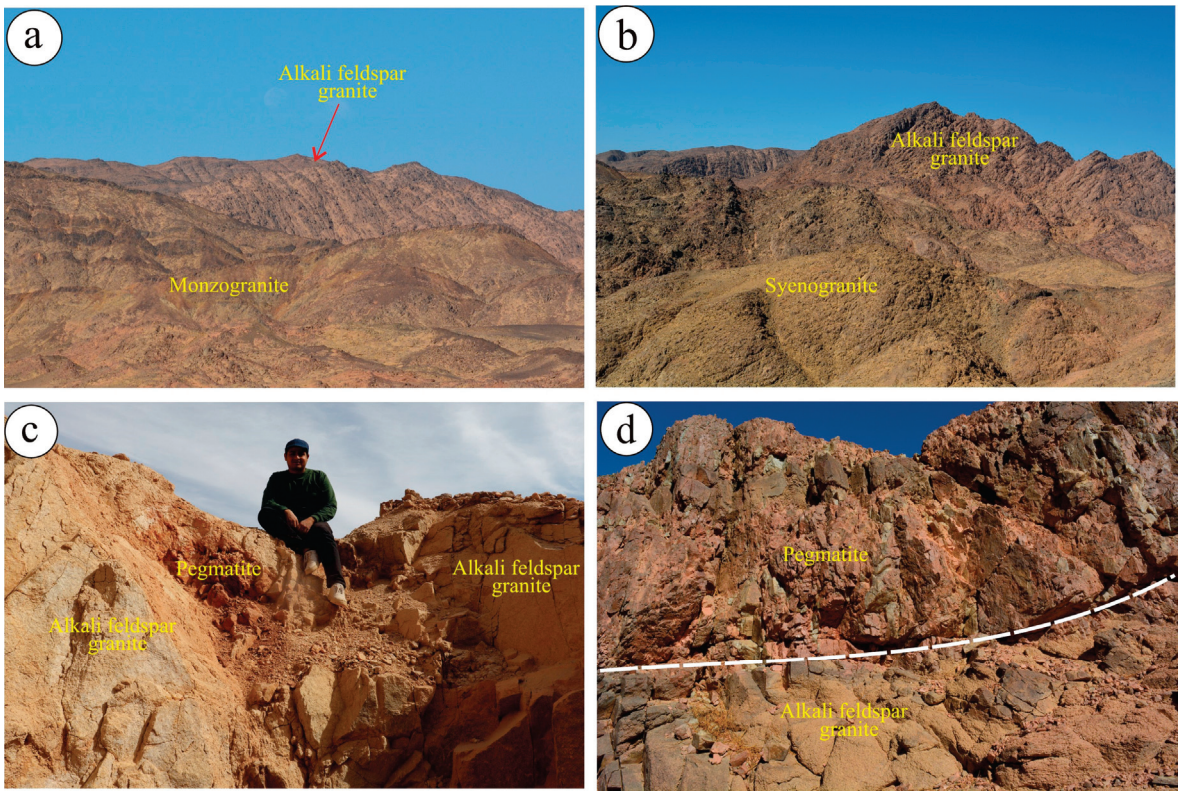


Figure 4. Field photographs show (**a**) sharp contact between alkali-feldspar granite and monzogranite; Note: dikes traversing the monzogranite and abutting the alkali-feldspar granite, (**b**) alkali-feldspar granite with pinkish color intruding syenogranite with yellowish color, (**c**) highly tectonized alkali-feldspar granite dissected by pegmatite and quartz veins, (**d**) granitic pegmatite dike.

Mineralized, coarse-grained granitic pegmatites and greisens are distributed along the margin of the alkali-feldspar granite, generally with gradational contacts. Pegmatites occur as plugs and dikes within the pluton and along its margin intruding the alkali-feldspar granite (Figure 4c,d). For the first time, pyroxmangite-rich pockets (5–15 cm in width) have been identified in the Gabal El-Bakriya pegmatites, representing a new component of the Neoproterozoic basement rocks of the Egyptian Nubian Shield. Pyroxmangite appears as massive, coarse-grained black segregations (Figure 5a), or as disseminated crystals within pegmatites (Figure 5b). Some pyroxmangite pockets also enclose clasts of pegmatite (Figure 5c) and quartz (Figure 5d). Greisenization is observed irregularly along the margin of the alkali-feldspar granite, where greisens occur as pockets, veins filling fractures, or selvages around quartz veins, occasionally extending into adjacent country rocks. Numerous veins and pods of fluorite are found cutting through the greisen bodies, further supporting the post-magmatic hydrothermal activity in the area.

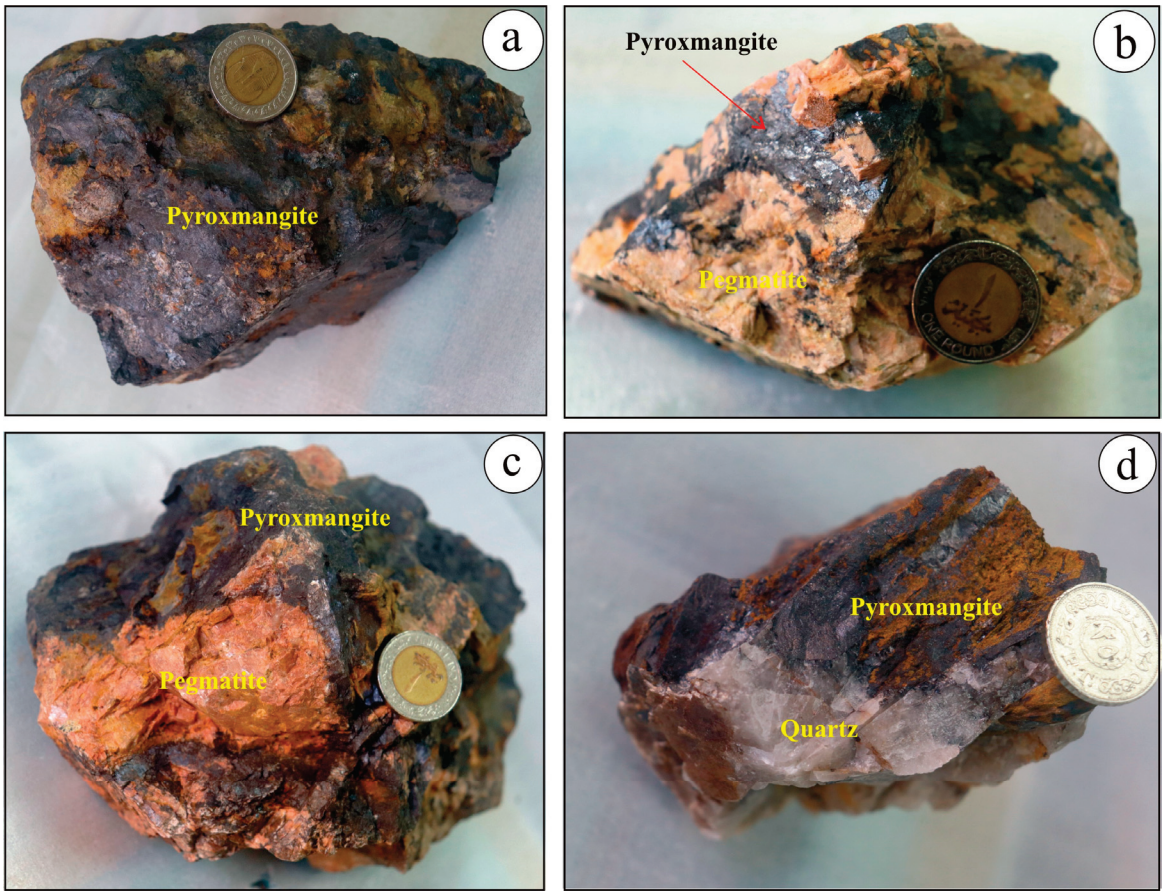


Figure 5. Hand specimen samples showing (**a**) massive pyroxmangite, (**b**) disseminated pyroxmangite in pegmatite, (**c**) inclusion of pegmatite in pyroxmangite, and (**d**) inclusion of quartz in pyroxmangite.

3. Petrography

This section provides a petrographic description of the alkali-feldspar granite, pegmatites, and pyroxmangite-bearing pockets associated with the Gabal El-Bakriya intrusion. Multiple mineral species were identified using SEM and EPMA techniques.

3.1. Alkali-Feldspar Granite

Alkali-feldspar granite is predominantly composed of K-feldspar and quartz with subordinate albite, amphibole, and micas. Accessory minerals include allanite, bastnäsite, thorite, fluorite, zircon, garnet, topaz, monazite-(Ce), fergusonite, Nb-Ta oxides, rutile,

and opaques. K-feldspar occurs mainly as subhedral, tabular crystals, primarily of orthoclase perthite, displaying Carlsbad and simple twinning. Microcline occurs as anhedral to subhedral crystals showing cross-hatching twinning. Quartz appears as subhedral crystals, commonly containing muscovite inclusions. Albite is present as subhedral crystals intergrown with other phases. Amphibole forms short, prismatic crystals and is strongly pleochroic, ranging from pale yellow and green to brownish green. The mica assemblage includes biotite and white mica (muscovite and zinnwaldite). Biotite is found as subhedral to anhedral tabular crystals, occupying interstitial spaces between feldspars and quartz or as fine anhedral flakes. Muscovite occurs as deformed crystals (Figure 6a) or also as fine, anhedral flakes between feldspars and quartz. Zinnwaldite is represented by anhedral, corroded crystals that contain albite inclusions and are associated with topaz.

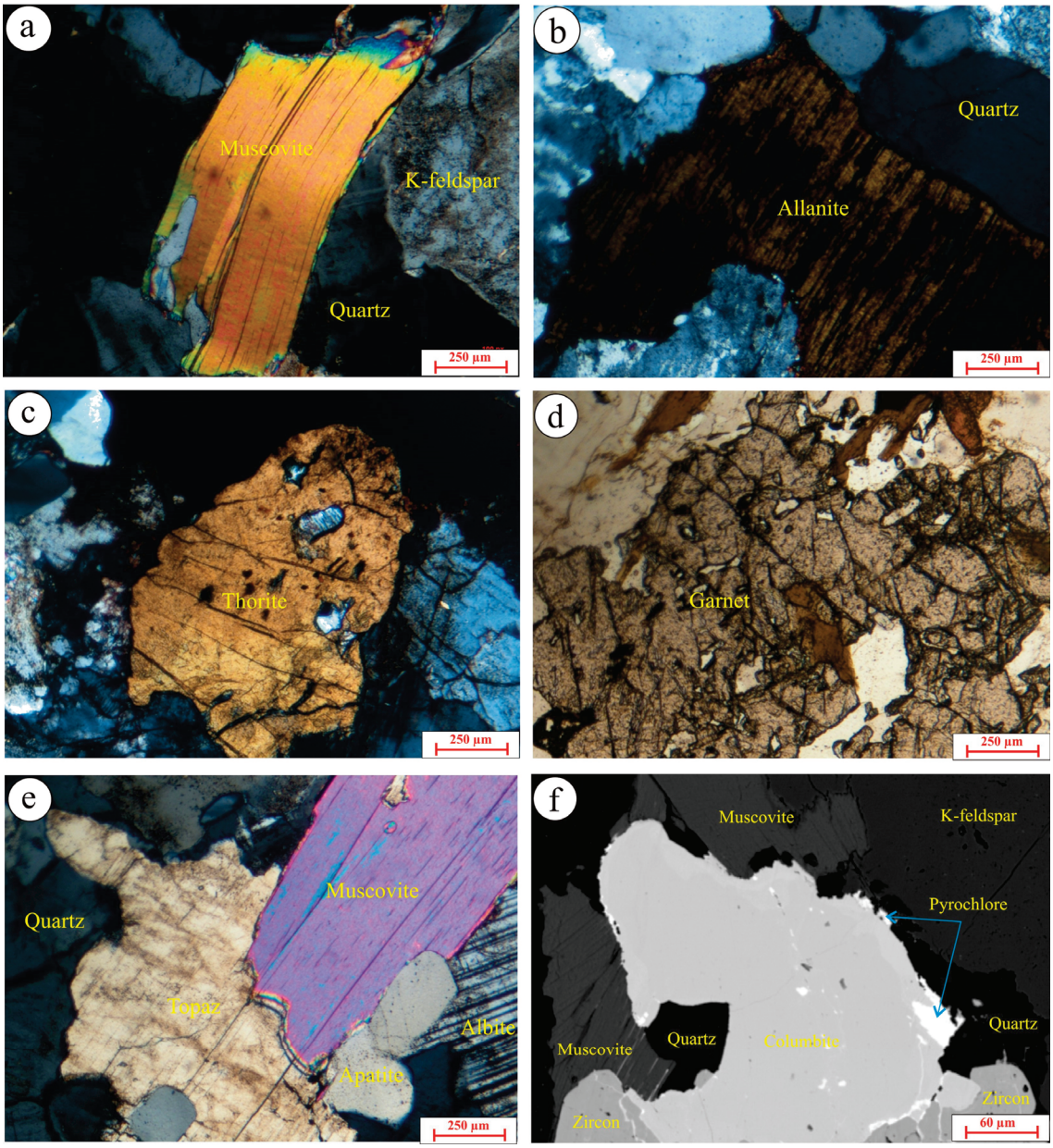


Figure 6. Microphotographs of alkali-feldspar granite ((**a**–**c**,**e**) are under crossed Nicols, "(**d**)" is under plane-polarized light, and "(**f**)" is a backscattered electron image); (**a**) deformed muscovite crystal; (**b**) deep-brown allanite crystal embayed by silicate minerals; (**c**) anhedral crystal of thorite containing small inclusions of monazite; (**d**) garnet with irregular outlines and high relief; (**e**) topaz crystals interstitial among other minerals; (**f**) pyrochlore replaced columbite along its margins.

Opaques are mainly Fe-Ti oxides such as magnetite and ilmenite. Zircon appears as prismatic and bipyramidal crystals, both homogeneous and zoned. Allanite occurs as subhedral to euhedral, metamict crystals with a deep brown and black color, corroded and in contact with silicate minerals (Figure 6b). Thorite is present as anhedral crystals that contain monazite inclusions (Figure 6c). Garnet occurs in various forms, including euhedral to subhedral, irregular, and rounded interstitial crystals (Figure 6d). Quartz inclusions are common within garnet. Topaz forms small anhedral interstitial crystals, associated with muscovite (Figure 6e). Bastnäsite is present as anhedral to euhedral tabular crystals ranging from colorless to pale greenish to yellow. Apatite occurs as small subhedral to euhedral crystals, commonly associated with topaz and muscovite. Titanite is rare and was found as a few anhedral grains. Monazite-(Ce) is disseminated throughout the rock and occurs as inclusions in amphibole and allanite. Fluorite is present as interstitial crystals and as veinlets filling fractures. Fergusonite forms dark-brown subhedral prismatic crystals, occasionally zoned and locally altered to pyrochlore. Columbite and rare tantalite occur as small subhedral to anhedral crystals with color varying from black to dark brown. Some columbite crystals are partially replaced along their margins by pyrochlore and tantalite (Figure 6f).

3.2. Pegmatite

The pegmatites are coarse-grained, reddish rocks primarily composed of perthitic K-feldspar and quartz, with minor albite, micas, and mafic minerals. Accessory minerals include opaque phases, monazite-(Ce), zircon, fergusonite, xenotime, fluorite, pyrochlore, allanite, thorite, bastnäsite, samarskite, cassiterite, beryl, and pyrochlore. K-feldspar, orthoclase and microcline, occurs as coarse subhedral to anhedral crystals. Some crystals enclose albite, iron oxide, and zircon inclusions. Orthoclase intergrown with albite forms perthitic texture (Figure 7a), whereas microcline shows tartan twinning. Quartz occurs in the following two generations: an early phase of coarse-grained crystals and a later phase forming fine-grained veinlets, crosscutting earlier developed minerals. Large quartz crystals commonly show undulose extinction and contain inclusions of K-feldspar and muscovite (Figure 7b). Some quartz crystals display graphic intergrowths with K-feldspar. Albite appears as euhedral to anhedral crystals with characteristic lamellar twinning. Some show deformation features such as deformed or broken twin planes, and others are altered to sericite. Muscovite occurs as large crystals with subhedral to anhedral crystals with perfect cleavage and high interference color (Figure 7c). Zinnwaldite forms large, fractured subhedral crystals, corroded and in contact with K-feldspar and quartz (Figure 7d). The corroded zinnwaldite crystals indicate successive replacement and a complex crystallization history.

Opaque phases mainly include Fe-Ti and Nb-Ta oxides. The Nb-Ta oxides exhibit color variation from black to dark brown and often show oscillatory zoning. Some crystals show patchy texture or resorption appearance due to disequilibrium crystallization. Partial replacement of columbite by secondary pyrochlore is also observed. Zircon appears as isolated, reddish brown anhedral to subhedral crystals, as well as inclusions in the other minerals. Monazite-(Ce) is found as an anhedral to euhedral prismatic crystals (Figure 7e). Fergusonite occurs as anhedral to subhedral crystals, partially replaced by pyrochlore. Xenotime is present as an anhedral to subhedral crystals scattered throughout the rock and usually has zircon inclusions (Figure 7f). Bastnäsite is found as euhedral to subhedral crystals associated with allanite. Some bastnäsite crystals show zoning or patchy texture, attributed to minor decarbonation or hydration along fractures due to the circulation of deuteric fluids during late-stage cooling.

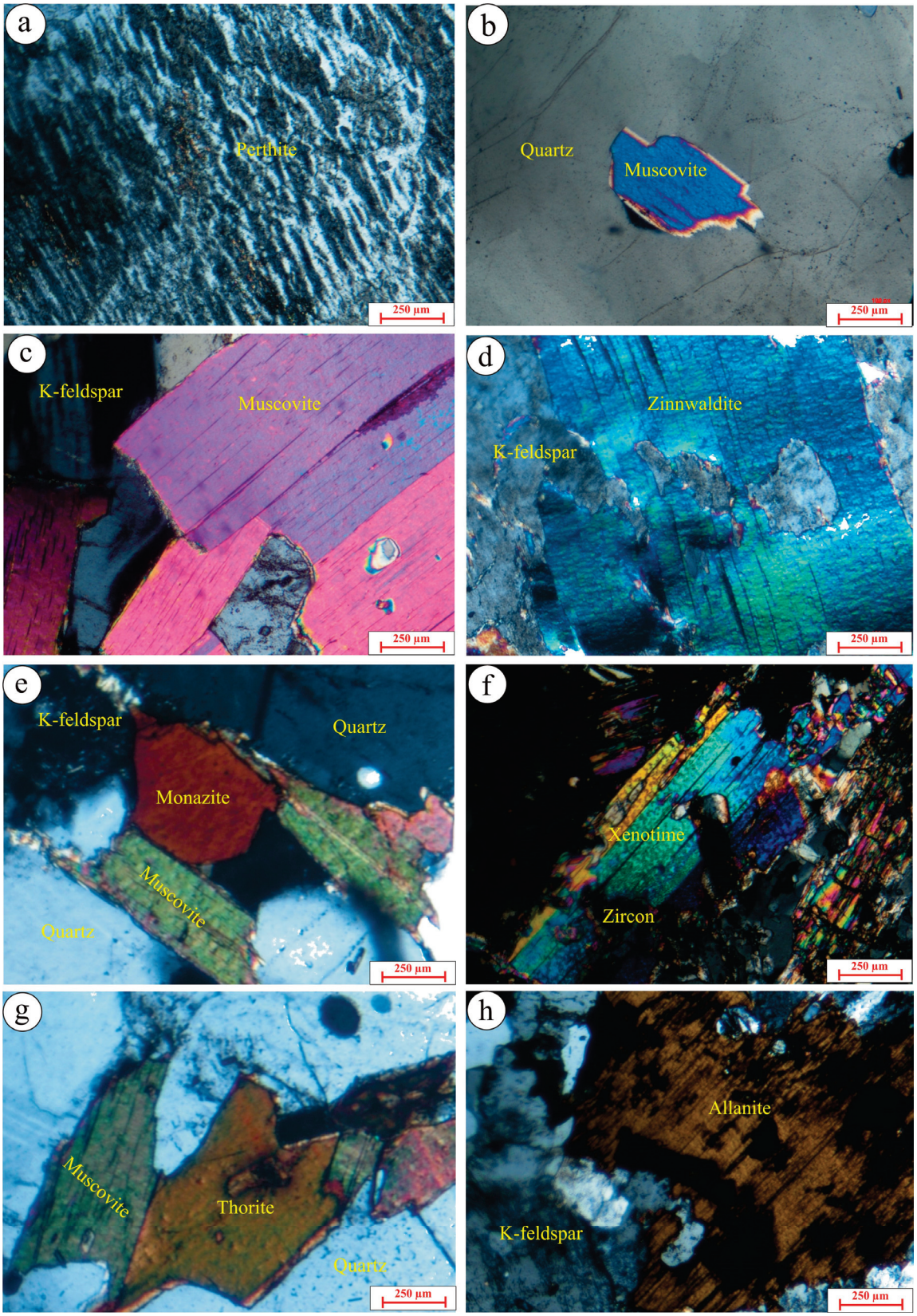


Figure 7. The minerals that occur in pegmatites (under crossed Nicols): (**a**) braid perthite; (**b**) muscovite inclusion in quartz; (**c**) muscovite with perfect cleavage and high-interference color; (**d**) zinnwaldite having irregular contact with K-feldspar and quartz; (**e**) monazite-(Ce) associated with muscovite; (**f**) xenotime with zircon inclusion; (**g**) thorite associated with muscovite; (**h**) allanite crystal having irregular contact with K-feldspar.

Thorite is present as subhedral to anhedral, cracked crystals often associated with muscovite (Figure 7g). Allanite appears as anhedral reddish brown crystals (Figure 7h). Cassiterite forms subhedral crystals characterized by oscillatory zoning. Pyrochlore appears as subhedral to rounded, yellowish-brown crystals, replacing fergusonite. Fluorite occurs as interstitial anhedral crystals or as veinlets.

3.3. Pyroxmangite

Pyroxmangite-rich pockets, identified for the first time within the Gabal El-Bakriya pegmatites, are composed mainly of pyroxmangite and garnet, with accessory pyrochroite, quartz, zircon, magnetite, rutile, and fluorite. Pyroxmangite occurs as large, anhedral crystals or as fine, needle-like crystals (Figure 8a). The large crystals exhibit fractures along perpendicular cleavage planes, filled with quartz and magnetite (Figure 8b). Garnet, represented by spessartine, occurs as anhedral crystals with internal cracks filled with secondary minerals (Figure 8c). Magnetite is present as anhedral crystals enclosed within pyroxmangite. Fluorite occurs as both large crystals and veinlets. Pyrochroite is present as anhedral crystals enclosed within fluorite or as veinlets (Figure 8d). Rutile forms fine clusters of reddish color.

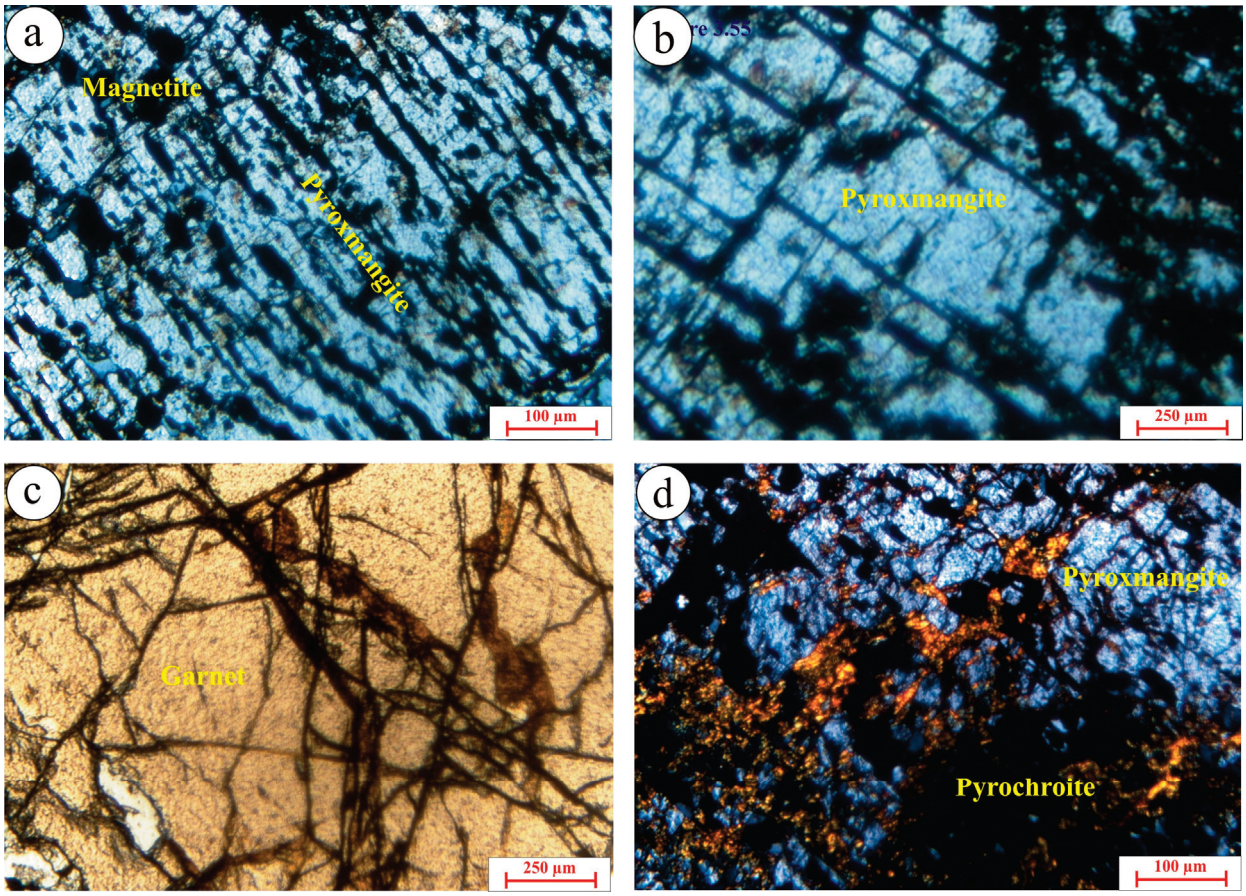


Figure 8. Microphotographs of pyroxmangite-rich pockets (all under crossed Nicols, except "c", under plane-polarized light): (**a**) needle-like pyroxmangite intercalated with magnetite; (**b**) fractured pyroxmangite crystal along perpendicular cleavage planes, narrow black fractures and veinlets are filled with magnetite, while black, poorly defined clusters are pyrochroite; (**c**) fractured anhedral garnet; (**d**) pyrochroite and reddish rutile clusters fill fractures and veinlets in pyroxmangite.

4. Analytical Method

Mineral chemical compositions and backscattered electron (BSE) images of both major and accessory minerals were obtained on polished thin sections using a CAMECA

SX100 electron microprobe (Agilent Technologies, Oslo, Norway) at the Department of Geosciences, University of Oslo, Norway. The sections were carbon-coated using a vacuum coater to ensure conductivity. Operating conditions were a 15 kV accelerating voltage, 20 nA beam current, peak counting time of 20 s, and a focused beam with a diameter of 2 μm. Analyses were calibrated using natural and synthetic mineral standards, and data were corrected using a ZAF matrix correction protocol. Mineral formula calculations were performed using both custom-built Excel spreadsheets and the Minpet software (Version 2.02, 1988–1997) package and were normalized on the basis of a fixed number of oxygen atoms specific to each mineral (as atom per formula unit, apfu).

Whole-rock, major, and trace element compositions of representative samples of the mineralized pegmatite of the Gabal El-Bakriya area were determined at the GeoAnalytical Laboratory, Washington State University, USA. Concentrations of major oxides and selected trace elements were measured using a ThermoARL XRF Spectrometer (Agilent Technologies, Bellevue, WA, USA). Calibration was performed using the USGS GSP2 standard. Loss on ignition (LOI) was calculated from weight loss after ignition at 1000 °C. Analytical precision was better than 1% (2σ) for most major elements and better than 5% (2σ) for most trace elements, except for Ni, Cr, Sc, V, and Cs.

Rare earth elements (REEs) and additional trace elements were determined by inductively coupled plasma mass spectrometry (ICP-MS) using an Agilent 7700 instrument (Bellevue, WA, USA). Approximately 50 mg of powdered sample was digested in acid-washed Teflon vessel with a 1:3 hydrofluoric and nitric acids at 250 °C for at least 8 h. Instrument sensitivity was calibrated using a blank fused bead from the same flux batch as the samples, along with USGS standards RGM-2 and AGV-2. Additional standards (DTS-2, BCR-1, and G-2) were analyzed as unknowns for quality control. Analytical precision was better than ±5% (2σ) for most trace elements and REEs.

5. Mineral Composition

We present data on composition of both essential and accessory minerals in the pegmatite and associated pyroxmangite from the Gabal El-Bakriya area. The complete dataset is provided in Supplementary Tables S1–S22.

5.1. Silicate Minerals

5.1.1. Feldspars

The feldspars (84 analyses) are compositionally indicative of crystallization under near-equilibrium conditions (Tables S1 and S2). The dominant K-feldspar has near-end member composition ($KAlSi_3O_8$), with a K_2O content of 15.72–15.5 wt.%, low Na_2O (0.21–0.45 wt.%), and negligible CaO (0.01–0.07 wt.%). The orthoclase content ranges between 95.68 and 98.0 mol.%. The albite analyses display high Na_2O (10.79–11.98 wt.%) and low CaO (0.01–0.46 wt.%), with albite content ranging between 96.10 and 99.34 mol.% and anorthite content <2 mol.%.

5.1.2. Micas

Mica compositions (23 of zinnwaldite and 27 of muscovite analyses; Tables S3 and S4) plot in the zinnwaldite, lithian muscovite, and lithian phengite fields of Tischendorf et al. [37] (Figure 9a). Based on the classification scheme of Miller et al. [38], muscovite is primarily of magmatic origin, with few compositions plotting in the secondary muscovite field (Figure 9b). Enrichment in Ti supports a magmatic origin [39], as Ti absent in secondary muscovite.

5.1.3. Pyroxmangite

Pyroxmangite, recorded here for the first time on the Nubian Shield, is a Mn-rich pyroxenoid ($MnSiO_3$), with gem-quality potential. It contains 27.19–39.22 wt.% MnO, 11.99–23.84 wt.% total iron (FeO^t) and 45.50–46.66 wt.% SiO_2, with minor CaO (0.88–1.06 wt.%) (Table S5).

5.1.4. Zircon

Zircon (20 analyses; Table S6) has low total major element content, occasionally <98 wt.%, likely due to metamictization. Contributions of TiO_2, Al_2O_3, and FeO* are minimal. Low ThO_2 (0.12–0.36 wt.%) and UO_2 (0.19–0.49 wt.%) contents are typical of magmatic zircon in the Eastern Desert [23,40,41]. The ThO_2/UO_2 (0.4–0.89) and position on SiO_2 vs. ThO_2/UO_2 diagram [42,43] support their magmatic origin (Figure 9c).

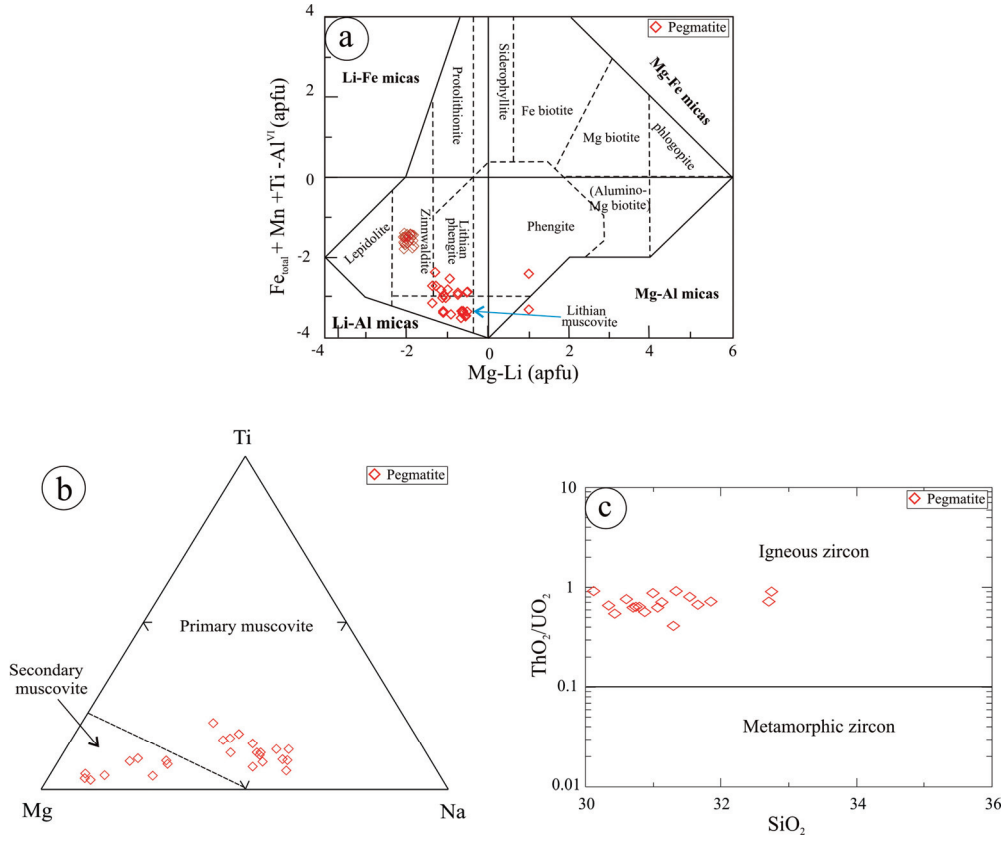


Figure 9. (**a**) Classification diagram of micas [37]; (**b**) Mg−Ti−Na ternary diagram of muscovite [38]; (**c**) ThO_2/UO_2 vs. SiO_2 diagram for zircon [42,43].

5.1.5. Thorite

Thorite (18 analyses; Table S7) exhibits total major element contents between 95.56 and 99.69 wt.% due to radiation damage. UO_2 contents (9.07–15.63 wt.%) suggest uranothorite composition. CaO content (0.41–1.26 wt.%) variations may reflect fluid composition or alteration [12]. Contents of P_2O_5 (0.92–2.01 wt.%) and trace REEs (e.g., Ce_2O_3, La_2O_3, Nd_2O_3, and Y_2O_3) suggest inclusions or minor substitution.

5.1.6. Topaz

Topaz (17 analyses; Table S8) shows limited compositional variations: the major oxide concentrations are Al_2O_3 (52.21–54.8 wt.%), SiO_2 (9.12–31.46 wt.%), and F (13.42–15.89 wt.%). Minor constituents include FeO, MnO, MgO, CaO, Na_2O, K_2O, P_2O_5, and TiO_2.

5.1.7. Chlorite

Chlorite (19 analyses; Table S9) shows a consistent composition, as follows: SiO_2 (27.02–28.56 wt.%), Al_2O_3 (17.06–20.21 wt.%), MgO (4.45–6.48 wt.%), and FeO (30.13–33.02 wt.%). The analyzed chlorite is chamosite and likely formed under reducing conditions [44,45]. Temperatures calculated using the Kranidiotis and MacLean [46] geothermometer yield 261–293 °C (avg. 271 °C).

5.2. Non-Silicate Minerals

5.2.1. Nb-Ta Oxides

The analyzed Nb-Ta oxide minerals in the pegmatite include columbite-(Mn) (24 analyses), fergusonite-(Y) (16 analyses), and pyrochlore (19 analyses). Chemical compositions and structural formulae of columbite are given in Table S10. Columbite is characterized by high contents of Nb_2O_5 (57.11–68.17 wt.%), Ta_2O_5 (9.27–19.94 wt.%), MnO (11.52–13.43 wt.%), and FeO (7.19–9.42 wt.%). On the classification diagram of Nb-Ta oxides, columbite composition plots within the Mn-dominant field (Figure 10a) [46]. Narrow ranges in FeO and MnO contents suggest lack of compositional zoning.

Fergusonite ($YNbO_4$) is a complex oxide that incorporates Nb, Y, and various REEs. Analytical data and calculated formulae are listed in Table S11. The fergusonite exhibits elevated Nb_2O_5 (39.77–41.32 wt.%) and Y_2O_3 (22.14–23.7 wt.%), with low TiO_2 (1.69–2.29 wt.%) FeO* (2.69–4.45 wt.%), CaO (0.7–1.77 wt.%), Ta_2O_5 (2.62–4.02 wt.%), UO_2 (4.17–4.67 wt.%), and ThO_2 (2.85–3.97 wt.%). REE content is dominated by HREEs, Dy_2O_3 (3.61–4.29 wt.%), Er_2O_3 (1.38–1.65 wt.%), and Yb_2O_3 (2.14–2.72 wt.%).

Pyrochlore compositions and structural formulae are reported in Table S12. Based on cation distribution at the B-site, the analyzed pyrochlores are Nb-dominant and fall within pyrochlore sensu stricto (Figure 10b) [47].

5.2.2. Niobian Rutile

Niobian rutile, Fe–Nb–Ti oxide, is reported here for the first time from pegmatites in the ANS. Fifteen analyses are presented in Table S13. The primary constituents are TiO_2, FeO*, and Nb_2O_5,with minor contribution of Ta_2O_5, SnO_2, and F.

5.2.3. Pyrochroite

Pyrochroite occurs exclusively in pyroxmangite-rich pockets within Gabal El-Bakriya pegmatite. It is a MnO-bearing phase, with low analytical totals (63.61–68.55 wt.%) due to its hydrous nature. Nineteen analyses and structural formulae are provided Table S14. Pyrochroite is composed mainly of MnO (63.61–68.55 wt.%), with subordinate FeO* (1.36–3.81 wt.%) and CaO (1.13–2.29 wt.%).

5.2.4. Cassiterite

Cassiterite occurs as a disseminated accessory mineral. Seventeen analyses are compiled in Table S15. It is compositionally homogeneous, with SnO_2 ranging between 95.35 and 96.65 wt.%. Other oxides are present in trace amounts, including SiO_2 (0.26–0.36 wt.%), TiO_2 (0.3–0.76 wt.%), FeO (0.06–0.32 wt.%), MgO (0.02–0.08 wt.%), CaO (0.11–0.12 wt.%), Na_2O (0.06–0.11 wt.%), K_2O (0.02–0.06 wt.%), Nb_2O_5 (0.53–1.24 wt.%), and Ta_2O_5 (0.12–0.58 wt.%).

5.2.5. Beryl

Beryl crystals (18 analyses; Table S16) exhibit chemical homogeneity, consistent with crystallization from Be-rich hydrothermal fluids. Major oxides include SiO_2 (62.74–65.31 wt.%), Al_2O_3 (16.43–18.04 wt.%), and BeO (12.11–13.96 wt.%). Minor constituents include FeO (0.73–1.4 wt.%), MgO (0.09–0.17 wt.%), CaO (0.02–0.13 wt.%), Na_2O (0.53–0.9 wt.%), and K_2O (0.01–0.18 wt.%).

5.2.6. Bastnäsite-(Y)

Bastnäsite, a rare earth fluorocarbonate [(Ce, La, Y) CO_3F], occurs as bastnäsite-(Y). Nineteen analyses are presented in Table S17. Bastnäsite-(Y) contains Y_2O_3 (36.92–38.51 wt.%), Gd_2O_3 (3.38–4.81 wt.%), Dy_2O_3 (2.74–3.73 wt.%), La_2O_3 (1.42–2.17 wt.%), Ce_2O_3 (4.41–5.74 wt.%), and ThO_2 (2.14–4.46 wt.%).

5.2.7. Monazite-(Ce)

Monazite, identified as monazite-(Ce), is represented by 23 analyses (Table S18). It contains significant P_2O_5 (23.48–26.93 wt.%), Ce_2O_3 (27.09–34.98 wt.%), La_2O_3 (5.59–7.85 wt.%), Pr_2O_3 (3.16–3.96 wt.%), Nd_2O_3 (8.15–9.74 wt.%), and Sm_2O_3 (2.04–2.79 wt.%), with minor Gd_2O_3 (0.6–0.8 wt.%), Dy_2O_3 (0.34–0.6 wt.%), and ThO_2 (7.55–19.22 wt.%).

5.2.8. Apatite

Some apatite analyses (Table S19) show low total major component content (up to 95.76wt.%) since Cl was not measured. Apatite composition includes CaO (50.26–53.93 wt.%), P_2O_5 (37.28–39.98 wt.%), and F (5.95–6.12 wt.%), along with minor SiO_2 (0.24–0.51 wt.%), total iron FeO^t (0.09–0.32 wt.%), MnO (0.08–0.34 wt.%), Na_2O (0.25–0.99 wt.%), and SO_3 (0.03–0.55 wt.%). High F content (2.64–3.25 wt.%) supports classification as fluorapatite.

Apatite occurs as an accessory phase and could preserve primary geochemical signature of the host magma [48–53]. On the discrimination diagrams of Chen et al. [48] and SiO_2 vs. MnO (Figure 10c,d) [48,51], the data indicate a magmatic origin for apatite, corroborated by its occurrence interstitially between feldspars and quartz or as inclusions within them.

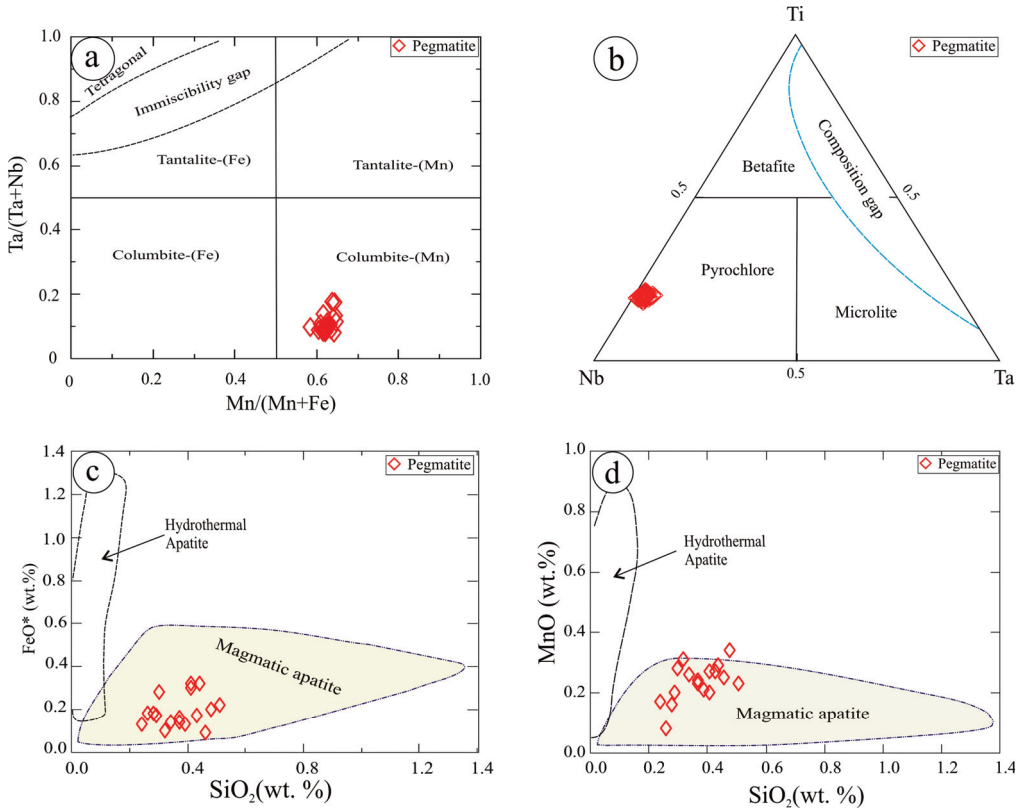


Figure 10. (**a**) Ta/(Ta + Nb) vs. Mn/(Mn + Fe) classification diagram for Nb-Ta oxides [46]; (**b**) Ti-Nb-Ta ternary classification diagram for pyrochlore group minerals based on B-site cations [47]; (**c**) FeO* vs. SiO_2 diagram for apatite [48]; (**d**) SiO_2 vs. MnO diagram for apatite [51].

5.2.9. Fluorite

Fluorite (25 analyses; Table S20) is composed predominantly of Ca (80.12–88.17 wt.%) and F (47.79–62.5 wt.%), with subordinate elements such as Si, Fe, Na, K, Mn, and Mg present in trace amounts (<1.0 wt.%).

Fe-Ti Oxides

The identified Fe-Ti oxides include magnetite (25 analyses) and ilmenite (14 analyses), with compositions and structural formulae reported in Tables S21 and S22. Magnetite is FeO*-rich (90–94.18 wt.%) and TiO_2-poor (0.0–0.44 wt.%). Ulvöspinel content, calculated following [54], is low (0.0–1.30 mol.%). Ilmenite exhibits compositional variation between $FeTiO_3$ and $MnTiO_3$ end-members, reflecting solid solution formation [55], as reflected by an elevated MnO content (3.07–10.14 wt.%). Calculated ilmenite composition ranges from 96.38 to 100.36 mol.% in the pegmatites.

6. Geochemical Characteristics

The results of major oxide compositions and calculated normative values of the pegmatite samples are represented in Table 1, while concentrations of trace elements and REEs are given in Table 2. The analyzed pegmatites display considerable compositional variability due to their coarse-grained nature and mineralogical heterogeneity. They are enriched in SiO_2 (76.51–80.69 wt.%), Al_2O_3 (7.62–10.76 wt.%), K_2O (4.09–6.76 wt.%), and Na_2O (1.96–3.94 wt.%), with notably low contents of total iron as FeO (0.24–1.64 wt.%), MgO (<0.7 wt.%), and CaO (<0.63 wt.%). Trace element abundances exhibit wide variation, with elevated concentrations of Nb (135.99–669.93 ppm), Y (51.32–464.47 ppm), Zr (318.96–763.68 ppm), Th (41.36–112.08 ppm), U (19.91–73.82 ppm), and REEs (ΣREE = 224.96–518.21 ppm). In contrast, Ba (40.53–89.63 ppm) and Sr (30.99–67.49 ppm) are relatively depleted. These geochemical characteristics, particularly the enrichment in Nb (Nb > Ta), Y, REE, Zr, Th, U, and F, are consistent with NYF-type pegmatites [56–58].

Table 1. Major oxides and normative compositions of pegmatite of Gabal El-Bakriya area.

Rock Type	**Pegmatite**								
Sample No	**BK52**	**BK53**	**BK54**	**BK103**	**BK104**	**BK107**	**BK108**	**BK132**	**BK135**
SiO_2	80.69	79.35	78.07	78.83	80.05	79.22	78.47	77.54	76.51
TiO_2	0.06	0.06	0.05	0.09	0.03	0.12	0.08	0.06	0.16
Al_2O_3	7.69	8.75	7.62	9.69	9.72	8.18	9.2	9.46	10.76
Fe_2O_3	1.28	1.32	1.24	1.18	1.39	1.62	1.93	1.43	1.64
MnO	0.01	0.01	0.01	0.01	0.03	0.02	0.02	0.3	0
MgO	0.07	0.08	0.09	0.04	0.05	0.03	0.06	0.14	0.17
CaO	0.24	0.16	0.2	0.15	0.3	0.24	0.23	0.28	0.63
Na_2O	3.08	3.04	1.96	2.94	2.98	3.94	3.18	3.19	3.12
K_2O	4.42	4.47	6.76	4.4	4.09	4.77	4.75	5.01	5.04
P_2O_5	0.01	0.01	0.01	0.02	0.02	0.01	0.03	0.02	0.04
LOI	0.95	1.09	1.03	0.78	0.82	0.54	0.61	0.71	0.83
Total	98.5	98.34	97.04	98.13	99.48	98.69	98.56	98.14	98.9
			Normative composition						
Quartz	45.28	46.34	47.68	44.42	42.67	38.07	52.22	47.83	50.15
Corundum	-	-	-	-	-	-	-	-	-
Orthoclase	26.74	24.53	28.76	28.7	30.42	30.41	26.8	27.19	41.65
Albite	25.58	25.59	15.82	21.33	21.32	26.95	15.32	20.69	1.61

Table 1. *Cont.*

Rock Type	Pegmatite								
Sample No	**BK52**	**BK53**	**BK54**	**BK103**	**BK104**	**BK107**	**BK108**	**BK132**	**BK135**
Anorthite	0.24	1.07	-	-	-	0.47	-	-	-
Acmite	-	-	0.78	0.9	0.81	-	0.6	0.62	0.59
Na-Metasilicate	-	-	4.03	1.2	1.28	-	2.5	1.18	3.49
Diopside	0.34	0.27	1.02	0.85	1.13	2.12	1.01	0.66	0.84
Hypersthene	1.3	1.77	1.66	2.35	2.2	1.16	1.39	1.67	1.52
Magnetite	0.29	0.32	-	-	-	0.4	-	-	-
Ilmenite	0.18	0.06	0.23	0.16	0.12	0.31	0.12	0.12	0.1
Apatite	0.04	0.04	0.02	0.07	0.04	0.09	0.02	0.02	0.02
Some chemical parameters									
R1	3212	3125	2890	3145	3280	2717	2935	2822	2763
R2	180	193	175	208	225	188	208	222	287
AI	1.28	1.12	1.38	0.99	0.96	1.42	1.13	1.13	0.98
ASI	0.75	0.86	0.70	0.98	0.98	0.68	0.85	0.89	0.92
Ti	360	360	300	540	180	719	480	360	959
K	36,692	37,107	56,117	36,526	33,952	39,597	39,431	41,590	41,839
P	44	44	44	87	87	44	131	87	175
Mg#	9.78	10.72	12.57	6.29	6.65	3.54	5.80	16.24	17.04
Colour Index	2.11	2.42	2.91	3.36	3.44	4	2.52	2.44	2.47
Diff. Index	97.59	96.45	92.25	94.46	94.41	95.43	94.34	95.72	93.42
ANOR	0.89	4.18	0.00	0.00	0.00	1.52	0.00	0.00	0.00
Q/	46.28	47.51	51.68	47.03	45.20	39.70	55.35	49.97	53.69

Table 2. Concentrations of trace-elements and REE in pegmatites of Gabal El-Bakriya area.

Rock Type	Pegmatite								
Sample No	**BK52**	**BK53**	**BK54**	**BK103**	**BK104**	**BK107**	**BK108**	**BK132**	**BK135**
Cr	2.33	4.11	2.45	3.09	2.37	3.77	1.89	2.25	1.54
Ni	4.59	2.74	3.32	5.11	3.68	14.02	2.75	3.21	12.63
Co	4.74	5.55	4.44	6.71	8.55	5.43	3.23	8.21	6.83
Sc	0.89	0.75	0.54	0.49	1.03	1.24	0.84	0.47	1.05
V	12.33	15.15	16.63	10.05	3.22	10.05	10.05	16.47	5.93
Cu	7.89	9.14	6.51	11.1	5.63	11.35	9.36	4.68	5.87
Pb	9.07	6.51	11.15	6.58	2.68	6.23	5.16	1.06	7.74
Zn	11.8	7.8	9.16	75.72	158.28	154.12	129.37	10.2	162.94
Rb	224.27	178.05	235.19	176.05	163.77	263.12	267.65	402.3	228.91
Ba	83.56	89.63	40.53	69.35	42.73	74.68	42.59	55.98	64.51
Sr	43.62	52.26	67.49	47.41	30.99	46.07	48.16	54.09	61.59
Ga	18.61	21.17	17.35	16.38	23.11	27.24	24.71	19.54	22.93
Ta	23.54	22.62	21.81	30.2	27.41	25.48	24.36	23.73	25.03
Nb	170.76	143.94	158.95	160.25	135.99	137.96	165.56	333.57	669.93
Hf	10.22	11.16	11.09	13.93	15.5	17.62	15.68	9.51	10.84
Zr	391.41	368.87	361.64	606.06	696.93	763.68	688.89	318.96	537.25
Y	126.36	157.96	130.98	57.62	70.64	63.21	51.32	334.53	464.47
Th	75.66	67.56	56.28	41.36	63.74	57.24	54.78	55.6	112.08
U	42.8	31.05	45.77	23.61	24.95	19.91	26.79	28.22	73.82
Li	39.66	34.46	34.9	35.13	30.58	30.61	34.56	33.41	35.91
Be	35.91	42.66	29.03	47.89	38.2	43.24	40.18	28.51	26.57
Mo	0.96	1.61	1.43	0.42	0.06	0.79	0.42	0.23	0.23
Cs	4.25	3.95	2.55	5.35	10.45	7.35	5.55	10.7	6.95
Sn	16.98	23.27	22.3	10.22	9.56	8.88	7.96	17.09	9.33
La	34.38	40.08	37.35	48.33	58.49	50.36	40.68	19.72	25.98

Table 2. *Cont.*

Rock Type	Pegmatite								
Sample No	**BK52**	**BK53**	**BK54**	**BK103**	**BK104**	**BK107**	**BK108**	**BK132**	**BK135**
Ce	69.86	83.48	80.4	131.58	170.39	142.59	119.24	60.5	80.45
Pr	9.5	11.59	10.53	21.44	29.03	23.04	20.07	11	15.05
Nd	40.76	49.81	46.03	100.14	138.47	111.17	94.4	57.08	81.29
Sm	10.74	12.6	12.23	26.46	38.45	30.99	24.5	21.54	32.23
Eu	2.14	1.58	1.8	1.04	1.05	1.1	0.86	1.02	1.04
Gd	12.06	13.38	13.38	23.73	33.36	26.88	21.2	34.98	48.24
Tb	2.28	2.58	2.43	3.12	4.34	3.56	2.75	7.73	10.53
Dy	16.02	18.16	16.78	15.87	22.26	18.42	14.09	57.18	77.99
Ho	3.78	4.34	3.98	2.72	3.72	3.05	2.36	12.46	16.79
Er	12.26	14.76	12.65	6.92	9.05	7.55	5.87	37.59	49.83
Tm	2.1	2.6	2.1	0.96	1.25	1.02	0.81	5.32	6.84
Yb	16.42	20.28	15.95	5.85	7.28	6.29	4.91	31.5	39.45
Lu	2.26	3.46	2.78	0.87	1.07	0.92	0.74	3.96	4.85
Geochemical parameters									
K/Rb	163.61	208.41	238.60	207.47	207.32	150.49	147.32	103.38	182.77
K/Ba	439.11	414.00	1384.57	526.69	794.58	530.22	925.83	742.94	648.56
Zr/Rb	1.75	2.07	1.54	3.44	4.26	2.90	2.57	0.79	2.35
Ba/Nb	0.49	0.62	0.25	0.43	0.31	0.54	0.26	0.17	0.10
Rb/Sr	5.14	3.41	3.48	3.71	5.28	5.71	5.56	7.44	3.72
Eu/Eu*	0.57	0.37	0.43	0.13	0.09	0.12	0.12	0.11	0.08
(La/Yb)n	1.42	1.34	1.58	5.59	5.43	5.41	5.60	0.42	0.45
(La/Sm)n	2.02	2.01	1.93	1.15	0.96	1.03	1.05	0.58	0.51
(Gd/Lu)n	0.65	0.47	0.59	3.34	3.82	3.58	3.51	1.08	1.22
(La/Lu)n	1.56	1.19	1.38	5.69	5.60	5.61	5.63	0.51	0.55

Primitive mantle (PM)-normalized multi-element patterns [59] (Figure 11a) exhibit pronounced enrichment in LILE (Rb, K, Th) and some HFSE (Ta, Zr), along with strong negative anomalies in Sr, Ti, and P. These features are typical of A-type granitoid sources [60]. The enrichment in Ta, Sn, and Cs further supports derivation from highly fractionated, evolved granitic melts.

REE concentrations are variable (173.94–518.21 ppm), and patterns show diversity in LREE versus HREE ratios [$(La/Lu)_n$ = 0.51–5.69]. The following three REE patterns can be distinguished (Figure 11b): group I (samples BK103, BK104, BK107, BK108) displays LREE-enriched patterns [$(La/Lu)_N$ = 5.69–5.60], group II (samples BK132 and BK135) is HREE-enriched [$(La/Lu)_N$ = 0.51–0.55], and group III (samples BK52, BK53, and BK54) shows V-shaped patterns [$(La/Lu)_N$ = 2.09–2.76]. Negative Eu anomalies (Eu/Eu* = 0.08–0.57) reflect plagioclase fractionation. The variation in REE patterns is interpreted to result from differences in the abundance and composition of accessory minerals such as monazite, zircon, fergusonite, xenotime, fluorite, pyrochlore, allanite, thorite, bastnäsite, samarskite, cassiterite, beryl, and pyrochlore.

Their alumina saturation index (ASI = molar $Al_2O_3/(CaO + Na_2O + K_2O)$) ranges from 0.68 to 0.98, indicating predominantly metaluminous composition. Agpaitic index [AI = molar (Na + K)/Al] values range between 0.96 and 1.38, suggesting alkaline to peralkaline affinity [61]. The presence of normative acmite (0.59–0.90) and Na-metasilicate (1.18–4.03) further supports the peralkaline character.

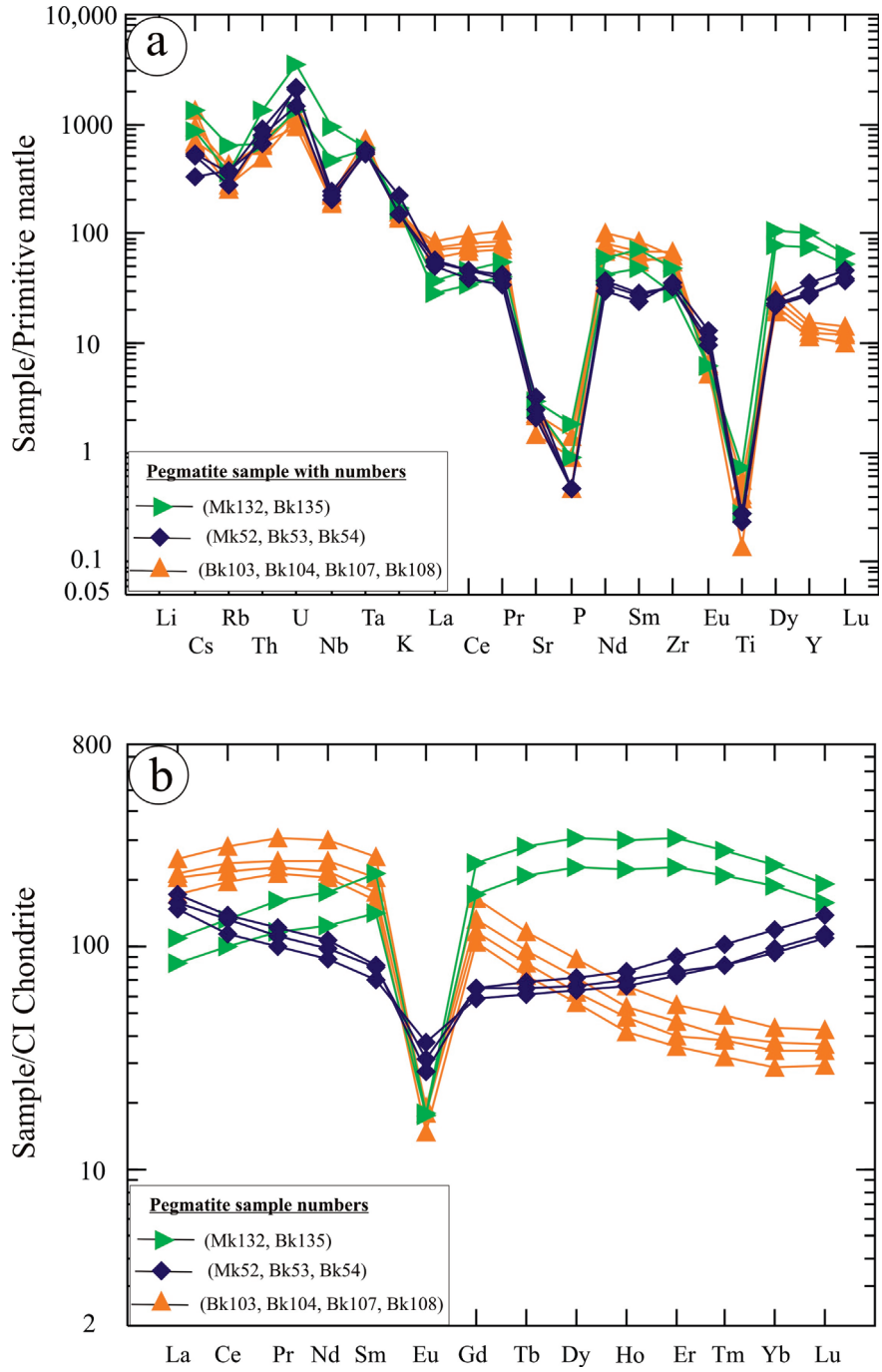


Figure 11. (**a**) Primitive mantle-normalized spider diagram, and (**b**) Chondrite-normalized REE-patterns. Normalization values are from Sun and McDonough [60].

Other key geochemical features consistent with A-type granites include high Ga/Al, Nb, Zr, Y, Ta, and Th, along with depletion in MgO, CaO, and P_2O_5 [61–65]. Further discrimination, using Whalen et al. [66] diagrams, confirms their A-type character (Figure 12a,b). Subdivision into A1 and A2 types following Eby [64,65] places the studied pegmatites in the A1 field on the Nb-Y-Ga diagrams (Figure 13a), suggesting that they represent differentiated products of an oceanic island basalt (OIB)-like source, typically emplaced in continental rifts or associated with intraplate magmatism.

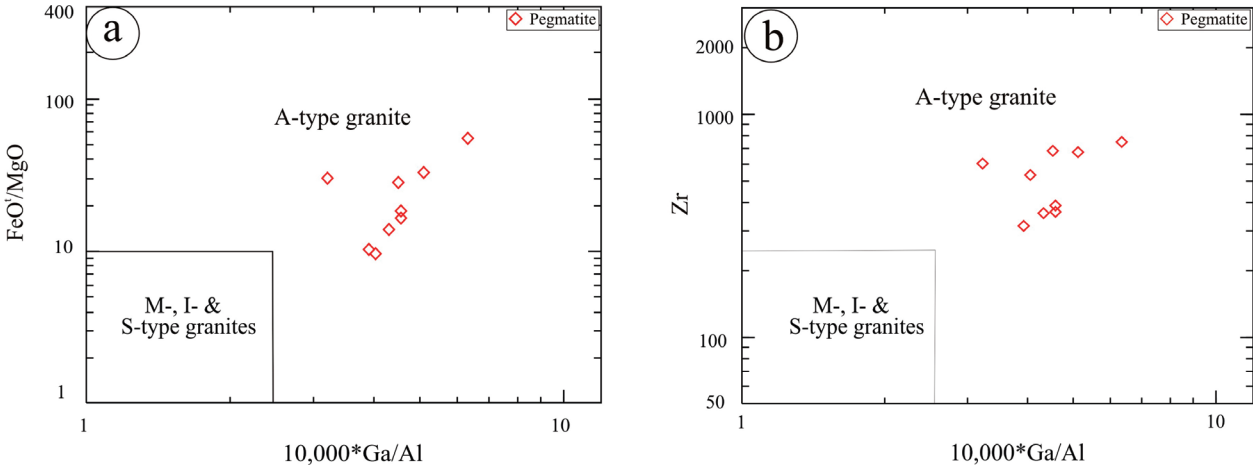


Figure 12. (**a**) Ga/Al vs. FeO^t/MgO [66], and (**b**) Ga/Al vs. Zr [66].

This within-plate (anorogenic) setting is further supported by high Rb/Sr (3.41–7.44) [67], and by discrimination diagrams of Pearce et al. [68], where the pegmatite data correspond to the within-plate field (Figure 13b).

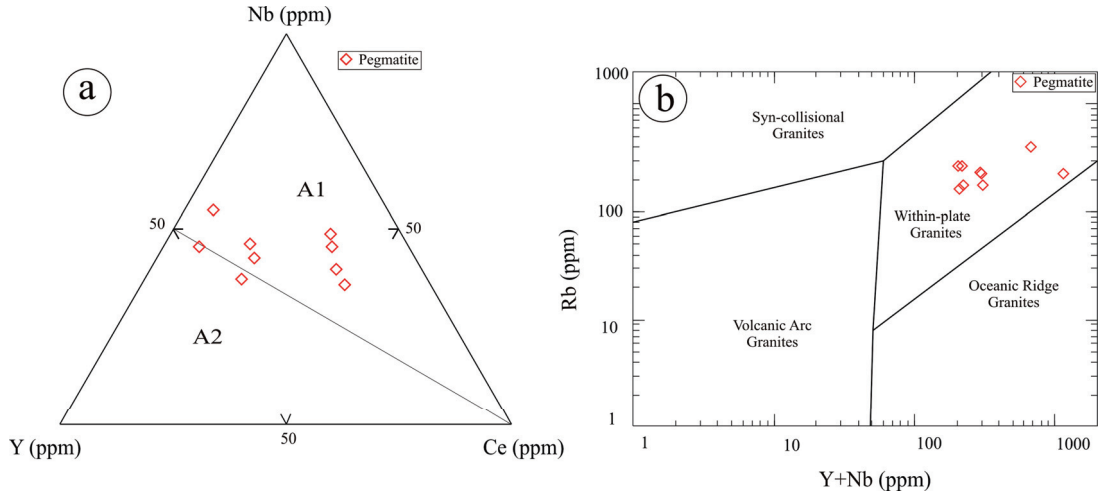


Figure 13. (**a**) Nb-Y-Ce ternary discrimination diagram [66], (**b**) Y + Nb vs. Rb tectonic discrimination diagram [68].

7. Discussion

7.1. Petrogenesis

7.1.1. Pegmatite

Granitic pegmatites typically form during the late stages of magma crystallization and are generally composed of quartz, feldspar, ±muscovite, and ±biotite. They exhibit diverse textures and mineral assemblages [12,69–73]. Granitic pegmatites are critical for understanding the processes governing magma differentiation, late-stage fluid evolution, and the geochemical behavior of rare-metal elements. Pegmatites are also of considerable economic interest as important sources of strategic elements such as Nb, Ta, Li, Be, and REEs [74–76].

The origin of pegmatites has been the subject of longstanding debate, with the following two primary models proposed: (i) residual pegmatites, which formed by extreme fractional crystallization of granitic magmas [72,76–81], and (ii) anatectic pegmatites, generated by low-degree partial melting of crustal rocks [53,76,82–88]. In this study, multiple pegmatite bodies are found intruding or closely associated with the A-type granite of the

GEBI. This spatial relationship implies that the pegmatites formed from a fluid-saturated granitic melt during the final stages of magmatic evolution [89–92]. The occurrence of fluorite in these pegmatites indicates significant fluorine enrichment in the parental magma. Furthermore, the observed gradational contacts between pegmatites and the host granite support a model of in situ magmatic fractionation and late-stage melt evolution.

Classification of the Gabal El-Bakriya pegmatites, based on field relationships and geochemical signatures, indicates they are simple, small-scale pegmatites with heterogeneous textures and compositions. They generated through late-stage fractional crystallization of the A-type granitic melt. The parental magma was likely derived from partial melting of the juvenile crust of the ANS, itself nearly contemporaneously sourced from the mantle. The hydrothermal fluids that influenced pegmatite crystallization are interpreted as magmatic in origin, as evidenced by the following: (i) the spatial and textural continuity between pegmatites and A-type granites; (ii) their preferential emplacement along the granite margins; and (iii) the presence of fluorine-bearing minerals and rare-metal enrichments. Late-stage fractional crystallization of the Gabal El-Bakriya granites produced volatile-rich, magmatic fluids that migrated toward the apex and periphery of the magma chamber. These fluids interacted with still-hot sub-solidus granite, were emplaced along fractures, and formed pegmatitic veins with gradational boundaries. The residual nature of these pegmatites is thus supported by (1) direct field relationships between pegmatites and hosts A-type granites, (2) the mineralogical and geochemical continuity between them, and (3) spatial proximity between the residual melt and its parental granite source. This genetic model aligns with numerous studies that support pegmatite formation via residual melts from granitic intrusions [57,76,85,93–97].

Based on mineralogical and geochemical criteria, the pegmatites are classified into the following three types: (i) Niobium–Yttrium–Fluorine (NYF) type, (ii) Lithium–Cesium–Tantalum (LCT) type, and (iii) a mixed NYF–LCT type. NYF-type pegmatites are enriched in Nb (Nb > Ta), Y, F, Zr, REE, and U, while LCT-type pegmatites are enriched in Ta (Ta > Nb), Cs, Li, Ga, Sn, Rb, and Be [56–58,98,99]. NYF pegmatites are typically small in size and emplaced in anorogenic settings, whereas LCT pegmatites tend to be larger in size and associated with orogenic environments [100,101]. Both types originate from highly evolved, volatile-rich melts that remobilize and concentrate critical metals [12,101]. Notably, the volatile-rich melts of NYF pegmatites are of pure magmatic origin, whereas LCT pegmatites often involve fluids derived from crustal anatexis [76,101]. The Gabal El-Bakriya pegmatites exhibit geochemical signatures, enrichments in Nb (Nb > Ta), Y, Zr, REE, U, and fluorine-bearing phases, and were emplaced in within-plate tectonic setting. These characteristics confirm that they are best classified as NYF-type pegmatites.

7.1.2. Pyroxmangite

This study documents the first reported occurrence of pyroxmangite hosted in pegmatites on the Nubian Shield, the western half of the ANS. It also represents the second reported occurrence on the ANS, with the first discovery being in pegmatites of Jabal Aja on the Arabian Shield, the eastern half of the ANS [102]. Pyroxmangite is the Mn-rich member of the pyroxenoid group, crystallizing in the triclinic system. The mineral typically shows two good cleavages, intersecting at 90 degrees. Pyroxmangite is structurally and compositionally similar to rhodonite. According to Maresch and Mottana [103], pyroxmangite forms under higher pressure and lower temperature conditions than rhodonite, a distinction that can be significant for interpreting the pressure–temperature (P–T) evolution of the host rocks.

The pyroxmangite-bearing pockets at Gabal El-Bakriya consist mainly of pyroxmangite and spessartine, with accessory quartz, pyrochroite, zircon, fluorite, and magnetite. The an-

alyzed pyroxmangite crystals contain MnO (27.19–39.22 wt.%) and SiO_2 (45.50–46.66 wt.%), with very low concentrations of CaO (0.88–1.06 wt.%) and MgO (0.05–0.11 wt.%), suggesting minimal substitution of Mn by Ca and Mg. The compositional dominance of Mn^{2+} indicates Mn-enriched microenvironment that promoted pyroxmangite saturation. The presence of pyroxmangite rather than rhodonite in the Gabal El-Bakriya pegmatite further implies crystallization under elevated pressure conditions, consistent with late-stage crystallization of volatile-rich pegmatitic melts. The mineralogical association, especially with fluorite and pyrochroite, supports a magmatic-hydrothermal origin involving Mn-rich fluids.

7.2. Mineralization of the GEBI

Dynamic Model of Mineralization Enrichment

Preliminary field investigation of the GEBI revealed notable zones of mineralization associated with pegmatites. Integrated geological, petrographic, and mineral chemical data suggest that these mineralized pegmatites formed in a post-collisional tectonic setting, representing the final evolutionary stage of the GEBI. While the main phase of the alkali-feldspar granite is of primarily magmatic origin, hydrothermal overprinting became increasingly significant in the marginal zone, resulting in the formation of pegmatites, greisens, and associated mineralization. The primary mineralization assemblage includes barite, fluorite, Nb-Ta oxides, REE minerals, and a uranium-bearing phase. This mineralization assemblage is interpreted to have formed during the final stages of granitic crystallization. Intense metasomatism associated with these fluids caused widespread fluid–rock interaction and mass transfer in the outer zone of the alkali-feldspar granite. The pegmatites formed first, then while they were still hot and reactive, infiltrating, acidic fluids caused hydrothermal overprint. Mineral replacement, especially with volume decreased, further promoted fluid migration, enhancing mineral deposition along fractures and lithological contacts. The localization of mineralization was restricted to the apical and marginal parts of the alkaline feldspar granite. These zones represent structural and geochemical traps where volatile-rich hydrothermal fluids accumulated during the late magmatic stage. Before complete solidification of the melt, these volatile phases became increasingly concentrated in the upper part of the magma chamber. The progressive build-up of internal pressure from fluid accumulation led to hydraulic fracturing, initiating greisenization and alteration of the surrounding rocks [104]. Pockets in pegmatites might be either primary (due to saturation in a peralkaline magma) or secondary, caused by dissolution with an influx of aggressive, acidic fluids. The mineralized zone extends approximately 20–50 m along the fracture-controlled contact between the alkali-feldspar granite and the surrounding syenogranite, with local extension to the adjacent country rocks. Metasomatism was likely caused by externally derived aqueous fluids. The simultaneous decrease in temperature and increase in pressure during fluid exsolution and magma crystallization facilitated destabilization of early-formed magmatic minerals and their replacement by quartz, mica, topaz, fluorite, cassiterite, REE minerals, and uranium-bearing phases.

Mineral paragenesis indicates that cassiterite and beryl crystallized concurrently with the alteration of muscovite to topaz and quartz, pointing to a sustained supply of F-rich fluids during hydrothermal alteration. The occurrence of fluorite within pegmatites further confirms the abundance of fluorine in the residual fluids [105,106]. This style of mineralization is consistent with a magmatic cupola model associated with A-type granitic intrusions [104]. Chemical homogeneity of fluorite, topaz, and cassiterite (see mineral chemistry section) likely reflects stable hydrothermal conditions, potentially maintained by prolonged and focused fluid flow within the apical part of the granite. These observations support a residual magmatic-hydrothermal model for the origin of the mineralization at the

GEBI, driven by the late-stage evolution of an evolved, volatile-rich A-type felsic magmatic system [11].

7.3. Ore Minerals

7.3.1. Nb-Ta Oxide Minerals

In the present study, Nb-Ta oxides are recognized in the pegmatites exhibiting notable compositional and textural variations, indicative of the complex evolutionary history of magmatic–hydrothermal system [107–109]. The main Nb-Ta oxide phases identified include columbite, fergusonite, and pyrochlore.

Some columbite crystals show oscillatory zoning, patchy textures, and resorption features, which are diagnostic of crystallization under dynamic magmatic conditions. Zoning in columbite reflects differential diffusion rates of Ta and Nb in silicate melts relative to the rate of crystal growth and is characteristic of late-stage magmatic evolution [110]. This interpretation is supported by the frequent association of columbite with magmatic micas [111,112]. Experimental data suggest that fluxing agents and melt composition significantly influence the solubility of Nb-Ta oxides in silicate melts [112–114]. Columbite can crystallize early from melts containing >0.05 wt.% of MnO and FeO and Nb concentrations of ~70–100 ppm, at temperatures as low as 600 °C [105]. As temperature decreases, the solubility of Nb and Ta complexes in the melt declines sharply [113], favoring their saturation and crystallization. In the GEBI pegmatites, columbite is interpreted as a primary magmatic phase, later modified by hydrothermal fluids. Overgrowth textures and partial replacement by pyrochlore suggest a multi-stage evolutionary sequence, wherein primary columbite was reworked during late-magmatic to early hydrothermal stages. Patchy textures and resorption rims are consistent with dissolution–reprecipitation processes, attributed to the influx of volatile-rich fluids capable of redissolving and remobilizing Nb and Ta [114–116]. The characteristics of Nb–Ta mineralization in the Gabal El-Bakriya pegmatites are comparable to those reported from post-collisional A-type granites and highly fractionated I-type granites in the Eastern Desert of Egypt [12,22,23,117–122].

Fergusonite, another major Nb–Ta-bearing phase, is a complex oxide enriched in REEs, Y, and Nb. The HREE-enrichment, along with fluorine content (0.39–0.78 wt.%), suggest crystallization from evolved, F-rich fluids. Minor Na_2O, K_2O, and P_2O_5 may reflect secondary substitution or inclusions.

The presence of significant UO_2 (4.17–4.67 wt.%) and ThO_2 (2.85–3.97 wt.%) in fergusonite resulted in partial metamictization, a common feature in U- and Th-rich minerals due to prolonged radiation damage [123–127]. Together, the Nb–Ta oxide mineral assemblage in the Gabal El-Bakriya pegmatites reflects a magmatic evolution, from high-temperature crystallization of columbite to hydrothermal alteration and metasomatic modification, culminating in the formation of economically significant mineralization in a volatile-rich, peralkaline A-type granite system.

7.3.2. Bastnäsite

In the Gabal El-Bakriya pegmatites, bastnäsite occurs as euhedral to subhedral crystals, consistent with late-stage magmatic crystallization. The absence of replacement textures and the presence of well-developed zoning in bastnäsite crystals support its primary magmatic origin rather than a secondary or metasomatic one. Moreover, its coexistence with allanite, a well-known magmatic REE-bearing phase, further indicates crystallization from an evolved, incompatible-element-rich melt.

Slight patchiness observed in some bastnäsite-(Y) grains may result from minor decarbonation or hydration along crystal boundaries or fractures, likely triggered by interaction with late-stage deuteric fluids during the cooling phase. However, the preservation of zon-

ing and the lack of pervasive alteration textures suggest minimal post-magmatic overprint, unless the bastnäsite-(Y) grew from the post-magmatic fluids.

7.3.3. Cassiterite

Cassiterite is observed within pegmatites, formed during a late-stage hydrothermal episode along newly developed fractures. The presence of oscillatory zoning in cassiterite crystals indicates episodic variations in fluid composition, possibly controlled by fluctuations in pH, redox conditions, or metal availability during crystallization [128].

7.3.4. Beryl

Beryl is identified in both pegmatite and greisen assemblages associated with the alkali-feldspar granite of the GEBI. Its presence reflects a Be-enriched fluid, underscoring the role of fluid-mediated metal transport in evolved A-type systems [129,130].

8. Conclusions

1. Pyroxmangite is reported for the first time in the Gabal El-Bakriya pegmatites and on the whole Nubian Shield. The pegmatites are hosted by post-collisional, A-type granites of the Gabal El-Bakriya intrusion (GEBI). They were emplaced as dikes and plugs along the margin of the alkali-feldspar granite.
2. The pyroxmangite pockets consist essentially of pyroxmangite mineral alongside garnet, pyrochroite, and fluorite. The composition of pyroxmangite reflects Mn-rich, low-Ca, and high-silica fluids that infiltrated at the hydrothermal stage.
3. The pegmatites are NYF-type, characterized by high SiO_2 content and significant enrichment in Nb, Y, REE, Zr, Th, U, and F. These geochemical characteristics indicate advanced magmatic differentiation under oxidizing, fluorine-rich conditions.
4. The NYF-pegmatites host a diverse suite of REE- and HFSE-bearing accessory minerals, including monazite-(Ce), xenotime, bastnäsite, fergusonite, and pyrochlore, indicating favorable conditions for the concentration of critical metals. The evolved nature of the GEBI system, combined with its complex mineralogy and REE–Nb–Ta–U–F enrichment, highlights its high potential for mineral exploration for critical minerals, particularly in the greisens, pegmatites, and quartz-fluorite veins. In addition, the studied pyroxmangite has potential economic value for its use in jewelry and decorative applications.

Supplementary Materials: The following supporting information can be downloaded at: https://www.mdpi.com/article/10.3390/min15101027/s1. All microprobe data are presented in the Supplementary Tables S1–S22.

Author Contributions: Conceptualization, M.K.A., D.M.F., S.A., E.S.F. and A.B.; methodology, D.M.F. and F.A.A.; software, D.M.F., M.K.A., D.M.F. and F.A.A.; validation, M.K.A., D.M.F., S.A., E.S.F. and A.B.; formal analysis, D.M.F. and F.A.A.; investigation, M.K.A., D.M.F., S.A., E.S.F., F.A.A. and A.B.; data curation, M.K.A., D.M.F. and S.A.; writing—original draft preparation, M.K.A., D.M.F. and S.A.; writing—review and editing, M.K.A., D.M.F., S.A., A.B. and F.A.A.; visualization, M.K.A., D.M.F., S.A. and E.S.F.; supervision, M.K.A., S.A. and E.S.F.; project administration, M.K.A. and F.A.A. All authors have read and agreed to the published version of the manuscript.

Funding: This research was funded by the Ongoing Research Funding Program (ORF-2025-1469), King Saud University, Saudi Arabia.

Data Availability Statement: All data derived from this research are presented in the enclosed figures, tables and Supplementary Tables S1–S22.

Acknowledgments: The authors express their sincere gratitude for the financial support provided by the Ongoing Research Funding Program (ORF-2025-1469), King Saud University, Riyadh, Saudi Arabia.

Conflicts of Interest: The authors declare that they have no known competing financial interests or personal relationships that could have appeared to influence the work reported in this paper.

References

1. Johnson, P.R.; Woldehaimanot, B. Development of the Arabian–Nubian Shield: Perspectives on accretion and deformation in the northern East African Orogen and the assembly of Gondwana. *Geol. Soc. Lond. Spec. Publ.* **2003**, *206*, 289–325. [CrossRef]
2. Stern, R.J. Arc assembly and collision in the Neoproterozoic African Orogen: Implications for the consolidation of Gondwanaland. *Annu. Rev. Earth Planet. Sci.* **1994**, *22*, 319–351. [CrossRef]
3. Stern, R.J. Crustal evolution in the East African Orogen: A neodymium isotopic perspective. *J. Afr. Earth Sci.* **2002**, *34*, 109–117. [CrossRef]
4. Meert, J.G.; Nédélec, A.; Hall, C. The stratoid granites of central Madagascar: Paleomagnetism and further age constraints on Neoproterozoic deformation. *Precambrian Res.* **2003**, *120*, 101–129. [CrossRef]
5. Hargrove, U.; Stern, R.; Kimura, J.-I.; Manton, W.; Johnson, P. How juvenile is the Arabian–Nubian Shield? Evidence from Nd isotopes and pre-Neoproterozoic inherited zircon in the Bi'r Umq suture zone, Saudi Arabia. *Earth Planet. Sci. Lett.* **2006**, *252*, 308–326. [CrossRef]
6. Liégeois, J.-P.; Stern, R.J. Sr–Nd isotopes and geochemistry of granite-gneiss complexes from the Meatiq and Hafafit domes, Eastern Desert, Egypt: No evidence for pre-Neoproterozoic crust. *J. Afr. Earth Sci.* **2010**, *57*, 31–40. [CrossRef]
7. Ali, K.A.; Azer, M.K.; Gahlan, H.A.; Wilde, S.A.; Samuel, M.D.; Stern, R.J. Age constraints on the formation and emplacement of Neoproterozoic ophiolites along the Allaqi–Heiani Suture, South Eastern Desert of Egypt. *Gondwana Res.* **2010**, *18*, 583–595. [CrossRef]
8. Johnson, P.; Andresen, A.; Collins, A.; Fowler, A.; Fritz, H.; Ghebreab, W.; Kusky, T.; Stern, R. Late Cryogenian–Ediacaran history of the Arabian–Nubian Shield: A review of depositional, plutonic, structural, and tectonic events in the closing stages of the northern East African Orogen. *J. Afr. Earth Sci.* **2011**, *61*, 167–232. [CrossRef]
9. Khalil, A.E.S.; Obeid, M.A.; Azer, M.K.; Asimow, P.D. Geochemistry and petrogenesis of post-collisional alkaline and peralkaline granites of the Arabian-Nubian Shield: A case study from the southern tip of Sinai Peninsula, Egypt. *Int. Geol. Rev.* **2017**, *60*, 998–1018. [CrossRef]
10. Azer, M.K.; Abdelfadil, K.M.; Asimow, P.D.; Khalil, A.E. Tracking the transition from subduction-related to post-collisional magmatism in the north Arabian–Nubian Shield: A case study from the Homrit Waggat area of the Eastern Desert of Egypt. *Geol. J.* **2019**, *55*, 4426–4452. [CrossRef]
11. Abuamarah, B.A.; Azer, M.K.; Seddik, A.M.; Asimow, P.D.; Guzman, P.; Fultz, B.T.; Wilner, O.; Dalleska, N.; Darwish, M.H. Magmatic and post-magmatic evolution of post-collisional rare-metal bearing granite: The Neoproterozoic Homrit Akarem Granitic Intrusion, south Eastern Desert of Egypt. *Geochemistry* **2022**, *82*, 125840. [CrossRef]
12. Elsagheer, M.A.; Azer, M.K.; Moussa, H.E.; Maurice, A.E.; Sami, M.; El Maaty, M.A.A.; Akarish, A.I.M.; Heikal, M.T.S.; Khedr, M.Z.; Elnazer, A.A.; et al. Late Neoproterozoic Rare-Metal Pegmatites with Mixed NYF-LCT Features: A Case Study from the Egyptian Nubian Shield. *Minerals* **2025**, *15*, 495. [CrossRef]
13. Bentor, Y. The crustal evolution of the Arabo-Nubian Massif with special reference to the Sinai Peninsula. *Precambrian Res.* **1985**, *28*, 1–74. [CrossRef]
14. Jarrar, G.; Stern, R.; Saffarini, G.; Al-Zubi, H. Late-and post-orogenic Neoproterozoic intrusions of Jordan: Implications for crustal growth in the northernmost segment of the East African Orogen. *Precambrian Res.* **2003**, *123*, 295–319. [CrossRef]
15. Moussa, E.M.; Stern, R.J.; Manton, W.I.; Ali, K.A. SHRIMP zircon dating and Sm/Nd isotopic investigations of Neoproterozoic granitoids, Eastern Desert, Egypt. *Precambrian Res.* **2008**, *160*, 341–356. [CrossRef]
16. Azer, M.; Obeid, M.; Ren, M. Geochemistry and petrogenesis of late Ediacaran (605–580 Ma) post-collisional alkaline rocks from the Katherina ring complex, south Sinai, Egypt. *J. Asian Earth Sci.* **2014**, *93*, 229–252. [CrossRef]
17. Be'ERi-Shlevin, Y.; Katzir, Y.; Valley, J.W. Crustal evolution and recycling in a juvenile continent: Oxygen isotope ratio of zircon in the northern Arabian Nubian Shield. *Lithos* **2009**, *107*, 169–184. [CrossRef]
18. Be'eRi-Shlevin, Y.; Samuel, M.D.; Azer, M.; Rämö, O.; Whitehouse, M.; Moussa, H. The Ediacaran Ferani and Rutig volcano-sedimentary successions of the northernmost Arabian-Nubian Shield (ANS): New insights from zircon U–Pb geochronology, geochemistry and O–Nd isotope ratios. *Precambrian Res.* **2011**, *188*, 21–44. [CrossRef]
19. Azer, M.K.; Stern, R.J.; Kimura, J.I. Origin of a late Neoproterozoic (605 ± 13 Ma) intrusive carbonate–albitite complex in Southern Sinai, Egypt. *Int. J. Earth Sci.* **2010**, *99*, 245–267. [CrossRef]

20. Eyal, M.; Litvinovsky, B.; Jahn, B.; Zanvilevich, A.; Katzir, Y. Origin and evolution of post-collisional magmatism: Coeval Neoproterozoic calc-alkaline and alkaline suites of the Sinai Peninsula. *Chem. Geol.* **2010**, *269*, 153–179. [CrossRef]
21. Abu El-Rus, M.A.; Mohamed, M.A.; Lindh, A. Mueilha rare metals granite, Eastern Desert of Egypt: An example of a magmatic-hydrothermal system in the Arabian-Nubian Shield. *Lithos* **2017**, *294–295*, 362–382. [CrossRef]
22. Azer, M.K.; Abdelfadil, K.M.; Ramadan, A.A. Geochemistry and petrogenesis of Late Ediacaran rare-metal albite granite of the Nubian Shield: Case study of Nuweibi intrusion, Eastern Desert, Egypt. *J. Geol.* **2019**, *127*, 665–689. [CrossRef]
23. Seddik, A.M.; Darwish, M.H.; Azer, M.K.; Asimow, P.D. Assessment of magmatic versus post-magmatic processes in the Mueilha rare-metal granite, Eastern Desert of Egypt, Arabian-Nubian Shield. *Lithos* **2020**, *366–367*, 105542. [CrossRef]
24. Moussa, H.E.; Asimow, P.D.; Azer, M.K.; El Maaty, M.A.A.; Akarish, A.I.; Yanni, N.N.; Mubarak, H.S.; Wilner, O.; Elsagheer, M.A. Magmatic and hydrothermal evolution of highly-fractionated rare-metal granites at Gabal Nuweibi, Eastern Desert, Egypt. *Lithos* **2021**, *400–401*, 106405. [CrossRef]
25. Heikal, M.T.S.; Shereif, A.S.; Azer, M.K. Gamma activity concentrations (226Ra, 232Th, 40K) of mineralized Homret Akarem composite granitic pluton, Egyptian Nubian Shield: Environmental hazards assessment. *Euro-Mediterranean J. Environ. Integr.* **2024**, *9*, 1629–1658. [CrossRef]
26. Heikal, M.T.S.; Azer, M.K.; Kamar, M.S.; Ibrahim, M.O.; El Monsef, M.A. Petrogenesis and geodynamic model for (Ta, Nb)-fertilized Nuweibi albite granite, Egyptian Nubian Shield: Juvenile crust-mantle mixing and metasomatic enhancement. *J. Afr. Earth Sci.* **2024**, *223*, 105530. [CrossRef]
27. Zoheir, B.; Carr, P.; Xu, X.; Zeh, A.; Kraemer, D.; McAleer, R.; Steele-MacInnis, M.; Ragab, A.; Deshesh, F. The Igla Sn-(W-Be) deposit, Egypt: Prolonged magmatic-metasomatic processes during the middle stage evolution of the Arabian-Nubian Shield. *Gondwana Res.* **2025**, *142*, 20–43. [CrossRef]
28. Saleeb-Roufaiel, G.S. Note on the possible occurrence of contact metamorphism Nubian sandstone at Bakriya, Eastern Desert of Egypt. *BNRC Egypt* **1977**, *2*, 283–286.
29. Moussa, H.E. Contribution to the Geology and Mineralization in the Area of Bakriya, Eastern Desert, Egypt. Master's Thesis, Ain Shams University, Cairo, Egypt, 1979; 129p.
30. Saleeb-Roufaiel, G.S.; Samuel, M.D.; Hilmy, M.E.; Moussa, H.E. Fluorite mineralization at El-Bakriya, Eastern Desert of Egypt. *Egypt. J. Geol.* **1982**, *26*, 9–18.
31. Samuel, M.D.; Roufaiel, G.S.; Hilmy, M.E.; Moussa, H. Study of Cretaceous fore-arc granite and associated rocks at Bakriya, Eastern Desert. *Egypt. J. Geol.* **1983**, *27*, 1–11.
32. El-Fatah, A.A.A.; Surour, A.A.; Azer, M.K.; Madani, A.A. Integration of Whole-Rock Geochemistry and Mineral Chemistry Data for the Petrogenesis of A-Type Ring Complex from Gebel El Bakriyah Area, Egypt. *Minerals* **2023**, *13*, 1273. [CrossRef]
33. Abd El-Fatah, A.A.; Abd El-Dayiem, A.; Madani, A.A.; Surour, A.A.A.; Azer, M.K. Integration of Landsat-8 and reflectance spectroscopy data for mapping of late Neoproterozoic igneous ring complexes in an arid environment: A case study of Gebel El-Bakriyah Area, Eastern Desert, Egypt. *JME* **2023**, *14*, 13–31.
34. El-Sayed, M.; Mohamed, F.; Furnes, H. Petrological and geochemical constraints on the evolution of late Pan-African Bakriya post-orogenic ring complex, Central Eastern Desert, Egypt. In Proceedings of the 7th EUREGEO, Zolder, Belgium, 11–12 September 2004; p. 688.
35. Abd EL-Wahed, M.; Hamimi, Z. Neoproterozoic tectonic events of Egypt. *Acta Geol. Sin.-Engl.* **2021**, *95*, 1366–1405. [CrossRef]
36. El-Amin, H. Radiometric and Geological Investigations of El-Bakriya Area, Eastern Desert, Egypt. Ph.D. Thesis, Cairo University, Cairo, Egypt, 1975.
37. Miller, C.F.; Stoddard, E.F. The role of manganese in the paragenesis of magmatic garnet: An example from the Old Woman-Piute Range, California. *J. Geol.* **1981**, *89*, 233–246. [CrossRef]
38. Tischendorf, G.; Förster, H.-J.; Gottesmann, B. Minor-and trace-element composition of trioctahedral micas: A review. *Miner. Mag.* **2001**, *65*, 249–276. [CrossRef]
39. Zen, E.A. Phase relations of peraluminous granitic rocks and their petrogenetic implications. *Annu. Rev. Earth Planet. Sci.* **1988**, *16*, 21–51. [CrossRef]
40. Mokhtar, H.; Surour, A.A.; Azer, M.K.; Ren, M.; Said, A. Petrogenesis and possible fingerprints of the Najd shear system on the evolution of deformed granitic rocks in the west Wadi Nugrus area, Egypt. *J. Afr. Earth Sci.* **2023**, *207*, 105045. [CrossRef]
41. Mokhtar, H.; Surour, A.A.; Azer, M.K.; Ren, M.; Said, A. Geochemistry and mineral chemistry of granitic rocks from west Wadi El Gemal area, southern Eastern Desert of Egypt: Indicators for highly fractionated syn-to post-collisional Neoproterozoic felsic magmatism. *Acta Geochim.* **2024**, *44*, 163–188. [CrossRef]
42. Vavra, G.; Gebauer, D.; Schmid, R.; Compston, W. Multiple zircon growth and recrystallization during polyphase Late Carboniferous to Triassic metamorphism in granulites of the Ivrea Zone (Southern Alps): An ion microprobe (SHRIMP) study. *Contrib. Miner. Pet.* **1996**, *122*, 337–358. [CrossRef]
43. Hoskin, P.; Black, L. Metamorphic zircon formation by solid-state recrystallization of protolith igneous zircon. *J. Metamorph. Geol.* **2000**, *18*, 423–439. [CrossRef]

44. Mücke, A. Chamosite, siderite and the environmental conditions of their formation in chamosite-type Phanerozoic ooidal ironstones. *Ore Geol. Rev.* **2006**, *28*, 235–249. [CrossRef]
45. Inoue, A. Formation of clay minerals in hydrothermal environments. In *Origin and Mineralogy of Clays: Clays and the Environment*; Springer: Berlin/Heidelberg, Germany, 1995; pp. 268–329.
46. Černý, P.; Ercit, T.S.; Wise, M.A. The tantalite-tapiolite gap; natural assemblages versus experimental data. *Can. Mineral.* **1992**, *30*, 587–596.
47. Atencio, D.; Andrade, M.B.; Christy, A.G.; Giere, R.; Kartashov, P.M. The pyrochlore supergroup of minerals: Nomenclature. *Can. Mineral.* **2010**, *48*, 673–698. [CrossRef]
48. Chen, L.; Yan, Z.; Wang, Z.Q.; Wang, K.M. Characteristics of apatite from 160–140 Ma Cu (Mo) and Mo (W) deposits in East Qinling. *Acta Geol. Sin.* **2017**, *91*, 1925–1941.
49. Du, J.; Wang, G.; Jia, L. In situ major and trace element compositions of apatites from Luanchuan orecluster: Implications for porphyry Mo mineralization. *Ore Geol. Rev.* **2019**, *115*, 103174. [CrossRef]
50. Yang, F.; Santosh, M.; Glorie, S.; Xue, F.; Zhang, S.; Zhang, X. Apatite geochronology and chemistry of Luanchuan granitoids in the East Qinling Orogen, China: Implications for petrogenesis, metallogenesis and exploration. *Lithos* **2020**, *378–379*, 105797. [CrossRef]
51. Feng, Y.; Lu, W.; Xiao, B.; Wu, C.; Zheng, H. Apatite geochronology and geochemistry of Gucheng granites: Implications for petrogenesis and REE metallogenesis in South China. *Ore Geol. Rev.* **2023**, *163*, 105791. [CrossRef]
52. Li, J.; Chen, S.-Y.; Zhao, Y.-H. Trace elements in apatite from Gejiu Sn polymetallic district: Implications for petrogenesis, metallogenesis and exploration. *Ore Geol. Rev.* **2022**, *145*, 104880. [CrossRef]
53. Li, J.; Yan, Q.; Li, P.; Jacobson, M.I. Formation of granitic pegmatites during orogenies: Indications from a case study of the pegmatites in China. *Ore Geol. Rev.* **2023**, *156*, 105391. [CrossRef]
54. Stormer, J.C. The effects of recalculation on estimates of temperature and oxygen fugacity from analyses of multicomponent iron-titanium oxides. *Am. Mineral.* **1983**, *68*, 586–594.
55. Deer, W.A.; Howie, R.A.; Zussman, J. *An Introduction to the Rock-Forming Minerals*, 2nd ed.; Longman Scientific & Technical: London, UK, 1992.
56. Černý, P. Distribution, affiliation and derivation of rare-element granitic pegmatites in the Canadian Shield. *Geol. Rundsch.* **1990**, *79*, 183–226. [CrossRef]
57. Cerny, P.; Ercit, T.S. The classification of granitic pegmatites revisited. *Can. Mineral.* **2005**, *43*, 2005–2026. [CrossRef]
58. Hanson, S.L. A tectonic evaluation of pegmatite parent granites. *Can. Mineral.* **2016**, *54*, 917–933. [CrossRef]
59. Sun, S.S.; McDonough, W.F. Chemical and isotopic systematics of oceanic basalts: Implications for mantle composition and processes. *Geol. Soc. Spec. Publ.* **1989**, *42*, 313–345. [CrossRef]
60. Wu, F.-Y.; Sun, D.-Y.; Li, H.; Jahn, B.-M.; Wilde, S. A-type granites in northeastern China: Age and geochemical constraints on their petrogenesis. *Chem. Geol.* **2002**, *187*, 143–173. [CrossRef]
61. Liégeois, J.P.; Black, R. Alkaline magmatism subsequent to collision in the Pan-African belt of the Adrar des Iforas (Mali). *Geol. Soc. Lond. Spec. Publ.* **1987**, *30*, 381–401. [CrossRef]
62. Bonin, B. A-type granites and related rocks: Evolution of a concept, problems and prospects. *Lithos* **2007**, *97*, 1–29. [CrossRef]
63. Eby, G. The A-type granitoids: A review of their occurrence and chemical characteristics and speculations on their petrogenesis. *Lithos* **1990**, *26*, 115–134. [CrossRef]
64. Eby, G.N. Chemical subdivision of the A-type granitoids:Petrogenetic and tectonic implications. *Geology* **1992**, *20*, 641–644. [CrossRef]
65. Whalen, J.B.; Currie, K.L.; Chappell, B.W. A-type granites: Geochemical characteristics, discrimination and petrogenesis. *Contrib. Mineral. Petrol.* **1987**, *95*, 407–419. [CrossRef]
66. Abdel-Rahman, A.F.M.; El-Kibbi, M.M. Anorogenic magmatism: Chemical evolution of the Mount El-Sibai A-type complex (Egypt), and implications for the origin of within-plate felsic magmas. *Geol. Mag.* **2001**, *138*, 67–85. [CrossRef]
67. Pearce, J.A.; Harris, N.B.W.; Tindle, A.G. Trace element discrimination diagrams for the tectonic interpretation of granitic rocks. *J. Pet.* **1984**, *25*, 956–983. [CrossRef]
68. London, D.; Evensen, J.M. Beryllium in silicic magmas and the origin of beryl-bearing pegmatites. *Rev. Mineral. Geochem.* **2002**, *50*, 445–486. [CrossRef]
69. Maphumulo, M.S. Mineralogical and Geochemical Characterisation of Mineralised and Regular NYF-Type Pegmatites from the Namaqualand Pegmatite Belt, Northern Cape, South Africa. Master's Thesis, University of Johannesburg, Johannesburg, South Africa, 2020.
70. Bonzi, W.M.-E.; Van Lichtervelde, M.; Vanderhaeghe, O.; André-Mayer, A.-S.; Salvi, S.; Wenmenga, U. Insights from mineral trace chemistry on the origin of NYF and mixed LCT+ NYF pegmatites and their mineralization at Mangodara, SW Burkina Faso. *Miner. Depos.* **2022**, *58*, 75–104. [CrossRef]
71. Simmons, W.B.; Webber, K.L.; Falster, A.U. Pegmatites. *Rocks Miner.* **2024**, *99*, 18–32. [CrossRef]

72. Xie, L.; Wang, R.; Rao, L.; Wu, F. Discovery of a petalite-type pegmatite in the eastern Himalaya and implications for rare-metal mineralization. *Lithos* **2025**, *510–511*, 108112. [CrossRef]
73. Dill, H.G. Pegmatitic Rocks and Economic Geology. In *The Hagendorf-Pleystein Province: The Center of Pegmatites in an Ensialic Orogen*; Springer International Publishing: Cham, Switzerland, 2015; pp. 1–54.
74. Xiong, Y.-Q.; Fan, Z.-W.; Yu, H.-Y.; Di, H.; Cao, Y.-H.; Wen, C.-H.; Jiang, S.-Y. Genetic linkage between parent granite and zoned rare metal pegmatite in the Renli-Chuanziyuan granite-pegmatite system, South China. *GSA Bull.* **2024**, *137*, 1607–1627. [CrossRef]
75. Zheng, S.; Su, J.-H.; Wang, J.; Liu, S.-J.; Zhao, X.-F. Origin and evolution of granitic pegmatite rare metal deposits in the northern Mufushan batholith, South China: Insights from muscovite chemistry. *Am. Mineral.* **2025**. [CrossRef]
76. Černý, P.; London, D.; Novák, M. Granitic pegmatites as reflections of their sources. *Elements* **2012**, *8*, 289–294. [CrossRef]
77. London, D. Ore-forming processes within granitic pegmatites. *Ore Geol. Rev.* **2018**, *101*, 349–383. [CrossRef]
78. Kaeter, D.; Barros, R.; Menuge, J.F.; Chew, D.M. The magmatic–hydrothermal transition in rare-element pegmatites from southeast Ireland: LA-ICP-MS chemical mapping of muscovite and columbite–tantalite. *Geochim. Cosmochim. Acta* **2018**, *240*, 98–130. [CrossRef]
79. Michaud, J.A.-S.; Pichavant, M. Magmatic fractionation and the magmatic-hydrothermal transition in rare metal granites: Evidence from Argemela (Central Portugal). *Geochim. Cosmochim. Acta* **2020**, *289*, 130–157. [CrossRef]
80. Xu, Y.-G.; Wang, R.-C.; Wang, C.Y.; Linnen, R.; Wu, F.-Y. Highly fractionated granites and rare-metal mineralization. *Lithos* **2021**, *398–399*, 106262. [CrossRef]
81. Xu, Z.; Zheng, B.; Zhu, W.; Chen, Y.; Li, G.; Gao, J.; Che, X.; Zhang, R.; Wei, H.; Li, W.; et al. Geologic scenario from granitic sheet to Li-rich pegmatite uncovered by Scientific Drilling at the Jiajika lithium deposit in eastern Tibetan Plateau. *Ore Geol. Rev.* **2023**, *161*, 105636. [CrossRef]
82. Liu, C.; Wang, R.-C.; Linnen, R.L.; Wu, F.-Y.; Xie, L.; Liu, X.-C. Continuous Be mineralization from two-mica granite to pegmatite: Critical element enrichment processes in a Himalayan leucogranite pluton. *Am. Mineral.* **2023**, *108*, 31–41. [CrossRef]
83. Yan, Q.-G.; Li, J.-K.; Wang, D.-H.; Zhu, Z.-Y.; Li, C.; Chen, Z.-Y. Petrogenesis of Ke'eryin granitic pegmatites and associated Li mineralization in the Songpan–Ganze orogenic belt, China: Evidence from apatite and bulk-rock chemistry. *Miner. Depos.* **2024**, *60*, 723–742. [CrossRef]
84. Goodenough, K.M.; Shaw, R.A.; Borst, A.M.; Nex, P.; Kinnaird, J.A.; van Lichtervelde, M.; Essaifi, A.; Koopmans, L.; Deady, E.A. Lithium pegmatites in Africa: A review. *Econ. Geol.* **2025**, *120*, 513–539. [CrossRef]
85. Müller, A.; Romer, R.L.; Szuszkiewicz, A.; Ilnicki, S.; Szełęg, E. Can pluton-related and pluton-unrelated granitic pegmatites be distinguished by their chemistry? In Proceedings of the 2nd Eugene E. Foord Pegmatite Symposium, Golden, CO, USA, 15–19 July 2016; p. 67.
86. Webber, K.; Simmons, W.B.; Falster, A.U.; Hanson, S.L. Anatectic Pegmatites of the Oxford County Pegmatite Field, Maine, USA. *Can. Mineral.* **2019**, *57*, 811–815. [CrossRef]
87. Martin, R.F.; De Vito, C. The patterns of enrichment in felsic pegmatites ultimately depend on tectonic setting. *Can. Mineral.* **2005**, *43*, 2027–2048. [CrossRef]
88. Konzett, J.; Schneider, T.; Nedyalkova, L.; Hauzenberger, C.; Melcher, F.; Gerdes, A.; Whitehouse, M. Anatectic granitic pegmatites from the Eastern Alps: A case of variable rare-metal enrichment during high-grade regional metamorphism–I: Mineral assemblages, geochemical characteristics, and emplacement ages. *Can. Mineral.* **2018**, *56*, 555–602. [CrossRef]
89. Fei, G.; Menuge, J.F.; Li, Y.; Yang, J.; Deng, Y.; Chen, C.; Yang, Y.; Yang, Z.; Qin, L.; Zheng, L.; et al. Petrogenesis of the Lijiagou spodumene pegmatites in Songpan-Garze Fold Belt, West Sichuan, China: Evidence from geochemistry, zircon, cassiterite and coltan U-Pb geochronology and Hf isotopic compositions. *Lithos* **2020**, *364–365*, 105555. [CrossRef]
90. Adoze, U.; Abubakar, F.; Ochu, G.; Danga, O.; Adamu, M.; Baba, Y. Geological and geochemical analyses of pegmatites in Egbe, Isanlu (sheet 225), Southwestern Nigeria. *Sci. Afr.* **2024**, *23*, 183–202. [CrossRef]
91. Sirbescu, M.-L.C.; Nabelek, P.I. Crystallization conditions and evolution of magmatic fluids in the Harney Peak Granite and associated pegmatites, Black Hills, South Dakota—Evidence from fluid inclusions. *Geochim. Cosmochim. Acta* **2003**, *67*, 2443–2465. [CrossRef]
92. London, D. Reading pegmatites: Part 1—What beryl says. *Rocks Miner.* **2015**, *90*, 138–153. [CrossRef]
93. Wu, F.-Y.; Liu, X.-C.; Liu, Z.-C.; Wang, R.-C.; Xie, L.; Wang, J.-M.; Ji, W.-Q.; Yang, L.; Liu, C.; Khanal, G.P.; et al. Highly fractionated Himalayan leucogranites and associated rare-metal mineralization. *Lithos* **2020**, *352–353*, 105319. [CrossRef]
94. Teixeira, L.M.F.; Troch, J.; Allaz, J.; Bachmann, O. Magmatic to hydrothermal conditions in the transition from the A-type Pikes Peak granite (Colorado) to its related pegmatite. *Front. Earth Sci.* **2022**, *10*, 976588. [CrossRef]
95. London, D. Granitic pegmatites: An assessment of current concepts and directions for the future. *Lithos* **2005**, *80*, 281–303. [CrossRef]
96. Stilling, A.; Ćerný, P.; Vanstone, P.J. The Tanco pegmatite at Bernic Lake, Manitoba. XVI. Zonal and bulk compositions and their petrogenetic significance. *Can. Mineral.* **2006**, *44*, 599–623. [CrossRef]

97. Buick, I.S.; Storkey, A.; Williams, I.S. Timing relationships between pegmatite emplacement, metamorphism and deformation during the intra-plate Alice Springs Orogeny, central Australia. *J. Metamorph. Geol.* **2008**, *26*, 915–936. [CrossRef]
98. London, D. A petrologic assessment of internal zonation in granitic pegmatites. *Lithos* **2014**, *184*, 74–104. [CrossRef]
99. Roda-Robles, E.; Pesquera, A.; Gil-Crespo, P.; Torres-Ruiz, J. From granite to highly evolved pegmatite: A case study of the Pinilla de Fermoselle granite–pegmatite system (Zamora, Spain). *Lithos* **2012**, *153*, 192–207. [CrossRef]
100. Simmons, W.B.S.; Webber, K.L. Pegmatite genesis: State of the art. *Eur. J. Miner.* **2008**, *20*, 421–438. [CrossRef]
101. Gahlan, H.A.; Asimow, P.D.; Azer, M.K.; Ma, C.; Al-Kahtany, K.M.; Hakeem, A.Y. Geochemistry and mineralogy of the Jebel Aja Igneous Intrusion and the associated exotic pegmatites, Arabian Shield, Saudi Arabia. *Lithos* **2021**, *400–401*, 106395. [CrossRef]
102. Partington, G.A.; McNaughton, N.J.; Williams, I.S. A review of the geology, mineralization, and geochronology of the Greenbushes pegmatite, Western Australia. *Econ. Geol.* **1995**, *90*, 616–635. [CrossRef]
103. Goodenough, K.M.; Shaw, R.A.; Smith, M.; Estrade, G.; Marqu, E.; Bernard, C.; Nex, P. Economic mineralization in pegmatites: Comparing and contrasting NYF and LCT examples. *Can. Mineral.* **2019**, *57*, 753–755. [CrossRef]
104. Elbialy, M.Y. Origin and Economic Profits of Pegmatites: A Case Study from Egypt. Ph.D. Thesis, Tanta University, Tanta, Egypt, 2022.
105. Maresch, W.V.; Mottana, A. The pyroxmangite-rhodonite transformation for the $MnSiO_3$ composition. *Contrib. Miner. Pet.* **1976**, *55*, 69–79. [CrossRef]
106. Azer, M.K.; Surour, A.A.; Moussa, H.E.; Maurice, A.E.; Sami, M.; El Maaty, M.A.A.; Akarish, A.I.M.; Heikal, M.T.S.; Elnazer, A.A.; Elsagheer, M.A.; et al. Homrit Akarem Post-Collisional Intrusion, Southeastern Desert, Egypt: Petrogenesis of Greisen Formed in a Cupola Structure and Enrichment in Strategic Minerals. *Geosciences* **2025**, *15*, 200. [CrossRef]
107. El Hadek, H.H.; Mohamed, M.A.; El Habaak, G.H.; Bishara, W.W.; Ali, K.A. Geochemical constraints on petrogenesis of Homrit Waggat rare metal granite, Egypt. *Int. J. Geo. Geochem.* **2016**, *3*, 33–48.
108. Kotlánová, M.K.; Dolníček, Z.; René, M.; Prochaska, W.; Ulmanová, J.; Kapusta, J.; Mašek, V.; Kropáč, K. Fluid evolution of greisens from Krupka Sn-W ore district, Bohemian Massif (Czech Republic). *Minerals* **2024**, *14*, 86. [CrossRef]
109. Linnen, R.L.; Keppler, H. Columbite solubility in granitic melts: Consequences for the enrichment and fractionation of Nb and Ta in the Earth's crust. *Contrib. Mineral. Petrol.* **1997**, *128*, 213–227. [CrossRef]
110. Bartels, A.; Holtz, F.; Linnen, R.L. Solubility of manganotantalite and manganocolumbite in pegmatitic melts. *Am. Miner.* **2010**, *95*, 537–544. [CrossRef]
111. Fiege, A.; Simon, A.; Linsler, S.A.; Bartels, A.; Linnen, R.L. Experimental constraints on the effect of phosphorous and boron on Nb and Ta ore formation. *Ore Geol. Rev.* **2018**, *94*, 383–395. [CrossRef]
112. Lahti, S.I. Zoning in columbite-tantalite crystals from the granitic pegmatites of the Eräjärvi area, southern Finland. *Geoch. Cosmochim. Acta* **1987**, *51*, 509–517. [CrossRef]
113. Roda, E.; Keller, P.; Pesquera, A.; Fontan, F. Micas of the muscovite–lepidolite series from Karibib pegmatites, Namibia. *Miner. Mag.* **2007**, *71*, 41–62. [CrossRef]
114. Van Lichtervelde, M.; Holtz, F.; Melcher, F. The effect of disequilibrium crystallization on Nb-Ta fractionation in pegmatites: Constraints from crystallization experiments of tantalite-tapiolite. *Am. Mineral.* **2018**, *103*, 1401–1416. [CrossRef]
115. Chevychelov, V.Y.; Borodulin, G.P.; Zaraisky, G.P. Solubility of columbite,(Mn, Fe)$(Nb, Ta)_2O_6$, in granitoid and alkaline melts at 650–850 °C and 30–400 MPa: An experimental investigation. *Geochem. Int.* **2010**, *48*, 456–464. [CrossRef]
116. McNeil, A.G.; Linnen, R.L.; Flemming, R.L. Solubility of wodginite, titanowodginite, microlite, pyrochlore, columbite-(Mn) and tantalite-(Mn) in flux-rich haplogranitic melts between 700° and 850 °C and 200 MPa. *Lithos* **2020**, *352–353*, 105239. [CrossRef]
117. Chevychelov, V.Y.; Zaraisky, G.P.; Borisovsky, S.E.; Nekrasov, A.N. Solubility of Columbite and Diffusion of Ta, Nb, Fe, and Mn in Li–F Granite Melts at 740–980 C and 1 kbar. In Proceedings of the 15th Russian Conference on Experimental Mineralogy, Syktyvkar, Russia, 22–24 June 2005; pp. 123–125.
118. London, D. The application of experimental petrology to the genesis and crystallization of granitic pegmatites. *Can. Min.* **1992**, *30*, 499–540.
119. Van Lichtervelde, M.; Salvi, S.; Beziat, D.; Linnen, R.L. Textural features and chemical evolution in tantalum oxides: Magmatic versus hydrothermal origins for Ta mineralization in the Tanco Lower pegmatite, Manitoba, Canada. *Econ. Geol.* **2007**, *102*, 257–276. [CrossRef]
120. Helba, H.; Trumbull, R.B.; Morteani, G.; Khalil, S.O.; Arslan, A. Geochemical and petrographic studies of Ta mineralization in the Nuweibi albite granite complex, Eastern Desert, Egypt. *Miner. Depos.* **1997**, *32*, 164–179. [CrossRef]
121. Abuamarah, B.A.; Azer, M.K.; Asimow, P.D.; Ghrefat, H.; Mubarak, H.S. Geochemistry and petrogenesis of late Ediacaran rare-metal albite granites of the Arabian-Nubian Shield. *Acta Geol. Sin. Engl.* **2019**, *95*, 459–480. [CrossRef]
122. Heikal, M.T.S.; Khedr, M.Z.; El Monsef, M.A.; Gomaa, S.R. Petrogenesis and geodynamic evolution of neoproterozoic Abu Dabbab albite granite, central Eastern Desert of Egypt: Petrological and geochemical constraints. *J. Afr. Earth Sci.* **2019**, *158*, 103518. [CrossRef]

123. Zozulya, D.; Macdonald, R.; Bagiński, B. REE fractionation during crystallization and alteration of fergusonite-(Y) from Zr-REE-Nb-rich late-to post-magmatic products of the Keivy alkali granite complex, NW Russia. *Ore Geol. Rev.* **2020**, *125*, 103693. [CrossRef]
124. Gawad, A.E.A.; Panova, E.G.; Ghoneim, M.M.; Yanson, S.Y.; Alsufyani, S.J.; Saftah, A.; Alresheedi, N.M.; Hanfi, M.Y. Radioactive Assessment and Th-, Nb-Ta-, Zr-, REE-Bearing Minerals in Alkaline Syenite: Environmental Implications for Radiological Safety. *Geosciences* **2025**, *15*, 138. [CrossRef]
125. Hisinger, W. *Lethoea Svecica: Seu, Petrificata Svecioe, Iconibus et Characteribus Illustrata*; PA Norstedt et filii: Stockholm, Sweden, 1838.
126. Andersen, T. Compositional variation of some rare earth minerals from the Fen complex (Telemark, SE Norway): Implications for the mobility of rare earths in a carbonatite system. *Miner. Mag.* **1986**, *50*, 503–509. [CrossRef]
127. Shore, M.; Fowler, A.D. Oscillatory zoning in minerals: A common phenomenon. *Can. Mineral.* **1996**, *34*, 1111–1126.
128. Christiansen, E.H.; Stuckless, J.S.; Funkhouser, M.J.; Howell, K.A.; Taylor, R.P.; Strong, D.F. Petrogenesis of rare-metal granites from depleted crustal sources: An example from the Cenozoic of western Utah, USA. Recent Advances in the Geology of Granite-Related Mineral Deposits. *CIM* **1988**, *39*, 307–321.
129. Ballouard, C.; Elburg, M.A.; Tappe, S.; Reinke, C.; Ueckermann, H.; Doggart, S. Magmatic-hydrothermal evolution of rare metal pegmatites from the Mesoproterozoic Orange River pegmatite belt (Namaqualand, South Africa. *Ore Geol. Rev.* **2020**, *116*, 103252. [CrossRef]
130. Wang, X.; Wang, K.-Y.; Ge, W.-C.; Yang, H.; Wu, H.-R.; Chen, J.-C. Fluid evolution and physicochemical constraints of the Nasigatu greisen-type Be deposit in Inner Mongolia. *Ore Geol. Rev.* **2024**, *176*, 106431. [CrossRef]

Disclaimer/Publisher's Note: The statements, opinions and data contained in all publications are solely those of the individual author(s) and contributor(s) and not of MDPI and/or the editor(s). MDPI and/or the editor(s) disclaim responsibility for any injury to people or property resulting from any ideas, methods, instructions or products referred to in the content.

minerals

MDPI

Article

Hydrothermal Scheelite Associated with Upper Cretaceous Intrusions in Romania: A Mineralogical Insight to the W Metallogeny

Ştefan Marincea [1,*], Delia-Georgeta Dumitraş [1], Cristina Sava Ghineț [1], George Dincă [1], Aurora-Măruța Iancu [1], Frédéric Hatert [2], Martin Depret [2] and Gelu Costin [3]

[1] Department INI, Geological Institute of Romania, 1 Caransebeş Str., RO-012271 Bucharest, Romania; d_deliaro@yahoo.com (D.-G.D.); ghinet.cristina@yahoo.com (C.S.G.); georgedinca@rocketmail.com (G.D.); iancu.maruta@yahoo.com (A.-M.I.)

[2] Laboratoire de Minéralogie, Université de Liège, Sart-Tilman, Bâtiment B 18, B-4000 Liège, Belgium; fhatert@uliege.be (F.H.); martin.depret@uliege.be (M.D.)

[3] Department of Earth, Environmental and Planetary Sciences, Rice University, Houston, TX 77005, USA; g.costin@rice.edu

* Correspondence: smarincea@yahoo.com or marincea@igr.ro

Abstract

Hydrothermal scheelite from three Romanian occurrences was analyzed in order to ascertain its structural, physical, vibrational, paragenetic, and crystal-chemical peculiarities as an important tool for characterizing the metallogenetic behavior and facilitating the ore-processing. All three occurrences, i.e., Ciclova and Oravița in Banat and Băița Bihor in the Bihor Mountains, are related to skarn deposits developed at the contact of Upper Cretaceous granodioritic bodies with Mesozoic calcareous deposits. Typical crystals show {001}, {111}, and {101} forms and are up to 15 mm across. The structure was successfully refined as tetragonal, space group $I4_1/a$, with R_1 = 0.0165 (Ciclova), 0.0204 (Oravița), and 0.0237 (Băița Bihor), respectively. The cell parameters refined for the same samples are a = 5.2459(10) Å and c = 11.3777(5) Å at Ciclova, a = 5.2380(2) Å and c = 11.3679(8) Å at Oravița, and a = 5.2409(2) Å and c = 11.3705(6) Å at Băița Bihor. The multiplicity of bands in both infrared absorption and Raman spectra is consistent with the S_4 punctual symmetry of the tungstate anion, agreeing with the structural data. In all cases, the analyzed scheelite is close to the $CaWO_4$ end-member. Cathodoluminescence peculiarities at the level of single crystals suggest that they crystallized in a slightly oxidizing to reducing environment from late hydrothermal solutions. Textural and paragenetic peculiarities suggest that scheelite from the three occurrences crystallized from epithermal, low-temperature, fluoride- and boron-bearing aqueous solutions.

Keywords: hydrothermal scheelite; physical properties; crystal chemistry; X-ray powder diffraction data; single-crystal X-ray diffraction; structure; infrared and Raman spectra; Cu-W skarn deposits; Upper Cretaceous; Romania

1. Introduction

Scheelite, ideally $CaWO_4$, accounts for a significant source of tungsten. Present in about 65% of the tungsten deposits throughout the world, the mineral is of major economic importance (e.g., [1–3] and referred works). Due to its very significant economic importance and high supply risk, tungsten was listed as one of the 32 critical materials in Europe (e.g., [4]) and 50 in the USA (e.g., [5]) and is also considered a hi-tech metal [6]. As

such, tungsten is primarily used to make wear-resistant metals but also in manufacturing electrodes, heating elements, field emitters, filaments in light bulbs, and cathode ray tubes. The detailed mineralogical study of scheelite as a major source for tungsten is then of great importance, offering an important tool to facilitate ore processing. Scheelite itself is widely used in scintillators for X-ray and gamma-ray detection, whereas compounds with scheelite structure were found to have extra low thermal conductivity [7] and were also investigated as photoanodes [8], photocatalysts [9], or even for nuclear waste immobilization [10]. Last but not least, scheelite can be used, in special conditions, as an appreciated gemstone [11,12].

Reported for the first time at the beginning of the 20th century [13], scheelite from Romania characteristically occurs in skarn deposits, the best-known occurrences being those at Ciclova (e.g., [13,14]), Oravița [14,15], and Băița Bihor: [14,16]. In all three of these occurrences, complex characterization mineralogy is lacking. The goal of this study is to fill the gaps existing in the mineralogical knowledge of the Romanian scheelite associated with Upper Cretaceous intrusions, insisting on its structural, physical, vibrational, paragenetic, and crystal-chemical peculiarities, of real use not only for mineralogists but also for prospectors, ore processors, and metallurgists. Last but not least, we appreciate that scheelite could represent, at least at Băița Bihor, an important component of a complex tungsten ore.

2. Geological Setting

The Ciclova, Oravița, and Băița Bihor occurrences are related to proximal or distal skarns developed at/near the contact of granodiorite bodies ascribed to the so-called "Banatitic Magmatic and Metallogenetic Belt"—BMMB [17]. The BMMB consists of a series of discontinuous magmatic and metallogenetic districts that are discordant over a Middle Cretaceous-aged nappe structure ([18–22] and references therein). The intrusive bodies are ascribed to calc-alkaline hydrated magmas and belong to I-type/magnetite series granitoids, derived from a primitive monzodiorite parent with a deep crust or upper mantle source region. These magmatic complexes (high-K calc-alkaline to calc-alkaline) are all productive in terms of ore formation [17,23].

The formation and evolution of the BMMB was early ascribed to subduction models involving either slab-rollback or slab-tear mechanisms affecting the subduction front of the Vardar Ocean ([20] and references therein). Other authors regarded magmatites in BMMB as post-collisional type I magmatites and ascribed the abundance of ore deposits in the eastern part of the Alpine–Balkan–Carpathian–Dinarides (ABCD) realm to a slab break-off of subducted lithosphere fragments during the Vardar Ocean closure, which imposed the rolling back and steepening of slabs. This process leads to upper crust extension and favors the access of melts to high crustal levels. The Cenozoic collision between the Tisia and Dacia blocks might be responsible for overall crustal thickening, for the formation of extensional faults that facilitated magma upwelling, and for a clockwise rotation of 60–80° with respect to the initial east-west trend at the time of magmatic emplacement ([19,21,22], and references therein).

The locations of the three occurrences in the general context of BMMB are given in Figure 1.

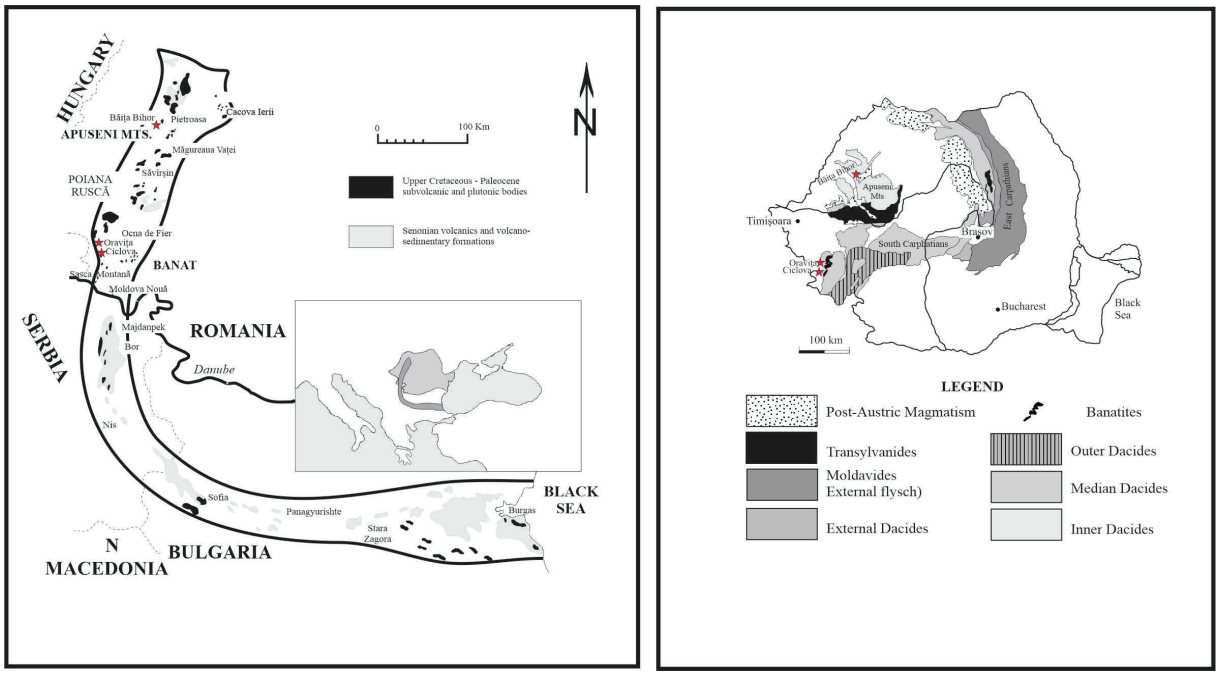


Figure 1. Sketch of the "Banatitic Magmatic and Metallogenetic Belt" ((**top left**): redrawn from [18]) showing its position in Europe (central detail, with BMMB painted in dark grey) and the structural context of Romania ((**top right**): from [24], simplified). The studied occurrences are marked with stars.

In all three occurrences, the granitoids were emplaced at shallow depths. Plutons show little evidence for differentiation, which is observed in other skarn systems (e.g., Fe, Au, and Zn skarns: [25]). Specific information on the analyzed bodies and on the skarn protolith is reported in Table 1.

Table 1. Geological features of the analyzed scheelite-bearing skarns.

Occurrence	Intrusion	Age of Intrusion	Protolith	Age of Protolith	Structural Unit
Ciclova Oraviţa	Ciclova-Oraviţa pluton	79 ± 3 to 74 ± 3 Ma [26] (1) 73.9 ± 3.2 to 71.2 ± 4.1 Ma [27] (2) 86.77 ± 0.5 to 87.70 ± 0.5 [20] (3)	carbonated veins in endoskarn	Mesozoic	Locva unit
Băiţa Bihor	Bihor batholith	77 ± 3 to 67 ± 3 Ma [28] (4) 70 ± 5 Ma [29] (5) 80.63 ± 0.3 to 78.69 ± 0.4 Ma [20] (3) 80.3 ± 1.6 Ma [27] (2)	dolostones	Anisian-Carnian; Carnian-Norian	Vălani unit; Vetre unit

(1) K-Ar on biotite; (2) U-Pb on zircon; (3) Re-Os data on molybdenite; (4) K-Ar ages on whole rock or on "femic" minerals; (5) Rb-Sr isochron.

Skarn deposits are one of the most representative types of mineralization from BMMB [17]. Copper metallogeny is predominant and distinguishes the BMMB in the context of the larger Alpine-Balkan–Carpathian–Dinaride belt [19]. A Cu-Mo zone can be distinguished in most of the Romanian deposits, including the Ciclova, Oravița, and Băița Bihor occurrences. Towards the external zones, Mo-rich ores grade into Mo-W-Bi-Te (in calcic skarns) or Cu-W-Bi (in magnesian skarns) [17,30,31].

Scheelite forms significant concentrations in the Cu-Mo (W) mineralization of Băița Bihor [30] and Oravița–Ciclova [15]. At Băiţa Bihor, scheelite occurs in distal magnesian skarns forming typical metasomatic columns whose outer zones contain magnesian borates (i.e., ludwigite, kotoite, suanite, fluoborite, and szaibélyite), whereas the inner zones typically contain magnesian silicates (e.g., diopside, forsterite, humite-group minerals, and

phlogopite) [32]. In this deposit, scheelite typically associates with chalcopyrite, galena, sphalerite, molybdenite, bornite, Bi-Cu sulphosalts, and Bi tellurides (e.g., [33,34]).

The scheelite occurrences from Ciclova and Oraviţa subscribe to vein systems developed at the level of endoskarn. The typical mineral association comprises, beside calcite, chalcopyrite, arsenopyrite, pyrite, gersdorffite, glaucodot, fluorite, and, according to [15], adularia, cobaltite, cubanite, molybdenite, and Bi-Cu sulphosalts.

3. Materials and Methods

The samples described in this paper were taken from three waste dumps pertaining to the Lobkowitz Gallery, located on Anton Brook in Ciclova (45°03′09″ N–21°44′25″ E); the Emil Gallery, located on Chinisea Valley in Oraviţa (45°04′42″ N–21°43′16″ E); and a collector located inside the Baia Roşie basal (transportation) Gallery, emergent on Crişul Negru Valley, in Băiţa Bihor (emergence: 46°29′14″ N–22°36′53″ E). Galleries from Ciclova and Oraviţa were mined for copper during the second half of the 19th century and reopened in the 50th year of the 20th century. The gallery at Băiţa Bihor is still active and is used for the Cu ore evacuation. The samples from Băiţa Bihor probably originate from Antoniu or Baia Roşie skarn bodies (metasomatic columns), where scheelite is particularly abundant [16].

Electron-microprobe analyses (EMPA) were performed using a Jeol JXA 8530F Hyperprobe (JEOL Ltd., Tokyo, Japan), equipped with a field emission-assisted thermo-ionic (Schottky) emitter, five wavelength-dispersive spectrometers (WDS), and one SD EDS detector. The apparatus is hosted by Rice University, Department of Earth, Environment, and Planetary Science (Houston, TX, USA). The apparatus was set at an accelerating voltage of 15 kV and a beam current of 20 nA (measured at the Faraday cup), for beam diameters of 5–10 μm. Natural chalcopyrite (Cu Kα), natural periclase (Mg Kα), natural hematite (Fe Kα), natural rhodonite (Mn Kα), natural scheelite (W Kα), natural molybdenite (Mo and S Kα), natural galena (Pb Kα), natural diopside (Ca Kα), metallic Bi (Bi Kα), and metallic Sb (Sb Kα) served as standards. Counting time was 20 s per element. Data were reduced using the Phi-Rho-Z matrix correction [35].

The fast identification of mineral phases in all samples was performed by Energy-Dispersive Spectrometry (EDS) analysis, using a JEOL Silicon Drift (SD) X-ray Detector with a 10 mm^2 active area and 133 eV resolution. The detector is attached and integrated into the JEOL JXA 8530F Hyperprobe described before. The analytical conditions used for EDS analysis were as follows: 15 kV accelerating voltage, 20 nA beam current, live time 20 s. Dead Time (DT) during the analysis was 35%–40% with count rates ranging from ~45,000 to ~100,000. The beam size used was "spot" size (~300 nm). Cathodoluminescence (CL) imaging was performed using a Gatan CL system (Gatan Inc., Pleasanton, CA, USA). Images were acquired at a voltage of 10 kV and contrast-enhanced for better observation.

X-ray powder diffraction (XRD) analysis of selected samples was performed on two different Brucker (AXS) D8 Advance diffractometers equipped with Bruker AXS Hi-star Area Detectors (Bruker, Karlsruhe, Germany) hosted by the Geological Institute of Romania (Bucharest) and by the University in Liège, Belgium, respectively. Both diffractometers used Ni-filtered Cu$K\alpha$ radiation ($K\alpha_1$ = 1.54056 Å) with Cu anode Kristalloflex K780 X-ray tubes, a step size of 0.02° 2θ, and a counting time of 6 s per step. An operating voltage of 40 kV for a current of 30 mA, a slit system of 1/0.1/1 with a receiving slit of 0.6 mm, and a scanning range of 4 to 100° 2θ were used for all measurements. Unit-cell parameters were calculated by least-squares refinement of the XRD data, using the computer program of [36] modified for PC use by [37]. Synthetic silicon (NBS 640b) was used as an external standard in order to verify the accuracy of the measurements. As the sample grinding seems to lower the crystallinity of the mineral, as well as to produce its partial carbonation, as in the

case of Ca silicates [38], separate determinations of the unit-cell values were carried out based on single-crystal X-ray diffraction.

Structure refinements of scheelite crystals were performed by single-crystal X-ray diffraction on a Rigaku Agilent Xcalibur EOS diffractometer equipped with a CCD Detector (both manufactured in Osaka, Japan), housed at the Laboratory of Mineralogy, University of Liège. Data were collected at room temperature (293 K) with monochromatized Mo$K\alpha$ radiation (λ = 0.71703 Å) at 40 kV and 40 mA. The instrument has Kappa geometry (ϕ/ω scan). Data collection, subsequent data reduction, and face-based absorption corrections were carried out using the CrysAlis Pro 41.123a software [39]. The initial solution of the structure in space group $I4_1/a$ was determined by the charge flipping method using the Superflip algorithm [40], and the structural model was subsequently refined on the basis of F^2 with the Jana2006 software [41].

The infrared-absorption spectrum of a sample from Oravița was obtained at the Geological Institute of Romania with a SPECORD M-80 IR spectrophotometer (Carl Zeiss, Jena, Germany), using a conventional pressed disk technique. Carefully dried mineral powders were embedded in KBr; a dilution of 2.5 wt.% was used. This spectrum was recorded between 250 and 4000 cm^{-1}. FT-IR spectra of representative samples from Ciclova and Băița Bihor, as well as details of the stretching region of $(WO_4)^{2-}$ groups in the scheelite structure, were obtained using a BRUKER FTIR S 12 spectrometer (Ettlingen, Germany) also hosted by the Geological Institute of Romania. In this case, the records were made in the frequency range between 400 and 4000 cm^{-1}, using the standard pressed-disk technique, after embedding 2 mg of mechanically ground mineral powder in 148 mg of dry KBr and compacting at 2500 N/cm^2 pressure. The spectral resolution was 0.1 cm^{-1}. All spectra were recorded at 25 °C.

Raman spectra were recorded using a Renishaw SEM-Raman system (Artisan Scientific, Champaign, IL, USA) hosted by the Geological Institute of Romania, at 25 °C, using both structural and chemical analysis (SCA) and inVia interfaces. The spectrometer was equipped with a 10 mW, 532 nm diode-pumped solid-state laser as an excitation source. The spectral resolution was 1 cm^{-1} for a 1 μm spatial resolution. Analyses were collected using a 50× objective, a confocal aperture of 400 μm, a 150 μm slit width, and 1800 lines·mm^{-1} grating. The spectra were collected in the range of 10–1500 cm^{-1} (10-s accumulation time, 10 scans). The instrument was calibrated with synthetic silicon.

The mean density of various crystals of scheelite was measured using a pycnometer (Rainhard Co., Austin, TX, USA) at 25 °C, using a mixture of methylene iodide and toluene as the immersion liquid.

Indices of refraction were measured at room temperature (25 °C) using a conventional JENAPOL-U petrographic microscope (Carl Zeiss, Jena, Germany) with a spindle stage and calibrated immersion liquids (Cargille or temperature-calibrated oils), with a 589-nm interference filter. Thin-section photographs were obtained using a Zeiss Axio Imager A2M microscope (Carl Zeiss, Jena, Germany) with 2.5×/10×/20× objectives.

UV-luminescence tests were performed using a portable Vetter ultraviolet lamp (Vetter, Lottstetten, Germany) with 254 and 366 nm filters, respectively.

4. Mode of Occurrence and Morphology

At the macroscopic level, scheelite crystals occur as roughly tetragonal crystals up to 30 mm across, easily identified in UV light (Figure 2). At Oravița, the crystals are generally anhedral, due to secondary overgrowths (see below). Previous studies have described scheelite nodules up to 1 cm in diameter at Ciclova [15], as well as well-formed crystals having {001} (basal pinacoid), {111} (pyramid), and {101} (prism) forms [13]. At Băița Bihor,

euhedral to subhedral crystals vary in size from microns to 3 cm [16]. Twinning on {110} was rarely recognized, as were contact twins with a composition plane of (110).



Figure 2. Hand-specimen photographs of scheelite-bearing skarns from Ciclova ((**left**), Sample 2575) and Băiţa Bihor ((**right**), Sample 2591) showing the UV phosphorescence color. The coin diameter is 2 cm.

The microscopic study reveals that the mineral can occur as clusters or streaks of crystals, but also as individual crystals, as already observed by [16]. The crystals are generally subhedral or even anhedral at Oravița [15]. In most of the cases, partly preserved tetragonal contours can be observed (Figure 2). The distinct cleavage on {101} can be observed, as it is sometimes lined by secondary hydrotungstite.

The CL imaging at the electron microscope is relevant for the tetragonal symmetry of the mineral. Transversal sections of typical crystals of scheelite from Ciclova, Oravița, and Băița Bihor are given in Figure 3 and generally reveal oscillatory CL zoning suggesting the tetragonal symmetry. Overgrowths of secondary scheelite on previous crystals (Figure 3B,C) could explain the anhedral contours observed in some cases [15].

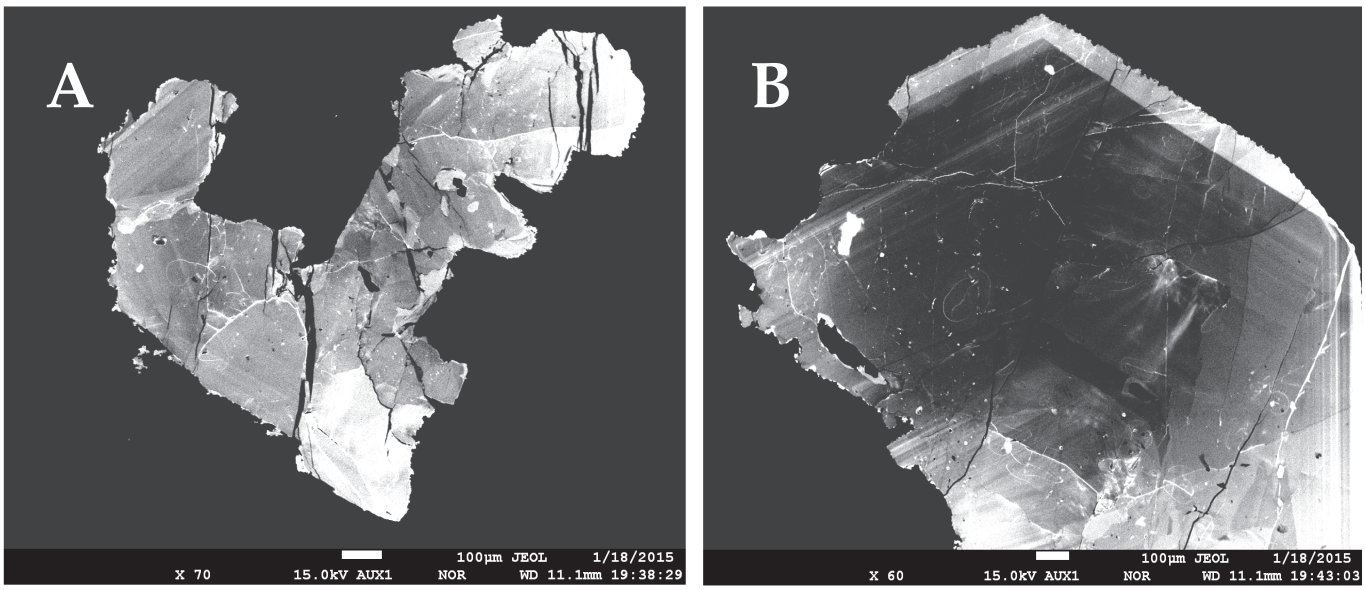


Figure 3. *Cont.*

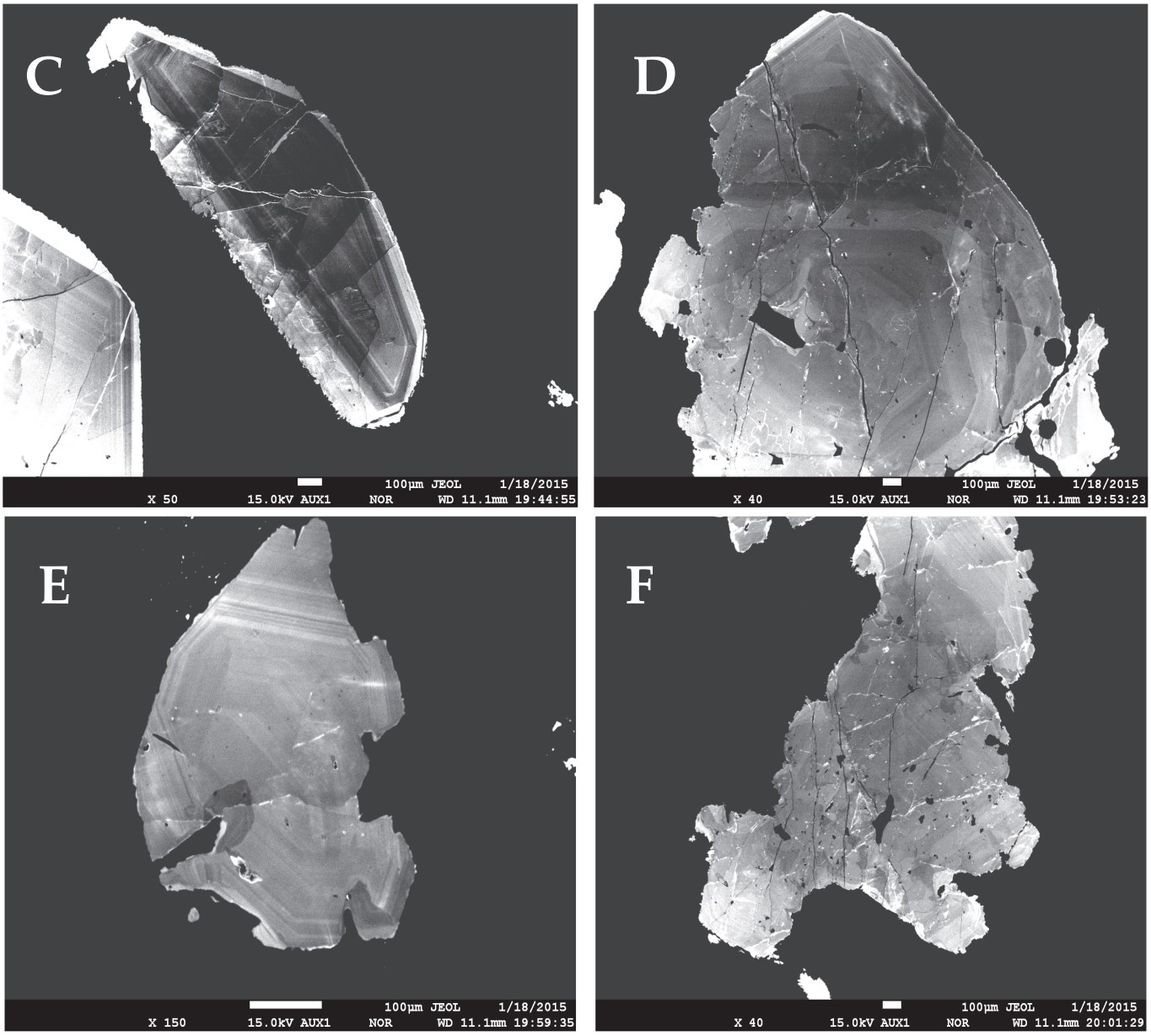


Figure 3. Cathodoluminescence images of scheelite from the analyzed skarns. (**A**) Internal structure of a scheelite grain as determined by CL, showing mainly irregular and diffuse zones. Sample 2506, Ciclova. (**B**,**C**) Oscillatory-zoned crystals with large regular dark CL zones (**B**) and late-stage overgrowth with lighter CL response (**B**,**C**). Sample 2569 Oravița. (**D**) Crystal of scheelite with diffuse CL zoning (center) with peripheral oscillatory zoning suggesting growth in tetrahedral symmetry. Note the recrystallized grains on the border with a light CL color. Sample 2536 Băița Bihor. (**E**) Oscillatory-zoned scheelite crystal, with peripheral regular (i.e., constant width), sharp, and distinct contacts. Sample 2544 Băița Bihor. (**F**) Homogenous CL-response scheelite grain (center) with peripheral irregular zones and lighter CL-response phases on fissures. Sample 2593 Băița Bihor.

5. Chemical Data

Electron-microprobe analyses of 30 representative scheelite crystals from Ciclova, Oravița, and Băița Bihor are given in Tables 2–4. The samples are indicated by numbers, whereas letters, when used, indicate different crystals in the same sample. Each analysis represents the average of N points of analysis across the same crystal from a thin section. Formulas were normalized on the basis of 4(O) atoms per formula unit (*apfu*), the resulting crystal-chemical formulas being, in all cases, definitory for terms close to the scheelite end-member of the scheelite-powellite solid solution series.

Table 2. Representative electron-microprobe analyses of scheelite from Ciclova *.

Sample	2506a	2506b	2506c	2509a	2509b	2509c	2534a	2534b	2575a	2575b	Mean
N (1)	12	15	16	11	13	13	14	11	12	11	128
WO_3	79.81	79.41	78.31	78.91	79.24	79.14	79.40	79.16	79.24	78.49	79.10
MoO_3	0.63	0.63	1.21	1.21	1.14	1.05	0.77	1.12	1.12	0.87	0.97
Bi_2O_3	0.03	0.02	0.03	0.01	0.04	0.02	0.01	0.03	0.03	0.04	0.03
CaO	19.44	19.40	19.45	19.49	19.38	19.37	19.31	19.31	19.32	19.25	19.37
MgO	0.00	0.02	0.00	0.00	0.00	0.00	0.00	0.00	0.00	0.00	0.00
MnO	0.02	0.03	0.04	0.03	0.02	0.03	0.06	0.04	0.03	0.02	0.03
FeO (2)	0.03	0.06	0.03	0.02	0.04	0.05	0.02	0.02	0.04	0.04	0.04
PbO	0.03	0.05	0.03	0.03	0.05	0.07	0.07	0.02	0.05	0.00	0.04
CuO	0.01	0.01	0.03	0.03	0.02	0.02	0.05	0.01	0.03	0.02	0.02
Total	100.00	99.63	99.13	99.73	99.93	99.75	99.67	99.71	99.86	98.73	99.60
Number of Cations on the Basis of 4(O)											
W	0.988	0.986	0.974	0.976	0.979	0.980	0.986	0.980	0.980	0.982	0.981
Mo	0.013	0.013	0.024	0.024	0.023	0.021	0.015	0.022	0.022	0.018	0.019
Bi	0.000	0.000	0.000	0.000	0.000	0.000	0.000	0.000	0.000	0.000	0.000
Ca	0.995	0.996	1.000	0.996	0.990	0.992	0.991	0.989	0.988	0.996	0.994
Mg	0.000	0.001	0.000	0.000	0.000	0.000	0.000	0.000	0.000	0.000	0.000
Mn	0.001	0.001	0.002	0.001	0.001	0.001	0.002	0.002	0.001	0.001	0.001
Fe^{2+}	0.001	0.002	0.001	0.001	0.002	0.002	0.001	0.001	0.002	0.002	0.002
Pb	0.000	0.001	0.000	0.000	0.001	0.001	0.001	0.000	0.001	0.000	0.001
Cu	0.000	0.000	0.001	0.001	0.001	0.001	0.002	0.000	0.001	0.001	0.001
Composition in End Members (mol.%)											
scheelite	98.70	98.70	97.60	97.60	97.70	97.90	98.50	97.80	97.80	98.20	98.10
powellite	1.30	1.30	2.40	2.40	2.30	2.10	1.50	2.20	2.20	1.80	1.90

* EMP analyses, results expressed in wt.%; (1) number of point analyses on the same crystal; (2) total iron taken as divalent.

Table 3. Representative electron-microprobe analyses of scheelite from Oraviţa *.

Sample	2537a	2537b	2537c	2538a	2538b	2538c	2539	2568	2569a	2569b	Mean
N (1)	5	6	7	9	7	6	11	16	12	11	90
WO_3	79.86	79.30	79.87	80.38	80.36	80.48	79.42	77.79	77.95	77.82	79.03
MoO_3	0.14	0.33	0.25	0.37	0.32	0.27	1.32	2.85	1.92	1.97	1.29
Bi_2O_3	0.01	0.01	0.00	0.01	0.01	0.00	0.02	0.02	0.00	0.01	0.01
CaO	19.29	19.53	19.55	19.42	19.36	19.44	19.56	19.90	19.46	19.42	19.53
MgO	0.00	0.01	0.01	0.00	0.01	0.01	0.01	0.01	0.00	0.00	0.01
MnO	0.00	0.00	0.01	0.00	0.00	0.00	0.00	0.00	0.01	0.01	0.00
FeO (2)	0.05	0.04	0.03	0.03	0.05	0.17	0.02	0.02	0.02	0.02	0.04
PbO	0.04	0.00	0.03	0.01	0.05	0.02	0.02	0.02	0.04	0.01	0.02
CuO	0.02	0.00	0.01	0.00	0.01	0.00	0.01	0.00	0.00	0.00	0.01
Total	99.41	99.22	99.76	100.22	100.17	100.39	100.38	100.61	99.40	99.26	99.94
Number of Cations on the Basis of 4(O)											
W	0.997	0.990	0.993	0.994	0.995	0.994	0.975	0.944	0.963	0.963	0.975
Mo	0.003	0.007	0.005	0.007	0.006	0.005	0.026	0.056	0.038	0.039	0.025
Bi	0.000	0.000	0.000	0.000	0.000	0.000	0.000	0.000	0.000	0.000	0.000
Ca	0.996	1.008	1.004	0.993	0.991	0.993	0.993	0.998	0.994	0.993	0.996
Mg	0.000	0.001	0.001	0.000	0.001	0.001	0.001	0.001	0.000	0.000	0.001
Mn	0.000	0.000	0.000	0.000	0.000	0.000	0.000	0.000	0.000	0.000	0.000
Fe^{2+}	0.002	0.002	0.001	0.001	0.002	0.007	0.001	0.001	0.001	0.001	0.002
Pb	0.001	0.000	0.000	0.000	0.001	0.000	0.000	0.000	0.001	0.000	0.001
Cu	0.001	0.000	0.000	0.000	0.000	0.000	0.000	0.000	0.000	0.000	0.000
Composition in End Members (mol.%)											
scheelite	99.70	99.30	99.50	99.30	99.40	99.50	97.40	94.40	96.20	96.11	97.50
powellite	0.30	0.70	0.50	0.70	0.60	0.50	2.60	5.60	3.80	3.89	2.50

* EMP analyses, results expressed in wt.%; (1) number of point analyses on the same crystal; (2) total iron taken as divalent.

Table 4. Representative electron-microprobe analyses of scheelite from Băița Bihor *.

Sample	2536	2544	2549	2552	2576	2577	2590	2591	2592	2593	Mean
N (1)	11	10	8	9	12	10	10	13	11	11	105
WO_3	79.70	79.48	79.56	78.41	78.81	78.93	78.60	79.28	79.49	78.97	79.13
MoO_3	0.63	0.73	0.61	1.13	1.29	0.88	1.16	1.17	0.84	0.88	0.95
Bi_2O_3	0.03	0.03	0.00	0.04	0.04	0.01	0.01	0.00	0.02	0.05	0.02
CaO	19.48	19.4	19.37	19.42	19.36	19.26	19.43	19.5	19.26	19.23	19.37
MgO	0.00	0.00	0.05	0.00	0.00	0.00	0.00	0.00	0.00	0.00	0.00
MnO	0.02	0.07	0.01	0.04	0.03	0.02	0.03	0.02	0.01	0.03	0.03
FeO (2)	0.04	0.03	0.09	0.03	0.07	0.03	0.01	0.03	0.04	0.03	0.04
PbO	0.04	0.02	0.08	0.03	0.04	0.01	0.03	0.05	0.04	0.00	0.03
CuO	0.01	0.00	0.01	0.02	0.03	0.03	0.03	0.03	0.03	0.01	0.02
Total	99.95	99.76	99.78	99.12	99.67	99.17	99.30	100.08	99.73	99.20	99.59
Number of Cations on the Basis of 4(O)											
W	0.987	0.986	0.987	0.976	0.975	0.984	0.976	0.978	0.986	0.984	0.982
Mo	0.013	0.015	0.012	0.023	0.026	0.018	0.023	0.023	0.017	0.018	0.019
Bi	0.000	0.000	0.000	0.000	0.000	0.000	0.000	0.000	0.000	0.001	0.000
Ca	0.997	0.995	0.993	0.999	0.991	0.992	0.998	0.994	0.988	0.991	0.994
Mg	0.000	0.000	0.004	0.000	0.000	0.000	0.000	0.000	0.000	0.000	0.000
Mn	0.001	0.003	0.000	0.002	0.001	0.001	0.001	0.001	0.000	0.001	0.001
Fe^{2+}	0.002	0.001	0.004	0.001	0.003	0.001	0.000	0.001	0.002	0.001	0.002
Pb	0.001	0.000	0.001	0.000	0.001	0.000	0.000	0.001	0.001	0.000	0.001
Cu	0.000	0.000	0.000	0.001	0.001	0.001	0.001	0.001	0.001	0.000	0.001
Composition in End Members (mol.%)											
scheelite	98.70	98.50	98.80	97.70	97.40	98.20	97.70	97.70	98.31	98.20	98.10
powellite	1.30	1.50	1.20	2.30	2.60	1.80	2.30	2.30	1.69	1.80	1.90

* EMP analyses, results expressed in wt.%; (1) number of point analyses on the same crystal; (2) total iron taken as divalent.

A few remarks must be drawn based on the results in Tables 2–4, as follows:

1. No obvious chemical zoning was observed at the level of individual crystals, in spite of the CL zoning described below. Qualitative elemental X-ray maps exemplified in Figure 4a,b don't show any zoning.
2. A slight overcompensation in the four-fold coordinated cations (i.e., W + Mo > 1) could be observed in some samples, particularly at Oraviţa (Table 3). This phenomenon was already observed in some other cases (e.g., [12,42,43]) and is probably due to the EMPA interference effect of tungstite (ideally $WO_3 \cdot H_2O$) or rather hydrotungstite (ideally $H_2WO_4 \cdot H_2O$), whose presence in all three occurrences was already mentioned [44].
3. The isomorphism in the scheelite–powellite solid solution series is very restricted, reaching up to 2.4 mol.% powellite at Ciclova, up to 5.6 mol.% at Oravița, and up to 2.6 mol.% at Băița Bihor. The X-ray elemental maps failed to identify a chemical zoning at the crystal level, in spite of the general opinion that the dark CL oscillatory bands described above are enriched in Mo (i.e., [45,46]).
4. Ba was sought but not detected, so the isomorphism toward ronpetersonite can't be considered.
5. The contents of stolzite (ideally $PbWO_4$) in the solid solution are insignificant, reaching up to 0.1 mol.%.
6. The small contents of Cu recorded in part of the samples could be rather due to submicrometer-sized cuprotungstite—ideally $Cu_2(WO_4)(OH)_2$—inclusions, probably intruded on the cleavage directions; these inclusions are too small to be seized by the X-ray imaging.

7. The collection of qualitative elemental X-ray maps (Figure 4a,b) together with SEM-EDS analyses confirmed that Sb and Bi are present in minor amounts in some scheelite grains. Apparently, both trivalent Sb and Bi are substitutes for Ca^{2+} through a mechanism similar to those reported by [47] and referred to in the case of REE and Y, i.e., $2Bi^{3+}(Sb^{3+}) + \square\ Ca = 3Ca^{2+}$, where $\square$ Ca represents a vacancy site.

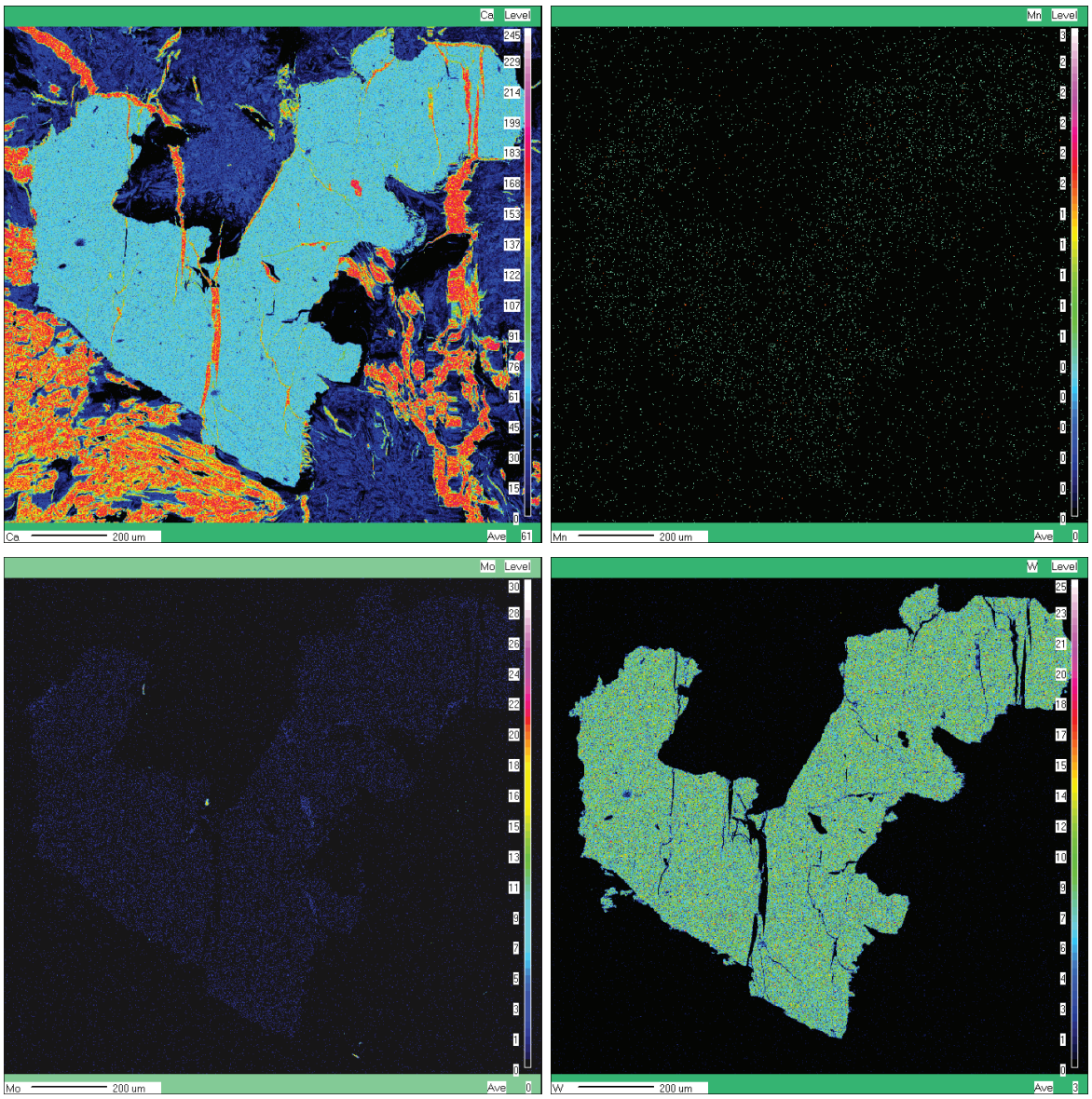
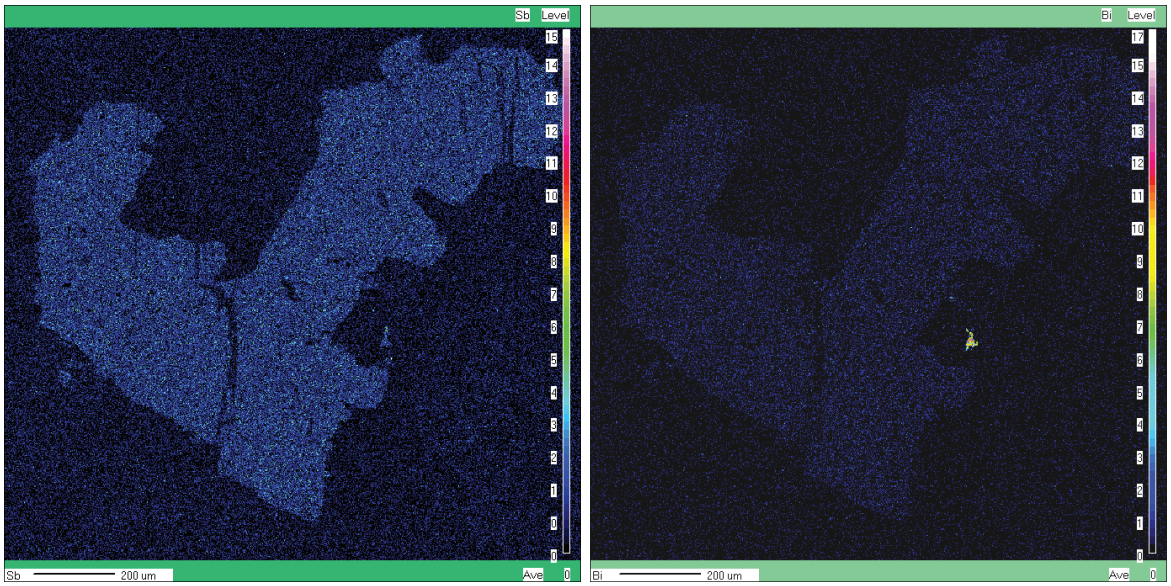


Figure 4. *Cont.*



(**a**)

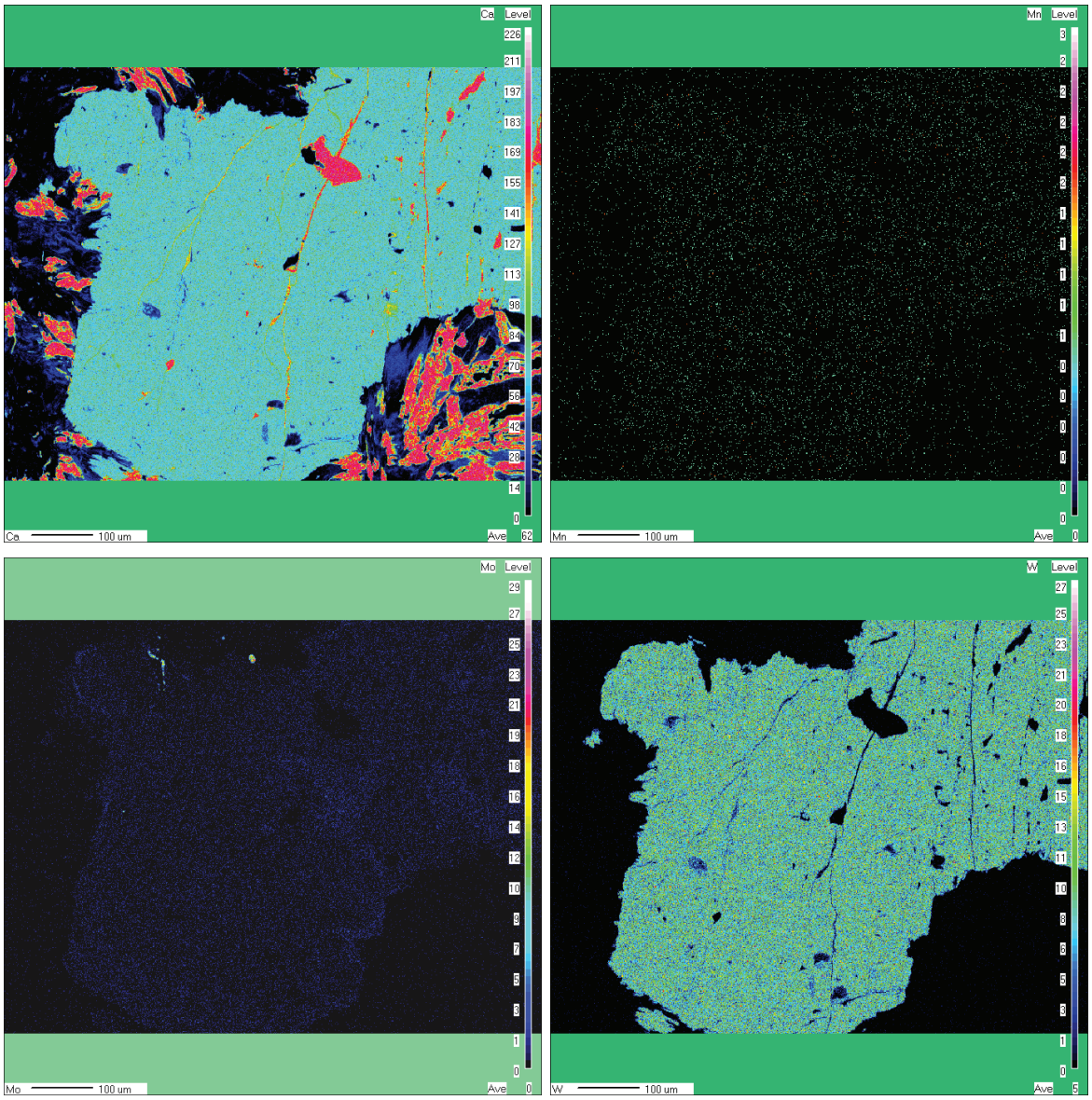
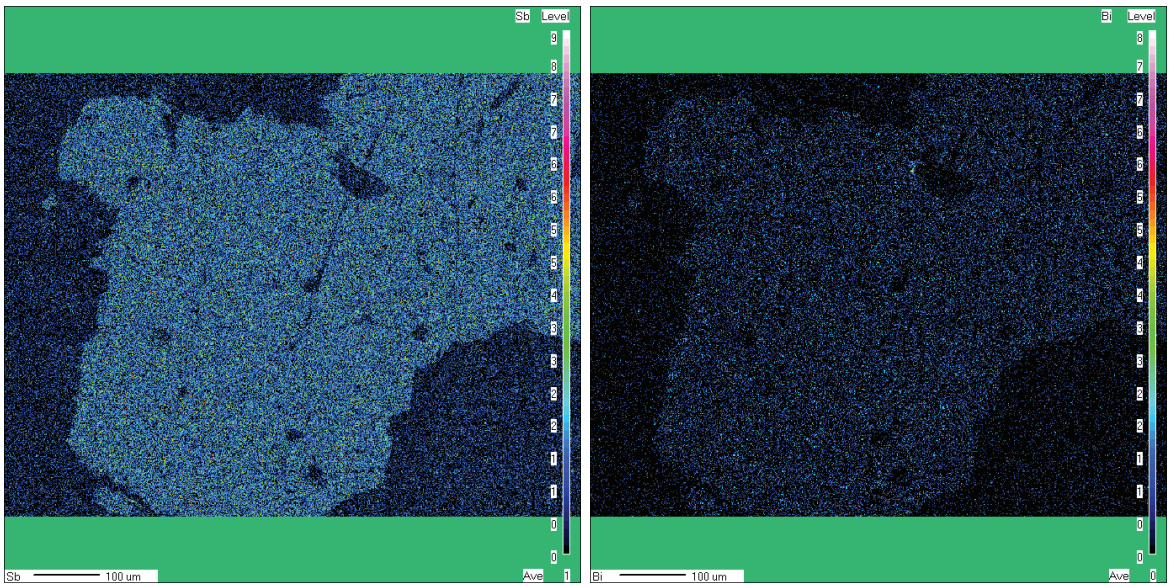


Figure 4. *Cont*.



(**b**)

Figure 4. (**a**) Elemental X-ray maps showing the spatial distribution of Ca, Mn, Mo, W, Sb, Bi in a selected crystal of scheelite from Ciclova (Sample 2506). (**b**) Elemental X-ray maps showing the spatial distribution of Ca, Mn, Mo, W, Sb, Bi in a selected crystal of scheelite from Băița Bihor (Sample 2593).

6. X-Ray Powder Diffraction Data

Cell parameters of 5 representative samples of scheelite were successfully refined by least squares, based on a tetragonal $I4_1/a$ cell (e.g., [48]). The patterns were indexed on the basis of Miller indices obtained by structural refinement that closely correspond to PDF 41-1431 [49]. Three XRD powder patterns given for scheelite samples from Băița Bihor by [16] and three others given for scheelite samples from Oravița–Ciclova and Băița Bihor by [44] were also used for calculation of cell parameters. The results are given in Table 5, together with 4 sets of cell parameters obtained by single-crystal X-ray refinement.

Table 5. Cell parameters of selected samples of scheelite from the analyzed skarn occurrences.

Sample	*a* (Å)	*c* (Å)	*V* (Å^3)
	Ciclova		
1189 [(1)]	5.230(2)	11.356(7)	310.67(8)
2492 [(2)]	5.2431(1)	11.3743(5)	312.68(2)
2506	5.243(4)	11.366(14)	312.46(53)
2509	5.234(2)	11.393 (15)	312.06(37)
	Oravița		
535 [(1)]	5.231(1)	11.343(3)	310.41(14)
2491	5.239(4)	11.402 (9)	313.02(53)
2537	5.229(4)	11.372(14)	310.92(57)
2569 [(2)]	5.2425(2)	11.3703(7)	312.499(2)
	Băița Bihor		
Sch 01 [(3)]	5.240(2)	11.373(5)	312.25(20)
Sch 02 [(3)]	5.2384(9)	11.370(4)	312.00(12)
Sch 03 [(3)]	5.2377(8)	11.366(2)	311.82(10)
1050 [(1)]	5.232(2)	11.375(8)	311.34(25)
2536	5.243(1)	11.380(4)	312.85(16)
2576 [(2)]	5.2409(2)	11.3705(6)	312.314(2)
2593 [(2)]	5.2388(2)	11.3667(9)	311.959(1)

[(1)]—calculated after the XRD powder patterns given by [44]. [(2)]—data obtained by single-crystal refinement. [(3)]—calculated after the XRD powder patterns given by [16].

The cell parameters in Table 5 are generally close to the cell parameters reported by various authors for stoichiometric scheelite {i.e., a = 5.24294(6) Å and c = 11.373(7) Å according to [49]; a = 5.2419(5) Å and c = 11.376(1) Å according to [50]; and a = 5.23643(5) Å and c = 11.33815(33) Å according to [51]} and also to similar values reported for scheelite samples close to stoichiometry: e.g., [43,52]. The low content of powellite in the solid solution series of the analyzed scheelite samples is quite evident since powellite has lower a and higher c cell parameters {e.g., a = 5.2256(5) Å and c = 11.434(1) Å according to [50], a = 5.222(1) Å and c = 11.425(3) Å according to [52], or a = 5.220(2) Å and c = 11.407(10) Å according to [53]}.

7. Physical Properties

Macroscopically, scheelite from all three occurrences occurs as translucent, turbid-white to yellow crystals. A glassy luster can be observed on the distinct cleavage on {101}, whereas the normal luster is waxy vitreous. The mineral is nonfluorescent in long-wave UV light (366 nm) and shows generally strong blue fluorescence in short-wave UV light (254 nm). Exceptions occur at some samples from Oravița, where a yellow tint of fluorescence also occurs. The usual fluorescence tints are better depicted in Figures 2 and 5 and indicate low contents of powellite in the solid-solution series [54].

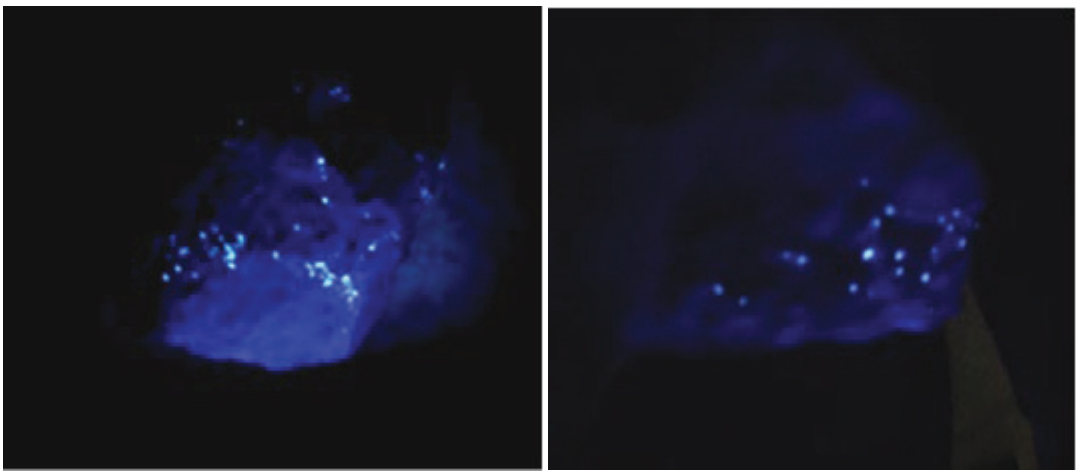


Figure 5. UV photographs of representative scheelite-bearing samples. (**Left**) Scheelite in a quartz-pyrite-chalcopyrite veinlet from Ciclova (Lobkowitz–Sample 2506). The biggest crystal is 12 mm across. (**Right**) Scheelite disseminated in a diopside–phlogopite skarn from Băiţa Bihor (Baia Roşie–Sample 2544). The biggest crystal is 15 mm across.

Compared with the standard color card proposed by [54], the scheelite samples from Ciclova, Băița Bihor, and the large majority of those from Oravița may contain up to 3 mol.% powellite in solid solutions, whereas the yellow-tinted scheelite from Oravița contains up to 6 mol.% powellite, which perfectly agrees with data in Tables 2–4. Scheelite samples from Băița Bihor seem to correspond to the scheelite III type described by [16] based on fluorescence colors.

Under the electron beam, scheelite samples show a strong cathodoluminescence (CL) response of light blue color, which can be due to the self-activated emission band (also referred to as a self-luminescence band, SB), which produces a broad spectral peak that is intrinsic to the mineral, this being attributed to the $(WO_4)^{2-}$ tetrahedral complex ([45] and referred works). A cathodoluminescence zoning of the individual crystals, described in many worldwide occurrences (e.g., [42,45–47,55,56]), can be observed in all the analyzed samples and is illustrated in Figure 3. The subhedral scheelite grains display in many cases oscillatory CL zones characterized by alternating dark and bright CL bands

with sharp boundaries, similar to Type 1 scheelite described by [46] or S-type described by [55]. Crystals of scheelite could also display bright peripheral CL concentric zones with central homogenous dark CL zones, suggesting the optical lamellar zoning of garnet and resembling Type 2 scheelite described by [46]: Figure 3.

Optically, the mineral is uniaxial positive. The indices of refraction of three representative samples (one for each occurrence), taken as the average of five measured values on 5 different crystals from the same sample, are given in Table 6. The indices of refraction in Table 6 are in the range of the higher values reported by [57] for scheelite, i.e., $\omega = 1.911 - 1.934$ and $\varepsilon = 1.926 - 1.953$. As the refraction indices presumably decrease with increasing content of Mo [57], the values in Table 6 are indicative of terms with low contents of powellite in the solid solution series. The mean refraction index, calculated as $n = (2\omega + \varepsilon)/3$ [58], is also given in Table 6.

Table 6. Physical constants of hydrothermal scheelite from the analyzed skarns.

Sample	**2509b**	**2539**	**2544**
Occurrence	Ciclova	Oraviţa	Băiţa Bihor
ω	1.928	1.929	1.931
ε	1.945	1.946	1.948
n	1.934	1.935	1.937
M_{mol} [(1)]	286.298	285.614	286.801
V (Å^3)	313.11	311.90	312.31
D_m (g/cm^3)	6.08(1)	6.08(1)	6.10(1)
D_x (g/cm^3)	6.071	6.080	6.098
K_P [(2)]	0.1536	0.1538	0.1536
K_C	0.1492	0.1494	0.1488
$1 - K_P/K_C$	−0.0298	−0.0294	−0.0323
K_P ′[(3)]	0.1538	0.1538	0.1537
$1 - K_P'/K_C$	−0.0313	−0.0293	−0.0327

[(1)] Molecular mass in atomic mass units; [(2)] based on measured density (D_m); [(3)] based on calculated density (D_x).

The D_x calculated densities of three representative samples (one for each occurrence) were obtained on the basis of chemical data in Tables 2–4 and of unit cell volumes in Table 6, for $Z = 4$ formula units per cell [59]. The values obtained are given in Table 6. The mean measured density D_m, taken as the average of measurements on 10 different grains, is also included in Table 6 and compares well with the calculated densities. Both values, as well as the mean refraction indices, were used to calculate the physical refractive energy as $K_P = (n - 1)/D$.

The chemical refractive energy (K_C) values in Table 6 are based on the oxide content issued from EMP analyses of the three samples and on the constants for oxides given by [58,60], excepting that for WO_3, taken from [61], i.e., k (WO_3) = 0.133.

The calculation of the Gladstone-Dale compatibility index ($1 - Kp/Kc$) yielded the values given in Table 6, indicative of excellent agreement between physical and chemical data [60]. The use of a Gladstone-Dale constant for WO_3 as indicated by [58,60], i.e., k (WO_3) = 0.152 or k (WO_3) = 0.171, respectively, results in poor compatibilities.

8. Structure

The atomic structure of scheelite was refined by both neutron diffraction [48] and single-crystal X-ray diffraction ([52,59]). The results are coincident in describing a structure consisting of two intercalated polyhedral lattices, one composed of slightly deformed WO_4 tetrahedra and another by CaO_8 dodecahedra (bidisphenoids) described by eight-fold coordinated Ca cations. The structure features a tetragonal unit cell with space group

$I4_1/a$ (Z = 4), which was confirmed during this study. As the powellite contents in the analysed samples are low, the eventual Mo atoms were not included in the refinement of the X-ray data.

Details of the scheelite structure obtained during this work are shown in Figure 6.

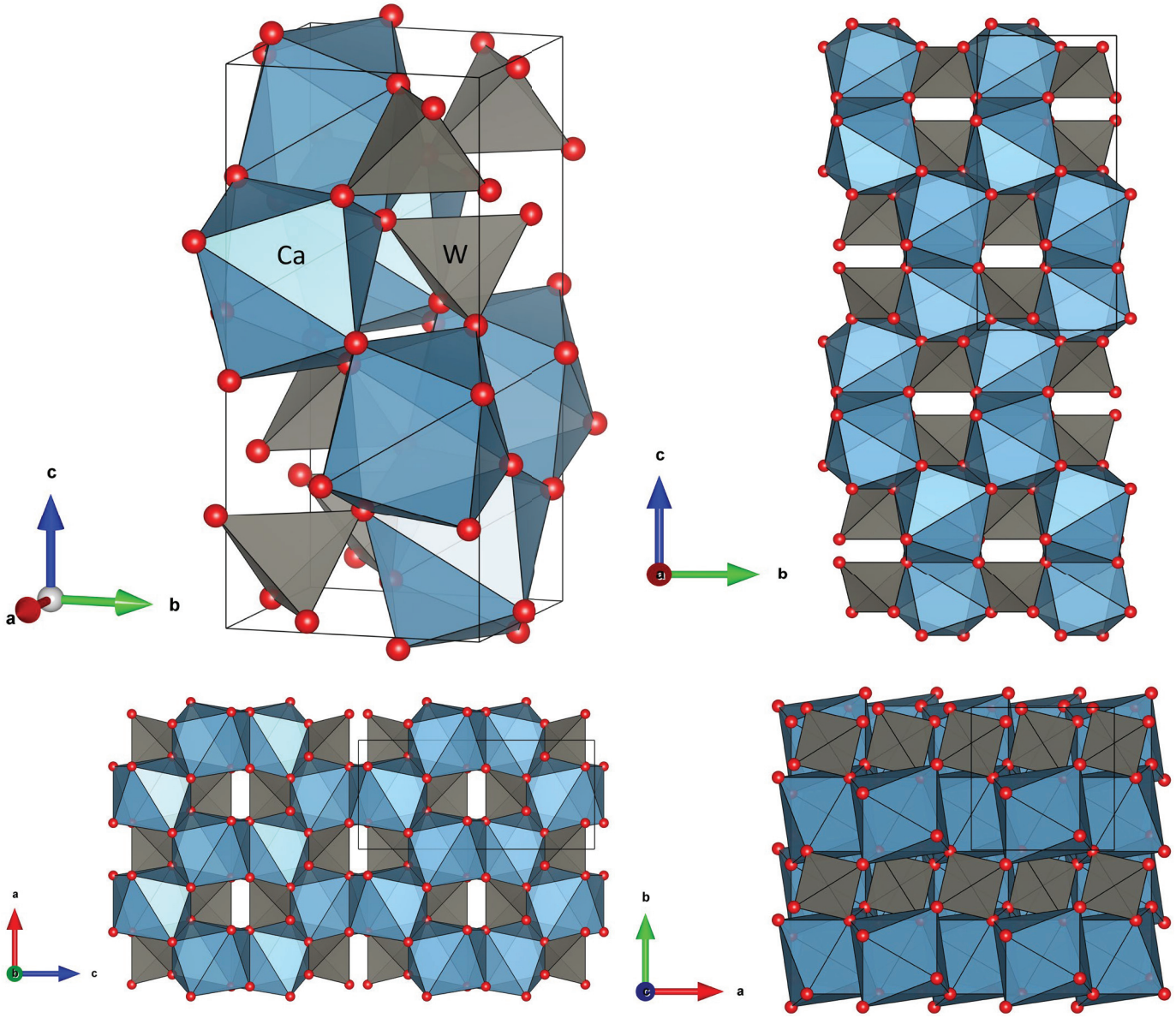


Figure 6. Projections of the structure of scheelite along the *c*-axis, showing the structural polyhedra. The grey tetrahedra represent WO_4, the gray-blue polyhedra represent CaO_8 dodecahedra, and the red balls represent O^{2-} corners. (**Top**): projection of the structure on (100), at the level of unit-cell (**left**), and at the level of the formula unit (**right**). (**Bottom**): projection of the structure at the level of the formula unit on (010)—(**left**) and (001), respectively (**right**).

Table 7 depicts the data collection and structure refinement details for the analyzed samples, whereas positional and displacement parameters are given in Tables 8–11. The corresponding *.cif files are given as Supplementary Materials.

Table 7. Data collection and structure refinement details for Romanian scheelite.

Sample **Occurrence**	**2509** **Ciclova**	**2538** **Oravița**	**2544** **Băița Bihor**
a (Å)	5.2459(10)	5.2380(2)	5.2409(2)
c (Å)	11.3777(5)	11.3679(8)	11.3705(6)
V (Å^3)	313.108(18)	311.90(3)	312.31(3)
Z	4	4	4
D_x (g/cm^3)	6.108	6.132	6.124
Crystal size (mm^3)	0.177 × 0.124 × 0.091	0.35 × 0.22 × 0.1	0.283 × 0.21 × 0.195
Absorption coefficient (mm^{-1})	38.351	38.502	38.449
F(000)	504	504	504
Max. 2ϴ (°)	56.994	57.766	57.74
Range of indices	$-6 \leq h \leq 6$	$-5 \leq h \leq 6$	$-7 \leq h \leq 6$
	$-5 \leq k \leq 6$	$-4 \leq k \leq 6$	$-7 \leq k \leq 5$
	$-13 \leq l \leq 15$	$-14 \leq l \leq 14$	$-12 \leq l \leq 15$
Number of measured reflections	1031	1011	1051
Number of unique reflections	188	191	194
Independent non-zero reflections	176	180	180
Criterion for observed reflections	$I > 2\sigma(I)$	$I > 2\sigma(I)$	$I > 2\sigma(I)$
Number of refined parameters	16	16	16
R int	0.0212	0.0261	0.0327
R sigma	0.0158	0.0181	0.0216
R_1 (F) with $F_0 > 4\ \sigma(F_0)$ *	0.0144	0.0189	0.0216
R_1 (F) for all the unique reflections *	0.0165	0.0204	0.0237
wR_2 (F_2) *	0.0348	0.0477	0.0539
S ("goodness of fit")	1.227	1.267	1.206
Min./max. residual *e* density, (*e*Å^{-3})	−0.88/0.61	−2.46/0.77	−1.71/1.00
Weighing scheme		$1/(\sigma^2(I)^2 + 0.0025(I)^2$	

* Notes: $R_1 = \Sigma(|Fobs| - |Fcalc|)/\Sigma|Fobs|$; $wR_2 = \{\Sigma[w(F^2obs - F^2calc)^2]/\Sigma[w(F^2obs)^2]\}^{1/2}$. $W = 1/[s^2(F_0^2) + (aP)^2 + bP]$, where $P = [2F_c^2 + Max(F_0^2,0)]/3$, where *a*, *b* are shown in the refinement process.

Table 8. Anisotropic displacement parameters (Å^2) for scheelite.

Atom	U_{11}	U_{22}	U_{33}	U_{23}	U_{13}	U_{12}
Sample 2509 Ciclova						
Ca	3.4(9)	3.4(9)	1.8(11)	0	0	0
W	3.96(17)	3.96(17)	4.9(2)	0	0	0
O	14.0(19)	14.7(18)	12.0(15)	−2.0(14)	−1.1(13)	−2.7(14)
Sample 2538 Oravița						
Ca	2.2(12)	2.2(12)	2.8(15)	0	0	0
W	2.6(2)	2.6(2)	6.2(3)	0	0	0
O	11(2)	11(2)	10(2)	1.9(17)	−2.0(17)	0.3(15)
Sample 2544 Băița Bihor						
Ca	7.7(13)	7.7(13)	4.2(16)	0	0	0
W	7.6(3)	7.6(3)	8.4(3)	0	0	0
O	16(2)	18(2)	15(2)	−1(2)	−3(2)	1.9(18)

Table 9. Atom coordinates and isotropic displacement parameters (Å^2) for scheelite.

Atom	*x*	*y*	*z*	*U* (eq)
Sample 2509 Ciclova				
Ca	0	7500	8750	2.9(8)
W	0	2500	6250	4.27(15)
O	1515(6)	4909(6)	7108(3)	13.6(10)
Sample 2538 Oravița				
Ca	0	7500	3750	2.4(10)
W	5000	7500	6250	3.8(2)
O	2594(7)	5980(7)	5392(4)	10.7(12)
Sample 2544 Băița Bihor				
Ca	0	7500	3750	6.5(11)
W	5000	7500	6250	7.8(2)
O	2592(9)	6000(8)	5393(4)	16.4(14)

Table 10. Bond distances (Å) and occupancies observed in the crystal structure of scheelite.

Sample	2509	2538	2544
Occurrence	**Ciclova**	**Oravița**	**Băița Bihor**
Bond distances (Å)			
Ca-O x 4	2.443(4)	2.442(5)	2.440(5)
Ca-O x 4	2.478(4)	2.474(4)	2.482(5)
W-O x 4	1.784(4)	1.781(4)	1.778(5)
Occupancy			
Ca	0.83(15)	0.84(2)	0.83(2)
W	0.91(10)	0.91(14)	0.87(15)

Table 11. Detailed bond-valence table (v_u) for the crystal structure of scheelite *.

	Sample 2509 Ciclova			Sample 2538 Oravița			Sample 2544 Băița Bihor		
	Ca	**W**	**Σ**	**Ca**	**W**	**Σ**	**Ca**	**W**	**Σ**
O	$0.276 \times 4\downarrow$	$1.436 \times 4\downarrow$	1.963	$0.277 \times 4\downarrow$	$1.444 \times 4\downarrow$	1.98	$0.278 \times 4\downarrow$	$1.456 \times 4\downarrow$	1.98
	$0.251 \times 4\downarrow$			$0.254 \times 4\downarrow$			$0.249 \times 4\downarrow$		
Σ	2.11	5.73		2.12	5.77		2.11	5.82	

* bond-valence parameters adjusted after [62].

The structure can be visualized as an assembly of CaO_8 dodecahedra and WO_4 tetrahedra. Each CaO_8 dodecahedron is connected to four other dodecahedra through edge-sharing, resulting in zigzag chains that develop along the c axis. WO_4 tetrahedra are isolated from each other and connected to CaO_8 dodecahedra via bridging oxygen atoms; each oxygen atom is connected to two Ca atoms and one W atom. CaO_8 dodecahedra are described by two distinct Ca−O distances (e.g., Table 11) and eight distinct O−Ca−O angles, while WO_4 tetrahedra could be fairly described by a single W−O distance and two distinct O−W−O angles. In fact, the isolated WO_4 tetrahedron is compressed along the c axis by 7% over a regular tetrahedron [51], which is better depicted by data in Table 10. Note that the site occupancies observed in Table 10 suggest mixed occupancies in both Ca and W sites and the non-stoichiometry of the analyzed samples with site populations involving substitutions in both structural sites, as given in Chapter 5.

9. Infrared and Raman Behavior

The infrared and Raman spectra recorded for representative scheelite samples from Ciclova, Oravița, and Băița Bihor are shown in Figures 7 and 8, respectively. An attempt to assign the vibrational bands in the Raman and infrared spectra to specific vibrational modes, together with the character and relative intensities of the bands in the infrared spectra, is included in Table 12.

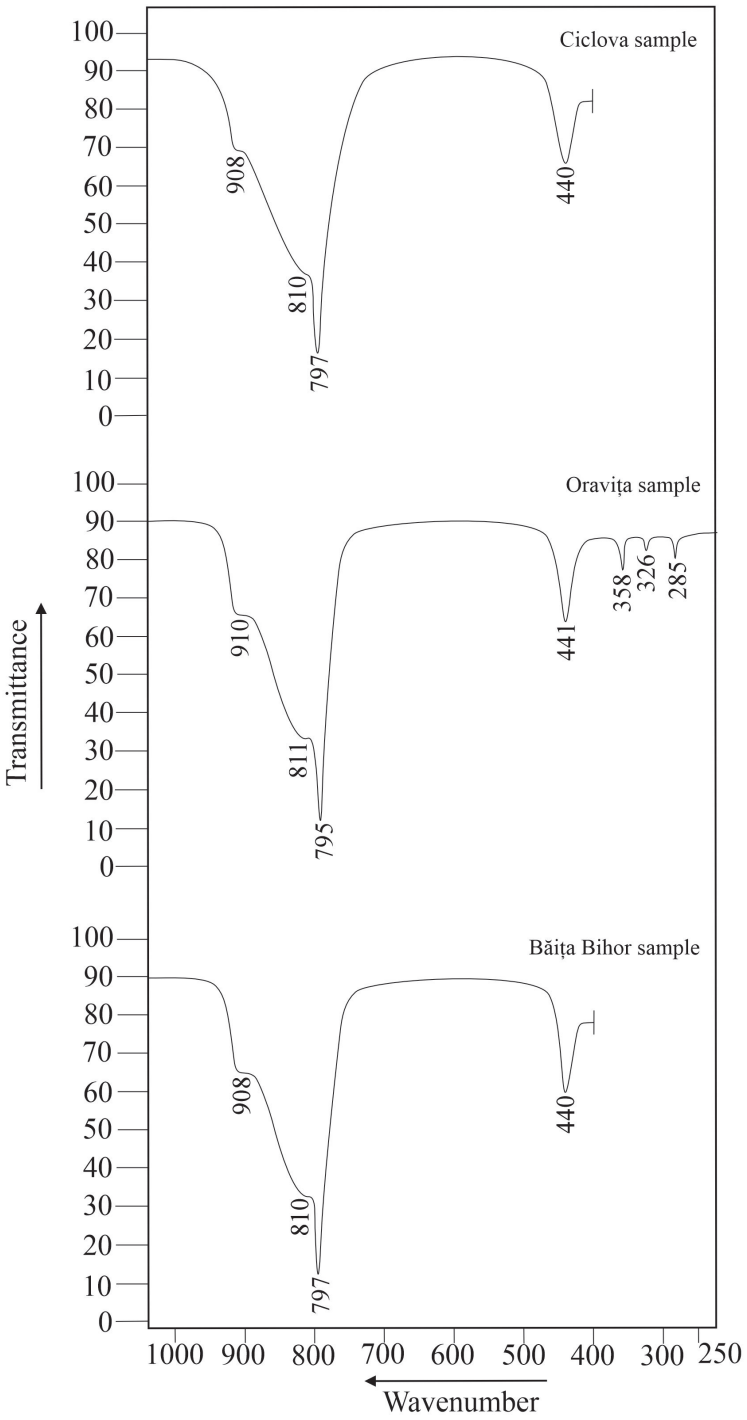


Figure 7. FTIR (**top**, **bottom**) and IR (**middle**) spectra of scheelite samples from Romanian skarns. From top to bottom: Sample 2509 Ciclova (**top**), sample 535 Oravița (**middle**), and sample 2544 Băița Bihor.

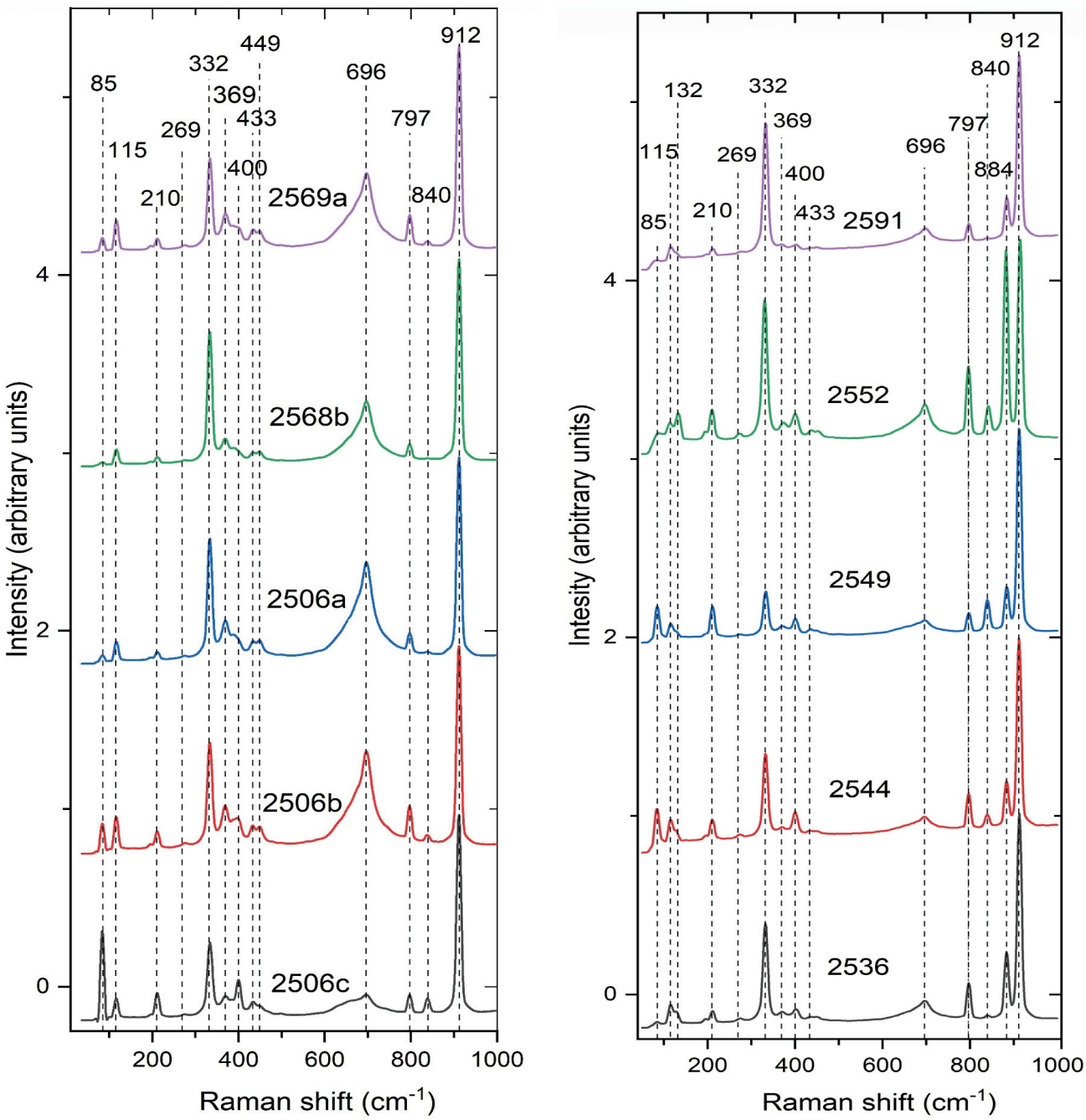


Figure 8. Raman spectra of selected samples of scheelite from Oravița (Samples 2569 a, 2568 b), Ciclova (Samples 2506 a, b, c), and Băița Bihor (Samples 2536, 2544, 2549, 2552, and 2591). Records were made aleatory, on different crystal faces.

Assigning vibrational bands in the Raman and infrared spectra to specific vibrational modes was considerably facilitated by the structure determinations, as well as by previous works of [11,12,63–71] for infrared spectra and of [11,65,70,72–78] for the Raman behavior.

IR spectra in Figure 7 show, at first view, the deviation of the main vibrational bands assignable to the WO_4 structural groups from the values given by [79] for the WO_4 tetrahedra with ideal T_d symmetry (i.e., ν_1 = 931 cm^{-1}, ν_3 = 833 cm^{-1}, ν_2 = 373 cm^{-1} and ν_4 = 320 cm^{-1}), as well as a superior band multiplicity. Note that, in scheelite, the ν_2 out-of-plane bending occurs at higher wavenumbers than the ν_4 in-plane bending, representing an opposite relation to the usual order. This relation, which implies that $\nu_2 > \nu_4$, was proven, based on force field studies, by [68]. Band assumptions in Table 12 were made consequently. Excepting the ν_1 symmetric stretching, vibrational modes of the $[WO_4]^{2-}$ group (i.e., the

ν_3 antisymmetric stretching and the two bending modes) are double degenerate. The band assignable to the ν_1 symmetric stretching, predicted by [68] to occur at 903 cm^{-1}, is materialized by a shoulder on the complex of bands at 750–900 cm^{-1}, which materializes the ν_3 antisymmetric stretching vibration of the WO_4 group (simply degenerate according to [67], and double degenerate according to [11,65,68,70]. The four bands found by [12] in the same region are certainly due to admixed secondary tungstates or, more probably, to the presence of two generations of scheelite, with different powellite contents. The ν_2 out-of-plane bending vibration of the $[WO_4]^{2-}$ group was found in the range of 428–441 cm^{-1}: [11,12,65–67,71]. Accepting that the two shoulders of the broad complex of bands centered at ~ 810 cm^{-1} materializes the ν_1 symmetric stretching (shoulder at higher frequency) and the ν'_3 antisymmetric stretching (shoulder at lower frequency) of the $[WO_4]^{2-}$ group, respectively, and that the band recorded at 286 cm^{-1} in the infrared spectrum in Figure 7 materializes in reality the ν'_4 in-plane bending [67], the multiplicity of bands in the infrared absorption spectrum ($1\nu_1 + 2\nu_3 + 2\nu_2 + 2\nu_4$) is consistent with the S_4 punctual symmetry of the tungstate anion, agreeing with the structural data. This point group symmetry was also deduced by [73,76,80] on the basis of the multiplicity of the Raman bands. Comparative studies on the IR behavior of $CaWO_4$ vs. $CaMoO_4$ (e.g., [65,67]) failed to prove any dependence of the positions of the main bands in the IR spectra on the Mo-for-W substitution. The slight differences in the position of the IR bands in our spectra do not consequently depend on the different powellite contents in the solid solution series of the analyzed samples.

Table 12. Positions and assignments of the FTIR and Raman bands recorded for scheelite from Romanian occurrences [(1)].

Structural Group	Vibrational Mode	Wavenumber (cm^{-1})								Character, Intensity [(4)]
		Calculated		Ciclova		Oravița		Băița Bihor		
		IR [(2)]	Raman [(3)]	FTIR	Raman	IR	Raman	FTIR	Raman	
WO_4	ν_1 (A_g) symmetric stretching	903	912	908	911	910	911	908	913	shd, s
WO_4 (?)	ν'_1 (B_g) (?)	-	893	-	-	-	-	-	883	-
WO_4	ν_3 (B_g) antisymmetric stretching	808	838	810	838	811	839	810	841	sh, vs
WO_4	ν'_3 (E_g) antisymmetric stretching	795	780	797	797	795	797	797	797	shd, s
WO_4	ν_2 (A_g) out-of-plane bending	418	439	440	434	441	434	440	437	sh, m
WO_4	ν'_2 ($E_g + B_g$) out-of-plane bending	-	403	-	401	-	400	-	402	-
WO_4	ν_4 (B_g) in-plane bending	359	-	-	369	358	369	-	370	sh, w
WO_4	ν'_4 (E_g) in-plane bending	348	330	-	333	326	333	-	332	sh, m
WO_4	rotation R$\parallel$ (A_g)	286	280	-	275	285	-	-	274	sh, w
WO_4	rotation R$\perp$ (E_g)	-	207	-	211	-	211	-	210	
CaO_8, WO_4	translation (E_g) Ca/Ca	-	196	-	193	-	193	-	193	
CaO_8, WO_4	translation (B_g) W/W	-	115	-	116	-	116	-	115	
CaO_8, WO_4	translation ($E_g + B_g$) W/W	-	83	-	84	-	84	-	85	

[(1)] Assumptions according to the authors referred to in the text; [(2)] after [68]; [(3)] after [70,80]; [(4)] character of the bands on IR (FTIR) spectra: s = strong; m = medium; w = weak; vs = very strong; sh = sharp; shd = shoulder.

All the 13 Raman-active vibrations recognized by [63] or [80] can be observed in our spectra (Table 12, Figure 8). In fact, the factor-group analysis indicates, for scheelite-group structures, a band multiplicity describing a representation of $\Gamma_i = 3A_g + 5B_g + 5E_g$ (13 vibrational modes), from which 7 are internal [stretching ν_1 (A_g); ν_3 (B_g) and ν'_3 (E_g); bending $\nu_2(A_g)$, $\nu'_2(B_g)$, $\nu_4(B_g)$ and $\nu'_4(E_g)$] and 6 are external (2 rotations, i.e., A_g and E_g, and 4 translations, i.e., $2B_g$ and 2 E_g): [70,73,75,81]. A fourteen-band, detected by us at 883 or 893 cm^{-1} (Table 12), is normally Raman inactive but was also observed by [78] and assumed to be strain-induced ν'_1 (B_g) symmetric stretching.

As a characteristic feature, the Raman spectrum displays an intense band at ~911 cm^{-1}, attributed to the ν_1 symmetric stretching vibration of the WO_4 tetrahedra (Table 12) and identified at 909 cm^{-1} by [77] and [78], at 910 cm^{-1} by [74], at 911 cm^{-1} by [76], and

at 916 cm^{-1} by [70]. The frequency of this band decreases with the progression of the Mo-for-W or Pb-for Ca substitutions [75,76].

The presence of two components of one ν_2 mode cannot be clearly observed because they probably overlap. A closer inspection of the mode located near 400 cm^{-1} allows us to conclude that it is indeed a double mode, as very weak additional bands or shoulders occur in its case (Figure 8).

The low-frequency translational E_g and B_g modes occur at 85 cm^{-1} and overlap [80].

A band located at ~695 cm^{-1} can be observed in all the Raman spectra in Figure 8. This band, which doesn't pertain to scheelite, can be assumed to be the O-W-O antisymmetric stretching in hydrotungstite [82]. Another band, not reproduced in Figure 8 and Table 12 and located at ~1092 cm^{-1}, was recorded in all but five of our Raman spectra and materializes the ν_1 symmetric stretching of the $(CO_3)^{2-}$ groups in the admixed calcite [83].

10. Genetic Considerations

Most tungsten deposits, including tungsten skarns, are typically associated with evolved A- or S-type granites. The three analyzed Romanian deposits, not included among the 203 worldwide W-skarn deposits identified by [25], can be defined and classified as Cu-W skarn deposits. As well as the "true" W-skarns described by [25], they associate with calc-alkaline equigranular plutons in an orogenic belt (i.e., BMMB).

In our specific case, tungsten mineralization is typically associated with fractionated felsic magmas that form under slightly oxidized to reduced fO_2 conditions [84]. In all three cases, the analyzed scheelite samples have low powellite (Mo) contents and are locally associated with molybdenite, which implies that they formed in a reduced environment [85,86]. Associated granodiorites pertain to the ilmenite series of I-type granites as defined by [87], which solidify under reducing conditions, differing from magnetite series magmas [87]. Sulfur in a reduced magma is kept in the silicate melt, whereas sulfur in an oxidized magma escapes to the aqueous phase [88]. The associated scheelite and sulfide-bearing deposits described in this paper seem to be genetically connected with the reducing nature of the ilmenite series granitic magma, as in part of similar Japanese deposits described by [89]. The ore-forming fluid is initially related to the magmatic fluid, particularly to the exolution and segregation of a hydrothermal fluid phase, which can afterwards mix with metamorphic or meteoric waters ([56] and references therein). The low Mo contents in the analyzed samples are compatible with a reducing environment; however, fluctuating Eh conditions may be evident. Mo migrates as Mo^{6+} in oxidizing conditions; thus, Mo substitution is likely to occur in oxidizing environments [90]. This is consistent with thermodynamic calculations, which indicate that scheelite and molybdenite exhibit an overlapping field of stability in terms of oxygen and sulfur fugacities under normal skarn system conditions [45,85].

The hosting skarns are formed at relatively low temperature (up to 600 °C) and pressure (up to 3 kbar according to [32]) in a reducing environment. Scheelite, however, appears to crystallize from late hydrothermal solutions during a retrograde stage of skarn evolution. At Ciclova and Oravița, the mineralizing solutions may have been supplied through original fissures, which were later filled with late quartz and calcite veins in tourmaline-rich endoskarns [15]. At Băița Bihor, scheelite-rich bands occur in the mass of diopside- and chondrodite + norbergite-rich magnesian skarn at the limit of the outer, borate-bearing zone of the metasomatic columns. In all three occurrences, fluorite occurs as micrometer- to millimeter-sized individual anhedral crystals (Figure 9), sometimes associated with scheelite, which is not unusual as it was also described in other scheelite occurrences throughout the world (e.g., [11,45,47,55,56,89]). Conversely, boron-bearing

minerals (i.e., schorlite at Ciclova and Oravița and magnesian borates at Băița Bihor) are particularly abundant in the scheelite-bearing skarns.

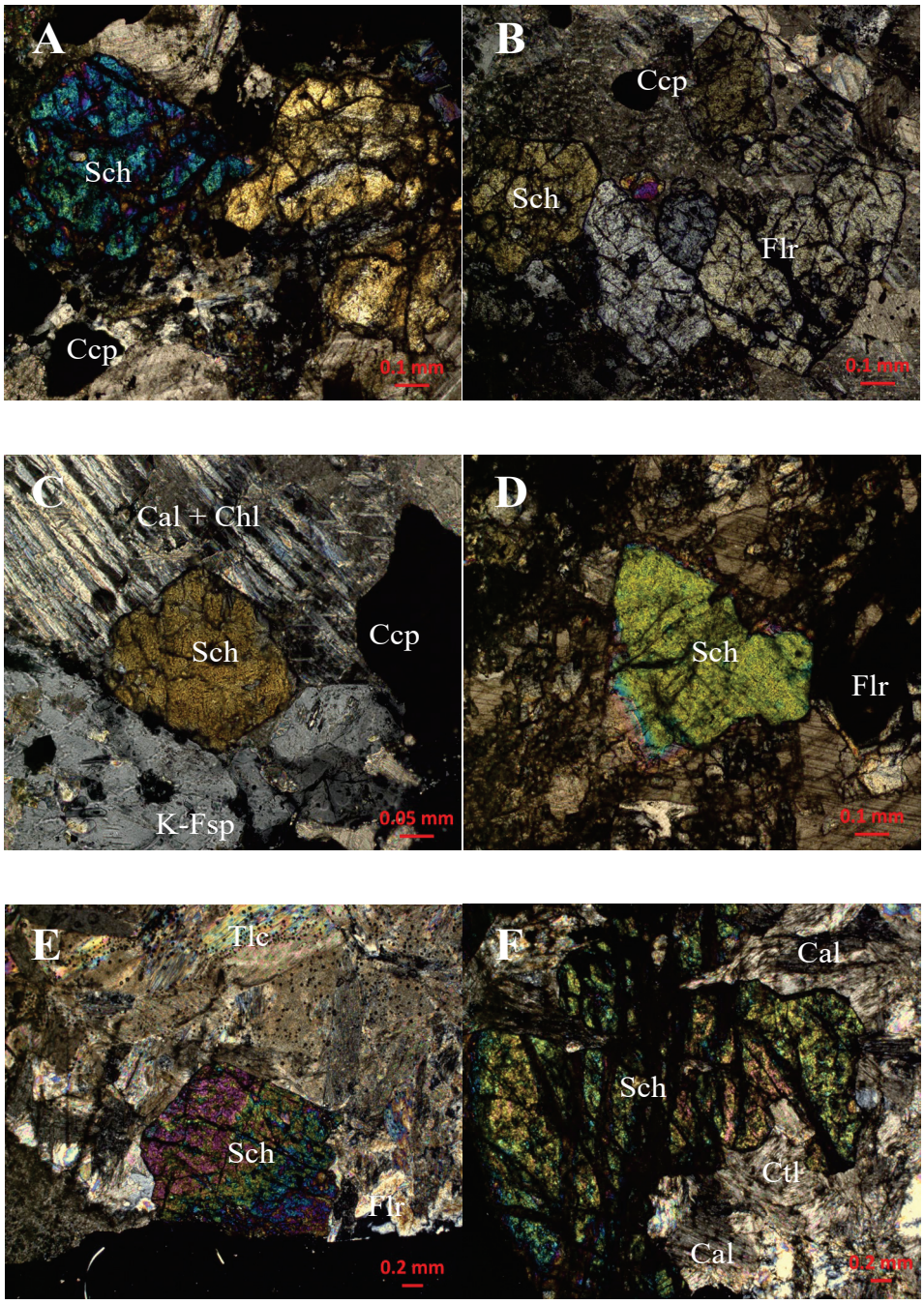


Figure 9. Photomicrographs showing characteristic relationships between scheelite and associated skarn minerals. Crossed polars. (**A**) Crystals of scheelite (Sch) associated with chalcopyrite (Ccp) in the calcite (Cal) mass. Sample 2506 Ciclova. (**B**) Crystals of scheelite (Sch) associated with chalcopyrite (Ccp) and fluorite (Flr). Sample 2575 Ciclova. (**C**) Crystals of scheelite (Sch) and chalcopyrite (Ccp) surrounded by calcite + chlorite (Cal + Chl) and adularia (K-Fsp). Sample 2537 Oravița. (**D**) Aggregate of scheelite (Sch) crystals associated with fluorite (Flr) in the calcite mass. Sample 2569 Oravița. (**E**) Crystal of scheelite (Sch) surrounded by carbonates (calcite, dolomite) and talc (Tlc). Sample 2544 Băița Bihor. (**F**) Aggregate of scheelite (Sch) crystals surrounded by calcite (Cal) and chrysotile (Ctl). Sample 2593 Băița Bihor. Abbreviations of mineral species after [91].

These observations suggest that W was introduced in the skarn system by fluoride-bearing aqueous fluids at relatively low temperatures and vapor-saturated water pressure

(e.g., as per experimental conditions used by [92]). Accepting that these experimental conditions were fulfilled during the hydrothermal evolution of the skarn systems described in this paper, we must accept that tungsten was dissolved predominantly as $H_3WO_4F^{2-}$ in solutions containing 0.05–0.30 m HF at pH (T) values between 1.5 and 3.4 and temperatures between 100 and 250 °C. The occurrence of abundant fluorite in scheelite-bearing samples from quartz-vein deposits from Ciclova and Oravița supports the hypothesis of scheelite crystallization from F-bearing fluids. The ideal reaction to form both scheelite and fluorite may be written, in our case, as: $2\ H_3WO_4F^{2-} + 3\ CaCO_3 = 2\ CaWO_4 + CaF_2 + 3\ H_2CO_3$.

Alternatively, a number of authors (e.g., [93] and referred works) showed that a large amount of boron can be dissolved in F-bearing hydrothermal solutions, which implies that speciation of B-bearing minerals is possible in similar conditions as for scheelite and explains the presence of boron minerals in the W-bearing skarns at Ciclova, Oravița, and Băița Bihor.

11. Conclusions

Physical and crystallographic properties and vibrational behavior, as well as crystal chemistry, show that scheelite from Ciclova, Oravița, and Băița Bihor is close to stoichiometry.

In all cases, the analyzed samples show, at least locally, oscillatory zonation in cathodoluminescence, characteristic of scheelite from proximal intrusion-related systems such as skarns. CL peculiarities suggest that, in the analyzed occurrences, scheelite formation was controlled by multiple factors, e.g., the nature of ore-forming fluids and crystal diffusion or growth rate. In all cases, the CL images of the crystals vary from homogenous to zoned, behaving like hydrothermal scheelite and suggesting slight oscillations in the Eh of the crystallizing solutions, from slightly oxidizing to reducing. Textural relations and petrographic evidence indicate that the analyzed scheelite crystallizes late in the skarn paragenesis, apparently from epigenetic hydrothermal fluids.

Scheelite described in this paper is typically associated with hydrous minerals and retrograde alteration but also with F- and B-bearing minerals, suggesting that the mineral crystallized from epithermal, low-temperature fluoride- and boron-bearing aqueous solutions.

The Ciclova, Oravița, and Băița Bihor deposits in Romania can be defined as Cu-W skarns but also contain significant contents of other metals (i.e., Pb, Zn, Bi, Mo, Ag, and Au). At least the deposit from Băița Bihor, which is a quite important source of Cu, Mo, and base metals, can produce a significant amount of byproduct W.

Supplementary Materials: The following supporting information can be downloaded at: https://www.mdpi.com/article/10.3390/min15080854/s1, Word-transposed *.cif files with structure data for representative samples of scheelite from Ciclova (Sample 2509), Oravița (Sample 2538) and Băița Bihor (Sample 2544).

Author Contributions: Conceptualization, Ş.M., D.-G.D., F.H. and M.D.; formal analysis, Ş.M., C.S.G., D.-G.D., M.D., F.H., G.D. and G.C.; funding acquisition, Ş.M., D.-G.D., C.S.G., A.-M.I., G.C. and F.H.; investigation, Ş.M., D.-G.D., F.H., C.S.G., M.D., G.D. and G.C.; methodology, Ş.M., D.-G.D., G.C. and F.H.; resources, Ş.M., D.-G.D., F.H., G.C. and C.S.G.; data curation, Ş.M., D.-G.D., C.S.G., F.H. and M.D.; writing—original draft preparation, Ş.M.; writing—review and editing, Ş.M.; visualization, Ş.M.; supervision, Ş.M.; project administration, Ş.M., D.-G.D., C.S.G. and F.H. All authors have read and agreed to the published version of the manuscript.

Funding: This study was partly supported by two scientific cooperative research grants awarded by the Walloon and Romanian Governments (4 BM/2021 and 1BCBE/2024). Other grants allowed to the first author by UEFISCDI in Romania (PN-III-P1-1.2-PCCDI-2017-0346 and PN-III-P1-1.1-MC-2018-3163) and by the Ministry of Education and Research (PN23-39-02-01/2023, PN23-39-02-06/2023 and PN23-39-02-07/2023) generously supported the final draft. C.S.G and A.-M.I. gratefully acknowledge

the receipt of two UEFISCDI grant (PN-III-P1-1.1-MC-2018-3199 and PN-III-P1-1.1-MC-2018-3211) which helped to obtain part of the structural data.

Data Availability Statement: Primary data presented in this study are available on request from the first author. More data for structure refinements, including *.cif files, are available on request from the fifth author (fhatert@uliege.be).

Acknowledgments: The use of the EPMA facility at the Department of Earth, Environmental, and Planetary Sciences, Rice University, Houston, Texas, is kindly acknowledged. The assistance of Gabriela Stelea (Geological Institute of Romania, Bucharest) in the acquisition of the infrared spectra is gratefully acknowledged. Corentin Amador del Valle (University in Liège) kindly communicated some of the XRD and EMP analyses used for this study. Fruitful discussions on the field with the late Jean Verkaeren, with André-Mathieu Fransolet, Bernard Guy, Essaïd Bilal, Gheorghe Ilinca, Jacqueline Vander Auwera, Hans-Peter Schertl, Walter Maresh, Evgheny Galuskin, Irina Galuskina, Robert Martin and Maxime Baijot were highly appreciated. Members of the staffs of SC Băița Bihor SA and Vast Resources PLC-Băița Plai mining companies are gratefully acknowledged for their assistance in the sampling activities. The authors are grateful to Alexandru Călin and to the Academic Editor for handling the manuscript, as well as to three anonymous referees for their thorough reviews of an earlier draft.

Conflicts of Interest: The authors declare no conflicts of interest.

References

1. British Geological Survey. Tungsten. In *British Geological Survey*; BGS: Keyworth, UK, 2011; pp. 1–34.
2. Yang, X. Beneficiation studies of tungsten ores—A review. *Min. Eng.* **2018**, *125*, 111–119. [CrossRef]
3. Han, Z.; Golev, A.; Edraki, M.A. Review of tungsten resources and potential extraction from mine waste. *Minerals* **2021**, *11*, 701. [CrossRef]
4. Grohol, M.; Veeh, C. *Study on the Critical Raw Materials for the EU 2023*; DG Grow, European Commission, Luxembourg Publication Office of the EU: Luxembourg, 2023; pp. 1–152.
5. Rowan, L.R. *Critical Mineral Resources: National Policy and Critical Minerals List*; Congressional Research Service Report: CRS Report R47982 2025; Library of Congress: Washington, DC, USA, 2025; pp. 1–22.
6. Hocquard, C. Les nouveaux métaux stratégiques: Métaux high-tech, «métaux verts», métaux stratégiques, vers une convergence. *Mag'Mat* **2008**, *26*, 1–30.
7. Liu, Y.; Jia, D.; Zhou, Y.; Zhou, Y.; Zhao, J.; Li, Q.; Liu, B. Discovery of ABO_4 scheelites with the extra low thermal conductivity through high-throughput calculations. *J. Mater.* **2020**, *6*, 702–711. [CrossRef]
8. Li, S.; Bychkov, K.L.; Butenko, D.S.; Terebilenko, K.V.; Zhu, Y.; Han, W.; Baumer, V.N.; Slobodyanik, M.S.; Ji, H.; Klyui, N.I. Scheelite-related $M^{II}_xBi_{1-x}V_{1-x}Mo_xO_4$ (M^{II}—Ca, Sr) solid solution-based photoanodes for enhanced photoelectrochemical water oxidation. *Dalton Trans.* **2020**, *49*, 2345–2355. [CrossRef]
9. Shivakumar, C.; Saraf, R.; Behera, S.; Dhananjaya, N.; Nagabhushana, H. Scheelite-type MWO_4 (M = Ca, Sr, and Ba) nanophosphors: Facile synthesis, structural characterization, photoluminescence, and photocatalytic properties. *Mater. Res. Bull.* **2015**, *61*, 422–432. [CrossRef]
10. Potanina, E.A.; Orlova, A.I.; Mikhailov, D.A.; Nokhrin, A.V.; Chuvil'deev, V.N.; Boldin, M.S.; Sakharov, N.V.; Lantcev, E.A.; Tokarev, M.G.; Murashov, A.A. Spark Plasma Sintering of fine-grained $SrWO_4$ and $NaNd(WO_4)_2$ tungstates ceramics with the scheelite structure for nuclear waste immobilization. *J. Alloys Compd.* **2019**, *774*, 182–190. [CrossRef]
11. Liu, X.; Yang, J.; Chen, Q. Study on spectral characteristics and color origin of scheelite from Xuebaoding, Pingwu County, Sichuan Province, P.R. China. *Minerals* **2022**, *12*, 1344. [CrossRef]
12. Cao, Q.; Shi, M.; Yuan, Y.; Ma, S.; Lu, H. Mineralogy and geochemical characteristics of scheelite deposit at Xuebaoding in Pingwu, Sichuan Province, China. *Minerals* **2024**, *14*, 38. [CrossRef]
13. Koch, A. Űber den Vesuvian und Scheelit von Csiklova. *Földtany Közlöny* **1924**, *54*, 85–90.
14. Superceanu, C. New occurrences of scheelite in contact deposits from the Banatitic geochemical province. *Rev. Min.* **1956**, *4–5*, 230–234. (In Romanian)
15. Constantinescu, E.; Ilinca, G.; Ilinca, A. Laramian hydrothermal alteration and ore deposition inthe Oravița—Ciclova area, South–western Banat. *D. S.—Inst. Geol. Geofiz.* **1988**, *72–73*, 13–26.
16. Cioflică, G.; Vlad, Ş.; Iosof, A.; Panican, A. Scheelite occurrences in the Bihor Massif. *Rev. Roum. Géol. Géoph. Géogr.* **1976**, *20*, 169–177.

17. Berza, T.; Constantinescu, E.; Vlad, Ş.N. Upper Cretaceous magmatic series and associated mineralization in the Carpatho-Balkan Orogen. *Res. Geol.* **1998**, *48*, 291–306. [CrossRef]
18. Cioflică, G.; Vlad, Ş. The correlation of the Laramian metallogenetic events belonging to the Carpatho-Balkan area. *Rev. Roum. Géol. Géophys. Géogr. Sér. Géol.* **1973**, *17*, 217–224.
19. Ciobanu, C.L.; Cook, N.J.; Stein, H. Regional setting and geochronology of the Late Cretaceous Banatitic Magmatic and Metallogenetic Belt. *Miner. Depos.* **2002**, *37*, 541–567. [CrossRef]
20. Zimmermann, A.; Stein, H.; Hannah, J.; Koželj, D.; Bogdanov, K.; Berza, T. Tectonic configuration of the Apuseni—Banat—Timok—Srednogorie belt, Balkans–Southern Carpathians, constrained by high precision Re–Os molybdenite ages. *Miner. Depos.* **2008**, *43*, 1–21. [CrossRef]
21. Ilinca, G. Classic skarn localities of Romania: Contact metamorphism and mineralization related to Late Cretaceous magmatism. *Acta Min.-Petr.* **2010**, *23*, 1–50.
22. Ilinca, G. Upper Cretaceous contact metamorphism and related mineralizations in Romania. *Acta Min.-Petr. Abstr. Ser.* **2012**, *7*, 59–64.
23. Vlad, Ş.N. Banatite metallogeny of North Poiana Ruscă Mts. Revisited. *Geol. Anali Balkanskoga Poluostrva* **2020**, *81*, 67–77. [CrossRef]
24. Săndulescu, M.; Kräutner, H.; Borcoş, M.; Năstăseanu, S.; Patrulius, D.; Ştefănescu, M.; Ghenea, C.; Lupu, M.; Savu, H.; Bercia, I.; et al. *Geological Map of Romania, scale 1:1,000,000*; Institute of Geology and Geophysics: Bucharest, Romania, 1978.
25. Meinert, L.D.; Dipple, G.M.; Nicolescu, Ş. World skarn deposits. In *Economic Geology 100th Anniversary Volume*; Society of Economic Geologists: Littleton, CO, USA, 2005; pp. 299–336.
26. Soroiu, M.; Catilina, R.; Strutinski, C. K-Ar ages on some igneous rocks from the southwestern end of the South Carpathians (Banat Hills). *Rev. Roum. Phys.* **1986**, *31*, 849–854.
27. Gallhofer, D. Magmatic Geochemistry and Geochronology in Relation to the Geodynamic and Metallogenetic Evolution of the Banat Region and Apuseni Mountains of Romania. Ph.D. Thesis, ETH Zürich, Zürich, Switzerland, 2015. Dissertation ETH no 22888. pp. 1–45.
28. Bleahu, M.; Soroiu, M.; Catilina, R. On the Cretaceous tectonic-magmatic evolution of the Apuseni Mountains as revealed by K-Ar dating. *Rev. Roum. Phys.* **1984**, *29*, 123–130.
29. Pavelescu, L.; Pop, G.O.; Weisz, E.; Popescu, G. La nature et l'âge du batholite banatitique de Bihor. *Rep. XII-th Congress K.B.G.A. Cracow* **1985**, 98–101.
30. Cioflică, G.; Jude, R.; Lupulescu, M. Cupriferous metallization processes associated with Upper Cretaceous–Eocene magmatites from Romania. *Rom. J. Mineral.* **1992**, *76*, 1–16.
31. Vlad, Ş.N. Calcic skarns and transversal zoning in the Banat Mountains, Romania: Indicators of an Andean–type setting. *Miner. Depos.* **1997**, *32*, 446–471. [CrossRef]
32. Marincea, Ş.; Dumitraş, D.-G. Contrasting types of boron-bearing deposits in magnesian skarns from Romania. *Ore Geol. Rev.* **2019**, *112*, 102952. [CrossRef]
33. Cioflică, G.; Vlad, Ş.; Stoici, S. Repartition de la mineralization dans le skarn de Băiţa Bihorului. *Rev. Roum. Géol. Géoph. Géogr.* **1971**, *15*, 43–58.
34. Tămaş, C.G.; Andrii, M.-P. Mineralogy of skarn ores from Băiţa Bihor, Northern Apuseni Mountains, Romania: A case study of Cu-, Bi- and Sn-minerals. *Minerals* **2020**, *10*, 436. [CrossRef]
35. Armstrong, J.T. Quantitative analysis of silicates and oxide minerals: Comparison of Monte Carlo, ZAF and Phi-Rho-Z procedures. In *Microbeam Analysis*; Newbury, D.E., Ed.; San Francisco Press: San Francisco, CA, USA, 1988; pp. 239–246.
36. Appleman, D.E.; Evans, H.T., Jr. Indexing and least-squares refinement of powder diffraction data. *U.S. Geol. Surv. Comput. Contrib.* **1973**, *20*, 60.
37. Benoit, P.H. Adaptation to microcomputer of the Appleman-Evans program for indexing and least-squares refinement of powder-diffraction data for unit-cell dimensions. *Am. Mineral.* **1987**, *72*, 1018–1019.
38. Kalinkina, E.V.; Kalinkin, A.M.; Forsling, W.; Makarov, A.M. Sorption of atmospheric carbon dioxide and structural changes of Ca and Mg silicate minerals during grinding. II. Enstatite, åkermanite and wollastonite. *Int. J. Miner. Process.* **2001**, *61*, 289–299. [CrossRef]
39. Agilent Technologies. *Xcalibur CCD System, CrysAlis Software System*; Agilent Technologies: Oxfordshire, UK, 2012.
40. Palatinus, L.; Chapuis, G. Superflip—A computer program for the solution of crystal structures by charge flipping in arbitrary dimensions. *J. Appl. Crystallogr.* **2007**, *40*, 786–790. [CrossRef]
41. Petříček, V.; Dušek, M.; Palatinus, L. Crystallographic computing system Jana2006: General features. *Z. Kristallogr.* **2014**, *229*, 345–352. [CrossRef]
42. Xu, J.; Ciobanu, C.L.; Cook, N.; Slattery, A. Crystals from the powellite-scheelite series at the nanoscale: A case study from the Zhibula Cu skarn, Gangdese Belt, Tibet. *Minerals* **2019**, *9*, 340. [CrossRef]

43. Wen, J.; Zheng, S.; Chu, X.; Jiang, H.; Zhao, Y. Mineralogical characteristics of scheelite in the Xi'an tungsten deposit, western Hunan. *IOP Conf. Ser. Earth Env. Sci.* **2021**, *658*, 012044. [CrossRef]
44. Ilinca, G.; Marincea, Ş. Hydrotungstite from Oraviţa-Ciclova and Băiţa Bihor: The first occurrences in Romania. *Rom. J. Mineral.* **1993**, *76* (Suppl. S1), 24–25.
45. Poulin, R.S.; McDonald, A.M.; Kontak, D.J.; McClenaghan, M.B. On the relationship between cathodoluminescence and the chemical composition of scheelite from geologically diverse ore-deposit environments. *Can. Mineral.* **2016**, *54*, 1147–1173. [CrossRef]
46. Xiao, X.; Zhou, T.; Shi, K.; White, N.C.; Fan, Y.; Wang, F.; Chen, X. Trace elements and textures of scheelite in porphyry-skarn Cu-Au systems: The example of Dongguashan deposit, eastern China. *Ore Geol. Rev.* **2022**, *149*, 105069. [CrossRef]
47. Miranda, A.C.R. Chemical Composition of Scheelite and its Application as An Indicator Mineral. Ph.D. Thesis, Laval University, Québec, QC, Canada, 2023; pp. 1–459.
48. Kay, M.I.; Frazer, B.C.; Almodovar, I. Neutron diffraction refinement of $CaWO_4$. *J. Chem. Phys.* **1964**, *40*, 504–506. [CrossRef]
49. Blanchard, F. X-ray powder data for $CaWO_4$, synthetic scheelite. *Powder Diffr.* **1989**, *4*, 220–222. [CrossRef]
50. Sleight, A.W. Accurate cell dimensions for ABO_4 molybdates and tungstates. *Acta Cryst.* **1972**, *28*, 2899–2902. [CrossRef]
51. Senyshyn, A.; Kraus, H.; Mikhailik, V.B.; Yakovyna, V. Lattice dynamics and thermal properties of $CaWO_4$. *Phys. Rev.* **2004**, *70*, 214306. [CrossRef]
52. Hazen, R.M.; Finger, L.W.; Mariathasan, J.W. High-pressure crystal chemistry of scheelite-type tungstates and molybdates. *J. Phys. Chem Solids* **1985**, *46*, 253–263. [CrossRef]
53. Rabuffetti, F.A.; Culver, S.P.; Suescun, L.; Brutchey, R.L. Structural disorder in $AMoO_4$ (A = Ca, Sr, Ba) scheelite nanocrystals. *Inorg. Chem.* **2014**, *53*, 1056–1061. [CrossRef]
54. Shoji, T.; Sasaki, N. Fluorescent color and X-ray powder data of synthesized scheelite- powellite series as guides to determine its composition. *Min. Geol.* **1978**, *28*, 397–404.
55. Palmer, M.C. Geochemical Characterisation of Scheelite from New Zealand. Ph.D. Thesis, Otago University, Dunedin, New Zealand, 2021; pp. 1–220.
56. Lu, D.; Mao, J.; Ye, H.; Wang, P.; Chao, W.; Yu, M. Geochemistry of scheelite from Jiangligou skarn W-(Cu-Mo) deposit in the West Qinling orogenic belt, Northwest China: Implication on the multistage ore-forming processes. *Ore Geol. Rev.* **2023**, *159*, 105525. [CrossRef]
57. Palache, C.; Berman, H.; Frondel, C. *The System of Mineralogy. II. Halides, Nitrates, Borates, Carbonates, Sulfates, Phosphates, Arsenates, Tungstates, Molybdates, etc.*; John Wiley and Sons: New York, NY, USA, 1951; pp. 1–1124.
58. Mandarino, J.A. The Gladstone-Dale relationship—Part I: Derivation of new constants. *Can. Mineral.* **1976**, *14*, 498–502.
59. Zalkin, A.; Templeton, D.H. X-ray diffraction refinement of the calcium tungstate structure. *J. Chem. Phys.* **1964**, *40*, 501–504. [CrossRef]
60. Mandarino, J.A. The Gladstone-Dale relationship. IV. The compatibility concept and its application. *Can. Mineral.* **1981**, *19*, 441–450.
61. Larsen, E.S. The microscopic determination of the nonopaque minerals. *U.S. Geol. Surv. Bull.* **1921**, *679*, 1–289.
62. Brown, I.D.; Altermatt, D. Bond-valence parameters obtained from a systematic analysis of the Inorganic Crystal Structure Database. *Acta Cryst. B* **1985**, *41*, 244–247. [CrossRef]
63. Barker, A.S. Infrared lattice vibrations in calcium tungstate and calcium molybdate. *Phys. Rev. A* **1964**, *135*, 742–747. [CrossRef]
64. Clark, G.M.; Doyle, W.P. IR spectra of anhydrous molybdates and tungstates. *Spectrochim. Acta* **1966**, *22*, 1441–1447. [CrossRef]
65. Khanna, R.K.; Lippincott, E.R. Infrared spectra of some scheelite structures. *Spectrochim. Acta A* **1968**, *24*, 905–908. [CrossRef]
66. Zorina, M.L.; Syritso, L.F. IR spectra and structures of tungstates. *J. Appl. Crystallogr.* **1972**, *16*, 774–776. [CrossRef]
67. Tarte, P.; Liegeois-Duyckaerts, M. Vibrational studies of molybdates, tungstates and related compounds—I. New infrared data and assignments for the scheelite-type compounds $X^{II}MoO_4$ and $X^{II}WO_4$. *Spectrochim. Acta A* **1972**, *28*, 2029–2036. [CrossRef]
68. Iishi, K. Study of the force field of scheelite. *Z. Kristallogr.* **1975**, *141*, 31–58. [CrossRef]
69. Zhou, P.L. Infrared spectra of wolframite and scheelite from tungsten ore deposits in Southern Ganzhou, Jiangxi Province. *Acta Mineral. Sinca* **1984**, *4*, 319–322.
70. Akimov, A.N.; Nikanovich, M.V.; Popov, V.G.; Umreiko, D.S. Calculation and investigation of the vibrational spectra of scheelite structures $MeWO_4$ (Me = Ca, Sr, Ba, Pb). *Zh. Prikladn. Spektr.* **1986**, *45*, 225–232. (In Russian) [CrossRef]
71. Chukanov, N.V. *Infrared Spectra of Mineral Species. Extended Library*; Springer Geochemistry/Mineralogy: Berlin/Heidelberg, Germany, 2014; pp. 1–1726.
72. Russell, J.P.; Loudon, R. The first-order Raman spectrum of calcium tungstate. *Proc. Phys. Soc.* **1965**, *85*, 1029–1033. [CrossRef]
73. Porto, S.P.S.; Scott, J.F. Raman Spectra of $CaWO_4$, $SrWO_4$, $CaMoO_4$, and $SrMoO_4$. *Phys. Rev.* **1967**, *157*, 716–721. [CrossRef]
74. Griffith, W.P. Raman studies on rock-forming minerals. Part II. Minerals containing MO_3, MO_4, and MO_6 groups. *J. Chem. Soc. A* **1970**, *2*, 286–291. [CrossRef]

75. Liegeois-Duyckaerts, M.; Tarte, P. Vibrational studies of molybdates, tungstates and related compounds—II. New Raman data and assignments for the scheelite-type compounds. *Spectrochim. Acta A* **1972**, *28*, 2037–2051. [CrossRef]
76. Basiev, T.T.; Sobol, A.A.; Voronko, Y.K.; Zverev, P.G. Spontaneous Raman spectroscopy of tungstate and molybdate crystals for Raman lasers. *Opt. Mater.* **2000**, *15*, 205–216. [CrossRef]
77. Crane, M.; Frost, R.L.; Williams, P.A.; Kloprogge, J.T. Raman spectroscopy of the molybdate minerals chillagite (tungstenian wulfenite-I4), stolzite, scheelite, wolframite and wulfenite. *J. Raman Spectrosc.* **2002**, *33*, 62–66. [CrossRef]
78. Frost, R.L.; Duong, L.; Weier, M. Raman microscopy of selected tungstate minerals. *Spectrochim. Acta A Mol. Biomol. Spectrosc.* **2004**, *60*, 1853–1859. [CrossRef]
79. Müller, A.; Krebs, B. Normal coordinate treatment of XY_4-type molecules and ions with T_d symmetry. Part I. Force constants of a modified valence force field and of the Urey-Bradley force field. *J. Molec. Spectr.* **1967**, *24*, 180–197. [CrossRef]
80. Khanna, R.K.; Brower, W.S.; Guscott, B.R.; Lippincott, E.R. Laser induced Raman spectra of some tungstates and molybdates. *J. Res. Nat. Inst. Stand. Techn. Phys. Chem. A* **1968**, *72*, 81–84. [CrossRef]
81. Kanamori, H.; Hayashi, S.; Ikeda, Y.Y. External lattice vibration modes in scheelites. *J. Phys. Soc. Jap.* **1974**, *36*, 511–516. [CrossRef]
82. Daniel, M.F.; Desbat, B.; Lassegues, J.C.; Gerand, B.; Figlarz, M. Infrared and Raman study of $WO_3 \cdot xH_2O$ tungsten trioxide hydrates. *J. Solid State Chem.* **1987**, *67*, 235–247. [CrossRef]
83. Gunasekaran, S.; Anbalagan, G.; Pandi, S. Raman and infrared spectra of carbonates of calcite structure. *J. Raman Spectr.* **2006**, *37*, 892–899. [CrossRef]
84. Newberry, R.; Swanson, S. Scheelite skarn granitoids: An evaluation of the roles of magmatic source and process. *Ore Geol. Rev.* **1986**, *1*, 57–81. [CrossRef]
85. Hsu, L.C.; Galli, P. E, Origin of the scheelite-powellite series of minerals. *Econ. Geol.* **1973**, *68*, 681–696. [CrossRef]
86. Hsu, L.C. Effects of oxygen and sulfur fugacities on the scheelite-tungstenite and powellite-molybdenite stability relations. *Econ. Geol.* **1977**, *72*, 664–670. [CrossRef]
87. Ishihara, S. The magnetite-series and ilmenite-series granitic rocks. *Mining Geol.* **1977**, *27*, 293–305.
88. Ishihara, S. The granitoid series and mineralization. In *Economic Geology 75th Anniversary Volume*; The Economic Geology Publishing Company: Littleton, CO, USA, 1981; pp. 458–484.
89. Sato, K. Tungsten skarn deposit of the Fujigatani Mine, Southwest Japan. *Econ. Geol.* **1980**, *75*, 1066–1082. [CrossRef]
90. Song, G.X.; Qin, K.Z.; Li, G.; Evans, N.J.; Chen, J. Scheelite elemental and isotopic signatures: Implication for the genesis of skarn-type W-Mo deposits in the Chizhou area, Anhui Province, eastern China. *Amer. Miner.* **2014**, *99*, 303–317. [CrossRef]
91. Warr, L.N. IMA-CNMNC approved mineral symbols. *Min. Mag.* **2021**, *85*, 291–320. [CrossRef]
92. Wang, X.-S.; Williams-Jones, A.E.; Hu, R.Z.; Lin-Bo, S.; Xian-Wu, B. The role of fluorine in granite-related hydrothermal tungsten ore genesis: Results of experiments and modelling. *Geochim. Cosmochim. Acta* **2021**, *292*, 170–187. [CrossRef]
93. Qiu, Y.; Zhang, R.; Chou, I.-M.; Wang, X.; Hu, W.; Zhang, W.; Lu, J.; Li, G.; Li, Z. Boron-rich ore-forming fluids in hydrothermal W-Sn deposits from South China: Insights from in situ Raman spectroscopic characterization of fluid inclusions. *Ore Geol. Rev.* **2021**, *132*, 104048. [CrossRef]

Disclaimer/Publisher's Note: The statements, opinions and data contained in all publications are solely those of the individual author(s) and contributor(s) and not of MDPI and/or the editor(s). MDPI and/or the editor(s) disclaim responsibility for any injury to people or property resulting from any ideas, methods, instructions or products referred to in the content.

minerals

MDPI

Article

Geological, Mineralogical, Geochemical, and Petrogenetic Characteristics of Plutonic Rocks in Çiftehan (Ulukışla-Niğde) Area, South-Central Türkiye: Implication for Genetic Link with Fe-Zn Skarn Mineralization

Emmanuel Daanoba Sunkari [1,2,3,*] and Abdurrahman Lermi [1]

[1] Department of Geological Engineering, Faculty of Engineering, Niğde Ömer Halisdemir University, Main Campus, 51240 Niğde, Türkiye; alermi@ohu.edu.tr
[2] Department of Mining Engineering, Faculty of Integrated and Advanced Technology, Sir Padampat Singhania University, N.H. 76, Bhatewar, Udaipur 313601, Rajasthan State, India
[3] Department of Geological Engineering, Faculty of Geosciences and Environmental Studies, University of Mines and Technology, Tarkwa P.O. Box 237, Ghana
* Correspondence: emmanueldaanoba.sunkari@spsu.ac.in or jenema23@gmail.com; Tel.: +233-241827727

Abstract: Globally, most skarn deposits show a direct relationship with magmatic activity, indicating a genetic link between the geochemical composition of causative plutons and the metal content of associated skarns. Therefore, this study investigated the Early–Middle Eocene plutonic rocks and their relationship with Fe-Zn skarn deposits in the Esendemirtepe-Koçak and Horoz areas of south-central Türkiye. Despite the regional significance, previous studies have not adequately addressed the petrogenetic evolution of these intrusions and the geochemical characteristics of the related skarns. In particular, the fluid-aided mobility of elements at the contact between the causative plutons and the volcano-sedimentary country rocks remains poorly understood. Therefore, in this study, field studies, petrographic and mineralogical analysis, and whole-rock geochemical analysis were conducted to investigate the genetic link between the plutonic rocks and the skarn deposits. Field studies reveal that the skarn zones are within volcano-sedimentary sequences and marble-schist units intruded by four distinct plutonic bodies: (1) Esendemirtepe diorite, (2) Koçak diorite, (3) Horoz granodiorite, and (4) Çifteköy monzogabbro. These rocks exhibit calc-alkaline, I-type, and metaluminous signatures, except for the Çifteköy monzogabbro, which shows I-type, tholeiitic, and alkaline characteristics. All the plutonic rocks associated with the skarn formation display steep LREE-enriched REE patterns with minor positive Eu anomalies (Eu/Eu* = 0.98–1.35), suggesting a subduction-related volcanic arc setting similar to other granitoids in the Ulukışla Basin. The Horoz skarn exhibits both endoskarn and exoskarn features, while the Esendemirtepe-Koçak deposit is characterized by typical exoskarn features. Dominant ore minerals in both skarn deposits include magnetite, hematite, sphalerite, chalcopyrite, and pyrite, with minor arsenopyrite, galena, and cobaltite. The mineral composition of the skarn also shows the dominance of Na-rich and Mg-rich minerals in both locations. The geochemical compositions of the I-type, metaluminous Esendemirtepe-Koçak, and Horoz plutonic rocks are compatible with Fe-Zn skarn type deposits based on the moderate MgO (0.36–4.44 wt.%) and K_2O (1.38–7.99 wt.%), and Rb/Zr and Sr/Zr ratios. They also show typical volcanic arc features, and the variation in various trace element concentrations shows similarity with Fe-Zn skarn type granitoids. These findings support a strong genetic relationship between the mineralization and the geochemical and mineralogical characteristics of the associated plutonic rocks.

Keywords: genetic link; I-type granitoids; petrogenesis; plutonic rocks; skarnization; skarn deposits; Fe-Zn mineralization; volcanic arc granites

1. Introduction

Skarn deposits are an important class of mineral deposits in Türkiye that formed between the Late Cretaceous and Oligo-Miocene period during the collision between the Afro-Arabian and Eurasian plates [1]. These deposits in Türkiye are mostly calcic exoskarns but sometimes occur as magnesian skarns with economic mineralization mainly restricted to the calcic exoskarns and some Fe-skarns hosted by endoskarns. There are many known and operating Fe-Pb-Zn deposits in the Taurus Mountains. In the Central Taurus Mountains, the main Fe-Zn skarn deposits are the Horoz, Esendemirtepe (Çiftehan, Niğde Province) and Karamadazi (Yahyali, Kayseri Province) deposits. These deposits have attracted the attention of several researchers in recent years, and many different ideas have been put forward regarding the origin of the deposits. Some of the researchers mentioned that the deposits are generally hosted in different stratigraphic units at different ages and are mostly epigenetic and sedimentary in origin [2]. Also, other authors working in the Central Taurus Mountains have proposed that the deposits in the region have a hydrothermal metasomatic origin and occur in a fault-controlled form and fill into karstic cavities (e.g., [3,4]).

It is estimated that the total reserve of the iron in the Fe-Zn skarn deposits in the Central Taurus Mountains is about 200,000 tonnes [5]. The endoskarn and exoskarn zones where the Fe-Zn skarn ore developed are in limestone/marble-granodiorite/volcanite contact, wherein the intrusions intersect the metacarbonate lithologies. The Fe-Zn skarns associated with granitoids in the Central Taurus Mountains, especially in the Niğde area, are the adakitic Horoz granitoids [6]. The exact age of the Horoz granitoids is still a controversy in the scientific discourse, though most authors have proposed an Early-Middle Eocene age (e.g., [6–8]). For instance, Ref. [7] reported a zircon U–Pb radiogenic age of 55 Ma for the Horoz granitoids, which is similar to the zircon U–Pb age of 54.74 $\pm$ 0.37 Ma reported by [9].

The granitoid plutons in the Niğde Province were emplaced in the eastern part of the Bolkar Mountains and in the valley where the Çiftehan village is located in Ulukışla District (Figure 1). In this area, there are several large- and small-scale mines but only a small number of them are currently under operation [10,11]. The geological [12–15], petrological [6–9,16,17], geodynamic and tectonic features [18–25], sediment and ore slag geochemical characteristics [26,27], and detailed studies on the mineral potential of the region [5,28–31] date back to the 1940s and still continue into the present day. However, the relationship between the Fe-Zn skarns and the associated granitoid plutons, and the possibility of identifying different styles of mineralization related to the granitoid emplacement, are not yet documented in the literature.

Studies on the petrogenetic characteristics of the intrusions in the Çiftehan (Ulukışla-Niğde) area and the skarn formation are lacking in the literature. In this regard, the fluid-aided mobility of elements at the contact between the intrusions and the volcano-sedimentary country rocks is not well understood. In addition, the relationship between the plutons and the associated Fe-Zn skarns, and the possibility of identifying different styles of mineralization related to the granitoid emplacement are not yet documented in the literature. Correlations between granitoid compositions and metal contents of the associated skarns have been reported elsewhere to provide vital constraints on the genetic relation between both. For instance, Ref. [32] analyzed the composition of the Evciler granitoid in Çanakkale, northwestern Türkiye, and found that its geochemical

characteristics closely resemble those of metasomatic zones in which the skarn deposits formed. This might indicate that both the emplacement of the granitoids and the skarn formation were contemporaneous from a common source. Similar observations were made in India [33], Mexico [34], Spain [35], Romania [36], Canada [37], Australia [38], Japan [39], and the USA [40]. Therefore, this study is aimed at investigating the geology, petrography, and whole-rock geochemistry of the skarns and associated granitoids in the Çiftehan (Ulukışla-Niğde) area, south-central Türkiye. The main objective is to constrain the petrogenesis of the granitoids and to establish the relationship between the metal contents in the skarns and the whole-rock geochemistry, degree of crystallization, and tectonic settings of the plutonic rocks. Overall, the present study will be the first detailed report of comparisons between the skarns and associated plutonic rocks in the Çiftehan (Ulukışla-Niğde) area, south-central Türkiye.

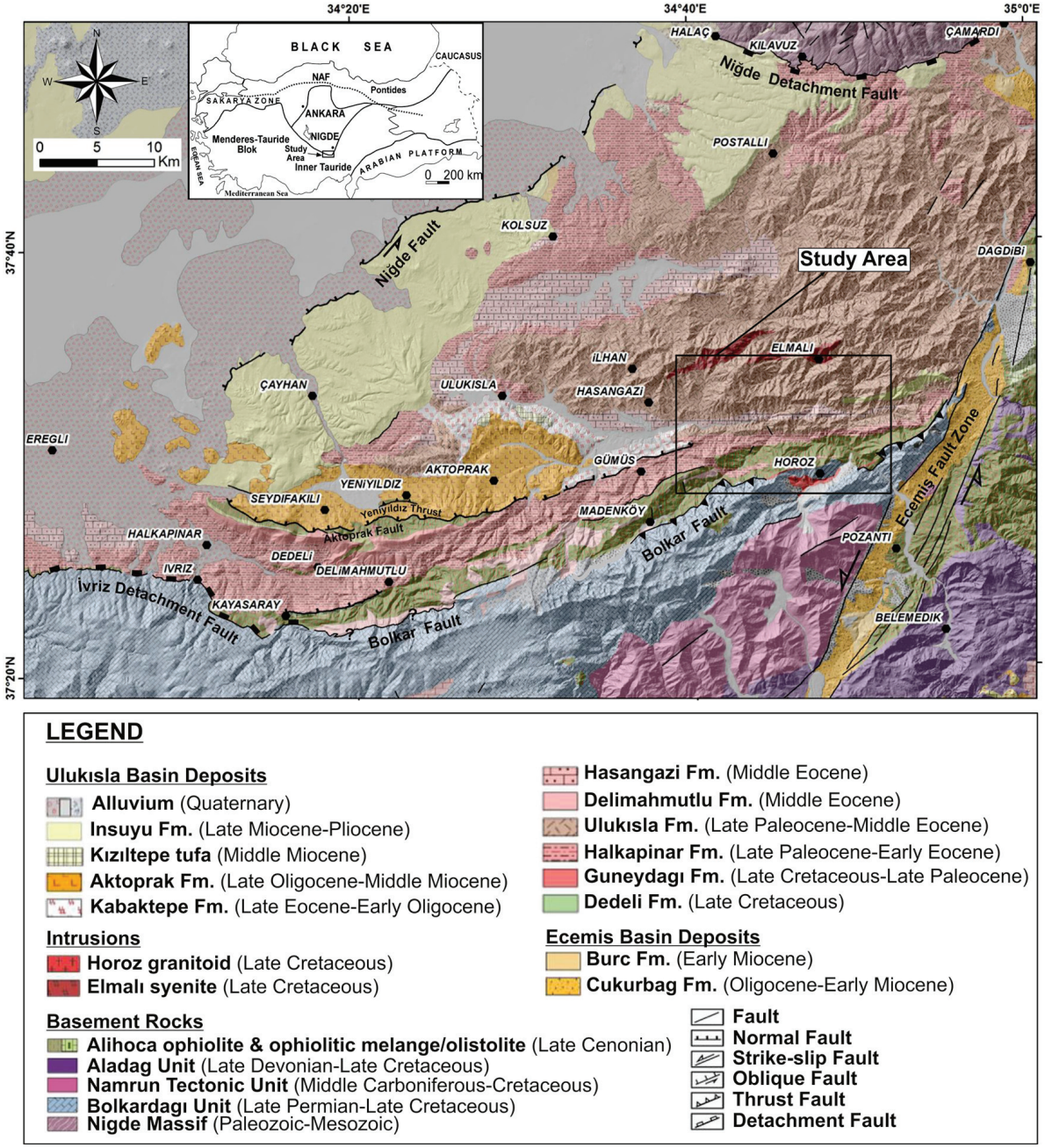


Figure 1. Geological map of the south of Central Anatolia, showing the rock types and formations in the study area (modified after [18]). The study area is indicated with a rectangle in the map.

2. Geological and Geodynamic Settings

The evolution of the Anatolian plate is related to tectonic regimes during the opening and closure of the Tethyan Ocean, which led to the development of paleo basins with different characteristics [18]. The Ulukışla Basin is one of the most important Late Cretaceous-Cenozoic basins in Central Anatolia. It is located in the southern fringe of Central Anatolia (Figure 1) and is geographically bordered to the north by the Niğde Massif, to the south by the Bolkar Mountains and the İvriz Detachment Fault, and to the east by the Aladağ Mountains and the Ecemiş Fault Zone [25,41].

A variety of rock types crop out in the area with age values mostly from Paleozoic to Quaternary. The basement rocks are composed of Late Permian to Late Cretaceous marble and schist belonging to the Bolkardagi Unit (Figure 1), which are then tectonically overlain by Late Cretaceous Alihoca ophiolite. The Alihoca ophiolite is adjacent to ophiolitic mélange made up of peridotite, gabbro, diabase, and diorite [42]. The Early-Middle Eocene adakitic Horoz granitoids intruded on the basement rocks near the Horoz stream [6]. The Cretaceous Kalkankaya Formation, which consists of limestone, sandstone, and shale, overlies the ophiolitic mélange and the basement rocks [26]. Quaternary alluvial deposits cover the Kalkankaya Formation and several units in the southwestern portion of the area (Figure 1). The volcano-sedimentary rocks in the region are approximately 5 km thick and are determined to be formed from the Late Cretaceous to Early Oligocene period [43], while volcanic rocks have a thickness of around 2 km [20]. Most of the volcano-sedimentary units formed in the Late Paleocene to Middle Eocene Ulukışla Formation; however, only sedimentary rocks are observed in the Middle Eocene Hasangazi Formation [26].

The volcanic rocks in the region consist of alkaline and potassic volcanic units. Alkaline volcanic rocks are present as pillow lavas and massive lavas, whereas the potassic volcanic rocks occur as dykes and massive lavas [43]. Most of the alkaline volcanic rocks are intercalated with sedimentary rocks and are intersected by the Upper Cretaceous Elmalı syenite (Figure 1).

Various ore deposits are found in the Ulukışla Basin within the Tauride belt in Türkiye. The primary mineral deposits in the area include Fe-Zn skarns at the Horoz granitoids and metacarbonate rocks interface, MVT- and CRD-type Pb-Zn and non-sulfide Zn deposits in carbonate rocks, podiform chromite in ophiolites, vein-type Sb-W-Hg-Au in the Niğde Massif, bauxite, Al and Fe-rich laterite, and Mn deposits [1,26,44–46]. Small-scale thrust faults greatly influence the rheology of the geological units and aid in ore settlement.

The Niğde Massif at the northern part of the Ulukışla Basin is predominantly composed of high-grade metamorphic rocks (quartzite, marble, and paragneiss) and ophiolites that are intruded on by slightly metamorphosed granitoids [47,48]. It is believed that the metamorphic rocks in the Niğde Massif, which are members of the Central Anatolian Crystalline Complex (CACC), were initially exposed in the late Cretaceous period and were exhumed prior to the end of the Maastrichtian period (e.g., [49,50]). Previous research works in the Niğde Massif have proposed that after the closure of the Neotethys Ocean during the late Cretaceous period, the massif was subjected to a different geodynamic evolutionary history when compared to the other parts of the CACC [19]. Moreover, Ref. [19] indicated that in the Oligocene-late Miocene, the Niğde Massif was exhumed under an extensional regime as a core complex with a low-angle normal fault trending from the southern to the northwestern fringes of the massif. This proposition that the Niğde Massif was exhumed as a core complex has largely been accepted but there are a lot of disagreements on the timing of the exhumation and the exact position of the low-angle normal fault that triggered the exhumation of the massif. For example, it has been proposed that the low-angle normal fault extended from the top to the northeastern part, which resulted in the exhumation of the massif in the Campanian-early Paleocene period [22,47]. Also,

other studies have suggested poly-burial exhumation episodes for the massif (e.g., [50–53]). Paleontological and geochronological data revealed that the first episode of exhumation occurred before the Eocene period [22] and in the Oligocene period, and reburial occurred at the eastern domain of the massif [53]. The second episode postdates the Oligocene period and may have occurred in the Miocene period [54].

In the southern fringe of the Ulukışla Basin, a fault developed along the northern margin of the Bolkar Mountains and is termed the "Bolkar Thrust Fault" [55]. It is along this fault that the rocks belonging to the Bolkar group were thrusted to fill up the Ulukışla Basin [18]. However, other studies have proposed that the fault in the northern margin of the Bolkar Mountains is actually a normal fault known as the "Bolkar Front Fault" [56]. Dilek et al. [56] mentioned that the Bolkar Front Fault is a high-angle normal fault that strongly contributed to the evolution of the Ulukışla Basin. This is consistent with the findings of [20,21], who further suggested that the normal fault facilitated the emplacement of ophiolites to the north of the Bolkar Mountains. However, more recent studies confirmed the earlier thrust fault hypothesis (e.g., [7,23,57]). Moreover, refs. [25,41] stated that the fault is rather a detachment type of fault that was active in the late Cretaceous-Eocene period and is termed the İvriz Detachment Fault, which is trending ENE–WSW and extending between the Bolkar Mountains and the Ulukışla Basin. This has since brought more understanding on the geological evolution of basins in Central Anatolia from a previous perception of collision-related basins to supradetachment basins.

The eastern fringe of the Ulukışla Basin features the left-lateral Ecemiş Fault Zone, one of the important active structures controlling the evolution of basins in Central Anatolia [58]. The Ecemiş Fault Zone was initiated in the late Eocene with geological offsets in the range of 60 $\pm$ 5 to 80 $\pm$ 10 km [59,60]. The fault kinematics suggest a transition from strike-slip during the middle-late Miocene period to transtensional and extensional in Pliocene-Quaternary period [24,61].

3. Materials and Methods

Field work for this study involved geological mapping, delineating the igneous plutons, the skarn, and contact with the carbonate rocks. The sampling traverses were carried out across the skarn and the host volcano-sedimentary rocks. During the field studies, more than 200 samples were collected from the various rocks in the Esendemirtepe and Horoz areas. Representative samples (n = 30) were selected for thin section preparation to help in understanding the mineral paragenetic sequence. A total of eleven (11) samples were selected and pulverized in an electric agate mortar for whole-rock geochemical analysis. The pulverized samples were analyzed for major elements and selected trace elements by XRF technique at the Central Laboratory of Niğde Ömer Halisdemir University, Türkiye. Some of the powders were analyzed for additional trace and rare earth element (REE) compositions by ICP-MS, following fusion with lithium metaborate/tetraborate, at the Department of Geological Engineering, Istanbul Technical University, Türkiye.

The mineralogical composition of the skarns was determined from twenty-two samples by a D8 ADVANCE BRUKER X-ray diffractometer (XRD) (Billerica, MA, USA) in the Central Research Laboratory of Niğde Ömer Halisdemir University. The XRD instrumentation comprised a theta with a copper sealed tube X-ray source producing Cu Kα radiation at a wavelength of 1.5406 Å from a generator operating at 40 kV and 40 mA. The X-ray energy range of operation was 3–30 keV with a detection limit of ~1% by volume. The XRD data were collected over a 2θ range of 2° to 70°, and the resulting diffraction patterns were identified and indexed with the aid of X'Pert HighScore Plus v. 3.0 software for mineral identification and semi-quantitative mineral content analysis.

4. Results

4.1. Geological, Stratigraphic, and Field Relations

The study area is part of the Late Cretaceous-Tertiary Ulukışla Basin, which developed in different tectonic units (Figure 2). The area is observed in three sections (southern, middle, and northern) that are distinct from stratigraphical and lithological points of view (Figure 2). Whilst the southern section consists of sedimentary rocks that are intruded on by some granitoids and dykes, which developed on the Bolkar Mountain Group, the northern section consists of volcano-sedimentary and plutonic rocks, which developed above the Niğde Group (Figure 2). Also, the middle section developed on the Alihoca ophiolite complex in the form of volcano-sedimentary rocks (Figure 2). The plutons related to the skarn mineralization were emplaced in the southern and middle sections. They are located at the eastern fringe of the Bolkar Mountains in the Niğde Province of south-central Türkiye. The Bolkar Mountains are contiguous to the Inner Taurides Suture Zone sandwiched between the Taurides and the CACC [8]. Details of the southern and middle sections, where the skarn mineralization occurs, are given in the following Sections.

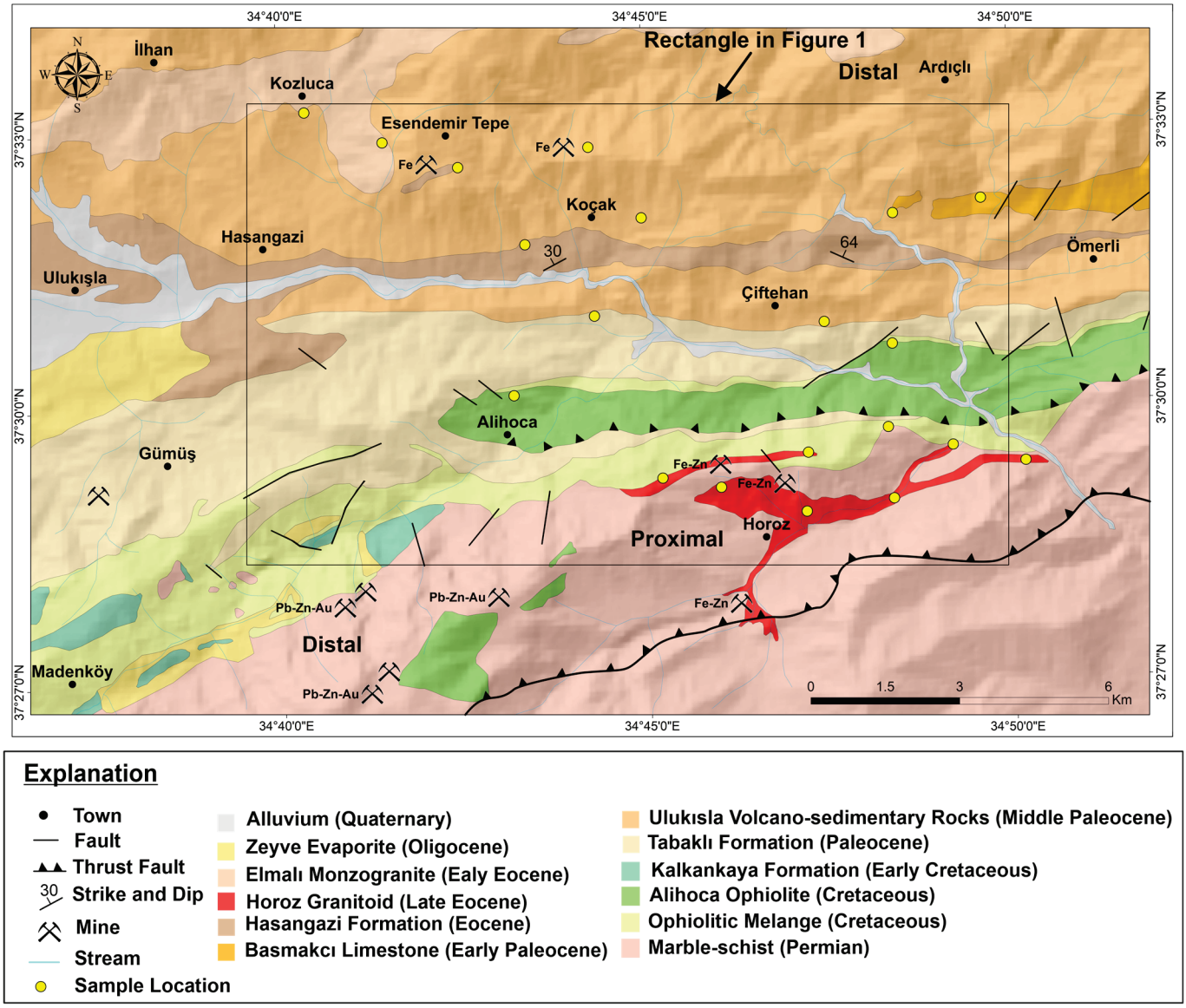


Figure 2. Geological and structural map of the Çiftehan (Ulukışla-Niğde) area, south-central Türkiye (modified after [26]).

4.1.1. Southern Section

The oldest lithological units in the area form the heights of the Bolkar Mountain with an anticlinal architecture. These units are composed of metamorphosed Permian-Triassic platform carbonates with intercalations of siliciclastic rocks, which were later intruded by the ENE–WSW-trending sill-like pluton known as the Horoz granitoid in the Horoz village with the associated economic skarn mineralization (Figure 2). Locally, the Horoz granitoid is a shallow-seated intrusion that crops out in the Horoz Valley towards the Horoz village. It is proposed that the Horoz granitoid was emplaced in the Early Eocene period (56.1 Ma) [7]. The Horoz granitoid appears as a light-colored medium-fine-grained intrusion with some chilled margins with the country rocks [8]. It contains mafic microgranular enclaves, indicative of mingling during the evolution of the felsic magma. Previous studies suggest that the granitoid can be classified into two different groups, granodiorite and felsic granite, which have a gradational contact [8]. Locally, the felsic granite is relatively fine-grained, fractured, and altered with fewer enclaves than the granodiorite.

The Horoz granitoid pluton intrudes marbles belonging to the Bolkar Mountain units, which are also intruded by tonalitic and dioritic dykes and some schist-like units (Figure 2). According to [8], aplite veins crosscut the unit. The entire unit is overlain by the Upper Cretaceous Alihoca Ophiolites (Figure 2), which have been thrusted to form an ophiolitic mélange. An erosional episode postdates the thrusting event with the Cretaceous Kalkankaya Formation unconformably overlying the ophiolitic unit. This formation generally consists of limestone and conglomerate (Figure 3). It was first named by [13] according to Kalkankaya Hill southwest of Alihoca village. Later, Refs. [55,62] also adopted the same name. The conglomerate level at the base is red and grain supported. The ophiolitic rocks cover the recrystallized limestone pebbles. The pebbles are generally medium sized and not very rounded. The limestone levels of the formation are light gray, medium-thick bedded (Figure 4a), and contain abundant Loftusia and rudist crustal limestone. The formation unconformably overlies the Bolkardağı Group, which contains marble-schist-like rocks interbedded with the Horoz granitoids (Figure 4b–d). There is also an aplite dyke intruding the Bolkardağı Group towards the Kalkankaya units (Figure 4e). Overlapping units known as the Madenköy ophiolitic mélange also underlie the formation after an erosion zone. However, the Madenköy ophiolitic mélange is mainly confined to the eastern boundary of the Ulukışla Basin and is therefore not part of the study area. The Yağbağ Formation conglomerates between Kevenniboyun and Sivri Tepe on the road to Horoz village also belong to this formation. The Kalkankaya Formation is about 300 m thick. Minor Luftusia and *Omphalocyclus* sp. obtained from the limestone levels indicate that the age of the unit is Late Maastrichtian [15]. However, the fauna of Miliolidae, Microcodium, and *Mississipina* sp. indicate Late Maastrichtian-Early Paleocene age [15]. On this basis, the formation may have been deposited under shallow shelf conditions.

The Yağbağ Formation consists of limestone, including sandy varieties (Figure 3). Yağbağ, located in the southwestern part of Alihoca village, is named after the Yağbağ stream [15]. The formation is mainly represented by black, thin-medium bedded, sometimes sandy, bituminous limestone. It occasionally includes black clayey limestone interbeds and brecciated dolomite (Figure 4f). The formation unconformably overlies the Madenköy ophiolitic mélange and is transitional with Saçkayası limestone on top. Its maximum thickness is 50 m. *Globorotallia* sp. and *Globigerina* sp. fauna obtained from the clayey limestone levels indicate Paleocene age [15]. It is likely that the formation was deposited beneath these features.

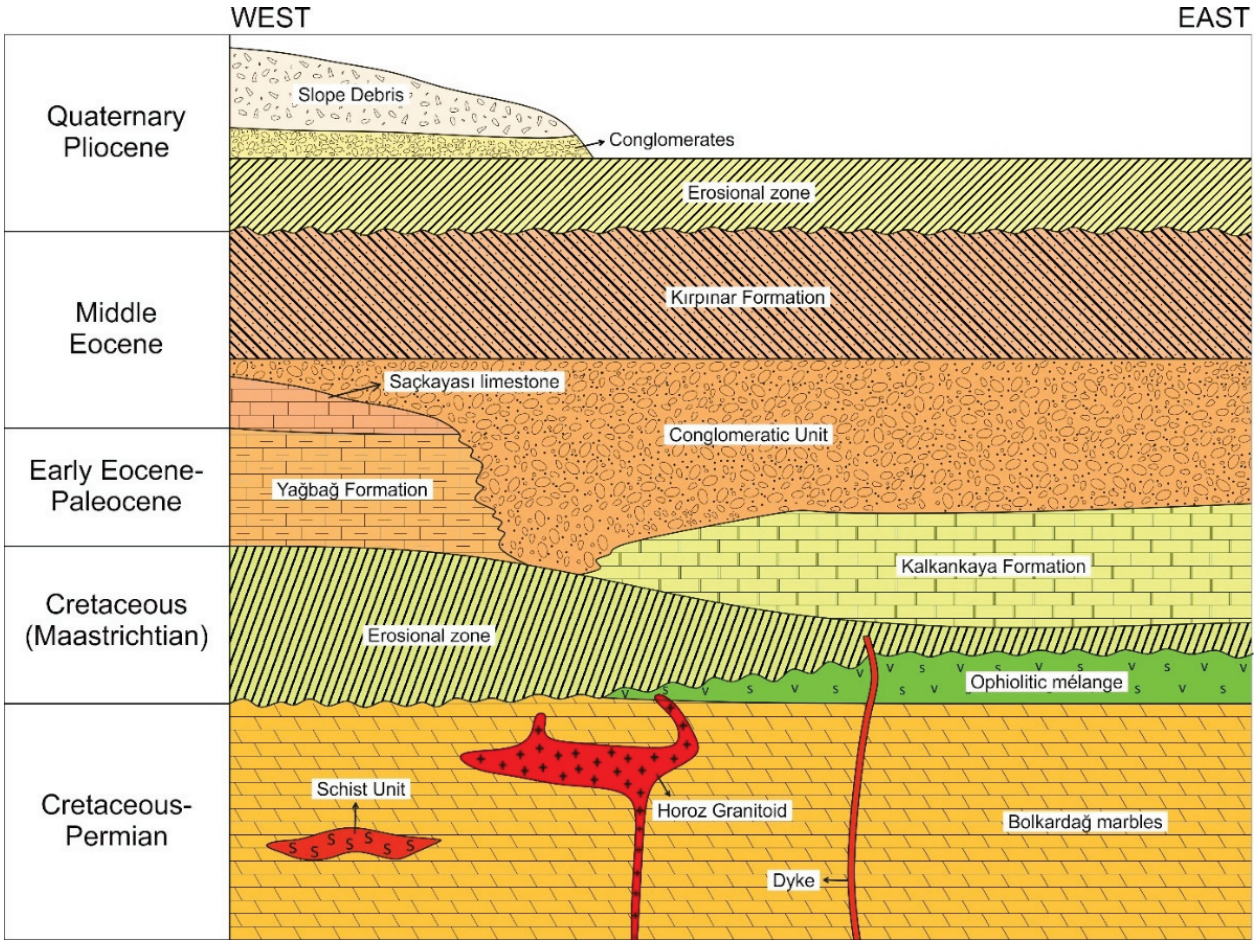


Figure 3. Schematic columnar section of the southern section of the study area (modified from [15]).

The Geyik Pinar conglomeratic unit is the conjugate unit of the Yağbağ Formation and consists entirely of conglomerate (Figure 3). It also contains small amounts of ophiolitic rock pebbles in a calc-silicate unit (Figure 4g). The pebbles are sub-angular and poorly sorted. The cracks in the calc-silicate unit are filled with sphalerite ore (Figure 4h). Previously, Ref. [55] included the Geyik Pinar conglomeratic unit in the Halkpinar Formation, but [15] separated it as a member of the Yağbağ Formation. Its thickness is a maximum of 100 m. It is transitional with the Kirkpinar Formation and was probably deposited under riverine conditions.

The Saçkayası limestone unit (Figure 3) is named after Saçkaya Hill in the north of Madenköy. It is also a member of the Yağbağ Formation. However, it appears to be a later unit. It consists of thin-medium-bedded claystone and alternating sandstone. The middle level consists of off-white, thick-bedded sandstone and abundant fossils. The upper level is represented by massive limestone. The unit is about 20 m thick and was probably deposited in a shallow shelf environment.

The Kırkpınar Formation consists of conglomerate, limestone and sandstone–cla–stone succession (Figure 3). It is named after the Kırkpınar Spring southwest of Madenköy. Demirtaşlı et al. [55] considered the unit as a part of the Halkpinar Formation. The formation consists of limestone at the lower levels and sandstone-shale succession at the upper levels. The limestone level is generally thin to medium-bedded. The upper-level units are laminated and contain sandstone lenses showing channel geometry. Within the sandstones, ophiolitic rock fragments and claystone forming fault breccia within the formation are observed (Figure 4h). The Kırkpınar Formation, which is transitional with

the underlying Yağbag Formation, is 350–400 m thick. According to the fauna found in it, the formation is Lutesian in age and was deposited in a wave base environment [15].

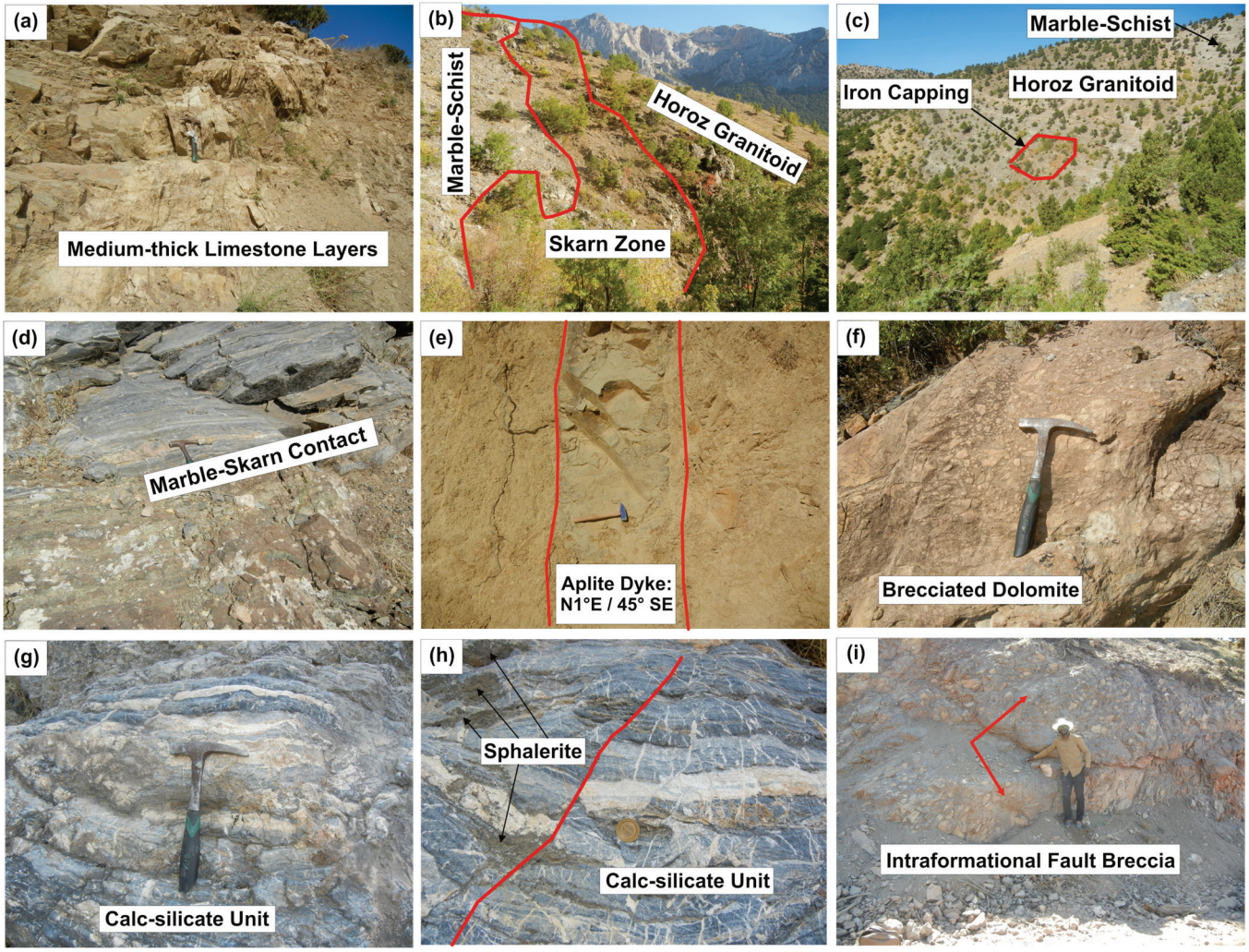


Figure 4. Field photographs of some outcrops in the southern part of the study area, (**a**) limestone layers of the Kalkankaya Formation, (**b**–**d**) the skarn zone observed at the contact of Horoz granitoid and marble-schist units, (**e**) aplite dyke intruding into Kalkankaya Formation, (**f**) brecciated dolomite in the Yağbağ Formation, (**g**) conglomeratic levels with ophiolitic rock pebbles in a calc-silicate unit, (**h**) sphalerite in fractures adjacent to basal calc-silicate unit, and (**i**) intraformational fault breccia in the Kirkpinar Formation.

4.1.2. Middle Section

The middle section of the Esendemirtepe-Koçak area predominantly consists of volcano-sedimentary formations intruded on by igneous rocks, dated from the Late Cretaceous to Middle Eocene (Figure 5). The basement begins with the Alihoca Ophiolitic Complex, including quartz porphyry and dioritic intrusions associated with skarn mineralization. These units are overlain by the Kırkgeçit Formation, which comprises limestone, sandstone, conglomerate, shale, and basalt [15,55].

The Kırkgeçit Formation, named after the Kırkgeçit Stream, includes limestone, sandstone–shale alternations, and basaltic units. Discontinuous limestone sections dominate from the northeastern border to the southwest (Figure 6a). The Karakaya basaltic unit, composed of pillow lavas and flow breccia, overlies the Alihoca Ophiolitic Complex and transitions into the Çiftehan Unit. Fossil evidence suggests a Maastrichtian age [15,55].

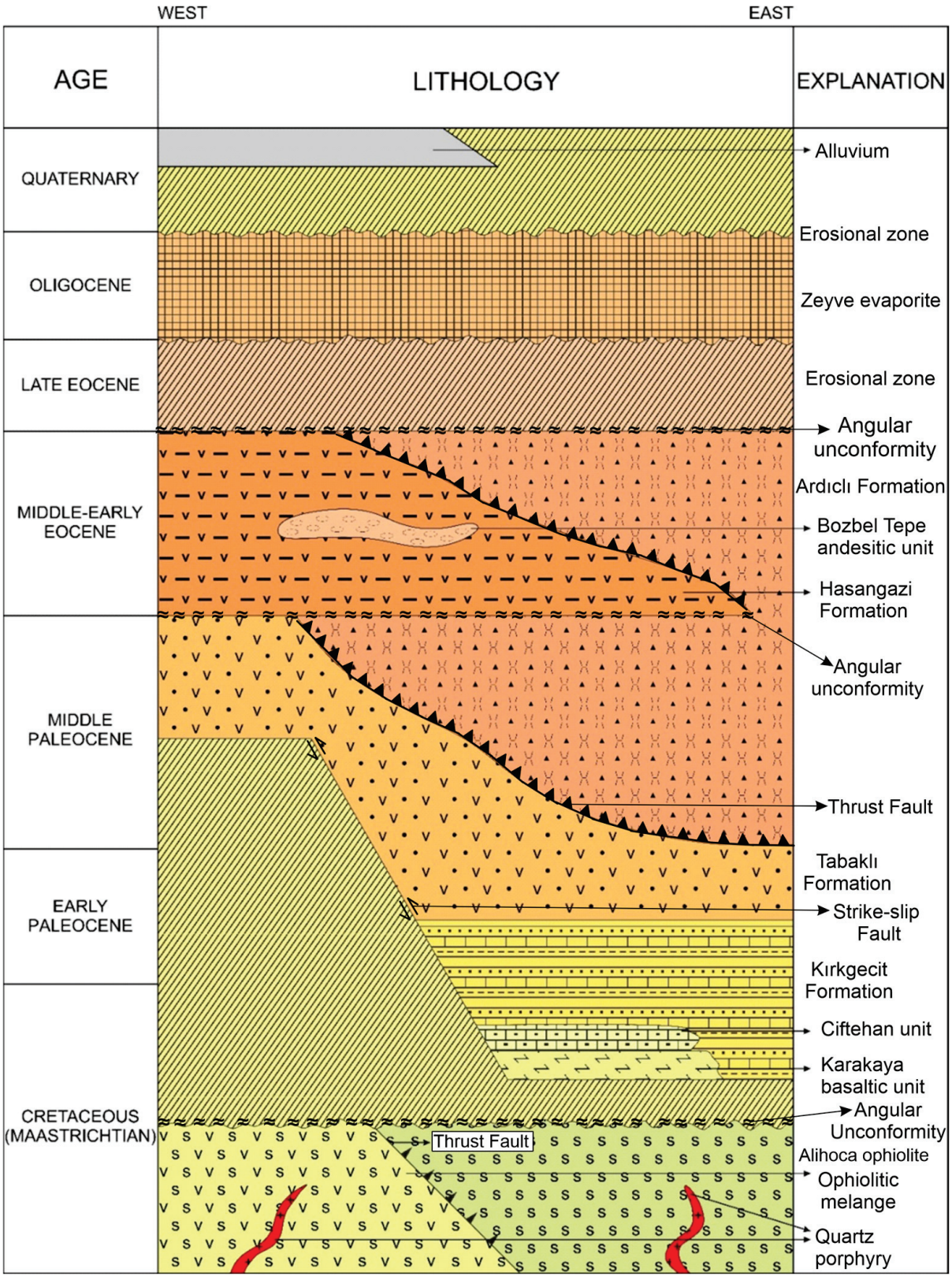


Figure 5. Schematic columnar section of the middle section of the study area (modified from [15]).

The Tabaklı Formation, named after the Tabaklı village, contains sandstone and limestone intercalations with planktonic foraminifera such as *Abathomphalus mayaroensis* and *Morozovella uncinata*. This formation, deposited under wave-base conditions, is Early-Middle Paleocene in age and transitions into the Hasangazi Formation [15].

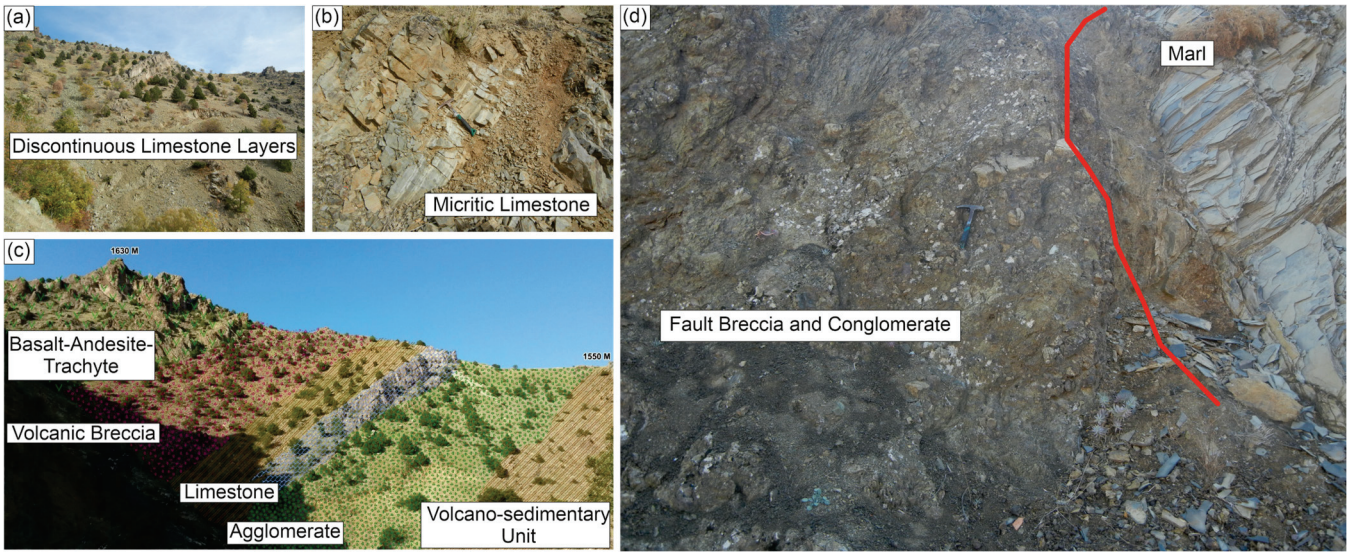


Figure 6. Field photographs of some outcrops in the middle section, (**a**) discontinuous limestone layers of the Kirkgeçit Formation, (**b**) beige and reddish micritic limestones of the Çiftehan Unit, (**c**) basalt-andesite-trachyte, agglomerate, and limestone of the Tabaklı Formation interbedded with volcano-sedimentary units of the Ulukışla Formation, and (**d**) fault breccia, conglomerate, and marl interbeds of the Ardıçlı Formation.

The Hasangazi Formation features sandstone–shale alternations interspersed with mudstones and conglomerates. Missing Bouma sequences and fossil records indicate a Middle-Early Eocene (Lutetian) age. The Bozbel Tepe andesitic unit, part of this formation, contains red micritic limestone fragments and continues with the Ardıçlı Formation [15,55].

The Ardıçlı Formation, characterized by andesite, trachyandesite, and pillow lavas, reflects Early-Middle Paleocene to Middle-Early Eocene seafloor development. Fossil micritic limestone fragments suggest a marine setting [15].

The Zeyve Evaporite, deposited after erosion, consists of gypsum, sandstone–mudstone, and anhydrite alternations. It shows angular unconformity with the underlying Hasangazi Formation and dates back to the Oligocene. Quaternary alluvium caps the sequence in this section of the study area [14,63].

4.2. Petrographic Characteristics of Plutonic Rocks

4.2.1. Monzogabbro

Monzogabbroic rocks are widespread in the Çifteköy village. They exhibit a granular (holocrystalline) texture containing biotite phenocrysts and some undifferentiated opaque minerals (Figure 7a,b). The minerals are partially altered so that the feldspars cannot be recognized. Plagioclase, orthoclase, and biotite minerals are highly altered due to alkaline metasomatism. Therefore, calcitization, epidotization, and argillization are very intense, indicating that calcic alteration developed over sodic alteration (Figure 7a,b).

4.2.2. Granodiorite

Granodiorites are found only in the Horoz region in the study area. They exhibit granular (holocrystalline) textures containing quartz, plagioclase, orthoclase, microcline, amphibole, and biotite phenocrysts (Figure 7c). They also show microcrystalline porphyritic textures, but locally glomeroporphyric textures are common. They contain phenocrysts of quartz, plagioclase, amphibole, biotite, and muscovite (Figure 7d,e). The minerals are partially altered towards the skarn zone, such that the feldspar minerals show intense epidotization. Wavy extinction is common in quartz minerals (Figure 7c–e). Lattice twinning is evident in microcline (Figure 7c), and zoning is observed in plagioclase (Figure 7d).

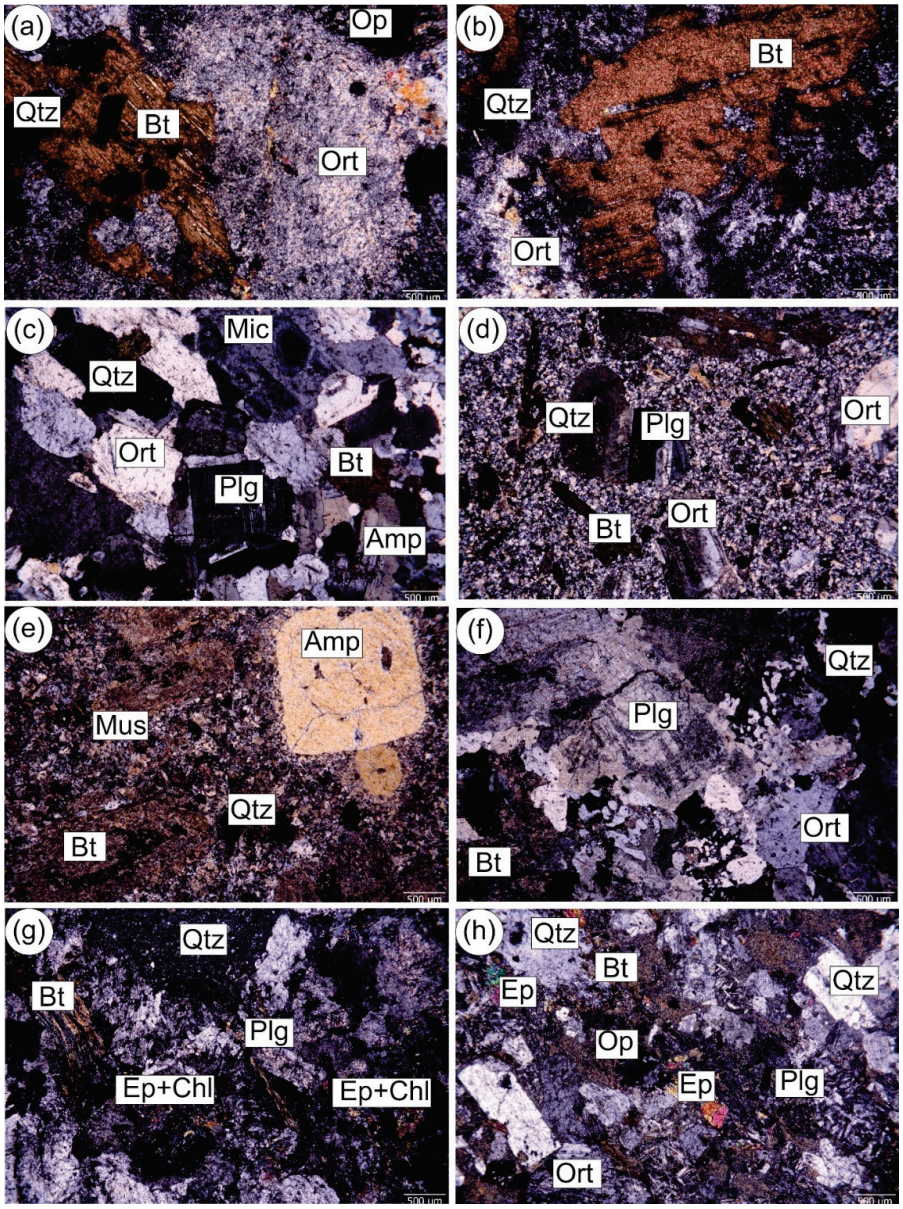


Figure 7. Photomicrograph images of the plutonic rocks in the Horoz and Esendemirtepe-Koçak areas; (**a**,**b**) Çifteköy monzogabbro showing a granular (holocrystalline) texture with biotite phenocrysts; (**c**) Horoz granodiorite (H003) showing a granular (holocrystalline) texture with quartz, plagioclase, orthoclase, microcline, amphibole, and biotite phenocrysts; (**d**) Horoz granodiorite (H016) displaying microcrystalline porphyritic, and locally glomeroporphyritic textures with quartz, plagioclase, and biotite phenocryst; (**e**) Horoz granodiorite (H005) displaying microcrystalline and porphyritic textures with phenocrystic quartz, muscovite, biotite, and amphibole; (**f**) Horoz granodiorite (H019) showing granular and myrmekitic textures with quartz, orthoclase, biotite, and plagioclase as the dominant phenocrysts; (**g**) Esendemirtepe diorite (ED002C) displaying microcrystalline and porphyritic textures, dominated by quartz, biotite, and plagioclase; and (**h**) Esendemirtepe diorite (ED002A) displaying microcrystalline and porphyritic textures with quartz, orthoclase, plagioclase, biotite, epidote, and opaque minerals (Qtz = Quartz; Plg = Plagioclase; Ort = Orthoclase; Mic = Microcline; Bt = Biotite; Mus = Muscovite; Amp = Amphibole; Ep = Epidote; Chl = Chlorite; Op = Opaque).

Other granodiorites in the Horoz area exhibit hypidiomorphic granular and myrmekitic textures with quartz, orthoclase, biotite, and plagioclase as the dominant phenocrysts (Figure 7f). Plagioclase typically shows polysynthetic twinning and zoning, while quartz shows undulose extinction (Figure 7f), indicating stages of deformation. Plagioclase

feldspar is partially altered around the skarn zone with calcitization and silicification as common types of alteration associated with the granodiorite.

4.2.3. Diorite

Among the intrusive rocks surfacing in the study area, diorites are mostly located in the Esendemirtepe-Koçak region. They exhibit microcrystalline and porphyritic textures where quartz, orthoclase, plagioclase, biotite, epidote, chlorite, and undifferentiated opaque minerals are the dominant minerals (Figure 7g,h). Plagioclase feldspar minerals are transformed into epidote (Figure 7g) during the skarnization process. Zonation is observed in places in plagioclase (Figure 7h). Sericitization and calcitization are also common (Figure 7h).

Overall, the microscopic images of the plutons in the region show that porphyritic textures are common and thus, it can be said that the plutons crystallized in a shallow environment.

4.3. Whole-Rock Geochemical Constraints

4.3.1. Major Element Variation and Rock Classification

The different types of plutons were distinguished by field observations and petrographic studies as monzogabbro, granodiorite, and diorite. Results of the whole-rock geochemical analysis of the plutonic rocks are presented in Table 1. The monzogabbro displays major element variation in SiO_2 (40.0–40.5 wt.%), Al_2O_3 (18.8–18.9 wt.%), Fe_2O_3 (13.9–14.9 wt.%), CaO (10.2–11.3 wt.%), MgO (4.14–4.49 wt.%), Na_2O (1.50–1.71 wt.%), K_2O (1.96–2.75 wt.%), MnO (0.07–0.07 wt.%), TiO_2 (1.84–2.16 wt.%), P_2O_5 (1.15–1.26 wt.%), and Cr_2O_3 (0.00–0.01 wt.%) (Table 1). The granodiorite also displays major element variations in SiO_2 (67.6–71.2 wt.%), Al_2O_3 (13.8–15.7 wt.%), Fe_2O_3 (2.15–4.83 wt.%), CaO (1.85–3.33 wt.%), MgO (0.36–0.60 wt.%), Na_2O (3.02–4.05 wt.%), K_2O (2.68–4.85 wt.%), MnO (0.01–0.02 wt.%), TiO_2 (0.18–0.33 wt.%), P_2O_5 (0.11–0.19 wt.%), and Cr_2O_3 (0.00–0.01 wt.%) (Table 1). Similarly, the diorite displays major element variations in SiO_2 (55.6–60.5 wt.%), Al_2O_3 (16.7–18.5 wt.%), Fe_2O_3 (5.08–8.69 wt.%), CaO (1.95–4.27 wt.%), MgO (0.95–2.80 wt.%), Na_2O (3.66–5.24 wt.%), K_2O (1.38–6.66 wt.%), MnO (0.02–0.09 wt.%), TiO_2 (0.50–0.93 wt.%), P_2O_5 (0.13–0.42 wt.%), and Cr_2O_3 (0.00–0.02 wt.%) (Table 1). This indicates that the plutons are fairly enriched in both alkali elements and ferromagnesian oxides, which is consistent with their mineralogy. The granodiorite and diorite are more abundant in alkali elements than the monzogabbro, whereas the monzogabbro contains more ferromagnesian oxides (Table 1). Also, the diorite is slightly more enriched in alkali elements than the granodiorite (Table 1). The Na_2O contents correlate positively with increasing silica (Figure 8a,b), whereas the K_2O, Al_2O_3, Fe_2O_3, CaO, MgO, TiO_2, and P_2O_5 contents correlate negatively with increasing silica content (Figure 8c–h). The major element variation diagrams also reveal that the Al_2O_3, Fe_2O_3, CaO, MgO, TiO_2, and P_2O_5 values appear to be more depleted in the granodiorite and diorite than in the monzogabbro (Figure 8a–h).

The major element compositions of most plutons associated with the skarn deposits indicate calc-alkaline affinities but the monozogabbro shows tholeiitic affinity in the [64] classification diagram (Figure 9a). All the studied plutons plot as two distinct groups in the AFM diagram [64]. The monzogabbro plots in the high Fe_2O_3 (Figure 9a) and low SiO_2 fields (Figure 9b), whereas the granodiorite and diorite plot in the moderate-to-high total alkali field (Figure 9a) and high SiO_2 fields (Figure 9b). This trend is similar to granitoids from the Ulukışla-Niğde area (Figure 9b) [7,16,17,65]. Also, on the Al-saturation index diagram of [66], the studied plutonic rocks all have metaluminous compositions except for the Koçak diorite and one sample from the Horoz granodiorite, which plots in the peraluminous field (Figure 9c).

Table 1. Whole-rock geochemistry of plutonic rocks in the Çiftehan (Ulukışla-Niğde) area, south-central Türkiye (ND = Not Detected).

Sample No.	C1	C3	H3B	H16	H19	KE1	EM13	EM10	E4B	ED2A	ED2C
Rock Name	**Çifteköy Monzogabbro**		**Horoz Granodiorite**			**Koçak Diorite**		**Esendemirtepe Diorite**			
Major elements (wt.%)											
SiO_2	40.5	40.0	71.0	67.6	71.2	56.4	59.9	56.4	60.5	57.8	55.6
Al_2O_3	18.9	18.8	15.7	15.2	13.8	17.8	16.7	17.2	17.2	18.5	18.5
Fe_2O_3	13.9	14.9	1.63	4.83	2.15	8.69	7.12	8.04	5.08	6.13	6.19
CaO	10.2	11.3	2.93	3.33	1.85	4.27	1.95	3.33	2.11	2.73	3.13
MgO	4.49	4.14	0.42	0.60	0.36	2.80	0.95	2.19	1.44	2.22	1.86
Na_2O	1.71	1.50	4.05	3.42	3.02	4.61	5.24	4.95	4.71	4.16	3.66
K_2O	2.75	1.96	2.68	3.11	4.85	2.13	3.96	1.38	5.18	4.58	6.66
MnO	0.07	0.07	0.02	0.02	0.01	0.05	0.06	0.02	0.04	0.09	0.09
TiO_2	1.84	2.16	0.33	0.29	0.18	0.66	0.50	0.76	0.90	0.77	0.93
P_2O_5	1.15	1.26	0.18	0.19	0.11	0.19	0.13	0.20	0.30	0.36	0.42
Cr_2O_3	0.01	0.00	0.01	0.00	0.01	0.01	0.00	0.00	0.01	0.02	0.01
LOI	3.50	2.29	0.84	1.15	2.30	2.03	2.95	3.82	1.83	1.90	1.95
Total	99.0	98.4	99.8	99.7	99.8	99.7	99.4	98.3	99.3	99.2	99.1
Trace elements (ppm)											
Cr	68.4	26.0	34.2	27.4	54.8	34.2	27.4	27.4	34.2	130	82.1
Ni	39.3	29.8	23.6	47.1	7.86	15.7	15.7	7.86	15.7	62.8	23.6
Pb	27.9	11.8	10.2	9.29	ND	ND	27.9	9.29	9.29	9.29	9.29
Cu	7.99	8.79	7.99	7.99	24.0	104	31.9	39.9	31.9	16.0	7.99
Mn	531	568	157	164	106	393	475	147	280	702	678
V	448	482	44.8	28.0	39.2	168	33.6	140	84.0	140	118
Ga	13.1	13.0	10.1	11.8	7.50	13.5	11.8	13.0	12.8	11.1	12.9
Rb	99.1	79.3	60.0	71.8	113	39.5	102	48.3	104	135	154
Pd	0.02	0.07	0.08	0.01	0.01	0.02	0.02	0.06	0.02	0.02	0.02
Rh	0.24	0.24	0.01	0.01	ND	0.02	ND	0.01	ND	0.04	0.01
In	0.00	0.00	0.00	0.00	0.00	0.02	0.02	0.08	0.00	0.00	0.05
Cs	3.17	4.30	0.53	0.56	3.02	0.68	0.84	3.21	0.49	2.68	0.86
Tl	0.47	0.42	0.07	0.22	0.26	0.16	0.69	0.23	0.45	0.78	0.74
Zr	133	112	111	118	59.2	81.4	355	81.4	311	185	185
Y	19.4	26.4	17.3	13.3	10.9	12.1	19.0	18.7	21.0	17.0	21.0
Th	8.26	12.0	13.7	9.72	14.9	3.14	35.0	2.12	33.7	19.6	23.3
U	1.39	2.16	3.66	3.35	3.10	0.80	6.32	0.31	3.62	1.86	2.65
Hf	3.05	15.9	0.79	1.73	0.56	0.21	5.61	0.17	3.28	2.06	2.53
Nb	8.50	4.30	7.70	10.5	6.60	10.9	5.80	4.86	8.30	5.95	8.70

Table 1. *Cont.*

Sample No.	C1	C3	H3B	H16	H19	KE1	EM13	EM10	E4B	ED2A	ED2C
Rock Name	**Çifteköy Monzogabbro**		**Horoz Granodiorite**			**Koçak Diorite**	**Esendemirtepe Diorite**				
Rare earth elements (ppm)											
La	63.1	68.4	19.9	113	20.7	11.9	88.0	11.4	123	87.2	109
Ce	138	148	44.0	160	39.8	24.5	157	24.9	232	158	209
Pr	17.1	18.5	5.25	5.18	4.22	2.93	16.0	3.24	25.0	17.2	22.8
Nd	65.3	72.0	18.6	19.4	15.2	11.9	50.1	14.2	87.8	61.4	75.7
Sm	12.6	12.6	3.54	3.30	2.69	2.81	7.57	3.38	14.15	9.88	13.6
Eu	3.29	4.11	1.01	0.95	0.80	1.01	2.11	1.29	4.22	3.55	4.58
Gd	8.36	9.99	2.80	2.65	2.01	2.57	5.17	3.70	8.52	6.56	8.42
Tb	1.09	1.33	0.46	0.44	0.37	0.35	0.73	0.57	1.07	0.89	1.13
Dy	4.85	6.12	2.91	2.21	2.31	1.97	3.97	3.50	4.88	3.92	5.18
Ho	0.82	0.91	0.52	0.44	0.34	0.41	0.74	0.68	0.79	0.68	0.75
Er	2.03	2.75	1.65	1.61	1.09	1.30	2.34	2.17	2.49	1.95	2.39
Tm	0.16	0.21	0.18	0.13	0.10	0.15	0.27	0.22	0.24	0.11	0.25
Yb	1.42	1.94	1.60	1.51	1.50	1.32	2.12	1.90	1.81	1.44	1.65
Lu	0.20	0.31	0.18	0.23	0.19	0.15	0.32	0.27	0.28	0.17	0.22
∑REE	318	347	103	311	91	63	336	71	506	353	455
Eu/Eu*	0.98	1.12	0.98	0.98	1.05	1.15	1.03	1.12	1.17	1.35	1.31
$(La/Yb)_N$	27.4	21.7	7.66	46.1	8.50	5.55	25.6	3.70	41.9	37.3	40.7
$(Gd/Yb)_N$	4.32	3.78	1.28	1.29	0.98	1.43	1.79	1.43	3.45	3.34	3.74
$(Ce/Yb)_N$	23.2	18.2	6.55	25.2	6.32	4.42	17.6	3.12	30.5	26.1	30.2

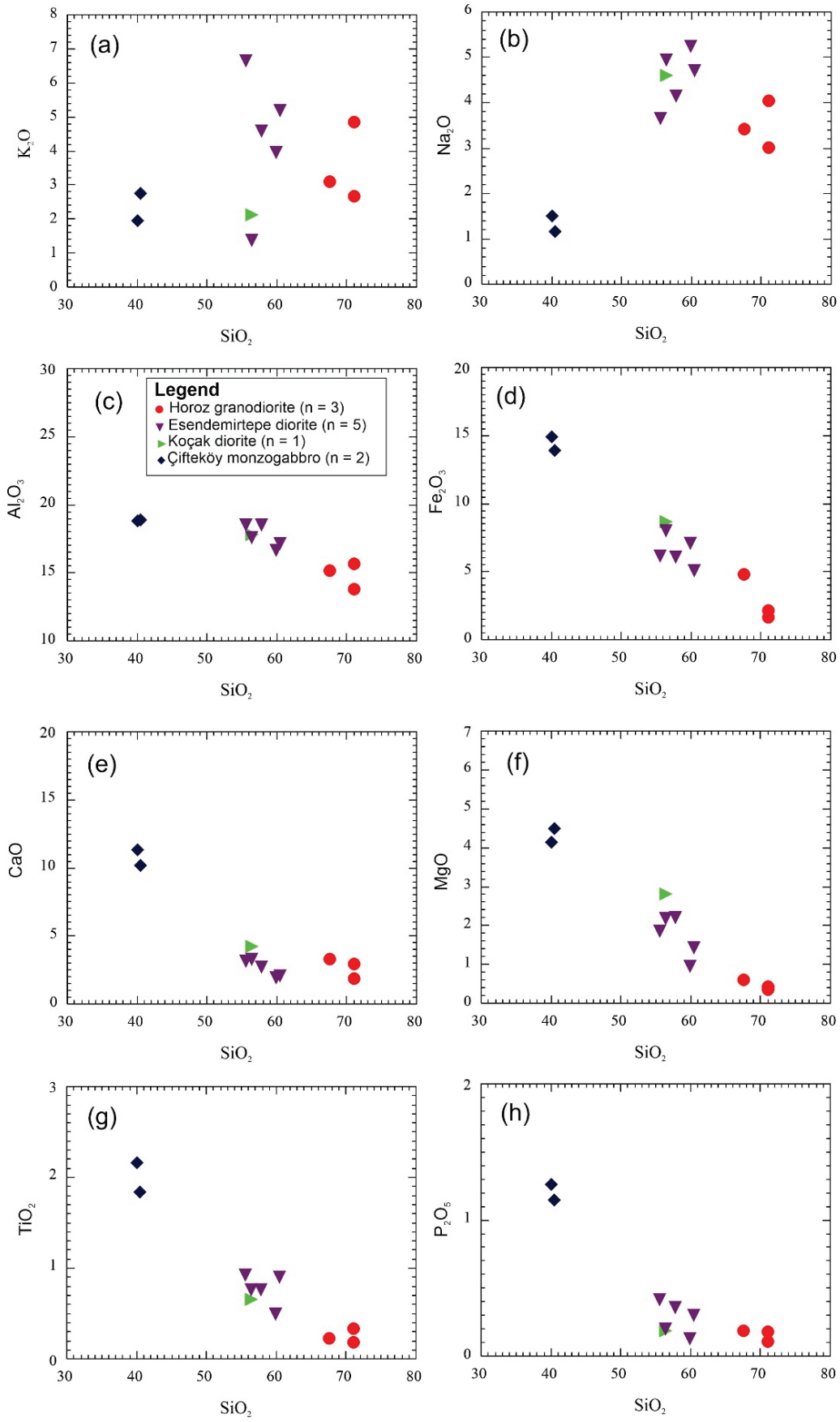


Figure 8. Major element variation diagrams for the plutonic rocks (**a**) K_2O versus SiO_2, (**b**) Na_2O versus SiO_2, (**c**) Al_2O_3 versus SiO_2, (**d**) Fe_2O_3 versus SiO_2, (**e**) CaO versus SiO_2, (**f**) MgO versus SiO_2, (**g**) TiO_2 versus SiO_2, and (**h**) P_2O_3 versus SiO_2.

In this study, granite discrimination diagrams were used to interpret the geochemical characteristics of monzogabbro, diorite, and granodiorite, despite their compositional differences, in order to provide a comparative framework for understanding their petrogenetic relationships. While granite diagrams are traditionally designed for felsic rocks and may not fully capture the geochemical behavior of mafic rocks like monzogabbro, their use here is justified by the need to evaluate all three rock types within a unified geochemical context. This approach allows for a clearer visualization of magmatic differentiation trends and potential genetic links among the rocks. The authors acknowledge the limitations of applying felsic-based diagrams to mafic compositions; however, by normalizing the data and interpreting the results cautiously, these diagrams offer valuable comparative insights, especially when the rocks are part of the same intrusive suite or magmatic system. Therefore, in the classification diagram of Winchester and Floyd [67], the plutonic rocks in the study area form a continuous spectrum from the field of felsic rocks (granodiorite) to the field of mafic-ultramafic plutonic rocks (Figure 9d). The Horoz granodiorite, Esendemirtepe diorite, and Koçak diorite all plot in the field of felsic rocks, whereas the Çifteköy monzogabbroic rocks characteristically plot in the field of mafic-ultramafic plutonic rocks due to their high TiO_2 and low Zr contents (Figure 9d).

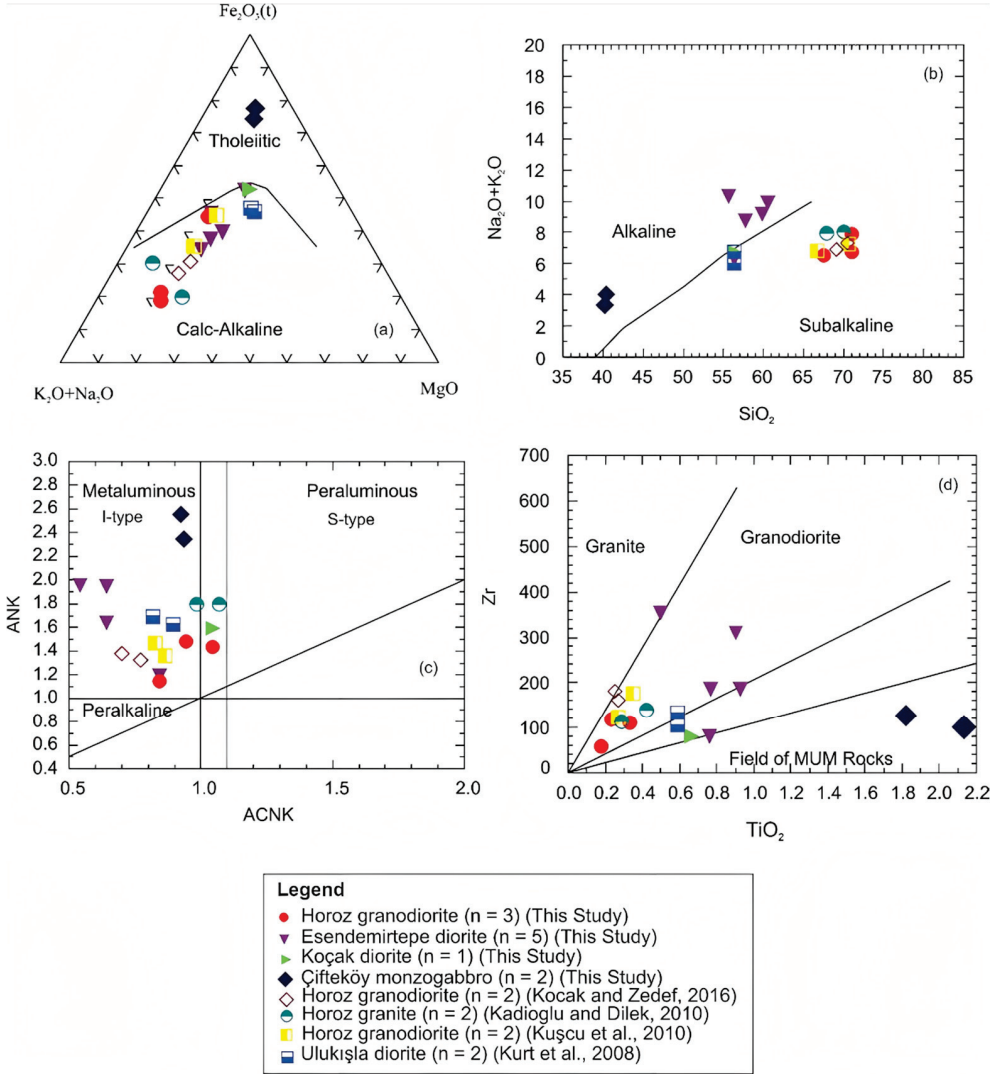


Figure 9. Rock classification showing (**a**) calc-alkaline affinity on the AFM diagram [64], (**b**) alkaline to subalkaline affinity, (**c**) the Al-saturation index [68], and (**d**) the continuous spectrum from the field of felsic rocks (granodiorite) to the field of mafic-ultramafic plutonic rocks [67]. Legend: [7,16,17,65].

4.3.2. Trace and Rare Earth Element (REE) Variations

Trace and REEs have been proven to be one of the best tools in petrogenetic studies since these elements can indicate the source of a melt as well as when a melt is differentiated or contaminated by crustal materials during its ascent [69]. The petrogenetic characteristics of the studied plutonic rocks show contrasting differences among the monzogabbro, granodiorite, and diorite. The emplacement of the monzogabbroic rocks likely played a significant role in the formation of the skarn deposits in the area and they display the lowest Rb (79.3–99.1 ppm) and Th (8.26–12.0 ppm) contents (Table 1; Figure 10). However, the diorite displays the highest Rb (39.5–154 ppm) and Th (2.12–34.95 ppm) contents (Table 1; Figure 9). The Rb (60.0–113 ppm) and Th (9.72–14.9 ppm) contents of the granodiorite are also more enriched than that of the monzogabbro (Table 1; Figure 10). The Y content of monzogabbro (19.4–26.4 ppm) is higher than that of the granodiorite (10.9–17.3 ppm) and the diorite (12.1–21.0 ppm) (Table 1; Figure 10). The monzogabbro is also fairly enriched in Zr (112–133 ppm), whereas the granodiorite (59.0–118 ppm) and diorite (81.4–355 ppm) show moderate to high enrichment in Zr, respectively (Table 1; Figure 10). The Cr content of the monzogabbro is low (26.0–68.4 ppm) compared to that of the granodiorite (27.4–54.8 ppm) and diorite (27.4–130 ppm) (Table 1; Figure 10). However, the V content of the monzogabbro (448–482 ppm) is higher than that of the granodiorite (28.0–44.8 ppm) and diorite (33.6–168 ppm) (Table 1). The other trace elements like Cr, Ni, Ga, Cd, In, Cs, Tl, and U show low concentrations in all the plutonic rocks (Table 1).

The diorite shows considerable enrichment in REEs compared to monzogabbro and the granodiorite (Table 1). The total REE abundance in the monzogabbro is in the range of 318–347 ppm, whereas those of the granodiorite and diorite are in the range of 91–311 ppm and 63–506 ppm, respectively (Table 1). The Eu/Eu* values for the monzogabbro vary from 0.98 to 1.12 while the Eu/Eu* values for the granodiorite and diorite vary from 0.98 to 1.05 and 1.03–1.35, respectively (Table 1). The monzogabbro exhibits $(La/Yb)_n$ ratios in the narrow range of 27.4–21.7 and $(Ce/Yb)_n$ ratios of 18.2–23.2. The $(Gd/Yb)_n$ ratios (3.78–4.32) of the monzogabbro are also elevated (Table 1). Moreover, the granodiorite shows a broader range of REE fractionation, with $(La/Yb)_n$ ratios in the range of 7.66–46.1, $(Ce/Yb)_n$ ratios in the range of 6.32–25.2, and $(Gd/Yb)_n$ ratios in the range of 0.98–1.29 (Table 1). The diorite also shows a wide range of REE fractionation characterized by $(La/Yb)_n$ ratios (3.70–40.7), $(Ce/Yb)_n$ ratios (3.12–30.5), and $(Gd/Yb)_n$ ratios (1.43–3.74) (Table 1).

4.4. Skarn Occurrences

4.4.1. Esendemirtepe-Koçak Skarn

The skarn mineralization in the Esendemirtepe-Koçak area occurs as an exoskarn characterized by various calc-silicate minerals along the skarn zone. It is classified as an exoskarn because these kinds of skarns are identified by the overlap in both location and timing of an intrusive body with sedimentary wall rocks [70]. However, in the field, there was no clear contact between the Esendemirtepe-Koçak diorites and the skarn mineralization and thus the endoskarn zone could not be determined. Moreover, mineralization was mostly determined within the exoskarn towards the outer zone, mostly in the hornfelsic zone. Therefore, alteration in the Esendemirtepe-Koçak area is predominantly affecting the sedimentary wall rocks with retrograde metamorphism evidenced by intense epidotization and transformation of pyroxene minerals into actinolite.

At the contact between the volcano-sedimentary rocks and the skarn, several centimeter-scale irregularly distributed hematite assemblages are accompanied by garnet, actinolite, calcite, and quartz (Figure 11a). At this contact, a highly fractured structure dominated by magnetite with calcite and chalcopyrite filling in the fractures was observed, indicating that magnetite formed before calcite (Figure 11b). Epidote and chalcopyrite

inclusions are observed around fracture-filling-type magnetite (Figure 11c). A few meters away from the skarn zone, epidote continues to develop within the volcanic breccia (Figure 11d). There are quartz veins cross-cutting the epidote grains (Figure 11e). The Esendemirtepe-Koçak skarn zone is characterized by irregular garnet aggregates coexisting with calcite, quartz, and hematite (Figure 11f). Such garnet aggregates are observed close to the ore body and range from centimeters to decimeters. Although there is no distinct zoning as one moves towards the wall rocks from the ore, epidotization and chloritization become more common as one moves away. Hematite is observed in rock fractures, and the width of the zone exceeds 200 m in places.

4.4.2. Horoz Skarn

The skarn mineralization in the Horoz area shows both endoskarn and exoskarn features considering the close contact between the Horoz granitoids and the calc-silicate-bearing sedimentary rocks in the area with alteration affecting both the sedimentary wall rocks and the intrusive bodies (Figure 4). In this area, garnets are coarse-crystalline and massive (Figure 12a). Sporadic nodular sphalerite and irregular quartz are common in the granitoids (Figure 12b). Banded crystallization of calcite, quartz, and sphalerite occurs towards the ore zone, which is at the contact of the granitoids and the carbonate unit (Figure 12c). The mineralization occurs as vein-type mineralization due to hydrothermal fluid ingress. Sphalerite formation between the contact of calcite (Figure 12d) indicates fracture-filling-type retrograde sphalerite. Other macroscopic endoskarn features are characterized by massive (Figure 12e) and large garnet crystals surrounded by smaller fine-grained garnet crystals (Figure 12f). These garnets may have formed simultaneously closer to the skarn zone suggesting reactive infiltration, which caused zoning [70–74].

4.5. Mineralogical Characteristics of the Skarn Deposits

XRD analyses were conducted to identify the various primary and secondary minerals in the skarn deposits. However, some analyses involving Electron Probe Microanalysis (EPMA) of the skarn deposits are reported in an upcoming related work. A summary of all minerals identified in skarn-related rocks is given in Table S1.

From the XRD analyses, skarns in the Esendemirtepe-Koçak area essentially consist of Na-rich minerals with calc-silicate minerals (Figure 13a). The volcano-sedimentary rocks in the Esendemirtepe-Koçak area also contain Na-rich clinopyroxene and orthopyroxene (Figure 13b). Therefore, in the calcic skarn zone, calc-silicate minerals such as grandite garnet (grossular-andradite), clinopyroxene (diopside-hedenbergite-johansenite), epidote, and actinolite, among others, are commonly observed. Hydrothermal alteration products in the Esendemirtepe-Koçak skarns include epidote, calcite, dolomite, and clinochlore (Figure 13c). The hydrothermal alteration also resulted in the formation of quartz, magnetite, hematite, and subordinate spinel in the skarns (Figure 13d).

A summary of all minerals identified in skarn-related rocks in the Horoz region is given in Table S1. On the basis of the XRD analyses, skarns in the Horoz area contain abundant calc-silicate minerals and Na-K-rich minerals (Figure 14a). The garnet crystals observed in the Horoz area are actually andraditic to grossularite in composition in view of the XRD patterns. Pyroxene end members (diopside) and augite alongside a sodium-rich member of the amphibole group of silicate minerals (riebeckite) also developed with the garnet end member andradite (Figure 14b). Alteration may have resulted in the formation of quartz, calcite, piemontite, actinolite, grossular, and vermiculite (Figure 14c) and continued with the formation of dolomite, muscovite, and kaolinite (Figure 14d).

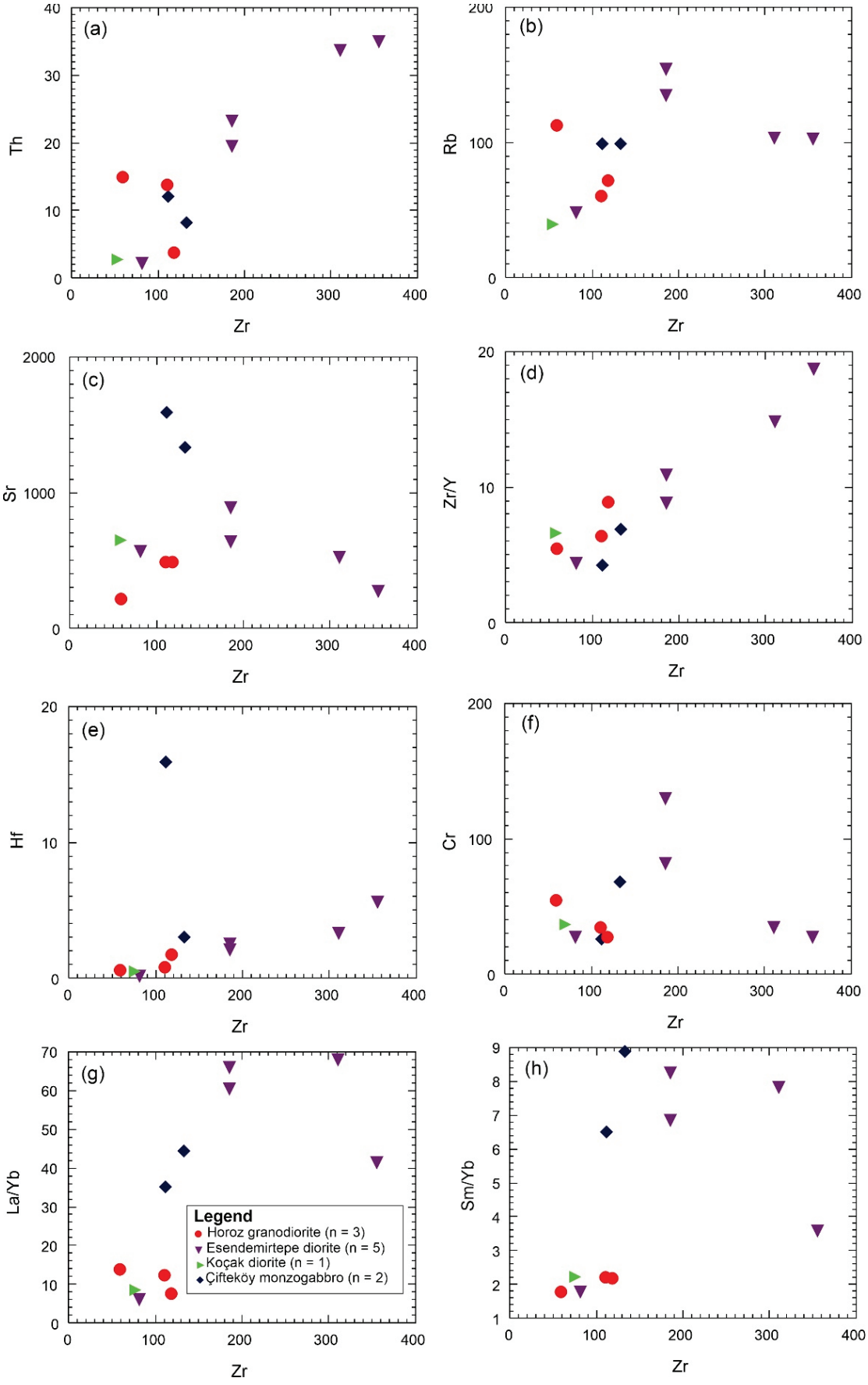


Figure 10. Trace element variation diagrams of (**a**) Th versus Zr, (**b**) Rb versus Zr, (**c**) Sr versus Zr, (**d**) Zr/Y versus Zr, (**e**) Hf versus Zr, (**f**) Cr versus Zr, (**g**) La/Yb versus Zr, and (**h**) Sm/Yb versus Zr.

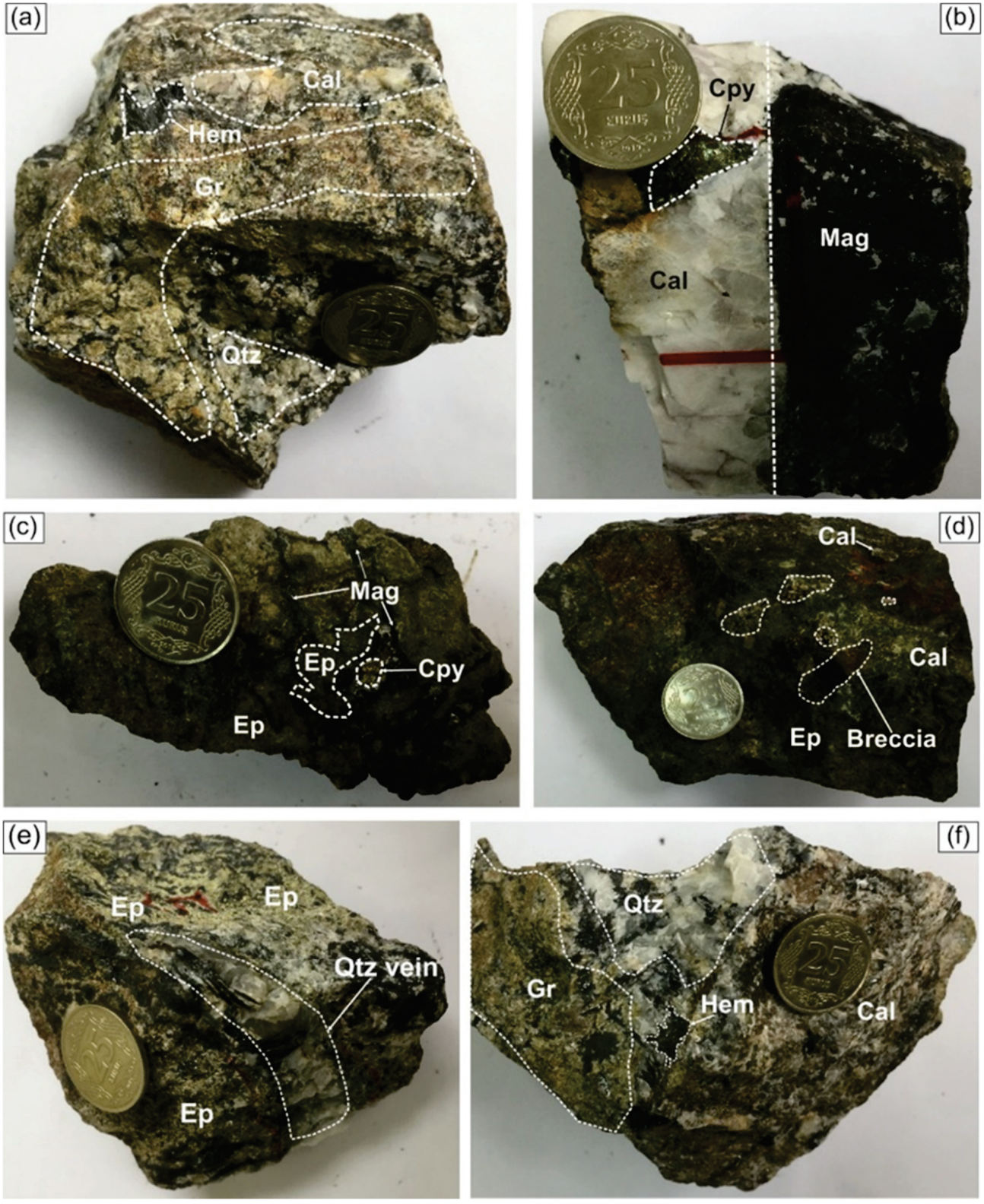


Figure 11. Macroscopic scale typical exoskarn features in Esendemirtepe-Koçak mineralization, with (**a**) irregularly distributed hematite assemblage in garnet; (**b**) a highly fractured structure dominated by magnetite with calcite and chalcopyrite filling in the fractures; (**c**) fracture-filling-type magnetite with epidote and chalcopyrite grains; (**d**) breccia-filling-type epidote and calcite precipitation in volcanic host rocks along the skarn zone; (**e**) quartz veining in the reactive front of epidote; and an (**f**) irregular garnet reaction front in contact with carbonate skarn (Cal = Calcite; Cpy = Chalcopyrite; Ep = Epidote; Gr = Garnet; Hem = Hematite; Mag = Magnetite; Qtz = Quartz).

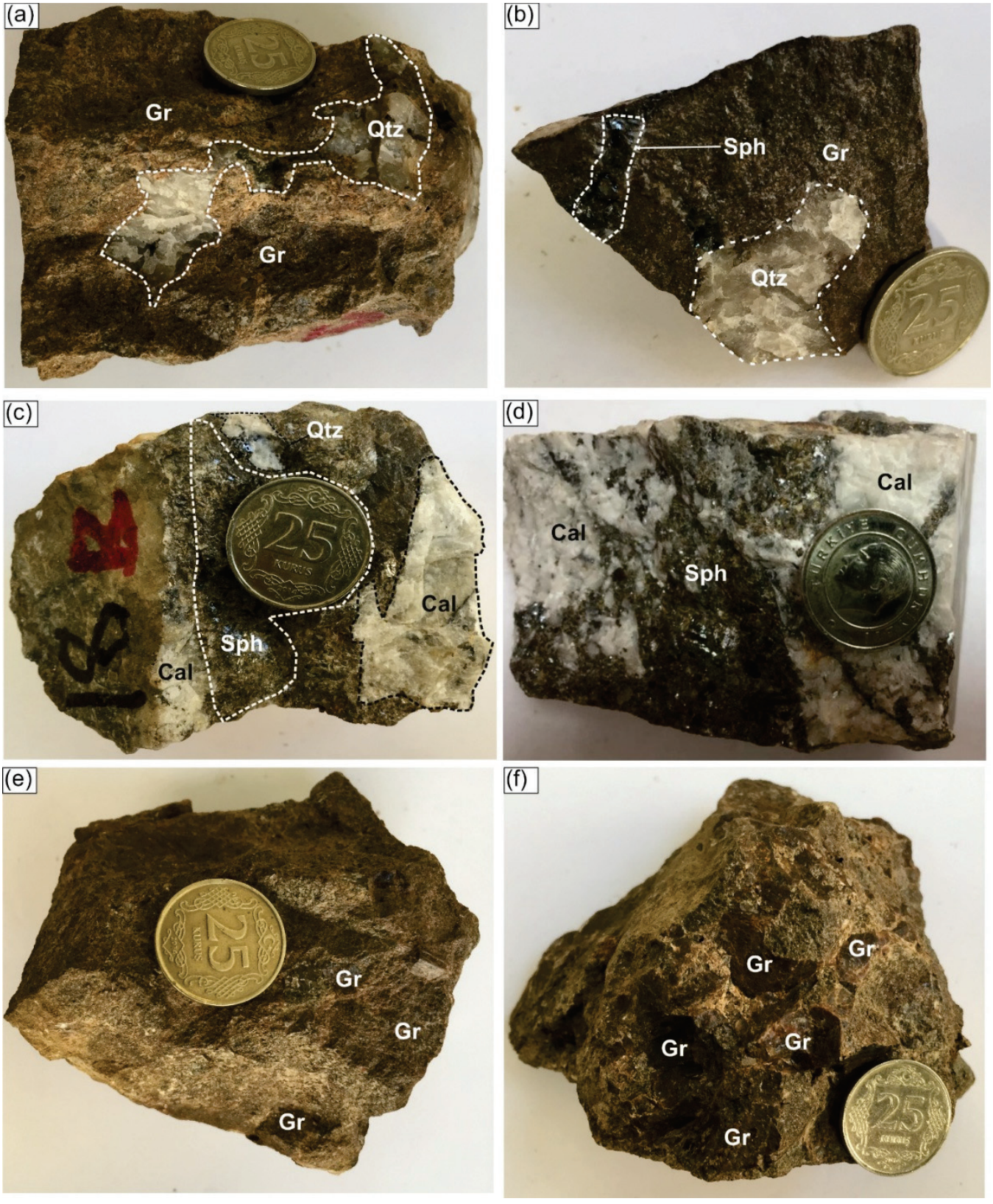


Figure 12. Macroscopic scale typical endoskarn features in the Horoz skarn with (**a**) massive garnets cut by quartz; (**b**) sporadic nodular-shaped sphalerite and irregular quartz along marble-schist skarn contact; (**c**) banded crystallization of calcite, quartz, and sphalerite towards the ore zone; (**d**) fracture-filling type sphalerite; (**e**) massive garnet; and (**f**) large garnet crystals, surrounded by smaller fine-grained garnet crystals (Cal = Calcite; Gr = Garnet; Qtz = Quartz; Sph = Sphalerite).

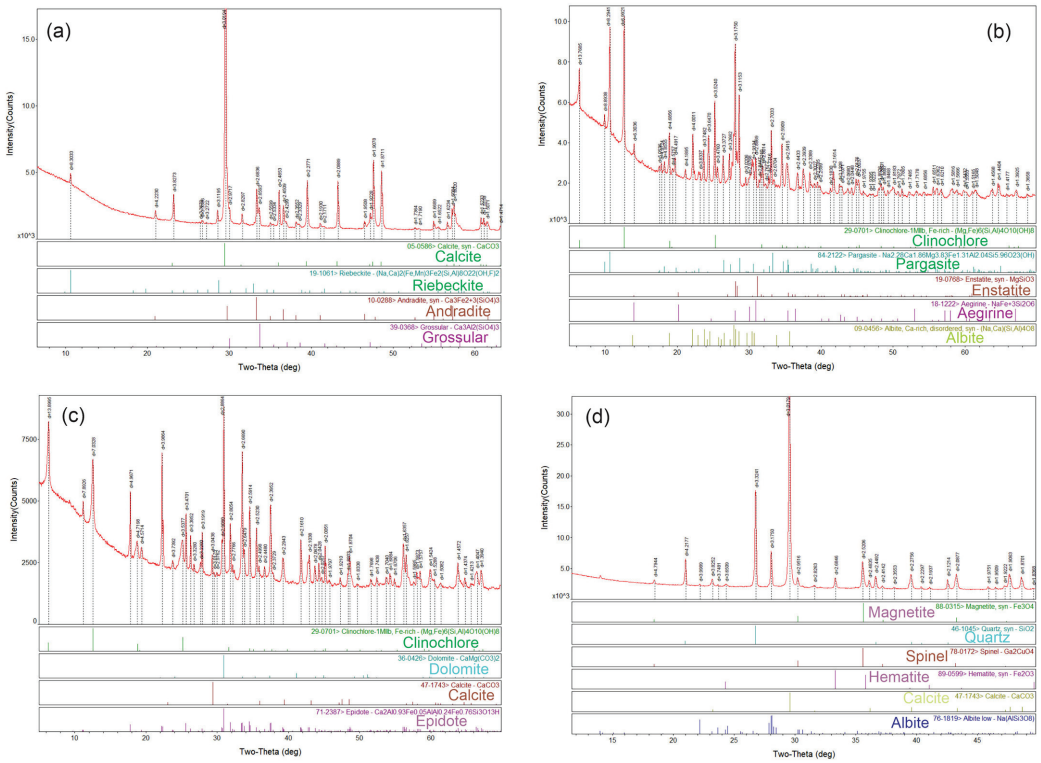


Figure 13. XRD patterns of selected samples from different skarn zones in the Esendemirtepe-Koçak area with dominance of (**a**) calcite, riebeckite, andradite, and grossular, (**b**) clinochlore, pargasite, enstatite, aegirine, and albite, (**c**) clinochlore, dolomite, calcite, and epidote, and (**d**) magnetite, quartz, spinel, hematite, calcite, and albite.

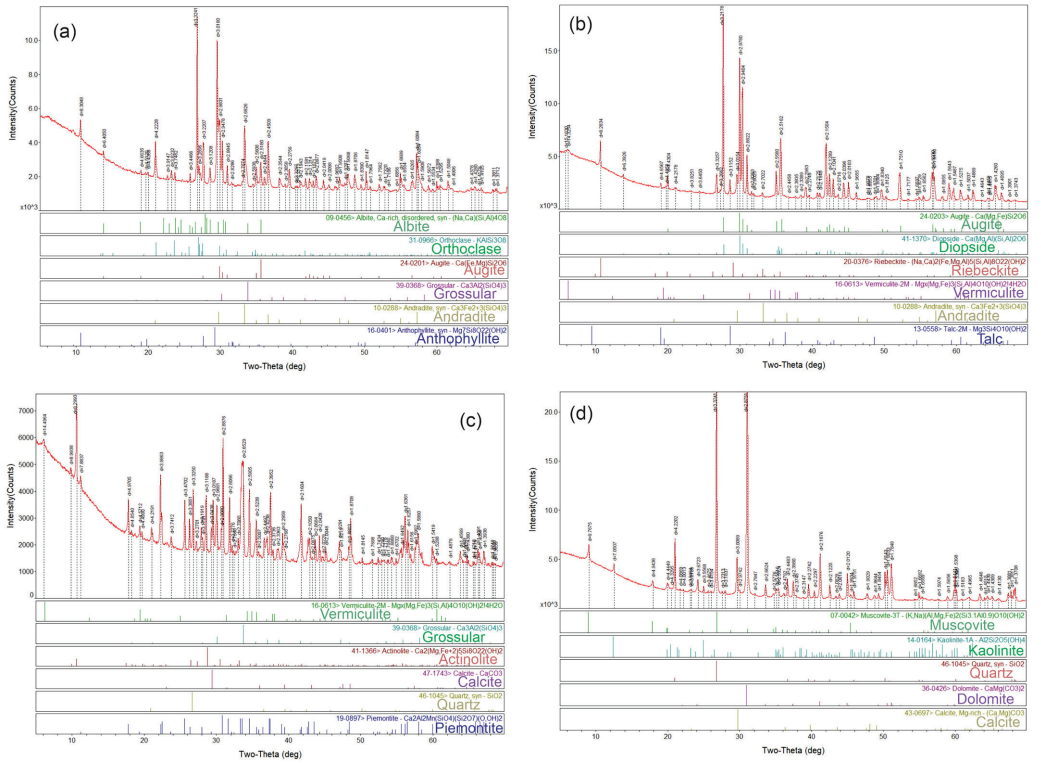


Figure 14. XRD patterns of selected samples from different skarn zones in the Horoz area with dominance of (**a**) albite, orthoclase, augite, grossular, andradite, and anthophyllite, (**b**) augite, diopside, riebeckite, vermiculite, andradite, and talc, (**c**) vermiculite, grossular, actinolite, calcite, quartz, and piemontite, and (**d**) muscovite, kaolinite, quartz, dolomite, and calcite.

5. Discussion

5.1. Petrogenetic Evolution of the Çiftehan Plutonic Rocks

The major element variations, especially the SiO_2 and Na_2O contents, K_2O/Na_2O ratios, molecular A/CNK ratios, and mineralogical composition, all suggest that the plutons in the Çiftehan (Ulukışla-Niğde) area show I-type characteristics when compared with the classification scheme of [75]. These characteristics also indicate that the monzogabbro, granodiorite, and diorite have a similar origin, probably derived from partial melting and crystallization from meta-igneous rocks, but due to magmatic differentiation and influence from crustal materials, the granodiorite and diorite became late-stage products of the same magma [32,76].

The observed geochemical trends in the studied samples revealing positive correlations of SiO_2 with Na_2O and negative correlations with K_2O, Al_2O_3, Fe_2O_3, MgO, and TiO_2 (Figure 8) are indicative of advanced fractional crystallization processes and evolving magma chemistry. As magmas differentiate, silica and alkali contents typically increase due to the progressive removal of early-crystallizing mafic minerals such as olivine, pyroxene, and amphibole, which preferentially incorporate Fe, Mg, and Ti. The depletion of Al_2O_3 may reflect the fractionation of plagioclase, which is a major Al-bearing phase, especially in intermediate to felsic magmas [77]. The positive trend with Na_2O suggests the increasing role of alkali feldspars and sodic plagioclase (e.g., albite) in the residual melt, consistent with I-type granitoid evolution [78]. The equilibrium between plagioclase and amphibole is particularly significant in controlling the trace element and major oxide evolution of the melt. Amphibole can incorporate significant amounts of Fe, Mg, and Ti, and its crystallization alongside plagioclase can drive the melt toward more felsic compositions. Moreover, the presence of amphibole suggests water-rich conditions, which can suppress plagioclase crystallization at early stages, delaying its appearance until lower temperatures, thereby influencing the observed Al_2O_3 depletion [79]. These mineralogical controls, combined with the redox-sensitive behavior of elements like Ti and Fe, further support a scenario of oxidizing to mildly reducing conditions during magma evolution.

The trace element concentrations of the studied plutonic rocks were normalized to the Chondrite, Ocean Ridge Granite (ORG), Upper Crust, and Lower Crust values of [80] to further confirm their source characteristics. The Chondrite, ORG, Upper Crust, and Lower Crust-normalized patterns of the plutonic rocks indicate enrichment in large ion lithophile elements (LILEs) like Rb and Th and depletion in Y (Figure 15a–d), implying interaction with crustal materials for all the plutonic rocks. However, the higher Rb and Th values for the granodiorite and the diorite than the monzogabbro is interpreted to be because of extensive crustal input from a subduction-related origin since Rb and Th are enriched in crustal sources [81,82].

According to Rudnick and Gao [81], plutonic rocks with a Zr content higher than 132 pm and a low Y content may point to crustal mixing with their magmas. Therefore, the low Zr and Y content in the monzogabbro imply limited crustal interaction, but most of the granodioritic and dioritic rocks, especially the Esendemirtepe diorite, show extremely high Zr and Y contents, implying extensive input from crustal materials during their emplacement. The low Cr content of the monzogabbro compared with that of the granodiorite and diorite further indicates more input from crustal materials to the magma of the granodiorite and diorite. The Çifteköy monzogabbro and the Esendemirtepe diorite are exceptionally rich in Cs when compared with the Horoz granodiorite and the Koçak diorite (Figure 15a–d). Such enrichment might be due to the presence of accessory minerals like apatite [83]. On the Upper Crust and Lower Crust-normalized diagrams (Figure 15c,d), the studied rocks are fairly enriched in LILEs compared to the Upper Crust and are more enriched than the Lower Crust, consistent with patterns of magma that have undergone

significant crustal mixing. When compared with geochemical data of granitoids in the Ulukışla-Niğde area [7,16,17,65], the studied rocks show overlapping patterns, indicating that they may be coeval members.

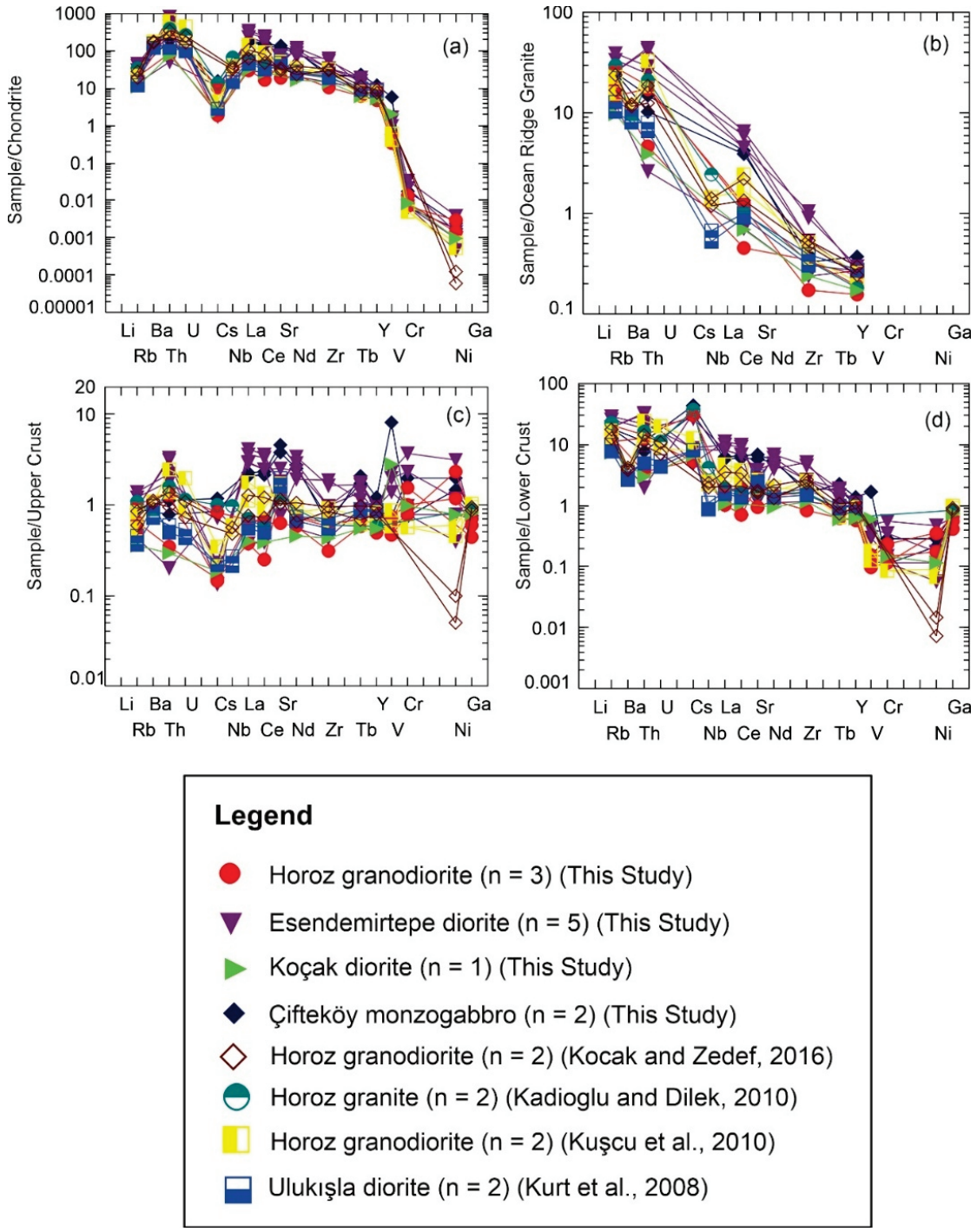


Figure 15. Normalized trace element diagrams for the studied rocks involving (**a**) Chondrite, (**b**) Ocean Ridge Granite, (**c**) the Upper Crust, and (**d**) the Lower Crust (normalization values from [80]), Legends: [7,16,17,65].

Overall, the trace element patterns of the studied plutonic rocks suggest that they may have been derived from a hybrid source, characterized by crustal and mantle components. This interpretation is supported by the Chondrite, ORG, Upper Crust, and Lower Crust-normalized trace element patterns of the studied rocks as discussed above.

The studied plutonic rocks were also normalized to the Chondrite and Continental Crust REE values of [80]. A steep negative REE slope (La > Yb) with considerable enrichment in LREEs against the MREEs and HREEs, smaller positive Eu anomalies (Eu/Eu* = 0.98–1.35), and a flat normalized pattern for the HREEs are observed in all the plutonic rocks (Figure 16a,b). This trend is also comparable to that of granitoids in the Ulukışla-Niğde area [7,16,17,65], which implies contribution from crustal sources to the melt composition and accumulation of plagioclase feldspars during partial melting [84,85].

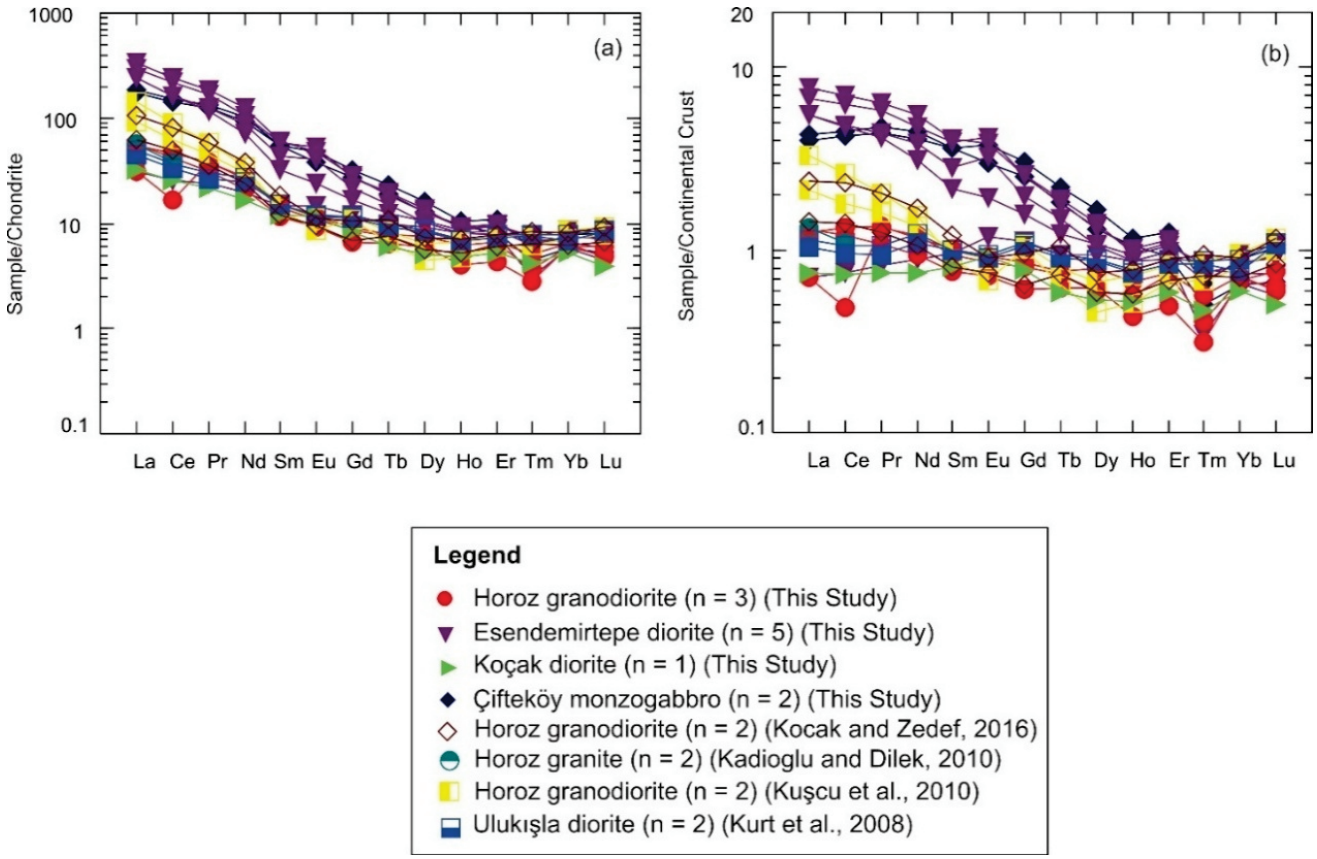


Figure 16. Normalized REE diagrams involving (**a**) Chondrite and (**b**) Continental Crust (normalization values from [80]). Legends: [7,16,17,65].

The Eu/Eu* ratios ranging from 0.98 to 1.35 suggest limited to moderate plagioclase accumulation or retention in the source magma and relatively reducing conditions that allowed for the partial stabilization of Eu^{2+}. Studies have shown that such ratios are typical of calc-alkaline granitoids where plagioclase crystallization plays a dominant role in early magmatic differentiation [86]. The presence of positive Eu anomalies in the monzogabbro or less-evolved rocks, and their gradual decline in more-evolved granodioritic and dioritic rocks, further supports the role of plagioclase fractionation in controlling Eu behavior [87]. The samples also show negative Tm anomalies, indicating the absence of Tm-bearing minerals [88]. The Continental Crust-normalized patterns of the Horoz granodiorite and Koçak diorite are fairly similar and thus, their magmas may have been derived from mantle sources and later mixed with continental crustal sources (Figure 16b).

The $(La/Yb)_n$, $(Ce/Yb)_n$, and $Gd/Yb)_n$ ratios of the monzogabbro indicate strong LREE and MREE enrichment relative to HREEs. These patterns are characteristic of magmas derived from a deep-seated, garnet-bearing source, where garnet retains HREEs during partial melting [89]. The elevated MREE/HREE ratios further imply that amphibole may also be present in the residue, contributing to the fractionation pattern [90]. Tectonically,

such REE signatures are typical of continental arc settings, where subduction-related fluids and melts metasomatize the overlying mantle wedge, enriching it in LREEs. The high-pressure melting conditions inferred from the garnet signature suggest that these magmas were generated in a thickened crustal environment, possibly during the early stages of arc development or post-collisional crustal reworking [91].

Nevertheless, the variability in the $(La/Yb)_n$, $(Ce/Yb)_n$, and $Gd/Yb)_n$ ratios of the granodiorite and diorite suggest heterogeneous source compositions or variable degrees of partial melting and fractional crystallization. The samples with lower $(La/Yb)_n$ and $(Ce/Yb)_n$ ratios (e.g., EM10 and EM13—Esendemirtepe diorite) likely reflect shallower melting conditions, where garnet is absent and clinopyroxene or plagioclase dominates the residue. In contrast, samples with higher ratios (e.g., samples H16, E4B, ED2A, and ED2C—Horoz granodiorite and Esendemirtepe diorite) resemble the monzogabbro, indicating deeper melting with garnet stability. This geochemical diversity implies a complex magmatic evolution, possibly involving magma mixing, crustal assimilation, or polybaric melting. The tectonic setting remains consistent with a continental arc to post-collisional regime, but the broader range of REE patterns suggests progressive crustal thickening, slab rollback, or delamination processes influencing magma genesis [92,93].

5.2. Tectonic Environments

Trace element data are widely used in discriminating the tectonic environments associated with the formation of different magma types (e.g., [66,94]). In the Rb versus Y + Nb (Figure 17a) and Rb/Zr versus SiO_2 (Figure 17b) diagrams, the plutonic rocks from the study area all plot in the Volcanic arc granite (VAG) and Syn-collisional granite (Syn-COLG) + VAG fields just as samples from previous studies in some localities within the Ulukışla-Niğde area. The tectonic discrimination of the rocks as volcanic arc granites and compositionally as calc-alkaline granites implies subduction-related settings for their emplacement [76,94]. It might also indicate regional metamorphism around active continental margins. Furthermore, on the [95] diagram (Figure 17c), the samples spread across the Late-orogenic to Syn-Collision granite zones that are consistent with previous studies [7,16,17,65] and this is a typical geochemical signature of late orogenic plutonic rocks. Late orogenic granites are known to be calc-alkaline rocks characterized by more than one tectonic environment [96], which reflects the hybrid composition of their source magmas like a depleted/enriched mantle and crust. The thick nature of the crust and extensive interaction between mantle-derived magma and the crust makes most late orogenic granites show evidence of crustal assimilation [96].

5.3. Genetic Link Between Plutonic Rocks and Skarn-Type Formation

Some studies have documented the relationship between the composition of plutonic rocks and skarn-type deposits (e.g., [32,70,97]). For example, Ref. [97] reported that plutonic rocks associated with the formation of Fe, Zn, Au, and Cu skarns contain moderate levels of MgO and K_2O. In contrast, plutonic rocks associated with Sn and Mo skarns have less MgO and more K_2O [97]. Furthermore, Ref. [70] revealed that most of the plutons associated with skarns show calc-alkaline trends and aluminum saturations that are mostly metaluminous.

In this study, with the exception of the Çifteköy monzogabbro, all plutonic rock samples from the Esendemirtepe-Koçak and Horoz areas were in the calc-alkaline field in the AFM diagram (Figure 18a). In addition, the aluminum saturation index values of the plutonic rocks ranged from 0.52 to 1.08 and therefore, they plot in the metaluminous field, except for some Horoz granodiorite and Koçak diorite samples, which plot in the peraluminous field (Figure 18b). In this context, the Esendemirtepe-Koçak and Horoz granitoids have the potential to produce skarns and their geochemical compositions are

similar to all skarn-forming plutonic rock types except the Sn-type. Similar findings were reported by Demir and Bayraktar [98] in the Düzköy Fe-Cu skarn deposit of Gümüşhane in northeastern Türkiye. In addition, the geochemical composition of the Esendemirtepe-Koçak and Horoz plutonic rocks is similar to Fe-, Au-, Cu-, and Zn-type skarn granitoids in SiO_2 versus K_2O (Figure 18c) and SiO_2 versus MgO (Figure 18d) diagrams. However, the Esendemirtepe-Koçak and Horoz plutonic rocks differ from the geochemical composition of W, Sn, and Mo skarn-type granitoids.

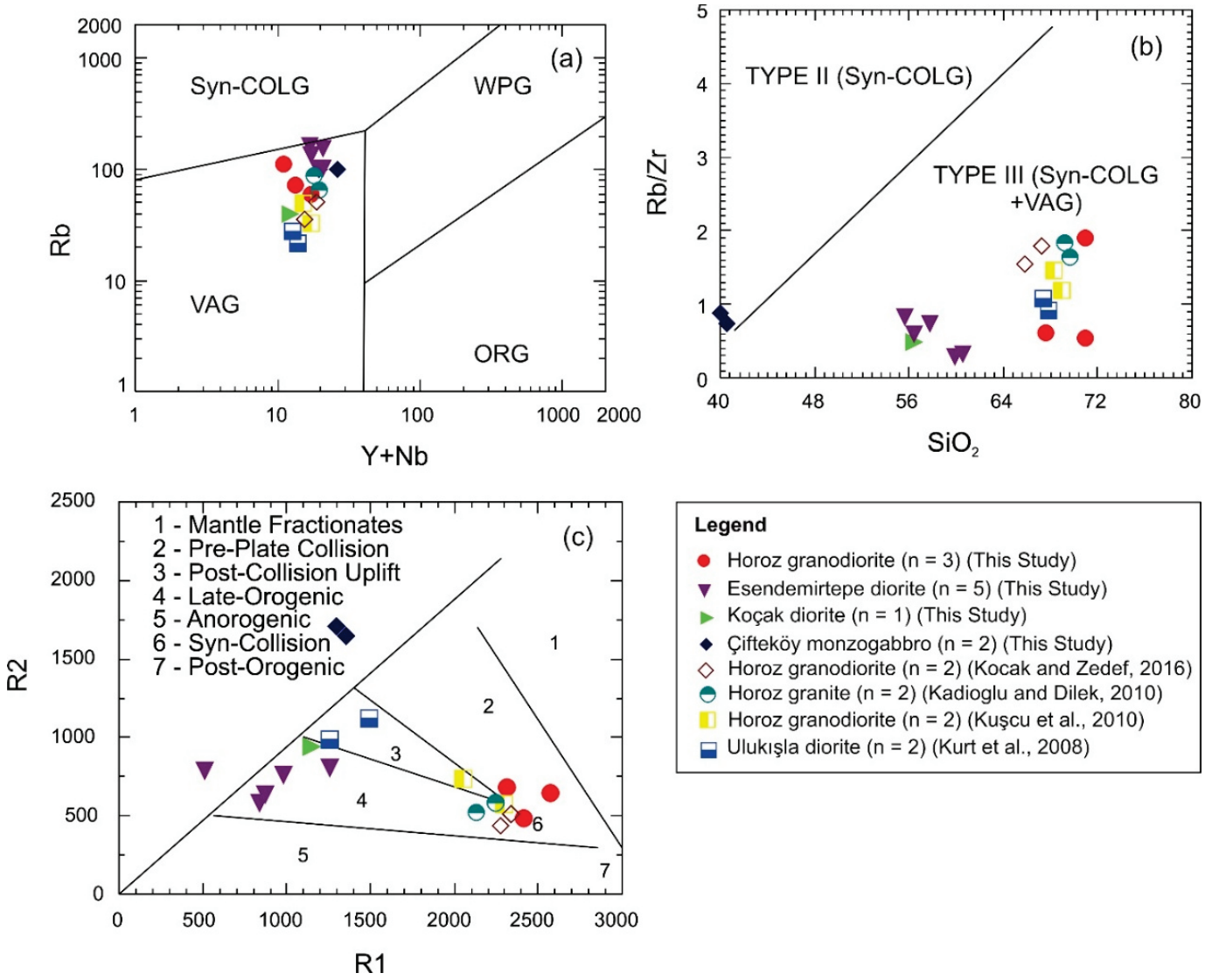


Figure 17. Tectonic discrimination diagrams of the studied rocks with (**a**) Rb versus (Y + Nb), (**b**) Rb/Zr versus SiO_2, and (**c**) R1-R2 of [95]. Legends: [7,16,17,65].

Accordingly, Fe-, Cu-, Zn-, and Au-type skarn granitoids occur as volcanic arc granitoids (VAGs) and are therefore usually located in the VAG area in tectonic discrimination diagrams such as Rb versus Y + Nb and Nb versus Y [70]. Such granitoids typically have lower Rb and Zr contents compared to W, Mo, and Sn skarn-related granitoids. The Esendemirtepe-Koçak and Horoz plutonic rocks have a similar composition to volcanic arc granitoids and a close relationship with Fe and Zn-type skarn granitoids and partly with Cu-type skarn granitoids in the Rb versus Y + Nb diagram (Figure 19a). In addition, the studied samples are similar to Fe-, Cu-, and Zn-producing granitoids in Rb/Zr and Sr/Zr diagrams (Figure 19b,c).

On the basis of the above explanations, both major and trace elements of the Esendemirtepe-Koçak and Horoz plutonic rocks show similar features and a close relationship with Fe- and Zn-type skarn granitoids with a slight overlap with Cu-type skarn granitoids. Similar findings have been reported in the skarn deposits of Düzköy (Gümüşhane), Sivrikaya (Rize), Dağbaşı (Trabzon), and Eğrikar (Gümüşhane) and a strong relationship between skarn mineralogy and the geochemical properties of skarn-related granitoids has been demonstrated [74,98–100].

Moreover, the mineral composition of the Esendemirtepe-Koçak skarns is characterized by a dominance of Na-rich and calc-silicate minerals, including grandite garnet (grossular-andradite), clinopyroxenes (diopside-hedenbergite-johansenite), epidote, and actinolite. Hydrothermal alteration in this area has produced secondary minerals such as epidote, calcite, dolomite, clinochlore, quartz, magnetite, hematite, and minor spinel. In comparison, skarns from the Horoz area also exhibit a rich assemblage of calc-silicate and alkali-rich minerals, but with a broader diversity. Garnets here range from andraditic to grossularite, and are associated with pyroxenes like diopside and augite, as well as sodium-rich amphiboles such as riebeckite. Alteration in the Horoz skarns has led to the formation of minerals like piemontite, vermiculite, muscovite, and kaolinite, in addition to those found in the Esendemirtepe-Koçak area. Overall, while both areas share common skarn-forming minerals, the Horoz area displays a more complex alteration assemblage and a wider range of alkali-bearing silicates, suggesting variations in fluid composition and metasomatic conditions during skarn formation. Most of these alkali-bearing silicates were observed in the plutonic rocks indicating consanguinity. Similar skarn mineralogy has been reported in the Biga Peninsula in Türkiye by [101]. Therefore, considering the genetic relationship between skarn mineral composition and the geochemical properties of the Esendemirtepe-Koçak and Horoz plutonic rocks, it is thought that this relationship may have occurred on a regional scale.

In Türkiye, recent research on skarn systems offers significant analogs for elucidating the genetic processes seen in the Çiftehan area. For example, Ref. [102] demonstrated that comprehensive mineral chemistry and iron isotope studies of magnetite from the Pertek Fe-skarn deposit can accurately delineate the origins and evolutionary trajectories of hydrothermal fluids. Likewise, the sulfur and carbon-oxygen isotopic compositions, together with fluid inclusion data from the Yolindi Cu-Fe skarn deposit, underscore the intricacy of fluid development and the multistage mineralization processes [101]. Furthermore, the genetic connection between calc-alkaline magmatic activity and skarn mineralization, as shown by [103] in the Biga Peninsula, robustly substantiates the hypothesis that the plutonic rocks associated with skarn formation in the Çiftehan region are probable outcomes of subduction-related magmatism. The findings of the comparison substantiate the perspective that the Çiftehan skarn system emerged via the interaction of developing magmatic-hydrothermal fluids with carbonate host rocks, under tectonic settings shaped by active subduction processes. Moreover, the tectonic and genetic evolution of granitoids associated with skarn formation in the Biga Peninsula, Kazdağ Massif, and the Eastern Taurus Belt of Türkiye also indicate similarity with the plutonic rocks associated with skarn formation in the Çiftehan (Ulukışla-Niğde) area. Their evolution reflects a complex interplay of magmatic, metasomatic, and tectonic processes. For instance, in the Biga Peninsula, the Yolindi Cu-Fe skarn deposit exemplifies the influence of calc-alkaline magmatism in an island-arc setting, where the Şaroluk quartz monzonite intruded Upper Palaeozoic metamorphic rocks, initiating prograde and retrograde metasomatic reactions that formed garnet-pyroxene skarns and later hydrous mineral assemblages [101]. Similarly, in the Kazdağ Massif, skarn alteration and Au-Cu mineralization are linked to Tertiary I-type, magnetite-series, calc-alkaline granitoids. These intrusions generated oxidized skarn sys-

tems with hedenbergitic pyroxene and andraditic garnet during early stages, followed by retrograde assemblages of amphibole, epidote, and chlorite, influenced by a transition from magmatic to meteoric fluid sources [104]. In the Eastern Taurus Belt, skarn systems are also genetically tied to post-collisional granitoids, reflecting a tectonic regime shift from subduction to continental collision, which facilitated the emplacement of metaluminous, calc-alkaline intrusions and the associated mineralization. These granitoids share geochemical signatures with global skarn-forming systems, indicating a convergent tectonic heritage and a consistent magmatic-hydrothermal evolution [1].

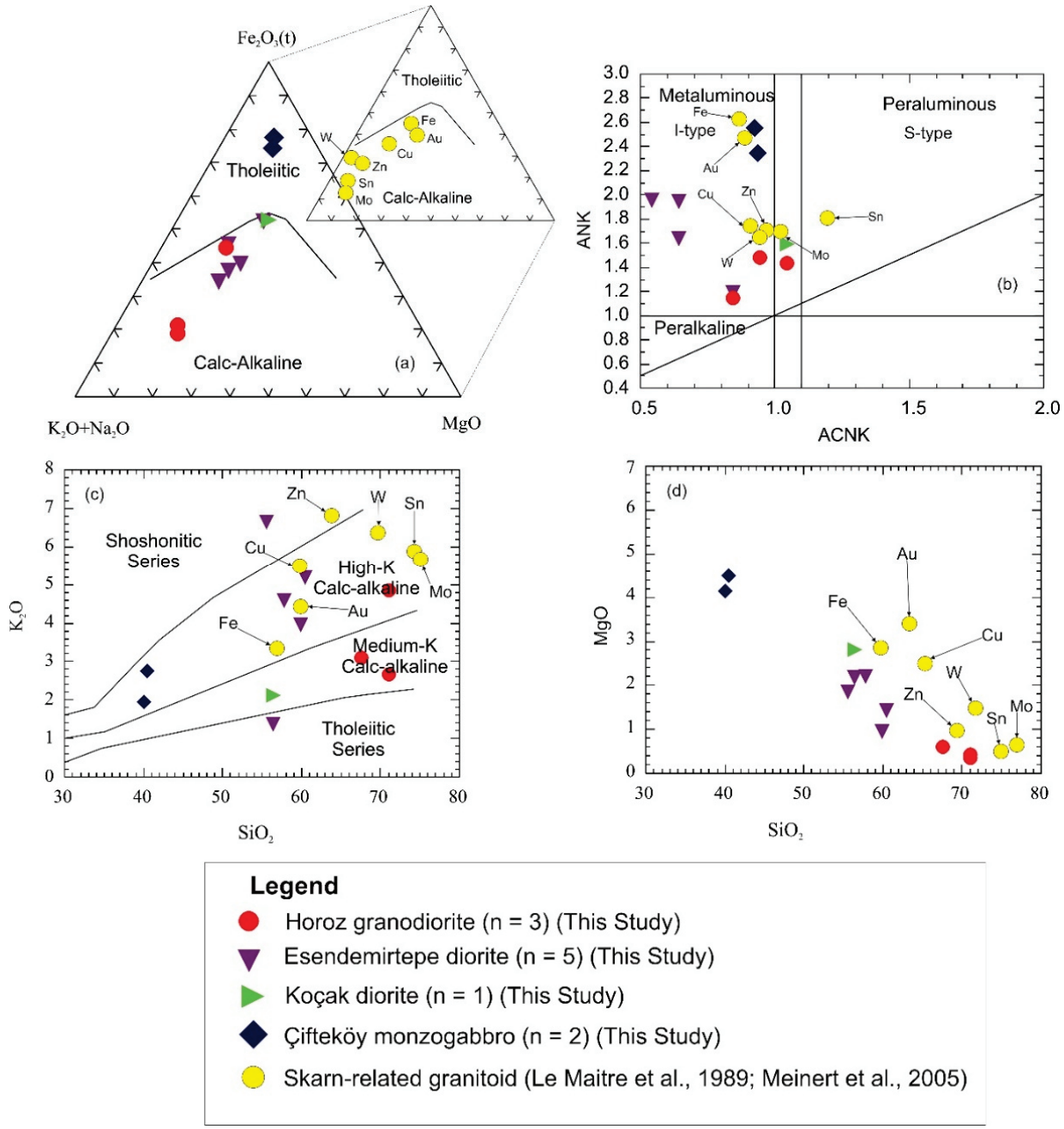


Figure 18. (**a**) Comparison of plutonic rock samples with plutonic rocks associated with skarn formation in the AFM diagram of Irvine and Baragar [64]; (**b**) Aluminum saturation index classification of plutonic rock samples with plutonic rocks associated with skarn formation in the A/CNK versus A/NK diagram [66]; (**c**,**d**) SiO_2 versus K_2O and SiO_2 versus MgO variation diagrams and comparison with the composition of plutonic rocks associated with skarn formation [70,105].

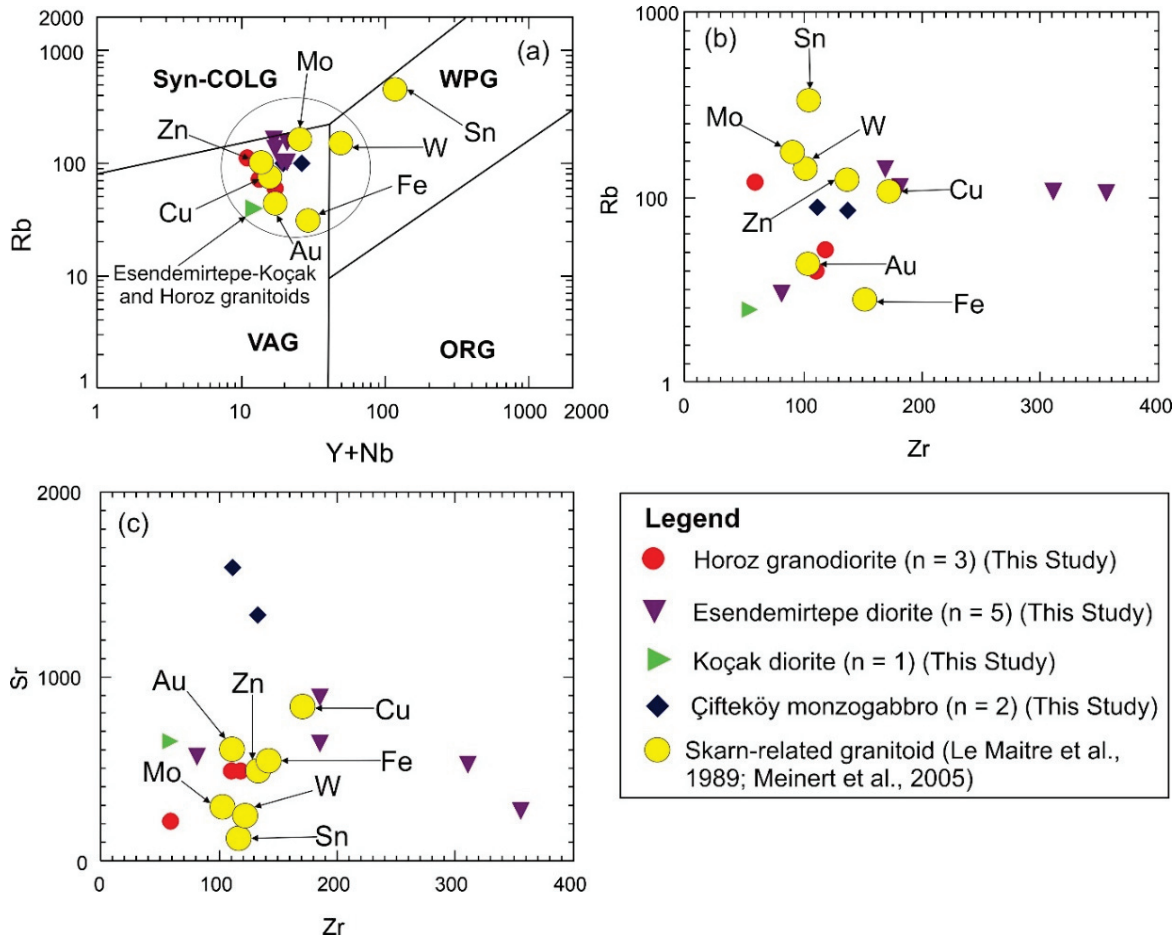


Figure 19. Classification of the plutonic rock samples on the (**a**) Rb versus Y+Nb tectonic discrimination diagram of [66] and comparison with the plutonic rocks associated with skarn formation (VAG: volcanic arc granitoids; syn-COLG: syn-collision granitoids; WPG: within plate granitoids; ORG: ocean ridge granitoids); (**b**,**c**) Rb versus Zr and Sr versus Zr trace element variation diagrams and comparison with the compositions of different types of plutonic rocks associated with skarn formation [97]. Legends: [70,105].

6. Conclusions

The Esendemirtepe-Koçak and Horoz Fe-Zn skarn deposits in the Çiftehan (Ulukışla-Niğde) area in south-central Türkiye formed in the Ulukışla Basin, which is predominantly composed of volcano-sedimentary rocks and various igneous intrusions. The skarn deposits formed due to the intrusion of the Esendemirtepe diorite and Horoz granodiorite into carbonate rocks of the Bolkar Mountain Carbonate Platform. These intrusions show calc-alkaline affinities with I-type and metaluminous characteristics. They are more enriched in LILEs and LREEs than HFSEs, MREEs, and HREEs with smaller positive Eu anomalies (Eu/Eu* = 0.98–1.35) indicating subduction-zone settings for their emplacement. All the plutonic rocks associated with skarn formation are classified as volcanic arc granites similar to other granitoids in the Ulukışla Basin. The tectonic discrimination of the rocks as volcanic arc granites and compositionally as calc-alkaline granitoids confirms their subduction-related settings during emplacement and regional metamorphism around active continental margins.

The endoskarn and exoskarn zones where the Fe-Zn skarn ore developed are located at the limestone-marble-granodiorite-volcanite contact, wherein the intrusions intersect with the metacarbonate lithologies. The plutonic rocks associated with the Fe-Zn skarn formation are Early-Middle Eocene in age. Endoskarn and exoskarn zones are mostly observed in the

Horoz area, whereas only the exoskarn zone is located in the Esendemirtepe-Koçak area. The endoskarn zone is characterized by the presence of actinolite and alteration product epidote, which are commonly observed in the calc-silicate rocks. Sporadic nodular-shaped sphalerite and irregular quartz developed along the marble-schist skarn contact. Banded crystallization of calcite, quartz, and sphalerite occurs towards the skarn zone. This zone also shows intensive fracturing and alteration of the granitoids with epidote as the main alteration product. Massive garnet crystals are also common in the endoskarn zone.

The exoskarn zone developed along the contacts of the plutonic rocks and the carbonate rocks due to the infiltration of magmatic hydrothermal fluids. The silicate minerals are richer in calcium than magnesium, thus making them calcic skarns rather than magnesian skarns. However, due to the metasomatic infiltration of the silicate melt into the carbonate lithologies, grossular-andradite pyroxene developed. The common minerals of the exoskarn zone are garnet, pyroxene, quartz, calcite, actinolite, and epidote. The presence of cobalt and nickel minerals is also common in this area. Magnetite and hematite in the skarns formed as massive and banded structures and were characterized by replacement features in both limestone and host volcanites. However, sulfide ore occurs as breccia-filling structures along the brecciated host rocks and sometimes as fracture-filling structures in the limestones and volcanites. The skarn deposits and their causative plutons show overlapping geochemical signatures, indicating their paragenetic occurrence.

Supplementary Materials: The following supporting information can be downloaded at https://www.mdpi.com/article/10.3390/min15060578/s1: Table S1: Summary of the mineralogical composition of selected skarn-related samples from the Esendemirtepe-Koçak and Horoz areas from XRD analysis.

Author Contributions: Conceptualization, E.D.S. and A.L.; methodology, E.D.S. and A.L.; software, E.D.S.; validation, E.D.S. and A.L.; formal analysis, E.D.S.; investigation, E.D.S.; resources, A.L.; data curation, E.D.S.; writing—original draft preparation, E.D.S.; writing—review and editing, E.D.S. and A.L.; visualization, E.D.S.; supervision, A.L.; project administration, A.L.; funding acquisition, A.L. All authors have read and agreed to the published version of the manuscript.

Funding: This research was funded by the Scientific Research Office of Niğde Ömer Halisdemir University in Türkiye, with the project/grant number MMT 2020/6-BAGEP.

Data Availability Statement: The original contributions presented in the study are included in the article/Supplementary Materials.

Acknowledgments: This research is part of the Ph.D. thesis of the first author at Niğde Ömer Halisdemir University, Türkiye. Faruk Aydin at the Department of Geological Engineering of Karadeniz Technical University, Türkiye, is acknowledged for assisting in the petrographic analysis of the plutonic rocks associated with skarn formation.

Conflicts of Interest: The authors declare no conflicts of interest.

Abbreviations

The following abbreviations are used in this manuscript:

AFM	Total Alkali Iron and Magnesium
A/CNK	Alkali/Calcium + Sodium + Potassium
CACC	Central Anatolian Crystalline Complex
CRD	Carbonate Replacement Deposits
HFSEs	High Field Strength Elements
HREEs	Heavy Rare Earth Elements
ICP-MS	Inductively Coupled Plasma Mass Spectrometry
LILEs	Large Ion Lithophile Elements
LREEs	Light Rare Earth Elements

MREEs	Middle Rare Earth Elements
MVT	Mississippi Valley-type Deposits
ORG	Ocean Ridge Granite
REEs	Rare Earth Elements
Syn-COLG	Syn-Collision Granite
VAG	Volcanic Arc Granite
WPG	Within Plate Granite
XRD	X-ray Diffraction

References

1. Kuşcu, İ. Skarns and skarn deposits of Turkey. In *Mineral Resources of Turkey*; Pirajno, F., Ünlü, T., Dönmez, C., Şahin, M.B., Eds.; Modern Approaches in Solid Earth Sciences; Springer: Cham, Switzerland, 2019; Volume 16, pp. 283–336. [CrossRef]
2. Çopuroğlu, İ. Mineralogy and Genesis of Zn-Pb Deposits of Yahyalı Kayseri-Demirkazık Niğde-Çamardı Region. *Bull. Miner. Res. Explor.* **1996**, *118*, 35–46.
3. Ayhan, A.; Langeranlı, Y.; Çeltek, N.; Aksoy, E. Study of the Geology of Zn-Pb Deposits in the Aladağlar (West Zamantı) and (Yahyalı-Çamardı) Areas. In *Mineral Research and Exploration Report*; General Directorate of Mineral Research and Exploration: Ankara, Turkey, 1984.
4. Çevikbaş, A.; Öztunalı, S. Mineral deposits of Ulukisla-Çamardı basin. *J. Geol. Eng.* **1991**, *39*, 22–40.
5. Temur, S.; Baş, H. Mineralogical and genetic study of iron deposits of the Çiftehan-Koçak (Ulukışla-Niğde) district. *Geol. Eng.* **1992**, *41*, 91–103.
6. Kuşcu, I.; Tosdal, R.M.; Gencalioğlu-Kuşcu, G.; Friedman, R.; Ullrich, T.D. Late Cretaceous to Middle Eocene magmatism and metallogeny of a portion of the Southeastern Anatolian orogenic belt, East-Central Turkey. *Econ. Geol.* **2013**, *108*, 641–666. [CrossRef]
7. Kadioglu, Y.K.; Dilek, Y. Structure and geochemistry of the adakitic Horoz granitoid, Bolkar Mountains, south-central turkey, and its tectonomagmatic evolution. *Int. Geol. Rev.* **2010**, *52*, 505–535. [CrossRef]
8. Kocak, K.; Zedef, V.; Kansun, G. Magma mixing/mingling in the Eocene Horoz (Niğde) granitoids, Central southern Turkey: Evidence from mafic microgranular enclaves. *Miner. Petrol.* **2011**, *103*, 149–167. [CrossRef]
9. Sünger, A.; Akyıldız, M.; Nurlu, N. Significance of the felsic sub–volcanics in development of related Au–Ag deposits at Maden village (Bolkar Mountain region), South Turkey: Constraints from whole–rock geochemistry, geochronology and Pb-S isotopes. *Geotectonics* **2022**, *56*, 361–381. [CrossRef]
10. Çiftçi, E.; Lermi, A.; Ghosh, N.; Basu, A. Carbonate-hosted gallium-bearing lead-zinc deposits of Tauride belt (Turkey): Genetic implications. *Acta Geol. Sin.* **2014**, *88*, 147. [CrossRef]
11. Lermi, A.; Çiftçi, E.; Koçak, A. Geochemical and mineralogical characterization of selected gossans developed on the carbonate-hosted Pb-Zn deposits occurring along the Central Tauride Belt (Turkey). In Proceedings of the 12th International Congress for Applied Mineralogy, İstanbul, Turkey, 10–12 August 2015; p. 43.
12. Blumenthal, M. *Belemedik Paleozoic Window and Its Mesozoic Limestone Frame (Kilikya, Taurus)*; Publication of the Mineral Research and Exploration Directorate: Ankara, Turkey, 1947.
13. Blumenthal, M. Geology of the Northern Margin and Western Extensions of the High Bolkar Mountains. *Miner. Res. Explor. Inst. Ser. D* **1956**, *7*, 153.
14. Oktay, F.Y. Stratigraphy and Geologic Evolution of Ulukisla and Its Vicinity. *Turk. Geol. Kur.* **1982**, *25*, 15–24.
15. Çevikbaş, A.; Öztunalı, S. Geology of the Ulukisla-Çamardı (Nigde) post-Mestrihtian sedimentary basin. *Bull. Miner. Res. Explor.* **1992**, *114*, 155–172.
16. Kurt, M.A.; Alpaslan, M.; Göncüoğlu, M.C.; Temel, A. Geochemistry of late-stage medium to high-K calc-alkaline and shoshonitic dykes in the Ulukişla Basin (Central Anatolia, Turkey): Petrogenesis and tectonic setting. *Geochem. Int.* **2008**, *46*, 1145–1163. [CrossRef]
17. Kocak, K.; Zedef, V. Interaction of the lithospheric mantle and crustal melts for the generation of the Horoz pluton (Nigde, Turkey): Whole-rock geochemical and Sr–Nd–Pb isotopic evidence. *Est. J. Earth Sci.* **2016**, *65*, 138. [CrossRef]
18. Gürbüz, E.; Seyitoğlu, G.; Güney, A. Late Cenozoic tectono-sedimentary evolution of the Ulukışla Basin: Progressive basin development in south-central turkey. *Int. J. Earth Sci.* **2020**, *109*, 345–371. [CrossRef]
19. Whitney, D.L.; Dilek, Y. Core complex development in central Anatolia, Turkey. *Geology* **1997**, *25*, 1023–1026. [CrossRef]
20. Clark, M.; Robertson, A.H.F. The role of the Early Tertiary Ulukisla Basin, southern Turkey, in suturing of the Mesozoic Tethys Ocean. *J. Geol. Soc.* **2002**, *159*, 673–690. [CrossRef]
21. Clark, M.; Robertson, A. Uppermost Cretaceous–Lower Tertiary Ulukışla Basin, south-central turkey: Sedimentary evolution of part of a unified basin complex within an evolving Neotethyan suture zone. *Sediment. Geol.* **2004**, *173*, 15–51. [CrossRef]

22. Gautier, P.; Bozkurt, E.; Bosse, V.; Hallot, E.; Dirik, K. Coeval extensional shearing and lateral underflow during Late Cretaceous core complex development in the Niğde Massif, Central Anatolia, Turkey. *Tectonics* **2008**, *27*, TC1003. [CrossRef]
23. Gürbüz, A.; Kazancı, N. Genetic framework of Neogene–Quaternary basin closure process in central Turkey. *Lithosphere* **2015**, *7*, 421–426. [CrossRef]
24. Sarıkaya, M.A.; Yıldırım, C.; Çiner, A. No surface breaking on the Ecemiş Fault, central Turkey, since Late Pleistocene (~64.5ka); new geomorphic and geochronologic data from cosmogenic dating of offset alluvial fans. *Tectonophysics* **2015**, *649*, 33–46. [CrossRef]
25. Gürer, D.; Plunder, A.; Kirst, F.; Corfu, F.; Schmid, S.M.; van Hinsbergen, D.J.J. A long-lived Late Cretaceous–Early Eocene extensional province in Anatolia? Structural evidence from the Ivriz Detachment, southern central Turkey. *Earth Planet. Sci. Lett.* **2018**, *481*, 111–124. [CrossRef]
26. Lermi, A.; Sunkari, E.D. Geochemistry, risk assessment, and Pb isotopic evidence for sources of heavy metals in stream sediments around the Ulukışla Basin, Niğde, southern Turkey. *Turk. J. Earth Sci.* **2020**, *29*, 1167–1188. [CrossRef]
27. Lermi, A.; Kelebek, G. Investigation of the potential of Gumuskoy (Ulukisla-Nigde) ore slags to form acid mine drainage and their impact on the environment, Nigde University. In Proceedings of the International Symposium on Geology of the Cappadocia Region with International Participation Proceedings, Nigde, Turkey, 17–29 October 2007; pp. 223–224.
28. Baş, H.; Temur, S. *Formation Conditions of Iron Barite and Copper in the Çiftehan-Koçak-Elmali (Ulukışla-Niğde) Region, Project Report to the Scientific and Technological Research Council of Turkey (TÜBİTAK)*; TÜBİTAK: Konya, Turkey, 1991.
29. Çevikbaş, A.; Ateş, M.Z. *Cu-Pb-Zn-Co Mineralization in the Vicinity of Çiftehan (Ulukışla-Niğde) [TJK Bulletin]*; Jeoloji Mühendisleri Odası: Ankara, Turkey, 1993.
30. Kahya, A. Geology and geochemistry of Madenköy (Ulukışla/Niğde) area carbonate-hosted Au-Ag-Zn±Pb deposits. *AKU J. Sci. Eng.* **2018**, *18*, 648–663. [CrossRef]
31. Sunkari, E.D.; Lermi, A.; Demir, Y. Fluid evolution of the Fe-Zn skarn deposits in the Çiftehan (Ulukışla-Niğde) area, south-central turkey. In *Recent Research on Sedimentology, Stratigraphy, Paleontology, Tectonics, Geochemistry, Volcanology and Petroleum Geology*; Çiner, A., Banerjee, S., Lucci, F., Radwan, A.E., Shah, A.A., Doronzo, D.M., Hamimi, Z., Bauer, W., Eds.; Advances in Science, Technology & Innovation, Springer Nature Book Series; Springer Nature: Cham, Switzerland, 2023; pp. 109–112. [CrossRef]
32. Öztürk, Y.Y.; Helvaci, C.; Satir, M. Genetic relations between skarn mineralization and petrogenesis of the Evciler Granitoid, Kazdağ, Çanakkale, Turkey and comparison with world skarn granitoids. *Turk. J. Earth Sci.* **2005**, *14*, 255–280.
33. Chowdhury, S.; Lentz, D.R. Mineralogical and geochemical characteristics of scheelite-bearing skarns, and genetic relations between skarn mineralization and petrogenesis of the associated granitoid pluton at Sargipali, Sundergarh District, Eastern India. *J. Geochem. Explor.* **2011**, *108*, 39–61. [CrossRef]
34. Meza-Figueroa, D.; Valencia-Moreno, M.; Valencia, V.A.; Ochoa-Landín, L.; Pérez-Segura, E.; Díaz-Salgado, C. Major and trace element geochemistry and 40Ar/39Ar geochronology of Laramide plutonic rocks associated with gold-bearing Fe skarn deposits in Guerrero state, southern Mexico. *J. S. Am. Earth Sci.* **2003**, *16*, 205–217. [CrossRef]
35. Martin-Izard, A.; Fuertes-Fuente, M.; Cepedal, A.; Moreiras, D.; Nieto, J.; Maldonado, C.; Pevida, L. The Rio Narcea gold belt intrusions: Geology, petrology, geochemistry and timing. *J. Geochem. Explor.* **2000**, *71*, 103–117. [CrossRef]
36. Nicolescu, Ş.; Cornell, D.H.; Bojar, A.V. Age and tectonic setting of Bocşa and Ocna de Fier—Dognecea granodiorites (southwest Romania) and of associated skarn mineralisation. *Miner. Depos.* **1999**, *34*, 743–753. [CrossRef]
37. Ray, G.E.; Webster, I.C.L.; Ettlinger, A.D. The distribution of skarns in British Columbia and the chemistry and ages of their related plutonic rocks. *Econ. Geol.* **1995**, *90*, 920–937. [CrossRef]
38. Blevin, P.L.; Chappell, B.W. The role of magma sources, oxidation states and fractionation in determining the granite metallogeny of eastern Australia. *Earth Environ. Sci. Trans. R. Soc. Edinb.* **1992**, *83*, 305–316. [CrossRef]
39. Ishihara, S.; Sasaki, A. Ore deposits related to granitic magmatism in Japan: A magmatic veiwpoint. *Episodes* **1991**, *14*, 286–292. [CrossRef]
40. Meinert, L.D.; Brooks, J.W.; Myers, G.L. (Eds.) Whole rock geochemistry and contrast among skarn types. In *Skarn Deposits in Nevada, Great Basin Symposium—Geology and Ore Deposits of the Great Basin, Geological Society of Nevada Field 2 Guidebook*; Geological Society of Nevada: Reno, NV, USA, 1990; pp. 179–192.
41. Seyitoğlu, G.; Işık, V.; Gürbüz, E.; Gürbüz, A. The discovery of a low-angle normal fault in the Taurus Mountains: The İvriz detachment and implications concerning the Cenozoic geology of southern Turkey. *Turk. J. Earth Sci.* **2017**, *26*, 189–205. [CrossRef]
42. Dilek, Y.; Thy, P.; Hacker, B.; Grundvig, S. Structure and petrology of Tauride ophiolites and mafic dike intrusions (Turkey): Implications for the Neotethyan ocean. *GSA Bull.* **1999**, *111*, 1192–1216. [CrossRef]
43. Alpaslan, M.; Boztuğ, D.; Frei, R.; Temel, A.; Kurt, M.A. Geochemical and Pb–Sr–Nd isotopic composition of the ultrapotassic volcanic rocks from the extension-related Çamardı-Ulukışla basin, Niğde Province, Central Anatolia, Turkey. *J. Asian Earth Sci.* **2006**, *27*, 613–627. [CrossRef]
44. Akçay, M. Fluid inclusions and chemistry of tourmalines from the Gümüşler Sb-Hg±W deposits of the Niğde Massif (Central Turkey). *Chem. Erde* **1995**, *55*, 225–236.

45. Lermi, A.; Sönmez, M.; Aydin, F. Mineralogy and geochemistry of the Kiziltepe (Çamardi-Niğde) Mn prospect in central Anatolia, Turkey. *Int. Multidiscip. Sci. Geoconf. SGEM Surv. Geol. Min. Ecol. Manag.* **2016**, *1*, 421–428.
46. Hanilçi, N. Bauxite deposits of Turkey. In *Mineral Resources of Turkey*; Pirajno, F., Ünlü, T., Dönmez, C., Şahin, M.B., Eds.; Modern Approaches in Solid Earth Sciences; Springer Nature: Cham, Switzerland, 2019; Volume 16, pp. 681–730. [CrossRef]
47. Dirik, K.; Bozkurt, E.; Gautier, P. *Development, Effects and Consequences of Stress Tectonism in the Kirsehir Massif and Vicinity*; TUBITAK YDABAG-100Y030; TÜBİTAK: Ankara, Turkey, 2003.
48. Altuncu, S.; Tümüklü, A.; Ozgur, Z.F. Trace elements geochemistry of Nigde (Turkey) antimony deposits. *J. Sci. Eng. Res.* **2018**, *5*, 622–631.
49. Gautier, P.; Bozkurt, E.; Hallot, E.; Dirik, K. Dating the exhumation of a metamorphic dome: Geological evidence for pre-Eocene unroofing of the Nigde Massif (Central Anatolia, Turkey). *Geol. Mag.* **2002**, *139*, 559–576. [CrossRef]
50. Umhoefer, P.J.; Whitney, D.L.; Teyssier, C.; Fayon, A.K.; Casale, G.; Heizler, M.T. Yo-Yo tectonics in a wrench zone, Central Anatolian fault zone, Turkey. In *Exhumation Associated with Continental Strike-Slip Fault Systems*; Special Paper 434; Geological Society of America: McLean, VA, USA, 2007; pp. 35–57. [CrossRef]
51. Whitney, D.L.; Teyssier, C.; Heizler, M.T. Gneiss domes, metamorphic core complexes, and wrench zones: Thermal and structural evolution of the Niğde Massif, central Anatolia. *Tectonics* **2007**, *26*, TC5002. [CrossRef]
52. Whitney, D.L.; Umhoefer, P.J.; Teyssier, C.; Fayon, A.K. Yo-Yo tectonics of the Niğde Massif during wrenching in Central Anatolia. *Turk. J. Earth Sci.* **2008**, *17*, 209–217.
53. Idleman, L.; Cosca, M.A.; Heizler, M.T.; Thomson, S.N.; Teyssier, C.; Whitney, D.L. Tectonic burial and exhumation cycles tracked by muscovite and K-feldspar $^{40}Ar/^{39}Ar$ thermochronology in a strike-slip fault zone, central Turkey. *Tectonophysics* **2014**, *612–613*, 134–146. [CrossRef]
54. Gürer, D.; van Hinsbergen, D.J.J.; Matenco, L.; Corfu, F.; Cascella, A. Kinematics of a former oceanic plate of the Neotethys revealed by deformation in the Ulukışla basin (Turkey). *Tectonics* **2016**, *35*, 2385–2416. [CrossRef]
55. Demirtaşlı, E.; Turhan, N.; Bilgin, A.Z.; Selim, M. *Geology of Bolkar Mountains, 50th Anniversary of the Republic, Book of Communiqués of the Congress of Earth Sciences*; MTA Magazine: Ankara, Turkey, 1975; pp. 42–57.
56. Dilek, Y.; Whitney, D.L.; Tekeli, O. Links between tectonic processes and landscape morphology in an alpine collision zone, south—Central Turkey. *Geomorphology* **1999**, *118*, 147–164.
57. Karaoğlan, F. Tracking the uplift of the Bolkar Mountains (south-central turkey): Evidence from apatite fission track thermochronology. *Turk. J. Earth Sci.* **2016**, *25*, 64–80. [CrossRef]
58. Koçyiğit, A.; Beyhan, A. A new intracontinental transcurrent structure: The Central Anatolian Fault Zone, Turkey. *Tectonophysics* **1998**, *284*, 317–336. [CrossRef]
59. Yetiş, C. A Geological Study of the Near and Far Vicinity of Çamardı (Niğde Province) and the Characteristics of the Ecemiş Yarılı Belt Between Maden Bogazi-Kamışlı. Ph.D. Thesis, Faculty of Science, Istanbul University, Istanbul, Turkey, 1978; p. 164.
60. Jaffey, N.; Robertson, A.H.F. New sedimentological and structural data from the Ecemiş Fault Zone, southern Turkey: Implications for its timing and offset and the Cenozoic tectonic escape of Anatolia. *J. Geol. Soc. Lond.* **2001**, *158*, 367–378. [CrossRef]
61. Higgins, M.; Schoenbohm, L.M.; Brocard, G.; Kaymakçı, N.; Gosse, J.C.; Cosca, M.A. New kinematic and geochronologic evidence for the quaternary evolution of the Central Anatolian fault zone (CAFZ). *Tectonics* **2015**, *34*, 2118–2141. [CrossRef]
62. Çalapkulu, F. Geological study of Horoz granodiorite. *Bol. Geol. Soc. Turkey* **1980**, *23*, 59–68.
63. Nazik, A. Stratigraphic Interpretation of the Ulukisla Tertiary Stack According to Foraminifera and Ostracod Fauna. *TJK Bull.* **1989**, *32*, 89–95.
64. Irvine, T.N.; Baragar, W.R.A. A guide to the chemical classification of the common volcanic rocks. *Can. J. Earth Sci.* **1971**, *8*, 523–548. [CrossRef]
65. Kuscu, I.; Kuscu, G.G.; Tosdal, R.M.; Ulrich, T.D.; Friedman, R. Magmatism in the southeastern Anatolian orogenic belt: Transition from arc to post-collisional setting in an evolving orogen. *Geol. Soc. Lond. Spéc. Publ.* **2010**, *340*, 437–460. [CrossRef]
66. Pearce, J.A.; Harris, N.B.W.; Tindle, A.G. Trace element discrimination diagrams for the tectonic interpretation of granitic rocks. *J. Petrol.* **1984**, *25*, 956–983. [CrossRef]
67. Winchester, J.A.; Floyd, P.A. Geochemical discrimination of different magma series and their differentiation products using immobile elements. *Chem. Geol.* **1977**, *20*, 325–343. [CrossRef]
68. Maniar, P.D.; Piccoli, P.M. Tectonic discrimination of granitoids. *Geol. Soc. Am. Bull.* **1989**, *101*, 635–643. [CrossRef]
69. Whalen, J.B.; Currie, K.L.; Chappell, B.W. A-type granites: Geochemical characteristics, discrimination and petrogenesis. *Contrib. Mineral. Petrol.* **1987**, *95*, 407–419. [CrossRef]
70. Meinert, L.D.; Dipple, G.M.; Nicolescu, S. World skarn deposits. In *Economic Geology One Hundredth Anniversary Volume*; Society of Economic Geologists: Littleton, CO, USA, 2005; pp. 299–336. [CrossRef]
71. Einaudi, M.T.; Meinert, L.D.; Newberry, R.J. Skarn deposits. In *Seventy-Fifth Anniversary*; Skinner, B.J., Ed.; Economic Geology Publishing Company: Littleton, CO, USA, 1981; pp. 317–391. [CrossRef]

72. Jamtveit, B. Oscillatory zonation patterns in hydrothermal grossular–andradite garnet: Nonlinear dynamics in regions of immiscibility. *Am. Mineral.* **1991**, *76*, 1319–1327.
73. Ciobanu, C.L.; Cook, N.J. Skarn textures and a case study: The Ocna de Fier-Dognecea orefield, Banat, Romania. *Ore Geol. Rev.* **2004**, *24*, 315–370. [CrossRef]
74. Demir, Y.; Uysal, İ.; Kandemir, R.; Jauss, A. Geochemistry, fluid inclusion and stable isotope constraints (C and O) of the Sivrikaya Fe-skarn mineralization (Rize, NE Turkey). *Ore Geol. Rev.* **2017**, *91*, 153–172. [CrossRef]
75. Chappel, B.W.; White, A.J.R. Two contrasting granite types. *Pac. Geol.* **1974**, *8*, 173–174.
76. Chukwu, A.; Obiora, S.C. Petrogenesis and tectonomagmatic updates on the origin of the igneous rocks in the lower Benue rift, southeastern Nigeria. *Arab. J. Geosci.* **2021**, *14*, 154. [CrossRef]
77. Li, Z.; Tainosho, Y.; Kimura, J.I.; Shiraishi, K. Characterization of the Mefjell plutonic complex from the Sør Rondane Mountains, East Antarctica: Implications for the petrogenesis of Pan-African plutonic rocks of east Gondwanaland. *Isl. Arc* **2005**, *14*, 636–652. [CrossRef]
78. Nelson, W.R.; Dorais, M.J.; Christiansen, E.H.; Hart, G.L. Petrogenesis of Sierra Nevada plutons inferred from the Sr, Nd, and O isotopic signatures of mafic igneous complexes in Yosemite Valley, California. *Contrib. Mineral. Petrol.* **2012**, *165*, 397–417. [CrossRef]
79. Wang, D.; Hou, T.; Botcharnikov, R.; Haselbach, S.; Pohl, F.; Almeev, R.R.; Klügel, A.; Wang, M.; Qin, J.; Zhang, Z.; et al. Experimental constraints on the storage conditions and differentiation of high-ti basalts from the Panzhihua and Hongge layered intrusions, SW China. *J. Petrol.* **2024**, *65*, egae078. [CrossRef]
80. McDonough, W.F.; Sun, S.S. The composition of the Earth. *Chem. Geol.* **1995**, *120*, 223–253. [CrossRef]
81. Rudnick, R.L.; Gao, S. Composition of the Continental Crust. In *Treatise on Geochemistry*; Elsevier: Oxford, UK, 2003; Volume 3, pp. 1–64.
82. Jing, Y.; Ge, W.; Santosh, M.; Dong, Y.; Yang, H.; Ji, Z.; Bi, J.; Zhou, H.; Xing, D. Generation of Nb-enriched mafic rocks and associated adakitic rocks from the southeastern Central Asian Orogenic Belt: Evidence of crust-mantle interaction. *Geosci. Front.* **2022**, *13*, 101341. [CrossRef]
83. Delaloye, M.; Blngol, E. Granitoids from Western and Northwestern Anatolia: Geochemistry and Modeling of Geodynamic Evolution. *Int. Geol. Rev.* **2000**, *42*, 241–268. [CrossRef]
84. Rudnick, R.L. Restites, Eu anomalies and the lower continental crust. *Geochim. Cosmochim. Acta* **1992**, *56*, 963–970. [CrossRef]
85. Nutman, A.; Ali, S.; Mohammad, Y.; Jones, B.G.; Zhang, Q. The Early Eocene (48 Ma) Qaladeza trondhjemite formed by wet partial remelting of mafic crust in the arc-related Bulfat Igneous Complex (Kurdistan, Iraq): Constraints on the timing of Neotethys closure. *Arab. J. Geosci.* **2022**, *15*, 679. [CrossRef]
86. Lee, S.G.; Tanaka, T.; Lee, M.J. Geochemical implication of Eu isotopic ratio in anorthosite: New evidence of Eu isotope fractionation during feldspar crystallization. *Geosci. J.* **2023**, *27*, 271–284. [CrossRef]
87. Grocolas, T.; Müntener, O. The role of peritectic biotite for the chemical and mechanical differentiation of felsic plutonic rocks (Western Adamello, Italy). *J. Petrol.* **2024**, *65*, egae009. [CrossRef]
88. Irzon, R.; Syafri, I.; Kurnia, P.; Sendjadja, P.; Setiawan, V.E.E.E.; Hutabarat, J. Rare earth elements on the A-type Unggan granite and its comparison to the A-type section of Sibolga Granite. *J. Phys. Conf. Ser.* **2018**, *1095*, 012033. [CrossRef]
89. Green, D.H.; Ringwood, A.E. The genesis of basaltic magmas. *Contrib. Mineral. Petrol.* **1967**, *15*, 103–190. [CrossRef]
90. Davidson, J.P. Crustal contamination versus subduction zone enrichment: Examples from the Lesser Antilles and implications for mantle source compositions of island arc volcanic rocks. *Geochim. Cosmochim. Acta* **1987**, *51*, 2185–2198. [CrossRef]
91. Pearce, J.A. Geochemical fingerprinting of oceanic basalts with applications to ophiolite classification and the search for Archean oceanic crust. *Lithos* **2008**, *100*, 14–48. [CrossRef]
92. Richards, J.P. Tectono-magmatic precursors for porphyry Cu–(Mo-Au) deposit formation. *Econ. Geol.* **2003**, *98*, 1515–1533. [CrossRef]
93. Rollinson, H.R. *Using Geochemical Data: Evaluation, Presentation, Interpretation*; Longman Scientific & Technical; Routledge: London, UK, 1993.
94. Gürsu, S.; Möller, A.; Usta, D.; Köksal, S.; Ateş, Ş.; Sunkari, E.D.; Göncüoğlu, M.C. Laser ablation inductively coupled plasma mass spectrometry U-Pb dating of detrital and magmatic zircons of glacial diamictites and pebbles in Late Ordovician sediments of the Taurides and Southeast Anatolian Autochthon Belt, Turkey: Indications for their Arabian-Nubian Provenance. *J. Geol.* **2017**, *125*, 165–202. [CrossRef]
95. Batchelor, R.A.; Bowden, P. Petrogenetic interpretation of granitoid rock series using multicationic parameters. *Chem. Geol.* **1985**, *48*, 43–55. [CrossRef]
96. Pearce, J. Sources and settings of granitic rocks. *Episodes* **1996**, *19*, 120–125. [CrossRef]
97. Meinert, L.D. Compositional variation of igneous rocks associated with skarn deposits-chemical evidence for a genetic connection between petrogenesis and mineralization. *Mineral. Assoc. Can. Short Course Ser.* **1995**, *23*, 401–418.

98. Demir, Y.; Bayraktar, K. Geochemistry, microthermometry, and C and O isotope constraints on the origin of the Düzköy Fe-Cu skarn deposit (Gümüşhane, NE Turkey). *Arab. J. Geosci.* **2020**, *13*, 1260. [CrossRef]
99. Orhan, A.; Demirbilek, M.; Mutlu, H. Geochemistry of the Topuk pluton associated with the Kozbudaklar W-skarn deposit (western Anatolia, Turkey): Implication for crystallization conditions. *J. Afr. Earth Sci.* **2017**, *130*, 141–160. [CrossRef]
100. Sipahi, F.; Akpınar, İ.; Eker, Ç.S.; Kaygusuz, A.; Vural, A.; Yılmaz, M. Formation of the Eğrikar (Gümüşhane) Fe–Cu skarn type mineralization in NE Turkey: U–Pb zircon age, lithogeochemistry, mineral chemistry, fluid inclusion, and O-H-C-S isotopic compositions. *J. Geochem. Explor.* **2017**, *182*, 32–52. [CrossRef]
101. Kaya, M.; Kumral, M.; Yalçın, C.; Abdelnasser, A. Genesis and evolution of the Yolindi Cu-Fe skarn deposit in the Biga Peninsula (NW Turkey): Insights from genetic relationships with calc-alkaline magmatic activity. *Minerals* **2023**, *13*, 1304. [CrossRef]
102. Kara, H.; Yalçın, C.; Ertürk, M.A.; Kalender, L. Mineral chemistry and iron isotope characteristics of magnetites in Pertek Fe-skarn Deposit (Türkiye). *Minerals* **2025**, *15*, 369. [CrossRef]
103. Kaya, M.; Kumral, M.; Yalçın, C.; Abdelnasser, A. Sulfur and carbon–oxygen isotopic geochemistry and fluid inclusion characteristics of the Yolindi Cu-Fe skarn mineralization, Biga Peninsula, NW Turkey: Implications for the source and evolution of hydrothermal fluids. *Minerals* **2023**, *13*, 1542. [CrossRef]
104. Ozturk, Y.Y.; Helvaci, C. Skarn Alteration and Au-Cu Mineralization Associated with Tertiary Granitoids in Northwestern Turkey: Evidence from the Evciler Deposit, Kazdag Massif, Turkey. *Econ. Geol.* **2008**, *103*, 1665–1682. [CrossRef]
105. Le Maitre, R.W.; Streckeisen, A.; Zanettin, B.; Le Bas, M.J.; Bonin, B.; Bateman, P. *Igneous Rocks: A Classification and Glossary of Terms*; Cambridge University Press: Cambridge, UK, 1989.

Disclaimer/Publisher's Note: The statements, opinions and data contained in all publications are solely those of the individual author(s) and contributor(s) and not of MDPI and/or the editor(s). MDPI and/or the editor(s) disclaim responsibility for any injury to people or property resulting from any ideas, methods, instructions or products referred to in the content.

minerals

MDPI

Review

Advances in Distribution Pattern and Enrichment Mechanism of Associated Cobalt Resources in Skarn-Type Deposits, China

Rongfang Zhang [1], Chong Cao [1,*], Yanbo Zhang [2], Shuzhi Wang [1], Yang Zhang [3], Zhaokang Yuan [1], Boxiao Dong [1], Qing Cao [1], Wenzhe Zuo [2] and Zhihua Guo [1]

[1] Tangshan Key Laboratory of Geological Resource Development and Disaster Prevention, School of Emergency Management and Safety Engineering, North China University of Science and Technology, Tangshan 063210, China; z15027507128@163.com (R.Z.); wangszh@ncst.edu.cn (S.W.); kk15130045445@163.com (Z.Y.); 13040043035@163.com (B.D.); caoqing131@163.com (Q.C.); huazifighting@163.com (Z.G.)

[2] Hebei Key Laboratory of Mining Development and Safety Technology, College of Mining Engineering, North China University of Science and Technology, Tangshan 063210, China; fzdn44444@163.com (Y.Z.); zuowenzhej@sina.com (W.Z.)

[3] Hebei Iron and Steel Group Shahe Zhongguan Iron Mine Co., Ltd., Xingtai 054100, China; zhang-yang-168@163.com

* Correspondence: caochong@ncst.edu.cn

Abstract

Although skarn-type deposits represent significant hosts for Co resources, the distribution patterns and enrichment mechanisms of associated Co resources within these deposits have not been systematically investigated. This study summarizes relevant data on Co resources from representative skarn-type deposits in China to comparatively reveal the grade and reserve characteristics, spatiotemporal distribution patterns, and coupled enrichment mechanisms of Co across three principal skarn mineralization subtypes: iron-, copper-, and lead–zinc polymetallic-dominated deposits. Studies demonstrate that Fe-dominated skarn-type cobalt deposits exhibit widespread distribution, high Co grades (100–2000 ppm), and abundant Co reserves (4000–32,000 t), demonstrating significantly superior Co resource potential compared to Cu-dominated (Co grades: 20–200 ppm, Co reserves: 3000–10,000 t) and Pb-Zn polymetallic-dominated (Co grades: 140–853 ppm, Co reserves: approximately 3000 t) subtypes. In these skarn-type cobalt deposits, cobalt is mainly hosted in sulfide minerals. Influenced by tectonic settings, magmatic activity, and hydrothermal fluid evolution, associated Co resources in these skarn-type deposits exhibit both regional zonation and stage-specific differential enrichment patterns. In the formation of skarn-type cobalt deposits, mantle-derived magmas play a critical role in the pre-enrichment of Co. The injection of mafic magmas, assimilation of evaporite sequences, and the dissolution–reprecipitation mechanism of hydrothermal fluids collectively promote the re-enrichment of Co during magmatic evolution. These findings provide a theoretical foundation for targeted exploration, sustainable development, and comprehensive utilization of associated Co resources in skarn-type deposits.

Keywords: skarn-type deposits; associated cobalt resources; distribution patterns; enrichment mechanisms

1. Introduction

Cobalt (Co), an emerging critical metal resource, is widely utilized in lithium-ion batteries, superalloys, and the aviation industry due to its ferromagnetism, low thermal

conductivity, and electrical conductivity, and its importance in modern industrial systems has grown substantially [1,2]. Global demand for Co, significantly driven by the transition towards low-carbon energy infrastructures, increased from less than 1×10^5 t in 2015 to 1.87×10^5 t in 2022, with a Compound Annual Growth Rate (CAGR) of approximately 9.6% [3]. Consequently, cobalt has been classified as a critical mineral resource by numerous nations, including the European Union, the United States, Japan, and China [4–6]. Against this global backdrop, China, the largest Co consumer globally, experiences a severe imbalance between resource scarcity and industrial demand. In 2022, domestic Co production in China was reported at only 2200 t, contrasting sharply with consumption of 1.41×10^5 t, resulting in an import dependency rate of 98% [3]. Furthermore, Chinese Co deposits are characterized by being small-scale and low-grade and having a dispersed distribution, further exacerbating the existing supply–demand imbalance [7]. To mitigate this critical bottleneck, intensifying exploration and development efforts targeting potential Co resources is imperative for enhancing future supply security.

Globally, principal Co deposit types comprise stratiform sediment-hosted Cu-Co deposits (41%), lateritic Ni-Co deposits (36%), magmatic Ni-Cu-Co deposits (15%), and hydrothermal–volcanic polymetallic Co deposits (8%) [6]. Conversely, Co deposits in China are primarily of magmatic and hydrothermal origin [8,9]. Hydrothermal Co deposits in China, which are widely distributed and cover diverse subtypes including skarn, hydrothermal metasomatic, and porphyry, are increasingly recognized as a focus for the exploration and development of Co resources [10,11]. Historically, research on skarn-type deposits has primarily focused on the metallogenic mechanisms of major elements such as Fe and Cu [12,13]. However, understanding of the distribution patterns and enrichment mechanisms of associated Co remains inadequate, reflecting a persistent tendency toward prioritizing major elements over associated elements. Given the high dependence on Co resources and surging demand from emerging industrial sectors, enhancing the understanding of Co metallogenic mechanisms in skarn-type deposits is considered essential and urgent [3].

Skarn-type deposits represent significant sources of Co in China, accounting for 28.2% of the national Co reserves, with Co mainly hosted in Fe-, Cu-, Pb-, and Zn-bearing minerals [14–20]. Furthermore, significant Co enrichment has recently been identified in skarn-type deposits within major metallogenic belts of China, including the Handan–Xingtai Mining Area, the Middle-Lower Yangtze River Metallogenic Belt, and the Gangdese Metallogenic Belt, underscoring the considerable Co metallogenic potential of such deposits [21–23]. Consequently, this study focuses on investigating the grade, reserves, distribution patterns, occurrence states, migration, precipitation, and enrichment mechanisms of associated Co resources in skarn-type deposits to comprehensively understand the key geological controls and processes of cobalt enrichment, thereby advancing the understanding of Co metallogenic mechanisms.

2. Grade and Reserves of Associated Cobalt Resources in Skarn-Type Deposits

Although skarn-type deposits represent significant hosts for Co resources [24,25], notable variations in Co grade and reserves are observed among different deposits. According to the Comprehensive Exploration and Evaluation Specification for Mineral Resources (GB/T 25283-2023) [26], the boundary grade for the comprehensive utilization of associated cobalt is 100 ppm. This study summarizes relevant data on associated Co resources from 42 skarn-type deposits and classifies these deposits into three subtypes for comprehensive assessment: Fe-dominated, Cu-dominated, and Pb-Zn polymetallic deposits (Figures 1 and 2).

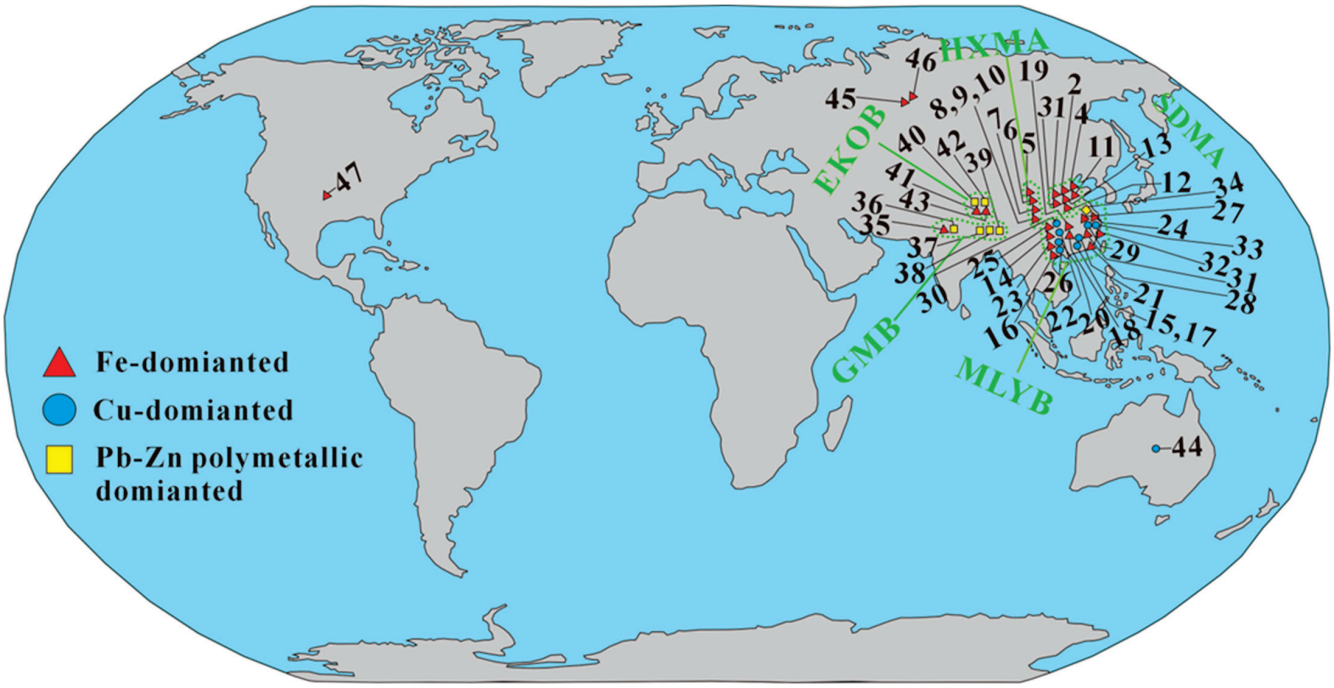


Figure 1. Regional distribution diagram of skarn-type cobalt deposits (the numbers in the figure are deposit numbers, and the corresponding information is listed in Table 1) (modified after [6]). Abbreviation: HXMA—Handan–Xingtai Mining Area, SDMA—Shandong Mining Area, MLYB—Middle-Lower Yangtze River Metallogenic Belt, GMB—Gangdese Metallogenic Belt, EKOB—East Kunlun Metallogenic Belt.

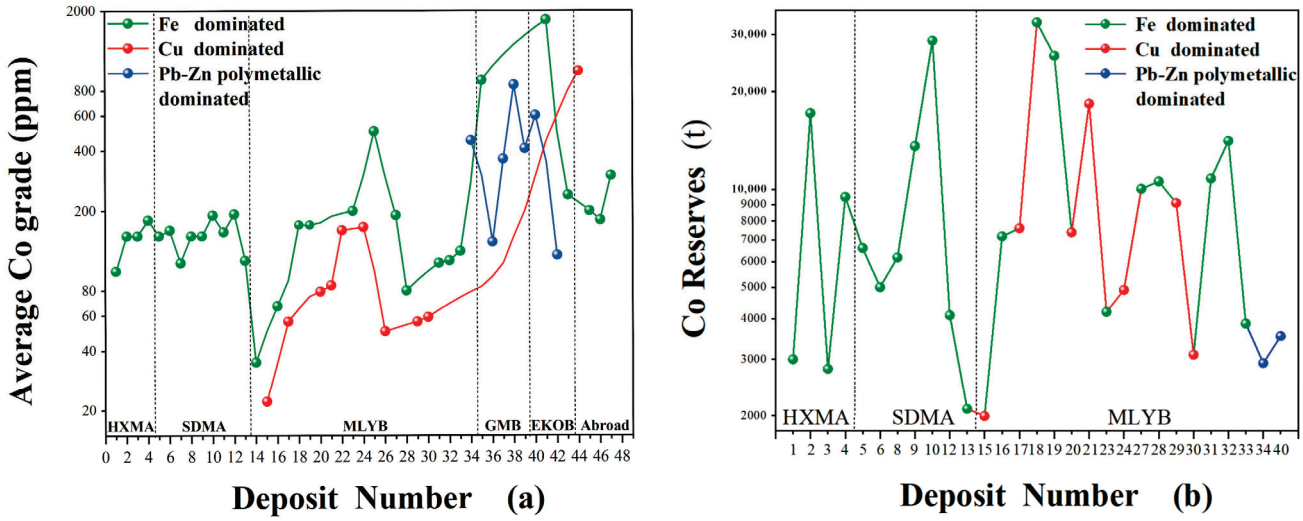


Figure 2. Grade (**a**) and reserves (**b**) diagram of associated cobalt resources in skarn-type deposits (detailed deposit information is listed in Table 1) (the abbreviations HXMA, SDMA, MLYB, GMB, and EKOB are defined in the abbreviation provided in Figure 1).

2.1. Fe-Dominated Skarn-Type Cobalt Deposits

Fe-dominated skarn-type cobalt deposits are globally distributed, with significant occurrences documented in the Sayan Mountains of Russia, Tuva–Mongolia region of Russia, Yamato mining area of Japan, Sesia–Lanzo metallogenic belt in the Western Alps, and Banatic Belt in Eastern Europe (Romania) [27–31]. In China, a significant concentration of such deposits primarily occurs in the Middle-Lower Yangtze River Metallogenic Belt (MLYB), Handan–Xingtai Mining Area (HXMA), and Shandong Mining Area of the eastern regions (SDMA), with minor occurrences in the Gangdese Metallogenic Belt (GMB) and

East Kunlun Metallogenic Belt (EKOB) of the western regions (Figure 2a). These deposits are characterized by high Co grades, ranging from 100 ppm to 2000 ppm. Co reserves commonly exceed 4000 t, and several deposits exceed 10,000 t, indicating substantial potential for economic exploitation (Figure 2b). Consequently, it is proposed that, given their widespread distribution, high grades, and abundant reserves, Fe-dominated skarn-type cobalt deposits represent critical targets for Co resource exploration.

The Zhongguan deposit, a representative "Hanxing-type" skarn Fe deposit, is dominated by primary magnetite ores with total reserves of 94.89 Mt [32]. Associated Co reserves are estimated at 9489 t, with an average Co grade of 180 ppm [32,33]. Notably, pyrite in the deposit is characterized by a generally elevated Co content, which facilitates effective Co resource extraction through optimized beneficiation to improve recovery rates [34]. Similarly, the Baijian Fe deposit, also located in the Handan–Xingtai Mining Area, has been identified as the largest recently discovered Fe deposit in the region [21]. This deposit hosts massive Fe ore reserves of 112 Mt, accompanied by associated Co reserves of 17,186 t, with an average Co grade of 150 ppm and localized high-grade zones reaching 320 ppm [35].

The Longqiao Fe deposit, located in the Luzong Basin of the Middle-Lower Yangtze River Metallogenic Belt, is characterized by a principal ore body extending 1000 m in length [19]. This ore body has been recognized as the largest single Fe ore body among the skarn-type deposits in eastern China [19]. It contains Fe ore resources estimated at 101 Mt, accompanied by Co reserves of 10,810 t with an average Co grade of 110 ppm [19,22]. Notably, sulfur–cobalt concentrates from this deposit exhibit an average Co content ranging from 0.16% to 0.20%, meeting the minimum grade requirement for Grade VI sulfur–cobalt fine powder, which demonstrates potential for Co resource utilization [36]. The Zhangjiawa Fe deposit, located in the Laiwu area of Shandong Province, represents the largest-scale deposit within the regional ore field and contains abundant reserves of open-hearth-furnace-rich ore [37]. Hosted by the inclined termination of the mineralized arc-shaped anticline, it comprises three distinct mining areas: Zhangjiawa I, II, and III. Total proven Fe ore resources are estimated at 290 Mt, accompanied by Co reserves of 48,548 t, which represents 63.66% of the total Co reserves within the ore field [38]. Within the Zhangjiawa I Mining Area, the associated Co reserves are estimated at 6180 t, with an average Co grade of 150 ppm. The Zhangjiawa II Mining Area (also known as Xiaoguanzhuang) contains Co reserves of 13,611.5 t, exhibiting an average Co grade of 150 ppm and localized zones reaching 410 ppm [38]. Meanwhile, Zhangjiawa III Mining Area (also known as Gangli) contains Co reserves of 28,757 t, with an average Co grade of 190 ppm and localized zones reaching up to 2600 ppm [38].

Among global Fe-dominated skarn-type cobalt deposits, the Cornwall deposit (Pennsylvania, USA) is recognized for its substantial Fe resources and high-grade associated critical metals, including Co, Au, and Ag [39]. The deposit exhibits an average Co grade of 300 ppm, making it a significant source of Co in the United States and serving as a representative example for associated Co recovery from skarn-type deposits [40,41]. In Russia, the Goroblagodat Fe deposit exhibits an average Co grade of 200 ppm, while the Magnitogorsk Fe deposit exhibits an average Co grade of 180 ppm [15,42].

2.2. Cu-Dominated Skarn-Type Cobalt Deposits

Compared to Fe-dominated skarn-type cobalt deposits, Cu-dominated skarn-type cobalt deposits are less abundant and primarily concentrated in the Middle-Lower Yangtze River Metallogenic Belt (MLYB). These deposits are typically characterized by low Co grades, ranging from 20 ppm to 200 ppm (Figure 2a). Despite the relatively low average Co grade, total Co reserves are substantial, mostly ranging from 3000 t to 10,000 t (Figure 2b). Consequently, it is proposed that, given their concentrated distribution, low grades, but

substantial reserves, Cu-dominated skarn-type cobalt deposits represent an important supplementary source for Co exploitation.

The Anqing Cu-Fe deposit (also known as Xima'anshan), located in the Middle-Lower Yangtze River Metallogenic Belt, is characterized by Cu and Fe as the principal ore types. Cu ore reserves are estimated at 23.28 Mt, accompanied by Co reserves of 4905 t, with an average Co grade of 166 ppm [25,43]. Through comparative analysis of porphyry-skarn deposits in the Middle-Lower Yangtze River Metallogenic Belt, Zhong et al. revealed that the average Co grade in Cu ores of the Anqing deposit is 3 to 8 times higher than that of the Cu ores in the Dongguashan, Xinqiao, and Wushan deposits (average Co grade: 20 ppm to 50 ppm) and approximately 33 times higher than that of the Cu ores in the Shaxi deposit (average Co grade: 5.2 ppm) [43,44]. This anomaly is attributed to the unique cobalt-hosting monoclinic pyrrhotite in the deposit, characterized by numerous crystallographic vacancies and strong magnetism that significantly enhance its Co enrichment ability, resulting in significantly higher Co grades relative to regional analogous deposits [43,45,46].

Significant spatial variations in Co resource distribution are observed between the Wushan and Chengmenshan Cu deposits, both located in the Jiurui Mining Area of the Middle-Lower Yangtze River Metallogenic Belt [22]. The Wushan deposit is divided into northern and southern ore zones, which exhibit distinct differences in Co grades and reserves. In the northern zone, associated Co reserves are estimated at 7603 t, with an average Co grade of 56 ppm. In contrast, the southern zone contains lower associated Co reserves of 1995 t, with a lower average Co grade of 22 ppm [44]. The Chengmenshan Cu deposit exhibits an average Co grade of 85 ppm, and its abundant ore reserves of 220 Mt result in substantial associated Co reserves of 18,382 t, demonstrating obvious low-grade but high-reserve characteristics [22,47].

The Mount Elliott deposit (Queensland, Australia) serves as a representative example of a global Cu-dominated skarn-type cobalt deposit. It exhibits an average Co grade of 1000 ppm [48], substantially higher than that in analogous deposits in China (Figure 2a), indicating significant Co metallogenic potential.

2.3. Pb-Zn Polymetallic-Dominated Skarn-Type Cobalt Deposits

Compared to Fe-dominated and Cu-dominated skarn-type cobalt deposits, Pb-Zn polymetallic-dominated skarn-type cobalt deposits are less numerous, with primary occurrences concentrated in the Gangdese and East Kunlun Metallogenic Belts of western China. Significant variations in Co grades are documented for this deposit type, ranging from 140 ppm to 853 ppm (Figure 2a). The total Co reserves are estimated at approximately 3000 t (Figure 2b). Consequently, it is proposed that Pb-Zn polymetallic-dominated skarn-type cobalt deposits are characterized by a spatially constrained distribution, moderate grades, and relatively low reserves and thus require further exploration and development.

The Galinge deposit, located in the Qimantage area of the East Kunlun Metallogenic Belt, is characterized by a polymetallic Fe-Cu-Pb-Zn mineralization assemblage [49]. Geological exploration data indicate that total Co resources (proven, controlled, and inferred) are estimated at 4.34 Mt of ore, accompanied by Co reserves of 3538 t. The average Co grade for the deposit is reported as 600 ppm, with the No. II ore body exhibiting a significantly higher grade of 1230 ppm, reflecting localized high Co enrichment [49]. The Pusangguo deposit, located in the Gangdese Metallogenic Belt, was formed primarily through late-stage mineralization and hydrothermal replacement [50]. Total proven metal resources of Cu, Pb, Zn, and Co in this deposit exceed 300,000 t, including Co reserves exceeding 280 t. An average Co grade of 140 ppm is recorded for this deposit [20,51].

The Yaojialing deposit, located in the Tongling Mining Area of the Middle-Lower Yangtze River Metallogenic Belt, is recognized as the sole large-scale Cu-Pb-Zn polymetallic

deposit [52]. Associated Co reserves in this deposit are estimated at 2920 t, with an average Co grade of 450 ppm [53]. Mineralization primarily comprises four ore body types: skarn, stratiform, vein-type, and stratabound-type. Significant Co enrichment is observed in skarn-type and stratiform ore bodies formed during the early high-temperature stage, indicating economic recovery potential [53].

Based on the preceding analysis, it is proposed that Fe-dominated skarn-type cobalt deposits are characterized by their abundance and wide distribution, with significantly higher Co grades than Cu-dominated and Pb-Zn polymetallic-dominated cobalt deposits, coupled with relatively abundant Co reserves. In contrast, Cu-dominated skarn-type cobalt deposits generally exhibit lower Co grades, although certain deposits exhibit relatively high grades along with considerable reserves. Pb-Zn polymetallic-dominated skarn-type cobalt deposits demonstrate higher Co grades than Cu-dominated deposits but are constrained by relatively limited Co reserves. Nevertheless, Liang et al. (2023) conducted a comparative analysis of Co grade and reserve characteristics in the Fe- and Cu-dominated skarn-type cobalt deposits in the Middle-Lower Yangtze River Metallogenic Belt and concluded that no obvious correlation exists between Co mineralization and specific deposit type [54]. Thus, further research is required to investigate the correlation between Co metallogenic potential and skarn-type deposit types.

Table 1. The grade and reserves of associated cobalt resources in skarn-type deposits.

No.	Name	Location	Type	Average Co Grade (ppm)	Co Reserves (t)	Reference
1	Henghui	Xingtai, Hebei Province, China	Fe	100	3000	[55]
2	Baijian	Xingtai, Hebei Province, China	Fe	150	17,186	[35]
3	Yushiwa	Handan, Hebei Province, China	Fe	150	2800	[33]
4	Zhongguan	Xingtai, Hebei Province, China	Fe	180	9489	[32,33]
5	Xishangzhuang	Laiwu, Shandong Province, China	Fe	150	6600	[33]
6	Gujiatai	Laiwu, Shandong Province, China	Fe	160	5000	[33]
7	Chuiyang	Laiwu, Shandong Province, China	Fe	110	——	[38]
8	Zhangjiawa I Mining Area	Laiwu, Shandong Province, China	Fe	150	6180	[38]
9	Zhangjiawa II Mining Area	Laiwu, Shandong Province, China	Fe	150	13,612	[38]
10	Zhangjiawa III Mining Area	Laiwu, Shandong Province, China	Fe	190	28,757	[38]
11	Xinzhuang	Zibo, Shandong Province, China	Fe	157	——	[56]
12	Jinzhao	Zibo, Shandong Province, China	Fe	193	4100	[33]
13	Houjiazhuang	Zibo, Shandong Province, China	Fe	113	2100	[33]
14	Tonglvshan Fe Ore	Daye, Hubei Province, China	Fe	35	——	[57]
15	Wushan South Ore Zones	Ruichang, Jiangxi Province, China	Cu	22	1995	[44]

Table 1. *Cont.*

No.	Name	Location	Type	Average Co Grade (ppm)	Co Reserves (t)	Reference
16	Jinshandian	Daye, Hubei Province, China	Fe	67	7178	[58]
17	Wushan North Ore Zones	Ruichang, Jiangxi Province, China	Cu	56	7603	[44]
18	Chengchao	Ezhou, Hubei Province, China	Fe	170	32,717	[59]
19	Tieshan	Huangshan, Hubei Province, China	Fe	170	25,818	[57]
20	Fengshandong	Huangshan, Hubei Province, China	Cu	79	7384	[60]
21	Chengmenshan	Jiujiang, Jiangxi Province, China	Cu	85	18,382	[22,47]
22	Xujiazu	Daye, Hubei Province, China	Cu	160	——	[57]
23	Daguangshan	Daye, Hubei Province, China	Fe	200	4200	[33]
24	Anqing Cu Ore	Anqing, Anhui Province, China	Cu	166	4905	[43]
25	Zhangsizhu	Daye, Hubei Province, China	Fe	500	——	[57]
26	Tonglvshan Cu Ore	Daye, Hubei Province, China	Cu	50	——	[57]
27	Zhuchong	Anqing, Anhui Province, China	Fe	190	10,045	[61]
28	Baixiangshan	Maan, Anhui Province, China	Fe	80	10,584	[62]
29	Dongguashan	Tongling, Anhui Province, China	Cu	56	9093	[63]
30	Tongshankou	Daye, Hubei Province, China	Cu	59	3099	[64,65]
31	Longqiao	Hefei, Anhui Province, China	Fe	110	10,810	[19]
32	Xinqiao	Tongling, Anhui Province, China	Fe	113	14,129	[66,67]
33	Anqing Fe Ore	Anqing, Anhui Province, China	Fe	126	3864	[43]
34	Yaojialing	Wuhu, Anhui Province, China	Pb-Zn polymetallic	450	2920	[53]
35	Chunzhe	Rikeze, Xizang Province, China	Fe	898	——	[68]
36	Pusangguo	Rikeze, Xizang Province, China	Pb-Zn polymetallic	140	——	[20]
37	Bangpu	Lasa, Xizang Province, China	Pb-Zn polymetallic	363	——	[68]
38	Jiama	Lasa, Xizang Province, China	Pb-Zn polymetallic	853	——	[68]
39	Zhibula	Lasa, Xizang Province, China	Pb-Zn polymetallic	410	——	[17]

Table 1. *Cont.*

No.	Name	Location	Type	Average Co Grade (ppm)	Co Reserves (t)	Reference
40	Galinge	Geermu, Qinghai Province, China	Pb-Zn polymetallic	600	3538	[49]
41	Haisi	Dulan, Qinghai Province, China	Fe	1800	——	[69]
42	Niukutou	Geermu, Qinghai Province, China	Pb-Zn polymetallic	120	——	[70]
43	Zhanbuzhale IV Mining Area	Dulan, Qinghai Province, China	Fe	240	——	[71]
44	Mount Elliott	Queensland, Australia	Cu	1000	——	[48]
45	Goroblagodat	Middle Urals, Russia	Fe	200	——	[15]
46	Magnitogorsk	Baimak-Buribai, Russia	Fe	180	——	[42]
47	Cornwall	Pennsylvania, America	Fe	300	——	[40]

3. Distribution Patterns of Associated Cobalt Resources in Skarn-Type Deposits

Distinct distribution patterns are observed for associated Co resources in skarn-type deposits. With respect to host minerals, Co enrichment is mainly associated with sulfide minerals, with Co occurrence states varying systematically across deposit types. Regionally, Co resources exhibit zonal distribution patterns controlled by tectonic settings and magmatic activity. During the mineralization process, stage-specific variations in Co enrichment are governed by the evolving composition of hydrothermal fluids and the physicochemical conditions.

3.1. Distribution Patterns of Cobalt in Host Minerals

In skarn-type deposits, Co occurs not only as independent cobalt minerals but is also mainly hosted in sulfides, arsenides, and oxides through isomorphic substitution [54,72–74]. To further elucidate its mineralogical distribution, available data on cobalt-hosting minerals and average Co grades in major cobalt-bearing minerals from skarn-type deposits are summarized (Table 2).

Early on, Xu et al. (1979) pointed out that in skarn-type Fe-Cu deposits, pyrite is the primary Co-bearing mineral, with its proportion of Co reaching as high as 50%–90% [75]. Based on this conclusion, we propose that Co in Fe-dominated skarn-type cobalt deposits is mainly hosted in pyrite and magnetite through isomorphic substitution for Fe, with a minor proportion occurring in pyrrhotite (Table 2). Additionally, Co occurs as independent Co minerals in specific deposits, such as cobaltite (CoAsS) in the Baijian deposit [35], grimmitte ($NiCo_2S_4$) in the Zhuchong deposit [54], and glaucodot [(Co,Fe)AsS] in the Longqiao deposit [76]. During hydrothermal mineralization, the complexity of fluid interactions leads to a wide variation in the average Co content of pyrite [17], ranging from 220 ppm to 13,000 ppm, and with most values exceeding 1000 ppm (Table 2). In contrast, magnetite, as the other major cobalt-bearing mineral, exhibits a narrower range of average Co content, from 17 ppm to 320 ppm, with most values below 100 ppm (Table 2). This distribution pattern is exemplified by the Baijian Fe deposit, where Co is mainly hosted in pyrite and magnetite through isomorphic substitution, with a minor proportion occurring as an independent cobalt mineral, cobaltite (CoAsS) [35]. Specifically, pyrite exhibits a significant Co content variation, ranging from 0.187 ppm to 33,331 ppm, while magnetite ranges from 15.2 ppm to 107 ppm [35].

In Cu-dominated skarn-type cobalt deposits, Co is mainly hosted in pyrite and chalcopyrite through isomorphic substitution, with a minor proportion occurring in bornite (Table 2). Additionally, Co occurs as independent cobalt minerals in specific deposits, such as cobaltite, carrollite, and glaucodot in the Dongguashan Cu deposit [63] and siegenite [$(Ni,Co)_3S_4$] in the Anqing Cu-Fe deposit [43]. In this subtype of deposits, pyrite exhibits an average Co content ranging from 626 ppm to 1365 ppm, values typically lower than that in pyrite from Fe-dominated skarn-type cobalt deposits (Table 2). Chalcopyrite (253–500 ppm) exhibits a lower average Co content than pyrite (Table 2). This distribution pattern is exemplified by the Anqing Cu-Fe deposit, where pyrite and chalcopyrite serve as primary cobalt-bearing minerals through isomorphic substitution, with an average content of 1358 ppm and 260 ppm, respectively, with a minor proportion occurring as an independent cobalt mineral, siegenite [43,77,78].

In Pb-Zn polymetallic-dominated skarn-type cobalt deposits, Co is mainly hosted in pyrite, arsenopyrite, and sphalerite through isomorphic substitution, with minor incorporation into chalcopyrite and pyrrhotite (Table 2). Distinct from skarn-type Fe and Cu deposits, these systems commonly develop abundant independent cobalt minerals, including cobaltite and glaucodot [(Co,Fe)AsS] in the Niukutou deposit [70], linnaeite in the Pusangguo deposit [20], and skutterudite ($CoAs_3$) in the Galinge deposit [73]. Notably, pyrite exhibits a highly variable average Co content, ranging from 42.5 ppm to 27,400 ppm, with most values exceeding 100 ppm (Table 2). Sphalerite, a distinctive cobalt-bearing mineral in this deposit type, exhibits an average Co content from 203.7 ppm to 8100 ppm (Table 2). This distribution pattern is exemplified by the Galinge deposit, where Co occurs in two principal modes: One is as independent cobalt minerals, including skutterudite and cobaltite [73]. The other is through isomorphic substitution in arsenopyrite, sphalerite, pyrite, pyrrhotite, and chalcopyrite, with average Co contents of 34,077 ppm, 471 ppm, 194 ppm, 145 ppm, and 2 ppm, respectively [73]. It is evident that the Co content in arsenopyrite is significantly higher than that in pyrite. This further indicates that when both arsenopyrite and pyrite are present in a deposit, Co primarily occurs in arsenopyrite, with only a minor proportion hosted in pyrite [75]. This phenomenon is attributed to the fact that sulfarsenides such as arsenopyrite have a crystal structure more conducive to accommodating cobalt compared to pyrite [70,79].

Based on the preceding analysis, pyrite, chalcopyrite, sphalerite, and arsenopyrite are identified as the primary cobalt-bearing minerals across the three types of the skarn-type deposits (Table 2). These minerals exhibit elevated Co contents, confirming sulfide minerals as the dominant hosts for Co enrichment [23,43,80]. Notably, the development of independent cobalt minerals is restricted to specific deposits.

Table 2. Summary table of host minerals of cobalt and the average content in typical skarn-type cobalt deposits.

Name	Type	Cobalt-Bearing Minerals	Main Cobalt-Bearing Minerals and the Average Content (ppm)	Independent Cobalt Minerals	Reference
Zhongguan	Fe	Pyrite, Magnetite, Pyrrhotite, Hematite	Pyrite (1750), Magnetite (42.8)		[34]
Baijian	Fe	Pyrite, Magnetite	Pyrite (4251), Magnetite (47.6)	Cobaltite	[35]
Henghui	Fe	Pyrite	Pyrite (5233)		[55]
Yushiwa	Fe	Pyrite, Magnetite	Pyrite (2800), Magnetite (320)		[75,81]
Zhangjiawa	Fe	Pyrite	Pyrite (6300)		[38]
Jinshandian	Fe	Pyrite, Magnetite	Pyrite (590), Magnetite (52)		[58]

Table 2. *Cont.*

Name	Type	Cobalt-Bearing Minerals	Main Cobalt-Bearing Minerals and the Average Content (ppm)	Independent Cobalt Minerals	Reference
Baixiangshan	Fe	Pyrite, Magnetite	Pyrite (785), Magnetite (17)		[62]
Chengchao	Fe	Pyrite, Magnetite	Pyrite (1550)		[57,59]
Tieshan	Fe	Pyrite, Magnetite	Pyrite (1580), Magnetite (1046)		[57]
Zhuchong	Fe	Pyrite, Magnetite, Pyrrhotite, Chalcopyrite	Pyrite (2138), Magnetite (72.1)	Grimmite	[43]
Longqiao	Fe	Pyrite, Magnetite	Pyrite (1115), Magnetite (30)	Cobaltite, Carrollite, Glaucodot	[19,82]
Goroblagodat	Fe	Pyrite	Pyrite (220)		[15]
Cornwall	Fe	Pyrite	Pyrite (13,000)		[40]
Peña Colorada	Fe	Pyrite	Pyrite (1200)		[83]
Dongguashan	Cu	Pyrite, Magnetite, Chalcopyrite, Pyrrhotite	Pyrite (626)	Carrollite, Cobaltite, Glaucodot	[63]
Tongshankou	Cu	Pyrite, Chalcopyrite	Pyrite (629), Chalcopyrite (253)		[64,65]
Fengshandong	Cu	Pyrite, Chalcopyrite	Pyrite (689)		[60]
Anqing	Cu	Pyrite, Magnetite, Chalcopyrite, Pyrrhotite	Pyrite (1358), Chalcopyrite (260)	Siegenite	[43,77,78]
Chengmenshan	Cu	Pyrite, Chalcopyrite	Pyrite (790)		[47]
Tonglvshan	Cu	Pyrite, Magnetite, Chalcopyrite, Bornite	Pyrite (1365), Chalcopyrite (500)	Carrollite, Cobaltite, Safflorite	[84]
Pusangguo	Pb-Zn polymetallic	Pyrite, Sphalerite, Chalcopyrite, Galena	Pyrite (490.9), Sphalerite (1102)	Cobaltite, Carrollite, Linnaeite	[20,85]
Niukutou	Pb-Zn polymetallic	Pyrite, Arsenopyrite, Pyrrhotite, Sphalerite, Chalcopyrite,	Pyrite (42.5), Sphalerite (230.7), Arsenopyrite (3755.9)	Cobaltite, Glaucodot	[70]
Yaojialing	Pb-Zn polymetallic	Pyrite, Sphalerite, Chalcopyrite	Pyrite (193.2), Sphalerite (733.9)	Carrollite	[53]
Lalingzaohuo	Pb-Zn polymetallic	Pyrite, Chalcopyrite, Pyrrhotite, Sphalerite	Pyrite (27,400), Sphalerite (8100)	Cobaltite	[18]
Zhibule	Pb-Zn polymetallic	Pyrite, Magnetite, Galena, Sphalerite	Pyrite (2454), Magnetite (228)	Siegenite	[17]
Galinge	Pb-Zn polymetallic	Pyrite, Arsenopyrite, Sphalerite, Pyrrhotite, Chalcopyrite	Pyrite (194), Sphalerite (471), Arsenopyrite (34,077)	Skutterudite, Cobaltite	[73]

3.2. Distribution Patterns of Cobalt in Metallogenic Regions

It is proposed that the distribution of Co resources in skarn-type deposits exhibits regional zonation patterns, as revealed by the preceding analysis. The Handan–Xingtai and Shandong Mining Areas are dominated by skarn-type Fe deposits, while the East Kunlun and Gangdese Metallogenic Belts mainly host skarn-type Pb-Zn polymetallic deposits. Furthermore, the Middle-Lower Yangtze River Metallogenic Belt hosts multiple types of skarn-type deposits, including Fe, Cu, and Pb-Zn polymetallic deposits (Figure 1). These regional distribution patterns are fundamentally controlled by regional tectonic settings and associated magmatic activities (Table 3).

The Handan–Xingtai Mineral Area (HXMA) is recognized as a prominent skarn-type Fe metallogenic province in China, hosting over 100 Fe deposits of various sizes, with total reserves exceeding 1000 Mt [12,86]. Notably, significant Co mineralization occurs at the Baijian, Zhongguan, and Henghui Fe deposits in the region, with Co grades consistently ranging from 100 ppm to 200 ppm (Figure 2a). This area is located in the southern segment of the Taihang Mountain Uplift Belt in the central North China Craton [12]. During the Indosinian period, a series of EW-NNE-trending concealed basement fault zones were developed through subduction interactions between the Paleo-Siberian Plate and the Yangtze Block, coupled with the Pacific Plate [21,87]. The metallogenic age of the skarn-type cobalt deposits in this region is primarily concentrated between 135 and 125 Ma [21], with rock types mainly comprising diorite, monzonite, and monzodiorite [21,34,35,55]. The mining area experienced three stages of magmatic activity consisting of eight intrusive episodes [12]. During this process, repeated injection of mafic magma into felsic magma chambers significantly increased the Co content in the hydrothermal fluids, while well-developed fault structures provided migration pathways for cobalt-bearing fluids from deep to shallow crustal levels [12,21,88]. Host strata are dominated by Ordovician carbonate sequences, primarily composed of dolomite, quartz sandstone, and gypsum breccia, which provide prerequisites for Co mobilization and enrichment [21].

The Gangdese Metallogenic Belt (GMB), which hosts numerous skarn-type Pb-Zn polymetallic deposits, is recognized as another Co-enriched belt comparable to the Middle-Lower Yangtze River Metallogenic Belt [23]. This belt exhibits distinct east–west contrasts in Co distribution patterns and enrichment mechanisms [23,68]. In the eastern segment of this belt, deposits such as Jiama, Zhibula, and Chunzhe exhibit an average Co content exceeding 400 ppm in ores, whereas ores from the Bangbule and Chagele deposits in the western segment generally exhibit values of less than 3 ppm [17,68]. This belt is located in the southern Lhasa Terrane, between the Indus-Yarlung Tsangpo Suture Zone and the Milashan–Luobadui Fault [89–92]. It was influenced by the Jurassic–Cretaceous subduction of the Neo-Tethyan oceanic crust, which resulted in the development of a nearly EW-trending tectonic–magmatic zone [93,94]. During the Paleogene, the region experienced the main collision (65–41 Ma) and late collision (40–26 Ma) between the Indian and Asian continents, entering the Miocene post-collisional tectonic stage (25–0 Ma) [17]. The mineralization ages of skarn-type cobalt deposits in the area are primarily concentrated in 65–41 Ma and 33–13 Ma [23], corresponding to four major stages of magmatic activities [95–100]. The rock types are predominantly granodiorite, quartz monzonite, and monzogranite [23]. Western cobalt-depleted deposits were formed in Paleocene continental collision settings, with mineralization ages concentrated around 61 Ma [23,101,102]. These deposits are associated with limited magmatic activity, lacking juvenile lower crust development or mantle-derived magma injection [23,103]. In contrast, eastern Co-enriched deposits were formed in Miocene post-collisional extensional or Oligocene late-collisional settings, with mineralization ages concentrated around 15 Ma [17,104–110]. This eastern mineralization phase demonstrates intense magmatic activity, featuring juvenile lower crustal

additions and mantle-derived magma injection [23,103]. Furthermore, the differential Co enrichment between segments is further enhanced by adakitic characteristics in eastern intrusions compared to inherited arc magma signatures in western intrusions [23,103].

Extensive Co geochemical anomalies identified at a 1:50,000 scale in the East Kunlun Metallogenic Belt (EKOB) are spatially associated with the Galinge, Haisi, and Niukutou Pb-Zn polymetallic deposits, indicating significant Co metallogenic potential [49]. Considerable variations in Co grades are observed in these deposits, ranging from 120 ppm to 1800 ppm (Figure 2a). The belt is located in the western Central Orogenic Belt, where its formation is closely related to the collision of the Bayan Har and Qiangtang terranes with the Qaidam Basin after the Paleo-Tethys closure [111–115]. The belt is tectonically subdivided by major crustal-scale fault zones, including the nearly EW-NWW-trending North Kunlun, Central Kunlun, and South Kunlun Faults [49]. The Paleozoic–Triassic development of a trench–island arc–backarc system facilitated Co deposit formation through continuous northward subduction–accretion along the Kunlun suture zone, as exemplified by the Haisi and Xiarihamu deposits [69,116,117]. The mineralization ages of skarn-type cobalt deposits in this belt are mainly concentrated between 237 and 212 Ma, with rock types mainly comprising granodiorite and monzogranite [49,69,70]. The mineralizing magmas were primarily derived from partial melting of the lower crust induced by upwelling asthenosphere, with additional mantle-derived contributions, representing typical crust–mantle mixed sources [118]. Intense magmatic activities promoted Co migration from the mantle to the crust, thus providing a material basis for the development of cobalt-bearing skarn-type deposits [18,119].

The Middle-Lower Yangtze River Metallogenic Belt (MYLB) hosts significant Co resources, totaling approximately 2.79×10^5 t, classified into three types based on the relationship between Co grades in deposits and the boundary grade for the comprehensive utilization of associated cobalt (100 ppm) [22]. Approximately 1.08×10^5 t is classified as favorably recoverable (reaching 100 ppm), while 4.6×10^4 t exhibits moderate recovery potential (approaching 100 ppm), and the remaining 1.25×10^5 t represents potential future resources (below 100 ppm) [22]. The belt is dominated by skarn-type Fe and Cu deposits, where Fe deposits exhibit average Co grades ranging from 35 ppm to 500 ppm, while Cu deposits range from 22.1 ppm to 166 ppm (Figure 2a). This belt is located in the northern margin of the Yangtze Craton, and it was formed through subduction and collision between the Yangtze and North China blocks along the Xiangfan–Guangji and the Tan–Lu Faults [120,121]. The mineralization ages of skarn-type cobalt deposits in this belt are mainly concentrated between 145 and 127 Ma [54], with rock types mainly comprising granodiorite, diorite, and quartz diorite [19,43,54,122]. The deep material sources for the mineralization system include mantle upwelling, partial melting of the lower crust, and crust–mantle mixing [123]. These magmatic activities were controlled by the Mesozoic tectonic regime transformation and are closely associated with large-scale Mesozoic mineralization events in eastern China [124]. However, systematic investigations into Co enrichment mechanisms in skarn-type deposits of this belt remain insufficient, hindering a comprehensive understanding of metallogenic processes.

Table 3. Summary table of characteristics and controls on cobalt resources in skarn-type cobalt deposits across metallogenic regions.

Metallogenic Region	Geotectonic Settings	Main Mineralization Ages of Deposits	Main Rock Types of Deposits	Magmatic Source	Main Types of Deposits	Typical Deposits	Distribution Patterns of Co Resources	Influencing Factors	Reference
Han–Xing Mining Area in China	Subduction of the Paleo-Siberian, Yangtze, and Pacific Plates	135–125 Ma	Diorite, Monzonite, Monzodiorite	Predominantly mantle-derived with minor crustal or mixed crust-mantle sources	Fe	Baijian, Henghui, Zhongguan	High Co grade and abundant Co reserves	Multi-stage magmatic activities, relatively developed fault structures, ordovician carbonate strata	[12,21,34,35, 55,88]
Gangdese Metallogenic Belt in China	Subduction of the Neo-Tethyan oceanic crust	65–41 Ma and 33–13 Ma	Granodiorite, Quartz Mozonite, Monzogranite	Predominantly mantle-derived with minor mixed crust-mantle sources	Pb-Zn polymetallic	Jiama, Zhibula	East segment Co-enriched, west segment Co-poor	Eastern Co-enriched deposits with adakitic ore-forming intrusions, young mineralization age, and intense magmatic activity	[23,68,93,94, 103]
East Kunlun Metallogenic Belt in China	Collision between the Bayan Har or Qiangtang terrane and the Qaidam Basin	237–212 Ma	Granodiorite, Monzogranite	Mantle-derived, mixed crust-mantle sources	Pb-Zn polymetallic	Galinge, Niukutou	Significant variation in Co grade	"Trench–island arc–back arc basin" tectonic system, intense magmatic activity	[49,69,70,111–115,118,119]
Middle-Lower Yangtze Metallogenic Belt in China	Subduction and collision of the Yangtze and North China blocks	145–127 Ma	Granodiorite, Diorite, Quartz diorite	Mantle-derived, mixed crust-mantle sources	Fe, Cu	Zhuchong, Anqing	Extremely abundant Co reserves	————	[19,22,43,54, 120–123]
Cornwall mining district in America	Variscan orogeny	295–270 Ma	Granite	————	Fe	Cornwall	Relatively high Co grade	————	[39,41,125]
Cloncurry mining district (Mount Isa Eastern Fold Belt) in Australia	Late tectonism	1510 Ma	Granite	————	Cu	Mount Elliott	Extremely high Co grade	————	[48]
Magnitogorsk zone in Russia	Island arc	Late-Devonian to Early Carboniferous	Gabbroid	Mantle-derived	Fe	Magnitogorsk	Relatively high Co grade	————	[126–128]

Based on the preceding analysis, significant Co enrichment occurs in skarn-type deposits across multiple major metallogenic regions. The spatially heterogeneous enrichment of Co is systematically controlled by regional geotectonic settings, rock types, and magmatic activities, which collectively govern the migration pathways, enrichment zones, and transport efficiency of ore-forming fluids, thereby influencing the effective enrichment of Co [12,18,21,23,88,103,119]. These factors result in a distinct zonal distribution pattern of associated Co resources in these regions (Figure 1).

3.3. Distribution Patterns of Cobalt in Metallogenic Process

The metallogenic process of skarn-type deposits is typically divided into distinct stages, including the dry skarn, wet skarn, oxide, sulfide, and carbonate stages [129]. During mineralization, the geochemical behavior of Co varies significantly with the evolving composition of hydrothermal fluids, resulting in stage-specific enrichment patterns [130,131]. Therefore, the distribution patterns of Co and its controlling factors are summarized for 10 skarn-type deposits (Table 4).

Table 4. Summary table of stage distribution patterns and controls on cobalt enrichment in typical skarn-type cobalt deposits.

Name	Main Metallogenic Stage	Enrichment Degree of Co Element	Influencing Factors	Reference
Zhongguan	Wet skarn	Depleted	Continuous high-temperature oxidation conditions prevent the decomposition of cobalt complexes	[34]
	Oxide	Enriched	Decreased fluid temperature, elevated oxygen fugacity	
Henghui	Early sulfide	Enriched	Magnetite crystallization and multi-stage mafic magmatism causing decreased fluid temperature and salinity	[55]
	Late sulfide	Depleted	Hydrothermal alterations release Co into fluid	
	Carbonate	Re-enriched	Meteoric water injection causes fluid cooling and dilution	
Anqing	Early quartz–sulfide	Enriched	Meteoric water injection causes fluid temperature and chloride complex concentration to decrease	[43]
	Late quartz–sulfide	Depleted	Continuous meteoric water injection causes further fluid cooling and dilution	
Zhuchong	Sulfide	Enriched	Magnetite crystallization and wall-rock Mg-Ca strata cause fluid temperature and oxygen fugacity to decrease	[54]
Wushan	Quartz–sulfide I Quartz–sulfide II	Depleted Enriched	Formation of limited pyrite amount Elevated fluid temperature, the massive formation of pyrite	[44]
Xinqiao	Quartz–sulfide	Enriched	Elevated fluid temperature	[122]
Galinge	Early sulfide I Early sulfide II Late sulfide	Enriched Re-enriched Depleted	———— Elevated fluid temperature and pH, fluid–rock interaction Decreased fluid temperature	[73]
Zhibula	Quartz–sulfide	Enriched	————	[17]
Yaojialing	Early sulfide Late sulfide	Enriched Depleted	———— Decreased fluid temperature	[53]
Niukutou	Pyrrhotite Chalcopyrite Sphalerite–Galena	Depleted Enriched Depleted	———— Decreased fluid temperature and oxygen fugacity ————	[70]

In the Henghui deposit, Co is mainly precipitated and enriched during the sulfide and carbonate mineralization stages [55]. During the early sulfide stage, the highest average Co content of 9122 ppm is recorded in coarse-grained disseminated pyrite (Py_{2a}), resulting from the combined effects of decreasing hydrothermal fluid temperature and salinity, extensive magnetite crystallization, and multi-stage mafic magma injection [55,88,132–136]. During the late sulfide stage, shearing fragmented Py_{2a} into coarse-grained cataclastic pyrite (Py_{2b}) [55]. Hydrothermal fluids infiltrating fractures generated abundant secondary pores, promoting extensive hydrothermal alteration that mobilized Co into the hydrother-

mal system and reduced the average Co content of Py_{2b} to 848 ppm [55,137]. During the carbonate stage, the injection of meteoric water caused cooling and dilution of the hydrothermal fluids, triggering the reprecipitation and enrichment of Co and elevating the average Co content in Py_3 to 6870 ppm [55,138,139].

In the Anqing Cu-Fe deposit, Co is mainly precipitated and enriched during the quartz–sulfide stage [43]. Although skarn minerals and magnetite crystallize during the skarn stage, Co enrichment remains limited due to low fluid–mineral partition coefficients in these phases [43]. During the early quartz–sulfide stage, the injection of meteoric water reduces the hydrothermal fluid temperature and the concentration of chloride complex [43]. These variations promote Co incorporation into pyrite and pyrrhotite lattices, resulting in precipitation and concentration, with their average Co contents reaching 4871 ppm and 753 ppm, respectively [43,131,138]. Progressive meteoric water injection during the late quartz–sulfide stage further cooled and diluted the hydrothermal fluids. These physicochemical changes decrease Co solubility, leading to inhibited significant precipitation and enrichment in pyrite and a decrease in the average Co content to 95.4 ppm [43,131,138].

In the Galinge Pb-Zn deposit, Co is mainly enriched during the sulfide stage [73]. In the early sulfide stage I, Co occurs primarily in arsenopyrite, with minor proportions occurring in pyrrhotite and pyrite, with an average content of 13,018 ppm, 67.7 ppm, and 192.6 ppm, respectively [73]. As the system progresses to early sulfide stage II, elevated As/S ratios in arsenopyrite indicate rising fluid temperatures, which increases the average Co content of arsenopyrite to 47,703 ppm and that of pyrrhotite to 359 ppm [73,140,141]. Concurrently, an increase in fluid pH promotes the reaction $CoCl_4^{2-} + 3H_3AsO_3^0 \rightarrow CoAs_3 + 4Cl^- + 2H^+ + 3.5H_2O + 2.75O_2$, facilitating the precipitation of abundant skutterudite ($CoAs_3$). Continuous fluid–rock interactions deplete the As concentrations, leading to decreased As/S ratios and the transformation of skutterudite into cobaltite (CoAsS) [73,142]. The formation of these cobalt independent minerals contributes to the highest Co concentrations observed in minerals [73]. During the late sulfide stage, fluid inclusion evidence indicates decreasing temperature, which reduces the average Co content in pyrrhotite to 69 ppm and in pyrite to 95 ppm, respectively [73,143].

Based on the preceding analysis, the stage-specific distribution patterns of Co reflect the cumulative effects of multi-stage mafic magma injection, fluid–rock interaction, and meteoric water injection. These processes collectively drive changes in physicochemical conditions of the hydrothermal fluids, including temperature, oxygen fugacity, and salinity, which govern differential Co enrichment across mineralization stages [43,55,73,88,131–136,138–143]. Precipitation and enrichment of Co mainly occur during sulfide stages, although notable variations exist between different deposits (Table 4).

4. Enrichment Mechanism of Associated Cobalt Resources in Skarn-Type Deposits

Cobalt, as a typical element with a pronounced mantle affinity, is enriched in skarn-type deposits via processes intrinsically linked to deep-seated magmatic activities [14,144]. Within the high-temperature, high-pressure, and reduced deep-seated magma chambers, Co mainly forms hydride or carbonyl–hydride complexes. These compounds migrate upward through magmatic–hydrothermal conduits along fractures [144–147]. The decomposition of cobalt-bearing compounds occurs in response to evolving physicochemical conditions in the hydrothermal system, enabling migration and culminating in the effective enrichment under favorable metallogenic constraints [34]. During this process, the material contribution from mantle-derived magmas provides the primary condition for Co enrichment, while the injection of mafic magmas, the assimilation of evaporite sequences, and the dissolution–reprecipitation mechanism of hydrothermal fluids during the mag-

matic evolution further promote the re-enrichment of Co [21,23,35,54,55,110]. These four factors synergistically drive the effective enrichment of Co in the magmatic–hydrothermal systems (Table 5).

4.1. Magmatic Source

Cobalt, a transition metal, is widely distributed throughout the Earth's layers with significant abundance variations, decreasing systematically from the core (420 ppm) through the lower mantle (200 ppm) and the upper mantle (160 ppm) to the crust (25 ppm) [148]. The mantle serves as a significant source reservoir due to its high Co abundance, which provides the material foundation for mantle-derived Co deposits such as Volcanogenic Massive Sulfide (VMS) deposits [149,150]. VMS deposits are volcanic in origin, and skarn-type deposits are of a hydrothermal–metasomatic origin [129]. Given their classification as hydrothermal deposits, Co enrichment in skarn-type deposits is inferred to be closely associated with mantle-derived magmas. Known mantle-derived magmatic skarn-type deposits are mainly restricted to the Handan–Xingtai Mining Area and the Gangdese Metallogenic Belt [23,151–154].

Table 5. Controlling factors and specific mechanisms of associated cobalt resources in skarn-type deposits.

Controlling Factors	Specific Mechanisms	Representative Examples	Reference
Mantle-derived magma sources	High Co content in mantle-derived magmas provides the additional Co source	Handan–Xingtai Ming Area, Gangdese Metallogenic Belt	[23,151–154]
Mafic magma injection	Inherited high Co content from mantle-derived magmas and mixed with felsic magmas	Baijian deposit, Henghui deposit	[21,55,110]
Assimilation of evaporite sequences	Extensive assimilation of evaporite sequences with magmatic–hydrothermal fluids alter fluid composition and metallogenic environment	Baijian deposit, Zhuchong deposit	[35,54]
Dissolution and re-precipitation mechanism of hydrothermal fluids	Enhanced activity of late-stage hydrothermal fluids drives the reprecipitation and enrichment of Co	Henghui deposit, Zhongguan deposit, Baijian deposit	[35,55]

Recent investigations into the attributes of magma sources in the Handan–Xingtai Mining Area have been conducted by many scholars [151–154]. Amphiboles from the Ziquan, Guzhen, Fushan, Wuan, and Qicun intrusions were analyzed by electron probe microanalysis (EPMA) and laser ablation inductively coupled plasma mass spectrometry (LA-ICP-MS) [151–154]. Integrated with TiO_2-Al_2O_3 discrimination diagrams, these data reveal that the magma source of these intrusions is mainly mantle-derived or crust–mantle-mixed, with minor crust-derived contributions [151–154]. Our research group performed Sr isotope analyses of apatite in diorite intrusions from the Zhongguan deposit using LA-ICP-MS. These analyses yield initial $^{87}Sr/^{86}Sr(i)$ ratios ranging from 0.7053 to 0.7076. Integrated with Sm-La-Th-Y relationships in apatite magma source discrimination diagrams, these isotopic signatures indicate a dominantly mantle-derived magma source with minor crustal-derived components (unpublished data). These results collectively demonstrate that the magma source in the Handan–Xingtai Mining Area is primarily mantle-derived. We propose that this mantle-dominated magma source characteristic is closely linked to the regional development of numerous skarn-type Fe deposits with significant Co enrichment.

For the Gangdese Metallogenic Belt, Wang et al. (2025) demonstrated that mantle-derived magmas or involvement of mafic juvenile lower crust provide the essential material basis for the significant enrichment of Co through a multi-isotope system (Pb-Hf-Os) [23].

The Pusangguo (18.555, 15.716, 39.044), Jiama (18.608, 15.618, 38.990), and Zhibula (18.437, 15.574, 38.536) deposits exhibit relatively low $^{206}Pb/^{204}Pb$, $^{207}Pb/^{204}Pb$, and $^{208}Pb/^{204}Pb$ ratios [155–160], whereas the Jiama (6.0), Nuri (6.4), and Zhibula (7.2) deposits exhibit higher ε_{Hf} (t) values [161–163]. Furthermore, the initial $^{187}Os/^{188}Os$ ratios of the Zhibula (0.49), Leqingla (~0.1), Chengba (~0.1), and Jiama (~0.05) deposits approach or fall below the mantle value (~0.13) [17,109,164–166]. These isotopic signatures, combined with widespread occurrences of mafic gabbro enclaves, collectively provide compelling evidence for contributions from mantle-derived magma sources or juvenile mafic lower crust [23]. The involvement of these components is consequently considered to provide additional sources of Co for the formation of cobalt-enriched skarn-type deposits throughout the belt, thereby promoting effective Co enrichment [23].

In summary, despite contrasting tectonic settings between the Handan–Xingtai Mining Area and the Gangdese Metallogenic Belt (Table 3), both regions exhibit significant Co enrichment in their skarn-type deposits that are primarily derived from mantle-derived magmas. Thus, we propose that mantle-derived magmas represent a key controlling factor for Co enrichment.

4.2. Injection of Mafic Magmas

Fe-dominated skarn-type cobalt deposits associated with intermediate-mafic magmas generally exhibit higher average Co grades than Cu-dominated deposits associated with intermediate-felsic magmas (Figure 2a). This contrast demonstrates the critical control of magma composition on Co enrichment. Regarding material sources, as products of mantle partial melting, mafic magmas provide abundant Co to metallogenic systems through inherited high Co content [167], while the mafic magmas' low viscosity and high mobility enable efficient Co migration and enrichment [168]. During the metallogenic processes, mafic magma injection modifies mineralization environments through mixing with magmatic–hydrothermal fluids and enables Co migration and precipitation [21,55]. This dual control mechanism, which encompasses both material source supplementation and modification of the metallogenic environment, drives significant Co enrichment in skarn-type deposits, as exemplified by the Baijian, Henghui, Zhongguan, and Pusangguo deposits [21,55,110].

The Baijian Fe deposit exhibits exceptional Co enrichment characterized by multi-stage precipitation at low temperatures, which contrasts with conventional hydrothermal mineralization theory that typically posits Co precipitation during high-temperature hydrothermal stages [21,130]. Notably, late-stage low-temperature veinlet pyrite exhibits an anomalously high Co content that mostly exceeds 10,000 ppm [21]. This phenomenon is genetically related to multiple injections of mafic magma into a felsic magmatic chamber, as evidenced by mineral chemical data of the Qicun intrusion [88]. Specifically, the $Mg^{\#}$ values of amphibole phenocrysts are positively correlated with temperature and pressure but negatively correlated with oxygen fugacity [88]. Based on this evidence, Qin (2022) proposed that the injection of mafic magma not only provides a supplementary Co source but also modifies physicochemical conditions of temperature, oxygen fugacity, and pressure in the metallogenic system through felsic magma mixing [21]. This process establishes favorable conditions for Co migration and precipitation, ultimately leading to significant Co enrichment in the late low-temperature stage [21].

In the Henghui deposit, the sulfide-stage pyrite exhibits a high Co content of 9122 ppm, attributed to the combined effects of decreasing temperature and salinity of hydrothermal fluids, among other factors [55]. Furthermore, mantle-derived mafic magma ascent and subsequent mixing with crust-derived felsic magma are demonstrated by plagioclase zoning data from the Wuan intrusion, amphibole thermobarometer calculations (yielding

temperatures of 697–754 °C and pressures of 39–65 MPa), and shallow-level metasomatic characteristics [169]. Based on this evidence, Dong et al. (2024) propose that Co enrichment in the pyrite is primarily controlled by multi-stage mafic magma injection and associated magma mixing processes [55]. Similarly, Cao et al. (2025) demonstrate that oscillatory zoning of Co in pyrite from the Jinchang porphyry deposit records multiple injections of mafic magma, proposing that such events significantly elevate the Co content in the ore-forming fluids and promote Co enrichment in the porphyry deposits [170]. Additional evidence for mafic magma injection is provided by the discovery of gabbroic inclusions in the Pusangguo deposit and mafic inclusions in the Zhongguan deposit (Figure 3), although their specific roles in Co enrichment remain underexplored [110] (unpublished data).

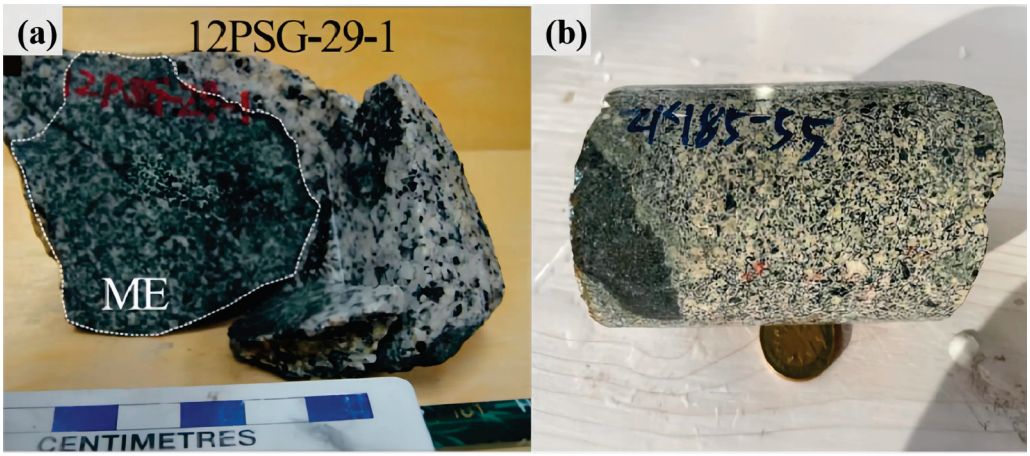


Figure 3. (**a**) Gabbro inclusions observed from the Pusangguo deposit, Gangdese Metallogenic Belt, China [110] (ME—microgranular enclave). (**b**) Mafic inclusions observed in the diorite from the Zhongguan deposit, Handan-Xingtai Mining Area, China.

In summary, the enrichment of Co in skarn-type deposits is significantly facilitated by multi-stage mafic magma injections and associated mixing processes. The Baijian, Henghui, Zhongguan, and Pusangguo deposits, which are primarily concentrated in the Handan–Xingtai Mining Area and Gangdese Metallogenic Belt, are associated with mantle-derived magmas, and this geological association provides both the material basis for Co enrichment and favorable conditions for mafic magma injections.

4.3. Assimilation of Evaporite Sequences

Evaporite sequences, which are evaporative sedimentary units primarily composed of gypsum, anhydrite, and sulfate minerals, contain abundant saline components including SO_4^{2-}, Cl^-, CO_3^{2-}, Na^+, and K^+. These constituents control metal enrichment and mineralization through diverse geochemical mechanisms [171–181]. SO_4^{2-} serves as an oxidizing agent that transforms low-valence Co into higher oxidation states. This process inhibits the premature removal of Co through sulfide precipitation during early mineralization stages, thereby preserving Co for subsequent enrichment in later stages [181]. On the other hand, other saline components including Cl^-, CO_3^{2-}, Na^+, and K^+ act as complexing agents that enhance the dissolution and migration of metallic elements through complexation reactions [181]. Furthermore, the low mechanical strength of evaporite sequences provides favorable conditions for magma emplacement and hydrothermal fluid migration [182]. While existing studies mainly focus on the controlling mechanisms of evaporite sequences on Fe mineralization in skarn-type deposits, systematic investigations into their influence on Co enrichment remain inadequate [181]. In this paper, the Baijian, Zhongguan, and Zhuchong deposits are examined to systematically investigate this mechanism [35,54].

The Baijian deposit is located in the contact zone between Yanshanian intermediate diorite and Middle Ordovician wall rocks dominated by a gypsum-bearing limestone formation [183–185]. The extensive development of evaporite sequences provides the sulfur source for mineralization and effectively promotes Co enrichment through extensive assimilation by magmatic–hydrothermal fluids [35]. Sulfur isotopic analyses reveal that $\delta^{34}S$ values of pyrite in magnetite ores (18.3%) are closely comparable to those of stratigraphic pyrite (18.9%), indicating a dominant evaporite-derived sulfur source for the ore body, with 45%–79% of the stratigraphic sulfur (mainly from gypsum–salt layers) participating in mineralization [35,186,187]. Meanwhile, substantial amounts of SO_4^{2-}, Cl^-, CO_3^{2-}, and other saline components were released through the assimilation of these layers [35]. Specifically, SO_4^{2-} oxidized Co^{2+} to Co^{3+}, facilitating Co incorporation through isomorphic substitution for Fe^{3+} and leading to significant Co enrichment [35]. Co mobility in hydrothermal fluids was substantially enhanced by chlorine complexation (e.g., $[CoCl_4]^{2-}$), a process driven by Cl^- [21,188,189]. Additionally, these saline components facilitated fluid-mediated Co extraction from wall rocks, providing an essential material source for subsequent enrichment [21,175,190]. In the Zhongguan deposit, we performed chemical analyses of major and trace elements in amphibole and apatite in diorite using EPMA and LA-ICP-MS. A distinct core–rim structure was observed in apatite, with rims showing enrichment in S, Na, and Cl, while cores were enriched in SiO_2, MnO, and Ce. Simultaneously, amphibole matrices were found enriched in Cl and Ca relative to phenocrysts. These results collectively demonstrate a similar extensive assimilation process involving evaporite sequences within the deposit. This process significantly altered hydrothermal fluid composition and magmatic–hydrothermal physicochemical conditions, creating favorable conditions for Co enrichment (unpublished data).

In contrast to the Baijian deposit, the Zhuchong deposit exhibits relatively limited Co enrichment despite extensive evaporite development. Sulfur isotopic analyses of pyrite reveal $\delta^{34}S$ values ranging from 5% to 12% [54]. These values are intermediate between magmatic sulfur (−3%–+3%) and stratigraphic sulfur (+25.4%–+34.4%), indicating a dominantly magmatic sulfur source with minor stratigraphic contributions [54,191,192]. Whole-rock Co analyses reveal a relatively elevated Co content in hydrothermally altered rocks: diopsidized diorite (26.34 ppm), diopside skarn (41.43 ppm), and skarn-proximal siltstone (17.21 ppm) [54]. Notably, high-Co pyrite (2088 ppm) in altered siltstone correlates with lower $\delta^{34}S$ values (6.1%–7.8%), whereas low-Co pyrite (94.5 ppm) in gypsum-bearing siltstone correlates with higher $\delta^{34}S$ values (12.0%–12.7%) [54]. Furthermore, early high-temperature pyrite spatially associated with magnetite and diopside in magnetite ores is enriched in Co relative to late low-temperature pyrite associated with calcite and anhydrite [54]. Collectively, these results indicate that Co was primarily derived from deep magmatic-hydrothermal fluids, with limited evaporite-derived sulfur involvement and insufficient assimilation, which consequently did not significantly promote cobalt mineralization [54].

In conclusion, the influence of evaporite sequences on Co enrichment in skarn-type deposits varies significantly. It is proposed that sufficient assimilation of evaporite sequences by magmatic–hydrothermal fluids, which effectively modifies fluid composition and physicochemical conditions of the ore-forming system, significantly enhances Co grades. In contrast, insufficient or localized assimilation exerts a negligible influence on Co enrichment.

4.4. Dissolution–Reprecipitation Mechanism of Hydrothermal Fluids

Based on the preceding analysis, it is proposed that sulfide minerals in skarn-type deposits exhibit significant enrichment of Co (Table 2), which is closely associated with

a dissolution–reprecipitation mechanism. This mechanism, essentially a dynamic equilibrium process, typically occurs during middle–late mineralization stages, where sulfide minerals thoroughly react with hydrothermal fluids, leading to the activation, mobilization, and reprecipitation of cobalt [193]. Specifically, under high-temperature hydrothermal conditions, increased Co solubility releases ionic Co^{2+} and Co^{3+} [139,194]. These ions subsequently complex with ligands such as Cl^- and HS^- to form stable migratory complexes [131]. Evolving physicochemical conditions trigger complex decomposition, causing Co to reprecipitate at favorable sites [195]. Throughout this process, porous textures that commonly develop in sulfide minerals such as pyrite enhance fluid–mineral interaction, thereby accelerating re-equilibration kinetics and promoting effective Co enrichment [196–198]. This mechanism is exemplified in the Henghui, Zhongguan, and Baijian deposits in the Handan–Xingtai Mining Area [35,55].

The sulfide stage of the Heng Hui Fe deposit was characterized by pervasive hydrothermal fluid infiltration along fracture margins, which induced hydrothermal alteration [55]. Concurrently, porous textures that developed along the margins of Py_{2b} further enhanced fluid–mineral interaction through increased reactive surface area [55]. This alteration process elevated fluid temperatures and pressures, increasing the solubility of Co [139,194]. Consequently, Co was activated and mobilized from pyrite lattices into the hydrothermal fluids, which decreased the Co content in Py_{2b} (average: 848 ppm) [55]. During the subsequent carbonate stage, H-O isotope compositions of fluid inclusions from the Fushan deposit ($\delta^{18}O$: 5.7% to 7.8%, δD_{H2O}: −78% to −83%) indicate the injection of meteoric water, which caused a further decrease in fluid temperature and salinity [138,139]. This physicochemical shift triggered the reprecipitation and enrichment of Co in Py_3, resulting in a significantly higher Co content (average: 6870 ppm) [55].

Two distinct stages of pyrite formation are recognized in the Baijian deposit. Early-stage pyrite exhibits a relatively low Co content (average: 2000–10,000 ppm), whereas late-stage pyrite exhibits a significantly elevated Co content (average: 10,000–47,340 ppm) [35]. Furthermore, the distribution of Co within individual late-stage pyrite grains is highly heterogeneous, with concentration variations approaching three orders of magnitude in single crystals [35]. Similarly, in the Zhongguan deposit, early-stage pyrite exhibits a relatively lower and uniform average Co content, ranging from 195 ppm to 331 ppm. In contrast, late-stage pyrite exhibits a higher Co content and substantial variability, ranging from 0.35 ppm to 10,000 ppm (unpublished data). Further analysis of Zhongguan late-stage pyrite reveals a distinct rim-enriched and core-depleted zoning pattern for Co, with rim concentrations exceeding core concentrations by approximately four orders of magnitude (Figure 4) (unpublished data). Based on these observations, it is proposed that these differential enrichment patterns are closely related to a dissolution–reprecipitation mechanism. Specifically, enhanced fluid activity during late hydrothermal stages promotes Co remobilization and re-enrichment through leaching of pre-existing cobalt-bearing minerals and intensified fluid–rock interaction.

In conclusion, the differential enrichment of Co in multistage pyrite from skarn-type deposits of the Handan–Xingtai Mining Area is primarily controlled by dissolution–reprecipitation mechanisms. Under this mechanism, enhanced late-stage hydrothermal fluid activity drives Co mobilization and reprecipitation through changes in temperature, pressure, salinity, and other physicochemical conditions [131,139,193–195].

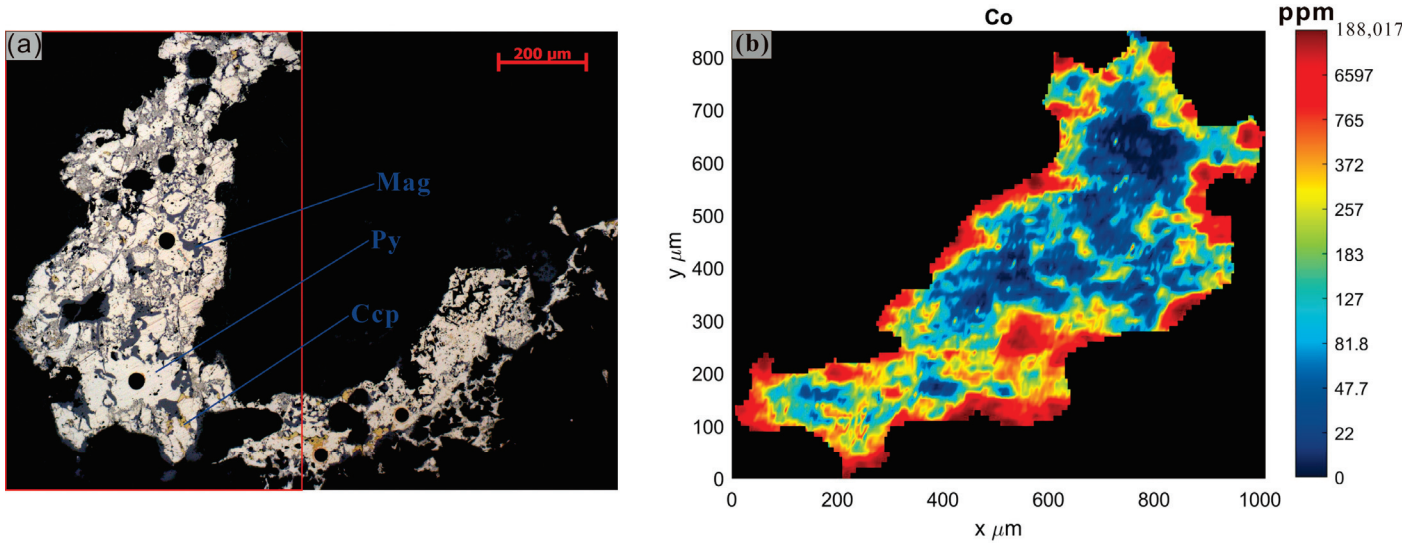


Figure 4. Reflected light photomicrographs (**a**) of pyrite and corresponding LA-ICP-MS mapping (**b**) from the Zhongguan deposit, Handan–Xingtai Mining Area, China. (Py—pyrite, Mag—magnetite, Ccp—chalcopyrite) (the red line indicates the area corresponding to the LA-ICP-MS mapping in (**b**).

5. Exploration Strategy of Associated Cobalt Recourses in Skarn-Type Deposits

Based on a comprehensive analysis of the distribution patterns and enrichment mechanisms of associated cobalt resources in global skarn-type deposits (Figure 1, Table 3), it is recommended that future cobalt exploration focus on the following aspects: (1) deposits with mantle-derived magmatic sources should be prioritized (Table 3); (2) regarding geotectonic settings, attention should be concentrated on subduction or collision zones at convergent plate margins (e.g., the Middle-Lower Yangtze River metallogenic belt in China and the Cornwall mining district in the USA); (3) the mineralization ages of these deposits vary widely, specifically exhibiting older ages in the United States and Australia and relatively young ages in China (mainly Mesozoic to Cenozoic); (4) the associated rock types exhibit a wide range, covering mafic to intermediate-felsic intrusive rocks (e.g., gabbro, diorite, monzonite, and granite), particularly gabbro and diorite.

Based on the above synthesis (Tables 3 and 5), the metallogenic model for associated cobalt resources in skarn-type deposits can be summarized as follows: (1) The higher Co abundance in the mantle provides the material basis for Co enrichment, making mantle-derived magmas a primary condition for mineralization. For instance, the skarn-type Fe deposits in the Han–Xing Mining Area of China and the Magnitogorsk zone in Russia are dominated by mantle-derived magmas, exhibiting significantly higher Co grades (Table 3). (2) The injection of mafic magmas serves as an additional source of Co and represents one of the important conditions contributing to enrichment. For instance, late-stage mafic magma injection in the Baijian and Henghui Fe deposits in China has resulted in significant Co enrichment (average Co content in pyrite reaching about 10,000 ppm) [21,55]. (3) The contribution of assimilation of evaporite sequences to Co enrichment remains unclear and requires further investigation. (4) The dissolution–reprecipitation mechanism of hydrothermal fluids facilitates Co enrichment and represents another important condition for mineralization. In the Zhongguan deposits in China, this mechanism enhanced Co concentrations in pyrite by approximately three to four orders of magnitude (Figure 4). In addition, deep major fault systems provide favorable pathways for Co migration. The coupling of these factors collectively promotes the enrichment of associated cobalt in skarn-type deposits. Based on this metallogenic model, utilizing artificial intelligence technology

to integrate multi-source geological data and exploring the cobalt mineralization patterns can optimize future exploration strategies for cobalt deposits.

6. Conclusions

1. Fe-dominated skarn-type cobalt deposits are characterized by a widespread distribution, high Co grades, and abundant reserves, exhibiting significantly superior cobalt resource potential compared to Cu-dominated or Pb-Zn polymetallic-dominated skarn-type deposits.
2. In skarn-type cobalt deposits, cobalt mainly occurs in sulfide minerals, particularly pyrite, while independent cobalt minerals occur only in specific deposits.
3. Associated cobalt resources in skarn-type deposits are observed to exhibit regionally zonal distribution features.
4. Associated cobalt resources in skarn-type deposits are characterized by stage-specific differential enrichment, with effective enrichment particularly exhibited during the sulfide stage.
5. Mantle-derived magmas provide additional cobalt sources for enrichment in associated skarn-type cobalt deposits.
6. The injection of mafic magmas creates favorable conditions for cobalt enrichment in skarn-type cobalt deposits.
7. The assimilation of evaporite sequences alters hydrothermal fluid composition, thereby affecting cobalt enrichment in skarn-type cobalt deposits.
8. The dissolution–reprecipitation mechanism of hydrothermal fluids drives the secondary enrichment of cobalt in skarn-type cobalt deposits, significantly contributing to cobalt enrichment.
9. The formation of skarn-type cobalt deposits is a complex process. Mantle-derived magmatic sources represent the primary condition for mineralization, while the injection of mafic magmas and the dissolution–reprecipitation mechanism of hydrothermal fluids play crucial roles in promoting cobalt enrichment.
10. Cobalt exploration should emphasize mantle-derived magmatic rocks (primarily mafic-intermediate lithologies) in convergent plate tectonic settings such as subduction or collision zones.
11. Given the multiple factors influencing cobalt enrichment, multidimensional data analysis under AI-aided frameworks will significantly enhance cobalt exploration efficiency.

Author Contributions: Conceptualization, C.C.; methodology, C.C.; software, R.Z.; validation, Z.Y., B.D. and Q.C.; formal analysis, C.C.; investigation, C.C. and R.Z.; resources, Y.Z. (Yang Zhang); data curation, R.Z.; writing—original draft preparation, R.Z.; writing—review and editing, C.C. and R.Z.; visualization, R.Z.; supervision, C.C., S.W., W.Z. and Z.G.; project administration, C.C.; funding acquisition, Y.Z. (Yanbo Zhang). All authors have read and agreed to the published version of the manuscript.

Funding: This research was funded by Natural Science Foundation of Hebei Province: D2023209016; The Innovation Capacity Enhancement Program Project of Hebei Province: 23564201D.

Data Availability Statement: Data are available on request from the authors.

Conflicts of Interest: Yang Zhang is an employee of Hebei Iron and Steel Group Shahe Zhongguan Iron Mine Co., Ltd. The paper reflects the views of the scientists and not the company. The remaining authors declare that the research was conducted in the absence of any commercial or financial relationships that could be construed as a potential conflict of interest.

References

1. Hitzman, M.W.; Bookstrom, A.A.; Slack, J.F.; Zientek, M.L. *Cobalt-Styles of Deposits and the Search for Primary Deposits*; Open-File Report 2017-1155; U.S. Geological Survey: Reston, VA, USA, 2017; p. 47.
2. Zhang, H.R.; Hou, Z.Q.; Yang, Z.M.; Song, Y.C.; Liu, Y.C.; Chai, P. A new division of genetic types of cobalt deposits: Implications for Tethyan cobalt-rich belt. *Miner. Depos.* **2020**, *39*, 501–510.
3. Duan, J.; Xu, G.; Tang, Z.L.; Yan, H.Q.; Liu, J.Q.; Chen, Y.Y.; Liu, Q. Analysis of development of China's cobalt industry: Current status, problems and countermeasures. *Eng. Sci.* **2024**, *26*, 98–107.
4. European Commission. *Report on Critical Raw Materials for the EU*; Report of the Ad Hoc Working Group on Defining Critical Raw Materials; European Commission: Brussels, Belgium, 2014; p. 41.
5. European Commission. *Study on the Review of the List of Critical Raw Materials*; Report of the Ad Hoc Working Group on Defining Critical Raw Materials; European Commission: Brussels, Belgium, 2017; p. 93.
6. Schulz, K.J.; DeYoung, J.H.; Seal, R.R.; Bradley, D.C. (Eds.) *Critical Mineral Resources of the United States—Economic and Environmental Geology and Prospects for Future Supply*; U.S. Geological Survey: Reston, VA, USA, 2017.
7. Li, P.; He, L.; Liang, T. Geochemical behavior, genetic type, resource distribution, and research prospects of the cobalt deposits. *Xinjiang Geol.* **2023**, *41*, 210–217.
8. Wang, H.; Feng, C.Y.; Zhang, M.Y. Characteristics of global cobalt resources and research progress in exploration. *Miner. Depos.* **2019**, *38*, 739–750.
9. Zhang, W.B.; Ye, J.H.; Chen, X.F.; Li, N.; He, X.Y.; Chen, X.F.; Liu, Y.F. Global cobalt resource distribution and exploration potential. *Resour. Ind.* **2018**, *20*, 56–61.
10. Roberts, S.; Gunn, G. Cobalt. In *Critical Metals Handbook*; Gunn, G., Ed.; John Wiley & Sons, Ltd.: Oxford, UK, 2014; pp. 122–149.
11. Smith, C.G. Always the bridesmaid, never the bride: Cobalt geology and resources. *Appl. Earth Sci.* **2001**, *110*, 75–80. [CrossRef]
12. Wen, G. Formation mechanism and key controlling factors of skarn-type rich iron deposits in Han-Xing area. *China Univ. Geosci.* **2017**, 1–227.
13. Shi, J. Geological characteristics and prospecting indicators of Zhuchong skarn iron-copper deposit in Anqing-Guichi ore concentration area, Anhui. *Anhui Geol.* **2023**, *33*, 113–115, 185.
14. Zhao, J.X.; Li, G.M.; Qin, K.Z.; Tang, D.M. A review of the types and ore mechanism of the cobalt deposits. *Chin. Sci. Bull.* **2019**, *64*, 2484–2500. [CrossRef]
15. Slack, J.F.; Kimball, B.E.; Sheed, K.B. *Cobalt. No. 1802-F*; US Geological Survey: Reston, VA, USA, 2017.
16. Wang, F.; Guo, Y.; Yan, H.; Gu, H.; Sun, H.; Ge, C. Geochronology and geochemistry of the W-Mo-ore-related granitic rocks from eastern Ningzhen, lower Yangtze river belt, eastern China. *Acta Geochim.* **2022**, *41*, 288–306. [CrossRef]
17. Wang, S.; Cao, M.; Li, G.; Evans, N.J.; Silang, W.; Qin, K. Tracing the genesis of the Zhibula skarn deposit, Tibet, using Co, Te, Au and Ag occurrence. *Ore Geol. Rev.* **2023**, *160*, 105601. [CrossRef]
18. Chen, J.; Wu, H.; Niu, X.; Niu, S.; Wang, Y.; Wang, J.; Wang, Z. Geology and geochronology of the Lalingzaohuo cobalt-bearing copper polymetallic skarn deposit, East Kunlun. *Ore Geol. Rev.* **2023**, *154*, 105349. [CrossRef]
19. Yan, L.; Fan, Y.; Liu, Y. The occurrence and spatial distribution of cobalt in Longqiao iron deposit in Luzong Basin, Anhui Province. *Acta Petrol. Sin.* **2021**, *37*, 2778–2796.
20. Wang, S.; Cao, M.; Li, G.; Silang, W.; Shan, P.; Qin, K. The occurrence of cobalt and implications for genesis of the Pusangguo cobalt-rich skarn deposit in Gangdese, Tibet. *Ore Geol. Rev.* **2022**, *150*, 105193. [CrossRef]
21. Qin, C. Study on occurrence state and enrichment mechanism of associated cobalt in Han-xing type iron deposits. *Hebei GEO Univ.* **2022**, 1–101. [CrossRef]
22. Shi, L.; Zhou, T.F.; Fan, Y.; Zhang, Y.F.; Yan, L.; Liang, X. Resource status and comprehensive utilization potential evaluation of associated cobalt in the Middle-Lower Yangtze River Metallogenic Belt. *Acta Petrol. Sin.* **2023**, *39*, 1144–1156. [CrossRef]
23. Wang, S.; Cao, M.J.; Shan, P.F. Study on cobalt enrichment and genesis of the (porphyry-) skarn deposits in Gangdese metallogenic belt, Tibet. *Acta Petrol. Sin.* **2025**, *41*, 492–509.
24. Meinert, L.D.; Dipple, G.M.; Nicolescu, S. World skarn deposits. *Econ. Geol.* **2005**, *100*, 299–336.
25. Zhou, T.F.; Fan, Y. Enrichment mechanisms, mineral exploration, and comprehensive utilization of critical metals: Preface. *Acta Petrol. Sin.* **2021**, *37*, 2599–2603.
26. *GB/T 25283-2023*; Specification for Comprehensive Exploration and Evaluation of Mineral Resources. Ministry of Land and Resources: Beijing, China, 2023.
27. Tretiakova, I.G.; Borisenko, A.S.; Lebedev, V.I.; Pavlova, G.G.; Goverdovsky, V.A.; Travin, A.V. Cobalt mineralization in the Altai-Sayan orogen: Age and correlation with magmatism. *Russ. Geol. Geophys.* **2010**, *51*, 1078–1090. [CrossRef]
28. Lebedev, V.I.; Lebedeva, M.F. Cobalt mineralization of Tuva, South-East Altai and North-West Mongolia. *Int. Multidiscip. Sci. Geo. Conf. Surv. Geol. Min. Ecol. Manag.* **2013**, *2*, 567–571.
29. Nagashima, M.; Akasaka, M.; Morifuku, Y. Ore and skarn mineralogy of the Yamato mine, Yamaguchi prefecture, Japan, with emphasis on silver-, bismuth-, cobalt-, and tin-bearing sulfides. *Resour. Geol.* **2016**, *66*, 37–54. [CrossRef]

30. Nimis, P.; Dalla Costa, L.; Guastoni, A. Cobaltite-rich mineralization in the iron skarn deposit of Traversella (Western Alps, Italy). *Mineral. Mag.* **2014**, *78*, 11–27. [CrossRef]
31. Cook, N.J.; Ciobanu, C.L. Paragenesis of Cu-Fe ores from Ocna de Fier-Dognecea (Romania), typifying fluid plume mineralization in a proximal skarn setting. *Mineral. Mag.* **2001**, *65*, 351–372. [CrossRef]
32. Xie, A.M.; Wang, S.G. Experimental study on cobalt recovery from Zhongguan iron deposit. *China New Technol. Prod.* **2014**, *32*, 137.
33. Liu, D.S.; Wang, X.Q.; Chen, Y.Y.; Zhang, B.M.; Zhou, J.; Liu, H.L.; Wang, W.; Nie, L.S.; Chi, Q.H. Cobalt distribution and its relationship with bedrocks and cobalt mineralizations in China. *Ore Geol. Rev.* **2024**, *167*, 105992. [CrossRef]
34. Zhang, D.Y.; Cao, C.; Wang, S.Z.; Cao, Q.; Dong, B.X.; Li, Y.; Dong, G.Y.; Wang, L. Distribution patterns and precipitation mechanisms of cobalt in Zhongguan skarn iron deposit, Hebei: Implications for mineralization. *Geol. Explor.* **2024**, *60*, 244–264.
35. Liang, X.; Wang, F.Y.; Zhang, J.Q.; Zhang, L.; Zhou, T.F.; Fan, Y.; Qin, C.; Zhang, J.W. Enrichment of cobalt at Baijian skarn Fe–Co deposit in the Handan—Xingtai region, North China Craton: Insights from mineral trace elements and pyrite sulfur isotopes. *J. Asian Earth Sci.* **2024**, *273*, 106265. [CrossRef]
36. Zhang, Y.F.; Fan, Y.; Chen, J.; Liu, L.H.; Li, M.M. Establishment of a research workflow for occurrence state of critical metal in ore concentrate power: A case study of the cobalt-rich sulfide ore concentrate from the Middle-Lower Yangtze River Valley Metallogenic Belt, China. *Acta Petrol. Sin.* **2021**, *37*, 2791–2804.
37. Duan, Z. The Mineralization and Mechanism of the Iron Skarn Deposits in Laiwu District, Shandong Province. *China Univ. Geosci.* **2019**, 1–148.
38. Zong, X.D.; Li, W.; Wang, J.; Qiao, W.; Zhang, J.F.; Liu, J.T. Study on rich iron ore for martin steel and the by-products of Cu and Co in Zhangjiawa iron deposit of Shandong province. *Contrib. Geol. Miner. Resour. Res.* **2012**, *27*, 60–65.
39. Rollinson, G.; Le Boutillier, N.; Selley, R. Cobalt mineralisation in Cornwall—A new discovery at Porthtowan. *Proc. Ussher Soc.* **2018**, *14*, 176–187.
40. Meinert, L.D. Skarns and Skarn Deposits. *Geosci. Can.* **1992**, *19*, 145–162.
41. Robinson, G.P., Jr. Magnetite skarn deposits of the Cornwall (Pennsylvania)type—A potential cobalt, gold, and silver resource. In Proceedings of the Second U.S. Geological Survey Workshop on the Early Mesozoic Basins of the Eastern United States, Reston, VA, USA, 11–14 May 1985; Volume 946, pp. 126–128.
42. Herrington, R.J.; Zaykov, V.V.; Maslennikov, V.V.; Brown, D.; Puchkov, V.N. Mineral Deposits of the Urals and Links to Geodynamic Evolution. In *Economic Geology, One Hundredth Anniversary Volume*; Society of Economic Geologists: Littleton, CO, USA, 2005; pp. 1069–1095.
43. Zhong, Z.H.; Wang, S.W.; Zhou, T.F.; Wang, B.; Wu, S.; Shu, Y. Study on the occurrence, distribution and enrichment of cobalt in Anqing copper-iron deposit, Anhui Province. *Acta Petrol. Sin.* **2024**, *40*, 629–641. [CrossRef]
44. Chen, X.Q.; Zhou, T.F.; Wang, B.; Liu, X.; Peng, K. Distribution, occurrence and enrichment mechanism of key metals of selenium, tellurium and cobalt in Wushan copper deposit, Jiurui ore concentration area, Jiangxi Province. *Acta Petrol. Sin.* **2023**, *39*, 3121–3138. [CrossRef]
45. Guo, W.M.; Lu, J.J.; Zhang, R.Q.; Xu, Z.W. Textural characteristics of pyrrhotite ore and their genetic significance in the Dongguashan deposit, Tongling, Anhui. *Miner. Depos.* **2010**, *29*, 405–414.
46. Lu, J.W.; Peng, X.L. *Microscopic Identification Manual for Metallic Minerals*; Geological Publishing House: Beijing, China, 2010; pp. 1–320.
47. Luo, J.A.; Yang, G.C. Geological characteristics and genesis of the Chengmenshan copper deposit, Jiangxi Province. *Miner. Resour. Geol.* **2007**, *21*, 284–288.
48. Wang, S.Q.; Williams, P.J. Geochemistry and origin of Proterozoic skarns at the Mount Elliott Cu-Au(-Co-Ni) deposit, Cloncurry district, NW Queensland, Australia. *Mineral. Depos.* **2001**, *36*, 109–124. [CrossRef]
49. Fan, D.X. Study on Occurrence State and Enrichment Mechanism of Cobalt in the Galinge Iron Polymetallic Deposit, East Kunlun Mountains, Qinghai Province. Ph.D. Dissertation, Yunnan University, Kunming, China, 2023.
50. Li, X.L.; Li, Z.Q.; Zhang, C.J.; Hu, T.; Zhang, Z.Z. Discussion on the genesis of the Pusangguo lead-zinc deposit, Tibet. *Yunnan Geol.* **2011**, *30*, 122–126.
51. Li, Z.; Lang, X.H.; Zhang, Q.Z.; He, L. Petrogenesis and geodynamic setting of intermediate-acidic rocks in the Pusangguo copper polymetallic deposit, Tibet: Constraints from geochronology, geochemistry and Sr-Nd-Pb-Hf isotopes. *Acta Petrol. Sin.* **2019**, *35*, 737–759.
52. Jiang, S.G. Exploration on the metallogenic model of the Yaojialing deposit. *World Nonferrous Met.* **2020**, *2*, 81–82.
53. Xiong, Y.; Zhou, T.; Fan, Y.; Chen, J.; Wang, B.; Liu, J.; Wang, F. Enrichment mechanisms and occurrence regularity of critical minerals resources in the Yaojialing Zn skarn polymetallic deposit, Tongling district, eastern China. *Ore Geol. Rev.* **2022**, *144*, 104822. [CrossRef]

54. Liang, X.; Wang, F.Y.; Zhou, T.F.; Wei, C.; Zhang, L.; Guo, X.; Zhang, K. Metallogenic mechanism of cobalt in the Zhuchong cobalt-rich skarn iron deposit in the Middle-Lower Yangtze River Valley Metallogenic Belt: Constrained by in-situ sulfur isotopes and zircon U-Pb dating. *Acta Petrol. Sin.* **2023**, *39*, 3015–3030. [CrossRef]
55. Dong, R.; Hu, J.; Wang, S.G.; Yu, D.S.; Guo, R.T.; Yan, Q.H.; Gao, S.P.; Guo, W.M. Mineralogy and geochemistry of the pyrite from the Henghui skarn iron deposit in central North China craton: Insights into cobalt mineralization. *Ore Geol. Rev.* **2024**, *168*, 106053. [CrossRef]
56. Zhang, B.T.; Hu, Z.G.; Mei, Z.H.; Wang, X.W.; Wei, Z.Y.; Zheng, Y.Y.; Zhao, X.B.; Chen, L.; Hu, C.Y. Geological and geophysical characteristics and deep prospecting prediction of Xinzhuang iron deposit in Jinling area, Zibo, Shandong. *Geol. Rev* **2022**, *68*, 2259–2268.
57. Wei, K.T.; Xu, J.Y.; Wu, C.X.; Liu, D.Q.; Yan, F. Discussion on the current status and comprehensive utilization prospects of cobalt resources in ore-concentrated area of Southeast Hubei. *Resour. Environ. Eng.* **2021**, *35*, 777–781.
58. Xiong, Q. Geological and Geochemical Characteristics and Fluid Inclusion Study of the Jinshandian Iron Deposit in Southeast Hubei Province. Master's Thesis, Yangtze University, Jingzhou, China, 2016.
59. Li, W. Discussion on the Formation-Mechanism of Chengchao Iron Skarn Deposit, Southeast Hubei Province. Ph.D. Dissertation, China University of Geosciences, Beijing, China, 2015.
60. Mao, J.R.; Chen, S.Y.; Zhao, S.L.; Cheng, Q.F. Geochemical characteristics and magmatic evolution processes of intrusive rock bodies in the Fengcheng-Ruichang-Jiujiang area. *Bull. Nanjing Inst. Geol. Miner. Res* **1985**, *6*, 1–15.
61. Liang, X.; Wang, F.Y.; Zhang, L.; Zhang, J.W.; Wei, C.S.; Fan, Y.; Guo, X.Z.; Zhou, T.F.; Zhang, J.Q.; Lü, Q.T. Cobalt distribution and enrichment in skarn iron deposits: A case study of the Zhuchong skarn iron deposit, Eastern China. *Ore Geol. Rev.* **2023**, *163*, 105778. [CrossRef]
62. Di, S.W. Geological and Geochemical Characteristics and Genesis of the Baixiangshan Iron Deposit in the Ningwu Basin. Master's Thesis, Hefei University of Technology, Hefei, China, 2010.
63. Luo, S. Metallogenic Geological Characteristics and Mineralization Regularity of the Dongguashan Copper Deposit in Tongling, Anhui Province. Master's Thesis, Central South University, Changsha, China, 2014.
64. Fang, K.D. Discussion on diagenetic and metallogenic evolution mechanism of the Tongshankou copper deposit. *Geol. Explor.* **1994**, *5*, 7–13.
65. Hubei Geological Survey. Resource reserve verification report for the Tongshankou copper mine verification area, Daye City, Hubei Province. *Geol. Surv. Rep.* **2010**.
66. Ma, H. Geological Characteristics and Genesis of the Xinqiao Copper-Iron-Sulfur Deposit in Tongling, Anhui Province. Master's Thesis, China University of Geosciences, Beijing, China, 2016.
67. Hua Dong Bureau of Metallurgical Geology and Exploration. Resource reserve utilization status verification report for the Xinqiao copper-iron-sulfur deposit verification area, Tongling County, Anhui Province. *Geol. Surv. Rep.* **2009**.
68. Wang, S.; Xu, Y.; Shan, P.F.; Silang, W.D.; Li, G.M.; Cao, M.J. Occurrence state and enrichment characteristics of cobalt in skarn deposits of the Gangdese Metallogenic Belt, Tibet. *Acta Geol. Sin.* **2024**, *98*, 163–180.
69. Ren, J.X.; Zeng, X.G.; Fang, G.; Luo, M.; Fan, L.K. Geological characteristics of cobalt deposits in east part of East Kunlun and its potential. *Miner. Resour. Geol.* **2006**, *20*, 4.
70. Che, Y.Y.; Su, H.M.; Liu, T.; Li, H.; He, S.Y. The occurrence and enrichment of cobalt in skarn Pb-Zn deposits: A case study of the Niukutou Co-rich deposit, East Kunlun metallogenic belt, western China. *Ore Geol. Rev.* **2024**, *172*, 106210. [CrossRef]
71. Liang, H.C.; Liu, H.C. Geological characteristics and preliminary discussion on genesis of the Zhanbuzhale iron deposit, Qinghai. *Min. Technol.* **2005**, *5*, 2.
72. Nadoll, P.; Angerer, T.; Mauk, J.L.; French, D.; Walshe, J. The chemistry of hydrothermal magnetite: A review. *Ore Geol. Rev.* **2014**, *61*, 1–32. [CrossRef]
73. Liu, T.; Jiang, S.Y.; Cao, S.; Wang, W.; Su, H.M.; Yang, D.; Li, H.; He, S. Cobalt enrichment and metallogenic mechanism of the Galinge skarn iron deposit in the Eastern Kunlun metallogenic belt, western China. *Ore Geol. Rev.* **2024**, *170*, 106147. [CrossRef]
74. Wen, G.; Deng, X.D.; Zhou, R.J.; Duan, Z.; Cui, B.Z.; Li, J.W. Geology, geochronology and stable isotope studies at the Baijian Fe-(Co) skarn deposit, eastern China, with implications for ore genesis and regional Fe skarn metallogeny. *Ore Geol. Rev.* **2024**, *166*, 105935. [CrossRef]
75. Xu, W.Y. Geochemical characteristics of co-occurring cobalt in skarn iron (copper) deposits in China. *Geol. Explor.* **1979**, *23*, 24–29.
76. Zhang, Y.F.; Fan, Y.; Liu, Y.; Zhou, T.F.; Ou, B.G. Distribution and enrichment processes of cobalt in the Longqiao iron skarn deposit in Eastern China. *Ore Geol. Rev.* **2024**, *174*, 106277. [CrossRef]
77. Xiang, W.S. Characteristics and Genesis of the Anqing Copper-Iron Deposit, Anhui Province. Master's Thesis, China University of Geosciences, Beijing, China, 2010.
78. Li, C.Q. Genesis and Metallogenic Regularity of the Anqing Copper-Iron Deposit, Anhui Province. Master's Thesis, Central South University, Changsha, China, 2000.

79. Rezazadeh, S.; Hosseinzadeh, M.R.; Raith, J.G.; Moayyed, M. Mineral Chemistry and Phase Relations of Co-Ni Arsenides and Sulfarsenides from the Baycheh-Bagh Deposit, Zanjan Province, Iran. *Ore Geol. Rev.* **2020**, *127*, 103836. [CrossRef]
80. Chen, B.; Qi, C.M. The Occurrence State of Cobalt and Its Significance in Prospecting and Resource Assessment. *J. Chang. Univ. Sci. Technol.* **2001**, *31*, 217–218.
81. Dai, P.G.; Long, Y.Z.; Li, P.Z. Occurrence state and comprehensive utilization of associated cobalt in Yushiwai iron deposit. *Hunan Geol.* **2000**, *19*, 54–57.
82. Duan, C. Geological and Geochemical Characteristics and Genesis of Longqiao Iron Deposit in Luzong Basin, Anhui Province. *Hefei Technol. Univ.* **2009**, 1–120.
83. Zuicher, L.; Ruiz, J.; Barton, M.D. Paragenesis, elemental distribution, and stable isotopes at the Peña Colorada iron skarn, Colima, Mexico. *Econ. Geol.* **2001**, *96*, 535–557. [CrossRef]
84. Wang, Y.B. Geochemical Characteristics and Genesis of Tonglushan Cu-Fe Deposit in Hubei Province. *China Univ. Geosci.* **2012**, 1–110.
85. Li, Z.; Tan, H.; Zhao, F.; Xiang, Z.; Wu, H.; Zhang, P. Sphalerite and Pyrite Geochemistry from the Pusangguo Co-Rich Cu–Zn–Pb Skarn Deposit, Tibet: Implications for Element Occurrence and Mineralization. *Minerals* **2023**, *13*, 1165. [CrossRef]
86. Zheng, J.M.; Mao, J.W.; Chen, M.H.; Li, G.D.; Ban, C.Y. Geological characteristics and metallogenic model of skarn iron deposits in *the* Handan-Xingtai area, southern Hebei, China. *Geol. Bull. China* **2007**, *26*, 150–154.
87. Li, L.M. Ore-controlling structural factors of Handan-Xingtai type iron deposits. *Geol. Explor.* **1986**, *22*, 1–11.
88. Fan, L.L.; Lu, J.; Zhang, J.Q.; Jin, Y.N.; Bai, F.S.; Tang, Y.Y.; Qin, C. The zoning and its geological significance of texture of amphibole from the Qicun porphyritic quartz monzonite in the southern Hebei. *Bull. Mineral. Petrol. Geochem.* **2021**, *40*, 903–913.
89. Qin, K.Z.; Xia, D.X.; Li, G.M.; Duo, J.; Jiang, G.W.; Zhao, J.X. Qulong Porphyry-Skarn Cu-Mo Deposit. *Sci. Press.* **2014**, 1–316.
90. Hou, Z.Q.; Cook, N.J.; Zaw, K. Metallogenesis of the Tibetan Collisional Orogen: A Review and Introduction to the Special Issue. *Ore Geol. Rev.* **2009**, *36*, 1. [CrossRef]
91. Zhu, D.-C.; Zhao, Z.-D.; Niu, Y.; Mo, X.-X.; Chung, S.-L.; Hou, Z.-Q.; Wang, L.-Q.; Wu, F.-Y. The Lhasa Terrane: Record of a Microcontinent and Its Histories of Drift and Growth. *Earth Planet. Sci. Lett.* **2011**, *301*, 241–255. [CrossRef]
92. Wang, R.; Zhu, D.-C.; Wang, Q.; Hou, Z.-Q.; Yang, Z.-M.; Zhao, Z.-D.; Mo, X.-X. Porphyry Mineralization in the Tethyan Orogen. *Sci. China Earth Sci.* **2020**, *63*, 2042–2067. [CrossRef]
93. Yin, A.; Harrison, T.M. Geologic evolution of the Himalayan-Tibetan orogen. *Annu. Rev. Earth Planet. Sci.* **2000**, *28*, 211–280. [CrossRef]
94. Zheng, W.B.; Chen, Y.C.; Tang, J.X.; Chang, Z.S.; Wang, X.W.; Ying, L.J.; Li, F.J.; Wang, H.; Tang, X.Q. Discovery of tubular ore body in Jiama ore district, Tibet and its geological significance. *Miner. Depos.* **2011**, *30*, 12.
95. Ji, W.Q.; Wu, F.Y.; Chung, S.L.; Li, J.X.; Liu, C.Z. Zircon U-Pb geochronology and Hf isotopic constraints on petrogenesis of the Gangdese batholith, southern Tibet. *Chem. Geol.* **2009**, *262*, 229–245. [CrossRef]
96. Ji, W.Q.; Wu, F.Y.; Liu, C.Z.; Chung, S.L. Geochronology and petrogenesis of granitic rocks in Gangdese batholith, southern Tibet. *Sci. China Earth Sci.* **2009**, *52*, 1240–1261. [CrossRef]
97. Lee, C.T.A.; Luffi, P.; Chin, E.J.; Bouchet, R.; Dasgupta, R.; Morton, D.M.; Le Roux, V.; Yin, Q.Z.; Jin, D. Copper systematics in arc magmas and implications for crust-mantle differentiation. *Science* **2012**, *336*, 64–68. [CrossRef] [PubMed]
98. Zhu, D.C.; Zhao, Z.D.; Pan, G.T.; Lee, H.Y.; Kang, Z.Q.; Liao, Z.L.; Wang, L.Q.; Li, G.M.; Dong, G.C.; Liu, B. Early Cretaceous subduction-related adakite-like rocks of the Gangdese belt, southern Tibet: Products of slab melting and subsequent melt-peridotite interaction? *J. Asian Earth Sci.* **2009**, *34*, 298–309. [CrossRef]
99. Kang, Z.Q.; Xu, J.F.; Wilde, S.A.; Feng, Z.H.; Chen, J.L.; Wang, B.D.; Fu, W.C.; Pan, H.B. Geochronology and geochemistry of the Sangri Group volcanic rocks, southern Lhasa Terrane: Implications for the early subduction history of the Neo-Tethys and Gangdese magmatic arc. *Lithos* **2014**, *200–201*, 157–168. [CrossRef]
100. Ma, X.X.; Xu, Z.Q.; Meert, J.G. Eocene slab breakoff of Neotethys as suggested by dioritic dykes in the Gangdese magmatic belt, southern Tibet. *Lithos* **2016**, *248–251*, 55–65. [CrossRef]
101. Tian, K. Study on Geological and Geochemical Characeristics and Genesis of Bangbule Pb-Zn-Cu-Fe Deposit, Western Gangdese, Tibet. Ph.D. Thesis, China University of Geosciences, Wuhan, China, 2019.
102. Gao, S.B.; Zheng, Y.Y.; Tian, L.M.; Zhang, Z.; Qu, W.J.; Liu, M.Y.; Zheng, H.T.; Zheng, L.; Zhu, J.H. Geochronology of magmatic intrusions and mineralization of Chagele Copper-Lead-Zinc Deposit in Tibet and its implications. *Earth Sci. China Univ. Geosci.* **2012**, *37*, 507–514.
103. Xie, F.W.; Lang, X.H.; Tang, J.X.; He, Q.; Deng, Y.L.; Wang, X.H.; Wang, Y. Metallogenic Regularity of Gangdese Metallogenic Belt, Tibet. *Miner. Depos.* **2022**, *41*, 952–974.
104. Li, G.M.; Liu, B.; Qu, W.J.; Lin, F.C.; She, H.Q.; Feng, C.Y. The Porphyry-Skarn Metallogenic System in the Gangdese Metallogenic Belt, Tibet: Re-Os Isotopic Age Evidence from Porphyry and Skarn-Type Cu Polymetallic Deposits. *Geotecton. Met.* **2005**, *29*, 60–68.

105. Qu, T.; He, R.Z.; Yu, P.L.; Wang, S.F.; Chen, X.L.; Liu, J.L. Statistics and Application of Rock Physical Properties in Jiama Mining Area, Tibet. *Geophys. Geochem. Explor.* **2021**, *45*, 661–668.
106. Shu, Q.H.; Deng, J.; Chang, Z.S.; Wang, Q.F.; Niu, X.D.; Xing, K.; Sun, X.; Zhang, Z.K.; Zeng, Q.W.; Zhao, H.S.; et al. Skarn Zonation of the Giant Jiama Cu-Mo-Au Deposit in Southern Tibet, SW China. *Econ. Geol.* **2024**, *119*, 1–22. [CrossRef]
107. Chen, L.; Qin, K.Z.; Li, G.M.; Li, J.X.; Xiao, B.; Jiang, H.Z.; Zhao, J.X.; Fan, X.; Jiang, S.Y. Geological Characteristics and Skarn Mineralogy of the Nuri Cu-W-Mo Deposit in the Southern Margin of Gangdese, Tibet. *Mineral. Depos.* **2012**, *31*, 417–437.
108. Zhang, K.J.; Zhang, Y.X.; Tang, X.C.; Xia, B. Late Mesozoic Tectonic Evolution and Growth of the Tibetan Plateau Prior to the Indo-Asian Collision. *Earth-Sci. Rev.* **2012**, *114*, 236–249. [CrossRef]
109. Ying, L.J.; Wang, D.H.; Tang, J.X.; Chang, Z.S.; Qu, W.J.; Zheng, W.B.; Wang, H. Re-Os dating of molybdenite from the Jiama Cu-polymetallic deposit in Tibet and its metallogenic significance. *Acta Geol. Sin.* **2010**, *84*, 1165–1174.
110. Cao, M.J.; Qin, K.Z.; Evans, N.J.; Li, G.M.; Ling, X.X.; McInnes, B.I.A.; Zhao, J.X. Titanite in situ SIMS U-Pb geochronology, elemental and Nd isotopic signatures record mineralization and fluid characteristics at the Pusangguo skarn deposit, Tibet. *Min. Depos.* **2021**, *56*, 907–916. [CrossRef]
111. Jiang, C.F.; Wang, Z.Q.; Li, J.Y. *Opening-Closing Tectonics of Central Orogenic Belt*; Geological Publishing Housing: Beijing, China, 2000.
112. Dong, Y.P.; He, D.F.; Sun, S.S.; Liu, X.M.; Zhou, X.H.; Zhang, F.F.; Yang, Z.; Cheng, B.; Zhao, G.C.; Li, J.H. Subduction and accretionary tectonics of the East Kunlun orogen, western segment of the Central China Orogenic System. *Earth-Sci. Rev.* **2018**, *186*, 231–261. [CrossRef]
113. Deng, J.; Zhai, Y.S.; Mo, X.X.; Wang, Q.F. Temporal-spatial distribution of metallic ore deposits in China and their geodynamic settings. *Econ. Geol. Spec. Publ.* **2019**, *22*, 103–132.
114. Wang, P.; Zhao, G.C.; Liu, Q.; Yao, J.L.; Han, Y.G. Evolution of the Paleo-Tethys Ocean in Eastern Kunlun, North Tibetan Plateau: From continental rift-drift to final closure. *Lithos* **2022**, *422–423*, 106717. [CrossRef]
115. Yu, M.; Dick, J.M.; Feng, C.Y.; Li, B.; Wang, H. The tectonic evolution of the East Kunlun Orogen, northern Tibetan Plateau: A critical review with an integrated geodynamic model. *J. Asian Earth Sci.* **2020**, *191*, 104168. [CrossRef]
116. Dong, Y.P.; Sun, S.S.; Santosh, M.; Zhao, J.; Sun, J.P.; He, D.F.; Shi, X.H.; Hui, B.; Cheng, C.; Zhang, G.W. Central China Orogenic Belt and Amalgamation of East Asian Continents. *Gondwana Res.* **2021**, *100*, 131–194. [CrossRef]
117. Chen, L.M.; Song, X.Y.; Hu, R.Z.; Yu, S.Y.; Yi, J.N.; Kang, J.; Huang, K.J. Mg-Sr-Nd isotopic insights into petrogenesis of the Xiarihamu mafic-ultramafic intrusion, northern Tibetan Plateau. *J. Petrol.* **2021**, *62*, 113. [CrossRef]
118. Wang, S.; Li, G.M.; Li, Z.S.; Su, H.M.; Shan, P.F.; Huang, X.S.; Cao, M.J. Occurrence and enrichment characteristics of cobalt in typical skarn deposits of the Qimantagh ore-concentrated area, East Kunlun, Qinghai. *Acta Petrol. Sin.* **2025**, *41*, 2648–2665.
119. Wang, Y.D.; Ma, Y.W.; Cao, C.G. Geological Characteristics of the East Kunlun Metallogenic Belt in Qinghai Province. *West. Resour.* **2022**, *5*, 166–168.
120. Faure, M.; Lin, W.; Le Breton, N. Where is the North China-South China Block Boundary in Eastern China? *Geology* **2001**, *29*, 119–122. [CrossRef]
121. Zhang, J.J. Early Cretaceous Magmatism and Porphyrite Iron Mineralization in the Middle-Lower Yangtze River Region Under Ridge Subduction. Ph.D. Dissertation, Institute of Oceanology, Chinese Academy of Sciences, Qingdao, China, 2024.
122. Shi, L.; Zhou, T.F.; Xiao, X. Distribution patterns, occurrence states and enrichment mechanisms of critical metals (Co-Se-Te) in the Xinqiao deposit, Tongling ore district, Anhui Province. *Acta Petrol. Sin.* **2023**, *39*, 3031–3047. [CrossRef]
123. Zhang, K.; Lü, Q.T.; Man, Z.H.; Lan, X.Y.; Guo, D.; Tao, L.; Zhao, J.H. Electrical constraints on the deep setting and process of magma-mineral system in the Middle-Lower Reaches of Yangtze River Metallogenic Belt. *Acta Petrol. Sin.* **2022**, *38*, 573–583.
124. Wang, Y.F. Genetic Study of Stratiform Sulfide Deposits in the Northern Ore Belt of Wushan Copper Deposit, Jiurui Area, Jiangxi Province. Ph.D. Dissertation, Chang'an University, Xi'an, China, 2019.
125. Ehser, A.; Borg, G.; Pernicka, E. Provenance of the Gold of the Early Bronze Age Nebra Sky Disk, Central Germany: Geochemical Characterization of Natural Gold from Cornwall. *Eur. J. Mineral.* **2011**, *23*, 895–910. [CrossRef]
126. Seravkin, I.B.; Kosarev, A.M.; Puchkov, V.N. Geodynamic Conditions of Formation of Massive Sulfide Deposits in the Magnitogorsk Megazone, Southern Urals, and Prospection Criteria. *Geol. Ore Depos.* **2017**, *59*, 227–243. [CrossRef]
127. Plotinskaya, O.Y.; Grabezhev, A.I.; Tessalina, S.; Seltmann, R.; Groznova, E.O.; Abramov, S.S. Porphyry Deposits of the Urals: Geological Framework and Metallogeny. *Ore Geol. Rev.* **2017**, *85*, 153–173. [CrossRef]
128. Grabezhev, A.I.; Kuznetsov, N.S.; Puzhakov, B.A. *Ore and Alteration Zoning of Sodium Type Copper-Porphyry Column (Paragonite-Bearing Aureoles, the Urals)*; IGG Publisher: Yekaterinburg, Russia, 1998.
129. Zhai, Y.S.; Yao, S.Z.; Cai, K.Q. *Ore Deposit Geology*, 3rd ed.; Geological Publishing House: Beijing, China, 2011; pp. 1–440.
130. Liu, Y.J.; Cao, L.M.; Li, Z.L. *Element Geochemistry*; Science Press: Beijing, China, 1984; pp. 113–137.
131. Williams-Jones, A.E.; Vasyukova, O.V. Constraints on the Genesis of Cobalt Deposits: Part I. Theoretical Considerations. *Econ. Geol.* **2022**, *117*, 513–528. [CrossRef]

132. Zhang, J.Q.; Li, S.R.; Santosh, M.; Wang, J.Z.; Li, Q. Mineral chemistry of high-Mg diorites and skarn in the Han-Xing Iron deposits of South Taihang Mountains, China: Constraints on mineralization process. *Ore Geol. Rev.* **2015**, *64*, 200–214. [CrossRef]
133. Zhang, J.Q.; Yan, L.N.; Santosh, M.; Li, S.R.; Lu, J.; Wang, D.X.; Liang, X.; Wang, L.X.; Li, Y.Q. Tracing the genesis of skarn-type iron deposit in central North China Craton: Insights from mineral zoning textures in ore-forming intrusion. *Geol. J.* **2020**, *55*, 6280–6295. [CrossRef]
134. Liu, L.L.; Su, S.G.; Wang, N.; Wang, W.B. Deep magmatic processes and shallow responses during the lithospheric thinning of North China Craton: Taking Tanling intrusive complex as an example. *Acta Petrol. Sin.* **2019**, *35*, 2873–2892.
135. Wen, G.; Li, J.; Hofstra, A.H.; Harlov, D.E.; Zhao, X.; Lowers, H.A.; Koenig, A.E. Trace element fractionation in magnetite as a function of Fe depletion from ore fluids at the Baijian Fe-(Co) skarn deposit, eastern China: Implications for Co mineralization in Fe skarns. *Am. Miner.* **2024**, *in press*. [CrossRef]
136. Zheng, J.M. The Ore-Forming Fluid and Mineralization of Skarn Fe Deposits in Handan-Xingtai, South Hebei. *China Univ. Geosci.* **2007**, 1–150.
137. Ma, Y.; Jiang, S.Y.; Frimmel, H.E.; Zhu, L.Y. In situ chemical and isotopic analyses and element mapping of multiple-generation pyrite: Evidence of episodic gold mobilization and deposition for the Qiucun epithermal gold deposit in Southeast China. *Am. Miner.* **2022**, *107*, 1133–1148. [CrossRef]
138. Liu, W.H.; Borg, S.J.; Testemale, D.; Etschmann, B.; Hazemann, J.L.; Brugger, J. Speciation and thermodynamic properties for cobalt chloride complexes in hydrothermal fluids at 35–440 °C and 600 bar: An in-situ XAS study. *Geochim. Cosmochim. Acta* **2011**, *75*, 1227–1248. [CrossRef]
139. Cao, M.J.; Shan, P.F.; Qin, K.Z. Cobalt-rich characteristics and existing problems of porphyry gold-copper deposit: A case study of Jinchang deposit in Heilongjiang Province. *Chin. Sci. Bull.* **2022**, *67*, 3708–3723. [CrossRef]
140. Kretschmar, U.; Scott, S.D. Phase relations involving arsenopyrite in the system Fe-As-S and their application. *Can. Miner.* **1976**, *14*, 364–386.
141. Sharp, Z.D.; Essene, E.J.; Kelly, W.C. A re-examination of the arsenopyrite geothermometer: Pressure considerations and applications to natural assemblages. *Can. Miner.* **1985**, *23*, 517–534.
142. Vasyukova, O.V.; Williams-Jones, A.E. Constraints on the genesis of Cobalt deposits: Part II. Applications to Natural Systems. *Econ. Geol.* **2022**, *117*, 529–544. [CrossRef]
143. Yu, M.; Feng, C.Y.; Bao, G.Y.; Liu, H.C.; Zhao, Y.M.; Li, D.X.; Xiao, Y.; Liu, J.N. Mineralogy and alteration zoning of skarn in the Galinge iron deposit, Qinghai Province. *Miner. Depos.* **2013**, *32*, 55–76.
144. Rudnick, R.L.; Gao, S.; Holland, H.D.; Turekian, K.K. Composition of the continental crust. *Treat. Crust* **2003**, *4*, 1–51.
145. Zheng, D.Z.; Zheng, R.F. Preliminary Study on Migration Forms and Metallogenic Mechanism of Cobalt. *Acta Geol. Sichuan* **2010**, *30*, 364–368.
146. Richards, J.P. Tectono-magmatic precursors for porphyry Cu-(Mo-Au) deposit formation. *Econ. Geol.* **2003**, *98*, 1515–1533. [CrossRef]
147. Sillitoe, R.H. Porphyry copper systems. *Econ. Geol.* **2010**, *105*, 3–41. [CrossRef]
148. Li, T. Chemical Element Abundances in the Earth and Its Major Shells. *Geochimica* **1976**, *3*, 167–174.
149. Wang, Y.; Zhong, H.; Cao, Y.H.; Wei, B.; Chen, C. Genetic classification, distribution and ore genesis of major PGE, Co and Cr deposits in China: A critical review. *Chin. Sci. Bull.* **2020**, *65*, 3825–3838. [CrossRef]
150. Wang, F.; Bai, M.; Zhu, D.; Dong, L.; Liu, S.; Li, X.; Lu, L. Study of Ore Features and Occurrence Status of Cobalt in the Hanxing Type Iron Deposit, Hebei Province. *Nonferrous Met. Miner. Process. Sect.* **2024**, *1*, 1–8.
151. Cui, X.L. Mineralogical characteristics and genesis of amphibole in intermediate-mafic intrusive complex from Wu'an, Hebei Province. *China Univ. Geosci.* **2017**. [CrossRef]
152. Bai, F.S.; Jin, Y.N.; Fan, L.L.; Tang, Y.Y.; Qin, C.; Zhang, J.Q. Genetic mineralogy of Ziquan diorite in eastern Han-Xing area. *J. Hebei GEO Univ.* **2021**, *44*, 1–7.
153. Fan, L.L. Genetic Mineralogy of Amphiboles in Mesozoic Intrusive Rocks from Handan-Xingtai Area, Southern Hebei Province, China. *Hebei GEO Univ.* **2022**. [CrossRef]
154. Gao, X.Y.; Zhang, J.Q.; Wang, Y.Q.; Sun, T.Q.; Zhao, K.C.; Wang, L.X.; Li, Y.Q.; Xu, C. Formation and Mineralogy of Porphyritic Biotite Hornblende Diorite in Qicun Pluton, Southern Hebei. *Geoscience* **2019**, *33*, 738–750.
155. Li, Z.; Wang, L.Q.; Li, H.F.; DanZhen, W.X.; Shi, S. Sulfur and Lead Isotopic Compositions *of* the Pusangguo Cu-Pb-Zn Polymetallic Deposit in Tibet: Implications for the Source of Ore-forming Material. *Geoscience* **2018**, *32*, 56–65.
156. Zhou, Y. Characteristics and Evolution of Ore-Forming Fluids in the Jiama Cu Polymetallic Deposit, Mozhugongka County, Tibet. Ph.D. Dissertation, Chengdu University of Technology, Chengdu, China, 2010.
157. Li, Y.S. Geological Characteristics and Genesis of the Jiama Cu Polymetallic Deposit in Tibet. Ph.D. Dissertation, China University of Geosciences, Wuhan, China, 2009.
158. Qu, X.M.; Hou, Z.Q.; Li, Y.G. S and Pb Isotopes as Indicators of Ore-Forming Material Sources and Orogenic Belt Material Cycling in the Gangdese Porphyry Copper Belt. *Geol. Bull. Chin.* **2002**, *21*, 768–775.

159. Yao, P.; Zheng, M.H.; Peng, Y.M.; Li, J.G.; Li, D.K.; Fan, W.Y. Study on the Sources of Ore-Forming Material and Genesis of the Jiama Copper and Polymetallic Deposit in Gangdese Island-arc Belt, Xizang. *J. Geol. Rev.* **2002**, *48*, 468–478.
160. She, H.Q.; Feng, C.Y.; Zhang, D.Q.; Pan, G.T.; Li, G.M. Characteristics and Metallogenic Prospective Analysis of Skarn Cu-Pb-Zn Polymetallic Deposits in the Middle-Eastern Gangdese Belt, Tibet. *Miner. Depos.* **2005**, *24*, 508–520.
161. Yao, X.F.; Tang, J.X.; Ding, S.; Zheng, W.B.; Yang, H.H.; Zhang, W.Y.; Feng, Y.F. Petrography, Geochronology and Hf Isotope Constraints on Origin of the of Ore-bearing Granodiorite in Zhibula copper Deposit, Tibet. *Geotecton. Met.* **2015**, *39*, 315–324.
162. Wang, Q.; Huang, Y.; Dong, S.L.; Yan, G.Q.; You, Q.; Jiang, H.Z.; Zhang, K. Zicron LA-ICP-MS U-Pb Geochronology, Geochemistry and implications of Ore-Forming Porphyry in Nuri skarn Cu-Mo-W Deposit, Eastern Gangdise. *Miner. Depos.* **2018**, *37*, 571–586.
163. Sun, F. Magmatic Evolution and Genesis of the Jiama Superlarge Porphyry-Skarn Deposit, Southern Tibet. Ph.D. Dissertation, China University of Geosciences, Wuhan, China, 2022.
164. Esser, B.K.; Turekian, K.K. The osmium isotopic composition of the continental crust. *Geochim. Cosmochim. Acta* **1993**, *57*, 3093–3104. [CrossRef]
165. Zhang, A.P.; Zheng, Y.C.; Xu, B.; Fu, Q.; Ma, W.; Wu, C.D.; Zhang, C.; Shen, Y.; Fei, F. Metallogeny of the Lietinggang-Leqingla Fe-Cu-(Mo)-Pb-Zn polymetallic deposit, evidence from geochronology, petrogenesis, and magmatic oxidation state, Lhasa terrane. *Ore Geol. Rev.* **2019**, *106*, 318–339. [CrossRef]
166. Sun, X.; Zheng, Y.Y.; Wu, S.; You, Z.M.; Wu, X.; Li, M.; Zhou, T.C.; Dong, J. Metallogenic epoch and genesis of ore-bearing rocks in the Mingze-Chengba porphyry-skarn Mo-Cu deposit, Gangdese. *Acta Petrol. Sin.* **2013**, *29*, 1392–1406.
167. Marsh, E.; Anderson, E.; Gray, F. *Nickel-Cobalt Laterites: A Deposit Model: Chapter H in Mineral Deposit Models for Resource Assessment*; U.S. Geological Survey: Reston, VA, USA, 2013.
168. Shu, L.S. *General Geology*; Geological Publishing House: Beijing, China, 2010.
169. Fan, L.L.; Jin, Y.N.; Bai, F.S.; Liang, X.; Wu, W.Z.; Li, Q.; Zhang, J.Q. Genetic mineralogical study of dioritic complex in Wu'an pluton, southern Hebei province. *J. Hebei GEO Univ.* **2020**, *43*, 16–21.
170. Shan, P.F.; Cao, M.J.; Tang, D.M.; Qiu, Z.J.; Evans, N.J.; Lazarov, M.; Wang, D.C.; Hu, W.; Qin, K.Z.; Horn, I.; et al. Cobalt-rich porphyry deposits derived from multiple mafic magma injections. *Geochim. Cosmochim. Acta* **2025**, *399*, 125–143. [CrossRef]
171. Barton, M.D.; Johnson, D.A. An evaporitic source model for igneous-related Fe oxide-(REE-Cu-Au-U) mineralization. *Geology* **1996**, *24*, 259–262. [CrossRef]
172. Sillitoe, R.H.; Burrows, D.R. New field evidence bearing on the origin of the El Laco magnetite deposit, Northern Chile. *Econ. Geol.* **2002**, *75*, 1101–1109.
173. Sillitoe, R.H. Iron oxide copper gold deposits: An Andean view. *Miner. Depos.* **2003**, *38*, 787–812. [CrossRef]
174. Jami, M.; Dunlop, A.C.; Cohen, D.R. Fluid inclusion and stable isotope study of the Esfordi apatite-magnetite deposit, Central Iran. *Econ. Geol.* **2007**, *102*, 1111–1128. [CrossRef]
175. Li, Y.; Xie, G.; Duan, C.; Han, D.; Wang, C. Effect of sulfate evaporate salt layer over the formation of skarn-type iron ores. *Acta Geol. Sin.* **2013**, *87*, 1324–1334.
176. Li, Y.H.; Duan, C.; Han, D.; Chen, X.W.; Wang, C.L.; Yang, B.Y.; Zhang, C.; Liu, F. Role of evaporite layers as oxidation barriers in the mineralization of porphyrite iron deposits in the Middle-Lower Yangtze River Belt. *Acta Petrol. Sin.* **2014**, *30*, 1355–1368.
177. Li, Y.H.; Duan, C.; Wang, C.L.; Yang, B.Y.; Hou, K.J.; Zhang, C.; Liu, J.L. *Mineralization of Porphyrite Iron Deposits in the Ningwu District: Case Study of the Washan Deposit, Anhui*; Geological Publishing House: Beijing, China, 2021; pp. 1–124.
178. Duan, C.; Li, Y.H.; Mao, J.W.; Zhu, Q.Q.; Xie, G.Q.; Wan, Q.; Jian, W.; Hou, K.J. The role of evaporite layers in the ore-forming processes of iron oxide-apatite and skarn Fe deposits: Examples from the Middle-Lower Yangtze River Metallogenic Belt, East China. *Ore Geol. Rev.* **2021**, *138*, 104352. [CrossRef]
179. Duan, C.; Li, Y.H.; Mao, J.W.; Wan, Q.; He, S.; Wang, C.L.; Yang, B.Y.; Hou, K.J. Zircon U-Pb ages, Hf-O isotopes and trace elements of the multi-volcanism in the Ningwu ore district, Eastern China: Implications for the magma evolution and fertility of iron oxide-apatite (IOA) deposits. *Gondwana Res.* **2023**, *116*, 149–167. [CrossRef]
180. Wang, Q.; Li, Y.H.; Li, H.M.; Hou, K.J.; Zhang, Z.J. Paleoproterozoic hydrothermal overprinting over Neoarchean banded iron formation produced high-grade iron ores in the giant Gongchangling deposit of North China: Evidence from O-S-B isotopes. *Ore Geol. Rev.* **2024**, *165*, 105911. [CrossRef]
181. Li, Y.H.; Duan, C.; Fan, C.F.; Hu, B.; Hou, K.J.; Zhu, Q.Q.; Wang, Q.; Guo, D.W. Study on the Role of Gypsum-Salt Layers in the Mineralization of Endogenic Metal Deposits. *Miner. Explor.* **2024**, *15*, 1391–1408.
182. Zhou, T.F.; Fan, Y.; Yuan, F.; Wu, M.A.; Zhao, W.G.; Qian, B.; Ma, L.; Wang, W.C.; Liu, Y.N.; Noel, W. The metallogenic model of Nihe iron deposit in Luzong basin and genetic relationship between Gypsum-Salt layer and deposit. *Acta Geol. Sin.* **2014**, *88*, 562–573.
183. Li, L.; Qin, Y.J.; Zhang, K. Metallogenic Geological Characteristics and Genesis of Skarn-Type Iron Deposits: A Review. *China Met. Bull.* **2018**, *11*, 252–253.
184. Ma, J.F.; Hu, Y.L.; Li, R.J. Skarn type iron ore ore-forming geological characteristics and genesis of review. *West. Resour.* **2016**, *4*, 21–23.

185. Zhu, Q.Q.; Xie, G.Q.; Wang, J.; Li, W.; Yu, B.F. The Relationship between the Evaporate and Skarn-Type Iron Deposits: A Case Study of the Jinshandian Iron Deposit in Hubei. *Acta Geol. Sin.* **2013**, *87*, 1419–1429.
186. Zhang, B.M.; Zhao, G.L.; Ma, G.X. *The Metallogenetic System and Ore-Forming Models of the Main Metallogenic Belts in Hebei Province*; Petroleum Industrial Publishing House: Beijing, China, 1996.
187. Cai, B.; Li, X.; Wei, S.; Cui, Y.; He, J. The Control of the Evaporite Beds in the Middle Ordovician Series over the Endogenic Iron (Sulfur) Ores of Han-Xing Type. *Mineral. Petrol.* **1983**, *4*, 31–44.
188. Zhai, Y.S.; Shi, Z.L.; Lin, X.D.; Xiong, P.F.; Wang, D.Y.; Yao, S.Z.; Jin, Z.M. Genesis of "Daye-Type" iron ore deposits in eastern Hubei, China. *Earth Sci.* **1982**, *3*, 239–251.
189. Zhao, Y.M.; Wu, J.S.; Han, F.; Luo, Z.K.; Feng, Y.M. Mineralization and Alteration Characteristics of Magnesian Skarn-Type Iron Deposits in Luonan Area, Shaanxi Province: Prospecting Indicators. *Bull. Inst. Miner. Resour. Chin. Acad. Geol. Sci.* **1982**, *1*, 29–50.
190. Li, Y.H.; Duan, C.; Han, D.; Liu, F.; Wan, D.F.; Wang, C.Y. Oxygen Isotope Discrimination Marker of Magmatic Iron Deposits: Ningwu Porphyry Iron ore as an Example. *Acta Petrol. Sin.* **2017**, *33*, 3411–3421.
191. Zhou, T.F.; Yuan, F.; Yue, S.C.; Liu, X.D.; Zhang, X.; Fan, Y. Geochemistry and Evolution of Ore-Forming Fluids of the Yueshan Cu-Au Skarn- and Vein-Type Deposits, Anhui Province, South China. *Ore Geol. Rev.* **2007**, *31*, 279–303. [CrossRef]
192. Zhou, T.F.; Yue, S.C.; Yuan, F. *Petrogenesis and Metallogenesis of the Yueshan Ore District, Anhui Province*; Geological Publishing House: Beijing, China, 2005; pp. 1–146.
193. Li, F.J.; Qi, Y.Q.; Gong, H.T. A Review of Researches on Mineral Dissolution and Reprecipitation Processes. *Bull. Mineral. Petrol. Geochem.* **2024**, *43*, 240–258.
194. Davey, J.; Roberts, S.; Wilkinson, J.J. Copper- and Cobalt-Rich, Ultrapotassic Bittern Brines Responsible for the Formation of the Nkana-Mindola Deposits, Zambian Copperbelt. *Geology* **2021**, *49*, 341–345. [CrossRef]
195. Ulrich, T.; Gunther, D.; Heinrich, C.A. The Evolution of a Porphyry Cu-Au Deposit Based on LA-ICP-MS Analysis of Fluid Inclusions: Bajo de la Alumbrera, Argentina. *Econ. Geol.* **2001**, *96*, 1743–1774. [CrossRef]
196. Putnis, A. Mineral Replacement Reactions. *Rev. Mineral. Geochem.* **2009**, *70*, 87–124. [CrossRef]
197. Ruiz-Agudo, E.; Putnis, C.V.; Putnis, A. Coupled Dissolution and Precipitation at Mineral-Fluid Interfaces. *Chem. Geol.* **2014**, *383*, 132–146. [CrossRef]
198. Putnis, A. Mineral Replacement Reactions: From Macroscopic Observations to Microscopic Mechanisms. *Mineral. Mag.* **2002**, *66*, 689–708. [CrossRef]

Disclaimer/Publisher's Note: The statements, opinions and data contained in all publications are solely those of the individual author(s) and contributor(s) and not of MDPI and/or the editor(s). MDPI and/or the editor(s) disclaim responsibility for any injury to people or property resulting from any ideas, methods, instructions or products referred to in the content.

MDPI AG
Grosspeteranlage 5
4052 Basel
Switzerland
Tel.: +41 61 683 77 34

Minerals Editorial Office
E-mail: minerals@mdpi.com
www.mdpi.com/journal/minerals



Disclaimer/Publisher's Note: The title and front matter of this reprint are at the discretion of the Guest Editors. The publisher is not responsible for their content or any associated concerns. The statements, opinions and data contained in all individual articles are solely those of the individual Editors and contributors and not of MDPI. MDPI disclaims responsibility for any injury to people or property resulting from any ideas, methods, instructions or products referred to in the content.





Academic Open
Access Publishing

mdpi.com

ISBN 978-3-7258-8922-8